

Fluorescent Nucleic Acid Probes for DNA Sensing and Imaging

Georgina Helen Leck



UNIVERSITY OF
BIRMINGHAM

A thesis submitted to the
University of Birmingham
for the degree of
Doctor of Philosophy

School of Chemistry
College of Engineering and Physical Sciences
University of Birmingham
May 2021

UNIVERSITY OF
BIRMINGHAM

University of Birmingham Research Archive

e-theses repository

This unpublished thesis/dissertation is copyright of the author and/or third parties. The intellectual property rights of the author or third parties in respect of this work are as defined by The Copyright Designs and Patents Act 1988 or as modified by any successor legislation.

Any use made of information contained in this thesis/dissertation must be in accordance with that legislation and must be properly acknowledged. Further distribution or reproduction in any format is prohibited without the permission of the copyright holder.

Abstract

Fluorescent probes are widely used to study biological samples. In recent years, fluorescently modified nucleic acid probes have been investigated for the detection of DNA single point variations. Single point variations have been linked to certain diseases with a genetic component and are viewed as biomarkers. Despite recent advances in the detection of such biomarkers, commercially available detection assays of this type are often time-consuming, complex in experimental design and tend to produce only qualitative data (i.e. simply denoting whether a mutation is present or not). As complex diseases such as cancer are becoming better understood, and in particular the way in which these diseases develop and mutate, there is a drive for the development of versatile probes that can detect several mutations at once, while also providing quantitative data (e.g. the proportion of a cancerous mutation present within a given sample). The work herein describes the development of such probes which aim to overcome the challenges that are currently faced.

The fluorescent probes developed in this thesis are simple in design, comprising a short nucleic acid sequence, which is complementary to the region of interest, and a fluorescent molecule incorporated directly into the sugar-phosphate backbone as a reporter group.

1,8-Naphthalimides were the choice of fluorophore for the majority of this work, owing to their longer wavelength absorption and emission profiles in comparison to many nucleic acid probes in the literature, their tuneable photophysical properties, large Stokes shift and photostability. They are also solvatochromic, giving emission profiles that are highly sensitive to their local environment. This effect has been explored as a method for discriminating between single nucleobases within a target sequence of DNA. In addition, their synthetic versatility has allowed the development of four different classes of fluorescent tag for probe incorporation, each with varying photophysical properties and DNA sensing capabilities.

Owing to their longer wavelength absorption and emission profiles, the naphthalimide probes are also suitable for use in imaging techniques; this aspect has been explored using fluorescence in-situ hybridisation (FISH) and DNA-PAINT.

Finally, building on work previously studied in the group, anthracene-based nucleic acid probes have also been developed. These probes were effective at sensing and quantifying the BRAF V600E mutation, a single point variation in genomic DNA associated with many types of cancer such as melanoma and colorectal cancer. Work in this thesis builds on the development of these probes into assays for use on patient samples.

Acknowledgements

Firstly, I would like to thank my supervisors Prof. James Tucker and Dr Robert Neely. I am truly grateful for the support and guidance you have given me throughout my PhD. Thank you for giving me the opportunity to take on this project, but also for providing me with the many other opportunities I have been lucky to be a part of throughout my PhD. Jim, thank you for your enormous support and positivity throughout the ICURE programme, I would not have ended up where I am without this experience and I will be forever grateful.

I would also like to thank the members of the Tucker group, who are the reason I can say that I truly enjoyed my PhD; Francia Allabush, Media Ismail, Aysha Ali, Klaudia Englert, Ed Wilkinson, Charlotte Farrow, Jake Carter, Marium Rana. Thank you for being such a friendly, supportive, and collaborative group to work in. A special thank you to Klaudia who supported me through my master's project and encouraged me to take on this PhD. Thank you also to Francia, who was always there from day one to give advice. Another special thank you to the Awesome Four girls for your friendship, and the countless coffee breaks, dinners, and days out. Thank you to members of the Neely group, who were always there for help with aspects of my research – another great group to be a part of. Not to forget, thank you to the other members of Office 408, the Cox and Grainger groups, who have also made this journey an enjoyable one!

Thank you to members of the Beggs Lab for your guidance with aspects of my research, and to the Birmingham Women's NHS Foundation Trust for providing me with samples that allowed me to conduct my research.

Thank you to all members of the analytical facility in the School of Chemistry; in particular, Dr Cecile Le Duff, Dr Chi Tsang, Peter Ashton and Allen Bowden. Thank you for being there to help with all of my NMR, mass spectrometry and HPLC problems over the years.

To my family, who without, I would not be where I am today. Thank you to the best parents, for your unconditional support and encouragement throughout the years. And to my Grandad, a fellow chemist, whom I would like to dedicate this thesis to. Thank you for inspiring me to achieve and for teaching me that “if it’s easy, then it ain’t worth having” – a saying that definitely holds for this PhD! Finally, Ed, I started this journey with you, and we have made so many happy memories since. Thank you for always being there for me, for your support and always answering my questions (I know there have been a lot!); you are the best.

Table of Contents

1. Introduction.....	1
1.1. Deoxyribonucleic Acid (DNA)	1
1.1.1. DNA Duplex Structure	2
1.2. Single Point Variations	3
1.2.1. Single Nucleotide Polymorphisms.....	4
1.2.2. Epigenetic Changes	6
1.3. Fluorescent Nucleic Acid Probes	8
1.3.1. Modified Nucleobase Sensors.....	10
1.3.2. Non-Nucleosidic Sensors.....	13
1.4. Detection of Single Point Variations Using Fluorescence	15
1.4.1. Commercially Available Base Discriminating Probes	16
1.4.2. Base Discriminating Probes Reported in the Literature.....	22
1.5. Solvatochromic Reporter Groups.....	29
1.5.1. Naphthalimide Reporter Groups.....	34
1.6. Future Directions of Fluorescent Nucleic Acid Probes for the Detection of Single Point Variations	38
1.7. References.....	39
2. Techniques	44
2.1. Automated Solid-Phase DNA Synthesis	44
2.1.1. Preparation of Phosphoramidite Monomers.....	44
2.1.2. Ultramild Conditions	48
2.2. High Performance Liquid Chromatography	49
2.2.1. Reversed-Phase High Performance Liquid Chromatography.....	50
2.3. Mass Spectrometry	50
2.3.1. Matrix Assisted Laser Desorption Ionisation.....	51
2.3.2. Electrospray Ionisation.....	51
2.3.3. Data Analysis	51
2.4. DNA Thermal Melting.....	52
2.5. Ultraviolet Visible Spectroscopy	53
2.5.1. Molar Extinction Coefficient.....	55
2.5.2. Determining Oligonucleotide Concentrations	55
2.6. Fluorescence Spectroscopy	56
2.6.1. Fluorescence Quantum Yields.....	58

2.7. Polymerase Chain Reaction.....	59
2.8. Gel Electrophoresis	61
2.8.1. Polyacrylamide Gel Electrophoresis (PAGE).....	62
2.8.2. Agarose Gel Electrophoresis	62
2.9. Fluorescence Microscopy.....	63
2.9.1. Epifluorescence Microscopy	63
2.10. References.....	65
3. Synthesis and Characterisation – Fluorescent Tags and DNA.....	67
3.1. 1,8-Naphthalimide Tag Synthesis.....	67
3.1.1. Design Considerations.....	67
3.1.2. Synthesis of Naph ^A _{Short} and Naph ^A _{Long}	70
3.1.3. Synthesis of Naph ^I _{Dimethyl} and Naph ^I _{Amine}	76
3.2. Oligo Probe Synthesis.....	82
3.2.1. Design Considerations.....	82
3.2.2. Oligonucleotide Synthesis	86
3.2.3. Oligonucleotide Purification.....	87
3.2.4. Oligonucleotide Characterisation and Quantification	90
3.3. References.....	93
4. Exploring the Photophysical Properties of 1,8-Naphthalimide Reporter Groups and Their Ability as Base Discrimination Probes.....	95
4.1. Photophysical Properties of the 1,8-Naphthalimide Tags as Monomers and When Incorporated Into DNA Probes.....	95
4.1.1. UV-Vis Absorption Studies	95
4.1.2. Fluorescence Studies.....	104
4.1.3. Fluorescence Quantum Yields.....	110
4.2. Duplex Formation and Stability.....	112
4.2.1. Duplex Melting Temperatures	113
4.2.2. Explaining the Differences in Duplex Melting Temperatures Between the Various Naphthalimide Reporter Groups.....	115
4.2.3. Duplex Melting Temperatures for the BRAF V600E Duplexes	117
4.3. Fluorescence Sensing of 1,8-Naphthalimide Modified Duplexes and Their Ability to Base Discriminate	118
4.3.1. Sensing Conditions	119
4.3.2. Fluorescence Sensing of Probes in the Base-Opposite Sensing System	119
4.3.3. Fluorescence Sensing of Probes in the Base-Adjacent Sensing System.....	129

4.3.4. Fluorescence Sensing of Probes in the Epigenetic Sensing System	137
4.3.5. Fluorescence Sensing of Probes in the BRAF V600E System.....	143
4.4. Conclusions	146
4.5. Future Work	147
4.6. References.....	148
5. The Development of a Fluorescent Nucleic Acid Sensing Assay to Detect and Quantify the BRAF V600E Mutation	150
5.1. Overview	150
5.2. Previous Work: Anthracene-Modified Nucleic Acid Probes.....	152
5.3. Project Aims	155
5.4. Synthesis of Anthracene Probe and Target Oligonucleotides.....	156
5.5. BRAF V600E Sensing Studies Using Short (15-mer) Oligonucleotide Targets.....	157
5.5.1. Fluorescence Emission Profile of the Anthracene BRAF V600E Probe	157
5.5.2. Fluorescence Sensing With Equimolar Amounts of Probe and Target	159
5.5.3. Fluorescence Sensing With 1 Equivalent of Probe and 3 Equivalents of Target.....	161
5.6. BRAF V600E Sensing Using Long (173-mer) Oligonucleotide Targets.....	163
5.6.1. Fluorescence Sensing With 1 Equivalent of Probe and 1.2 Equivalents of Target.....	164
5.6.2. Fluorescence Sensing With 1 Equivalent of Probe and 3 Equivalents of Target.....	165
5.6.3. Investigating the Increase in Fluorescence Observed Upon Formation of Duplexes Containing Long Oligonucleotide Targets	171
5.7. BRAF V600E Sensing Using PCR-Amplified DNA From Genomic DNA.....	172
5.7.2. PCR Amplification of Genomic DNA	173
5.7.3. T7 Exonuclease Digestion of PCR Amplicon	175
5.7.4. Fluorescence Sensing of the Single-Stranded PCR Product	177
5.8. Conclusions	180
5.9. Future Work	181
5.10. References.....	182
6. The Development of Naphthalimide Nucleic Acid Probes for Use in Fluorescence In Situ Hybridisation (FISH) and Super-Resolution Imaging Experiments	184
6.1. Introduction	184
6.1.1. Fluorescence In Situ Hybridisation (FISH)	184
6.1.2. DNA PAINT.....	188
6.2. Project Aims	192
6.3. The Development of OligoFISH Centromeric Probes for the Detection and Discrimination of Known Polymorphisms at α -Satellite DNA Regions Within Centromeres of Chromosome 17	194

6.3.1. Probe Design	194
6.3.2. Naph 17CEN Probe Strand Synthesis	195
6.3.3. Preliminary Fluorescence Sensing Studies With Duplexes.....	196
6.3.4. FISH Sensing Using the Naph 17CEN Oligo Probe	199
6.4. The Development of Imaging Probes for DNA PAINT Super-Resolution Imaging Methods	204
6.4.1. Experimental Set-Up and Probe Design	204
6.4.2. Imager Probe Strand Synthesis	209
6.4.3. Preliminary Duplex Studies to Test the Suitability of the Naphthalimide Imager Strands for DNA PAINT Imaging.....	209
6.4.4. DNA PAINT Imaging Using Naphthalimide Imager Strands to Produce Super-Resolution Images of DNA Origami Triangles.....	213
6.5. Conclusions and Future Work	227
6.6. References.....	229
7. Experimental	231
7.1. Materials and Methods	231
7.2. Monomer Synthesis	232
7.2.1. Naph ^A _{Short} Synthesis	232
7.2.2. Naph ^A _{Long} Synthesis.....	240
7.2.3. Naph ^I _{Dimethyl} Synthesis	248
7.2.4. Naph ^I _{Amine} Synthesis	256
7.3. DNA Synthesis	266
7.3.1. Standard Synthesis – Unmodified DNA.....	266
7.3.2. Ultramild Synthesis - Modified Probe DNA.....	266
7.4. DNA Purification.....	267
7.5. DNA Characterisation	268
7.6. Naphthalimide Duplex Sensing	269
7.6.1. Duplex Annealing Conditions	269
7.6.2. Fluorescence Sensing Parameters.....	269
7.6.3. Duplex Melting Temperatures	269
7.7. Fluorescent Nucleic Acid Assay for the Detection and Quantification of the BRAF V600E Mutation.....	270
7.7.1. Duplex Annealing Conditions	270
7.7.2. Fluorescence Sensing Parameters.....	270
7.7.3. DNA Extraction	270
7.7.4. PCR Amplification	271

7.7.5. DNA Clean and Purification	272
7.7.6. T7 Exonuclease Digestion.....	272
7.7.7. TapeStation DNA Electrophoresis	273
7.7.8. QuBit DNA Quantification	273
7.7.9. Polyacrylamide Gel Electrophoresis (PAGE).....	273
7.8. Naphthalimide Modified Nucleic Acid Probes for Use in Imaging Techniques.....	274
7.8.1. Fluorescence In Situ Hybridisation.....	274
7.8.2. DNA PAINT.....	275
7.9. References.....	278
8. Appendix	279
8.1. DNA Synthesis, Purification, Characterisation and Quantification.....	279
8.1.1. Oligonucleotide Mass Spectrometry Results.....	279
8.1.2. Purified Oligonucleotide HPLC Traces	280
8.1.3. Determining Molar Extinction Coefficients	287
8.2. Exploring the Photophysical Properties of 1,8-Naphthalimide Reporter Groups and Their Ability as Base Discriminating Probes	291
8.2.1. Absorption Spectra of 1,8-Naphthalimide Tag Monomers	291
8.2.2. Effect of Solvent on the Absorption Profiles of the Naphthalimide Tag Monomers	293
8.2.3. Absorption Studies of 1,8-Naphthalimide Tag Monomers and the Affect Upon Incorporation Into DNA.....	297
8.2.4. Fluorescence Spectra of Naphthalimide Tag Monomers in Water	297
8.2.5. Solvatochromic Properties of Naphthalimide Tag Monomers.....	299
8.2.6. Sensing Results With 1:1 Probe: Target Equivalents.....	303
8.3. The Development of a Fluorescent Nucleic Acid Sensing Assay to Detect and Quantify the BRAF V600E Mutation	308
8.3.1. Previous Work	308
8.3.2. Probe Synthesis and Characterisation.....	309
8.3.3. Raman Scattering From Water	310
8.3.4. Fluorescence Sensing of PCR Product	310
8.4. The Development of Naphthalimide Nucleic Acid Probes for Use in Fluorescence In Situ Hybridisation (FISH) and Super-Resolution Imaging Experiments.....	311
8.4.1. Naph 17CEN Probe and Target Characterisation	311
8.4.2. TAMRA 17CEN1 Probe.....	316
8.4.3. FISH Sensing.....	317
8.4.4. DNA PAINT Imager Strand Characterisation.....	317

8.4.5.	DNA Origami Triangle Staple Strand Sequences	320
8.4.6.	DNA PAINT Background Intensity Plots	327
8.5.	Naphthalimide Oligo Probe Mass Spectra	328

List of Abbreviations

A	Adenine
AFM	Atomic force microscopy
ALL	Acute lymphocytic leukaemia
API	4-aminophthalimide
Ar	Aromatic
BAC	Bacterial artificial chromosomes
BDP	Base discriminating probe
Bp	Base pair
BSA	Bovine serum albumin
C	Cytosine
CCD	Charged-coupled device
cfDNA	Circulating free deoxyribonucleic acid
CPG	Controlled pore glass
CRC	Colorectal cancer
ctDNA	Circulating tumour deoxyribonucleic acid
DCM	Dichloromethane
(d)dPCR	(Droplet) Digital polymerase chain reaction
DIPEA	N,N-Diisopropylethylamine
DMAP	N,N-Dimethylpyridin-4-amine
DMSO	Dimethyl sulfoxide
DMT	4,4'-dimethoxytrityl
DNA	Deoxyribonucleic acid
dsDNA	Double-stranded DNA

E	Energy
λ_{em}	Emission wavelength
Eq	Equivalents
ESI	Electrospray ionisation
Et	Ethyl
$E_T(30)$	Dimroth-Reichardt parameter
E_T^N	Nomaised Dimroth-Reichardt parameter
λ_{ex}	Excitation wavelength
FISH	Fluorescence in situ hybridisation
(f)PALM	(Fluorescence) Photoactivation localisation microscopy
G	Guanine
GLRT	Generalised likelihood ratio
H	Hours
HBTU	N,N,N',N'-Tetramethyl-O-(1H-benzotriazol-1-yl)uronium hexafluorophosphate
hmC	Hydroxymethylcytosine
HMPA	Tris(dimethylamino)phosphine oxide
HOMO	Highest occupied molecular orbital
IC	Internal conversion
ICT	Intramolecular charge transfer
LNA	Locked nucleic acid
LUMO	Lowest unoccupied molecular orbital
m/z	Mass-to-charge ratio
MALDI	Matrix assisted laser desorption ionisation
λ_{max}	Maximum wavelength

mC	Methylcytosine
Me	Methyl
Mer	Oligomer
Min	Minutes
Mut	Mutant
Napth	Naphthalimide tags
NMR	Nuclear magnetic resonance
S_NAr	Nucleophilic aromatic substitution
OD	Optical density
Oligo	Oligonucleotide
PAGE	Polyacrylamide gel electrophoresis
PAINT	Points accumulation in nanoscale topography
PCR	Polymerase chain reaction
PET	Photoinduced electron transfer
RFLP	Restriction fragment length polymorphism
(RP-)HPLC	(Reverse phase-) High performance liquid chromatography
PSF	Point spread function
RT	Room temperature
S	Seconds
S/N	Signal-to-noise ratio
SNP	Single nucleotide polymorphism
ssDNA	Single-stranded DNA
STORM	Stochastic optical reconstruction microscopy
T	Thymine
TCA	Trichloroacetic acid

TEA	Triethylamine
TEAA	Triethylammonium acetate
THF	Tetrahydrofuran
TIRF	Total internal reflection fluorescence
T_m	Thermal melting temperature
TOF	Time of flight
U	Uracil
UV(-Vis)	Ultraviolet (-visible)
WT	Wild-type

1. Introduction

1.1. Deoxyribonucleic Acid (DNA)

Deoxyribonucleic acid (DNA) holds the genetic information essential for all living organisms to develop, function and reproduce. DNA is a biopolymer consisting of repeating nucleotide monomer units which are often described as the 'building blocks of life'. A nucleotide comprises a pentose sugar, a phosphate group and a nucleobase; of which there are four types in nature, Figure 1.1.

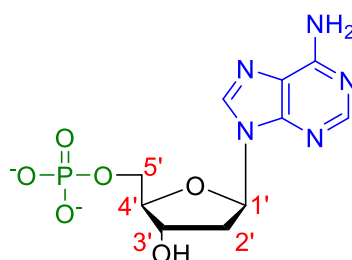


Figure 1.1: Structure of a DNA nucleotide, showing the phosphate group (green) attached to the ribose sugar at the 5'-hydroxyl and the nucleobase (blue) at position 1. The phosphate groups are deprotonated at biological pH.

The natural nucleobases (adenine, A; guanine, G; cytosine, C; and thymine, T) can be either monocyclic or bicyclic, and are classified as pyrimidines or purines, respectively. Their structures are shown in Figure 1.2.

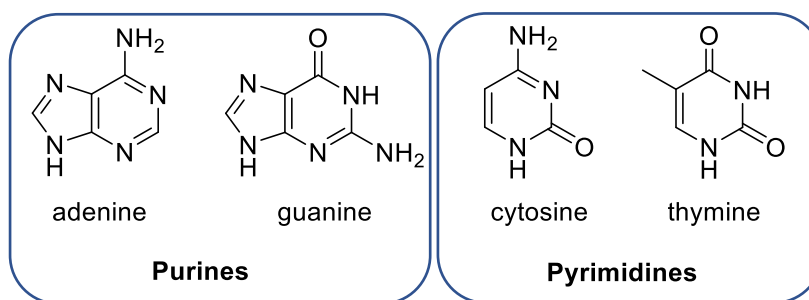


Figure 1.2: Structures of the four DNA nucleobases. The bicyclic purines; adenine (A) and guanine (G) and the monocyclic pyrimidines; cytosine (C) and thymine (T).

1.1.1. DNA Duplex Structure

Phosphodiester bonds are formed sequentially between the phosphate group of one nucleotide and the 3'-hydroxyl group of the ribose sugar of another, allowing the DNA strand to develop with what is known as 3' to 5' directionality. A single DNA strand comprises a negatively charged sugar-phosphate backbone owing to the phosphate groups, with protruding aromatic nucleobases. The secondary structure of DNA was first hypothesised as a double helix in 1953 by Watson and Crick.¹ In this helical structure, two antiparallel strands of DNA are held together *via* hydrogen bonding between complementary nucleobase pairs, with A and T forming two hydrogen bonds and C and G forming three, as shown in Figure 1.3. In the duplex, the aromatic nucleobases are able to π -stack for added stability.² It was later discovered that the dimensions and geometry of the DNA duplex varies; however, in Nature there are three main types which are depicted in Figure 1.4. The most common form of DNA is B-DNA, which describes a right-handed helix with a 0.34 nm distance between each base pair in the stack (a similar thickness to the π system of an aromatic ring). There are roughly 10 base pairs per turn. In order for the bases to effectively π -stack in the helix, the bases must twist and roll into a favourable conformation, thus creating asymmetric major and minor grooves upon helical formation. The A-form differs by having a tighter right-handed helical twist than the B-form, meanwhile the Z-form has a left-handed loose helical twist.

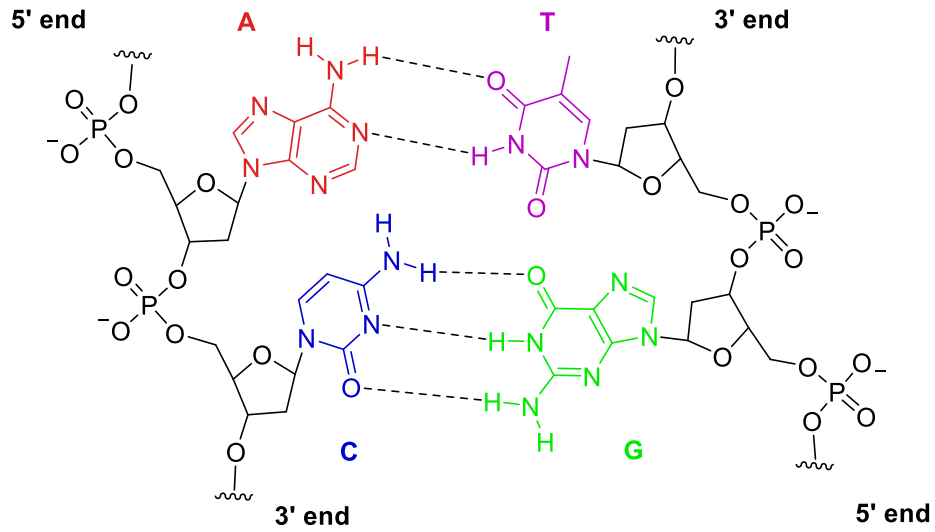


Figure 1.3: Hydrogen bonding that holds two antiparallel DNA strands together in the duplex. Showing the three hydrogen bonds formed between the CG pair and the two hydrogen bonds formed between the AT pair. The negatively charged sugar-phosphate backbone is also shown.

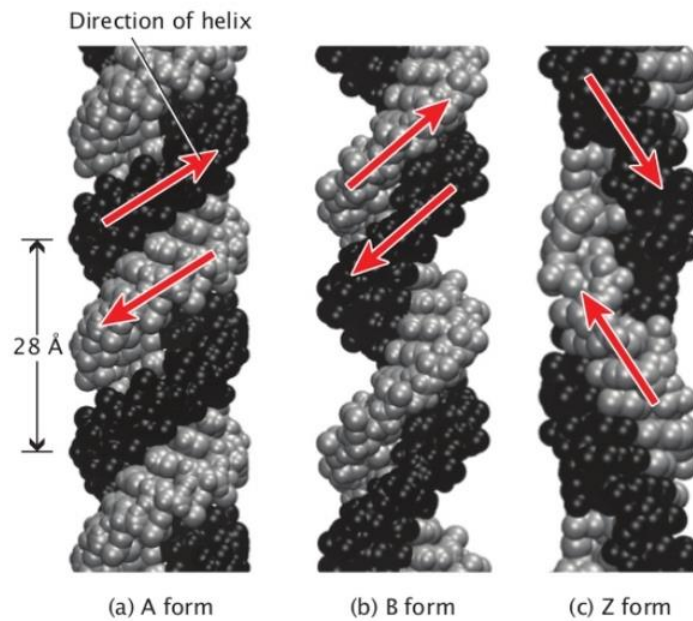


Figure 1.4: The three conformations of DNA. (a) A-DNA, a short, wide, right-handed helix. (b) B-DNA, the most common conformation, the structure proposed by Watson and Crick,¹ (c) Z-DNA, loose, left-handed helix.³

1.2. Single Point Variations

A single point variation describes a structural change to the nucleobase at a single nucleobase site within the genome. This can include the substitution of a nucleobase for one of the other nucleobase variants, or a structural modification to the nucleobase. Despite the growing research into the

discovery and detection of these variations, the literature lacks clarity on the terms used to describe these variations at single positions within the genome, with the terms ‘mutation’ and ‘polymorphism’ often used interchangeably.⁴ Here, the term ‘single point variation’ is used as an umbrella term to cover any type of nucleobase mutation and/or polymorphism, including; single nucleotide polymorphisms (SNPs)^{5, 6}, as well as cancer causing mutations that occur over the lifetime of an individual,^{7, 8} and epigenetic changes.^{4, 9} Figure 1.5 demonstrates a single point variation involving a base substitution. As outlined later in this chapter, modified DNA in the form of a hybridisation probe is ideal for the detection of single point variations within the genome, many of which are associated with diseases containing a genetic component.

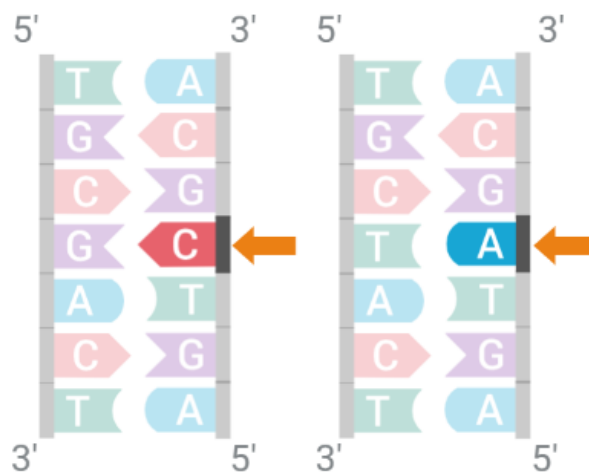


Figure 1.5: Diagram highlighting a single point variation site within a DNA sequence (orange arrow). In this example, a base substitution occurs at a single position within the DNA sequence, C > A.

1.2.1. Single Nucleotide Polymorphisms

A cell contains two copies of DNA, one from each parent, and each copy is called an allele. At particular regions, these alleles can be the same (homozygous) or different (heterozygous), and the variation between alleles contributes to the different phenotypes among individuals. >99% of the human genome is identical between individuals, however, single base changes can occur every 1000 bases or

so.¹⁰ Single nucleotide polymorphisms (SNPs) are defined as variations at specific base positions within the genome in >1% of the population⁹ and they account for genetic diversity across the population.

Most frequently, SNPs occur between genes and have no effect on genetic variation. However, SNPs that fall within a protein encoding region of DNA may cause an effect, as they can alter the amino acid sequence, and subsequently the protein produced. SNPs occurring within a regulatory region close to a gene may also have an effect by causing alterations to DNA transcription by affecting the efficiency of the proteins encoded further along the DNA sequence.¹¹

It is of interest to detect SNPs as they are seen as biological markers (biomarkers) for genetic diseases, for example many types of cancer. It is important to note that SNPs do not directly cause cancer, however, they can act as an indicator to the chances of an individual developing the disease.

1.2.1.1. BRAF V600E Mutation

The BRAF gene encodes the BRAF protein, a serine/threonine protein kinase involved in regulating MAP kinase/ERK-signalling pathway. The MAP kinase/ERK-signalling pathway is a cell signalling pathway that sends information from receptors on the cell surface to DNA in the nucleus *via* a chain of proteins, including the RAF family of proteins. Mutations in the BRAF gene have been linked with many types of cancer, including colorectal, lung, thyroid, hairy-cell leukaemia and more prevalently, melanoma.¹²⁻¹⁴ The BRAF V600E is a single point variation of particular interest as it is the most common BRAF mutation found in malignancies.¹⁵ The wild-type (WT) variant has the amino acid valine (V) at codon 600, whereas the mutant (Mut) variant has a glutamic acid (E) at this position instead. This amino acid change is a result of a single point variation in the BRAF gene; with the wild-type sequence containing T and the mutant containing A. There is need to detect this variation as the mutated version causes the MAP kinase pathway to keep sending signals to the nucleus and hence causes uncontrolled cell growth, Figure 1.6.

In recent years, there has been the development of targeted therapies which aim to inhibit these mutated pathways; for example, vemurafenib is a BRAF inhibitor which interrupts the signalling pathway. A variety of targeted therapy drugs have now been developed each with the aim of targeting specific genes and proteins involved in the growth of cancer cells. The use of mutation detection assays enables clinicians to identify the mutated gene and prescribe the appropriate treatment. Additionally, clinicians can use mutation detection assays to monitor cancer patients over the course of their treatment.

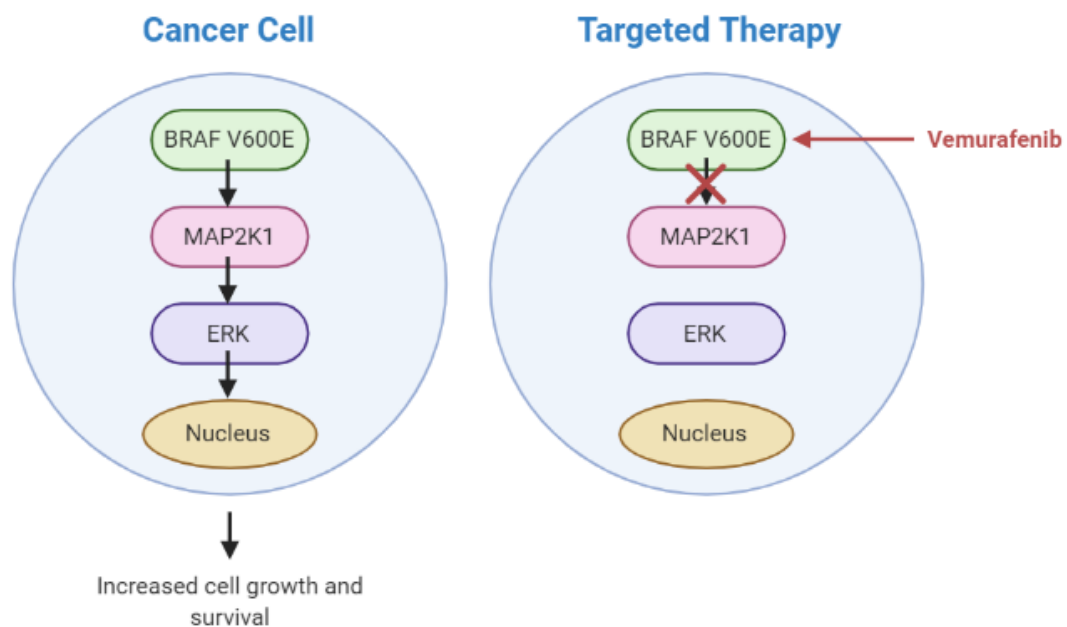


Figure 1.6: (Left) Cell signalling pathway in cancer cell with BRAF V600E mutation. No signal from the cell surface receptor is needed, so this pathway is always on, leading to increased cell growth. (Right) Effect of the BRAF inhibitor drugs. They stop the BRAF protein from turning on the rest of the pathway.

1.2.2. Epigenetic Changes

Epigenetics describes the study of heritable changes in the expression of genes that are not due to the changes in the genome sequence, such as a C > A base substitution.¹⁶ Epigenetic regulation of gene expression plays an important role in normal cell development and functions.¹⁷ However, disordered epigenetic gene expression has been linked to certain genetic diseases, including some cancers.¹⁸ DNA

methylation has been implicated in epigenetic gene regulation and is widely studied as a biological marker.

1.2.2.1. DNA Methylation

DNA methylation describes the addition of a methyl substituent to DNA, with the most widely characterised DNA methylation process being the addition of a methyl group to the 5-carbon of the cytosine ring resulting in 5-methylcytosine (5-mC), Figure 1.7. This epigenetic change represses DNA transcription as the methyl group protrudes into the major groove of DNA.

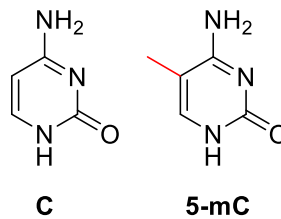


Figure 1.7: Structures of cytosine (left) and 5-methylcytosine (right).

In somatic cells, 5-mC occurs almost entirely at CpG sites (so named because of their sequence; cytosine-phosphate-guanine) and most CpG dinucleotides in the human genome are methylated. Unmethylated CpG dinucleotides usually form clusters called CpG islands, which mainly form in the promotor regions of many genes and allow normal gene transcription to take place. However, when a CpG island in the promotor region of a gene is methylated, silencing of gene expression occurs. Recent research has shown that cancer cells tend to have hypermethylated promotor regions, causing silencing of key tumour suppressor genes and hence leads to tumorigenesis.¹⁸ CpG methylation in protein encoding regions has also been linked to cancerous cells. With methylated cytosines being highly unstable, they are predisposed to gene mutation. Methylated cytosines are often deaminated and converted to thymine which may alter the amino acids produced, for example the formation of a stop codon, which has the effect of prematurely truncating the protein on translation and leads to subsequent inactivation of tumour suppressor genes.¹⁹ DNA hypomethylation has also been proposed

as a molecular marker for cancer.²⁰ Lack of methylation in promotor regions may activate the transcription of oncogenes, causing loss of imprinting or genomic instability by reactivation of repetitive elements which would normally be repressed.^{20, 21}

1.3. Fluorescent Nucleic Acid Probes

Modified DNA has useful applications in biological sensing and can be used as a hybridisation probe to detect specific nucleotide sequences and polymorphisms, including single point variations and epigenetic changes within DNA sequences. DNA modified with reporter groups, for example fluorescent or redox-active groups,²² can give read-out signals for the detection of such changes at the single base level. Fluorescence is a simple and easy to use technique that can be employed as a read-out signal for sensing systems, and fluorescence is the method focussed on in this work.

Before discussing the various types of fluorescent reporter groups and hybridisation probes, the methods in which these reporter groups are incorporated into the nucleic acid sequence are discussed.

There are three general methods used for the incorporation of such groups into DNA:

1. Direct oligonucleotide synthesis using solid-phase DNA synthesis and phosphoramidite chemistry (developed by Beaucage and Caruthers²³).
2. Post oligonucleotide synthesis modification using mild coupling conditions.
3. Enzymatic incorporation using primers that contain the fluorescently modified nucleobases.

The direct incorporation of a reporter group *via* solid-phase synthesis is the most desirable route, owing to the site-specific incorporation at any position along the oligonucleotide sequence and the minimal constraints on reporter group structure.²⁴ Unlike direct synthesis incorporation, post-synthesis incorporation may provide limitations on the structures of the reporter group to be incorporated. This method of labelling is still in early stages of research, and hence it is held back by

the limited number of coupling methods currently available.²⁵ Despite this, post-synthesis incorporation may provide a cheaper alternative to the direct synthesis labelling method. Out of all three approaches, enzymatic incorporation is the cheapest method and allows for much longer oligonucleotides to be synthesised (100-1000 nucleotides in length). However, there are constraints on the positional labelling and the reporter group modification structure may be restricted by enzyme constraints.²⁶

Fluorescent hybridisation probes are widely used in research and clinical diagnostic testing. There are many types of probe, some of which are commercially available, and each type employs different methods of inducing fluorescent character into the probe. These methods will now be discussed.

The fluorescent labelling of nucleic acid sequences with commercial fluorophores (such as Cy3 and Cy5) at the 3' and/or 5' end of the nucleic acid sequence is a common approach for creating fluorescent nucleic acid probes. These types of probes are widely used for the detection of specific nucleic acid sequences, and in fluorescence microscopy, *via* target hybridisation (i.e. duplex formation). They typically use unmodified nucleobases for base-pairing interactions with the target, with the fluorophore(s) tagged at the end of the sequence. Molecular beacons and TaqMan™ probes are good examples of commercially available probes of this type and are described in more detail later in this section.^{27, 28}

In contrast to commercial probes, academic research has generally focused more on developing probes that contain internal modifications, and in which the nucleobases themselves are often modified with the fluorophore. Using this approach, the reporter groups tend to play a greater role in the target-binding process, for example in producing distinct read-out signals that result from fluorophore-duplex interactions. The literature demonstrates several ways of introducing fluorescent character into a nucleic acid sequence in this way:

I. **Modified nucleobase tags;**

Modifying natural nucleobases to make them fluorescent *via* substituent modifications, base ring fusions and base ring extensions using conjugated linkers.

II. **Non-nucleosidic tags;**

- a) Removal of the nucleobase from the sugar ring and replacing it with a fluorescent moiety.
- b) Insertion of a fluorescent moiety into the backbone of DNA, which can be seen as taking the place of a whole nucleoside (sugar plus nucleobase) unit.

The following sections below describe these different types of fluorescent reporter groups in more detail and some literature examples of each are given.

1.3.1. Modified Nucleobase Sensors

DNA nucleobases are not naturally fluorescent but can be chemically modified to possess fluorescent properties. Any chemical modifications that are made must ideally retain the chemical and biological functions of the natural nucleobase, such as Watson and Crick base pairing and π -stacking. There are many literature examples of fluorescent nucleobases, dating back over 50 years. Furthermore, with more recent discoveries, the understanding of nucleic acid structures and their interactions are becoming better understood.²⁶ Many different approaches have now been used to tag nucleobases with fluorophores, as outlined below.

1.3.1.1. Substituent Modifications

Purine analogues were one of the first types of modified base to be studied, with Stryer *et al.* reporting the first example of a fluorescent nucleobase in 1969.²⁷ Figure 1.8 shows the structure of the fluorescent nucleobase, 2AP, which demonstrates a simple substituent modification at the 2-position of the nucleobase adenine. This modification does not block the pairing potential of the molecule.

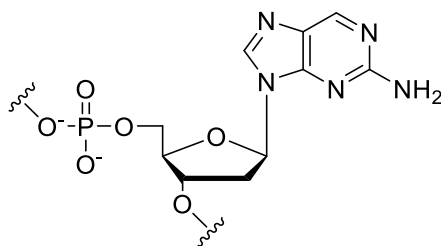


Figure 1.8: Structure of 2AP.

Initial research involving 2AP demonstrated the utility of fluorescent nucleobases in probing the conformation of nucleic acids. In later years, the development of pyrimidine fluorescent analogues began. The smaller size and simplicity of the ring system means that there are fewer modification sites compared to purines. An example of a pyrimidine analogue where the modification involves the substitution of the amino group on the pyrimidine ring for a methyl group is m^5K , developed by McLaughlin *et al.* in 1990, and its structure is shown in Figure 1.9.²⁸ This modification introduces a weak push-pull system within the electronic structure of the molecule, with the methyl serving as a donor and the carbonyl as an acceptor. This ‘push-pull’ character has a dramatic effect on the emission, red shifting the maximum emission wavelength from 324 nm to 400 nm.

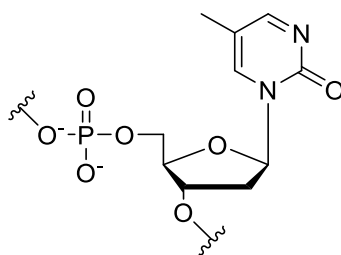


Figure 1.9: Structure of m^5K .

1.3.1.2. Base Ring Fusions

The pteridines were developed by Hawkins *et al.* in 1995.²⁹ and comprise the fusion of the pyrimidine ring of the nucleobase with a pyrazine. 3-MI shown in Figure 1.10, is one example which can be modified at different sites around the ring to produce a variety of pteridine structures. The extension

of the pyrimidine π -system affords a bathochromic shift in absorption and emission wavelengths and a significant increase in quantum yields compared to natural nucleobases.³⁰⁻³² This effect is observed due to the lowering of the HOMO “highest occupied molecular orbital”- LUMO “lowest unoccupied molecular orbital” orbital gap between the ground and excited states, a result of the extended conjugation. It is clear from this example that extended conjugation provides a useful method for tuning excitation and emission wavelength towards the red, an important factor when designing fluorescent probes for biological sensing – this minimalises any background emission that naturally occurs within the cell and avoids the need for ultraviolet radiation which could be potentially harmful.

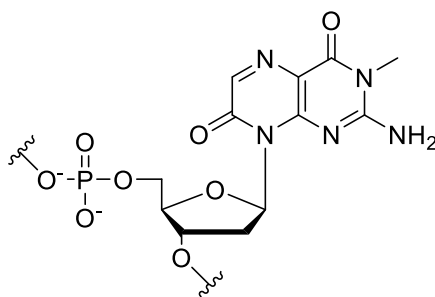


Figure 1.10: Structure of 3-MI, an example amongst the pteridines class of structures.

1.3.1.3. Extended Base Ring Structures Through Conjugated Linkers

Extended conjugated systems were first discovered in the late 1990s and 2000s, beginning with Moreau *et al.* developing the extended pyrimidine structure, BgQ.³³ Figure 1.11 shows the structure of BgQ, which is much larger than a natural nucleobase. The additional ring improves the fluorescence properties of the natural nucleobase, in a similar way to those mentioned above. However, when incorporated into DNA this larger nucleobase analogue perturbs the natural DNA helical structure which is not ideal for sensing applications. The size of the modification must be carefully considered when developing probes for DNA sensing - ideally modifications of a similar size to natural nucleobases should be used.

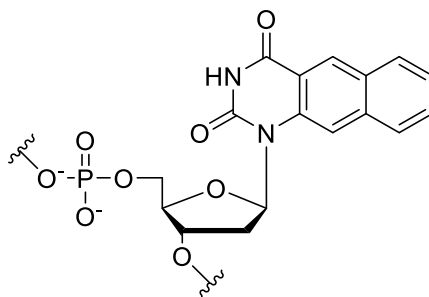


Figure 1.11: Structure of BgQ.

1.3.2. Non-Nucleosidic Sensors

1.3.2.1. Sugar Modifications

There are many literature examples of the direct addition of a fluorophore to a deoxyribose sugar by replacement of the purine or pyrimidine ring. Unlike nucleosidic sensors, non-nucleosidic sensors are not limited by the purine or pyrimidine structures, thus allowing the development of sensors with a wider range of fluorescent properties. This gives more freedom to create sensors with absorption and emission bands at higher wavelengths.

Kool *et al.* reported the direct addition of pyrene to deoxyribose, Figure 1.12.³⁴ Pyrene is a good choice of reporter group, due to its ability to π -stack more effectively than nucleobases and its comparable size to a nucleobase, allowing it to intercalate nicely into the helical structure of DNA. In addition, pyrene molecules can also form intramolecular excimers; if two pyrene molecules are held closely together within a DNA sequence, a resulting excimer may form which emits at a longer wavelength than that of a single pyrene molecule. Kool also reported the addition of other hydrocarbons, such as phenanthrene and perylene, to create a variety of non-natural nucleobases that exploited their different fluorescent properties.³⁴

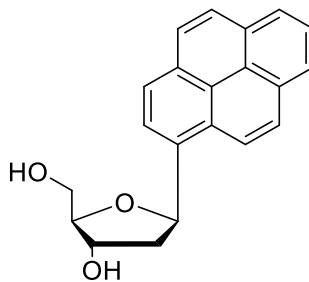


Figure 1.12: Structure of pyrene nucleoside reported by Kool *et al.*

1.3.2.2. Backbone Modifications

Fluorophores may also be directly incorporated into the DNA backbone using phosphoramidite chemistry and solid-phase DNA synthesis. Using this method, the fluorophore can be incorporated at a specific site and at any position within a DNA sequence. The minimal constraints on fluorophore structure and its position within a DNA sequence make this an exciting method for DNA probe synthesis. In addition, fluorescent monomer synthesis can be achieved with relative ease.

Despite there being few limitations with this method, the choice of fluorescent reporter group must be carefully selected; as mentioned above, those with longer wavelength absorption and emission profiles and with a comparable size to nucleobases are more desirable for the incorporation into a probe for DNA sensing applications. The synthetic design of the fluorescent reporter group must also be thought through carefully. To ensure the effective incorporation of the reporter group monomer into the DNA strand during automated solid-phase DNA synthesis, there is a requirement for the monomer to contain two hydroxyl groups. One of these groups is reacted to form a phosphoramidite group which will subsequently create a phosphate group during DNA synthesis, and the other is reacted with a protecting group. The simplest, most effective way of achieving this is to design the reporter group to contain a diol that mimics the 3'- and 5'-hydroxyl groups of a nucleoside. Appropriate linkers may also be employed to link the aromatic fluorophore moiety to the DNA backbone. This

creates space between the rigid sugar-phosphate backbone and the fluorophore which may improve the intercalation of the fluorophore into the DNA helix.

Tucker *et al.* have utilised serinol or threoninol diols as non-nucleosidic base analogues, which mimic the 5'- and 3'-hydroxyl groups of the sugar unit in a nucleoside, as shown in Figure 1.13. The use of threoninol is particularly advantageous as it is a chiral molecule with readily available L and D isomers. Once incorporated into the DNA probe, the different isomers affect the helical winding of DNA to different extents. Upon binding of the DNA probe with its complement, the threoninol isomer selectively positions the fluorophore within the duplex, which influences its intercalating ability and therefore duplex stability.^{35, 36} Asanuma *et al.* first reported the use D-threoninol to incorporate an azobenzene derivative and methyl red into oligonucleotides.³⁷ Others have also used threoninol to develop sensing systems with fluorophores, pyrene^{22, 24, 25} and thiazole orange.³⁸⁻⁴⁰

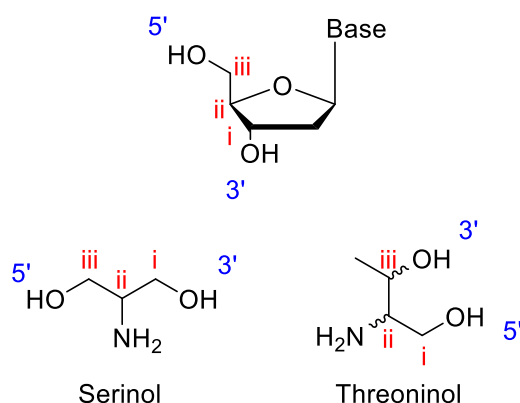


Figure 1.13: Structures of serinol and threoninol linkers showing the similarity in spacing between the 3'- and 5'-hydroxyl groups of a natural nucleobase.

1.4. Detection of Single Point Variations Using Fluorescence

Examples from the above section describe the modification of nucleic acids to generate probes with fluorescent character. The fluorescent reporter groups described above are not used for base discrimination and are therefore ineffective for the detection of single point variations.

Fluorescent hybridisation probes which are able to discriminate between bases in a target sequence have been developed; these are called base discriminating probes (BDPs). These probes are able to sense single point variations and examples of commercially available BDPs, and examples from academic literature are discussed in this section.

1.4.1. Commercially Available Base Discriminating Probes

DNA sequencing methods (e.g. whole genome, Sanger, next-generation) are seen as the gold standard for the detection of single point variations. However, sequencing methods are generally costly and time-consuming and whereas they can provide an abundance of genomic information, this is often much more than what is required for the detection of one single point variant at one locus. With increasing testing numbers within the NHS in the UK, there is an urgent need to develop rapid testing methods to allow high-throughput screening for genetic diseases.

Over recent years, there has been particular interest in the development of fluorescent hybridisation probe detection methods in clinical genetic testing.^{10, 41} Such fluorescence-based methods can be detected using simple equipment and are relatively straightforward techniques to use. They are highly sensitive techniques and effective at low concentrations (< μM). However, despite fluorescence-based methods being able to detect low concentrations, currently their limits of sensitivity are not low enough for very small quantities of DNA extracted from some types of patient sample, such as tumour samples or circulating free DNA (cfDNA) in liquid biopsies. Therefore, many fluorescence-based techniques require DNA amplification, such as polymerase chain reaction (PCR), to amplify patient DNA to produce a sufficiently strong fluorescence signal for accurate detection. PCR amplifies only the region of DNA of interest and hence removes any problems caused by the interference from other DNA sequences. However, it is required that the region of interest is known prior to sensing. Detailed below are some examples of commercially available assays for single point variation detection.

1.4.1.1. Molecular Beacon

Tyagi and Kramer were the first to introduce the molecular beacon concept in 1996.⁴² Molecular beacons consist of an oligonucleotide probe with a fluorophore and a quencher attached at opposite ends. The oligonucleotide probe contains self-complementary regions which allow the strand to fold and form a hairpin structure, where the fluorophore and quencher come into close proximity. When the molecular beacon's fully complementary 'match' target strand is present, the hairpin unfolds to favour hybridisation to the target strand. In the probe/target duplex hybrid, the fluorophore is distant from the quencher and so fluorescence emission is high. In the presence of a point variant, i.e. a 'mismatch' target, the molecular beacon has less affinity to hybridise and so remains in the hairpin structure with the fluorophore and quencher in close proximity and the fluorescence emission is quenched.⁴³ Figure 1.14 shows the molecular beacon strategy for single point variation detection. Molecular beacons have their drawbacks; they rely entirely on the thermodynamics of binding and quite frequently give false-positive signals.^{44, 45}

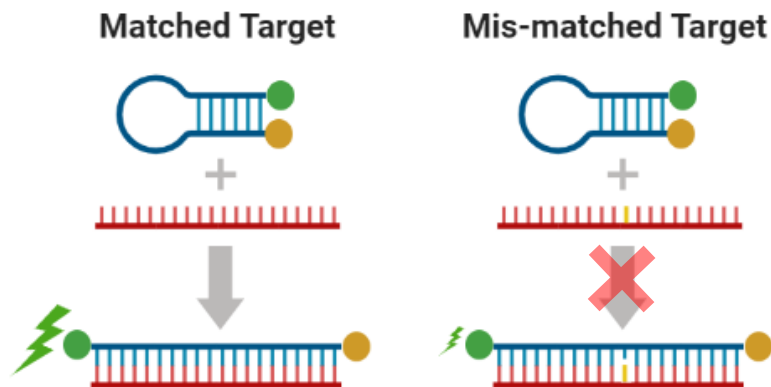


Figure 1.14: Schematic of molecular beacons for sensing single point variations.

1.4.1.2. TaqMan™ Assay

TaqMan™ assays (Applied Biosystems) are based on PCR techniques. The probe consists of an oligonucleotide with a fluorophore at the 5' end and a quencher at the 3' end. The oligonucleotide sequence is complementary to the sequence of interest, including the single point variant site. When the probe is intact, the fluorophore and quencher are in close enough proximity so that the fluorescence emission is reduced. During PCR, the forward primer extends and causes the degradation of the probe strand by the 5'-3' exonuclease activity of the DNA *Thermus aquaticus* (*Taq*) polymerase. The fluorophore is released from the probe strand and can fluoresce. With each round of amplification, the fluorescence signal increases as a result of accumulation of the PCR product. In addition to the sample of interest, control samples are also included. At the end point of PCR, the variant can be determined by calculating the ratio of fluorescence emission originating from each fluorophore on the probe of interest, compared to that of the control probes. Figure 1.15 illustrates how TaqMan™ assays detect single point variations. TaqMan™ is a relatively accurate and time-saving technique; however, it can only be used to detect one point variation at a time due to the limited quantity of fluorophores that can be read at any one time. Although TaqMan™ is an improvement on previous techniques of this type, such as restriction fragment length polymorphism (RFLP), it is still not high throughput and requires strict temperature windows to ensure that the probe binds to the target.⁴⁶⁻⁴⁸

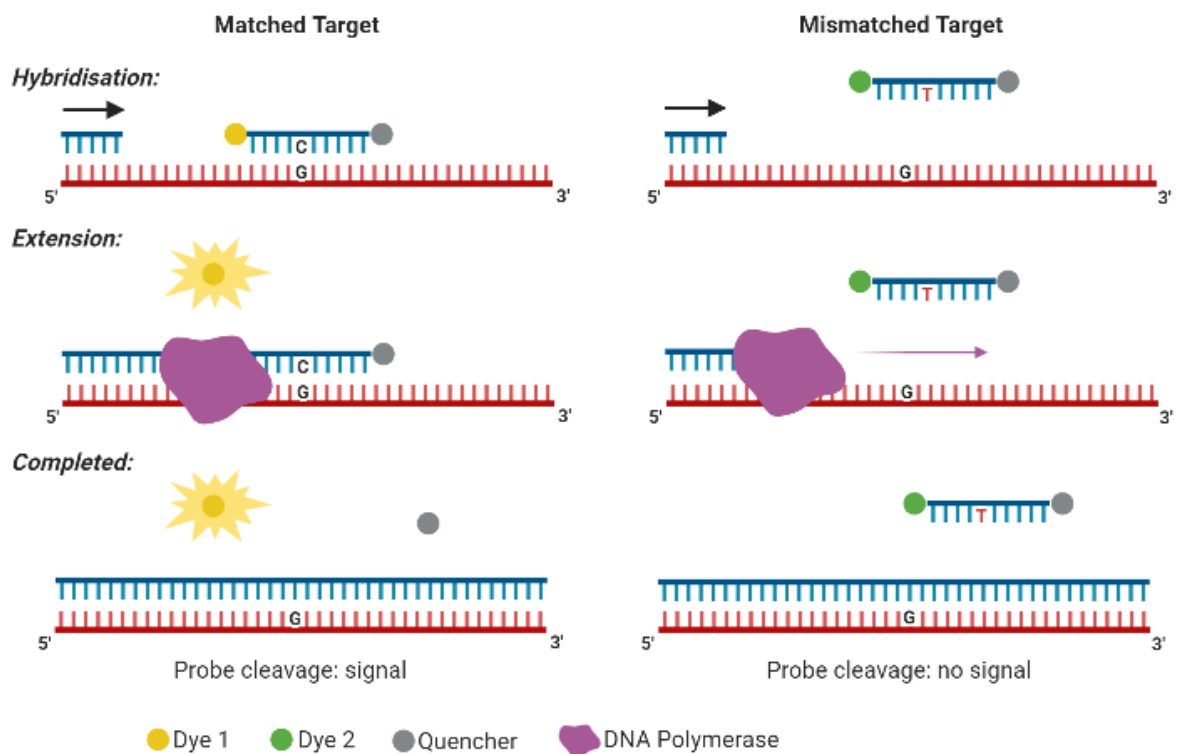


Figure 1.15: Schematic diagram of TaqMan™ assay for the detection of single point variations.

1.4.1.3. Scorpion Primers

Like TaqMan™, Scorpion Primers are a fluorescence-based technique used to analyse PCR products. Compared to TaqMan™, scorpion primers only require one probe strand so may be deemed more efficient. A scorpion probe consists of an oligonucleotide held in a hairpin loop by self-complementary regions at the 5' and 3' ends of the strand. A fluorophore is attached to the 5' end and a quencher to the 3' end. In its hairpin configuration the fluorescence signal is quenched due to the close proximity of the fluorophore and quencher. A PCR stopper links the hairpin loop to the 5' end of a PCR primer. The role of the PCR stopper is to prevent read-through, which could lead to the opening of the hairpin loop and the generation of a false-positive signal. The amplification process extends the primer and generates a sequence complementary to the probe sequence. This causes the hairpin loop to fully open and the probe to hybridise. The opening of the hairpin loop leads to an increase in fluorescence signal as the quencher is no longer held in close proximity to the fluorophore. Mutation detection is

achieved by monitoring the fluorescence emission at a temperature in which the probe has dissociated from the target when a 'mismatch' is present, but also remains bound to the fully complementary 'match' target. The full process of Scorpion primers is illustrated in Figure 1.16. The signalling speed associated with scorpion primers is highly desirable for high throughput sensing, but the probes are long and complex and rely on secondary structure for their operation.⁴⁹

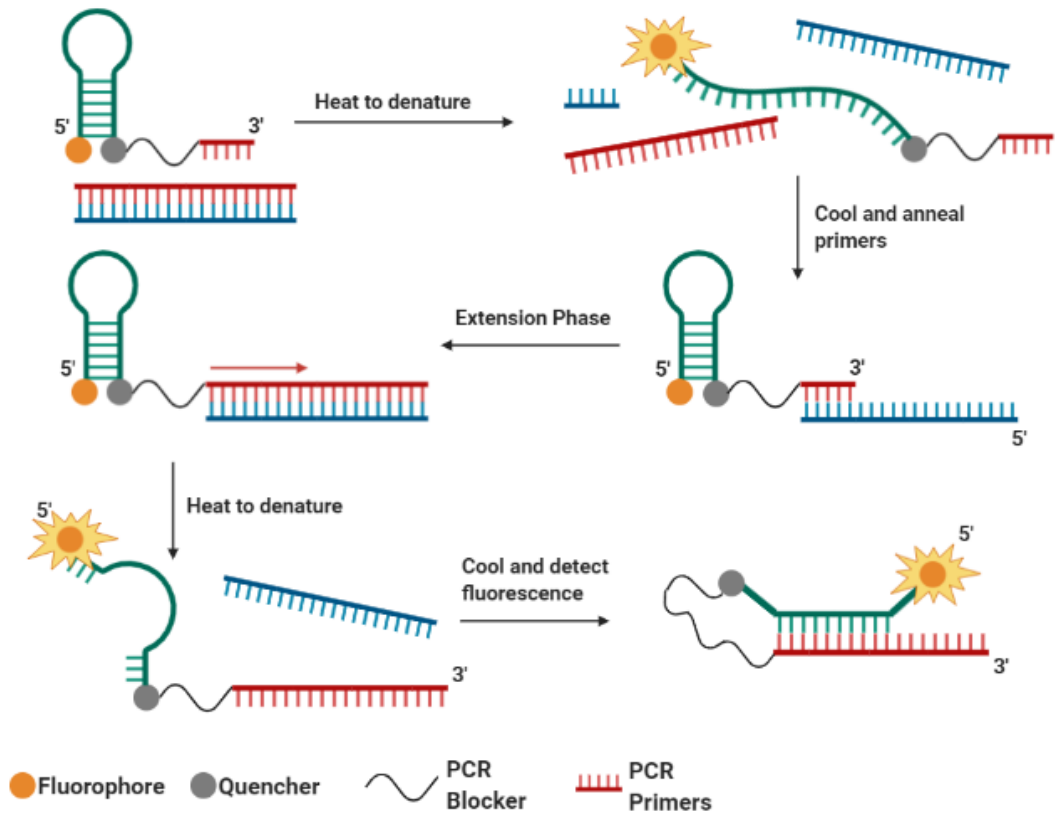


Figure 1.16: Schematic of Scorpion primers in the detection of single point variations.

Despite the variety of commercially available single point variation detection assays, research in recent years has shown a growing precedent for improved methods for single point variation detection in clinical settings. The current drawbacks of commercial assays, and the future directions of single point variation detection assays are summarised in the points below:

- The commercially available fluorescence-based assays described above rely upon hybridisation of probe strands to the DNA sequence of interest. This often requires strict temperature windows, restricting the temperature at which sensing can be performed. Room temperature sensing is not achievable using these methods; a feature which could be advantageous with certain methods such as isothermal amplification and could reduce the overall detection time for the assay.
- With growing complexity within the molecular diagnostic field, and with hundreds of single point mutations now linked to a single malignancy, there is increased interest in assays that can detect multiple single point variations within a DNA sequence at one time (i.e. multiplexing). Multiplexing to this extent is not currently possible with TaqMan™ assays and this is a major disadvantage of these technologies.
- The commercially available fluorescence-based assays can only distinguish between a wild-type (WT) and mutant (Mut) DNA sequence and cannot provide any information on the mutant variant identity.
- Current research in cancer progression and treatment focusses on tumour heterogeneity and simple, rapid methods for quantifying single point mutations would be beneficial. Quantitative read-outs are either not possible, or difficult to achieve using the methods above.
- There has been significant progress in the development of highly sensitive detection methods over the past few years.⁵⁰ Despite this, there is a need to improve the sensitivity and make the detection of low concentrations of rare DNA mutations easier and more cost effective. This need has been emphasised through the emergence of biomarkers within circulating free DNA

(cfDNA). cfDNA is degraded fragments of DNA that circulate in the blood plasma. It includes circulating tumour DNA (ctDNA) which is short, tumour-derived DNA fragments that circulate in the bloodstream which can reflect the tumour genome. For this reason, extracting ctDNA *via* a liquid biopsy may be used as a less invasive testing method for patients in comparison to a tissue sample taken directly from the tumour site. Due to the nature of ctDNA, it is only present at very low concentrations within the bloodstream (in the nanomolar range), hence why there is a push to develop highly sensitive techniques.

1.4.2. Base Discriminating Probes Reported in the Literature

As mentioned earlier, and in comparison to the commercially available probes above, academic research has focussed on the direct interactions of fluorescent reporter groups with target DNA as a way of base discrimination. In the early 2000s, the discovery of fluorescent base discriminating probes (BDPs) resulted in significant advancements towards the detection of single point variations and there are many examples of fluorescent BDPs in the literature.

The majority of fluorescent BDPs involve the hybridisation of a fluorescently modified probe strand to a specific target. By simply monitoring changes in the probe fluorescence emission intensity upon duplex formation, it is possible to detect the identity of the target. Recently developed fluorescent BDPs are able to distinguish between all four nucleobases, and a few examples can also detect epigenetic markers, such as 5-mC. Generally, the use of BDPs for base discrimination is relatively simple and avoids the complexity associated with many commercially available assays (as discussed above).

The specific response of a BDP to a particular target is often related to the exact positioning of the fluorophore within the duplex, its interactions with neighbouring bases and its microenvironment (including surrounding solvent molecules). One common problem that may occur is the quenching of the fluorescent reporter group emission from flanking base pairs.⁵¹ It is therefore imperative that the

fluorescent reporter group signal is strong, with a relatively high fluorescence quantum yield and is detectable at the low concentrations required for sensing applications.

1.4.2.1. Pyrene BDPs

Saito *et al.* developed pyrene labelled BDPs, Figure 1.17. The pyrene modified nucleotides ^{Py}U and ^{Py}C were incorporated into a probe strand and provided unique fluorescence emission profiles depending on the nature of the base at the site directly opposite the modification in the target strand upon binding. ^{Py}U and ^{Py}C were particularly effective at distinguishing between A and G, showing a distinctive change in fluorescence emission between the two nucleobases.^{52, 53}

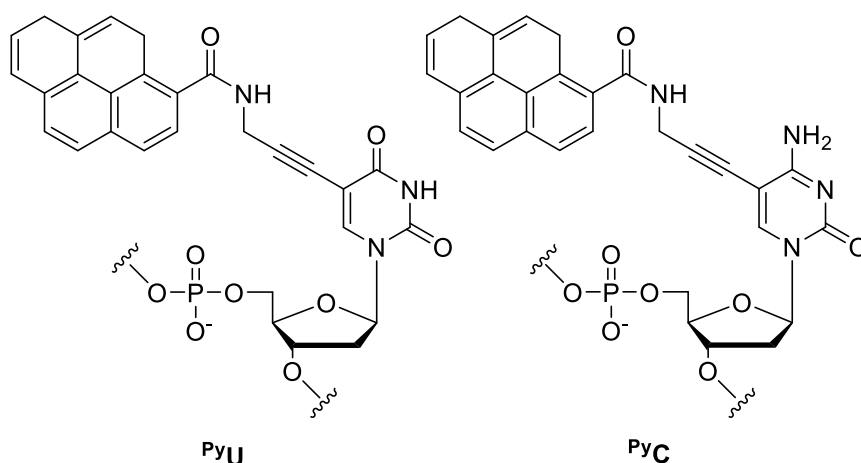


Figure 1.17: Structures of pyrene modified nucleobases, ^{Py}U (left) and ^{Py}C (right).

BDPs containing pyrene reporter groups have certain drawbacks; including their low fluorescence intensity, owing to their susceptibility to quenching from surrounding nucleobases and their relatively short wavelength emission. Hrdlicka *et al.* envisaged improving the fluorescent properties of Saito's ^{Py}U BDP system by incorporating the same pyrene reporter group within a locked nucleic acid (LNA). LNA nucleotides consist of a modified sugar unit in which a bridge connects the 2' oxygen and the 4' carbon, as shown in Figure 1.18. The presence of the bridge causes puckering of the ribose sugar ring and results in higher positional control of the pyrene moiety and subsequently improved sensing properties. The LNA monomers are incorporated into oligonucleotides and the fluorescence intensity

is monitored upon hybridisation of the probes with their complementary targets. Higher fluorescence quantum yields of the probe/target duplexes are observed with these LNA pyrene modified probes, which can be explained by a reduction in quenching interactions with surrounding nucleobases, a consequence of the more rigid positioning of the fluorophore within the duplex. This sensing system allows for a clear differentiation in fluorescent signal between 'matched' and 'mismatched' targets which is attractive for sensing applications.⁵⁴

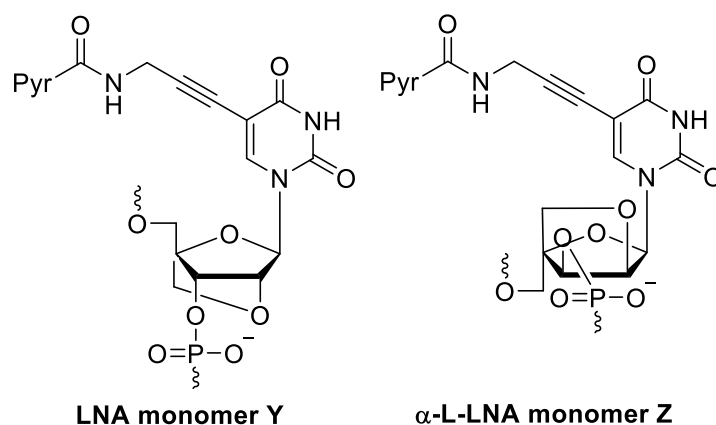


Figure 1.18: Structures of both isomers of the pyrene (Pyr) modified LNA monomers, showing the constrained bridge from the 2' oxygen to the 4' carbon.

In addition to the two pyrene BDPs described above, Saito *et al.* developed another pyrene labelled BDP which is capable of specifically sensing thymine (T). The probe consists of an oligodeoxynucleotide containing 7-deaza-7-(1-pyrenecarboxamido)propyl-2A-deoxyadenosine (^PYA) as part of its sequence. The structure of ^PYA is demonstrated in Figure 1.19. Unlike other BDP systems, which typically display increases in probe fluorescence signals upon sensing a specific target, this system utilises the quenching of the fluorescence signal as a way to detect a 'matching' target (i.e. target containing T). Although 'switch on' probes are usually preferred for sensing applications as increases in fluorescence intensity are easier to accurately detect, this system was successfully used to test the T (wild type)/C (mutant) single point variation associated with the human breast cancer gene 1 (BRACA1) and the

system demonstrated the success of these types of 'switch off' probes in single point variation detection.^{53, 55}

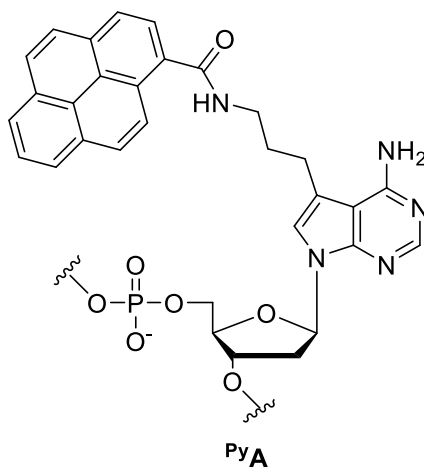


Figure 1.19: Structure of pyrene modified nucleobase, PyA.

1.4.2.2. Anthracene BDPs

Brown *et al.* developed a BDP consisting of a modified thymine nucleotide.⁵⁶ Anthracene was tagged to the thymine base at position 9 *via* a single or double ethynyl linker group, as demonstrated in Figure 1.20. A five-fold increase in fluorescence emission was seen upon hybridisation of the probe strand with both 'matching' and 'mismatching' target strands, apart from a 'mismatching' strand containing guanine, where fluorescence emission decreased, which made discrimination between A and G possible.

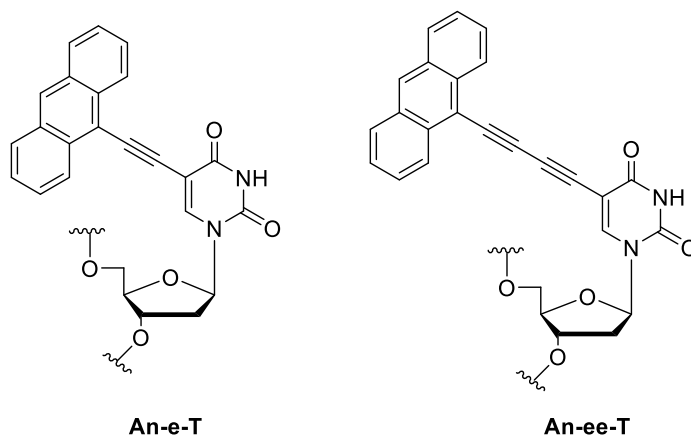


Figure 1.20: Structures of anthracene modified thymine nucleotides. The anthracene group is attached to the thymine base via single (An-e-T) or double (An-ee-T) ethynyl linkers.

A similar BDP system was developed by Saito *et al.* through the attachment of anthracene to 2-deoxyuridine *via* a carboxamide and an acetylenic linker group, Figure 1.21.⁵⁷ They varied the position at which the anthracene was attached to the linker group at positions 2 (^{2-Ant}U) and 9 (^{9-Ant}U) and incorporated the modified nucleotides into DNA. For both probe strands, the fluorescence emission was shown to increase upon hybridisation with its 'matching' target, where A base pairs with the modified base. However, ^{2-Ant}U showed much stronger fluorescence emission compared to ^{9-Ant}U, owing to the positioning of ^{2-Ant}U further outside the major groove than ^{9-Ant}U, away from quenching interactions from surrounding nucleobases. The very low signal produced by the ^{9-Ant}U system made it an undesirable choice for sensing applications.

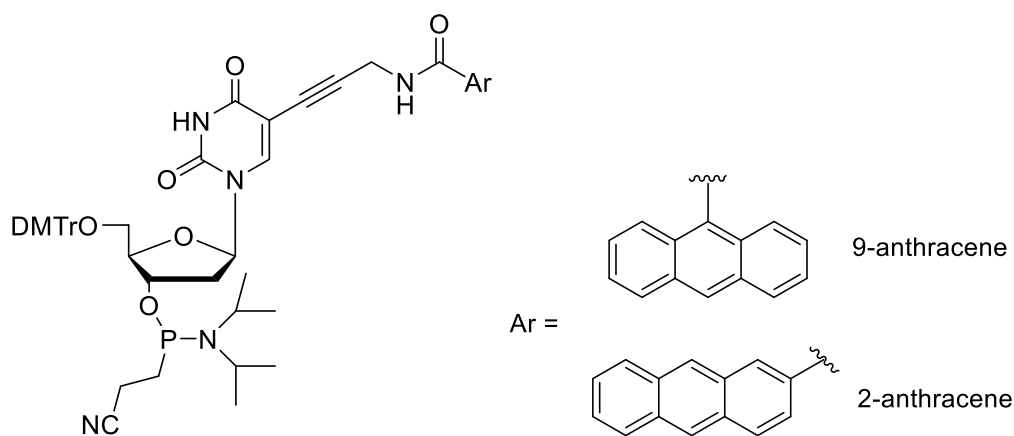


Figure 1.21: Structure of anthracene modified 2-deoxyuridine phosphoramidite, where Ar = 2-anthracene or 9-anthracene. The anthracene moiety is attached via a carboxamide and acetylenic linker.

Initial developments by Tucker *et al.* involved an anthracene BDP in which serinol was used as a non-nucleosidic analogue to incorporate the anthracene fluorophore into the DNA backbone.⁵⁸ However, as previously discussed, the chiral threoninol molecule is a better choice for a non-nucleosidic analogue and so Tucker *et al.* improved this initial system by moving to the development of threoninol-containing analogues.

One example developed by Tucker *et al.* involved a BDP containing an alkoxy-anthracene group that was inserted into the DNA backbone *via* a D-threoninol non-nucleosidic analogue, Figure 1.22.⁵⁹ This is a versatile probe system as the length of the alkyl spacer between the anthracene reporter group and the DNA backbone can be varied. Probe strands were hybridised with target strands in which the nucleobase site directly opposite the anthracene modification was varied. The probe containing the shortest linker length (where $n = 1$, Figure 1.22), gave decreases in fluorescence intensity for all target strands upon duplex formation. In contrast, the probe containing a longer linker length (where $n = 4$, Figure 1.22) gave either an increase or decrease in emission, depending on the base, see Figure 1.23.⁶⁰ Thus, it was shown that the linker length could have a pronounced effect on the sensing properties of the system. While still being quenched by proximate bases upon duplex formation, the short and relatively inflexible linker is relatively insensitive to a change in the identity of the base opposite the tag. In contrast, the longer linker length system can intercalate more effectively and also interact more with bases in the target strand and is therefore a better choice as a BDP.

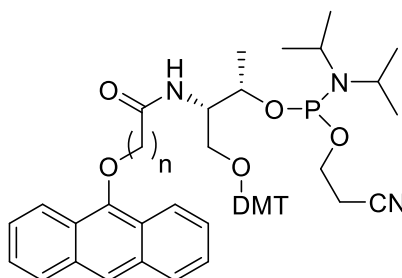


Figure 1.22: Anthracene phosphoramidite with linker lengths $n = 1$ or $n = 4$.

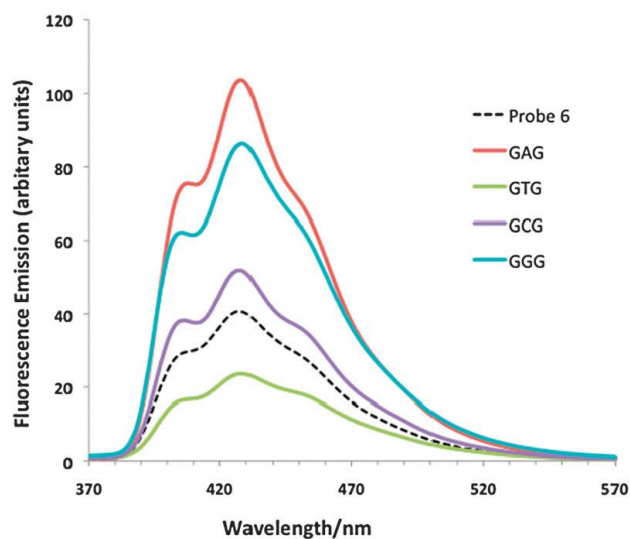


Figure 1.23: Fluorescence spectra of the anthracene probe strand containing the longer linker length (dotted line) and duplexes of the probe strand with targets containing all 4 base variants at the site opposite the anthracene modification. (100 mM NaCl, 10 mM sodium phosphate buffer, pH 7.0, $\lambda_{ex} = 350$ nm).⁶⁰

Using a similar anthracene BDP as described above, Tucker *et al.* showed that sensing the epigenetic markers, 5-methyl and 5-hydroxymethylcytosine was also achievable using this system, as shown in Figure 1.24.⁶¹ The linker lengths $n = 4$ and $n = 5$ were particularly effective at sensing these epigenetic markers. Target strands were varied at the site opposite the anthracene modification with either cytosine (C), 5-methylcytosine (5-mC) or 5-hydroxymethylcytosine (5-hmC). Probe strands involving the linker length $n = 4$ showed a distinct increase in fluorescence signal for target strands containing C, whereas a decrease in signal was seen for both 5-mC and 5-hmC. In contrast, for linker length $n = 5$, an increase in fluorescence signal was observed for both C and 5-mC and a decrease for 5-hmC only. By combining all these observations, discrimination between all three major epigenetic DNA methylation markers could be achieved. Following on from this, it may be possible to be able to detect other epigenetic variants, such as formylcytosine and carboxylcytosine, which have also been linked to certain types of cancer.⁶²

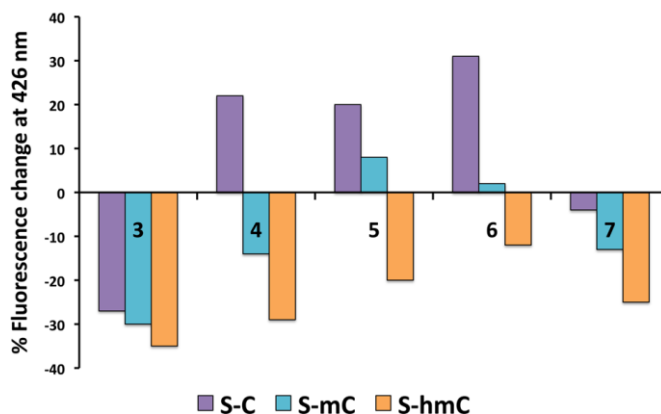


Figure 1.24: Fluorescent responses (at 426 nm) of the probe strand to target strands, showing the differences between linker lengths. [DNA] = 1 μ M, 100 mM NaCl, 10 mM sodium phosphate buffer, pH 7.0, λ_{ex} = 350 nm.⁶¹

1.5. Solvatochromic Reporter Groups

Solvatochromic fluorophores display shifts in absorption and emission bands depending on the nature and composition of their surrounding solvent. For a solvatochromic effect to occur, the molecule must possess intramolecular charge transfer (ICT) from a donor group to an acceptor group. During the excitation of the fluorophore, changes in charge distribution throughout the molecule occur. This leads to changes in the dipole moment, which alter the interactions of the fluorophore with the environment. The difference in the dipole moment between the fluorophore's ground and excited states determines the sign of solvatochromism. Negative solvatochromism relates to the hypsochromic (blue) shift with increasing solvent polarity whereas a bathochromic (red) shift with increasing solvent polarity is termed positive solvatochromism.

The work in this thesis concerns molecules that display positive solvatochromism, so this effect will now be described in more detail. Upon excitation, the dipole moment of the molecules increases, and a more polar solvent stabilises the excited state more than the ground state, as demonstrated in Figure 1.25. This leads to shifts in the absorption profiles of molecules to longer wavelengths when present in more polar solvents.

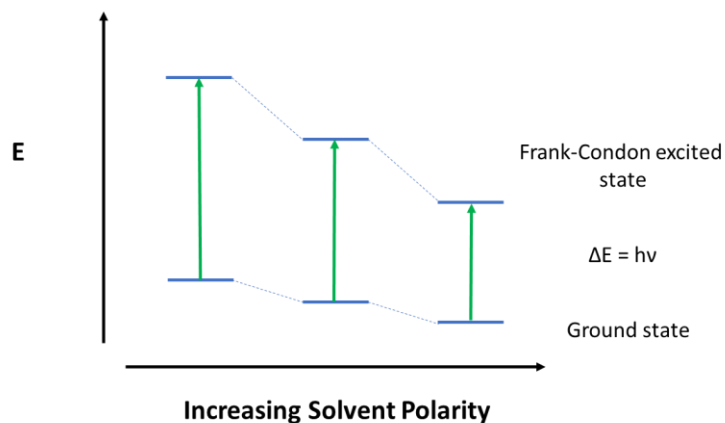


Figure 1.25: Energy level diagram showing the solvent effects on the absorption wavelengths, demonstrating the positive solvatochromism stabilising effect of solute molecules in more polar solvents. Where E is energy (J), h is Planck's constant (6.626×10^{-34} J s) and ν is frequency (s^{-1} or Hz). Diagram adapted from Rutan et al.⁶³

This solvatochromic effect is also evident in the emission profiles of solvatochromic molecules. With fluorescence emission being the most common detection method used in DNA sensing applications, this effect is studied to a greater extent in the work in this thesis. As mentioned above, when a molecule is excited, there is a change in the dipole moment, with the excited molecule experiencing a larger dipole moment than its ground state. The solvent molecules that surround the fluorophore are able to reorient themselves in response to this change in dipole moment through a process called solvent relaxation. In the case of positive solvatochromism, due to the more prominent dipole moment that is present in the excited state, more polar solvents cause stronger solvent-solute interactions and an increase in solvent relaxation; this leads to a lowering in the energy of the excited state and hence a longer emission wavelength. Upon emission of radiation, the excited molecule returns to the ground state configuration. However, the fluorescence emission timescale does not allow the solvent molecules enough time to reorganise themselves back to their original orientation, leading to a slightly higher ground state energy than to begin with.⁶³ Figure 1.26 describes this process.

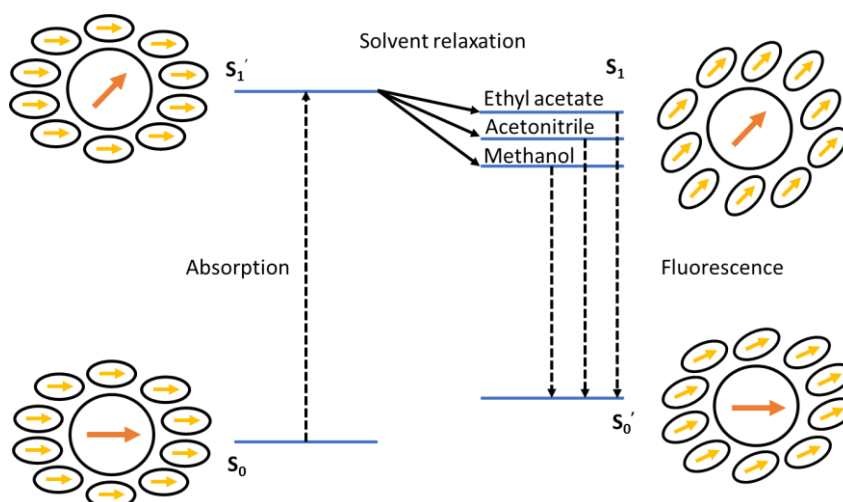


Figure 1.26: Solvent effects on electronic state energy. Dashed arrows represent radiative processes and solid lines represent non-radiative processes. Figure adapted from Rutan et al.⁶³

More prominent solvatochromic effects are commonly observed in the emission profiles compared to the absorption profiles a result of the presence of these solvent relaxation effects, which can be detected over longer fluorescence timescales and increase the bathochromic shifts of the emission profiles in more polar solvents.

A fluorescent BDP works by producing a sensing signal *via* a change in fluorescence intensity upon duplex formation. However, a solvatochromic BDP could provide an additional benefit by also displaying a shift in the emission wavelength as a result of small changes in the micro-environment surrounding the tag. This could improve results obtained from BDPs in cases where only small fluorescence intensity changes are observed, which makes base discrimination difficult. There are relatively few examples of DNA probes containing fluorophore reporter groups that exhibit such solvatochromic properties in the literature, as described below. Quite often, the solvatochromic effect of the reporter group monomer is reduced after DNA incorporation due to interactions with neighbouring bases. As well as base discrimination, there are also recent literature examples demonstrating the use of solvatochromic DNA probes for sensing DNA-protein interactions.^{64, 65}

Solvatochromic reporter groups are incorporated into DNA probes using similar methods to those described in the previous section, *via* (I) modifying the natural nucleobase to induce fluorescent character by either (a) extending the nucleobase aromatic system, or (b) simply attaching a solvatochromic group, or (II) removal of the nucleobase from the sugar ring and substituting it with a solvatochromic group. Examples of each are given in Figure 1.27 and are discussed further below.⁶⁶

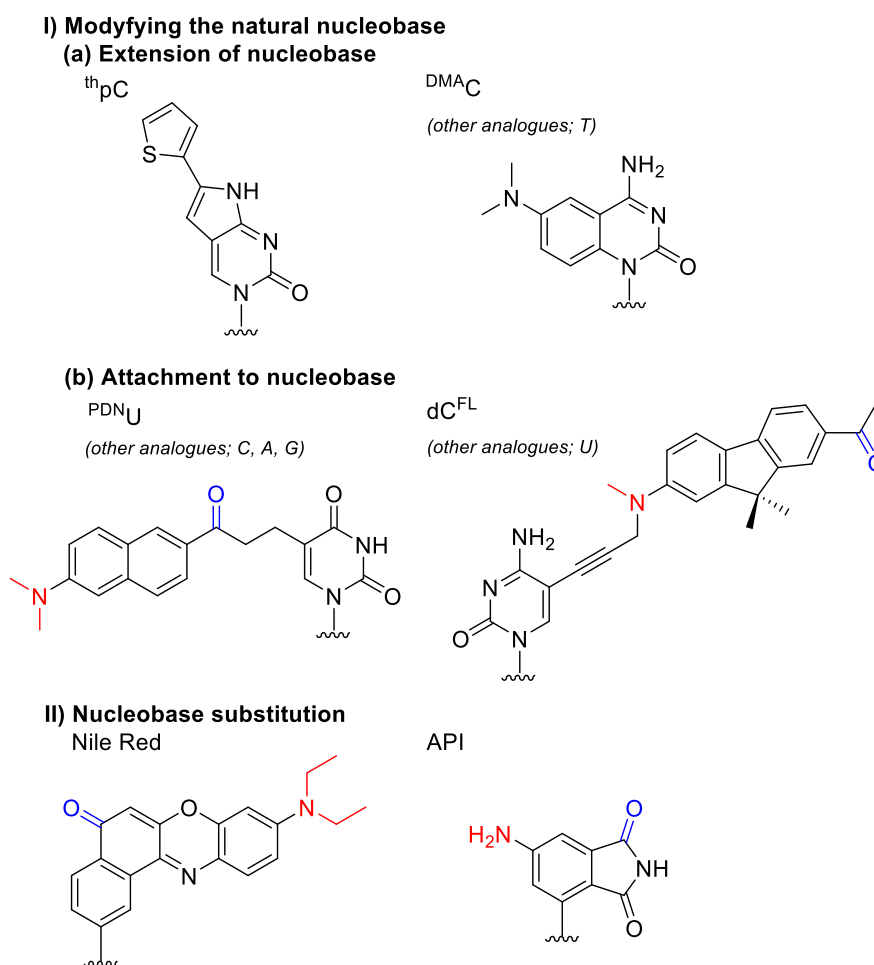


Figure 1.27: Solvatochromic nucleic acid analogues demonstrating intramolecular charge transfer (ICT) via donor and acceptor groups, shown in red and blue respectively.

Non-nucleosidic analogues Nile Red and 4-aminophthalimide (API), Figure 1.27 II, produce a strong solvatochromic affect when present in monomer form, displaying solvent-dependent shifts in their emission spectra; however, this effect is drastically reduced when they are incorporated into DNA probes. The resulting DNA probes provide little sensitivity to changes in their microenvironment as

evidenced by the minor shifts observed in their emission bands when transitioning from single- to double-stranded DNA (10 nm spectral shift for API and 0 nm shift for Nile Red).^{67, 68} This reduction in solvatochromic behaviour occurs because the prominent interactions within the DNA probe result from the π - π stacking interactions of the aromatic reporter groups with neighbouring bases, interactions which do not substantially change upon duplex formation.

Chemical modifications of natural nucleobases have given rise to the development of the solvatochromic tags thpC and ^{DMA}C, whose structures are shown in Figure 1.27, **I (a)**.^{69, 70} However, once again, when these compounds are present within DNA probes, any changes to their environment produce only small shifts in their emission bands. With this type of modification, it is difficult to tune/improve the solvatochromic properties of the reporter group because of the limitations of modifications which can be applied to the natural nucleobases. For this reason, fluorescent probes developed through chemical modifications of the natural nucleobases are more suited to base discrimination *via* intensity changes rather than monitoring any spectral shifts.

The systems ^{PDNU} and ^{dC^{FL}}, Figure 1.27 **I (b)**, involve the attachment of solvatochromic fluorophores to nucleobases *via* linker groups. When incorporated into DNA, these fluorophores position themselves within the major and minor grooves, making them more exposed to changes in the surrounding environment, which in turn provides significant shifts in their emission bands.^{65, 71} The solvatochromic properties of the nucleoside monomers modified with the PRODAN solvatochromic fluorophore, ^{PDNU}, are demonstrated in Figure 1.28. DNA probes containing various modified nucleobases, ^{PDNX} (where X= U, C, A and G), are of particular interest due to their base discrimination properties which are shown in Figure 1.29. Shifts in probe emission profiles of one or two nanometers were observed depending upon the base variant present in the target at the site directly opposite the PRODAN modified nucleobase.⁷¹ The spectral shifts observed in this example are only minimal and it would be difficult to accurately differentiate between nucleobases in sensing applications, hence further investigations into

the use of solvatochromic probes for this purpose are required. The use of an appropriate fluorophore, with a larger dipole moment across the molecule could resolve this issue and provide markedly larger spectral shifts for clearer base discrimination.

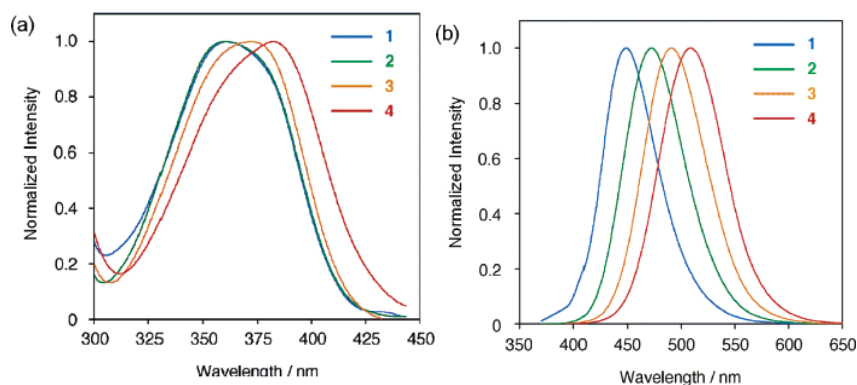


Figure 1.28: Photochemical behaviour of PDNU nucleoside. a) Normalised excitation spectra in different solvents; 1 = HMPA, 2 = acetonitrile, 3 = ethanol, 4 = ethylene glycol. b) Normalised emission spectra in different solvents; 1 = HMPA, 2 = acetonitrile, 3 = ethanol, 4 = ethylene glycol.⁷¹

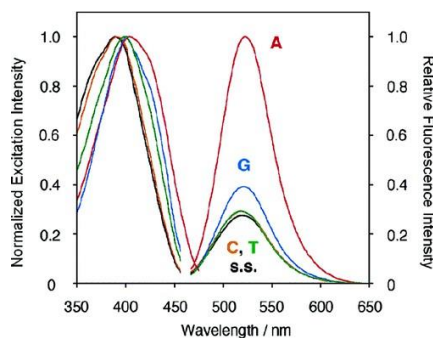


Figure 1.29: Fluorescence excitation and emission spectra of the PDNU probe strand and its targets. Normalised excitation (left) and relative emission (right) of 2.5 μ M probe hybridised with 2.5 μ M of target were measured in 50 mM sodium phosphate, pH = 7.0, and 0.1 M NaCl at 25 $^{\circ}$ C. For excitation spectra, λ_{em} = 520 nm and for emission spectra, λ_{ex} = 450 nm.⁷¹

1.5.1. Naphthalimide Reporter Groups

As solvatochromic molecules, 1,8-naphthalimides shown in Figure 1.30, are very sensitive to their surrounding environment, making their emissive properties very solvent-dependent.⁷²⁻⁷⁴ In addition, chemical modifications to their structure can drastically alter their optical and photophysical properties, especially the addition of substituents around the naphthalimide aromatic ring.^{75, 76} There

are many examples in the literature relating to the introduction of amines around the 1,8-naphthalimide core. This modification in particular has a pronounced effect on its fluorescence properties due to the presence of the lone pair on the nitrogen acting as the donor in ICT.^{72, 77} Many 1,8-naphthalimide compounds are highly fluorescent, have large Stokes shifts and emission bands in the green region of the visible spectrum. The emission band can be tuned and directed further towards the red by altering substituents around the aromatic ring, or at the imide position. As previously mentioned, emission bands shifted further towards the red are beneficial for biological sensing applications.

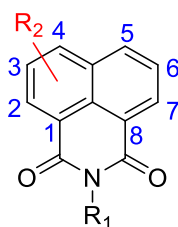


Figure 1.30: Structure and numbering of 1,8-naphthalimide molecules.

The convenient synthesis of 1,8-naphthalimides from 1,8-naphthalic anhydrides by reaction with an amine, along with the ease of substitution at various positions around the aromatic ring, allow for the production of a large family of naphthalimide derivatives, each with different chemical and photophysical properties. The production of such an expansive library of compounds is highly desirable for the development of probes for a variety of applications, including; fluorescent sensors, cell imaging, logic gates, chemical probes, dyes, sensing of biological cations/anions, and anticancer treatments.^{75, 78-81} A recent review was published discussing the wide sensing applications of 1,8-naphthalimide derivatives.⁸²

Although there is no evidence in the literature of the use of 1,8-naphthalimides as BDPs, their ability to target and interact with biomolecules, such as nucleic acids, is well-known. For example, its planar and aromatic core allows for DNA intercalation and its ability to bind to the grooves of DNA has also

been demonstrated.⁷⁵ For these reasons, naphthalimide molecules have been adapted for many sensor applications involving biomolecules.^{75, 83} A few examples are highlighted below.

de Silva *et al.* developed the naphthalimide sensor shown in Figure 1.31.⁸⁴ This sensor was able to sense thiols *via* interaction of a thiol at the maleimide unit of the sensor. The sensing was achieved through a photoinduced electron transfer (PET) mechanism.

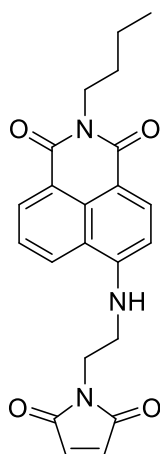


Figure 1.31: Naphthalimide sensor developed by de Silva *et al.* based on PET sensing. Thiol molecules are detected through the interaction with the maleimide moiety in the sensor.

Another naphthalimide sensor developed by Imperiali *et al.*, Figure 1.32, demonstrated the incorporation of naphthalimide sensors into polypeptides and their potential use for sensing protein interactions.⁸⁵

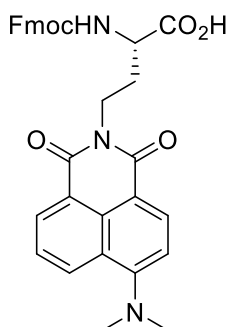


Figure 1.32: Naphthalimide sensor developed by Imperiali *et al.* for the incorporation into polypeptides.

With regards to DNA sensing, until now naphthalimide sensors have been mostly concerned with small molecules (i.e. not oligos) that bind to DNA. Positively charged naphthalimide sensors have been developed to bind to the polyanion DNA through electrostatic, hydrogen bonding and π - π intercalating binding interactions. These binding interactions usually give rise to changes in the photophysical properties of the naphthalimide molecules and in many cases also lead to DNA damage and programmed cell death. For example, naphthalimide sensors developed by Brana *et al.*⁸⁶ and Wilson *et al.*,⁸⁷ shown in Figure 1.33, were shown to be anticancer agents that bind to DNA directly *via* electrostatic interactions at physiological pH through the protonation of the tertiary amine. Naphthalimide molecules attached to metal compounds have also been explored for DNA binding, in which the metal centre is thought to provide additional affinity for the negatively charged phosphate backbone.⁸⁸⁻⁹⁰

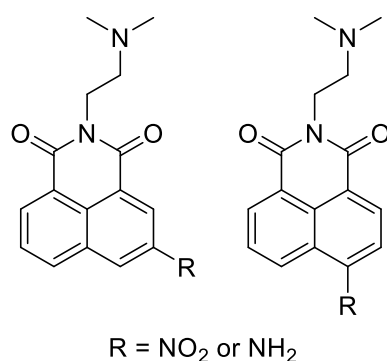


Figure 1.33: Naphthalimide sensor developed by Brana *et al.* (left) and Wilson *et al.* (right) for the binding to DNA. The positioning of the nitro group at the 3' or 4' position alters the intercalating ability of the sensor, with the 4'-nitro analogue perturbing the stacking intercalating ability.

The literature examples above show promise for the utilisation of naphthalimides in BDPs, owing to their well-studied interactions with DNA and photophysical properties.

1.6. Future Directions of Fluorescent Nucleic Acid Probes for the Detection of Single Point Variations

This past year, the COVID-19 pandemic has only highlighted the growing need and importance for the development of rapid, effective, and inexpensive methods for the detection of single point variations. The emergence of various SARS-CoV-2 mutations, such as the Alpha, Beta, Gamma and Delta are examples in which the RNA genome differs by just a few changes at the single base level. Being able to detect these mutations (currently done using sequencing technology) has helped in the tracking of COVID-19 and reducing its spread. But as a nation leading the way in genetic profiling, the UK requires ever faster and cheaper methods for detecting these variants to keep up with increasing testing demands.

Much of this thesis concerns the development of new fluorescent BDPs for improving the current methods used to detect single point variations, as described in this Introduction. The incorporation of the solvatochromic reporter group, 1,8-naphthalimide, into a nucleic acid hybridisation probe builds on what little research there currently is into the use of solvatochromic probes as BDPs. This adds a new dimension to sensing single point variations, with the potential for changes in emission wavelengths in addition to changes in emission intensity.

In addition, the development of fluorescent BDPs involving anthracenes is explored as a simple method for the quantification of single point variations, improving on commercially available detection assays which are unable to provide quantitative read-outs, or are expensive to do so.

1.7. References

1. J. D. Watson and F. H. C. Crick, *Nature*, 1953, **171**, 737.
2. E. T. Kool, J. C. Morales and K. M. Guckian, *Angew. Chem. Int. Ed.*, 2000, **39**, 990.
3. A. f. B. P. Nature Education, *Genetics: A Conceptual Approach*, 2nd Edition, *Journal*, 2014.
4. R. Karki, D. Pandya, R. C. Elston and C. Ferlini, *BMC Med. Genomics*, 2015, **8**, 37.
5. K. Nakatani, *ChemBioChem*, 2004, **5**, 1623.
6. A. L. Price, C. C. A. Spencer and P. Donnelly, *Proc. R. Soc. B*, 2015, **282**, 1684.
7. J. R. Hart, Y. Zhang, L. Liao, L. Ueno, L. Du, M. Jonkers, J. R. Yates and P. K. Vogt, *Proc. Natl. Acad. Sci. U.S.A*, 2015, **112**, 1131.
8. E. R. Cantwell-Dorris, J. J. O'Leary and O. M. Shiels, 2011, **10**, 385.
9. J.-L. H. A. Duprey, D. M. Bassani, E. I. Hyde, G. Jonusauskas, C. Ludwig, A. Rodger, N. Spencer, J. S. Vyle, J. Wilkie, Z.-Y. Zhao and J. H. R. Tucker, *Org. Biomol. Chem.*, 2018, 6576.
10. R. T. Ranasinghe and T. Brown, *Chem. Commun.*, 2005, 5487.
11. K. Nakatani, *Chembiochem*, 2004, **5**, 1623.
12. H. Davies, G. R. Bignell, C. Cox, P. Stephens, S. Edkins and S. Clegg, *Nature*, 2002, **417**, 949.
13. E. Tiacci, V. Trifonov, G. Schiavoni, A. Holmes, W. Kern, M. P. Martelli, A. Pucciarini, B. Bigerna, R. Pacini, V. A. Wells, P. Sportoletti, V. Pettrossi, R. Mannucci, O. Elliott, A. Liso, A. Ambrosetti, A. Pulsoni, F. Forconi, L. Trentin, G. Semenzato, G. Inghirami, M. Capponi, F. DeRaimondo, C. Patti, L. Arcaini, P. Musto, S. Pileri, C. Haferlach, S. Schnittger, G. Pizzolo, R. Foa, L. Farinelli, T. Haferlach, L. Pasqualussi, R. Rabadan and B. Falini, *N Engl J Med*, 2011, **364**, 2305.
14. M. Sobrinho-Simoes, A. Preto, A. S. Rocha, P. Castro, V. Maximo, E. Fonesca and P. Soares, *Virchows Arch*, 2005, **447**, 787.
15. W. O. Greaves, S. Verma, K. P. Patel, M. A. Davies, B. A. Barkoh, J. M. Galbincea, H. Yao, A. J. Lazar, K. D. Aldape, L. J. Medeiros and R. Luthra, *J Mol Diagn*, 2013, **15**, 220.
16. G. Egger, G. Liang, A. Aparicio and P. A. Jones, *Nature*, 2004, **429**, 457.

17. P. A. Jones and D. Takai, *Science*, 2001, **293**, 1068.
18. P. A. Jones and S. B. Baylin, *Nat. Rev. Genet.* , 2002, **3**, 415.
19. W. M. Rideout, G. A. Coetzee, A. F. Olumi and P. A. Jones, *Science*, 1990, **249**, 1288.
20. R. Z. Chen, U. Pettersson, C. Beard, L. Jackson-Grusby and R. Jaenisch, *Nature*, 1998, **395**, 89.
21. S. Gonzalo and M. A. Blasco, *Cell Cycle*, 2005, **4**, 752.
22. J.-L. H. A. Duprey, J. Carr-Smith, S. L. Horswell, J. Kowalski and J. H. R. Tucker, *J. Am. Chem. Soc.*, 2016, **138**, 746.
23. S. L. Beaucage and M. H. Caruthers, *Tetrahedron Lett.*, 1981, **22**, 1859.
24. S. Kosuri and G. M. Church, *Nat Methods*, 2014, **11**, 499.
25. S. Verma and F. Eckstein, *Annu Rev Biochem*, 1998, **67**, 99.
26. W. Xu, K. M. Chan and E. T. Kool, *Nat. Chem.* , 2017, **9**, 1043.
27. D. C. Ward, E. Reich and L. Stryer, *J. Biol. Chem.*, 1969, **244**, 1228.
28. P. Wu, T. M. Nordlund, B. Gildea and L. W. McLaughlin, *Biochemistry*, 1990, **29**, 6508.
29. M. E. Hawkins, W. Pfeleiderer, A. Mazumder, Y. G. Pommier and F. M. Balis, *Nucleic Acids Res.* , 1995, **23**, 2872.
30. M. E. Hawkins, W. Pfeleiderer, F. M. Balis, D. Porter and J. R. Knutson, *Anal. Biochem.*, 1997, **244**, 86.
31. M. E. Hawkins, *Cell Biochem. Biophys.*, 2001, **34**, 257.
32. M. E. Hawkins, W. Pfeleiderer, O. Jungmann and F. M. Balis, *Anal. Biochem.*, 2001, **298**, 231.
33. F. Godde, J. J. Toulme and S. Moreau, *Biochemistry*, 1998, **37**, 13765.
34. R. X. Ren, N. C. Chaudhuri, P. L. Paris, S. Rumney and E. T. Kool, *J. Am. Chem. Soc.* , 1996, **118**, 7671.
35. X. Liang, H. Asanuma, H. Kashida, A. Takasu, T. Sakamoto, G. Kawai and M. Komiyama, *J. Am. Chem. Soc.*, 2003, **125**, 16408.

36. H. Kashida, M. Tanaka, S. Baba, T. Sakamoto, G. Kawai, H. Asanuma and M. Komiyama, *Chem. Eur. J.*, 2006, **12**, 777.
37. H. Kashida, T. Fujii and H. Asanuma, *Org. Biomol. Chem.*, 2008, **6**, 2892.
38. S. Berndl, S. D. Dimitrov, F. Menacher, T. Fiebig and H. A. Wagenknecht, *Chem. Eur. J.*, 2016, **22**, 2386.
39. E. Socher, D. V. Jarikote, A. Knoll, L. Roglin, J. Burmeister and O. Seitz, *Anal. BioChem.*, 2008, 318.
40. O. Kohler, D. Venkatrao, D. V. Jarikote and O. Seitz, *ChemBioChem*, 2005, **6**, 69.
41. L. J. Engle, C. L. Simpson and J. E. Landers, *Oncogene*, 2006, **25**, 1594.
42. S. Tyagi and F. R. Kramer, *Nat. Biotechnol.*, 1996, **14**, 303.
43. P. Zhang, T. Beck and W. Tan, *Angew. Chem. Int. Ed.*, 2001, **40**, 402.
44. J. Guo, J. Ju and N. J. Turro, *Anal. Bioanal. Chem.*, 2012, **402**, 3115.
45. P. J. Santangelo, B. Nix, A. Tsourkas and G. Bao, *Nucleic Acids Res.*, 2004, **32**, 57.
46. F. E. A. McGuigan and S. H. Ralston, *Psychiatric Genetics*, 2002, **12**, 133.
47. P. M. Holland, R. D. Abramson, R. Watson and D. H. Gelfand, *Proc. Natl. Acad. Sci. U.S.A*, 1991, **88**, 7278.
48. K. J. Livak, S. J. A. Flood, J. Marmaro, W. Giusti and K. Deetz, *Genome Res.*, 1995, **4**, 357.
49. N. Thelwell, S. Millington, A. Solinas, J. Booth and T. Brown, *Nucleic Acids Res.*, 2000, **28**, 3752.
50. L. Dong, S. Wang and B. Fu, *Sci Rep*, 2018, **8**, 9650.
51. A. Okamoto, Y. Saito and I. Saito, *J. Photochem. Photobiol. C: Photochem. Rev*, 2005, **6**, 108.
52. A. Okamoto, K. Kanatani and I. Saito, *J. Am. Chem. Soc.*, 2004, **126**, 4820.
53. A. Okamoto, Y. Saito and I. Saito, *J. Photochem. Photobiol C: Photochem. Rev.*, 2005, **6**, 108.
54. M. E. Ostergaard, P. Kumar, B. Baral, D. C. Guenther, B. A. Anderson, F. M. Ytreberg, L. Deobald, A. J. Paszczyński, P. K. Sharma and P. J. Hrdlicka, *Chem. Eur. J.*, 2011, **17**, 3157.
55. H. Haga, R. Yamada, Y. Ohnishi, Y. Nakamura and T. Tanaka, *J. Hum. Genet.*, 2002, **47**, 605.

56. Q. Xiao, R. T. Ranasinghe, A. M. P. Tang and T. Brown, *Tetrahedron Lett.*, 2007, **63**, 3483.
57. Y. Saito, K. Motegi, S. S. Bag and I. Saito, *Bioorg. Med. Chem.*, 2008, **16**, 107.
58. N. Moran, D. M. Bassani, J.-P. Desvergne, S. Keiper, P. A. S. Lowden, J. S. Vyle and J. H. R. Tucker, *Chem. Commun.*, 2006, 5003.
59. Z. Zhao, M. San, J. H. A. Duprey, J. R. Arrand, J. S. Vyle and J. H. R. Tucker, *Bioorg. & Med. Chem. Lett.*, 2012, **22**, 129.
60. J.-L. H. A. Duprey, Z.-Y. Zhao, D. M. Bassani, J. Manchester, J. S. Vyle and J. H. R. Tucker, *Chem. Commun.*, 2011, **47**, 6629.
61. J.-L. H. A. Duprey, G. A. Bullen, Z.-y. Zhao, D. M. Bassani, A. F. A. Peacock, J. Wilkie and J. H. R. Tucker, *ACS Chem. Biol.*, 2016, **11**, 717.
62. B. Chowdhury, I.-H. Cho and J. Irudayaraj, *Journal of Biological Engineering*, 2017, **11**.
63. S. Nigam and S. Rutan, *Applied Spectroscopy*, 2001, **55**, 362.
64. J. Riedl, R. Pohl, N. P. Ernsting, P. Orsag, M. Fojta and M. Hocek, *Chem. Sci.*, 2012, **3**, 2797.
65. D. Dziuba, P. Pospisil, J. Matyasovsky, J. Brynda, D. Nachtigallova, L. Rulisek, R. Pohl, M. Hof and M. Hocek, *Chem. Sci.*, 2016, **7**, 5775.
66. B. Y. Michel, D. Dziuba, R. Benhida, A. P. Demchenko and A. Burger, *Front. Chem.*, 2020, **8**, 112.
67. M. Weinberger, F. Berndt, R. Mahrwald, N. P. Ernsting and H.-A. Wagenknecht, *J. Org. Chem.*, 2013, **78**, 2589.
68. A. Okamoto, K. Tainaka and Y. Fujiwara, *J. Org. Chem.*, 2006, **71**, 3592.
69. M. S. Noe, A. C. Ros and Y. Tor, *Org. Lett.*, 2012, **14**, 3150.
70. G. Mata and N. W. Luedtke, *Org. Lett.*, 2013, **15**, 2462.
71. K. Tainaka, K. Tanaka, S. Ikeda, K.-I. Nishiza, T. Unzai, Y. Fujiwara, I. Saito and A. Okamoto, *J. Am. Chem. Soc.*, 2007, **129**, 4776.
72. X. Poteau, A. I. Brown, R. G. Brown, C. Holmes and D. Matthew, *Dyes Pigm.*, 2000, **47**, 91.

73. J. R. Lakowicz, *Principles of fluorescence spectroscopy*, Springer, Berlin, Germany, 3rd edn edn., 2006.
74. I. Grabtchev, T. Konstantinov, S. Guittonneau and P. Meallier, *Dyes Pigm.*, 1997, **35**, 361.
75. R. M. Duke, E. B. Veale, F. M. Pfeffer, P. E. Kruger and T. Gunnlaugsson, *Chem. Soc. Rev.*, 2010, **39**, 3936.
76. S. Banerjee, E. B. Veale, C. M. Phelan, S. A. Murphy, G. M. Tocci, L. J. Gillespie, D. O. Frimannsson, J. M. Kelly and T. Gunnlaugsson, *Chem. Soc. Rev.*, 2013, **42**, 1601.
77. T. Gunnlaugsson, C. P. McCoy, R. J. Morrow, C. Phelan and F. Stomeo, *ARKIVOC*, 2003, 216.
78. S. W. Thomas, G. D. Joly and T. M. Swager, *Chem. Rev.*, 2007, **107**, 1339.
79. M. J. Ruedas-Rama, J. D. Walters, A. Orte and E. A. H. Hall, *Analytica Chimica Acta*, 2012, **751**, 1.
80. G. Saito, D. Velluto and M. Resmini, *R. Soc. open sci.*, 2018, **5**, 172137.
81. M. H. Lee, J. S. Kim and J. L. Sessler, *Chem. Soc. Rev.*, 2015, **44**, 4185.
82. H.-Q. Dong, T.-B. Wei, X.-Q. Ma, Q.-Y. Yang, Y.-F. Zhang, Y.-J. Sun, B.-B. Shi, H. Yao, Y.-M. Zhang and Q. Lin, *J. Mater. Chem*, 2020, **8**, 13501.
83. Z. Liu, K. H. Hecker and R. L. Rill, *J. Biomol. Struct. Dyn.*, 1996, **14**, 331.
84. A. P. d. Silva, H. Q. N. Gunaratne and T. Gunnlaugsson, *Tetrahedron Lett.*, 1998, **39**, 5077.
85. G. Loving and B. Imperiali, *J. Am. Chem. Soc.*, 2008, **130**, 13630.
86. M. F. Brana, J. M. Castellano, C. M. Roldan, A. Santos, D. Vazquez and A. Jimenez, *Cancer Chemother. Pharmacol.*, 1980, **4**, 61.
87. K. A. Stevenson, S.-F. Yen, N.-C. Yang, D. W. Boykin and W. D. Wilson, *J. Med. Chem.* , 1984, **27**, 1677.
88. E. B. Veale, D. O. Frimannsson, M. Lawler and T. Gunnlaugsson, *Org. Lett.*, 2009, **11**, 4040.
89. S. Roy, S. Saha, R. Majumdar, R. R. Dighe and A. R. Chakravarty, *Inorg. Chem.* , 2009, **48**, 9501.
90. G. J. Ryan, S. Quinn and T. Gunnlaugsson, *Inorg. Chem.*, 2008, **47**, 401.

2. Techniques

2.1. Automated Solid-Phase DNA Synthesis

Since the synthesis of the first dinucleotide in 1955,⁹¹ oligonucleotide synthesis has progressed significantly. Driven by the work by Caruthers *et al.*, automated synthesis methods using phosphoramidite chemistry were developed to synthesise long oligonucleotides up to 100 nucleobases in length.^{23, 92} An automated solid-phase synthesis method was used in this work which performed the stepwise building of the oligonucleotide, one nucleotide at a time in a 3'-5' direction. The synthesis occurs whilst bound to a solid support/resin; in this work, controlled pore glass (CPG) was used as the solid support. This method allows for the incorporation of modifications into the oligonucleotide sequence providing that the modifications can be phosphitylated to produce the phosphoramidite monomers, the essential building blocks for DNA synthesis. The benefits of using automated solid-phase DNA synthesis over solution-based methods is that they are typically quicker and higher yielding. This is owing to the large excess of reagents that can be passed through the solid support, forcing the coupling reaction to completion. Any impurities and unwanted reagents can be easily removed by washing steps, removing the need for subsequent purification.⁹³

2.1.1. Preparation of Phosphoramidite Monomers

To construct a DNA strand *via* the phosphoramidite method, the 3' hydroxyl group of the nucleoside monomer (or modifications) must be phosphitylated with a phosphoramidite group; this will form a phosphate group during the DNA synthesis procedure. Any remaining nucleophilic sites, such as the 5'-hydroxyl group, must be protected to ensure the regioselectivity of the coupling reactions. Figure 2.1 demonstrates the nucleophilic sites of natural nucleosides. A trityl protecting group is coupled to the 5'-hydroxyl group of the nucleoside monomer. This group is acid-sensitive and not stable to certain steps of the DNA synthesis cycle, allowing for detritylation and subsequent coupling of the next

nucleoside during the stepwise process. Other nucleophilic sites include the amine groups on the adenine, cytosine and guanine nucleobases. These sites must be protected with protecting groups that are able to withstand the DNA synthesis cycle conditions to ensure the regioselective coupling of subsequent nucleosides. Acyl groups are frequently used as protecting groups for this purpose and are shown in Figure 2.2. All protecting groups are removed after the oligonucleotide is fully synthesised.

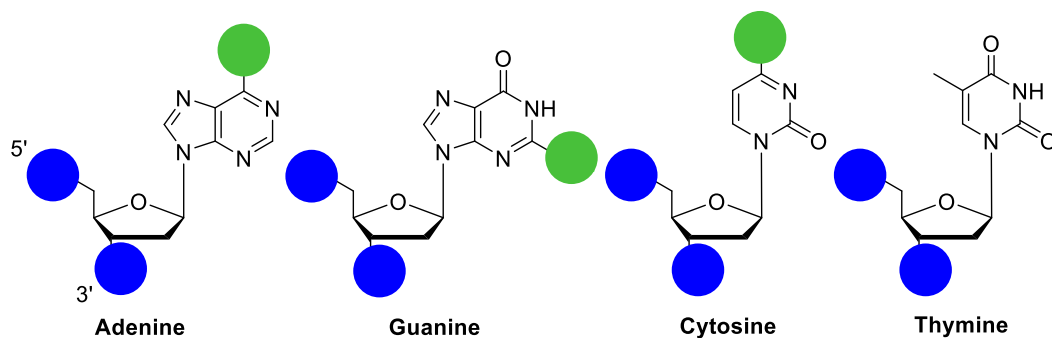


Figure 2.1: Nucleosides and their nucleophilic sites (circles). Hydroxyl groups (blue circles) on the sugar unit and amine groups (green circles) on the nucleobases must be protected for effective solid-phase DNA synthesis.

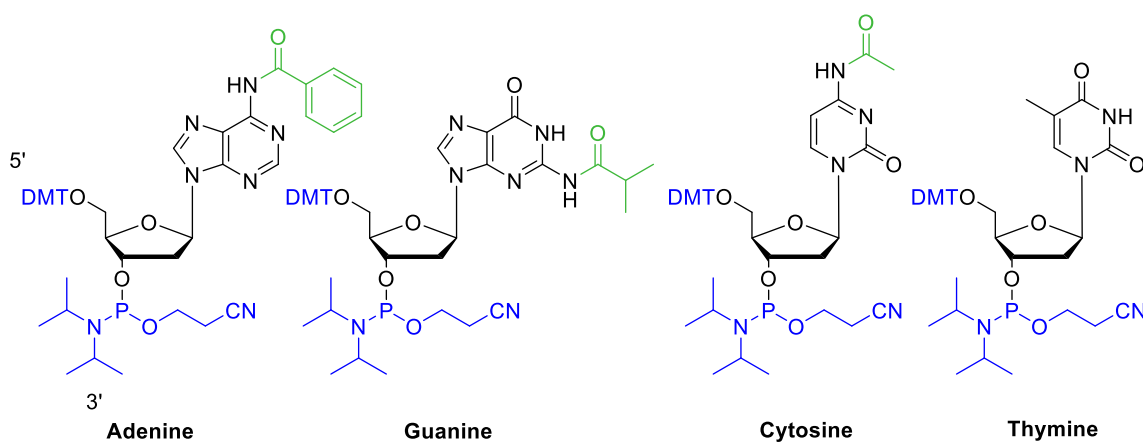
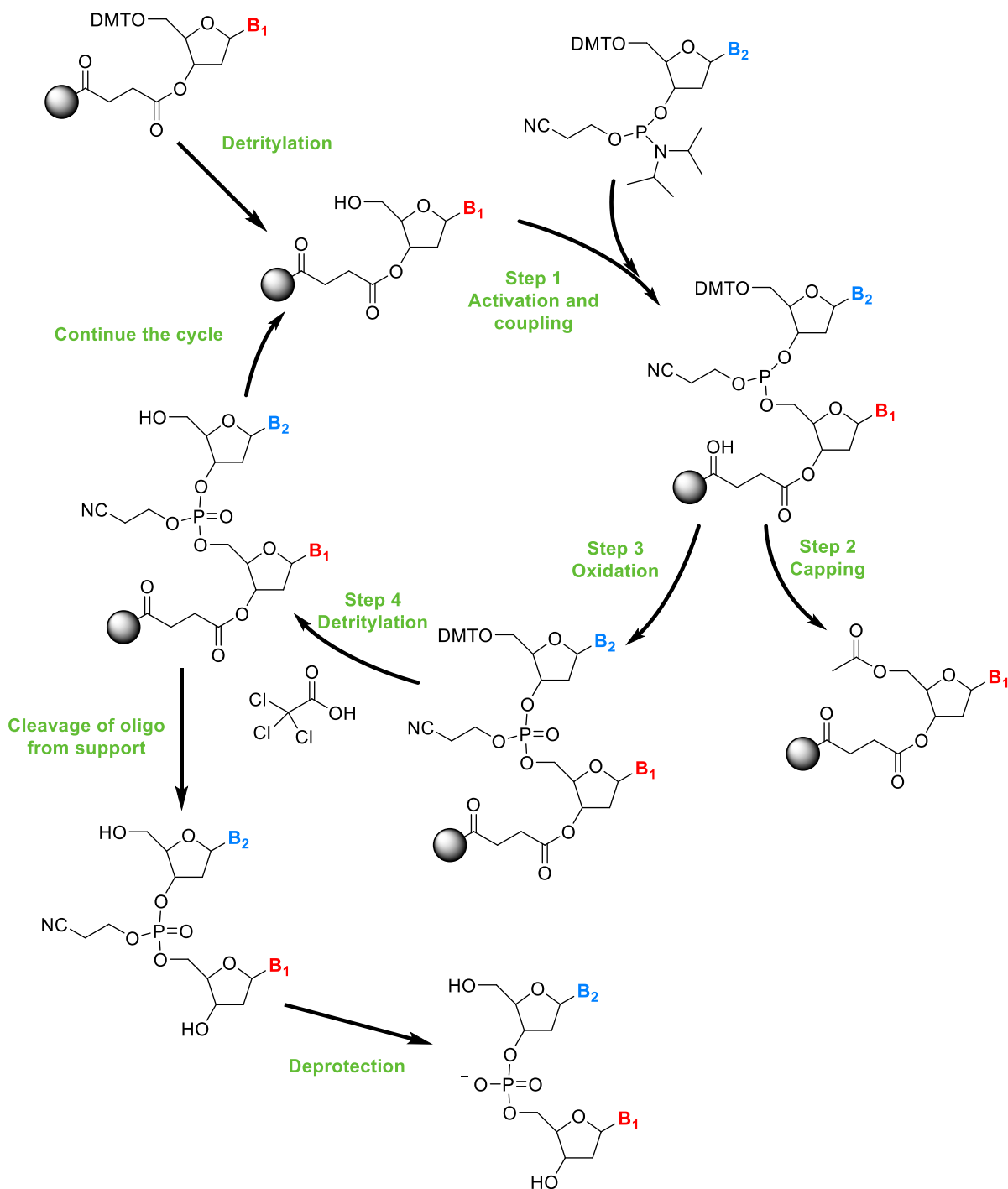


Figure 2.2: Protecting groups used on nucleoside monomers for solid-phase DNA synthesis.

Scheme 2.1 shows the stepwise DNA synthesis cycle using the solid-phase method. The steps in this cycle will now be discussed in detail.



Scheme 2.1: Solid-phase DNA synthesis cycle.

2.1.1.1. Detritylation of the Solid Support-Bound Nucleoside

The first protected nucleoside at the 3' end of the oligonucleotide to be synthesised is attached to the CPG solid support *via* a succinyl linker to the 3'-hydroxyl group. The 5'-hydroxyl group is protected with a 4,4'-dimethoxytrityl (DMT) protecting group which must then be removed in a detritylation step using trichloroacetic acid (TCA) in DCM so that the hydroxyl group is free to form a phosphodiester bond with the next nucleoside in the sequence and to begin the DNA synthesis cycle.

2.1.1.2. Step 1 - Activation and Coupling

Following detritylation, the 5'-hydroxyl group is free to react with the next nucleoside phosphoramidite. The nucleoside phosphoramidite is activated with tetrazole in acetonitrile, with the nucleoside present in excess to ensure the coupling reaction goes to completion. During the coupling reaction, a new oxygen-phosphorus bond is formed to produce the phosphite triester.

2.1.1.3. Step 2 – Capping of Unwanted Reagents

Despite the relatively high yields of the coupling step, the coupling yields are not 100% efficient. For this reason, any unreacted 5'-hydroxyl groups on the solid support-bound oligonucleotide must be capped to prevent the unwanted reaction with the next phosphoramidite in the following coupling step. This unwanted side reaction would result in a deletion mutation which could give a complex mixture of oligonucleotides in the final product and would be difficult to purify. Capping solutions of acetic anhydride and N-methylimidazole are used to prevent the unwanted side reactions.

2.1.1.4. Step 3 – Oxidation of the Phosphite Triester

The phosphite triester (P(III)) formed in previous steps must be oxidised to the stable species (P(V)) before the next detritylation step as the P(III) species is unstable to TCA. Oxidation occurs with iodine in pyridine and water. Pyridine is used to neutralise the hydrogen iodide by-product in the reaction.

2.1.1.5. Step 4 – Detritylation

At the end of the cycle, the 5'-DMT group of the solid support-bound oligonucleotide chain must be removed ready for the addition of the next nucleoside. Detritylation is achieved by addition of TCA in DCM. The detritylation step can be monitored *via* the absorbance of the removed dimethoxytrityl cation at 495 nm (which gives an orange solution). The intensity of this absorption can be used to determine the coupling efficiency of each added nucleoside.

Steps 1-4 are repeated, adding one nucleotide for each cycle until the oligonucleotide is fully synthesised. At this point, the strand can be cleaved from the CPG solid support and fully deprotected.

2.1.1.6. Cleavage from Solid Support and Deprotection

The succinyl linker is stable to all steps in the DNA synthesis cycle. However, it is removed once the desired oligonucleotide is fully synthesised by adding concentrated aqueous ammonia. This also removes the cyanoethyl protecting groups. The solution is then heated to 60 °C for 6 hours to ensure the removal of the acyl protecting groups from the nucleobases. Post cleavage and deprotection, the aqueous ammonia solution is evaporated to leave the desired oligonucleotide and any capped strands.⁹³

2.1.2. Ultramild Conditions

The final cleavage and deprotection steps involve the use of harsh conditions (heating in aqueous ammonia) which can cause sample degradation in some cases; especially those with sensitive chemical modifications. In this instance, milder deprotection conditions are used and different protecting groups are adopted on the nucleophilic sites of the nucleobases. These ultramild protecting groups, shown in Figure 2.3, are much more labile and can be removed using a methanolic solution of potassium carbonate at room temperature.⁹³

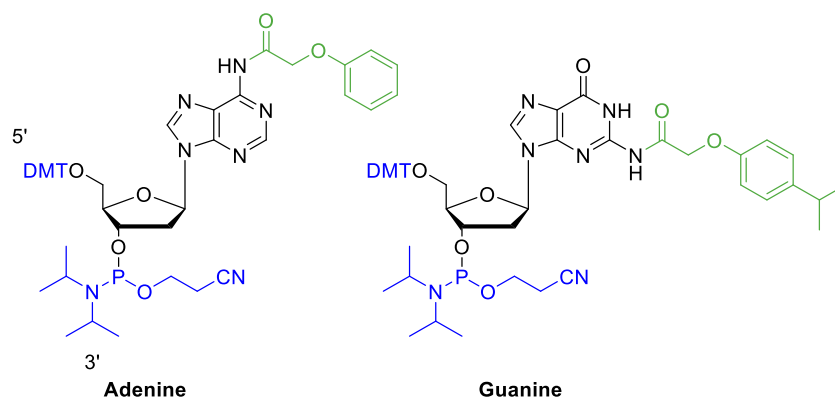


Figure 2.3: Ultramild protecting groups employed for ultramild solid-phase DNA synthesis.

In this work, ultramild conditions were used for the cleavage and deprotection of the naphthalimide modified oligonucleotides. All unmodified strands were deprotected using standard conditions.

2.2. High Performance Liquid Chromatography

High performance liquid chromatography (HPLC) is a purification technique used to separate molecules depending on their interactions with a stationary and mobile phase. Molecules in a mixture adsorb to the surface of the solid stationary phase. When the liquid mobile phase is passed through the stationary phase under high pressure, molecules desorb from the stationary phase surface and dissolve into the liquid mobile phase. Each molecule in the mixture interacts to varying extents with the stationary and mobile phases depending on the polarity of the molecules and their affinity to interact with the two phases. The stationary phase (often silica based) is polar, and the mobile phase is non-polar. Therefore, more polar molecules have a higher affinity for the polar stationary phase and take longer to elute. On the other hand, non-polar molecules have a greater affinity to the non-polar mobile phase and easily desorb from the stationary phase into the mobile phase to elute quicker. The eluent is monitored using UV-Vis or fluorescence and peaks arise when the analyte passes through the detector at a set wavelength.

2.2.1. Reversed-Phase High Performance Liquid Chromatography

Reversed-phase high performance liquid chromatography (RP-HPLC) differs from standard HPLC as the stationary phase is made non-polar by coating it with hydrocarbon chains, typically C18 molecules. A polar mobile phase is then used, for example water.⁹⁴ Hydrophilic molecules such as oligonucleotides are better suited to this method and oligonucleotides with lengths between 8-40 nucleobases can be separated using this method. RP-HPLC can also successfully separate modified oligonucleotides from unmodified. Longer oligonucleotides contain more hydrophobic nucleobases and retain longer on the stationary phase compared to shorter oligonucleotides, thus eluting at longer times. In this work, the mobile phase used is 0.1 M triethylammonium acetate (TEAA), pH 7.0, with an increasing gradient of acetonitrile. The addition of TEAA to the mobile phase causes ion-pairing. The triethylammonium molecules indirectly increase the interactions between the oligonucleotide and the stationary phase and this enhances the resolution. In addition, the pH of the mobile phase must be controlled as pH can affect the hydrophobic character of the molecules. The ion-pairing salt remains in the purified DNA sample and must be removed before further studies are performed using a NAP-10 desalting column.

^{95, 96}

2.3. Mass Spectrometry

Mass spectrometry is a technique used to determine the molecular weight of compounds and is the main method for characterising oligonucleotides of a known sequence.⁹⁷ This technique ionises a sample and then analyses the ions that are formed by their mass-to-charge ratio (m/z). Mass spectrometers consist of an ionisation source, mass analyser and an ion detector. The main ionisation methods used for DNA characterisation are electrospray ionisation (ESI) and matrix assisted laser desorption ionisation (MALDI), both of which are soft ionisation techniques. The introduction of these ionisation methods made it possible to analyse larger nucleic acids.⁹⁸ Once ionised, the ions are then accelerated through electric/magnetic fields, with the same kinetic energy. The electric/magnetic field

deflects the ions to differing extents depending upon their mass-to-charge ratio. This creates an ion beam which enters the mass analyser where their mass-to-charge ratio (m/z) is determined. The detection method uses a time-of-flight (TOF) detector in which lower mass species reach the detector first. Whilst mass spectrometry is a destructive technique, only a small amount of sample is injected.⁹⁹

2.3.1. Matrix Assisted Laser Desorption Ionisation

Karas and Hillenkamp first reported the MALDI method in 1988.¹⁰⁰ The MALDI method describes a 'matrix' containing a small amount of analyte which is then ionised by a short laser pulse. This produces ions that are predominantly singly charged (+1) *via* protonation. For oligonucleotide characterisation, the matrix solution often consists of 3-hydroxypicolinic acid. The MALDI method is a fast process (milliseconds) and enables the analysis of complex mixtures.

2.3.2. Electrospray Ionisation

ESI has been used for many years for the characterisation of organic compounds. However, Fenn *et al.* was the first to discover the use of ESI method for the analysis of biomolecules.¹⁰¹ In ESI-MS, a needle injector sprays the liquid sample into the mass spectrometer under the presence of an electric field. For biomolecules, the ionisation process produces species with multiple charges.

2.3.3. Data Analysis

For MALDI methods, the m/z signals given in a spectrum correspond to the singly charged species of the molecular ion and a proton. The molecular mass is determined by simple subtraction of the mass of a proton from the given signal.

For ESI methods, mass determination is more complex because of the multiply charged species present. Raw data from ESI-MS displays several clusters of signals, with each cluster corresponding to the various charged species. To determine the charge of the species relating to a particular cluster of signals, the spacing between each signal in the cluster is calculated and the inverse of this value

equates to the charge. The signal is then multiplied by the charge and the charge then added to compensate for the protons lost during ionisation to determine the final mass. The raw data can be processed using deconvolution software to give a single signal, with the m/z value the same as the mass. All mass spectra presented in this work are shown as the processed spectra.

2.4. DNA Thermal Melting

In solution, under physiological conditions, DNA strands are held together to form a secondary helical duplex structure *via* hydrogen bonding interactions between base pairs. During biological processes such as DNA transcription, the DNA strands unwind. This cellular DNA unwinding can be replicated with solutions of purified DNA. In the 1950s it was found that heating DNA solutions above room temperature causes the unwinding of DNA into separate single-stranded DNA.^{102, 103} The temperature at which 50% of the double-stranded DNA is denatured to single-stranded DNA is known as the melting temperature (T_m).¹⁰⁴

In this work, thermal melting experiments use heat to denature the DNA. DNA denaturation is monitored *via* fluorescence using the DNA intercalating dye, SYBR Green. SYBR Green is a well-known DNA intercalating dye that is highly fluorescent when intercalating within the duplex. Its fluorescence intensity diminishes when no longer in an intercalating position. These fluorescent properties are ideal for monitoring the denaturation of DNA duplexes of a reasonable length.^{105, 106} The duplex DNA sample, combined with SYBR Green, is heated in small increments to slowly denature the DNA duplex until the point of full denaturation. The fluorescence intensity of the SYBR Green is monitored at each temperature point. The denatured sample is then slowly cooled so the DNA strands anneal to reform the duplex (thermal cooling). A melt curve can then be plotted, showing the fluorescence emission of the SYBR Green as a function of temperature. Figure 2.4 shows an example of a thermal melt curve. The melting temperature of the duplex, T_m , is calculated from the midpoint on the curve, as highlighted in Figure 2.4. The T_m value correlates with duplex stability; a higher T_m value is a result of a more stable

duplex. The T_m value is very sensitive to salt concentration, pH and the DNA concentration. A higher salt concentration will aid duplex stability and cause an increase in the T_m . It is important to keep these factors constant between experiments so that results can be accurately compared. SYBR Green is also known to affect the T_m values by raising the melting temperatures by roughly 10 °C.¹⁰⁷ This increase must be accounted for when comparing duplex melting temperatures obtained *via* other methods, such as UV absorption. Duplexes that are GC rich have higher melting temperatures owing to the increased energy required to break the three hydrogen bond interactions compared to the two hydrogen bonds formed between a AT base pair. In addition, DNA modifications may disrupt DNA stability and therefore reduce the melting temperature of the duplex. The extent of disruption caused by modifications can be monitored using thermal melting experiments and comparing to the unmodified duplex analogue.

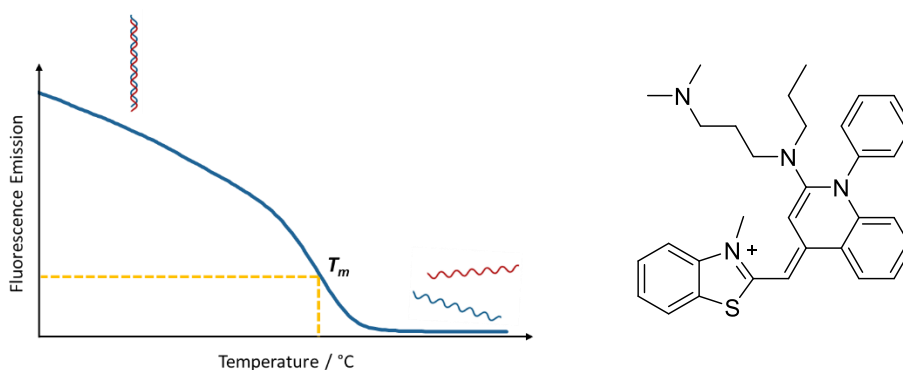


Figure 2.4: Thermal melting curve using the fluorescence emission of an intercalating dye, such as SYBR Green (right), to measure the T_m value of a duplex.

2.5. Ultraviolet Visible Spectroscopy

Ultraviolet visible (UV-Vis) spectroscopy is a technique used to determine the absorbance profile of a molecule. Light energy is used to excite electrons within a molecule *via* the absorption of UV or visible light energy (photons). During the excitation process and the absorption of photons, the excess energy obtained by the molecules is used to move electrons from the highest occupied molecular orbital

(HOMO) to the lowest unoccupied molecular orbital (LUMO). The relationship between the energy difference of the ground and excited state and the wavelength is described by Planck's equation, Equation 2.1.

Equation 2.1: Planck's equation. Where E is energy, h is Planck's constant, v is the frequency, c is the speed of light and λ is the wavelength.

$$\Delta E = h\nu = hc/\lambda$$

The spectrometer 'counts' the number of photons entering a sample and relates it with the number of photons exiting the sample. The spectrometer passes a monochromatic beam through the sample at a set wavelength, allowing examination with around 1 nm resolution.

As the monochromatic light beam is passed through an absorbing sample from the spectrophotometer to the detector, the intensity of light leaving the sample to the detector (transmitted light, I) is less than that of the light sent to the sample from the spectrophotometer (incident light, I_0). The transmittance (T) of light gives an indication of what light entering the sample was found to excite the sample and can be calculated by measuring the incident light (I_0) and comparing it with the transmitted light (I) as demonstrated in Equation 2.2.

Equation 2.2: Transmittance (T) of light. Where I is the light exiting the sample (transmitted light) and I_0 is the light entering the sample (incident light).

$$T = \left(\frac{I}{I_0}\right)$$

The ratio between the incident (I_0) and transmitted light (I) can be used to calculate the absorbance (A), as demonstrated by Equation 2.3.¹⁰⁸

Equation 2.3: Relationship between absorbance (A) and the incidence light (I_0) and the transmitted light (I).

$$A = \log \left(\frac{I_0}{I}\right)$$

Using the Beer-Lambert law, Equation 2.4, the absorbance is related to the molar extinction coefficient (ϵ) of the molecule at a particular wavelength, the concentration (c) of the molecule in the sample

being measured and the pathlength (l) the light has to travel through the sample solution. The Beer-Lambert law is used in many fields of science to determine the concentration of solutions and is routinely used to determine the concentrations of DNA oligonucleotide samples.

Equation 2.4: Beer-Lambert law. Where A is absorbance, ϵ is the molar extinction coefficient, c is the concentration and l is the path length.

$$A = \epsilon cl$$

2.5.1. Molar Extinction Coefficient

The molar extinction coefficient (ϵ) is a measure of how strongly a chemical species absorbs light of a particular wavelength. It is an intrinsic property that is dependent upon the chemical structure and composition.

Molar extinction coefficients are calculated for each oligonucleotide by adding the extinction coefficients for each nucleobase in the sequence and considering the effects from neighbouring bases.¹⁰⁹ In this work, for modified sequences, the molar extinction coefficients of the modifications were determined experimentally. This value was then added to the total molar extinction coefficients of the flanking DNA sequences. The molar extinction coefficients for unmodified DNA sequences in this work were calculated using ChemDraw.

2.5.2. Determining Oligonucleotide Concentrations

The Beer-Lambert law is routinely used to determine the concentrations of aqueous oligonucleotide samples. Using a set wavelength at 260 nm, where the DNA bases π - π^* transition occurs, the absorbance value of a sample can be determined.¹¹⁰

In this work, concentrations were determined using the BioSpec-nano Spectrophotometer; a UV-Vis technique that allows DNA quantification at low volumes. This method uses only a small amount of sample for quantification (1-2 μ L droplets). An optical density value at 260 nm is obtained which can

be used to determine the concentration using the Beer-Lambert law (Equation 2.4). The software accounts for the pathlength, l , and so this can be ignored in any calculations.

2.6. Fluorescence Spectroscopy

Fluorescence is a luminescence process caused by the excitement of a molecule using photons (light energy) to an electronic excited state. Relaxation from a singlet excited state produces a photon of energy (light) and is known as fluorescence. Relaxation from the triplet state is known as phosphorescence and is not associated with this work.

The simplified Jablonski diagram shown below, Figure 2.5, demonstrates the absorption of photons by molecules to produce the first (S_1) or second (S_2) singlet excited states. Excitation can cause the molecules to reach any of the vibrational sub-levels associated with each electronic state. There are also rotational levels associated with each vibrational level; these additional rotational bands increase the number of possible absorption bands to an extent that it becomes impossible to resolve each individual transition. Therefore, most molecules only have broad absorption bands where rotational levels are restricted. Vibrational fine structure may be present in the absorption or fluorescence spectrum if permitted.

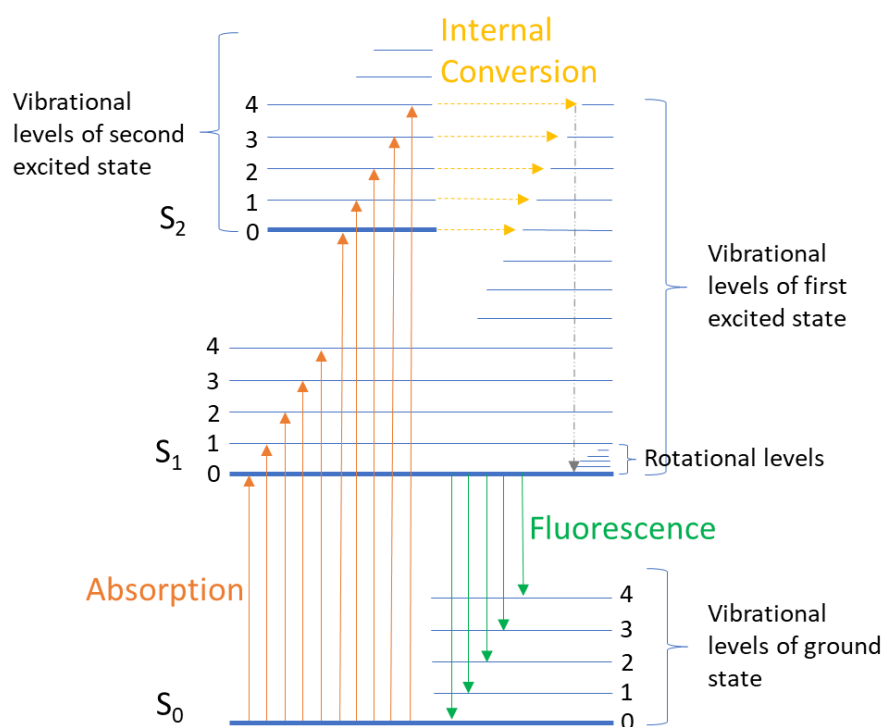


Figure 2.5: Simplified Jablonski diagram showing the transitions giving rise to absorption and fluorescence emission spectra.

After absorbing energy and reaching one of the higher vibrational levels of the excited state, the molecule then relaxes down to the lowest vibrational level of the first excited state, S_1 . If a molecule occupies an electronic excited state above the second excited state, S_2 , then a process of internal conversion (IC) allows the molecule to pass from the lower vibrational level of the higher electronic state to a higher vibrational level of a lower electronic state of similar energy. The molecule now relaxes down the lowest vibrational level of the first excited state, S_1 . Once the molecule reaches the lowest vibrational level of the first electronic state, S_1 , the molecule passes to any of the vibrational levels associated with the ground state, emitting light as it goes.¹¹¹

The 0-0 transition, a transition from the lowest vibrational level in the ground state to the lowest vibrational level in the first excited state, S_1 , is common in both the absorption and emission spectra. Hence, the absorption and emission spectra overlap at a wavelength that corresponds to this transition. All other transitions require more energy for absorption in comparison to fluorescence, due

to non-radiative processes (for example, IC) that can occur after absorption and lead to a reduction in energy. This results in fluorescence bands appearing at higher wavelengths than the absorption bands. The difference in wavelength between the absorption and emission profiles is known as the Stokes Shift.¹¹² An emission spectrum is produced as a plot of emission intensity against wavelength for any given excitation wavelength.

A fluorimeter consists of a source of light (typically an Xenon arc lamp), a sample holder and a detector (photomultiplier tubes). The incident radiation and detector must be selectable for a specified wavelength; this can be achieved using monochromators. A right-angled collection method is used to minimise any light scattering from the sample solution or cell.

2.6.1. Fluorescence Quantum Yields

The fluorescence quantum yield (Φ_F) is described as the ratio of the number of photons emitted through fluorescence to the number of photons absorbed by the molecule (Equation 2.5). Φ_F describes the efficiency of deactivation of the excited state *via* the fluorescence pathway compared to other non-radiative deactivation pathways.¹¹³

Equation 2.5: Simple representation of the fluorescence quantum yield, Φ_F .

$$\Phi_F = \frac{\text{Number of photons emitted through fluorescence}}{\text{Number of photons absorbed}}$$

There are two methods for measuring the fluorescence quantum yield; the relative method and the absolute method, with the former method being used for this work. The absolute method requires the use of an integrating sphere to collect all the photons emitted from the sample. The Φ_F is then calculated simply by comparing the number of emitted photons with the number of absorbed photons. This method allows the measurement to be taken in a single reading.^{114, 115} On the other hand, the relative method requires the use of well-characterised reference standards with similar optical properties to that of the sample being measured and is the most common method for measuring Φ_F .

Using this method, the integrated fluorescence intensity of an unknown sample is compared to that of a reference sample with known Φ_F .¹¹⁶ The absorbance and the integrated fluorescence intensity of the reference and unknown sample is recorded at a specified excitation wavelength. For improved accuracy, several measurements are taken for each sample over a range of absorbances. A calibration curve is then plotted using absorbance vs integrated fluorescence intensity to determine Φ_F , as demonstrated by Equation 2.6.

Equation 2.6: Determining the quantum yield of an unknown sample (Q_S) using the relative method. Quantum yield of reference sample (Q_R), absorbance of reference (A_R) and unknown sample (A_S), integrated fluorescence intensity of reference (F_R) and unknown sample (F_S), refractive index of reference solvent (η_R) and unknown sample solvent (η_S).

$$Q_S = Q_R \left(\frac{A_R}{A_S} \right) \left(\frac{F_S}{F_R} \right) \left(\frac{\eta_S}{\eta_R} \right)^2$$

2.7. Polymerase Chain Reaction

The polymerase chain reaction (PCR) was discovered by K. Mullis in the 1980s and has revolutionised the study of DNA. The polymerase chain reaction is a technique used to amplify small sections of DNA. It is a relatively fast and inexpensive technique and without it, the analysis of isolated pieces of DNA would be almost impossible.

The mechanism for DNA amplification is based on the DNA replication process in an organism, in particular, the ability of the DNA polymerase enzyme to synthesise a new strand of DNA which is complementary to the template strand. A *Taq* polymerase enzyme is used for PCR amplification. *Taq* polymerase requires a primer as a starting point for the PCR to which the first nucleobase can be added. The primers define the region of DNA to be amplified.

The PCR master mix contains all the components required for PCR amplification to occur, including *Taq* polymerase, forward and reverse primers, template DNA and free nucleotides. The samples are then

put through repeated cycles of heating and cooling that allow the synthesis of the DNA strands. Each PCR cycle involves the following steps and is demonstrated in Figure 2.6:

1. Denaturation – The reaction is heated to around 96 °C to denature the template DNA in the sample. This results in single-stranded DNA ready for the next step.
2. Annealing – The reaction is cooled to roughly 55-65 °C (depending on the primers used) to allow the primers to bind to their complementary regions on the single-stranded template DNA.
3. Extension – The temperature is raised so that *Taq* polymerase can extend the primer sequence by addition of the free nucleotides.

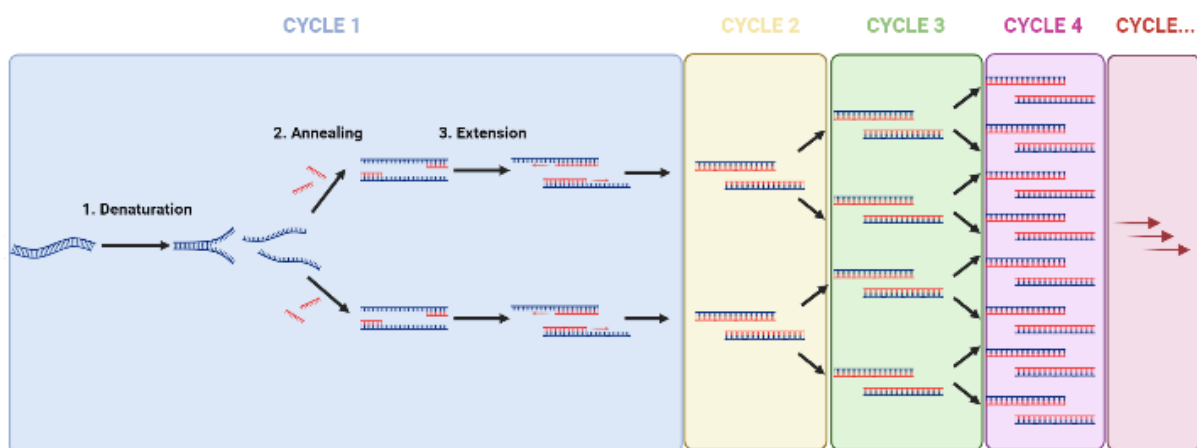


Figure 2.6: Schematic representation demonstrating the various steps involved in a PCR cycle, with each cycle amplifying DNA exponentially.

This cycle is repeated roughly 25-35 times, resulting in the production of millions (or even billions) of copies of the region of interest, providing the reaction was efficient. The DNA is amplified exponentially as any new DNA that is made is used in subsequent cycles to provide template DNA for the synthesis, as shown in Figure 2.6.

The success of PCR experiments are often checked using gel electrophoresis, by comparison of the PCR amplicon with a DNA ladder, showing the predicted length of the amplicon.

2.8. Gel Electrophoresis

Gel electrophoresis is a method used for the separation and analysis of biomolecules such as DNA and proteins. Separation of molecules and their fragments is based on shape/conformation, size and charge.

A mixture of nucleic acid molecules can be separated based on their size by passing an electric field through a gel polymer matrix from a positive to negative electrode. DNA molecules are loaded onto the gel at the positive electrode. When current is passed through the gel, DNA molecules migrate towards the negative electrode, as DNA molecules are negatively charged. Smaller/shorter molecules migrate through the gel pores faster and further, while the movement of larger/longer molecules through the gel pores is more hindered and so they remain closer to the positive electrode.¹¹⁷ This is depicted in Figure 2.7.

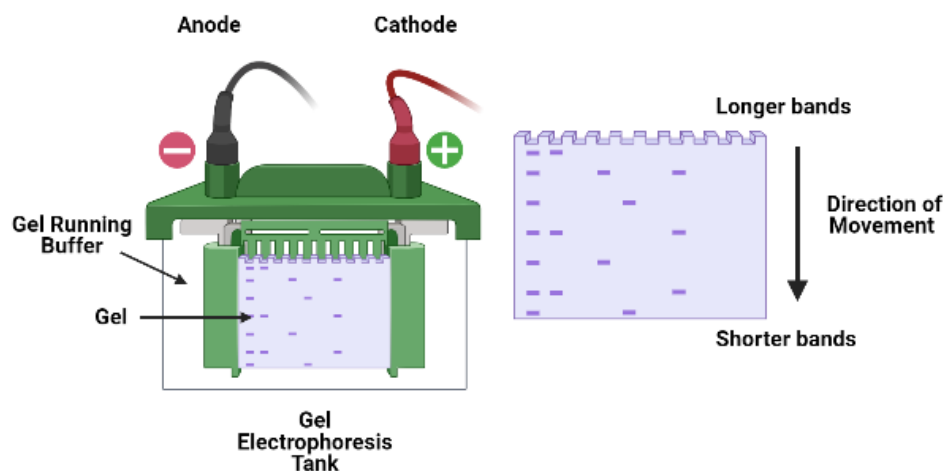


Figure 2.7: Diagram showing a gel electrophoresis set up for PAGE. The resulting gel shows the separation of bands by the varied movement down the gel.

The gels are cast containing lanes to which samples can be loaded. Dyes can be run alongside samples to indicate the expected electrophoretic mobilities of the DNA samples during the run. The voltage that is passed through the gel can be adapted to aid resolution and alter the run time. The running

buffer used may also have an effect. Post run, the gel is stained with a dye to aid the visualisation of any DNA bands.

Typically, agarose and polyacrylamide gel types are used, with preference for each depending on the type and size of the analyte. These two gel types are discussed below.

2.8.1. Polyacrylamide Gel Electrophoresis (PAGE)

Polyacrylamide gels are commonly used for smaller DNA fragments, such as the oligonucleotide strands synthesised in this research, with a range of 5-500 base pairs (bp) and they provide high resolving power. The pore sizes generated in the polyacrylamide gel matrix are much smaller than those when using agarose gels and so are more well suited to smaller fragments. Pore sizes can be altered by changing the percentage of polyacrylamide used. Polyacrylamide gels are run in an electrophoresis chamber in a vertical configuration.

There are two main types of polyacrylamide gels used for the separation of DNA fragments: native and denaturing. A native gel will contain no denaturing agents and allows for any DNA interactions and confirmations to remain intact, thus allowing the study of double-stranded DNA. On the other hand, denaturing gels contain denaturing agents, such as urea, that prevent all non-covalent interactions forming (i.e. only single-stranded DNA is present).

2.8.2. Agarose Gel Electrophoresis

Typically, agarose gels have lower resolving power but can separate DNA fragments of larger sizes, in the range of roughly 50-20,000 bp due to the formation of larger pores in the gel matrix, compared to those using polyacrylamide. The pore sizes may be altered by changing the concentration of agarose used. Agarose gels are more easily cast and handled than polyacrylamide gels, which can be quite fragile. Commonly, agarose gels are used to analyse PCR products or larger DNA structures, such as DNA origami.

2.9. Fluorescence Microscopy

Fluorescence microscopy is an essential technique in biology, biomedical and life sciences. With the use of fluorophores, of which there is now a wide variety, the identification and/or visualisation of cells and sub-microscopic cellular components has been made possible using this technique. Moreover, using this technique, methods to visualise single molecules have also been established.^{118, 119} A multi-labelling approach can also be employed, utilising different fluorophores to generate probes that target different molecules within a sample simultaneously.

The key components of a microscope are:

- Light source – usually xenon arc or mercury vapor lamp but more recently, laser light sources are used to excite the specimen.
- Filters – allow only light of specific wavelengths to pass through. Excitation and emission bandpass filters may be used.
- Objective lens – transmits excitation light onto the sample and simultaneously transmits any emitted light to the detector.
- Dichroitic mirrors – reflects the excitation light onto the sample and transmits only emitted light from the sample to the detector.
- Camera/detector - to detect and visualise the light that reaches the camera/detector. Charged-coupled device (CCD)-based cameras are often used for high resolution fluorescence imaging.

2.9.1. Epifluorescence Microscopy

An inverted epifluorescence microscope was used in this research. A typical set up is demonstrated in Figure 2.8. The principle of epifluorescence microscopy involves the irradiation of a specimen at specific wavelengths to excite the sample and any emitted fluorescent light from the sample is then separated from the excitation light before it reaches the detector. This generates images that have

high resolution and high signal-to-noise ratios. If the wavelength of the excitation light is not well separated from the emitted fluorescent light, then this can lead to reduced imaging quality due to the simultaneous detection of any excited light that is reflected from optical surfaces along with the desired emitted light.¹²⁰

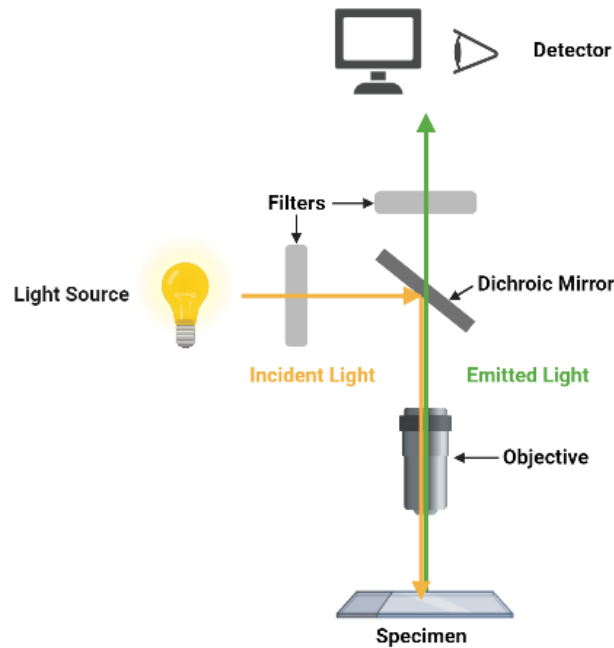


Figure 2.8: Schematic diagram of an inverted epifluorescence microscope, highlighting the key components and the direction of light travel. The incident light is shown in yellow and the emitted light from the sample in green.

The excitation light of a specific wavelength, from a laser light source in this instance, is reflected off a dichroitic mirror (mounted at 45°) at a 90° angle through the objective lens and onto the sample. Molecules in the sample absorb the light energy to become excited and then emit light energy at a longer wavelength (fluorescence) in all directions. The objective lens then collects the emitted fluorescent light from the sample, which then passes through the same dichroitic mirror. Any reflected excitation light may also be collected with the emitted light from the sample, but this is blocked by a filter before any light reaches the detector. Only emitted light from the sample reaches the detector, a CCD camera, which captures the emitted light and is visualised on a computer.¹²⁰

2.10. References

1. A. M. Michelson and A. R. Todd, *J. Chem. Soc. Perkin Trans. 2*, 1955, 2632.
2. S. L. Beaucage and M. H. Caruthers, *Tetrahedron Lett.*, 1981, **22**, 1859.
3. M. H. Caruthers, S. L. Beaucage, C. Becker, J. W. Efcavitch, E. F. Fisher, G. Galluppi, R. Goldman, P. deHaseh, M. Matteucci and L. McBride, *Gene Amplification and Analysis*, 1983, **3**, 1.
4. T. Brown, Solid-phase Oligonucleotide Synthesis, <https://www.atdbio.com/content/17/Solid-phase-oligonucleotide-synthesis>, (accessed 15/06/2020).
5. K. Ashman, A. Bosserhoff and R. Frank, *J Chromatogr.*, 1987, **397**, 137.
6. M. Gilar, K. J. Fountain, Y. Budman, U. D. Neue, K. R. Yardley, P. D. Rainville, R. J. Russell and J. C. Gebler, *Journal of Chromatography A.* , 2002, **958**, 167.
7. T. Brown, Purification of Oligonucleotides, <https://www.atdbio.com/content/7/Purification-of-oligonucleotides>, (accessed 16/06/2020).
8. B. Guo, *Anal. Chem.* , 1999, **71**, 333.
9. D. Fabris, *J. Am. Chem. Soc. Mass Spectrom*, 2010, **21**, 1.
10. W. M. Albers, A. Annala, N. J. G. G. Patonay and E. Soini, *Handbook of Spectroscopy*, WILEY, Weinheim, 2003.
11. M. Karas and F. Hillenkamp, *Anal. CHem.*, 1988, **60**, 2299.
12. J. B. Fenn, M. Mann and C. K. Meng, *Science*, 1989, **246**, 64.
13. R. Thomas, *Biochim. Biophys. Acta*, 1954, **14**, 231.
14. S. A. Rice and P. Doty, *J. Amer. Chem. Soc.*, 1957, **79**, 3937.
15. R. M. Wartell and A. S. Benight, *Physics Reports*, 1985, **126**, 67.
16. C. T. Wittwer, M. G. Herrmann, A. A. Moss and R. P. Rasmussen, *Biotechniques*, 1997, **22**, 130.
17. K. M. Ririe, R. P. Rasmussen and C. T. Wittwer, *Anal. Biochem.*, 1997, **245**, 154.
18. H. Gudnason, M. Dufva, D. D. Bang and A. Wolff, *Nucleic Acids Res.*, 2007, **35**, 127.

19. D. H. Williams and I. Fleming, *Spectroscopic methods in organic chemistry*, McGraw-Hill, Fifth edn., 1995.
20. Oligo Analyzer, <https://eu.idtdna.com/calc/analyzer>, 2020.
21. G. D. Fasman, *Handbook of Biochemistry and Molecular Biology*, CRC Press, 1975.
22. A. T. R. Williams, *An Introduction to Fluorescence Spectroscopy*, Perkin-Elmer, Buckinghamshire, 1981.
23. G. G. Stokes, *Phil. Trans. R. Soc.*, 1852, **142**, 463.
24. P. Atkins, J. D. Paula and J. Keeler, *Atkins' Physical Chemistry*, Oxford University Press, Oxford, 2018.
25. D. O. Faulkner, J. J. McDowell, A. J. Price, D. D. Perovic, N. P. Kherani and G. A. Ozin, *Laser Photonics Rev.*, 2012, **6**, 802.
26. L. Porres, A. Holland, A. Monkman, C. Kemp, A. Beeby and P. Lars-Olof, *Journal of Fluorescence* 2006, **16**.
27. K. Rurack, *Fluorescence Quantum Yields: Methods of Determination and Standards*, Springer, Berlin, 2008.
28. Nucleic Acid Gel Electrophoresis - A Brief Overview and History <https://www.thermofisher.com/uk/en/home/life-science/cloning/cloning-learning-center/invitrogen-school-of-molecular-biology/na-electrophoresis-education/na-separation-overview.html>, (accessed 02/02/21).
29. E. Lang, J. Baier and J. Kohler, *J. Microsc.* 2006, **222**, 118.
30. A. Triller and D. Choquet, *Neuron*, 2008, **59**, 359.
31. D. J. W. C. M. Brown, *Methods Mol Biol*, 2013, **931**, 29.

3. Synthesis and Characterisation – Fluorescent Tags and DNA

3.1. 1,8-Naphthalimide Tag Synthesis

3.1.1. Design Considerations

As outlined in Chapter 1, the use of 1,8-naphthalimides as reporter groups in DNA probes may lead to advancements in the detection of single point variations, owing to their solvatochromic properties and higher fluorescence quantum yields (in comparison to the previously studied anthracene probes).⁹ The focus of the work in this section was to produce a range of naphthalimide reporter groups to incorporate into DNA using solid-phase synthesis. The four naphthalimide tags prepared are shown in Figure 3.1. The synthesis routes for the chosen reporter groups are demonstrated in Scheme 3.1 and Scheme 3.6, and firstly involve the preparation of a diol monomer unit. This diol allows for the formation of a phosphoramidite compound that is compatible with solid-phase DNA synthesis, methods which were adapted from previous work by N. Moran.¹²¹

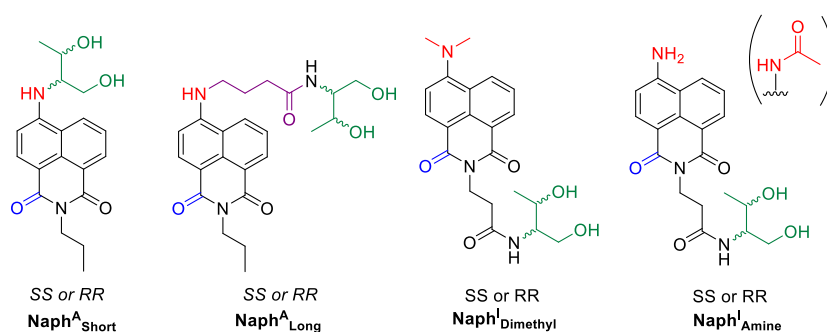


Figure 3.1: Structures of 1,8-naphthalimide tags highlighting the donor and acceptor groups in red and blue, respectively. The diol, threoninol (green), is used to mimic the pentose sugar of a nucleotide. Threoninol is chiral, hence the SS and RR isomers are produced from reaction with SS (D) and RR (L) threoninol, respectively.

Moving on from previous work in the group involving anthracene fluorophores, this research focuses on the use of 1,8-naphthalimide derivatives as reporter groups due to their improved spectroscopic and photophysical properties. In comparison to anthracene, 1,8-naphthalimides have absorption and

emission bands shifted towards higher wavelengths, removing the need for excitation at harmful UV wavelengths and minimising background fluorescence from biological environments. 1,8-Naphthalimides are also solvatochromic molecules resulting in additional sensing benefits through exhibiting spectral shifts depending on their microenvironment, as explored in Chapter 4.

The photophysical properties of 1,8-naphthalimides can be tuned depending on the substituents around the aromatic ring. The substituent must contain 'donor' character for a reasonable solvatochromic effect to occur. In this research, a variety of donor groups were adopted, as shown in red in Figure 3.1. The modification can be positioned at various points of the aromatic ring. However, only the 4-position is explored in this research as this position can be easily modified from the commercially available 4-bromo- or 4-chloro-1,8-naphthalic anhydride starting material.^{122, 123} The substituents, NH₂, NHR and NMe₂ all have differing strengths of donor character, which subsequently affects the strength of the solvatochromic effect produced.¹²³ In addition, the NH₂ substituent was selected for its potential hydrogen bonding capabilities with surrounding nucleobases once incorporated into a DNA probe strand. However, the NH₂ group must be protected before it undergoes solid-phase DNA synthesis, to prevent any unwanted side reactions occurring with the reagents used in the process. The acetyl protecting group was chosen as it is often used to protect the NH₂ groups of standard nucleoside phosphoramidite analogues.¹²⁴

It was also decided to explore the orientation of the incorporated naphthalimide tag and understand its effect on the sensing capability of the probe strand. Two approaches were chosen (shown in Figure 3.2 below):

- (i) Incorporation into the DNA backbone at the **imide** side of the naphthalimide molecule (Naph^I_{Dimethyl} and Naph^I_{Amine}), or
- (ii) Incorporation into the DNA backbone at the **aromatic** side of the naphthalimide molecule (Naph^A_{Long} and Naph^A_{Short}).

It was expected that the incorporation of the naphthalimide molecules into DNA probes *via* these two orientations would allow different interactions to take place between the reporter group and neighbouring bases and/or solvent molecules within or around the DNA duplex, which in turn would affect the sensing results. For those naphthalimide reporter groups incorporated at the aromatic face ($\text{Naph}^{\text{A}_{\text{Long}}}$ and $\text{Naph}^{\text{A}_{\text{Short}}}$), different linker lengths could also be explored. Previous work in the Tucker group has shown that varying the distance between the reporter group and DNA backbone dictates the positioning of the reporter group within the duplex and the effectiveness of tag intercalation.^{60, 125} For this reason, it was decided to connect the naphthalimide unit either directly to the diol unit or *via* an aliphatic chain consisting of three carbons. It was hypothesised that this would create a rigid and flexible system respectively that would afford different positioning of the 1,8-naphthalimide in the DNA duplex, subsequently leading to different sensing results.

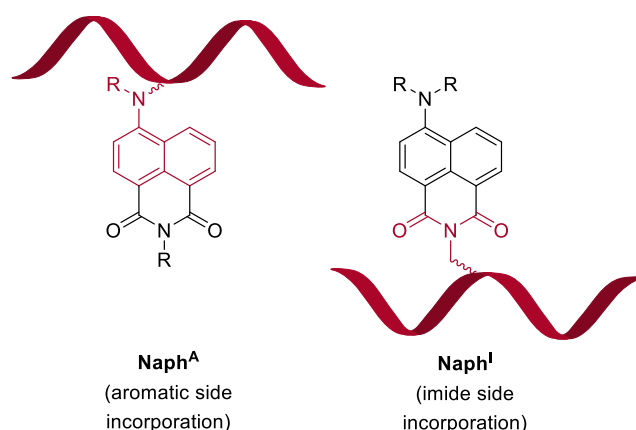


Figure 3.2: Diagram showing the different sides at which the naphthalimide molecules were incorporated into DNA.

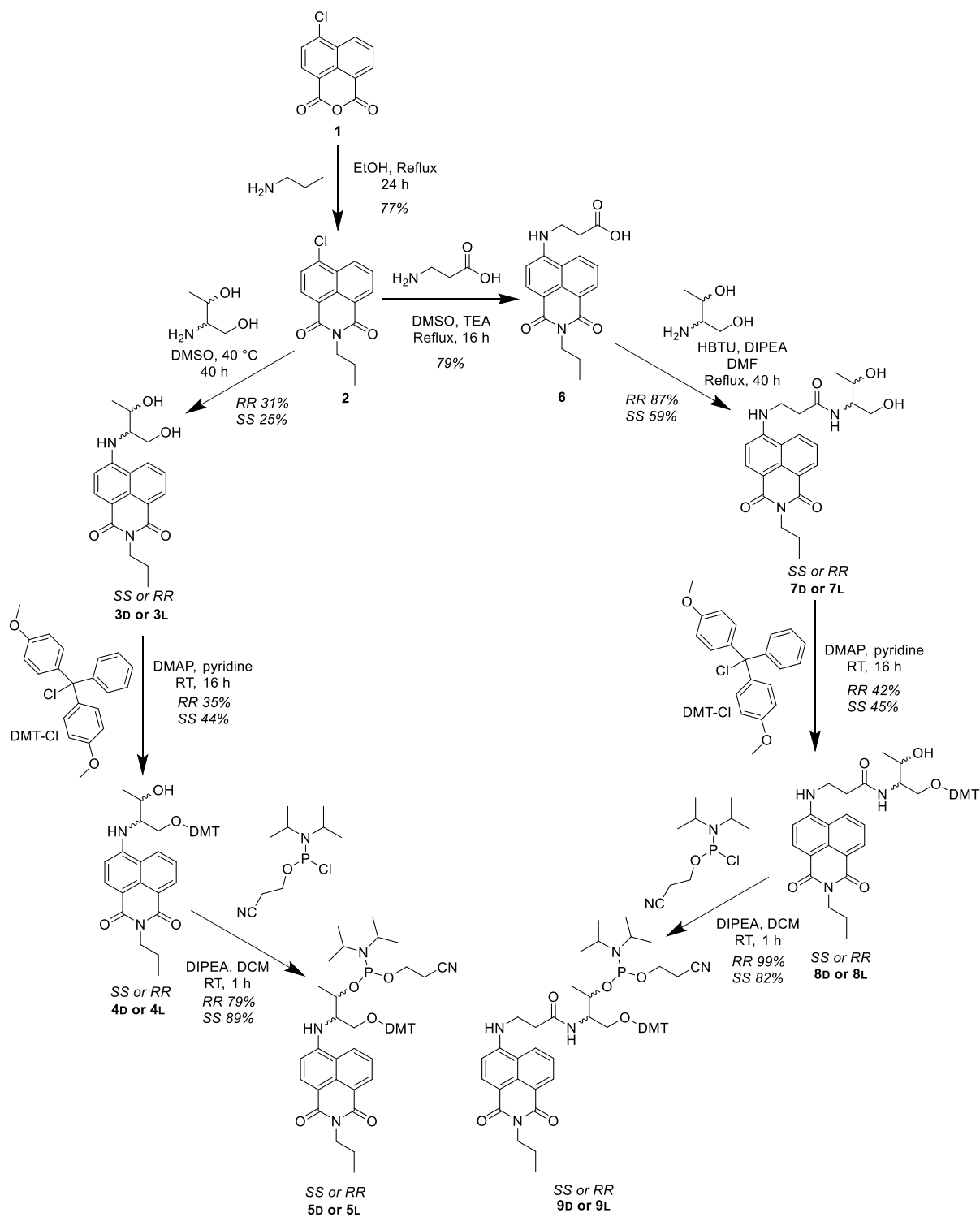
As mentioned in Chapter 1, the most effective fluorescent DNA probes aim to have reporter groups that have comparable size to a natural nucleotide, so not to greatly disturb the DNA structure, and to also allow for intercalation of the reporter group into the helical structure. This is often achieved by creating reporter groups that replicate and/or aim to mimic some structural features of a natural nucleotide. In this case, threoninol is employed as a ribose sugar alternative, aiming to mimic the 5'- and 3'-hydroxyl groups of the natural sugar unit. This analogue has been previously used in the Tucker

group for this purpose and has proven to successfully allow the incorporation of reporter groups into DNA *via* solid-phase synthesis. The enantiopure L and D threoninol molecules were used to produce only the L and D phosphoramidites respectively. As discussed in Chapter 1, it is known that the stereochemistry of the threoninol that is employed has an effect on the sensing abilities of the resulting probe.⁹ The different stereochemistry of the threoninol molecules influences the positioning of the reporter group within a duplex, hence dictating the sensing interactions that take place.^{9, 35, 36} The diol is an essential precursor for phosphoramidite chemistry and the DNA solid-phase synthesis process. The presence of the primary and secondary hydroxyl groups of threoninol produces specificity and makes the subsequent DMT protection and phosphitylation reactions relatively simple and high yielding.

3.1.2. Synthesis of Naph^A_{Short} and Naph^A_{Long}

It was decided to firstly synthesise the 1,8-naphthalimide tags in which the phosphoramidite modifications take place at the aromatic face of the naphthalimide. The synthetic route is shown in Scheme 3.1.

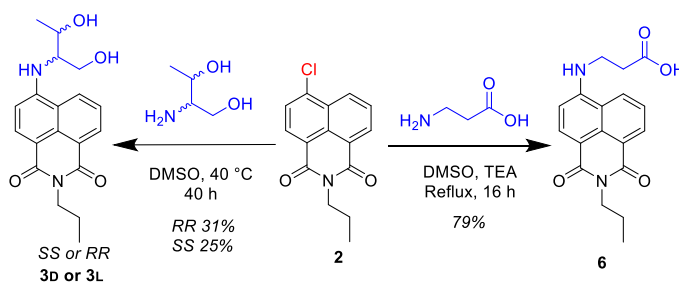
The synthesis of 6-chloro-2-propyl-1H-benzo[de]isoquinoline-1,3(2H)-dione (**2**) from 4-chloro-1,8-naphthalic anhydride (**1**) is drawn from work by K. N. de Oliveira *et al.*¹²⁶ The implementation of the short and long linker lengths occurs at the beginning of the synthesis route, before the threoninol sugar mimic is added.



Scheme 3.1: Synthetic route for the production of the phosphoramidites, $\text{Naph}^{\text{A}}_{\text{Short}}$ and $\text{Naph}^{\text{A}}_{\text{Long}}$.

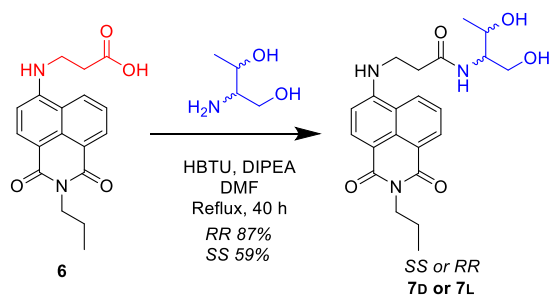
3.1.2.1. Preparation of the Diol Monomer Units

The chloro-substituent at the 4-position is a sufficiently good leaving group to allow for a nucleophilic aromatic substitution reaction (S_NAr) to occur directly with the amine group of threoninol (L or D) to form compounds **3L** and **3D**, or with the amine group of 3-amino propanoic acid to form compound **6** (Scheme 3.2). For ease, products synthesised from D or L threoninol are labelled as D or L, denoting the *SS* (D) and *RR* (L) configuration of the resulting phosphoramidites. The formation of compounds **3L** and **3D** was relatively slow and low yielding (31% and 25% respectively). This could be due to the increased steric hinderance between the amine in the threoninol and naphthalene groups, in comparison to the amine in 3-amino propanoic acid. The purification of these compounds *via* column chromatography on silica was also problematic, owing to the polar nature of the compounds, and this could have also contributed to the low yields.



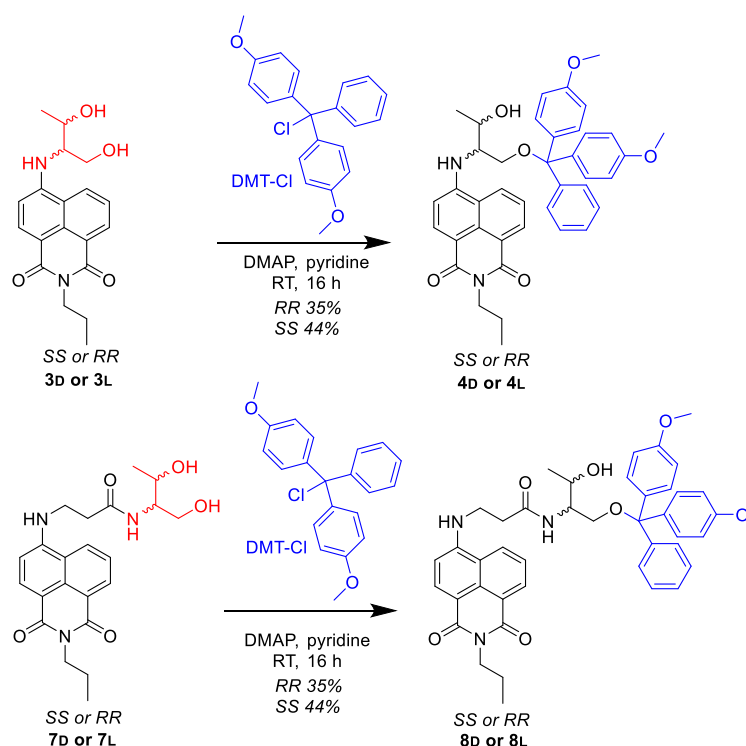
Scheme 3.2: Nucleophilic aromatic substitution at the 4-position at the naphthalimide core.

Subsequent amide coupling between the carboxylic acid group of **6** with threoninol (L or D) *via* a condensation reaction afforded compounds **7** in good yield (Scheme 3.3).



Scheme 3.3: Condensation reaction between the carboxylic acid and amine to afford the amide.

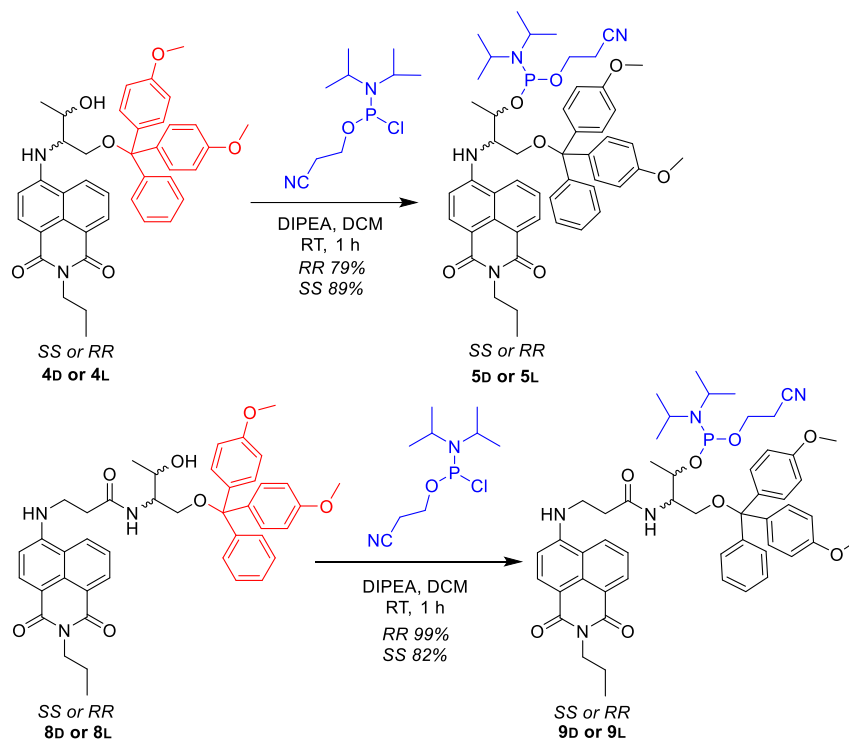
Solid-phase DNA synthesis requires protection of the primary hydroxyl group (comparable to the 5'-hydroxyl group of a nucleotide) with an acid labile protecting group, such as dimethoxytrityl (DMT). The method for hydroxyl protection is shown in Scheme 3.4 and was adapted from the procedure by Houlton et al.¹²⁷ The reaction was performed at room temperature to aid the sole formation of the mono-substituted product and to prevent the formation of the thermodynamic bis-substituted product. The work up and purification steps were performed in the absence of acid due to the acid-lability of the protecting group. This was achieved by neutralising the silica in column chromatography purification by the addition of triethylamine. The DMT-products (**4** and **8**) were formed with yields of 35%, 44%, 42%, 45% for **4L**, **4D**, **8L** and **8D** respectively. The low yields can be explained by the mild reaction conditions and the controlled equivalents of DMT used, which were required to prevent the formation of the bis substituted product.



Scheme 3.4: Reaction of the primary hydroxy group with DMT-Cl to produce the mono-protected product.

Phosphitylation occurred by reaction of the remaining hydroxyl group of the mono-DMT protected products (**4** and **8**) with 2-cyanoethyl *N,N*-diisopropylchlorophosphoramidite and *N,N*-diisopropylethylamine in anhydrous dichloromethane (Scheme 3.5). The phosphitylation requires anhydrous reaction conditions due to the unstable nature of the phosphitylating reagent and the subsequent phosphoramidite product. The phosphorous centre can be readily oxidised from P(III) to P(V) in the presence of air or H₂O. This is an unwanted side reaction as P(V) is incompatible with DNA synthesis and reduces the overall yield of the reaction. As in the previous step, the reaction, work up and purification steps were performed in the absence of any acid because of the acid-labile DMT group. The phosphoramidite products (**5** and **9**) were characterised by mass spectrometry, ¹H NMR and ³¹P NMR spectroscopy. ¹³C NMR spectra were not recorded due to the long run times of the scans and the unstable nature of the compounds. The phosphorus centre is chiral, leading to diastereomeric products. This is shown in the ³¹P NMR spectra of compounds **5** and **9** as two peaks around the 147

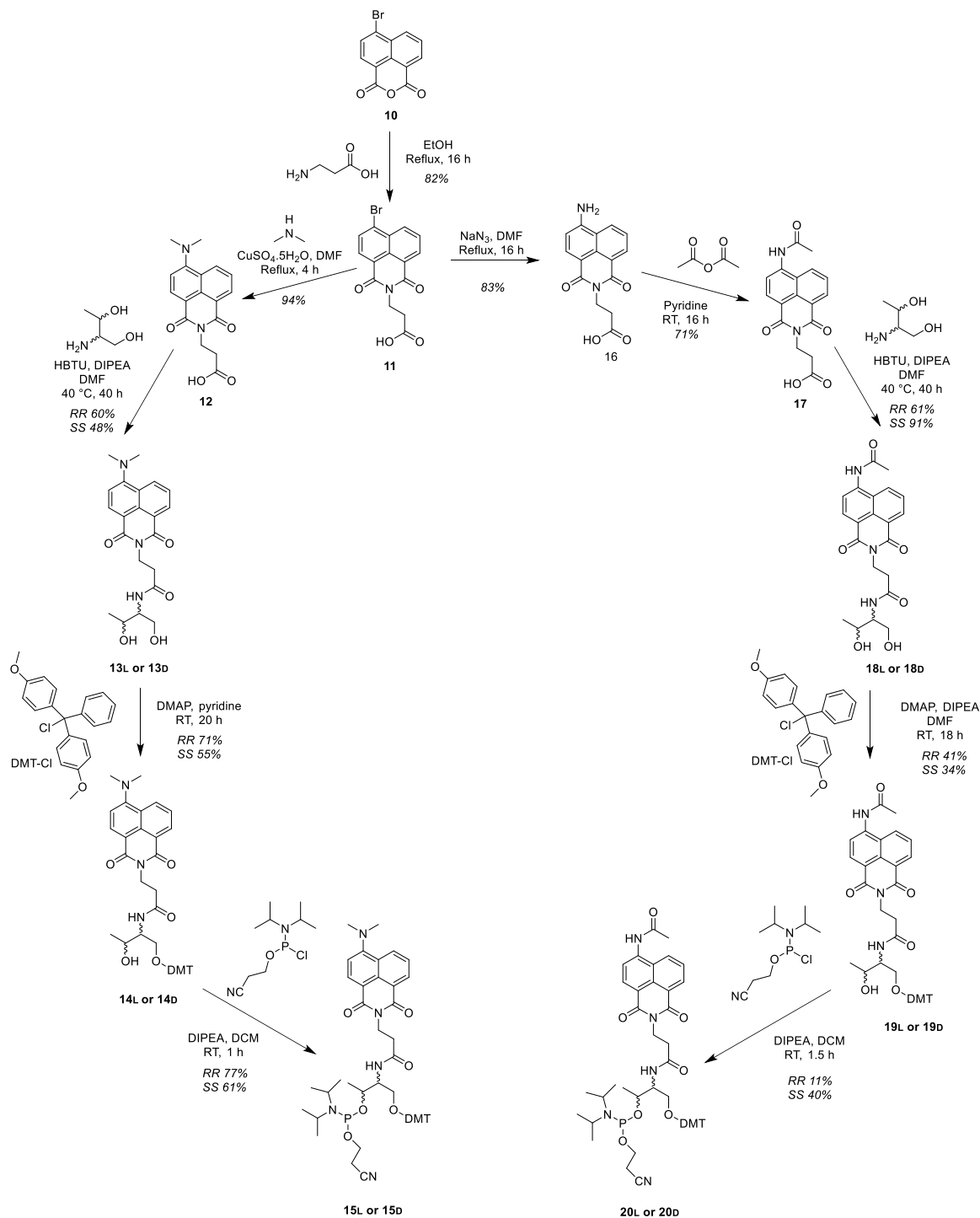
ppm region. Any peaks in the higher field region of the ^{31}P NMR spectrum (> 20 ppm) are due to the formation of oxidised products containing P(V).



Scheme 3.5: Reaction of the remaining hydroxyl group with chlorophosphitylating reagent.

3.1.3. Synthesis of Naph^I_{Dimethyl} and Naph^I_{Amine}

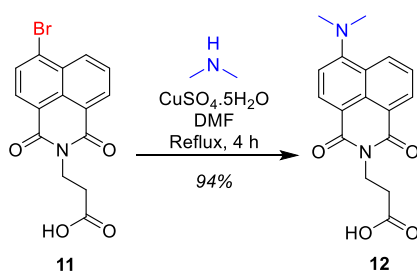
The synthetic route for the 1,8-naphthalimide tags in which the phosphoramidite groups are added at the imide side of the naphthalimide is shown in Scheme 3.6.



Scheme 3.6: Synthetic route for the formation of Naph^I_{Dimethyl} and Naph^I_{Amine}.

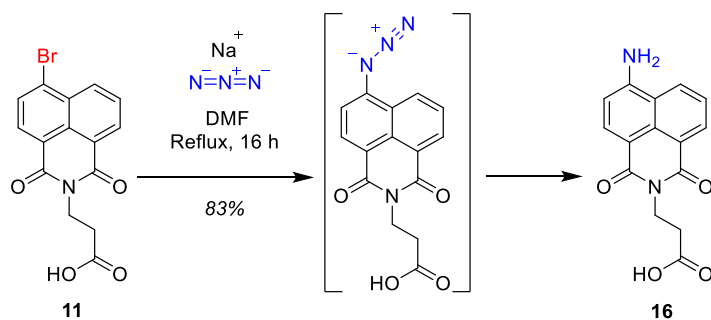
The method for the formation of compound **11** from 4-bromo-1,8-naphthalic anhydride (**10**) is drawn from work by X. Zhou *et al.*¹²² The donor groups were then introduced to the naphthalimide core at the 4-position, to substitute the bromo group.

To synthesise compound **12**, a nucleophilic aromatic substitution (S_NAr) reaction occurs between the dimethylamine and compound **11** which is catalysed by copper (II) sulfate (Scheme 3.7). This procedure was adapted from work by P. J. Dyson *et al.* and is shown in Scheme 3.7.¹²⁸



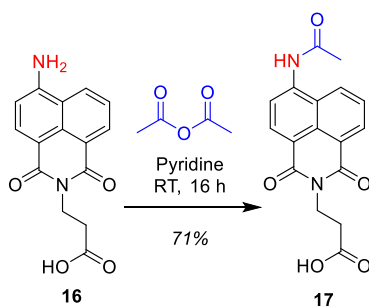
Scheme 3.7: Addition of NMe₂ to the naphthalimide aromatic core.

For the synthesis of compound **16**, the formation of the NH₂ group is achieved through an azide intermediate. In one step, the azide is formed at the 4-position and is reduced to an amine (Scheme 3.8).¹²² This procedure was followed from work reported by X. Zhou *et al.*¹²² The reaction was monitored by IR and reaction completion determined *via* the disappearance of the azide peak in the IR spectrum at ca. 2165 cm⁻¹. Following the procedure, purification was achieved by column chromatography on silica. However, this proved arduous and very forcing conditions were required due to the polar nature of the compound and the presence of the amine functional group.



Scheme 3.8: Formation of the NH_2 group through the azide intermediate.

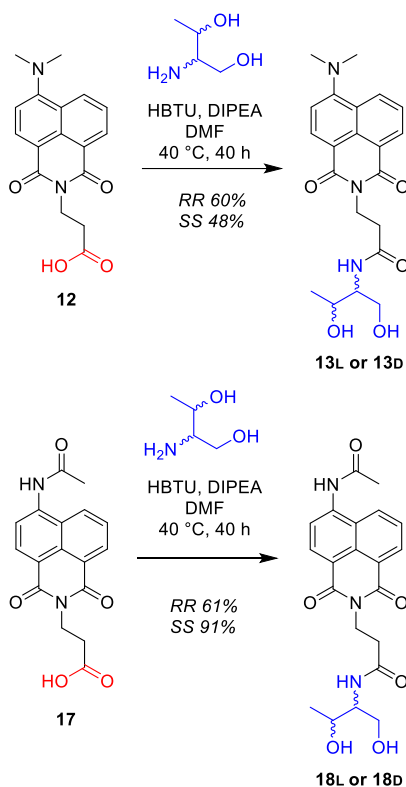
The amine was then protected with an acetyl group for compatibility with DNA synthesis (Scheme 3.9).¹²⁴ The acetyl protecting group is base sensitive, so it was important to ensure that the remaining synthesis steps did not involve the use of any strong bases. The acetyl group is a good choice of protecting group as it is not as base sensitive as the other protecting groups employed in DNA synthesis, and thus can withstand subsequent synthesis steps. Other milder protecting groups, such as 4-isopropyl phenoxyacetyl, were tested. However, they did not withstand the following reaction with threoninol and purification steps. It was decided to protect the amine at this stage in the synthesis and not later, as it was thought this would make the subsequent purification steps simpler due to the reduced hydrophilicity of the NH_2 group. Confirmation of successful amine protection was shown in the ^1H NMR spectrum by the appearance of a singlet peak at around 2.1 ppm corresponding to the methyl moiety of the acetyl group, with this peak remaining in subsequent products.



Scheme 3.9: Protection of the NH_2 group with an acetyl group.

3.1.3.1. Preparation of the Diol Monomer Units

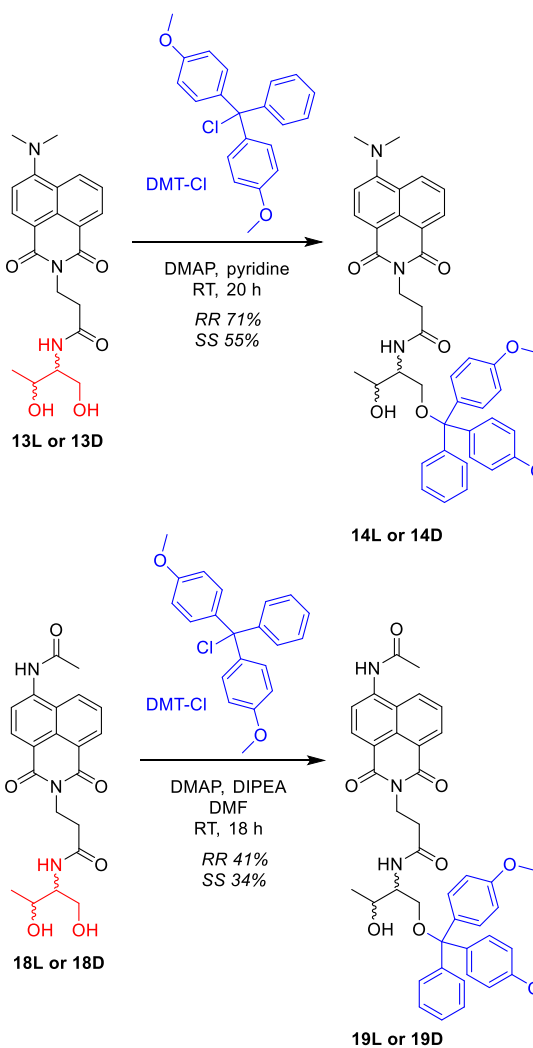
Amide coupling between the carboxylic acid group of **12** and **17** with threoninol (L or D) *via* a condensation reaction afforded compounds **13** and **18**, respectively (Scheme 3.10).



Scheme 3.10: Coupling of threoninol to the carboxylic acid functional group.

As before, hydroxyl protection using the dimethoxytrityl group was adapted from the procedure by Houlton *et al.*¹²⁷ Again, the reaction was performed at room temperature to aid the sole formation of the mono-substituted product. The work up and purification steps were performed in the absence of acid due to the acid-labile protecting group. This involves neutralising the silica in column chromatography purification by the addition of triethylamine. The DMT protection of compounds **18L** and **18D** was very slow and did not go to completion. To force the reaction to proceed, the reaction was heated to 40 °C after 14 h and another 0.5 eq of DMT-Cl was added and left for another 4 h. This helped but the reaction was stopped before reaching completion, which accounts for the very low

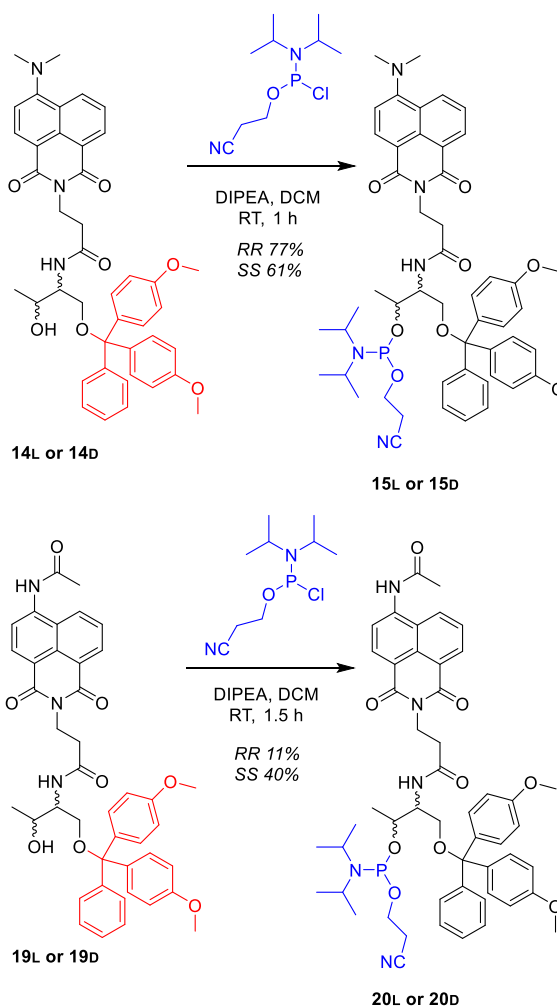
yields for compounds **19L** and **19D**. The low yields (**14L**, 77%; **14D** 61%; **19L**, 41%; **19D**, 34%) can be explained by the mild reaction conditions and the controlled equivalents of DMT used, which were required to prevent the formation of the bis-substituted product.



Scheme 3.11: Reaction of the primary hydroxy group with DMT-Cl to produce the mono-protected product.

As described previously, phosphorylation occurred by reaction of the remaining hydroxyl group of the mono-DMT protected products (**14** and **19**) with 2-cyanoethyl *N,N*-diisopropylchlorophosphoramidite and *N,N*-diisopropylethylamine in anhydrous dichloromethane (Scheme 3.12). The low yield for the synthesis of **20L** (11%) was due to a problematic work up and purification. The high retention of the product on the silica column resulted in a significant amount of oxidised product (P(V)). The oxidised

product was removed by trituration of the product in ethyl acetate with hexane. The phosphoramidite products (**15** and **20**) were characterised by mass spectrometry, ^1H NMR and ^{31}P NMR spectroscopy. Again, two peaks are observed in the ^{31}P NMR spectra of compounds **15** and **20** at around the 147 ppm region. There were small peaks around 8 ppm in the ^{31}P NMR spectra, which correspond to the formation of oxidised products containing P(V).



Scheme 3.12: Reaction of the remaining hydroxyl group with chlorophosphitylating reagent.

3.2. Oligo Probe Synthesis

3.2.1. Design Considerations

The prepared 1,8-naphthalimide tags described in the above section were incorporated into DNA using automated solid-phase DNA synthesis. This technique is described in more detail in Chapter 2. This method allows for the site-specific incorporation of the 1,8-naphthalimide tag anywhere within a DNA sequence. This automated method is reliable and consistent and produces oligo strands in relatively high yields.

The probe sequence chosen, Table 3.1, was based on previous sensing work performed in the Tucker group.^{9, 58, 60, 125} This sequence was chosen as it has been thoroughly studied and is well understood. It also allows for comparison between results.

Table 3.1: Probe sequences.

	Modification (X)	Sequence (5'→3')
Probe Strand P1AL	L Naph ^A _{Short}	TGG ACT C X C TCA ATG
Probe Strand P1AD	D Naph ^A _{Short}	TGG ACT C X C TCA ATG
Probe Strand P1BL	L Naph ^A _{Long}	TGG ACT C X C TCA ATG
Probe Strand P1BD	D Naph ^A _{Long}	TGG ACT C X C TCA ATG
Probe Strand P1CL	L Naph ^I _{Dimethyl}	TGG ACT C X C TCA ATG
Probe Strand P1CD	D Naph ^I _{Dimethyl}	TGG ACT C X C TCA ATG
Probe Strand P1DL	L Naph ^I _{Amine}	TGG ACT C X C TCA ATG
Probe Strand P1DD	D Naph ^I _{Amine}	TGG ACT C X C TCA ATG
Probe Strand P1	Unmodified	TGG ACT CGC TCA ATG

The probe sequence comprises 15 monomer units (15-mer), with the naphthalimide tag inserted at the centre of the strand. An oligo strand with a length of 15 bases is long enough to allow binding with its complementary target with high specificity, while still being simple enough to synthesise and purify. The strand length also ensures that more complex secondary structures are not formed, such as hairpin loops. This is also prevented by the choice of bases within the sequence, of which there is roughly equal amounts of each nucleobase at regular intervals. The decision to place the 1,8-naphthalimide

tag at the centre of the probe strand ensures that a stable duplex is formed, with a melting temperature well above room temperature. It was hypothesised that the 1,8-naphthalimide tag would reduce the duplex melting temperature slightly, but not to the extent that duplex formation would not occur at room temperature.

In addition to the modified probe, an unmodified probe was synthesised for comparison. In this sequence, the 1,8-naphthalimide tag modification site (X) is replaced with a guanine (G). The unmodified probe sequence is shown below.

3.2.1.1. Base-Opposite Sensing

To investigate the ability of the probe to sense and distinguish between various bases opposite the modification site, target oligos in which the site opposite the 1,8-naphthalimide tag was varied were synthesised. These target strands are shown in Table 3.2 and are named accordingly.

Table 3.2: Target sequences for base-opposite sensing.

	Sequence (5'→3')
GCG Target; T1C	CAT TGA GCG AGT CCA
GGG Target; T1G	CAT TGA GGG AGT CCA
GTG Target; T1T	CAT TGA GTG AGT CCA
GAG Target; T1A	CAT TGA GAG AGT CCA

The sensing mechanism is shown schematically in Figure 3.3.

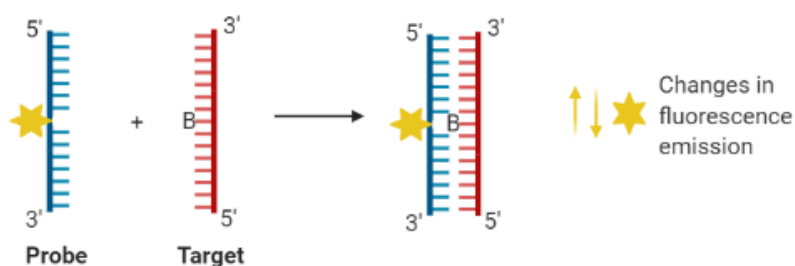


Figure 3.3: Schematic showing base-opposite sensing design. Where B = A, G, C or T. The fluorescent signal produced from the reporter group (star) is monitored upon duplex formation of the probe with the target.

3.2.1.2. Base-Adjacent Sensing

In previous work by the Tucker group, it has been shown that a similar system involving anthracene was particularly effective at sensing the environment of the base adjacent to the modification site, when a relatively short linker sequence was used.^{9, 129} Modifying at this site produces a 'match' versus 'mismatch' sensing system. Based on previous work, it was decided to vary the base in the target sequence upstream of the 1,8-naphthalimide modification from a guanine (G) to an adenine (A) to create the 'mismatch' sequence as this sequence produced the best sensing results for the anthracene system, as demonstrated in Table 3.3.

Table 3.3: Target sequence for base-adjacent sensing.

	Sequence (5'→3')
Mismatch Target; T1MM	CAT TGA GAA AGT CCA
Matched Target; T1A	CAT TGA GAG AGT CCA

This sensing mechanism is shown schematically in Figure 3.4.

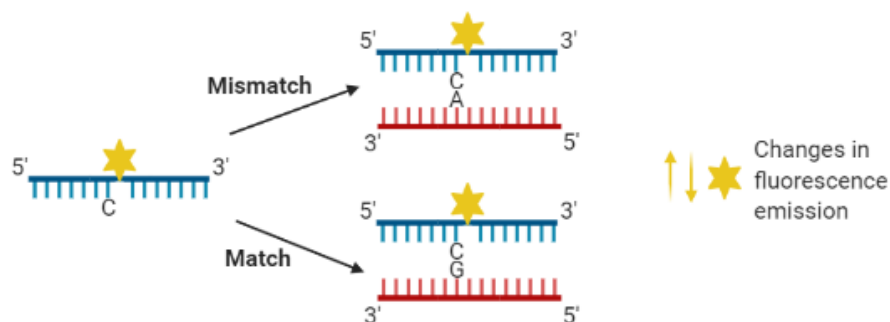


Figure 3.4: Schematic showing base adjacent, 'match' vs 'mismatch' sensing. The fluorescent signal produced from the reporter group (star) is monitored upon duplex formation of the probe with the target.

3.2.1.3. Epigenetic Sensing

The ability of the probes to sense the epigenetic marker, 5-methylcytosine (mC), was investigated. In a similar way to the base-opposite sensing, the site opposite the 1,8-naphthalimide modification site was altered with the epigenetic marker. The strand that was synthesised is shown in Table 3.4.

Table 3.4: Target sequence for the epigenetic sensing.

	Sequence (5'→3')
GmCG Target; T1mC	CAT TGA GmCG AGT CCA

3.2.1.4. Sensing Biomarkers – BRAF V600E

A 'real-life' single point variation associated with cancers, BRAF V600E, was also investigated. As described in Chapter 1, this is a T (WT) > A (Mut) mutation. The sequence is known, and so short target sequences were synthesised for initial sensing purposes, Table 3.5. Sensing results obtained from these short targets would provide a good proof-of-concept for the probe system as a mutation detection assay.

Table 3.5: Target sequences for BRAF V600E sensing.

	Sequence (5'→3')
BRAF WT Target; T2WT	GCT ACA GTG AAA TCT
BRAF Mut Target; T2Mut	GCT ACA GAG AAA TCT

A probe was accordingly designed that was complementary to the target sequence of interest. The 1,8-naphthalimide modification was positioned directly opposite the point variant site. The probe synthesised is shown in Table 3.6 and is also a 15-mer, with the modification directly at the centre of the strand. The oligo length and positioning of the modification was chosen for similar reasons to those mentioned for P1X. In addition to the 1,8-naphthalimide tag, the previously studied anthracene 5L tag was also incorporated into the BRAF probe.¹³⁰ This is discussed in more detail in Chapter 5.

Table 3.6: Probe sequences for BRAF V600E sensing.

	Modification (X)	Sequence (5'→3')
BRAF Probe Strand; P2AL	L Naph ^A _{Short}	AGA TTT C X C TGT AGC
BRAF Probe Strand; PAD	D Naph ^A _{Short}	AGA TTT C X C TGT AGC
BRAF Probe Strand; P2Anth	Anthracene 5L	AGA TTT C X C TGT AGC
BRAF Probe Strand; P2WT	Unmodified	AGA TTT CAC TGT AGC
BRAF Probe Strand; P2Mut	Unmodified	AGA TTT CTC TGT AGC

Along with the modified probe strands, unmodified probe strands were also synthesised for comparison. Two unmodified probe strands complementary to both the wild-type and mutant BRAF V600E sequences were synthesised as shown Table 3.6.

3.2.2. Oligonucleotide Synthesis

Oligos were synthesised using solid-phase DNA synthesis performed on an Applied Biosystems ABI 394 DNA/RNA synthesiser. There are two different sets of conditions that can be employed for DNA synthesis; standard conditions and ultramild conditions. Standard synthesis is the most commonly used method and was used to synthesise all unmodified oligonucleotides. This method is the highest yielding, but it uses relatively harsh chemical conditions and any modifications must be able to withstand them. On the other hand, ultramild synthesis provides a milder alternative for any modifications that are particularly sensitive. However, this method slightly reduces the overall yield as less-forcing conditions are used, whilst the ultramild reagents are more costly.

To determine whether the 1,8-naphthalimide modifications could withstand standard DNA deprotection conditions, it was decided to test the 1,8-naphthalimide diol monomer **3L** by heating to 60 °C in aqueous ammonia for 6 h. However, it was found that the compound degraded under these harsh conditions, as evidenced by ¹H NMR through the emergence of additional peaks. Therefore, it was decided to use ultramild DNA synthesis conditions for all 1,8-naphthalimide modified strands. The ultramild deprotection method involves agitating the strands in methanolic potassium carbonate

solution overnight at room temperature, a much milder approach. This approach is possible due to the more labile protecting groups on the ultramild phosphoramidite reagents.

All 1,8-naphthalimide phosphoramidites (**5L**, **5D**, **9L**, **9D**, **15L**, **15D**, **20L**, **20D**) were successfully incorporated into DNA. The stepwise yields for the coupling of the modifications into the DNA strand were significantly lower (by around 30-40%) than those achieved when coupling standard DNA phosphoramidites. A slight drop in yield may be expected for modifications due to steric hindrance that may occur between the modification site and nucleotide, making coupling more difficult. However, this large drop in yield could be attributed to the limited solubility of the tag molecules in acetonitrile, the solvent used to dissolve phosphoramidites for automated DNA synthesis. Hence coupling is reduced because the concentration of the phosphoramidite solution was lower than expected (< 0.1 M). To overcome this, a longer coupling time of 15 minutes (as opposed to the standard 30 second coupling time) was used for the coupling of the modification. This approach was successful in improving the overall strand yields for the modified oligonucleotides by up to 10-15%. For detailed oligonucleotide synthesis procedures and sequences of the strands synthesised, see Experimental 7.3 and Appendix 8.1.

3.2.3. Oligonucleotide Purification

Oligonucleotides were purified by semi-preparative reversed-phase HPLC using a Clarity Oligo column. 0.1 M triethylammonium acetate buffer was used with an increasing acetonitrile gradient from 5-18% acetonitrile over 25 minutes (see Experimental 7.4 for full method). The HPLC detection wavelengths were set at 260 nm for DNA and 430 nm for the 1,8-naphthalimide modification. The retention times of all purified oligonucleotides using analytical HPLC are demonstrated in Table 3.7. The retention times of the unmodified 15-mer oligonucleotides were consistent at around 17-18 minutes, as shown in Figure 3.5 (see Appendix 8.1.2 for all other HPLC traces).

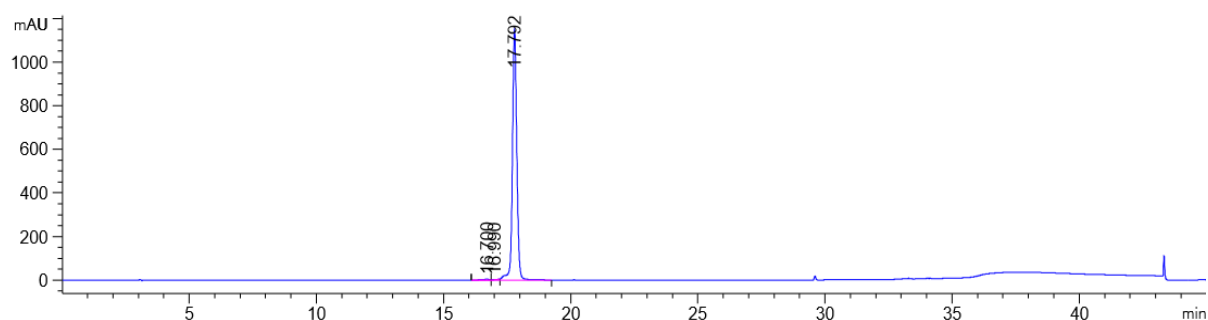


Figure 3.5: HPLC trace of the purified T1C target strand (unmodified oligo). Detector wavelength at 260 nm for DNA.

Table 3.7: Analytical HPLC retention times and purity of all purified oligonucleotides. *very broad, weak intensity peak detected as two peaks – further investigations detected this peak as a single entity.

Oligonucleotide	Modification	Retention Time (min)	Purity of isolated sample (%)
T1C	Unmodified	17.79	99.32
T1G	Unmodified	17.18	98.41
T1T	Unmodified	17.76	96.71
T1A	Unmodified	17.18	98.98
T1MM	Unmodified	17.53	98.32
T1mC	Unmodified	18.00	98.62
T2WT	Unmodified	18.54	100.00
T2Mut	Unmodified	18.01	96.22
P1AL	L Naph ^A _{Short}	23.61	100.00
P1AD	D Naph ^A _{Short}	24.07	100.00
P1BL	L Naph ^A _{Long}	26.57	100.00
P1BD	D Naph ^A _{Long}	26.98	100.00
P1CL	L Naph ^I _{Dimethyl}	23.66	100.00
P1CD	D Naph ^I _{Dimethyl}	24.02	100.00
P1DL	L Naph ^I _{Amine}	20.89	100.00
P1DD	D Naph ^I _{Amine}	20.75	100.00
P2AL	L Naph ^A _{Short}	23.26/23.69*	62.28/23.69*
P2AD	D Naph ^A _{Short}	23.72/24.17*	66.43/24.17*

The 1,8-naphthalimide modified strands have a significantly longer retention time than the unmodified strands (an example HPLC trace of the purified P1AL probe is given in Figure 3.6 for comparison), indicating that the 1,8-naphthalimide modification interacts with the stationary phase to a reasonable extent. The retention times of the modified probe varied slightly depending on the modification and

stereochemistry (L or D) (see Appendix 8.1.2 for HPLC traces of all modified probes). The probe containing the Naph^A_{Short} modification had a retention time at around 24 minutes. In comparison, probes containing Naph^A_{Long} had longer retention times of around 27 minutes. This longer retention time is due to the aliphatic linker which interacts with the hydrophobic stationary phase. Interestingly, for the majority of modifications, the probes with D stereochemistry had slightly longer retention times than the L. This suggests that in the single-stranded form, the L modifications are slightly more shielded from the external interactions than the D. This observation is consistent with previous work in the Tucker group on strands involving anthracene tags.¹³¹ The crude HPLC traces also contain a significant peak at around 14-18 minutes, which after mass spectrometry analysis equates to the truncated oligonucleotide at the modification site (i.e. 5' - TGG ACT CXC TCA ATG - 3'). This shows that the coupling of the 1,8-naphthalimide modification into the oligonucleotide is not 100% effective, which correlates with the low stepwise yield observed in DNA synthesis for the modification step.

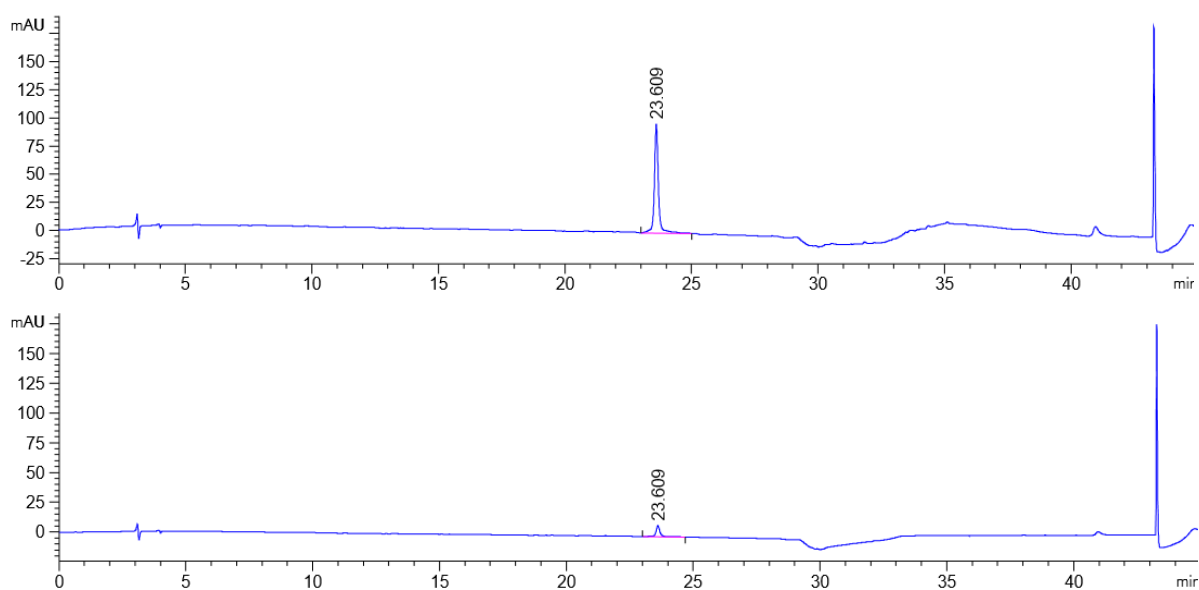


Figure 3.6: HPLC trace of the purified P1AL probe containing the naphthalimide reporter group. Detection wavelengths shown are 260 nm (top) for DNA and 430 nm (bottom) for naphthalimide.

Following purification, oligos were desalted using a NAP-10 column. Analytical reverse-phase HPLC was then performed on the purified samples using the same conditions as above to confirm a purity of

>95%. Any strands that did not show a purity of >95% were re-purified using the same semi-preparative method above.

3.2.4. Oligonucleotide Characterisation and Quantification

Oligonucleotide characterisation was achieved *via* mass spectrometry and UV-Vis spectroscopy. Mass spectrometry was carried out using negative mode electrospray methods. The results from these agreed with the calculated masses determined *via* ChemDraw analysis, Table 3.8.

Table 3.8: Oligonucleotide mass spectrometry results.

Name	Modification (X)	Sequence 5' → 3'	Calculated Mass (g mol ⁻¹)	Mass Found (m/z)
P1AL	L Naph ^A _{Short}	TGG ACT CXC TCA ATG	4642.84	4642.8
P1AD	D Naph ^A _{Short}	TGG ACT CXC TCA ATG	4642.84	4642.5
P1BL	L Naph ^A _{Long}	TGG ACT CXC TCA ATG	4725.91	4726.02
P1BD	D Naph ^A _{Long}	TGG ACT CXC TCA ATG	4725.91	4726.03
P1CL	L Naph ^I _{Dimethyl}	TGG ACT CXC TCA ATG	4697.88	4698.0
P1CD	D Naph ^I _{Dimethyl}	TGG ACT CXC TCA ATG	4697.88	4697.98
P1DL	L Naph ^I _{Amine}	TGG ACT CXC TCA ATG	4669.85	4669.96
P1DD	D Naph ^I _{Amine}	TGG ACT CXC TCA ATG	4669.85	4670.00
P2AL	L Naph ^A _{Short}	AGA TTT CXC TGT AGC	4655.86	4655.74
P2AD	D Naph ^A _{Short}	AGA TTT CXC TGT AGC	4655.86	4656.80
T1G	Unmodified	CAT TGA GGG AGT CCA	4617.1	4617.0
T1A	Unmodified	CAT TGA GAG AGT CCA	4601.1	4600.9
T1C	Unmodified	CAT TGA GCG AGT CCA	4577	4576.6
T1T	Unmodified	CAT TGA GTG AGT CCA	4592	4591.8
T1MM	Unmodified	CAT TGA GAA AGT CCA	4585.1	4587.5
T1mC	Unmodified	CAT TGA GmCG AGT CCA	4591.06	4591.0
T2WT	Unmodified	GCT ACA GTG AAA TCT	4576	4573.93
T2Mut	Unmodified	GCT ACA GAG AAA TCT	4585.1	4582.95

The UV-Vis spectra of the modified probe strands (aqueous solution, Milli-Q, 100 mM NaCl, 10 mM sodium phosphate, pH 7.0) show the successful incorporation of the 1,8-naphthalimide tags into DNA through the presence of a peak at around 430 nm. The peak at 260 nm mainly corresponds to the

absorbance by nucleic acids in DNA. The naphthalimide modification also absorbs in this region and contributes to this signal. Figure 3.7 shows the shift of the 1,8-naphthalimide absorbance between the P1A vs P1B probe and Figure 3.8 shows the absorbance of the P1C and P1D probes.

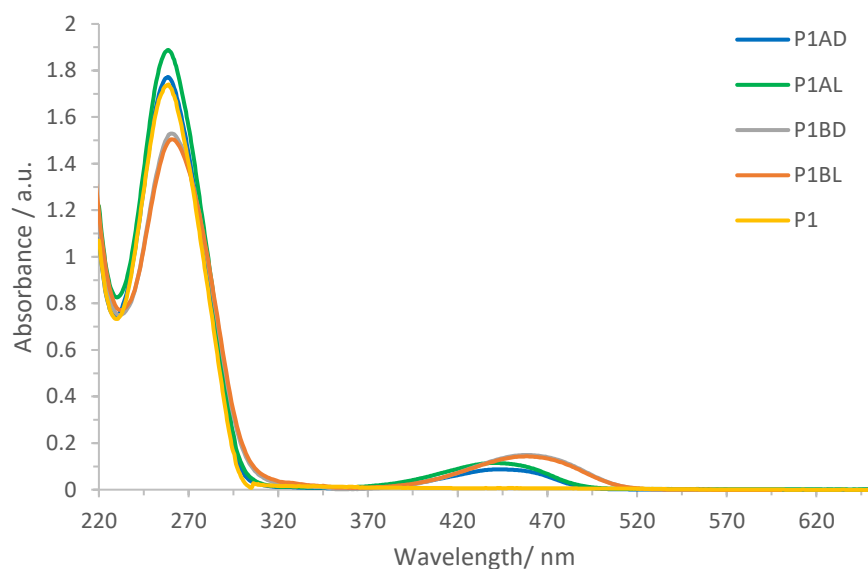


Figure 3.7: UV-Vis spectra of $Naph^A_{Short}$ and $Naph^A_{Long}$ probes (P1AL/D and P1BL/D). Aqueous solution, Milli-Q, 100 mM NaCl, 10 mM sodium phosphate, pH 7.0.

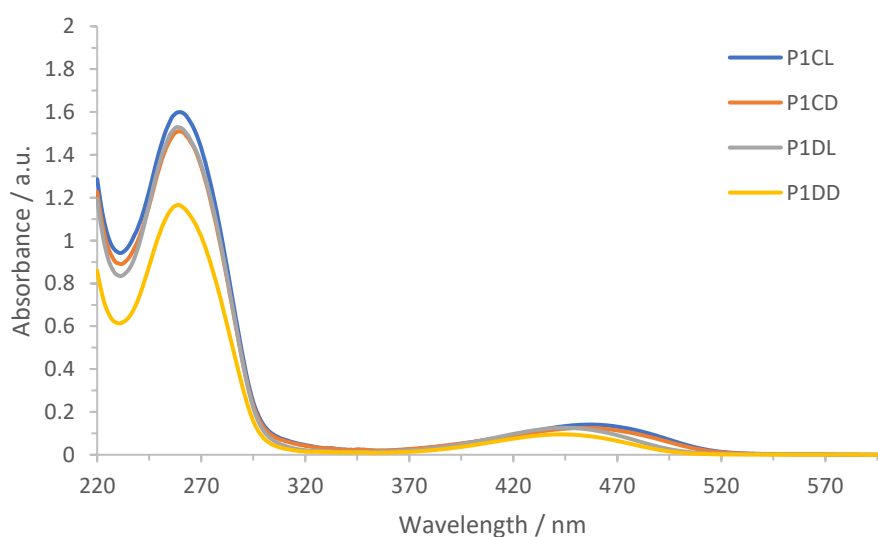


Figure 3.8: UV-Vis spectra of $Naph^{Dimethyl}$ and $Naph^{Amine}$ probes (P1CL/D and P1DL/D). Aqueous solution, Milli-Q, 100 mM NaCl, 10 mM sodium phosphate, pH 7.0.

Oligonucleotide quantification was achieved using a BioSpec-nano micro-volume UV-Vis spectrophotometer (nanodrop). The optical density (OD) at 260 nm is recorded and can be used directly as the absorbance at 260 nm. The nanodrop software converts the OD at 260 nm to absorbance using a set path length of 0.2 mm and internal calculations. Knowing the absorbance at 260 nm, the concentration can be determined using the Beer Lambert law, Equation 7.

Equation 7: Beer Lambert Law. Where the absorbance at 260 nm, A, is equal to the product of the molar extinction coefficient, ϵ , by the concentration, c, and path length, l.

$$A = \epsilon cl$$

The molar extinction coefficients of the unmodified oligonucleotides were determined from Integrated DNA Technologies' online web tool, OligoAnalyzer.¹⁰⁹ The 1,8-naphthalimide tag molar extinction coefficients were determined by recording the absorbance of the 1,8-naphthalimide diol monomer units (**3**, **7**, **13**, **18**) at 260 nm at various known concentrations in 85:15 water/acetonitrile. This information can be found in the Appendix 8.1.3.

Following synthesis and characterisation, the use of the naphthalimide modified probes were explored for sensing applications, as detailed in the following chapters.

3.3. References

1. J.-L. H. A. Duprey, D. M. Bassani, E. I. Hyde, G. Jonusauskas, C. Ludwig, A. Rodger, N. Spencer, J. S. Vyle, J. Wilkie, Z.-Y. Zhao and J. H. R. Tucker, *Org. Biomol. Chem.*, 2018, 6576.
2. N. Moran, PhD Thesis, University of Exeter, 2006.
3. Q. Zeng, Q. Guo, Y. Yuan, Y. Yang, B. Zhang, L. Ren, X. Zhang, Q. Luo, M. Liu, L.-S. Bouchard and X. Zhou, *Anal. Chem.*, 2017, **89**, 2288.
4. M. S. Alexiou, V. Tychopoulos, S. Ghorbanian, J. H. P. Tyman, R. G. Brown and P. I. Brittain, *J. Chem. Soc. Perkin Trans. 2*, 1990, 837.
5. J. C. Kim, M. Kim, J. Jung, J. Lee, B. J. Ree, H. Kim, I. J. Kim, J. R. Kim and M. Ree, *J. Polym. Sci., Part A: Polym. Chem.*, 2015, **53**, 1151.
6. J.-L. H. A. Duprey, G. A. Bullen, Z.-Y. Zhao, D. M. Bassani, A. F. A. Peacock, J. Wilkie and J. H. R. Tucker, *ACS Chem. Biol.*, 2016, **11**, 717.
7. J.-L. H. A. Duprey, Z.-Y. Zhao, D. M. Bassani, J. Manchester, J. S. Vyle and J. H. R. Tucker, *Chem. Commun.*, 2011, **47**, 6629.
8. X. Liang, H. Asanuma, H. Kashida, A. Takasu, T. Sakamoto, G. Kawai and M. Komiyama, *J. Am. Chem. Soc.*, 2003, **125**, 16408.
9. H. Kashida, M. Tanaka, S. Baba, T. Sakamoto, G. Kawai, H. Asanuma and M. Komiyama, *Chem. Eur. J.*, 2006, **12**, 777.
10. K. N. Oliveira, P. Costa, J. R. Santin, L. Mazzambani, C. Burger, C. Mora, R. J. Nunes and M. N. Souza, *Bioorg. Med. Chem*, 2011, **19**, 4295.
11. A. Pike, L. C. Ryder, B. R. Horrocks, W. Clegg, M. R. J. Elsegood, B. A. Connolly and A. Houlton, *Chem. Eur. J.*, 2002, **8**, 2891.
12. K. J. Kilpin, C. M. Clavel, F. Edefe and P. J. Dyson, *Organometallics*, 2012, **31**, 7031.
13. N. Moran, D. M. Bassani, J.-P. Desvergne, S. Keiper, P. A. S. Lowden, J. S. Vyle and J. H. R. Tucker, *Chem. Commun.*, 2006, 5003.

14. N. Moran, D. M. Bassani, J. P. Desvergne, S. Keiper, P. A. S. Lowden, J. S. Vyle and J. H. R. Tucker, *Chem. Commun.*, 2006, **48**, 5003.
15. A. Ali, University of Birmingham, 2018.
16. J.-L. H. A. Duprey, PhD Thesis, University of Birmingham, 2010.
17. Oligo Analyzer, <https://eu.idtdna.com/calc/analyzer>, 2020.

4. Exploring the Photophysical Properties of 1,8-Naphthalimide Reporter Groups and Their Ability as Base Discrimination Probes

This chapter describes the investigation of the photophysical properties of the naphthalimide reporter group monomers synthesised in the previous chapter. In particular, the solvatochromic properties were studied; for a detailed explanation of solvatochromism, see Chapter 1. The photophysical properties of the naphthalimide probes were also studied prior to sensing.

The second part of this chapter focuses on the sensing ability of the naphthalimide probes to detect single point variations within short complementary targets. The sensing systems explored are those synthesised in Chapter 3 and include the sensing of all four canonical nucleobases, 5-methylcytosine and the BRAF V600E mutation.

4.1. Photophysical Properties of the 1,8-Naphthalimide Tags as Monomers and When Incorporated Into DNA Probes

4.1.1. UV-Vis Absorption Studies

4.1.1.1. UV-Vis Absorption Studies of the 1,8-Naphthalimide Tag Monomers

The absorption profiles of the 1,8-naphthalimide tag monomers in 85:15 water/acetonitrile exhibited broad peaks in the region of 450 nm (see Figure 4.1 for the absorption spectrum of D Naph^A_{Short} monomer and Appendix 8.2.1 for others). The broad peak can be attributed to the π - π^* transition ($S_0 \rightarrow S_1$).^{123, 132}

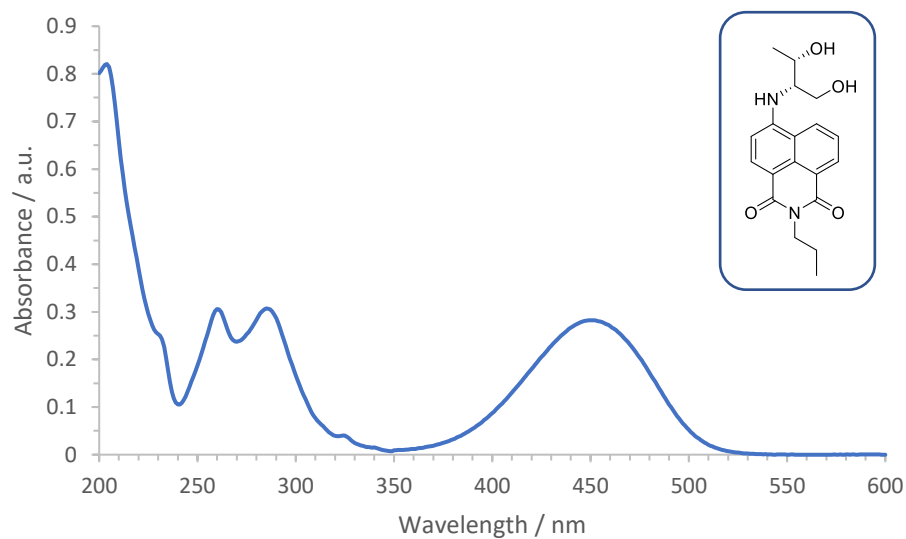


Figure 4.1: Absorption spectrum of D Naph^A_{Short} tag monomer (44 μ M) in 85:15 water/acetonitrile.

The position of the peak at \sim 450 nm is sensitive to the polarity of the surrounding environment. Figure 4.2 and Table 4.1 demonstrate the bathochromic shifts observed in the absorption spectrum of the D Naph^A_{Short} tag monomer in a range of solvents. This is caused by a change in solvent polarity from toluene to water (see Appendix 8.2.2 for other tags). These bathochromic shifts are typical for a charge-transfer (CT) transition and arise due to changes in the dipole moment of the naphthalimide molecules upon excitation.

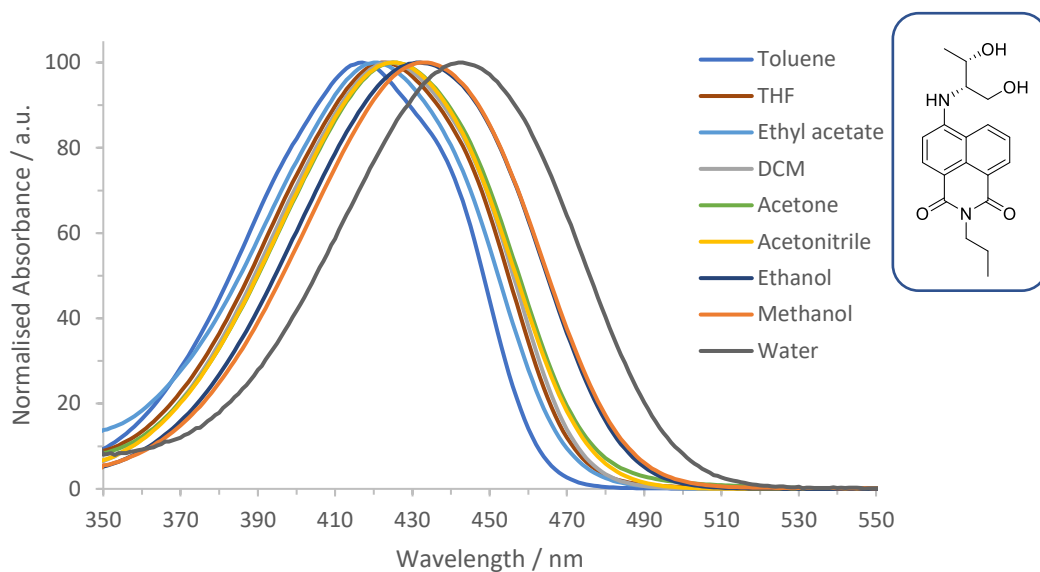


Figure 4.2: Absorption of $D\text{ Naph}^A_{\text{Short}}$ tag monomer in solvents of varying polarity.

Table 4.1: Maximum absorption wavelength of $D\text{ Naph}^A_{\text{Short}}$ tag monomer in solvents of varying polarity. $E_T(30)$ is the Dimroth-Reichardt solvent polarity parameter.

Solvent	$\lambda_{\text{max}} / \text{nm}$	$E_T(30) / \text{kcal mol}^{-1}$
Water	443	63.1
Methanol	433	55.4
Ethanol	432	51.9
Acetonitrile	425	45.6
Acetone	425	42.2
DCM	424	40.7
Ethyl acetate	421	38.1
THF	422	37.4
Toluene	417	33.9

Upon excitation, the dipole moment of the molecule increases and a more polar solvent (indicated by increasing $E_T(30)$ value, a solvent polarity parameter described in further detail in Section 4.1.2.1.1) stabilises the excited state more than the ground state. This results in emission profiles shifting to longer wavelengths, in what is described as positive solvatochromism.⁶³ All four of the naphthalimide tag monomers ($\text{Naph}^A_{\text{Short}}$, $\text{Naph}^A_{\text{Long}}$, $\text{Naph}^I_{\text{Dimethyl}}$, $\text{Naph}^I_{\text{Amine}}$) demonstrate this solvatochromic effect, albeit to differing extents, owing to their different structures and the extent of ICT within each

molecule. The Naph^A_{Long} tags showed the largest range in spectral shifts of the absorption spectra when present in the various solvent environments. On the other hand, the Naph^I_{Amine} tags demonstrated the smallest range. This may be attributed to the interactions of the NH₂ group with the various solvents, an effect which is described further below when considering the fluorescence emission. The proposed ICT within the naphthalimide molecules is from the donor amine group to the acceptor imide group, as illustrated in Figure 4.3.

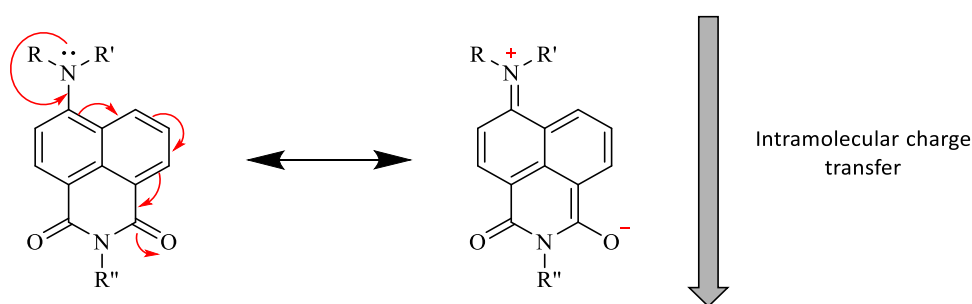
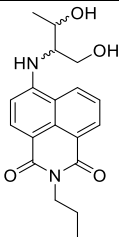
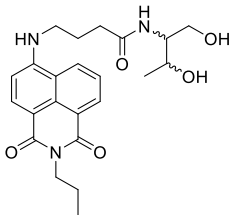
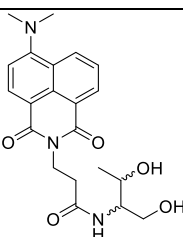
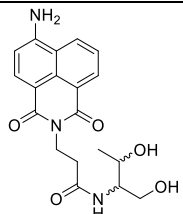


Figure 4.3: Proposed intramolecular charge transfer within 1,8-naphthalimide tag monomers.

The solvatochromic nature of naphthalimide molecules is also evident in their fluorescence emission profiles, which is more marked than the changes in absorption profiles. This is described in more detail in the following sections.

As well as the solvent, the electron-donating power of the substituent at the 4-position on the aromatic ring can affect the absorption profiles of the naphthalimide tag monomers. Work by Brittain *et al.* provided an extensive library of 1-8-naphthalimides and an examination of how varying the substituent at the 4-position affected their absorption spectra (in ethanol).¹²³ The results reported show similar trends to the naphthalimide tag monomer variants discussed here. The absorption maxima of the different naphthalimide tag monomers (in ethanol for comparison with literature examples) are presented in Table 4.2.

Table 4.2: Maximum absorption wavelengths of the different naphthalimide tag monomer variants in ethanol. L and D isomers of the reporter groups gave the same $\lambda_{\max, \text{abs}}$ so only one value is shown.

		$\lambda_{\max, \text{abs}} / \text{nm}$
Naph ^A _{Short}	 <p>SS or RR</p>	432
Naph ^A _{Long}	 <p>SS or RR</p>	442
Naph ^I _{Dimethyl}	 <p>SS or RR</p>	421
Naph ^I _{Amine}	 <p>SS or RR</p>	436

In the case of the Naph^I_{Dimethyl} tag monomers, a slightly lower absorption maximum ($\lambda_{\max, \text{abs}}$) could be attributed to steric interactions between methyl groups of the 4-dimethylamino substituent group and the hydrogen at the 5-position; a so-called *peri* effect. These steric interactions with the *peri* hydrogen cause a reduction in the planarity of the 4-amino substituent with the aromatic ring system. This in turn inhibits the intramolecular charge transfer, destabilising the excited state, and resulting in a shorter maximum absorption wavelength. This effect was also observed by Brittain *et al.*¹²³ The *peri*

effect is lessened in the other tag compounds which substitute a methyl group on the 4-amino group for a hydrogen. This allows the alkyl group to align away from the *peri* hydrogen, as demonstrated in Figure 4.4. In particular, the nitrogen substituents of the Naph^A_{Long} compounds are less bulky around the amine nitrogen compared to the Naph^A_{Short} counterparts, allowing for less of a steric interaction with the *peri* hydrogen and a longer maximum absorption wavelength.

Increased steric hinderance

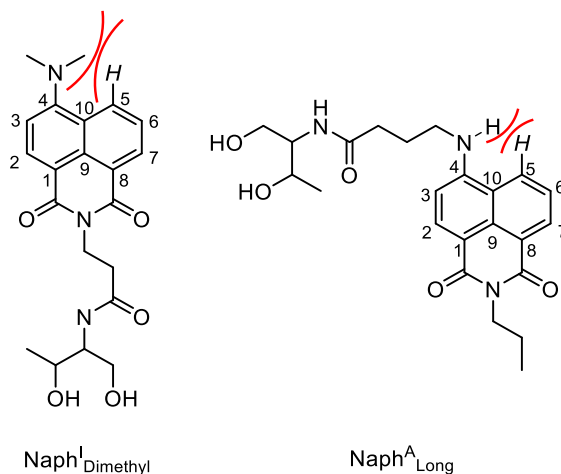


Figure 4.4: Steric hinderance between the 4-amino groups and hydrogen at the 5-position (the *peri* effect). There is increased steric hinderance for the Naph^I_{Dimethyl} tags.

Based on sterics alone, the predicted order of naphthalimide molecules with increasing maximum absorption wavelength is demonstrated in Figure 4.5. Naph^I_{Dimethyl} is expected to experience the greatest steric interactions and thus have the shortest maximum absorption wavelength out of all the naphthalimide tag variants. In comparison, Naph^I_{Amine} is expected to experience the least steric interactions and have the longest maximum absorption wavelength. However, this is not what is observed, and the highest maximum absorption wavelength is Naph^A_{Long}, Table 4.2.

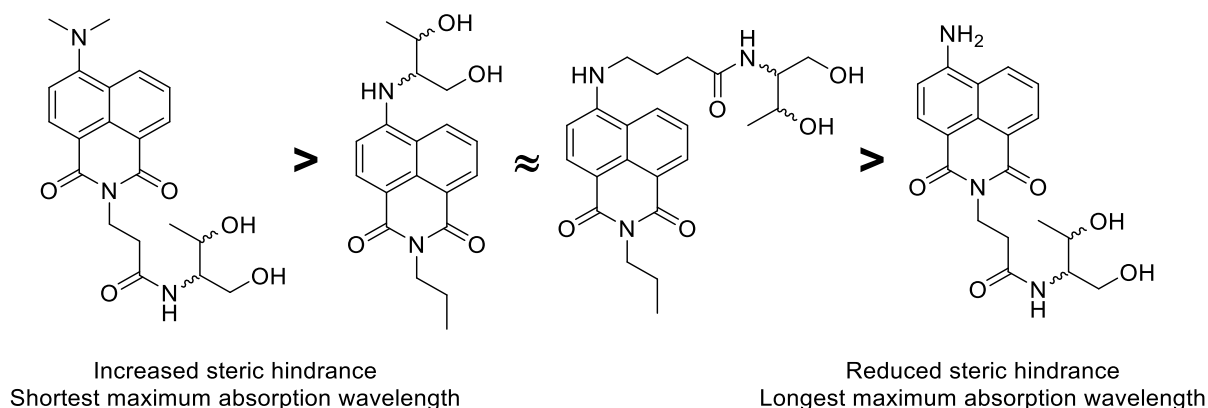


Figure 4.5: Naphthalimide reporter groups in order of predicted increasing maximum absorption wavelength based on steric interactions alone.

As mentioned earlier, the electron donating power of the substituent also contributes to the absorption properties.^{133, 134} Based only on the inductive effect of the substituents, a different order of naphthalimide molecules with increasing maximum absorption wavelength can be predicted, Figure 4.6. The presence of methyl substituents (as in Naph^{Dimethyl} reporter groups) or an *R* group (hydrocarbon chain) creates a positive inductive effect to the nitrogen atom at the 4- position. This positive inductive effect increases the electron donating power of the substituent, resulting in higher wavelength absorption profiles. This inductive effect is reduced for the Naph^{Amine} reporter group. The balance of steric interactions and the electron donating power of the substituents at the 4-position explains the differing absorption profiles for the various reporter groups.

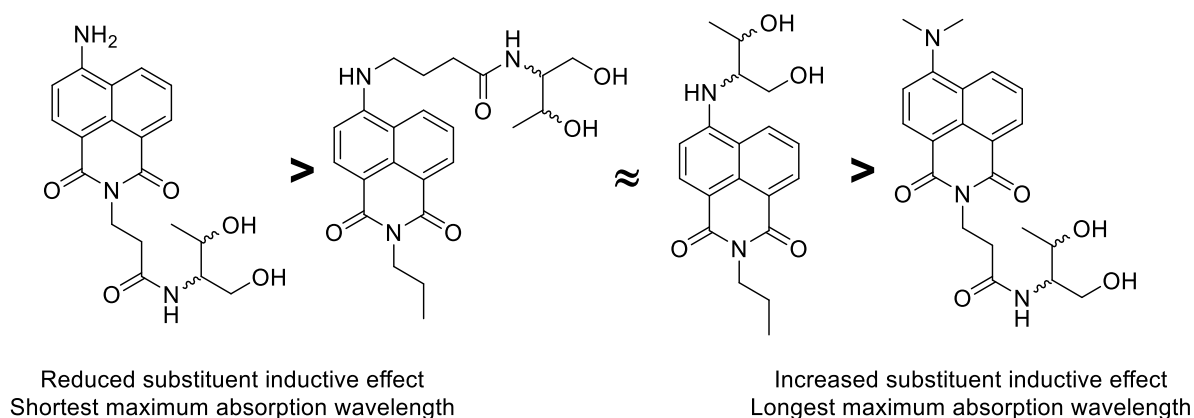


Figure 4.6: Naphthalimide reporter groups in order of predicted increasing maximum absorption wavelength based on substituent inductive effect alone.

4.1.1.2. Changes in the 1,8-Naphthalimide Absorption Profile Upon DNA Incorporation and Duplex Formation

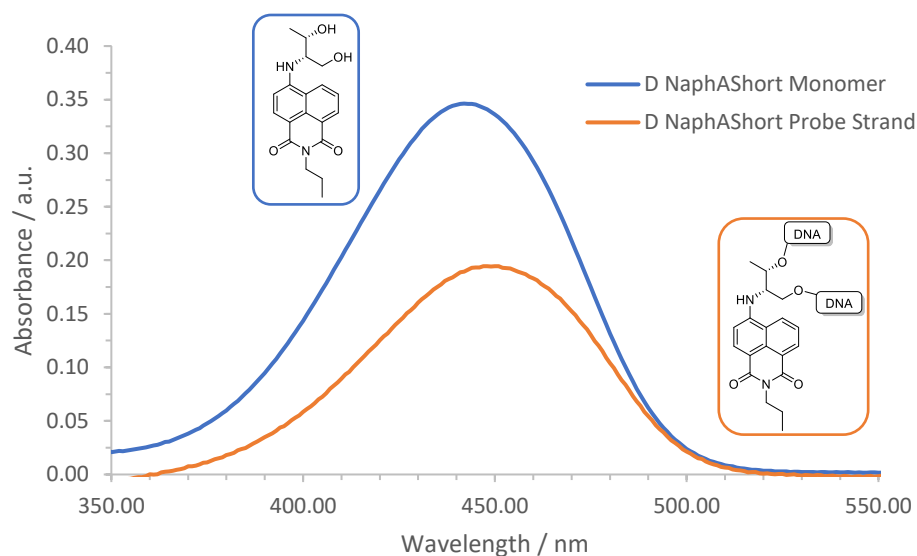


Figure 4.7: Absorption spectra of D Naph^A_{short} diol monomer and D Naph^A_{short} probe strand (P1AD). Showing the bathochromic shift in the absorption maximum upon DNA incorporation.

A significant bathochromic shift in the naphthalimide absorption band was observed upon incorporation of all the naphthalimide tag monomers into the DNA probe strands. While all the data can be found in the Appendix 8.2.3, a representative example is presented in Figure 4.7, showing the effect for the D Naph^A_{short} system. Similar trends were observed in previous work by the Tucker group involving the incorporation of anthracene into DNA.¹³¹ Other groups have also reported similar bathochromic shifts upon the incorporation of various aromatic molecules into DNA. For example, Sarkar *et al.* have attributed the bathochromic shift to the change in the local polarity around the fluorophore,¹³⁵ with DNA incorporation resulting in a decrease in the local polarity of the fluorophore compared to the 'free' fluorophore in solution. This reduces the energy gap between the HOMO and LUMO of the fluorophore, hence giving rise to the bathochromic shift, Figure 4.8. As naphthalimide molecules have been shown to be very sensitive to their microenvironment,^{123, 136, 137} this is a reasonable explanation. In contrast, Asanuma has ascribed the bathochromic shift observed upon fluorophore incorporation into DNA to exciton coupling of the intercalated molecule with the

surrounding natural nucleobases.¹³⁸ Although this explanation can be applied to the previously studied anthracene system,¹³¹ owing to the well-known intercalation of anthracene derivatives into DNA, this reasoning might not apply as readily to the naphthalimides as their DNA intercalating ability is not as well studied.

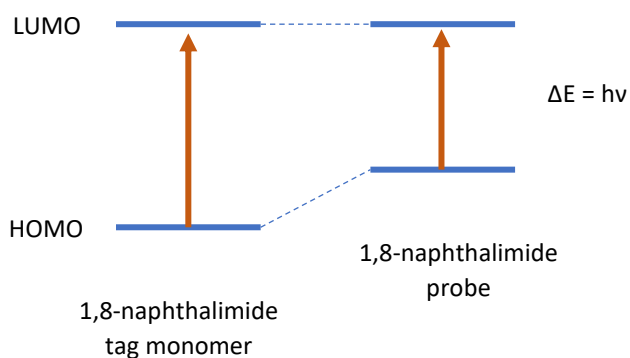


Figure 4.8: Energy level diagram explaining the observed shift of the naphthalimide absorption maximum to a longer wavelength upon DNA incorporation. D Naph^A_{Short} probe (P1AD) used. Where E is energy, h is Planck's constant and ν is frequency.

Interestingly, the Naph^A_{Short} probes display differences in the naphthalimide maximum absorption wavelengths between the L and D stereochemistry. The D Naph^A_{Short} probe exhibits a larger bathochromic shift (+8 nm to 450 nm) in comparison to the L Naph^A_{Short} probe (+5 nm to 447 nm), which implies different environments for each fluorophore. It would be expected that this effect would be more apparent for tags with shorter and more inflexible linkers to the chiral threoninol units. Indeed, a change in threoninol stereochemistry for the longer linker probe systems (L Naph^A_{Long} and D Naph^A_{Long} probes) does not affect the maximum absorption wavelength, as the more flexible tether allows each tag to move into a similar position within the DNA stack. Similar trends are also observed in the fluorescence sensing and duplex melting studies, which are discussed further in later sections.

4.1.2. Fluorescence Studies

4.1.2.1. Fluorescence Profiles of the 1,8-Naphthalimide Monomers

Fluorescence emission is the most commonly studied method for the detection of single point variations using fluorescently-modified DNA probes. It is therefore of great importance to investigate the fluorescence properties of the naphthalimide reporter groups to demonstrate their suitability for sensing applications.

The naphthalimide emission profiles are shifted towards higher wavelengths compared to many other fluorescent DNA probes in the literature.¹²⁵ This is advantageous for sensing applications as it minimalises the background emission from biological environments. The fluorescence spectra of the naphthalimide tag monomers exhibit broad bands at around 540 nm (upon excitation at 450 nm); an example of D Naph^A_{Short} tag monomer in Milli-Q water is given in Figure 4.9 (see Appendix 8.2.4 for the emission profiles of the other tag monomers). These broad and intense bands are typical of ICT within the fluorophore. The ICT within naphthalimides has been ascribed as a π - π^* transition occurring from the nitrogen to the carbonyl group.^{123, 136, 139}

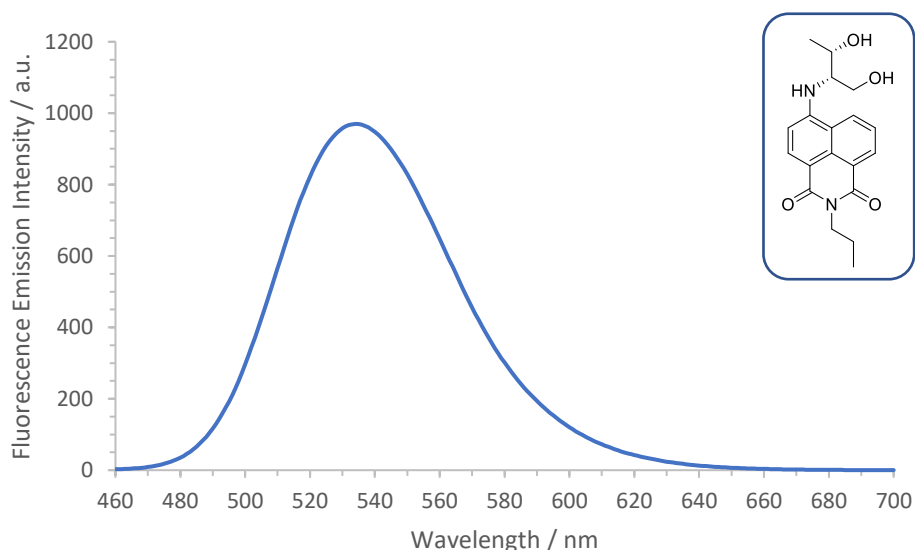


Figure 4.9: Fluorescence emission spectrum of D Naph^A_{Short} tag monomer in Milli-Q water. $\lambda_{ex} = 450$ nm, 298 K.

As mentioned earlier, the solvatochromic effect is relevant to both the naphthalimide absorption and emission spectra. The solvatochromic effect on the absorption spectra was shown above and now the effect on the emission spectra is explored. The naphthalimide tag monomers exhibit positive solvatochromism as demonstrated by the bathochromic shift in naphthalimide emission when placed in more polar solvents. Figure 4.10 shows the fluorescence emission profiles of the D Naph^A_{Short} tag monomer in solvents of varying polarity (data shown in Table 4.3). See the Appendix 8.2.5 for the other naphthalimide tag monomers.

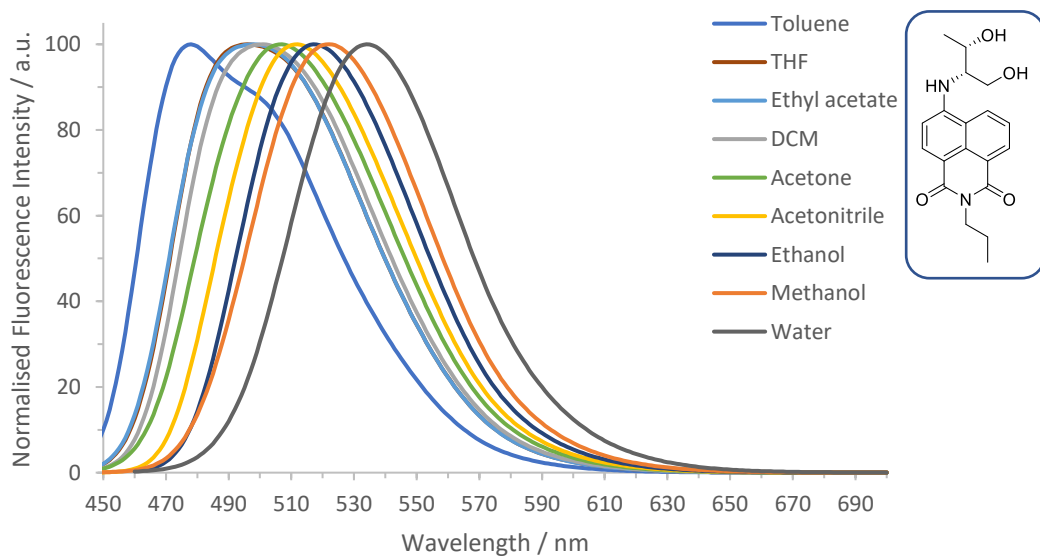


Figure 4.10: Fluorescence emission profiles of D Naph^A_{Short} tag monomer in solvents of varying polarity. The naphthalimide emission is shifted to longer wavelengths in more polar solvents.

Table 4.3: Fluorescence emission data for the D Naph^A_{Short} tag monomer in a variety of solvents with varying polarity. Solvent polarity indicated using the $E_T(30)$ solvent polarity parameter.

Solvent	λ_{\max} / nm	$E_T(30)$ / kcal mol ⁻¹
Water	534	63.1
Methanol	522	55.4
Ethanol	517	51.9
Acetonitrile	512	45.6
Acetone	507	42.2
DCM	501	40.7
Ethyl acetate	498	38.1
THF	496	37.4
Toluene	478	33.9

As described in detail in Chapter 1, this positive solvatochromic effect is due to the stabilisation of the excited state in more polar solvents and solvent relaxation effects. During excitation, there is a change in the dipole moment throughout the naphthalimide molecule. In its excited state, charge separation between the nitrogen at the 4-position and the carbonyl groups is more prominent in comparison to the ground state, as shown Figure 4.3. Therefore, naphthalimides experience a larger dipole moment in their excited state compared to their ground state. Surrounding solvent molecules are able to reorient to stabilise this excited state dipole moment, with more polar solvents causing stronger solvent-solute interactions and increased solvent relaxation effects. An increase in solvent relaxation results in a longer wavelength emission profile. Solvent relaxation effects are the reason more prominent solvatochromic effects are observed in the naphthalimide emission profiles compared to their absorption profiles.

4.1.2.1.1. Using the Dimroth-Reichardt Parameter to Assess the Extent of Solvatochromism of the 1,8-Naphthalimide Tag Monomers

The inadequacy of defining solvent polarity has led to the development of various models and empirical solvent polarity scales. In 1963, Dimroth, Reichardt and co-workers proposed the use of pyridinium *N*-phenoxide betaine indicator dyes as UV-Vis probes for solvent polarity.^{140, 141} This betaine dye (4-(2,4,6-triphenylpyridinium)-2,6-diphenylphenoxide, ET-30) was used to develop the $E_T(30)$ scale of solvent polarity. This solvent polarity scale gives an indication of dipolarity and hydrogen bond donating acidity of the solvent.¹⁴⁰ The normalised values, E_T^N , provide a polarity scale of 0 – 1, where a value of zero defines the shift of ET-30 in tetramethylsilane and a value to one in water. The E_T^N values employed in this section are defined as ‘a measure of the ionising power of a solvent based on the maximum wavenumber of the longest-wavelength electronic absorption band of a zwitterion in the given solvent’.¹⁴²

To demonstrate and assess the solvatochromic nature of the naphthalimide tag monomers, the normalised Dimroth-Reichardt parameter (E_T^N) for a variety of solvents, depicted in Table 4.4, was plotted against the maximum emission wavelength of the naphthalimide tag monomers in the given solvent. Figure 4.11 and Figure 4.12 demonstrate the relationship between the two parameters for the different naphthalimide tag monomers. The $\text{Naph}^{\text{A}}_{\text{Long}}$ molecules correlate well between the two parameters, with a linear relationship observed. The $\text{Naph}^{\text{A}}_{\text{Short}}$ and $\text{Naph}^{\text{I}}_{\text{Dimethyl}}$ compounds show a weaker correlation, and this is weaker still for the $\text{Naph}^{\text{I}}_{\text{Amine}}$ tag monomers. Considering the $\text{Naph}^{\text{I}}_{\text{Amine}}$ tag, the extent of hydrogen bonding in this system may change more as the solvent changes because the NH_2 group is both a hydrogen bond donor and acceptor. This may be causing the reduction in the correlation between the two parameters as the NH_2 group interacts differently with each solvent. This reduction in the solvatochromic nature is also evident in DNA sensing observations, as discussed later in the chapter.

Table 4.4: Normalised Dimroth-Reichardt values (E_T^N) of given solvents.

Solvent	Normalised Dimroth-Reichardt Solvent Polarity Parameter (E_T^N)
Acetonitrile	0.460
Acetone	0.355
DCM	0.309
Ethyl acetate	0.228
THF	0.207
Toluene	0.099

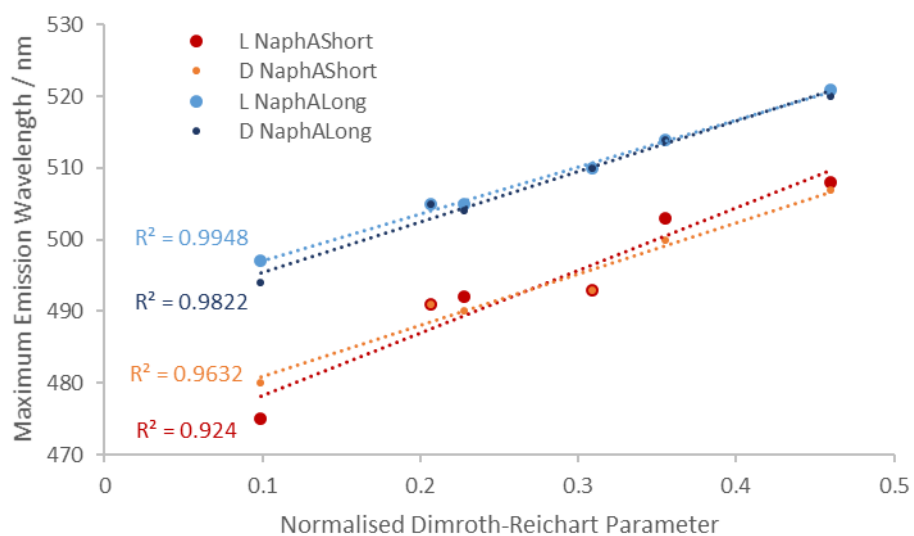


Figure 4.11: Relationship between the maximum fluorescence emission wavelength of $Naph^A_{Short}$ and $Naph^A_{Long}$ monomer tags in different solvents of varying polarity.

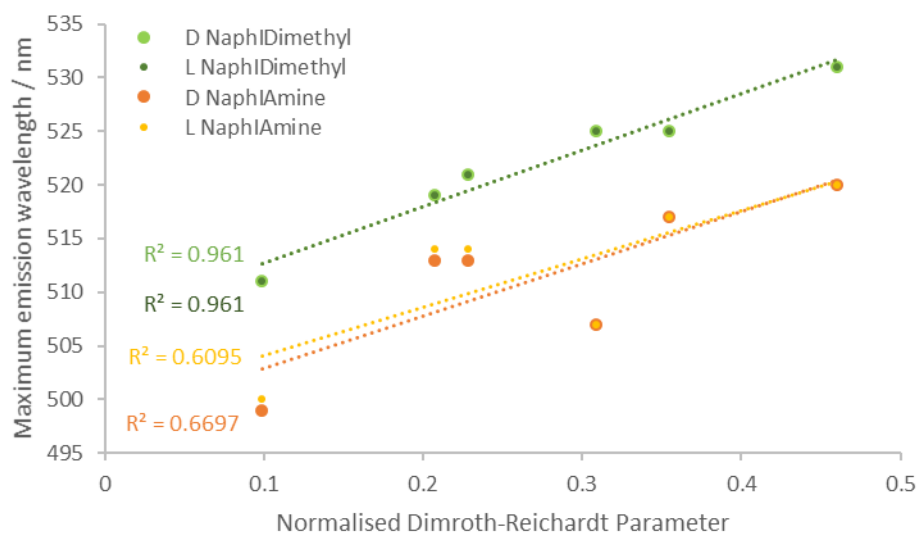


Figure 4.12: Relationship between the maximum fluorescence emission wavelength of $Naph^{Dimethyl}$ and $Naph^{Amine}$ monomer tags in different solvents of varying polarity.

4.1.2.2. Changes to the Naphthalimide Fluorescence Profiles Upon Incorporation into DNA Probe Strands and Duplex DNA

The high sensitivity of the naphthalimide molecules to their microenvironment enables the detection of various interactions that take place once incorporated into a DNA probe and upon duplex formation. As a free monomer, the naphthalimide is fully exposed to the external environment (solvent). However, upon incorporation into the DNA probe strands, it experiences a more hydrophobic environment, shielded from the polar external aqueous environment by neighbouring nucleobases. This produces a shift in the naphthalimide fluorescence emission profile to a lower wavelength, as shown in Figure 4.13. This effect is seen to a larger extent upon duplex formation where the naphthalimide experiences an even more hydrophobic environment, owing to the formation of a hydrophobic core through stacking base pairs. Furthermore, in this helical duplex structure, the naphthalimide reporter groups have the potential to intercalate or position themselves within the major or minor grooves of the DNA helix. Figure 4.13 demonstrates this effect for the D Naph^A_{Short} reporter group, which is also observed for all Naph^A_{Short} and Naph^A_{Long} reporter groups. However, the Naph^I_{Dimethyl} and Naph^I_{Amine} reporter groups do not reliably follow this trend in that shifts to lower emission wavelengths are not always observed with duplex formation, as demonstrated later in this chapter. This may be a result of the different orientations of these tags within the probe structures and the extent to which they can intercalate within the duplex.

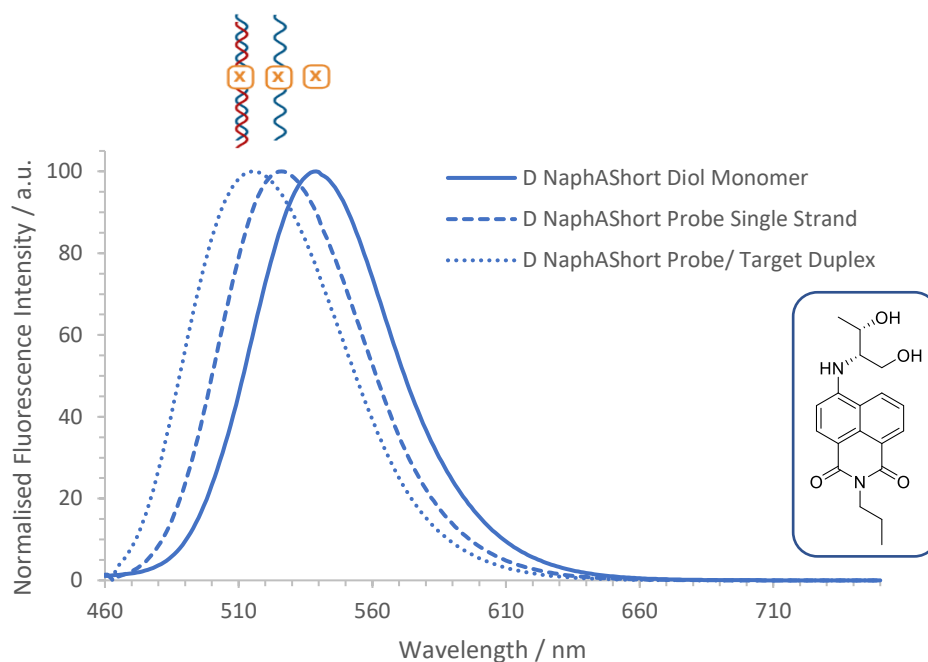


Figure 4.13 Fluorescence emission profiles of the D Naph^A_{Short} reporter group as a monomer (bold line), single probe strand (P1AD) (dashed line), and upon duplex formation (P1AD:T1G) (dotted line); showing shifts in the maximum emission wavelengths between the different forms. The duplex example given is with the base opposite T target (T1T). Samples prepared in aqueous solution of 100 mM NaCl, 10 mM sodium phosphate buffer pH 7.0.

4.1.3. Fluorescence Quantum Yields

4.1.3.1. Fluorescence Quantum Yield of Naphthalimide Diol Monomers

The fluorescence quantum yields (Φ) of the naphthalimide tag monomers in various solvents are shown in Table 4.5 and were measured using the relative method, with Coumarin 153 as a reference standard. The quantum yields are comparable to similar naphthalimide derivatives reported in the literature.^{123, 136, 143} The naphthalimide tag monomers, with the exception of Naph^I_{Dimethyl}, have a higher quantum yield value compared to the anthracene diol monomer previously studied in the Tucker group, which has a quantum yield of 0.08 in 90:10 water/methanol.^{9, 131} This demonstrates the improved fluorescence efficiency of the naphthalimide derivatives as reporter groups for sensing applications.

The very low quantum yield of the Naph^I_{Dimethyl} diol monomers is presumably caused by the steric interactions between the methyl groups of the 4-dimethylamino substituent and the *peri* hydrogen at the 5-position, as discussed in Section 4.1.1.1.

Table 4.5 also reveals the effect of solvent on the quantum yield. The highest values are seen in the aprotic solvent acetonitrile, with lower values in ethanol and then water.

Table 4.5: Fluorescence quantum yields of naphthalimide monomer tags ($\pm 10\%$).

Sample	Fluorescence Quantum Yield (Φ)		
	Water	Ethanol	Acetonitrile
L Naph ^A _{Short}	0.29	0.53	0.63
D Naph ^A _{Short}	0.30	0.53	0.64
D Naph ^A _{Long}	0.16	0.46	0.55
L Naph ^A _{Long}	0.17	0.44	0.56
D Naph ^I _{Dimethyl}	0.00065	0.0057	0.015
L Naph ^I _{Dimethyl}	0.00078	0.0077	0.012
D Naph ^I _{Amine}	0.11	0.33	0.52
L Naph ^I _{Amine}	0.10	0.35	0.48

The lower quantum yield values in polar and/or protic solvents are due to increased efficiencies of non-radiative pathways, although there are different explanations in the literature as to why this is the case for naphthalimides.^{137, 144, 145} Internal motion effects, such as nitrogen inversion, has been proposed as one explanation.¹⁴⁵ On the other hand, this effect has been ascribed to strong interactions with solvent molecules.¹⁴⁴ To explore this effect further, glycerol was titrated into an ethanol solution of the Naph^I_{Dimethyl} monomer sample, the monomer variant with the lowest quantum yield. Glycerol is a viscous liquid and should hinder any internal motion effects. However, the data displayed in Table 4.6 shows that the addition of glycerol has no significant effect, which suggests against internal motion effects. Therefore, the increase in solvent interactions (e.g. through H-bonding) is a more plausible explanation and correlates well with the red shifts in emission profiles of the naphthalimide tag monomers in more polar solvents (as previously discussed).

Table 4.6: Exploring the effects of non-radiative emission processes on the fluorescence quantum yield. Titration of glycerol into Naph^I_{Dimethyl} tag monomer sample to explore the effects of internal motion.

	Solvent			
	100% Ethanol	90% Ethanol : 10% Glycerol	70% Ethanol : 30% Glycerol	50% Ethanol : 50% Glycerol
L Naph ^I _{Dimethyl}	0.008	0.007	0.007	0.01

4.1.3.2. Fluorescence Quantum Yield of the Naphthalimide Probes

The fluorescence quantum yields of the naphthalimide probes in aqueous solution (Milli-Q water, 100 mM NaCl, 10 mM sodium phosphate buffer pH 7.0) are shown in Table 4.7 and obtained using the relative method, with Coumarin 153 as a reference standard. The quantum yields go down upon DNA incorporation due to quenching effects from proximal bases. However, the quantum yields of the probes are still an improvement on the previously studied anthracene system,⁹ once again illustrating the advantages of employing naphthalimides as reporter groups for sensing applications.

Table 4.7: Fluorescence quantum yield of naphthalimide probes ($\pm 10\%$).

Sample	Fluorescence Quantum Yield (Φ)
	Aqueous solution (Milli-Q water, 100 mM NaCl, 10 mM sodium phosphate buffer, pH 7.0)
P1AL (L Naph ^A _{Short})	0.035
P1AD (D Naph ^A _{Short})	0.032
P1BL (L Naph ^A _{Long})	0.032
P1BD (D Naph ^A _{Long})	0.033
P1CL (L Naph ^I _{Dimethyl})	0.0017
P1CD (D Naph ^I _{Dimethyl})	0.0017
P1DL (L Naph ^I _{Amine})	0.013
P1DD (D Naph ^I _{Amine})	0.020

4.2. Duplex Formation and Stability

Successful duplex formation and stability is a key factor in ensuring that the read-out detection signals are reliable, reproduceable, and that the maximum signal output is achieved. Internal DNA modifications, such as the insertion of naphthalimide reporter groups as described here, reduce duplex

stability by removing base pairing interactions and associated stacking interactions. Any disruption to duplex stability must be minimised to ensure the effectiveness of the modified DNA as a probe system. The naphthalimide modifications were designed to minimise disruptions to duplex stability, through the use of a threoninol linker that has the same phosphate spacing in the backbone as a sugar unit. Furthermore, the naphthalimide core unit itself is of a comparable size to a nucleobase and has the ability to π -stack within the duplex.

4.2.1. Duplex Melting Temperatures

Melting temperature (T_m) studies were performed on the naphthalimide-modified probe: target duplexes, with the melting temperatures of the unmodified duplexes also recorded for comparison (10 μ M probe, 10 μ M target; aqueous solution, 100 mM NaCl, 10 mM sodium phosphate buffer, pH 7.0; see Experimental 7.6.3 for detailed method). The duplex melting temperatures were recorded using the DNA intercalating dye, SYBR Green. As mentioned in Chapter 2, SYBR Green is known to affect the T_m values by raising the melting temperatures by roughly 10 °C.¹⁰⁷ This must be considered when comparing the melting temperatures reported here to other literature values which may have been determined using different methods. The melting temperature data is shown in Table 4.8.

All duplexes have T_m values well above room temperature (25 °C) meaning that all probe DNA strands should hybridise with their targets efficiently at room temperature. This room temperature sensing is highly beneficial for sensing applications as it removes the need for a heating step that slows down the testing procedure. The relatively high melting temperatures of all the modified duplexes should, in theory, allow optimal binding to occur with equal equivalents of probe and target DNA.

The naphthalimide modification replaces the site of a base pairing nucleotide, which causes a reduction in T_m values for all modified duplexes in comparison to the unmodified duplexes. This was also observed for the anthracene duplexes, despite its ability to provide stability *via* intercalation into the duplex and π -stack with adjacent bases.¹³¹

Table 4.8: Duplex melting temperatures (T_m) for all unmodified and naphthalimide-modified duplexes. 10 μ M probe: 10 μ M target, 100 mM NaCl, 10 mM sodium phosphate, pH 7.0, Milli-Q water, 1X SYBR Green. The values reported are the average T_m value from triplicate repeats, with the errors shown in brackets (). Values reported to the nearest 0.5 $^{\circ}$ C.

	T_m / $^{\circ}$ C	
Unmodified Duplex	67.5 (\pm 1.0)	
	Naph^A_{Short}	Naph^A_{Long}
L Probe : GGG Target (T1G)	57.5 (\pm 0.0)	56.5 (\pm 0.5)
L Probe : GAG Target (T1A)	57.0 (\pm 0.5)	56.5 (\pm 0.5)
L Probe : GCG Target (T1C)	59.0 (\pm 1.0)	56.5 (\pm 0.5)
L Probe : GTG Target (T1T)	57.5 (\pm 0.5)	56.0 (\pm 1.0)
L Probe : GAA Target (T1MM)	45.0 (\pm 1.0)	45.0 (\pm 0.5)
L Probe : GmCG Target (T1mC)	57.5 (\pm 0.5)	56.0 (\pm 0.0)
D Probe : GGG Target (T1G)	55.0 (\pm 1.5)	57.5 (\pm 0.5)
D Probe : GAG Target (T1A)	56.0 (\pm 1.0)	57.0 (\pm 0.0)
D Probe : GCG Target (T1C)	58.5 (\pm 0.5)	57.0 (\pm 1.0)
D Probe : GTG Target (T1T)	56.0 (\pm 1.0)	56.5 (\pm 0.0)
D Probe : GAA Target (T1MM)	44.0 (\pm 1.0)	47.0 (\pm 0.5)
D Probe : GmCG Target (T1mC)	53.5 (\pm 0.5)	56.5 (\pm 1.0)
	Naph^I_{Dimethyl}	Naph^I_{Amine}
L Probe : GGG Target (T1G)	62.5 (\pm 0.0)	62.5 (\pm 0.0)
L Probe : GAG Target (T1A)	60.5 (\pm 1.0)	61.5 (\pm 0.5)
L Probe : GCG Target (T1C)	57.0 (\pm 0.5)	60.5 (\pm 1.5)
L Probe : GTG Target (T1T)	60.0 (\pm 1.0)	60.5 (\pm 1.5)
L Probe : GAA Target (T1MM)	46.0 (\pm 0.5)	48.0 (\pm 0.5)
L Probe : GmCG Target (T1mC)	56.0 (\pm 0.5)	62.0 (\pm 0.5)
D Probe : GGG Target (T1G)	62.5 (\pm 0.5)	64.0 (\pm 1.0)
D Probe : GAG Target (T1A)	60.0 (\pm 0.5)	63.0 (\pm 0.5)
D Probe : GCG Target (T1C)	61.0 (\pm 0.5)	63.0 (\pm 0.5)
D Probe : GTG Target (T1T)	61.0 (\pm 0.5)	62.5 (\pm 0.5)
D Probe : GAA Target (T1MM)	48.0 (\pm 0.5)	48.5 (\pm 1.0)
D Probe : GmCG Target (T1mC)	59.0 (\pm 3.5)	62.0 (\pm 1.0)

4.2.2. Explaining the Differences in Duplex Melting Temperatures Between the Various Naphthalimide Reporter Groups

The different naphthalimide reporter groups have varying effects on the duplex stability due to their different orientations and interactions within the duplex. These effects are discussed below.

4.2.2.1. Comparing Melting Temperatures Between Naph^A_{Short} and Naph^A_{Long} Duplexes

The differences in the duplex melting temperatures are dependent on both the linker length between the naphthalimide unit and the threoninol sugar analogue and the stereochemistry of the threoninol. In the case of the Naph^A_{Short} duplexes, the L duplexes having higher melting temperatures overall in comparison to the D duplexes, which can be explained by the positioning of the reporter group imposed by the threoninol stereochemistry. Due to the short linker length between the threoninol and the naphthalimide, the system is quite rigid and therefore the threoninol stereochemistry may have a greater impact on where the reporter group resides within the duplex.

Interestingly, a similar trend was observed with the anthracene with a n=1 linker length system (a comparable linker length to Naph^A_{Short}) shown in Figure 4.14, with the L threoninol systems having higher melting temperatures than the D.⁶ This effect was explained through the use of molecular dynamics simulations of the L and D anthracene n=1 modified duplexes. Figure 4.15 highlights the structural effects that the threoninol stereochemistry has on the positioning of the anthracene moiety within the duplex, and the effect that this poses to the stability of the duplex. The model on the left, Figure 4.15, shows the L threoninol isomer, where the anthracene is directed towards the major groove of DNA. In this position the anthracene is able to intercalate effectively into the duplex with minimal disruption, which is consistent with the higher T_m values observed. In comparison, the model on the right, Figure 4.15, shows the D threoninol isomer, where the anthracene is now directed towards the minor groove of DNA. This more external anthracene positioning appears to disrupt the DNA helical structure by kinking the DNA, which would explain the lower T_m values. Owing to the similarity in size

and linker length of the anthracene and naphthalimide systems, it is reasonable to infer that the naphthalimide tags in the $\text{Naph}^{\text{A}}_{\text{Short}}$ duplexes experience a similar positioning to those in the anthracene systems, given the similarity in trends of the T_m values for these systems.

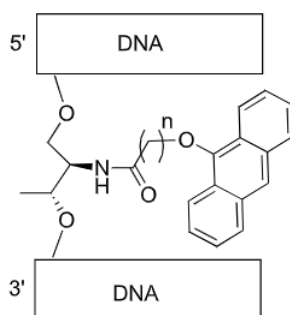


Figure 4.14: Anthracene reporter group with short linker length, comparable to $\text{Naph}^{\text{A}}_{\text{Short}}$, where $n = 1$.

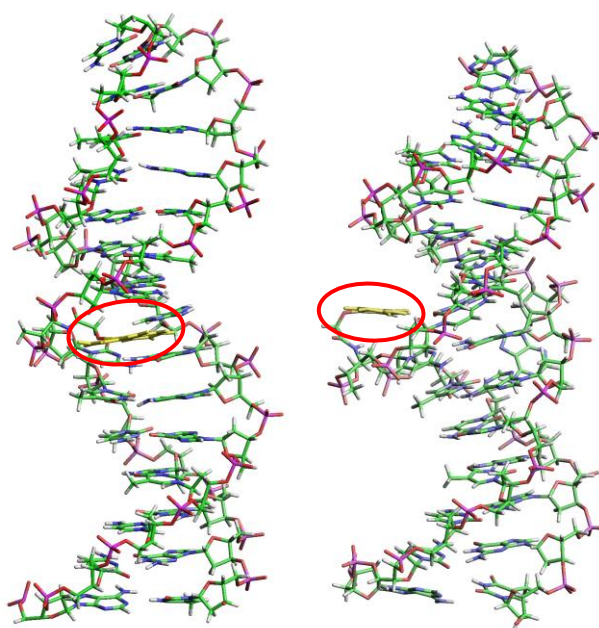


Figure 4.15: AMBER computational models of anthracene $n=1$ (circled in red) duplexes with L threoninol stereochemistry (left) and D stereochemistry (right). Figure taken from J. -L. H. A. Duprey Thesis, 2010.⁶

The $\text{Naph}^{\text{A}}_{\text{Long}}$ duplexes have T_m values that are fairly similar between the two threoninol isomers, see Table 4.8. This can be explained by the longer linker creating space between the threoninol unit and naphthalimide reporter group, giving more flexibility in the movement of the naphthalimide within the

duplex. This would result in the threoninol stereochemistry no longer dictating the positioning of the naphthalimide unit.

4.2.2.2. Comparing Melting Temperatures Between the Naph^A and Naph^I Duplexes

The Naph^I duplexes have slightly higher melting temperatures than the Naph^A duplexes, as shown in Table 4.8. This is most probably due to the differences in the orientation of the naphthalimide reporter group within the DNA probe strand. The Naph^A probes have an alkyl chain at the imide position, which may protrude into the duplex and cause a slight disruption to duplex stability. In addition, when considering the Naph^I duplexes, the naphthalene unit is in a better orientation to maximise any π -stacking interactions with neighbouring bases. This minimal disruption to duplex stability for the Naph^I duplexes accounts for the slightly higher T_m values. The linker also creates space and flexibility between the naphthalimide reporter group and the backbone which allows for a more favourable positioning of the tag within the duplex.

Furthermore, duplexes formed with mC targets show lower T_m values when compared to duplexes formed with C targets (in the majority of cases), Table 4.8. This implies that the addition of the methyl group in mC targets destabilises the duplex and may have an effect on reporter group positioning. A similar observation was also reported with the anthracene system.¹¹

4.2.3. Duplex Melting Temperatures for the BRAF V600E Duplexes

The BRAF duplexes have slightly lower melting temperatures compared to the duplexes above; a result of differences in the DNA sequence, see Table 4.9. Although all duplexes are identical in length, the BRAF sequence contains fewer CG base pairs in comparison to the other duplexes, which leads to a reduction in hydrogen bonding interactions between the probe and target strands. However, as the BRAF duplex T_m values are all well above room temperature, this slight reduction in T_m value is not significant enough to affect the sensing results. Interestingly, similar trends are observed here as with

the duplexes above, in that the D probe/target duplexes have lower T_m values than the L probe/target duplexes, again demonstrating the influence of the threoninol stereochemistry on the overall positioning of the naphthalimide tag within the duplex.

Table 4.9: Duplex melting temperatures (T_m) for the BRAF Naph^A_{short} duplexes. 10 μ M probe: 10 μ M target, 100 mM NaCl, 10 mM sodium phosphate, pH 7.0, Milli-Q water, 1X SYBR Green. Values reported to the nearest 0.5 °C. Repeats could not be performed due to limited sample.

	T_m /°C
Unmodified Duplex	63.0
BRAF Naph^A_{short}	
L Probe : A Target	54.5
L Probe : T Target	56.5
D Probe : A Target	51.5
D Probe : T Target	53

4.3. Fluorescence Sensing of 1,8-Naphthalimide Modified Duplexes and Their Ability to Base Discriminate

Previous work in the Tucker group has involved the sensing of anthracene probes upon hybridisation with complementary DNA targets *via* monitoring changes in fluorescence emission intensities.^{6, 11, 17}

The work described in this section demonstrates the additional benefits that solvatochromic fluorophores, such as naphthalimides, provide to the sensing read-out signals by not only displaying changes in the emission intensity but also shifts in their emission profiles upon duplex formation with a target strand. The aim of this work has been to discriminate between different base variants in the target strand *via* monitoring changes in the fluorescence emission of the naphthalimide reporter group in the probe strand.

The following sections describe the sensing results obtained from the various duplex systems introduced in Chapter 3; base-opposite sensing, base-adjacent sensing, epigenetic sensing and sensing of the BRAF V600E mutation. For each system, the resulting sensing read-outs (both intensity changes and spectral shifts) will be discussed. Drawing on some similarities in the molecular structure of the

naphthalimide tags, the Naph^A_{Short} and Naph^A_{Long} probes have been discussed and compared separately to the Naph^I_{Dimethyl} and Naph^I_{Amine} probes.

4.3.1. Sensing Conditions

Throughout the sensing experiments, the excitation wavelength remained constant at 450 nm so that comparisons could be made between the different naphthalimide systems.

For the DNA hybridisation studies, at first equal equivalents of probe and target DNA were used at micromolar concentrations as it was anticipated that these conditions should result in all probe strands binding sufficiently to their targets, owing to their relatively high duplex melting temperatures (see Section 4.2.1 for a detailed discussion of duplex melting temperature experiments). However, as seen with previous work,⁶ in reality higher equivalents of target were required to reach the optimal fluorescence signal upon duplex formation. For this reason, a 1:3 probe: target ratio was used for sensing experiments to ensure that all the probe strands were bound in solution to achieve an optimal read-out. These results are accordingly shown in the following sections (for the 1:1 sensing results, see Appendix 8.2.6).

All sensing experiments were carried out using 0.5 μ M probe DNA and 1.5 μ M target DNA in an aqueous solution of 100 mM NaCl and 10 mM sodium phosphate buffer, pH 7.0 at 298 K.

4.3.2. Fluorescence Sensing of Probes in the Base-Opposite Sensing System

Base-opposite sensing describes the sensing of base variants in a target strand at a site directly opposite the naphthalimide modification site in the probe strand. In this system, the base opposite the modification site cannot base pair with the naphthalimide reporter group but may interact with it.

4.3.2.1. Fluorescence Sensing Using Naph^A_{Short} and Naph^A_{Long} Probes

Figure 4.16 to Figure 4.19 show the emission profiles of the Naph^A_{Short} and Naph^A_{Long} reporter groups upon duplex formation with complementary targets. The figures demonstrate the intensity changes

and Table 4.10 summarises the shifts in maximum emission wavelength upon duplex formation. Due to the solvatochromic nature of the naphthalimide reporter groups and their sensitivity to their local environment, significant shifts in the maximum emission wavelength between the different base variants are observed. These shifts in emission provide a new dimension to sensing read-outs that was not previously seen with the anthracene sensing systems, whereby only intensity changes were observed.

Shifts in the fluorescence emission maximum between the various target strands allow a detection wavelength to be selected where the most significant changes in fluorescence intensities are observed. Taking the D Naph^A_{Short} system as an example, Figure 4.17, by changing the detection wavelength from the maximum emission of the probe (527 nm) to 509 nm we can detect a A > C point variation *via* a signal enhancement of 37% upon binding of the C target variant. This compares to a smaller signal enhancement of 21 % at the maximum emission of the probe (527 nm). This allows for effective base discrimination owing to the differences in the emission profiles upon binding each target variant, and the selection of the detection wavelength that provides the largest change in fluorescence intensity.

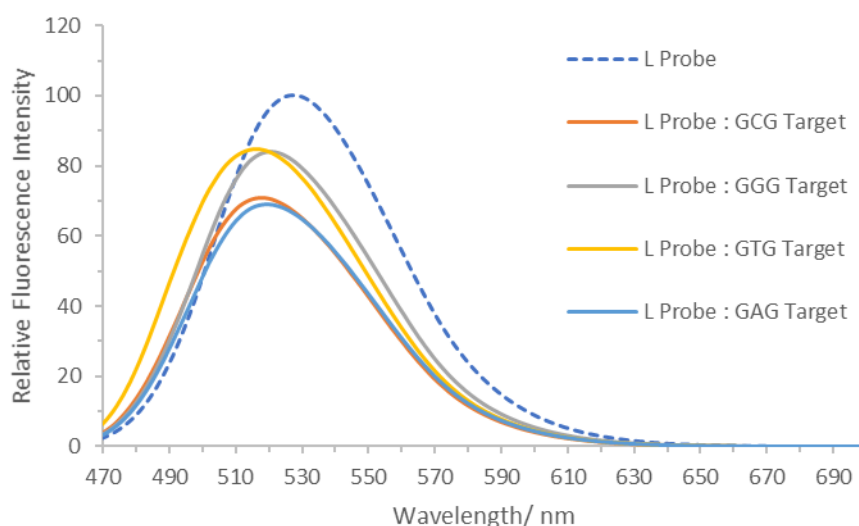


Figure 4.16: Sensing results of L Naph^A_{Short} (P1AL) probes with base-opposite system; T1C, T1G, T1T, T1A targets. 0.5 μ M [Probe], 1.5 μ M [Target], 100 mM NaCl, 10 mM sodium phosphate buffer pH 7.0, Milli-Q water, 298 K, λ_{ex} = 450 nm.

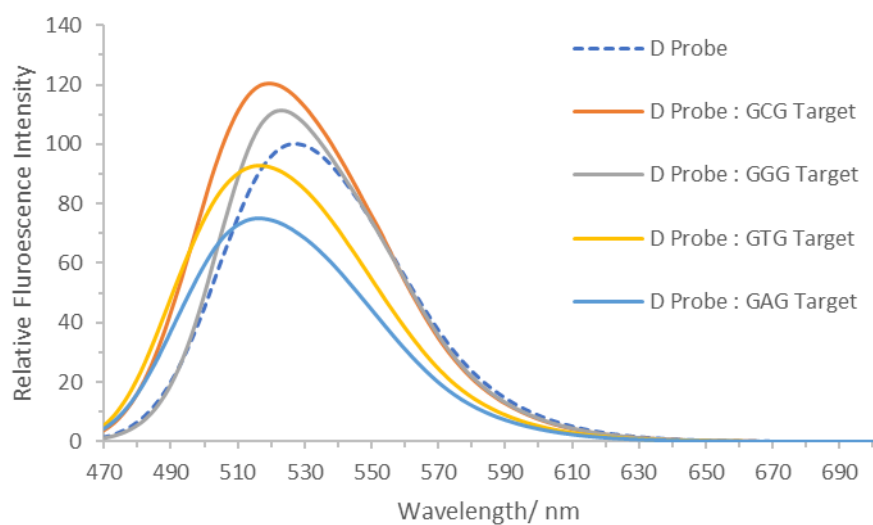


Figure 4.17: Sensing results of D Naph^A_{Short} (P1AD) probes with base-opposite system; T1C, T1G, T1T, T1A targets. 0.5 μ M [Probe], 1.5 μ M [Target], 100 mM NaCl, 10 mM sodium phosphate buffer pH 7.0, Milli-Q water, 298 K, λ_{ex} = 450 nm.

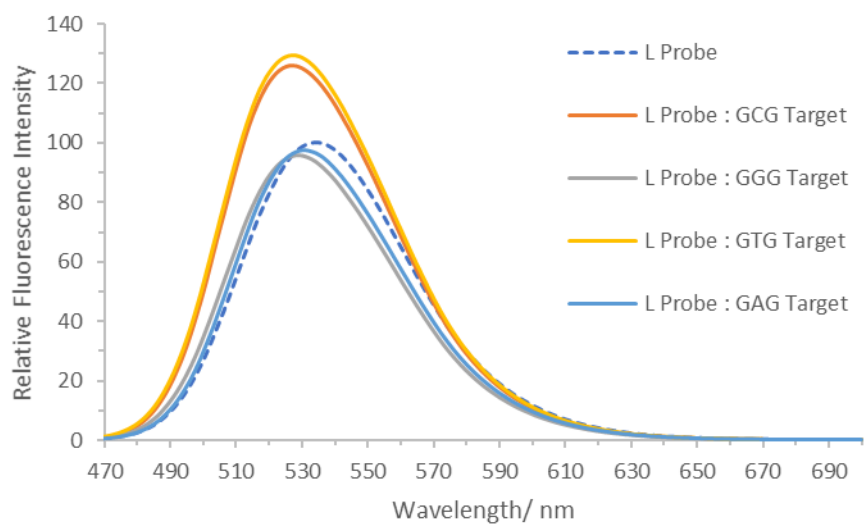


Figure 4.18: Sensing results of L Naph^A_{Long} (P1BL) probes with base-opposite system; T1C, T1G, T1T, T1A targets. 0.5 μ M [Probe], 1.5 μ M [Target], 100 mM NaCl, 10 mM sodium phosphate buffer pH 7.0, Milli-Q water, 298 K, λ_{ex} = 450 nm.

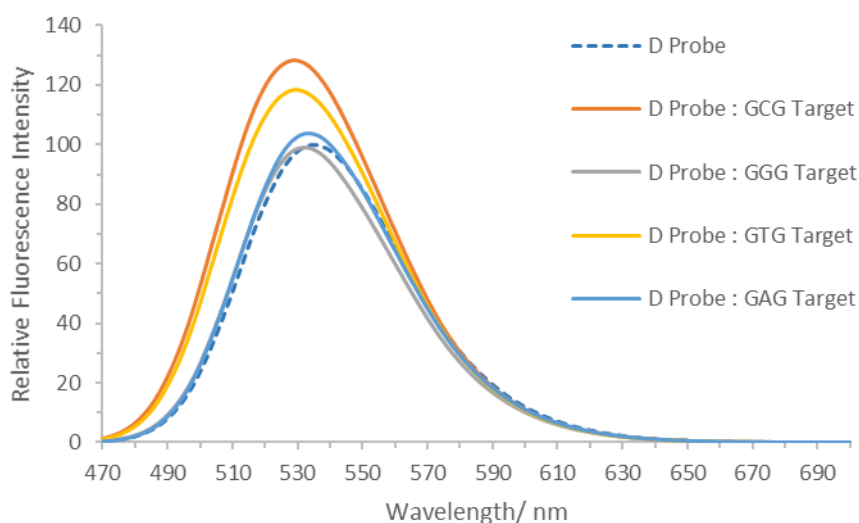


Figure 4.19: Sensing results of D Naph^A_{Long} (P1BD) probes with base-opposite system; T1C, T1G, T1T, T1A targets. 0.5 μ M [Probe], 1.5 μ M [Target], 100 mM NaCl, 10 mM sodium phosphate buffer pH 7.0, Milli-Q water, 298 K, λ_{ex} = 450 nm.

As expected from previous work involving anthracenes, the linker length, short vs long, has a pronounced effect on the sensing results. The Naph^A_{Short} probes, Figure 4.16 and Figure 4.17, are overall more sensitive to base discrimination than the Naph^A_{Long} probes, Figure 4.18 and Figure 4.19. In addition to linker length, stereochemistry may also contribute to differences in sensing read-outs. For the Naph^A_{Long} probes, the threoninol stereochemistry does not seem to affect the sensing results, whereas it plays a more important role with the Naph^A_{Short} probes, with differences observed in the sensing read-outs between the L and D probes. Differences in sensing read-outs for the different tag types can be explained by the positioning of the naphthalimide fluorophore within the duplex. The Naph^A_{Short} probes hold the naphthalimide fluorophore in close proximity to the sugar-phosphate backbone as it is attached directly to the threoninol sugar analogue, producing a rigid sensing system. In such a system, the fluorophore is held close to the base opposite in the target strand, resulting in stronger interactions between the two, and more sensitive base discrimination. On the other hand, the Naph^A_{Long} probes introduce a flexible tether between the naphthalimide fluorophore and the threoninol sugar mimic, and produces a flexible sensing system. This system allows the free movement of the naphthalimide reporter group in and out of the duplex structure. Consequently, there are fewer

and/or weaker interactions between the reporter group and the base opposite in the target strand, and thus there are less definitive intensity and shift changes between the base variants using these systems. These observations correlate well with duplex melting temperature results discussed above.

Table 4.10 summarises the effect of the linker length on the shifts between the base variants. The data demonstrates the increased sensitivity in base discrimination of the Naph^A_{Short} probes by displaying greater shifts in λ_{\max} between the different base variants compared to the various Naph^A_{Long} duplexes. This observation supports the explanation that the Naph^A_{Long} system is more flexible and therefore the naphthalimide is free to move in and out of the duplex and experience more varied changes in its local environment; this in turn produces more averaged shifts in the λ_{\max} of the fluorescence emission between the various duplex variants.

Table 4.10: Shifts in maximum emission wavelength of Naph^A_{Short} (P1AL/D) and Naph^A_{Long} (P1BL/D) probes between the target variants. 0.5 μ M probe: 1.5 μ M target. 100 mM NaCl, 10 mM sodium phosphate buffer pH 7.0, Milli-Q, 298 K, $\lambda_{\text{ex}} = 450$ nm.

	Naph ^A _{Short}		Naph ^A _{Long}	
	λ_{\max} /nm	λ_{\max} wavelength shift (in comparison to probe alone) /nm	λ_{\max} /nm	λ_{\max} wavelength shift (in comparison to probe alone) /nm
L Probe	527	-	534	-
L Probe : GGG Target (T1G)	521	-6	529	-5
L Probe : GAG Target (T1A)	519	-8	530	-4
L Probe : GCG Target (T1C)	517	-10	527	-7
L Probe : GTG Target (T1T)	516	-11	527	-7
D Probe	527	-	534	-
D Probe : GGG Target (T1G)	523	-4	532	-2
D Probe : GAG Target (T1A)	516	-11	533	-1
D Probe : GCG Target (T1C)	519	-8	529	-5
D Probe : GTG Target (T1T)	516	-11	529	-5

The size of the base opposite in the target strand also seems to influence the signal read-outs obtained with the $\text{Naph}^{\text{A}}_{\text{Long}}$ system. The larger bicyclic purine bases, adenine and guanine, provide similar intensity read-outs to the probe alone, whereas the smaller monocyclic pyrimidines, cytosine and thymine, show an increase in fluorescence intensity. The increase in fluorescence intensity upon binding the C and T targets, in addition to the larger shifts in λ_{max} to lower wavelengths, implies that the naphthalimide reporter groups in these duplexes experience a more hydrophobic environment, shielded from any quenching effects from the external aqueous environment. This increased hydrophobic environment could be a result of the additional space created in the base-opposite system when the smaller pyrimidine bases are present, creating a 'pocket' in which the naphthalimide reporter group can reside. The flexibility of the $\text{Naph}^{\text{A}}_{\text{Long}}$ system allows the naphthalimide to fill the additional space created by the pyrimidine bases and the ability of the naphthalimide to π -stack with the surrounding bases makes the positioning favourable. In contrast, the $\text{Naph}^{\text{A}}_{\text{Short}}$ probes have a much more fixed positioning of the reporter groups and the additional space provided by the smaller pyrimidine bases has little effect as the reporter group may not be free to adopt this space. The ability of the $\text{Naph}^{\text{A}}_{\text{Long}}$ probes to distinguish between purine and pyrimidine bases *via* the enhancement of the fluorescent signal, makes them promising probe systems for the detection of point variations involving the change from purines to pyrimidines by providing 'on/off' sensing read-outs.

4.3.2.2. Fluorescence Sensing Using $\text{Naph}^{\text{I}}_{\text{Dimethyl}}$ and $\text{Naph}^{\text{I}}_{\text{Amine}}$ Probes

Changing the orientation at which the naphthalimide reporter group is incorporated into DNA has a consequent effect on the sensing read-outs. The $\text{Naph}^{\text{I}}_{\text{Dimethyl}}$ and $\text{Naph}^{\text{I}}_{\text{Amine}}$ probes hold the naphthalimide in the opposite orientation compared to the $\text{Naph}^{\text{A}}_{\text{Short}}$ and $\text{Naph}^{\text{A}}_{\text{Long}}$ probes, with the naphthalene aromatic core in a position furthest away from the sugar-phosphate backbone. This enables different interactions to occur between the reporter group and the base opposite in the target strand. The different sensing read-outs produced as a result of this will now be discussed.

Figure 4.20 to Figure 4.23 shows the fluorescence emission read-outs obtained from the Naph¹_{Dimethyl} and Naph¹_{Amine} probes upon duplex formation with the complementary targets. Once again, fluorescence emission intensity changes are observed upon duplex formation with the various target variants, in addition to shifts in the λ_{max} of fluorescence emission. This again proves that the solvatochromic nature of the naphthalimide reporter groups are providing an additional dimension to the sensing read-outs that were not observed with the anthracene sensing systems.

Interestingly, significantly large increases in fluorescence emission intensity were observed upon target binding with the Naph¹_{Dimethyl} probes (in the majority of cases), despite the naphthalimide probes being weakly fluorescent in their single-stranded forms. This significant increase in fluorescence intensity could be attributed to an increase in planarity of the Naph¹_{Dimethyl} tag upon duplex formation. As monomer units, the interaction of the methyl group in the 4-dimethylamino substituent with the hydrogen at the 5-position causes a reduction in molecular planarity and leads to a diminution of the fluorescence intensity, as discussed in Section 4.1.3. However, once duplexed and interacting with the base stack, the Naph¹_{Dimethyl} may experience a more restricted position within the duplex, which would restrict rotation of the 4-dimethylamino group. This in turn would cause an increase in planarity throughout the molecule as the nitrogenous lone pairs are optimally aligned for the intramolecular charge transfer that occurs throughout the molecule. This 'switch on' or 'light up' sensing of a DNA binding event is particularly useful for DNA PAINT applications and is explored further in Chapter 6.

The signal enhancement effect upon DNA binding is seen to a greater extent for the L Naph¹_{Dimethyl} probe, indicating that threoninol stereochemistry plays a role in the positioning of the naphthalimide reporter group within the duplex and the environment the reporter group experiences. The results suggest that the L Naph¹_{Dimethyl} tag intercalates quite well upon duplex formation with all target variants, as demonstrated by the fluorescence intensity increases for all duplex variants.

With the D Naph^l_{Dimethyl} probes, varying the base opposite the tag has a greater effect on the tag positioning, with large increases in fluorescence only observed with the pyrimidine (cytosine and thymine) target variants. A possible explanation for this may be that the larger purine bases, adenine and guanine, ‘push’ the naphthalimide reporter group further out of the duplex, and into the more polar external environment. This external, more polar environment is reflected by the reduced fluorescence emission intensity in duplexes formed with A and G targets and the shift in the λ_{\max} fluorescence emission to a higher wavelength for these duplexes. These results indicate that the D Naph^l_{Dimethyl} probes may also be particularly effective at sensing point variations involving a change from a purine to pyrimidine, resulting in an ‘on/off’ sensing system.

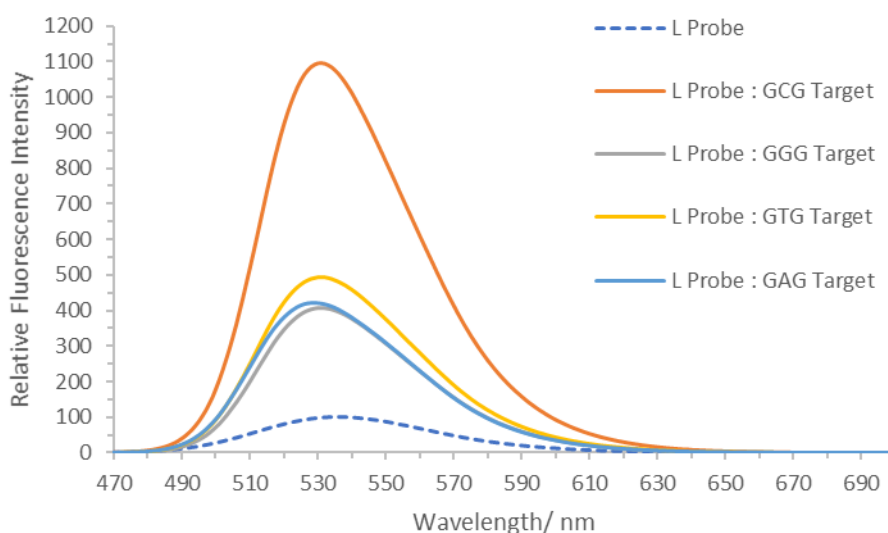


Figure 4.20: Sensing results of L Naph^l_{Dimethyl} (P1CL) probes with base-opposite system; T1C, T1G, T1T, T1A targets. 0.5 μ M [Probe], 1.5 μ M [Target], 100 mM NaCl, 10 mM sodium phosphate buffer pH 7.0, Milli-Q water, 298 K, $\lambda_{\text{ex}} = 450$ nm.

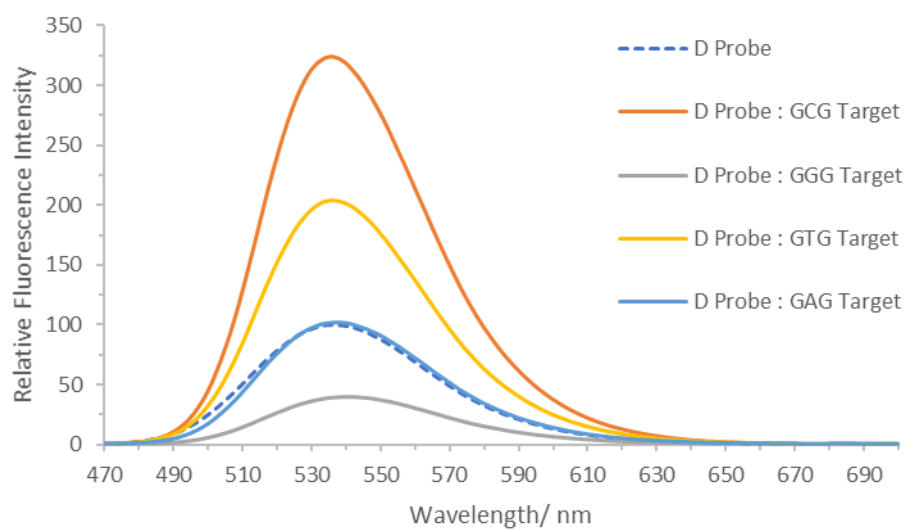


Figure 4.21: Sensing results of D Naph¹_{Dimethyl} (P1CD) probes with base-opposite system; T1C, T1G, T1T, T1A targets. 0.5 μ M [Probe], 1.5 μ M [Target], 100 mM NaCl, 10 mM sodium phosphate buffer pH 7.0, Milli-Q water, 298 K, λ_{ex} = 450 nm.

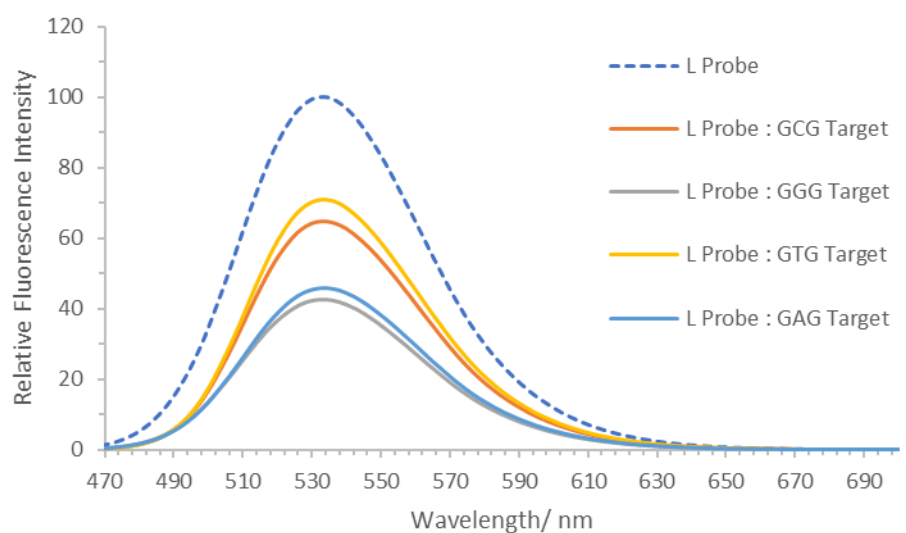


Figure 4.22: Sensing results of L Naph¹_{Amine} (P1DL) probes with base-opposite system; T1C, T1G, T1T, T1A targets. 0.5 μ M [Probe], 1.5 μ M [Target], 100 mM NaCl, 10 mM sodium phosphate buffer pH 7.0, Milli-Q water, 298 K, λ_{ex} = 450 nm.

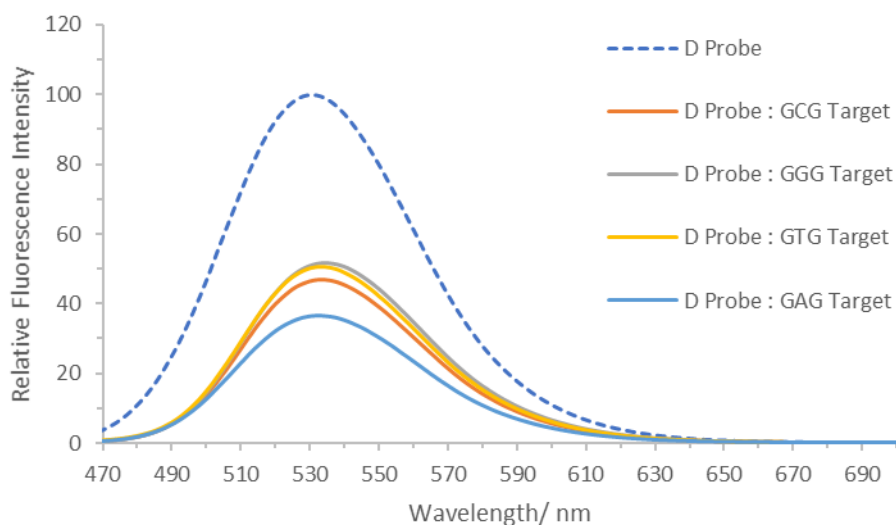


Figure 4.23: Sensing results of D Naph^I_{Amine} (P1DD) probes with base-opposite system; T1C, T1G, T1T, T1A targets. 0.5 μ M [Probe], 1.5 μ M [Target], 100 mM NaCl, 10 mM sodium phosphate buffer pH 7.0, Milli-Q water, 298 K, λ_{ex} = 450 nm.

In contrast, the Naph^I_{Amine} probes exhibit a significant reduction in the fluorescence emission intensity upon DNA binding, Figure 4.22 and Figure 4.23. The nature of the 4-amino group and its ability to form hydrogen bonds with the aqueous external environment, may provide a more favourable interaction over the intercalation of the naphthalimide reporter group within the duplex. This may result in the naphthalimide reporter group residing in a position outside of the duplex, with H-bonding between the NH₂ group and the surrounding water molecules causing a quenching in the fluorescence signal. Such interactions may also stabilise the excited state, which subsequently causes a shift in the λ_{max} of the fluorescence emission towards higher wavelengths, as shown in Table 4.11. As the reporter group is further removed from the base opposite in the target strand, it does not interact effectively, hence base discrimination is difficult. The effect of threoninol stereochemistry is also minimal, with both isomers of the probe giving similar results.

Table 4.11: Shifts in the maximum emission wavelength of $Naph^{Dimethyl}$ (P1CL/D) and $Naph^{Amine}$ (P1DL/D) probes between the target variants. 0.5 μ M probe: 1.5 μ M target. 100 mM NaCl, 10 mM sodium phosphate buffer pH 7.0, Milli-Q, 298 K, λ_{ex} = 450 nm.

	$Naph^{Dimethyl}$		$Naph^{Amine}$	
	λ_{max} /nm	λ_{max} wavelength shift (in comparison to probe alone) /nm	λ_{max} /nm	λ_{max} wavelength shift (in comparison to probe alone) /nm
L Probe	536	-	533	-
L Probe : GGG Target (T1G)	530	-6	533	0
L Probe : GAG Target (T1A)	529	-7	534	1
L Probe : GCG Target (T1C)	531	-5	533	0
L Probe : GTG Target (T1T)	531	-5	534	1
D Probe	536	-	531	-
D Probe : GGG Target (T1G)	541	5	534	3
D Probe : GAG Target (T1A)	537	1	532	1
D Probe : GCG Target (T1C)	536	0	534	3
D Probe : GTG Target (T1T)	536	0	533	2

4.3.3. Fluorescence Sensing of Probes in the Base-Adjacent Sensing System

The base-adjacent sensing system involves the detection of a base variation in the target strand at the site adjacent (3' end) to the modification site in the probe strand and creates 'match' and 'mismatch' duplexes, see Chapter 3 for a detailed explanation. Based on previous work,⁶ the G > A point variation at the site adjacent to the modification site, towards the 3' end of the target strand was sensed and the results are shown below.

4.3.3.1. Fluorescence Sensing Using Naph^A_{Short} and Naph^A_{Long} Probes

Figure 4.24 to Figure 4.27 demonstrate the sensing results obtained from the ‘match’ vs ‘mismatch’ sensing using the Naph^A_{Short} and Naph^A_{Long} probes. Fluorescence intensity changes and shifts in the λ_{max} emission, Table 4.12, are observed upon binding target strands, once again proving the sensitivity of the naphthalimide reporter groups to their local environment.

The ‘match’ duplexes produce a weaker fluorescent signal in comparison to the ‘mismatch’ duplexes, Figure 4.24 to Figure 4.27. In the ‘mismatch’ duplex, the base pair adjacent to the naphthalimide reporter group does not form a hydrogen bonding base pair. This creates some space within the duplex as the strands are not held tightly together at this position. This may allow the naphthalimide reporter group to insert into the duplex to a greater extent (more hydrophobic) and could explain why a slight increase in fluorescence emission is observed for the ‘mismatch’ target in comparison to the ‘match’ target. This would also explain why a smaller hypsochromic shift in λ_{max} emission is observed for some of the ‘mismatch’ duplexes.

The Naph^A_{Long} probes have a more flexible linker which allows the naphthalimide reporter group to move more freely. The additional space created by the ‘mismatch’ target within the duplex, combined with the more flexible movement of the reporter group, may result in the positioning of the naphthalimide within this free space. Thus, the reporter group experiences a more shielded environment in this inserted position, away from quenching effects experienced in the surrounding aqueous environment and may be a plausible explanation for the observed increase in fluorescence intensity of the Naph^A_{Long} probes upon binding the ‘mismatch’ target.

In particular, the D Naph^A_{Long} probe is effective for sensing the ‘mismatch’ target from the ‘matched’ target *via* an increase in fluorescence emission of 31% when monitored at 534 nm, Figure 4.27. Thus, providing a ‘switch on’ sensing read-out.

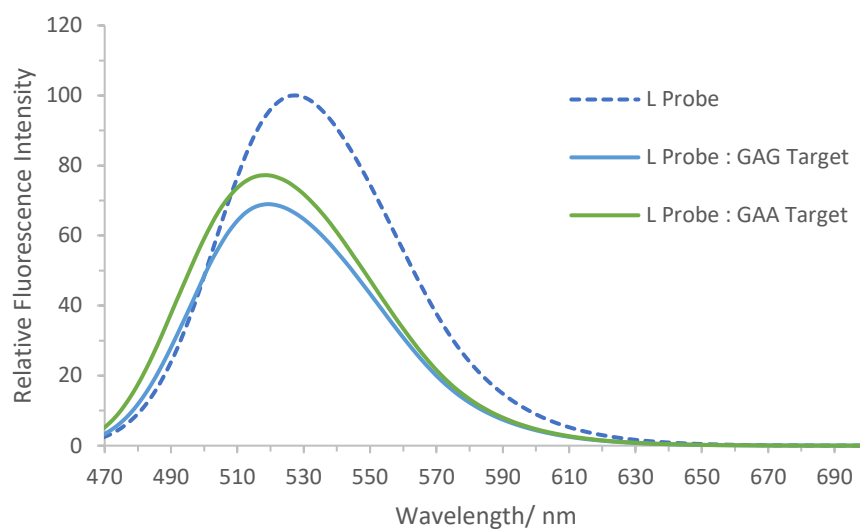


Figure 4.24: Sensing results of L Naph^A_{Short} probes (P1AL) with base-adjacent system; T1A, T1MM targets. 0.5 μ M [Probe], 1.5 μ M [Target], 100 mM NaCl, 10 mM sodium phosphate buffer pH 7.0, Milli-Q water, 298 K, λ_{ex} = 450 nm.

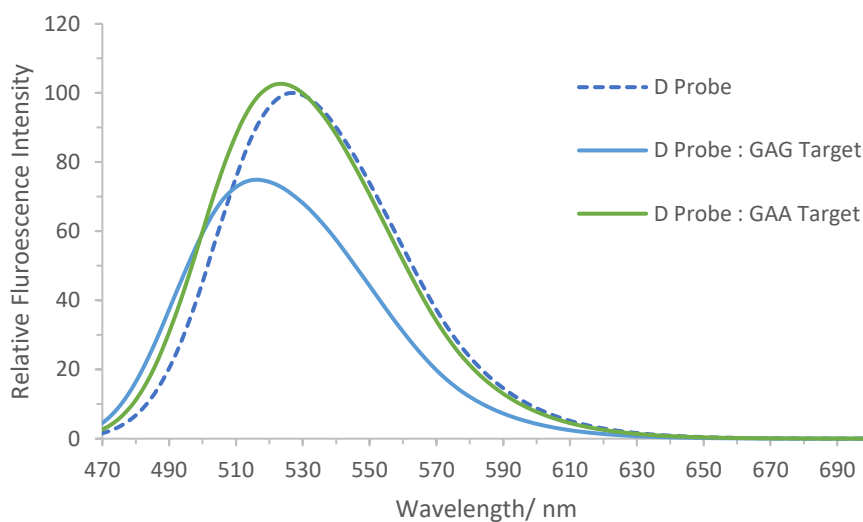


Figure 4.25: Sensing results of D Naph^A_{Short} (P1AD) probes with base-adjacent system; T1A, T1MM targets. 0.5 μ M [Probe], 1.5 μ M [Target], 100 mM NaCl, 10 mM sodium phosphate buffer pH 7.0, Milli-Q water, 298 K, λ_{ex} = 450 nm.

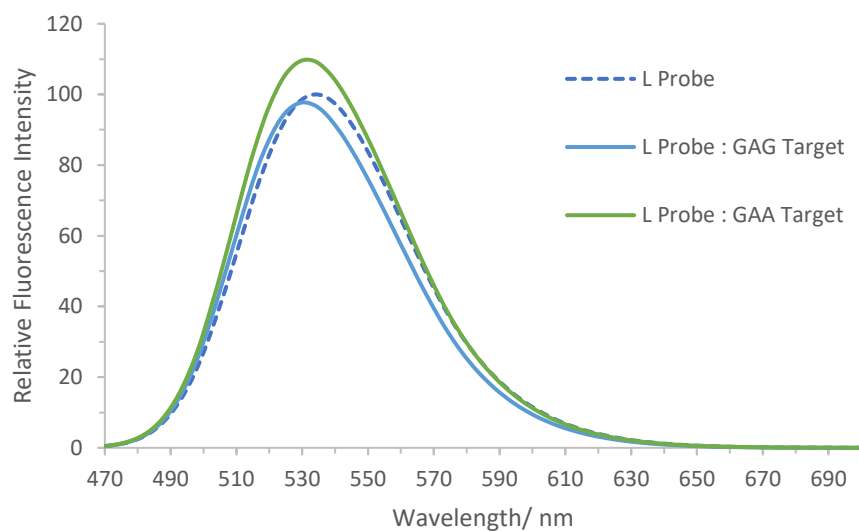


Figure 4.26: Sensing results of L Naph^A_{Long} (P1BL) probes with base-adjacent system; T1A, T1MM target. 0.5 μM [Probe], 1.5 μM [Target], 100 mM NaCl, 10 mM sodium phosphate buffer pH 7.0, Milli-Q water, 298 K, $\lambda_{\text{ex}} = 450 \text{ nm}$.

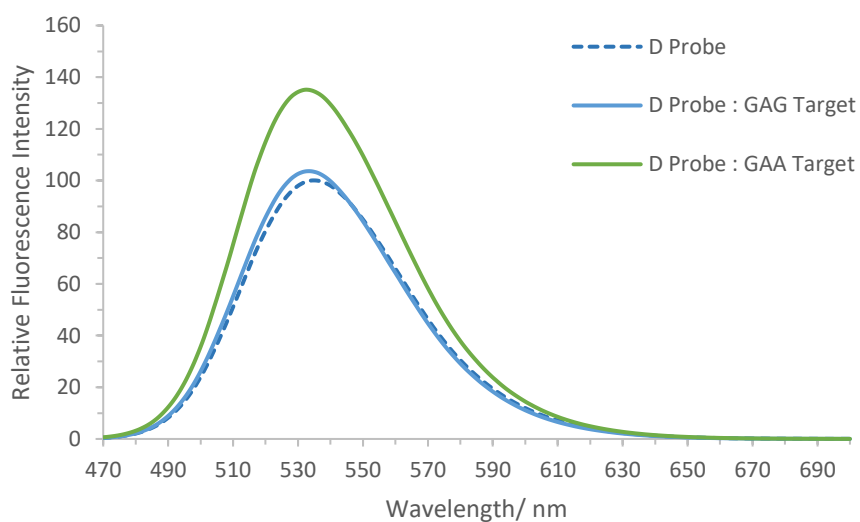


Figure 4.27: Sensing results of D Naph^A_{Long} (P1BD) probes with base-adjacent system; T1A, T1MM target. 0.5 μM [Probe], 1.5 μM [Target], 100 mM NaCl, 10 mM sodium phosphate buffer pH 7.0, Milli-Q water, 298 K, $\lambda_{\text{ex}} = 450 \text{ nm}$.

Table 4.12: Shifts in the maximum emission wavelength of Naph^A_{Short} (P1AL/D) and Naph^A_{Long} (P1BL/D) probes between ‘match’ (P1A) and ‘mismatch’ (P1MM) targets. 0.5 μM probe: 1.5 μM target. 100 mM NaCl, 10 mM sodium phosphate buffer pH 7.0, Milli-Q, 298 K, λ_{ex} = 450 nm.

	Naph ^A _{Short}		Naph ^A _{Long}	
	λ _{max} /nm	λ _{max} wavelength shift (in comparison to probe alone) /nm	λ _{max} /nm	λ _{max} wavelength shift (in comparison to probe alone) /nm
L Probe	527	-	534	-
L Probe : GAG Target (T1A)	519	-8	530	-4
L Probe : GAA Target (T1MM)	519	-8	532	-2
D Probe	527	-	534	-
D Probe : GAG Target (T1A)	516	-11	533	-1
D Probe : GAA Target (T1MM)	524	-3	533	-1

4.3.3.2. Fluorescence Sensing Using Naph^I_{Dimethyl} and Naph^I_{Amine} Probes

Figure 4.28 to Figure 4.31 show the sensing results of the Naph^I_{Dimethyl} and Naph^I_{Amine} probes to distinguish between a ‘match’ and ‘mismatch’ target.

As previously mentioned during the base-opposite sensing section, the L Naph^I_{Dimethyl} probes observe vast increases (up to 10-fold) in fluorescence emission intensity upon binding a target. However, the increase in fluorescence emission intensity upon binding the ‘mismatch’ target is less significant than for any of the ‘matching’ targets, Figure 4.28. As mentioned above, the removal of the hydrogen bonding base pair adjacent to the modification site in the ‘mismatched’ duplex creates space within the duplex. This additional space may lessen the restricted rotation of the methyl groups in the 4-dimethylamino substituent when compared to the fully ‘matched’ duplex. The increased movement/rotation of the methyl groups disrupts the planarity throughout the naphthalimide

molecule and could lead to the observed reduction in fluorescence emission intensity for the 'mismatched' duplex.

In comparison, the $\text{Naph}^{\text{I}}_{\text{Amine}}$ probes produce a higher fluorescence emission signal for the 'mismatch' target in comparison to the 'matched' target, Figure 4.30 and Figure 4.31. However, with these probes, no distinctive increase in fluorescence signal is observed for 'match' or 'mismatch' sensing.

Ideally, for an effective sensing system, a 'switch on' or enhancement in fluorescence signal is preferred for the detection of a single point variation, owing to the ease of detection and reduction of false-positive results. The $\text{Naph}^{\text{I}}_{\text{Dimethyl}}$ and $\text{Naph}^{\text{I}}_{\text{Amine}}$ probes do not exhibit a signal enhancement when binding the 'mismatched' target in comparison to the 'matched' target or probe alone, making these probe systems less effective for sensing these single point variations.

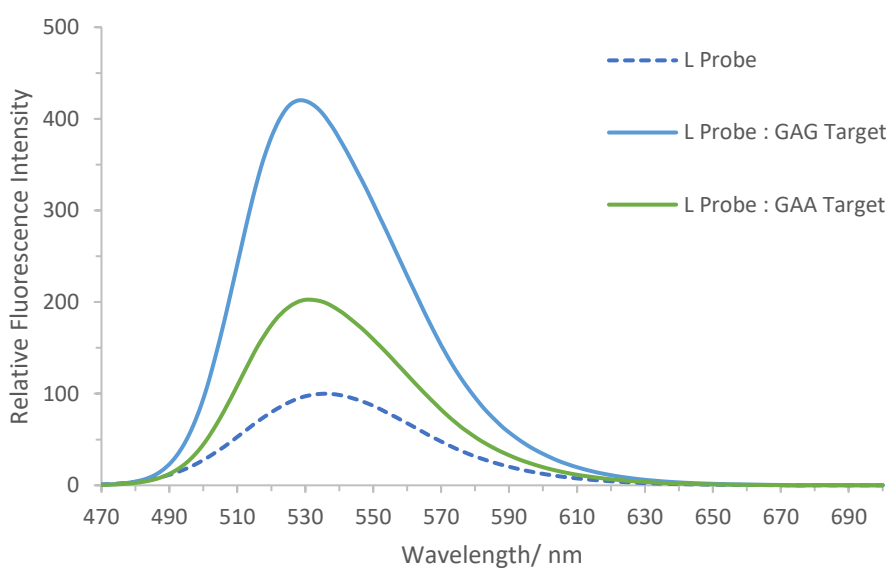


Figure 4.28: Sensing results of L $\text{Naph}^{\text{I}}_{\text{Dimethyl}}$ (P1CL) probes with base-adjacent system; T1A, T1MM targets. 0.5 μM [Probe], 1.5 μM [Target], 100 mM NaCl, 10 mM sodium phosphate buffer pH 7.0, Milli-Q water, 298 K, $\lambda_{\text{ex}} = 450$ nm.

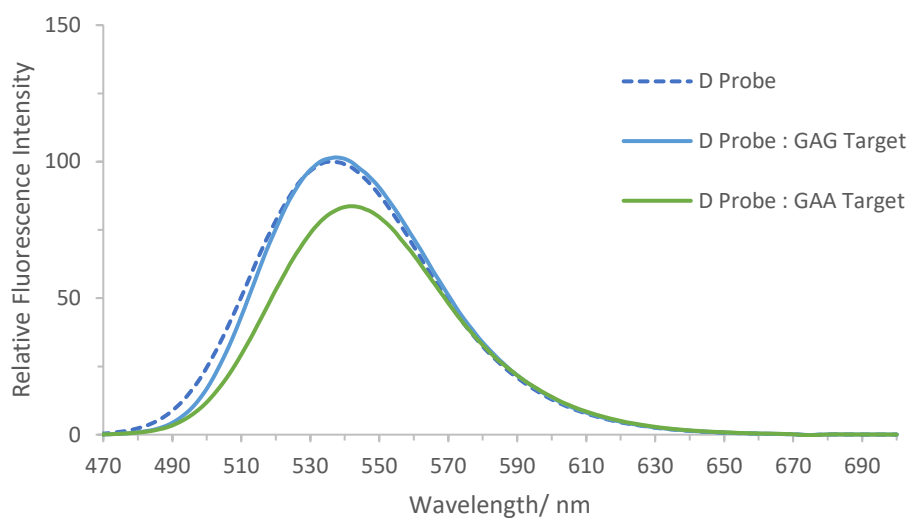


Figure 4.29: Sensing results of D Naph^{Dimethyl} (P1CD) probes with base-adjacent system; T1A, T1MM targets. 0.5 μM [Probe], 1.5 μM [Target], 100 mM NaCl, 10 mM sodium phosphate buffer pH 7.0, Milli-Q water, 298 K, $\lambda_{\text{ex}} = 450 \text{ nm}$.

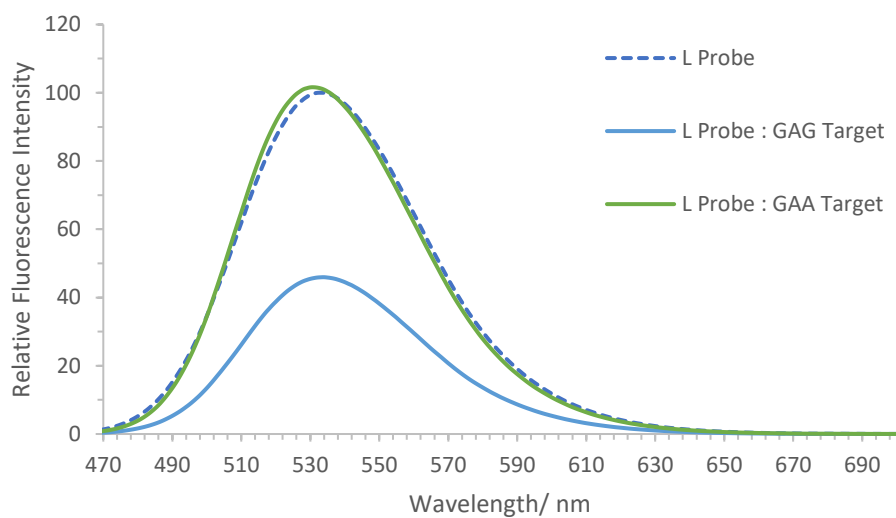


Figure 4.30: Sensing results of L Naph^{Amine} (P1DL) probes with base-adjacent system; T1A, T1MM targets. 0.5 μM [Probe], 1.5 μM [Target], 100 mM NaCl, 10 mM sodium phosphate buffer pH 7.0, Milli-Q water, 298 K, $\lambda_{\text{ex}} = 450 \text{ nm}$.

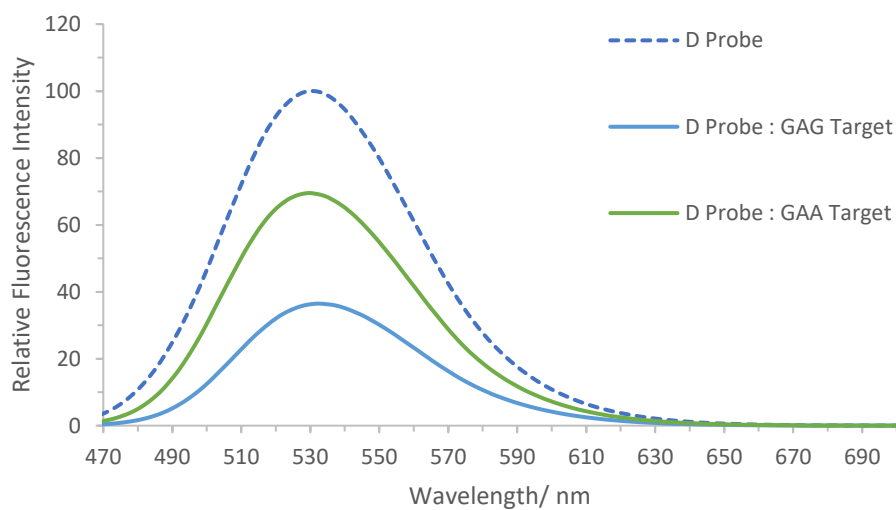


Figure 4.31: Sensing results of D Naph^{Amine} (P1DD) probes with base-adjacent system; T1A, T1MM targets. 0.5 μ M [Probe], 1.5 μ M [Target], 100 mM NaCl, 10 mM sodium phosphate buffer pH 7.0, Milli-Q water, 298 K, λ_{ex} = 450 nm.

Table 4.13: Shifts in the maximum emission wavelength of Naph^{Dimethyl} (P1CL/D) and Naph^{Amine} (P1DL/D) probes between 'match' (T1A) and 'mismatch' (T1MM) targets. 0.5 μ M probe: 1.5 μ M target. 100 mM NaCl, 10 mM sodium phosphate buffer pH 7.0, Milli-Q, 298 K, λ_{ex} = 450 nm.

	Naph ^{Dimethyl}		Naph ^{Amine}	
	λ_{max} /nm	λ_{max} wavelength shift (in comparison to probe alone) /nm	λ_{max} /nm	λ_{max} wavelength shift (in comparison to probe alone) /nm
L Probe	536	-	533	-
L Probe : GAG Target (T1A)	529	-7	534	1
L Probe : GAA Target (T1MM)	531	-5	531	-2
D Probe	536	-	531	-
D Probe : GAG Target (T1A)	537	1	532	1
D Probe : GAA Target (T1MM)	542	6	530	-1

4.3.4. Fluorescence Sensing of Probes in the Epigenetic Sensing System

The epigenetic biomarker, 5-methylcytosine (mC), consists of only a small structural change from the natural cytosine nucleobase and involves the methylation at position 5 on cytosine. This small structural change can alter the interactions with surrounding nucleobases. Given previous encouraging results with anthracene systems,¹¹ and owing to the high sensitivity of the naphthalimide reporter groups to their local environment, it was decided to check whether these naphthalimide-modified probes could detect such a small change in the target. The sensing results are discussed in the following sections.

4.3.4.1. Fluorescence Sensing Using Naph^A_{Short} and Naph^A_{Long} Probes

Figure 4.32 to Figure 4.35 show the fluorescence emission read-outs upon hybridisation of the Naph^A_{Short} and Naph^A_{Long} probes with C and mC targets.

The Naph^A_{Short} probes can effectively detect the small structural change in the point variation C > mC through changes in fluorescence emission intensity, Figure 4.32 and Figure 4.33, as well as shifts in the maximum emission wavelength as shown in Table 4.14. As discussed in the base-opposite sensing results section, the stereochemistry of the threoninol in the shorter linker probe systems has an effect on the positioning of the naphthalimide reporter group within the duplex, and ultimately affects the sensing read-outs. A similar trend is observed here; the L Naph^A_{Short} probe shows a reduction in the fluorescence emission signal upon binding both C and mC targets, Figure 4.32, whereas the D Naph^A_{Short} probe shows fluorescence enhancements in both cases, Figure 4.33. The L Naph^A_{Short} probe is less effective at discriminating between these targets, as only small changes in fluorescence intensity are observed, with no changes in the maximum emission wavelength, Table 4.14. However, the D Naph^A_{Short} probe shows more promise in demonstrating larger changes between the two targets.

The Naph^A_{Long} probes are less effective at detecting this small epigenetic change, Figure 4.34 and Figure 4.35. As discussed earlier, the Naph^A_{Long} reporter groups have a longer flexible linker, which allows freer

movement in and out of the duplex, which makes the tag less sensitive to slight modifications between closely related variants.

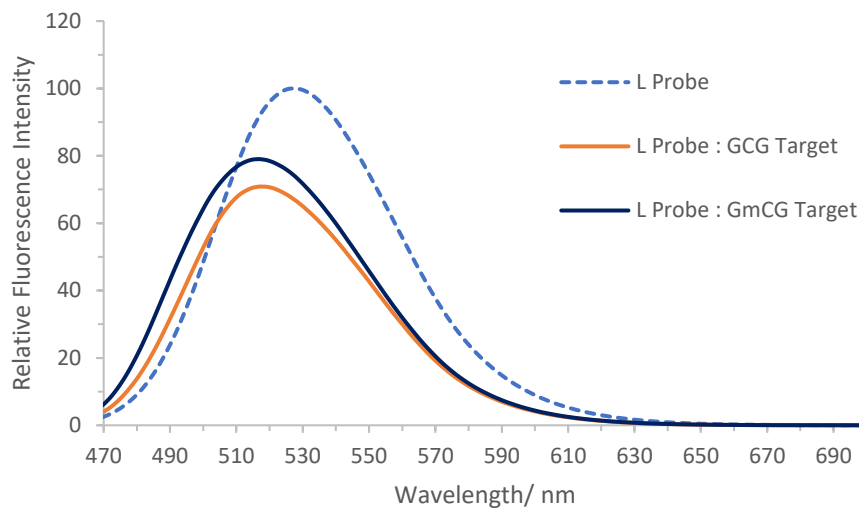


Figure 4.32: Sensing results of L Naph^A_{Short} (P1AL) probes with epigenetic sensing system; T1C, T1mC targets. 0.5 μ M [Probe], 1.5 μ M [Target], 100 mM NaCl, 10 mM sodium phosphate buffer pH 7.0, Milli-Q water, 298 K, λ_{ex} = 450 nm.

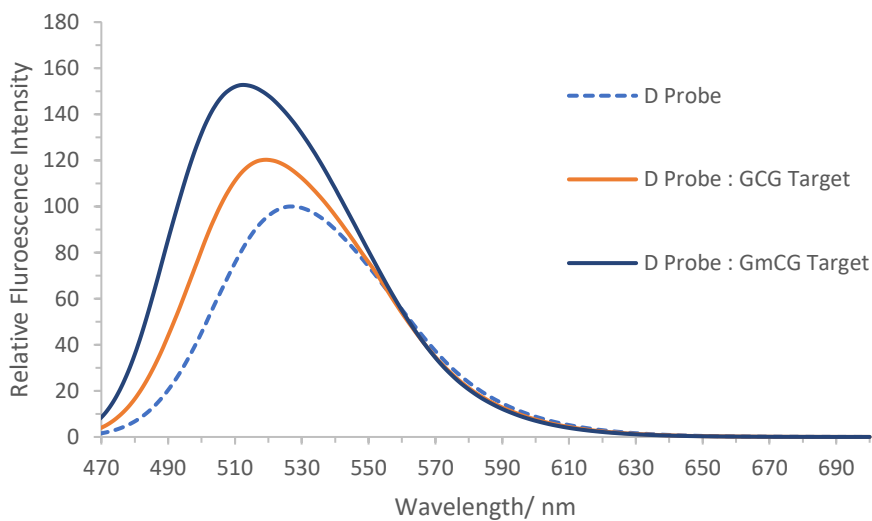


Figure 4.33: Sensing results of D Naph^A_{Short} (P1AD) probes with epigenetic sensing system; T1C, T1mC targets. 0.5 μ M [Probe], 1.5 μ M [Target], 100 mM NaCl, 10 mM sodium phosphate buffer pH 7.0, Milli-Q water, 298 K, λ_{ex} = 450 nm.

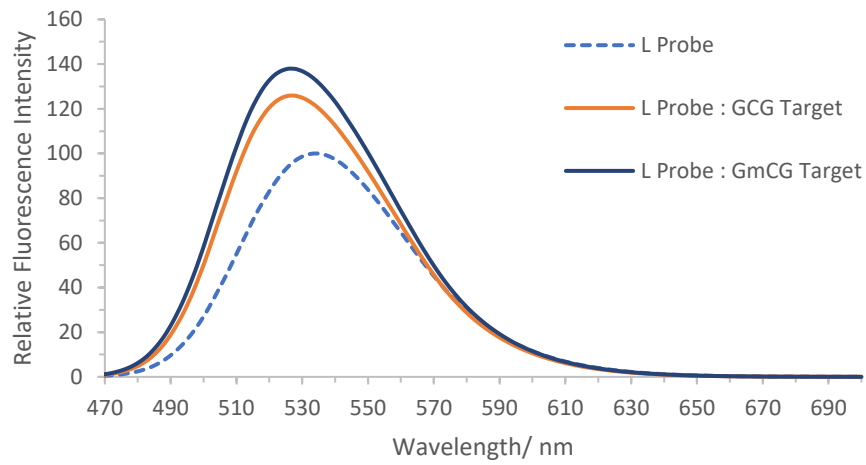


Figure 4.34: Sensing results of L Naph^A_{Long} (P1BL) probes with epigenetic sensing system; T1C, T1mC targets. 0.5 μ M [Probe], 1.5 μ M [Target], 100 mM NaCl, 10 mM sodium phosphate buffer pH 7.0, Milli-Q water, 298 K, λ_{ex} = 450 nm.

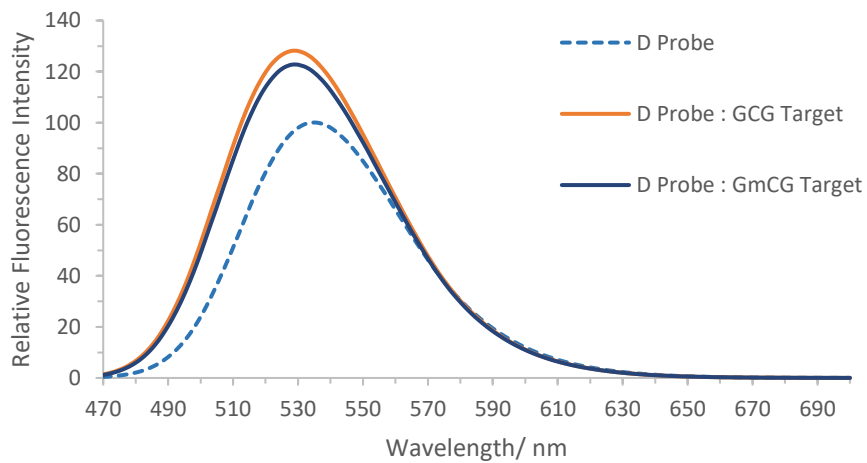


Figure 4.35: Sensing results of D Naph^A_{Long} (P1BD) probes with epigenetic sensing system; T1C, T1mC targets. 0.5 μ M [Probe], 1.5 μ M [Target], 100 mM NaCl, 10 mM sodium phosphate buffer pH 7.0, Milli-Q water, 298 K, λ_{ex} = 450 nm.

Table 4.14: Shifts in the maximum emission wavelength of $\text{Naph}^{\text{A}_{\text{Short}}}$ (P1AL/D) and $\text{Naph}^{\text{A}_{\text{Long}}}$ (P1BL/D) probes for epigenetic sensing. 0.5 μM probe: 1.5 μM target. 100 mM NaCl, 10 mM sodium phosphate buffer pH 7.0, Milli-Q, 298 K, $\lambda_{\text{ex}} = 450 \text{ nm}$.

	$\text{Naph}^{\text{A}_{\text{Short}}}$		$\text{Naph}^{\text{A}_{\text{Long}}}$	
	λ_{max} /nm	λ_{max} wavelength shift (in comparison to probe alone) /nm	λ_{max} /nm	λ_{max} wavelength shift (in comparison to probe alone) /nm
L Probe	527	-	534	-
L Probe : GCG Target (T1C)	517	-10	527	-7
L Probe : GmCG Target (T1mC)	517	-10	526	-8
D Probe	527	-	534	-
D Probe : GCG Target (T1C)	519	-8	529	-5
D Probe : GmCG Target (T1mC)	512	-15	529	-5

4.3.4.2. Fluorescence Sensing Using $\text{Naph}^{\text{Dimethyl}}$ and $\text{Naph}^{\text{Amine}}$ Probes

Figure 4.36 to Figure 4.39 show the fluorescence emission read-outs of the $\text{Naph}^{\text{Dimethyl}}$ and $\text{Naph}^{\text{Amine}}$ probes for epigenetic C > mC sensing, with Table 4.15 listing the shifts in the maximum fluorescence emission wavelengths. As discussed earlier, the $\text{Naph}^{\text{Dimethyl}}$ probes show a vast enhancement in their fluorescent emission signal upon DNA binding. Once again, similar increases in fluorescence emission are observed here, Figure 4.36 and Figure 4.37. The results for the D $\text{Naph}^{\text{Dimethyl}}$ probe are better in that larger differences are observed between the two targets.

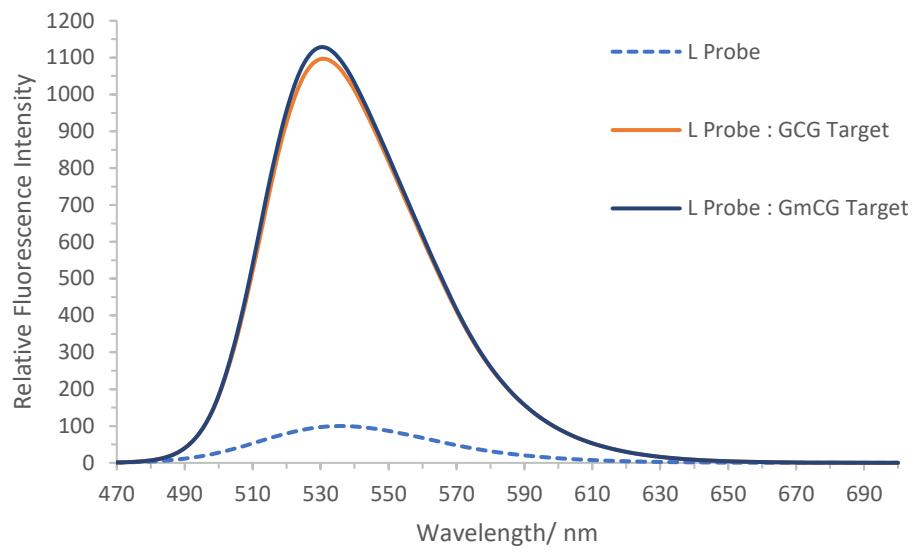


Figure 4.36: Sensing results of L $Naph^1_{Dimethyl}$ (P1CL) probes with the epigenetic sensing system; T1C, T1mC targets. $0.5 \mu M$ [Probe], $1.5 \mu M$ [Target], 100 mM NaCl , $10 \text{ mM sodium phosphate buffer pH 7.0}$, Milli-Q water, 298 K , $\lambda_{ex} = 450 \text{ nm}$.

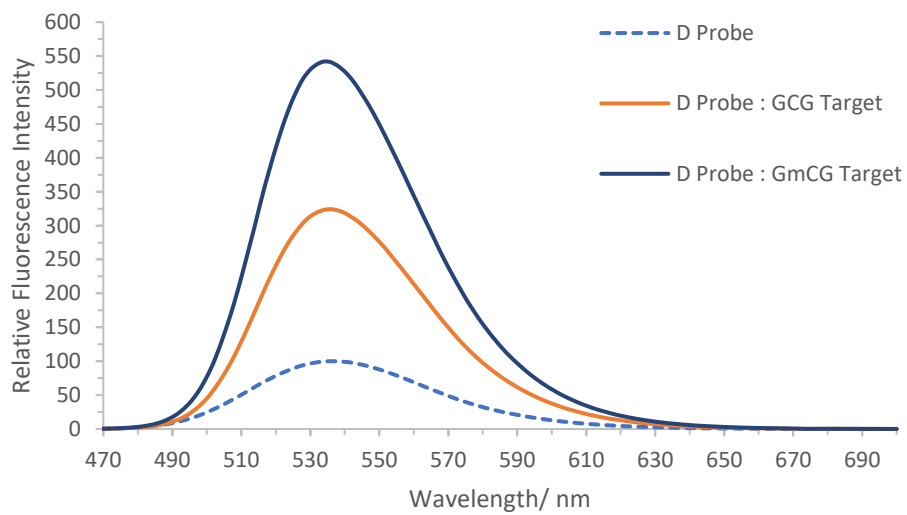


Figure 4.37: Sensing results of D $Naph^1_{Dimethyl}$ (P1CD) probes with the epigenetic sensing system; T1C, T1mC targets. $0.5 \mu M$ [Probe], $1.5 \mu M$ [Target], 100 mM NaCl , $10 \text{ mM sodium phosphate buffer pH 7.0}$, Milli-Q water, 298 K , $\lambda_{ex} = 450 \text{ nm}$.

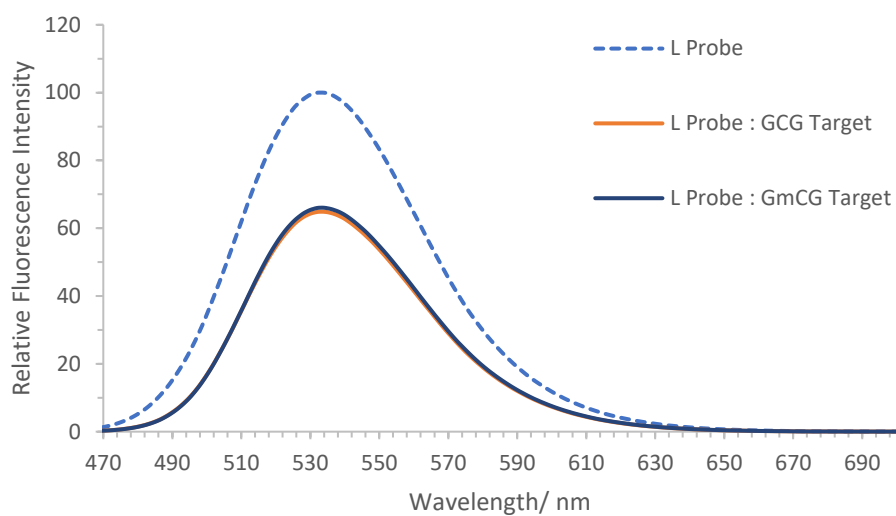


Figure 4.38: Sensing results of L Naph^I_{Amine} (P1DL) probes with the epigenetic sensing system; T1C, T1mC targets. 0.5 μ M [Probe], 1.5 μ M [Target], 100 mM NaCl, 10 mM sodium phosphate buffer pH 7.0, Milli-Q water, 298 K, λ_{ex} = 450 nm.

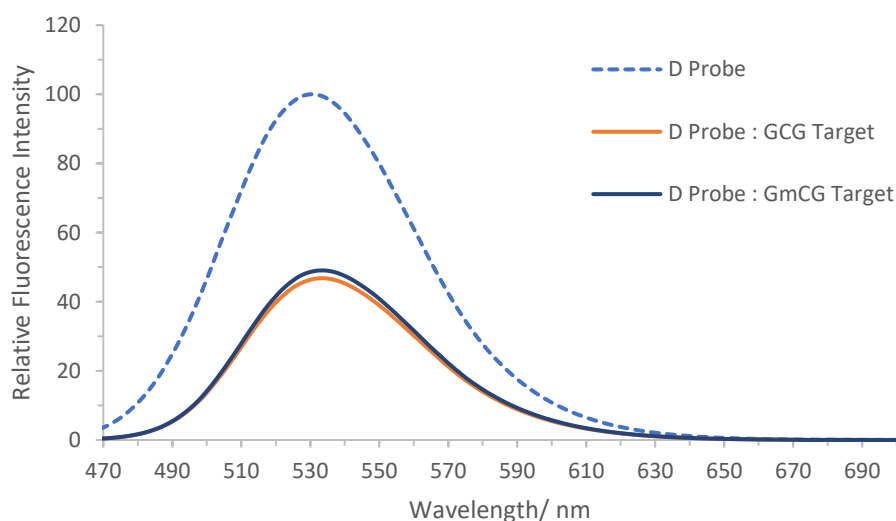


Figure 4.39: Sensing results of D Naph^I_{Amine} (P1DD) probes with the epigenetic sensing system; T1C, T1mC targets. 0.5 μ M [Probe], 1.5 μ M [Target], 100 mM NaCl, 10 mM sodium phosphate buffer pH 7.0, Milli-Q water, 298 K, λ_{ex} = 450 nm.

On the other hand, the Naph^I_{Amine} probes are relatively poor sensing systems for the C > mC epigenetic marker, with similar changes for each target, making discrimination impossible, Figure 4.38 - Figure 4.39. Similar observations were demonstrated earlier with the base discrimination results, showing minimal signal changes between the target variants and the reduction fluorescence intensity upon duplex formation with all targets.

Table 4.15: Shifts in the maximum emission wavelength of $Naph^{Dimethyl}$ (P1CL/D) and $Naph^{Amine}$ (P1DL/D) probes for epigenetic sensing. 0.5 μ M probe: 1.5 μ M target. 100 mM NaCl, 10 mM sodium phosphate buffer pH 7.0, Milli-Q, 298 K, λ_{ex} = 450 nm.

	$Naph^{Dimethyl}$		$Naph^{Amine}$	
	λ_{max} /nm	λ_{max} wavelength shift (in comparison to probe alone) /nm	λ_{max} /nm	λ_{max} wavelength shift (in comparison to probe alone) /nm
L Probe	536	-	533	-
L Probe : GCG Target (T1C)	531	-5	533	0
L Probe : GmCG Target (T1mC)	530	-6	532	-1
D Probe	536	-	531	-
D Probe : GCG Target (T1C)	536	0	534	3
D Probe : GmCG Target (T1mC)	534	-2	534	3

4.3.5. Fluorescence Sensing of Probes in the BRAF V600E System

The BRAF V600E biomarker involves a single T > A mutation, with the mutant A variant linked to the development of many types of cancer (see Chapter 1 for more information on the BRAF V600E mutation).²¹ The core DNA detection sequence in the BRAF V600E gene, 5'- GA/TG -3', is similar to the core sequence in the base-opposite target strands, 5'- GA/T/G/CG -3'. Consequently, the most effective reporter group from the base-opposite sensing results ($Naph^{A_{Short}}$) was chosen for incorporation into the BRAF V600E probe. As before, an excess of target was used for these sensing experiments (1 equivalent of probe and 3 equivalents of target). The sensing results are detailed in the following section.

4.3.5.1. Fluorescence Sensing Using $Naph^{A_{Short}}$ Probes

Figure 4.40 and Figure 4.41 show the sensing results obtained from the L and D $Naph^{A_{Short}}$ probes for the detection of the BRAF V600E sing point variant and Table 4.16 displays the shifts in λ_{max} emission for the different duplex variants. The L and D $Naph^{A_{Short}}$ probes both exhibit a decrease in fluorescence

emission upon binding the A and T targets, Figure 4.40 and Figure 4.41, an observation that correlates with the results observed for the base-opposite sensing system, Figure 4.16 and Figure 4.17. This demonstrates the reproducibility of the sensing results for various target sequences if the core sequence remains the same, implying that only the bases in immediate proximity to the modification site would have an effect on the signal produced by the reporter groups. The shifts in the maximum emission wavelength for the different target variants also correlates with the previous results, see Table 4.16.

As both probes show a decrease in their fluorescence emission intensity signal upon binding both of the target variants, the base discrimination of these probes is not very effective. However, the L Naph^A_{Short} probe provides detectable shifts between the maximum emission wavelength between different targets, Table 4.16, which could provide a way to detect the mutant target variant. The previously studied anthracene sensing system was particularly effective at sensing the BRAF V600E mutation, showing much greater fluorescence intensity changes between the Mut and WT target variants and this system is explored further in Chapter 5.

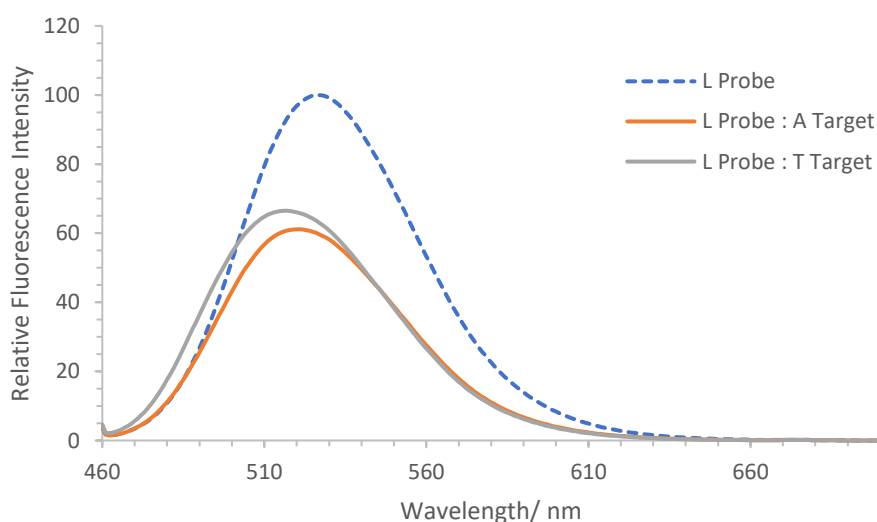


Figure 4.40: Sensing results of L Naph^A_{Short} probes (P2AL) with the BRAF V600E sensing system. 0.5 μ M [Probe], 1.5 μ M [Target], 100 mM NaCl, 10 mM sodium phosphate buffer pH 7.0, Milli-Q water, 298 K, λ_{ex} = 450 nm.

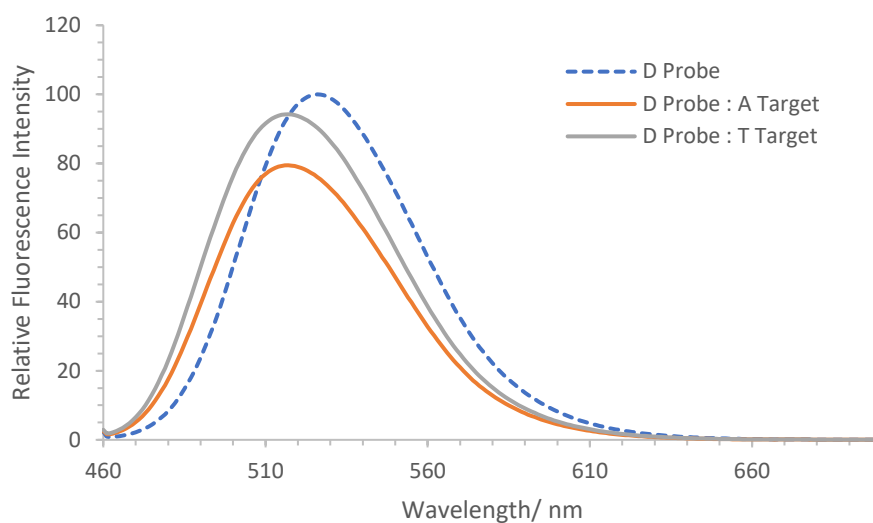


Figure 4.41: Sensing results of D Naph^A_{Short} probes (P2AD) with the BRAF V600E sensing system. 0.5 μM [Probe], 1.5 μM [Target], 100 mM NaCl, 10 mM sodium phosphate buffer pH 7.0, Milli-Q water, 298 K, $\lambda_{\text{ex}} = 450 \text{ nm}$.

Table 4.16: Shifts in the maximum emission wavelength of Naph^A_{Short} probes (P2AL/D) for BRAF V600E sensing. 0.5 μM probe: 1.5 μM target. 100 mM NaCl, 10 mM sodium phosphate buffer pH 7.0, Milli-Q, 298 K, $\lambda_{\text{ex}} = 450 \text{ nm}$.

	Naph ^A _{Short}	
	λ_{max} /nm	λ_{max} wavelength shift (in comparison to probe alone) /nm
L Probe	526	-
L Probe : A Target	520	-6
L Probe : T Target	516	-10
D Probe	526	-
D Probe : A Target	517	-9
D Probe : T Target	517	-9

4.4. Conclusions

The fluorescent and solvatochromic nature of the naphthalimide monomers synthesised in Chapter 3 have been investigated. The naphthalimide reporter groups are sensitive to their local environment, as demonstrated by the shifts in their emission spectra being dependent upon the polarity of their microenvironment. This is also evident upon incorporation into DNA probe strands and upon duplex formation. The spectral shifts in emission spectra, in addition to any fluorescence intensity changes, provide a new dimension to DNA sensing which was not observed with the previously studied anthracene systems. The advantages of naphthalimide reporter groups over the previously studied anthracene systems include longer wavelength absorption and emission profiles and higher quantum yields, making them more suitable for imaging experiments (including cellular imaging) which are explored in later chapters.

It has been shown that base discrimination is possible *via* monitoring changes in fluorescence intensity and/or shifts in emission profiles of the naphthalimide-modified probes upon duplex formation with their corresponding targets. As expected, the different naphthalimide tag variants and their stereochemistry provide different sensing read-outs. For base discrimination using the base-opposite sensing system, the Naph^A_{Short} probe variant proves more effective at base discrimination and produces promising sensing read-outs, with larger intensity changes and spectral shifts observed upon duplex formation with varying target variants. In addition, the Naph^A_{Short} probes are also more effective at epigenetic sensing. Interesting comparisons can be made between the Naph^A_{Short} and Naph^A_{Long} probes, in terms of the effect of linker length on the positioning of the reporter groups within the duplexes and how this affects the subsequent fluorescence read-outs observed.

The L Naph^I_{Dimethyl} probes display interesting fluorescence properties, with vast increases in fluorescence emission observed upon duplex formation. This discovery of this phenomenon may prove useful in DNA PAINT techniques as discussed in Chapter 6.

In contrast, the Naph^I_{Amine} probes were shown to be the least effective for DNA sensing purposes, displaying limited fluorescence intensity changes and spectral shifts between the target variants. This was indicated during initial experiments performed on the reporter group monomers which demonstrated that the Naph^I_{Amine} tags possessed limited solvatochromic properties compared to the other reporter groups.

The most promising probes, Naph^A_{Short}, were also tested for the detection of the BRAF V600E mutation. Although no distinctive fluorescence intensity changes were observed between the mutant and wild type variants, the significant spectral shifts between the variants may provide a way of sensing this mutation.

4.5. [Future Work](#)

Future work would include the investigation of the positioning of the fluorescent tags upon duplex formation with different targets *via* computational analysis or X-ray crystallography. This would allow more definitive reasoning for the sensing read-outs that are observed. Although current reasoning for the varied sensing read-outs are drawn from various sets of data (for example, thermal melting studies, fluorescence studies on monomer units, and fluorescence duplex sensing), more structural analysis would help to confirm these current explanations.

4.6. References

1. E. Martin, R. Weigand and A. Padro, *J. Lumin.*, 1996, **68**, 157.
2. M. S. Alexiou, V. Tychopoulos, S. Ghorbanian, J. H. P. Tyman, R. G. Brown and P. I. Brittain, *J. Chem. Soc. Perkin Trans. 2*, 1990, 837.
3. S. Nigam and S. Rutan, *Applied Spectroscopy*, 2001, **55**, 362.
4. D. Staneva, S. Angelova and I. Grabchev, *Sensors*, 2020, **20**, 3501.
5. K. G. Leslie, D. Jacquemin, E. J. New and K. A. Jolliffe, *Chem. Eur. J.*, 2018, **24**, 5569.
6. J.-L. H. A. Duprey, PhD Thesis, University of Birmingham, 2010.
7. D. Sarkar, P. Das, S. Basak and N. Chattopadhyay, *J. Phys. Chem. B.*, 2008, **112**, 9243.
8. S. Dhar, S. S. Roy, D. K. Rana, S. Bhattacharya, S. Bhattacharya and S. C. Bhattacharya, *J. Phys. Chem. A.*, 2011, **115**.
9. Z. Li, Q. Yang, R. Chang, G. Ma, M. Chen and W. Zhang, *Dyes and Pigments*, 2011, **88**.
10. T. Fujii, H. Kashida and H. Asanuma, *Chem. Eur. J.*, 2009, **15**.
11. J.-L. H. A. Duprey, G. A. Bullen, Z.-Y. Zhao, D. M. Bassani, A. F. A. Peacock, J. Wilkie and J. H. R. Tucker, *ACS Chem. Biol.*, 2016, **11**, 717.
12. B. Ramachandram and A. Samanta, *Chem. Commun.*, 1997, 1037.
13. C. Reichardt, *Solvent and Solvent Effects in organic Chemistry*, Weinheim, VCH, 2nd ed. edn., 1988.
14. K. Dimroth, C. Reichardt, T. Siepmann and F. Bohlmann, *Liebigs Ann. Chem.*, 1963, **1**, 661.
15. R. S. Szabadai, J. R-Barton, K. P. Ghiggino, J. M. White and D. J. D. Wilson, *Aust. J. Chem.*, 2014, **67**, 1330.
16. Q. Qiao, W. Liu, J. Chen, W. Zhou, W. Yin, L. Miao, J. Cui and Z. Xu, *Dyes and Pigments*, 2017, **147**, 327.
17. J.-L. H. A. Duprey, D. M. Bassani, E. I. Hyde, G. Jonusauskas, C. Ludwig, A. Rodger, N. Spencer, J. S. Vyle, J. Wilkie, Z.-Y. Zhao and J. H. R. Tucker, *Org. Biomol. Chem.*, 2018, 6576.

18. N. R. Deprez, K. A. McNitt, M. E. Peterson, R. G. Brown and D. E. Lewis, *Tetrahedron Lett.*, 2005, **46**, 2149.
19. S. Saha and A. Samanta, *J. Phys. Chem. A.*, 2002, **106**, 4763.
20. H. Gudnason, M. Dufva, D. D. Bang and A. Wolff, *Nucleic Acids Res.*, 2007, **35**, 127.
21. W. O. Greaves, S. Verma, K. P. Patel, M. A. Davies, B. A. Barkoh, J. M. Galbincea, H. Yao, A. J. Lazar, K. D. Aldape, L. J. Medeiros and R. Luthra, *J Mol Diagn*, 2013, **15**, 220.

5. The Development of a Fluorescent Nucleic Acid Sensing Assay to Detect and Quantify the BRAF V600E Mutation

5.1. Overview

Previous chapters have showcased the ability of fluorescently modified nucleic acid probes to discriminate between the canonical DNA bases and demonstrated their potential in the detection of single point variations. This chapter details the use of an anthracene-modified nucleic acid probe for the detection of the BRAF V600E single point mutation and explores the development of this probe technology into a more 'real-life' detection assay.

As mentioned in the introduction to this thesis (Chapter 1), single point variations within the genome can be viewed as molecular markers for certain genetic diseases, and the BRAF V600E mutation is classed as such. The BRAF V600E mutation occurs in the BRAF gene at codon 600, exon 15 and the c.T1799A substitution accounts for 80-100% of all BRAF mutations.¹⁻⁴ This mutation is a T > A transversion and results in an amino acid change from valine (V) to glutamic acid (E), which results in the mutation of Raf enzymes (called BRAF) and ultimately causes uncontrolled cell growth.⁵ The BRAF V600E mutation is associated with many types of cancer including malignant melanoma and colorectal cancer.⁶

The BRAF V600E mutation is a somatic mutation. Somatic mutations occur over the lifetime of an individual and differ from germ line mutations, which are inherited genetic alterations that occur in the germ cells. The BRAF V600E mutation is homozygous for the wild-type (WT), i.e. displaying T-A, T-A in both types of allele, and heterozygous for the mutant (Mut), i.e. displaying T-A, A-T in each allele. However, cancerous DNA extracted from patient tumour samples may not be a simple 50% T:50% A mixture. As the tumour develops, WT DNA is converted to Mut DNA, thus having effect on the overall local tumour cell population; which may be different to another local tumour cell population at a different site.⁷ It is therefore of growing interest in clinical diagnostics and medicine to not only detect

these single point variations within the genome, but in addition, be able to quantify the amount of Mut DNA present within a patient tumour sample.

The heterogeneity of tumour tissue can be an important indication for prescribing the most effective treatment and for the close monitoring of tumour suppression during a course of treatment. Until recently, the main focus of mutation detection assays is to simply detect if a mutation is present (i.e. qualitative testing). However, knowing how much of a mutated allele is present within a heterogenous tumour sample could help guide the course of the patient treatment. Most recent developments in the field have started to address this need, such as the emergence of digital polymerase chain reaction (dPCR).

The recent development of dPCR in 2006 has greatly increased the sensitivity of single point variation detection assays and has improved experimental reproducibility by allowing direct quantification of somatic mutations without the need of external calibrators.⁸ Droplet digital PCR (ddPCR) is the most sensitive and innovative branch of dPCR.⁸ ddPCR splits DNA molecules into approximately 20,000 droplets, with each droplet containing roughly 1 copy of DNA. Each droplet is analysed individually using PCR and base discriminating probes. Commonly, the mutant specific probe is labelled with a FAM fluorophore and the WT specific probe with a HEX fluorophore. Quantification is achieved by counting each droplet individually using a droplet reader.⁹ Both WT and mutant DNA-containing droplets are distributed randomly and are counted to provide absolute quantification of somatic mutations within the initial sample.¹⁰ Due to the nature of dPCR, it is possible to detect the presence of rare mutations. The DNA molecules are split into 20,000 droplets and each droplet is amplified and counted individually, thus reducing the chances of missing the rare mutation sequence which will be present at very low concentrations. This method has great potential for detecting somatic mutations within circulating tumour DNA (ctDNA), where very low concentrations of DNA are present.⁸

Despite these most recent advances, dPCR methods require specialist equipment, thus increasing the cost of diagnostic testing. More rapid, inexpensive and versatile methods for quantifying the amount of Mut DNA in heterozygous cancer samples, otherwise known as the allelic ratio, are becoming increasingly important as scientists begin to understand more about how molecular markers are implementing cancer growth and how precision medicine may be used to treat cancer patients more effectively and specifically.

5.2. Previous Work: Anthracene-Modified Nucleic Acid Probes

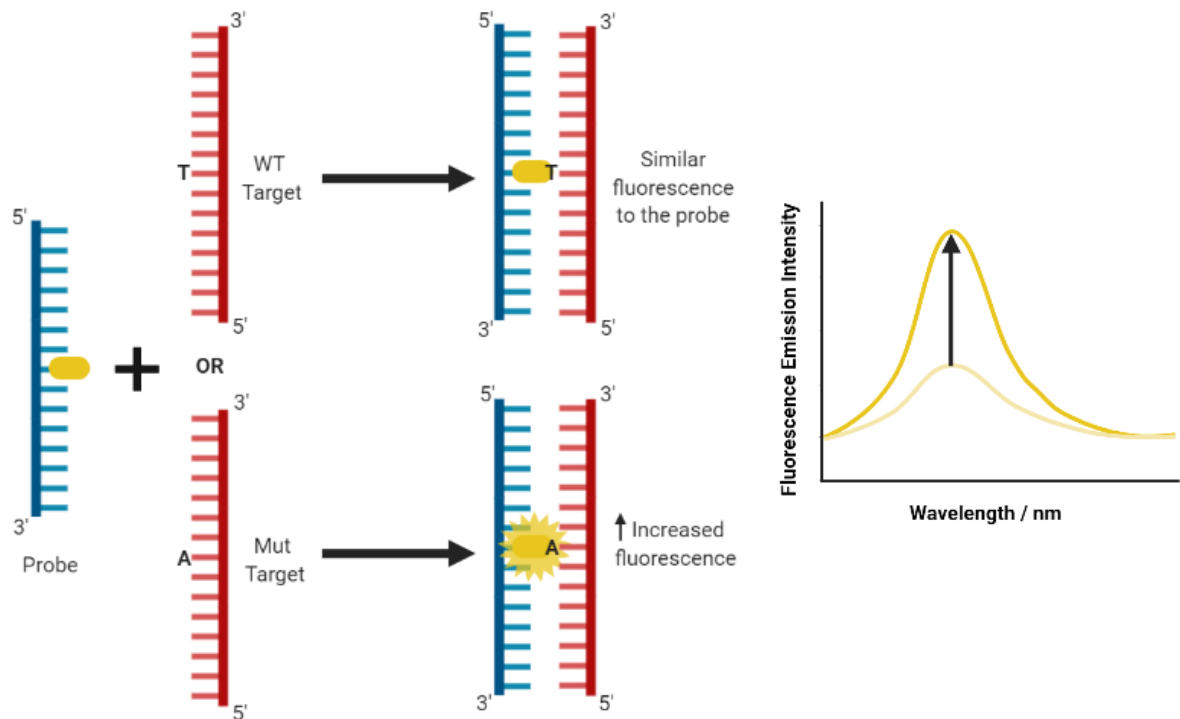


Figure 5.1: Anthracene probe design for detecting the BRAF V600E (T > A) mutation with the anthracene reporter group (yellow) at the centre of the strand which interacts with the base opposite in the target strand upon hybridisation. When the wild type (WT) target is present, the anthracene signal remains at a similar intensity to that of the probe alone. However, when the mutant (Mut) target strand is present, a significant increase in anthracene signal is observed as demonstrated by the emission spectra on the right.

The Tucker group previously reported the use of anthracene-modified nucleic acid probes that detect single point variations associated with prostate cancer, including a T > A mutation similar to the BRAF V600E mutation.¹¹ More recent unpublished work has focussed on developing these anthracene

probes to detect the BRAF V600E mutation. The probe design is shown in Figure 5.1 and the anthracene tag nucleotide substitution shown in Figure 5.2. The probe strand comprised a 15-mer oligonucleotide with the anthracene tag incorporated as a nucleotide substitution at the centre of the strand. Figure 5.1 demonstrates the method in which a Mut target is detected from the WT. Upon duplex formation of the probe with a WT target, there is no significant change in the fluorescence intensity of the anthracene reporter group. In comparison, upon duplex formation with the Mut target, a 'switch on' signal is observed, with the fluorescence intensity of the anthracene reporter group increasing significantly when compared to the fluorescence signal of the probe alone.

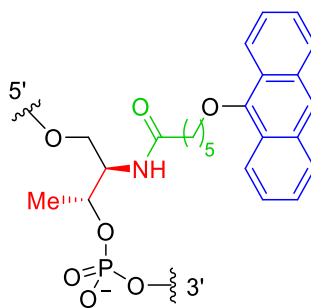


Figure 5.2: Structure of anthracene nucleotide mimic. Showing the anthracene unit (blue), the L threoninol sugar mimic (red) and hydrocarbon linker with five carbon units separating the anthracene unit and the amide bond (green).

The sequence of the probe strand is complementary to the genome region of interest where the BRAF V600E mutation occurs, with the anthracene tag positioned directly opposite the mutation site. In previous work, initial studies have mainly focussed on mutation sensing using short synthetic oligonucleotide target strands rather than extracted DNA from patient samples, providing proof-of-concept studies. The sequences of these target strands are 15 bases long (15-mer) and are identical to that found in the genome region of interest. The sequences of the probe and target strands used in these initial studies are shown below, Table 5.1.

Table 5.1: Probe and 15-mer target oligonucleotide sequences.

	Sequence
Anthracene BRAF V600E Probe	5' - AGATTTTCXCTGTAGC - 3' (where X = anthracene tag)
Wild type (WT) Target (15-mer)	5' - GCTACAGTGAATCT - 3'
Mutant (Mut) Target (15-mer)	5' - GCTACAGAGAAATCT - 3'

The initial results from this sensing system were very promising, with vast enhancement of the anthracene fluorescence signal upon duplex formation of the probe and Mut target, compared to very small fluorescence intensity changes upon duplex formation with the WT target. Even more exciting was the discovery of linear correlation behaviour between the anthracene fluorescence signal and percentage of Mut target within a sample of varying ratios of WT and Mut target, as shown in Figure 5.3.¹² This linear correlation effect has the potential to allow for the determination of allelic ratios in heterozygous samples. Quantification of Mut DNA can be achieved *via* generation of a calibration plot using samples of known percentages of Mut DNA. Subsequently, by recording the fluorescence intensity of a sample of unknown percentage of Mut DNA, the linear calibration plot can be used to determine the expected percentage of Mut DNA.

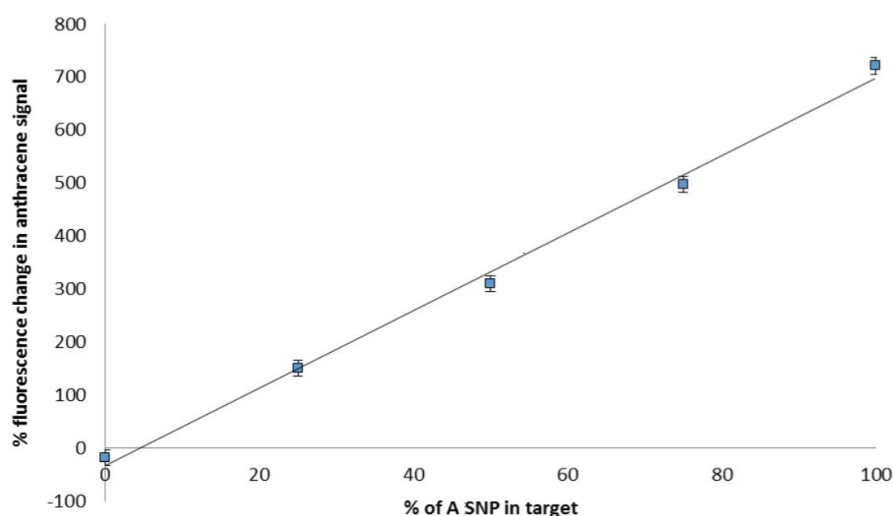


Figure 5.3: Previous work involving initial studies using the anthracene BRAF probe to detect varying percentages of the mutant target in a sample (using short synthetic oligonucleotide targets (15-mer) as proof-of-concept). 1 μ M probe: 1 μ M X% A target (100 mM NaCl, 10 mM sodium phosphate buffer pH 7.0, aqueous solution). λ_{ex} = 350 nm, 298 K.¹²

Unlike many other commercially available mutation detection assays,¹³ this simplified approach utilises only one probe to detect both the Mut and WT targets. This is achieved due to the probe binding with equal affinity for both the WT and Mut target, owing to the ‘probe: WT target’ and ‘probe: Mut target’ duplexes having similar melting temperatures (T_m), as shown below in Table 5.2. Therefore, unlike assays that utilise two probes to sense either the WT or Mut target, such as the TaqMan™ assay mentioned in the Chapter 1, this approach does not rely on a difference in binding strength between the two probes and their complementary targets, thus eliminating the need for a sensing temperature window.¹⁴ This allows for sensing at room temperature to occur, which in turn could reduce the testing time of the assay. Once bound to either the WT or Mut target, the anthracene probe provides an emission intensity that is indicative of the target variant present within the sample, removing the need for the use of different fluorophores/probes to detect each variant.

Table 5.2: Thermal melting temperatures (T_m) of the BRAF probes hybridised with the 15-mer targets. [DNA] = 5 μ M, aqueous solution, 100 mM NaCl, 10 mM sodium phosphate buffer, pH 7.0. Data from previous work.¹²

	Duplex Melting Temperature (T_m) / °C
Probe: WT target (15-mer)	45.5
Probe: Mut target (15-mer)	46.0

This is a very simple method for allelic quantification and does not require any specialist equipment, unlike other commercial methods for allelic quantification such as digital PCR.^{15, 16} Owing to its simplicity and functionality, the technology giving rise to this linear correlation effect is the subject of a University of Birmingham patent (GB201714068D0) and has been trademarked as *BaseSense*™.

5.3. [Project Aims](#)

Although promising, the initial studies detailed above used only short synthetic oligonucleotide target strands (15-mers) as a proof-of-concept, rather than target strands more representative of a patient sample. The work described in this chapter builds on these results by testing the sensing ability of the

anthracene probe system with longer DNA target sequences, including PCR amplicons derived from genomic DNA, which more closely replicate mutation detection assays used in a clinical environment. Some initial studies using PCR-amplified DNA targets from genomic DNA of BRAF V600E WT and Mut samples were carried out by Dr A. Ali,¹² but time constraints forced the preliminary work to conclude with inconclusive results. The data obtained from experiments sensing the PCR-amplified target DNA did not correlate with what was observed in initial studies using the 15-mer targets, with increases in anthracene signal observed for both the WT and Mut samples upon duplex formation (see Appendix 8.3.1 for data). Consequently, further research was required to investigate these results when sensing longer oligonucleotide target sequences, including those generated through PCR amplification.

Fluorescence sensing using the anthracene BRAF probe was to be tested using long synthetic oligos target strands that replicate the targets produced from PCR amplification. Using these longer targets would also enable the limits of detection of the anthracene probe to be explored. Moving on, the anthracene probe system would then be tested on genomic DNA by developing a protocol for PCR DNA amplification followed by probe hybridisation and fluorescence sensing.

5.4. Synthesis of Anthracene Probe and Target Oligonucleotides

The anthracene tag, as shown above in Figure 5.2, was synthesised using known methods established by Dr J. Duprey and as demonstrated in other published work.^{11, 12, 17, 18} The anthracene tag was incorporated into the centre of a 15-mer nucleic acid probe as a nucleotide substitution using solid-phase DNA synthesis. It was then purified by HPLC and characterised by mass spectrometry using methods similar to those described in Chapter 3 and detailed in the Experimental 7.4 and 7.5. Short oligonucleotide target strands (15-mers) with sequences identical to that found in the BRAF V600E genome region of interest and containing the T (WT) and A (Mut) mutation site at the position opposite the anthracene tag were also synthesised. The sequences of these probe and target strands are the same as those mentioned in previous studies (see Table 5.1) and their characterisation data can be

found in the Appendix 8.3.2. The long synthetic target oligos (173-mers) were purchased from Sigma-Aldrich (desalted, dried, with no further purification) and their sequences are shown in Table 5.3.

Table 5.3: Sequences of 173-mer target strands.

	Sequence
Wild Type (WT) Target (173-mer)	5' - GCTTGCTCTGATAGGAAAATGAGATCTACTGTTTTTCCTTTACTTACTACTACTC AGATATATTTCTTCATGAAGACCTCACAGTAAAAATAGGTGATTTTGGTCTAG CTACAGTGAATCTCGATGGAGTGGGTCCCATCAGTTTGAACAGTTGTCTGGA TCCATTTTGTGG - 3'
Mutant (Mut) Target (173-mer)	5' - GCTTGCTCTGATAGGAAAATGAGATCTACTGTTTTTCCTTTACTTACTACTACTC AGATATATTTCTTCATGAAGACCTCACAGTAAAAATAGGTGATTTTGGTCTAG CTACAGA GAAATCTCGATGGAGTGGGTCCCATCAGTTTGAACAGTTGTCTGGA TCCATTTTGTGG - 3'

5.5. BRAF V600E Sensing Studies Using Short (15-mer) Oligonucleotide Targets

With previous work establishing the sensing ability of the probe with synthetic 15-mer oligo targets, the work presented herein aims to explore the limits of detection at which the probe will display linear correlation behaviour and secondly, to increase the accuracy of the linear correlation plot by expanding the number of recorded samples at various percentages of Mut target (i.e. recording the fluorescence of samples at 10% increments of Mut Target, rather than every 20% as previously recorded in Figure 5.3).

An advantage of using the anthracene probe system over other commercially available assays is that probe hybridisation occurs at room temperature in 5 min, allowing for more rapid results. Standard salt and buffer solutions used for the sensing experiments in the previous chapter are used again here to aid duplex formation. See Experimental (7.7.1, 7.7.2) for full annealing and sensing parameters.

5.5.1. Fluorescence Emission Profile of the Anthracene BRAF V600E Probe

The anthracene probe displays a characteristic absorption signal in the region of 330-410 nm, Figure 5.4. Vibrational structure is observed in the absorption profile owing to the conjugated, planar nature

of the polyaromatic anthracene system. The wavelength of 350 nm was selected as the excitation wavelength for all sensing experiments in this chapter. Although there are stronger absorbance bands in the anthracene absorbance profile, e.g. 357 nm and 374 nm, these alternative wavelengths are not ideal as the Raman scattering peak resulting from the aqueous nature of the sample interferes with peaks in the fluorescence emission (see Appendix 8.3.3). At 350 nm, the Raman scattering of water is minimalised and does not interfere with the fluorescence detection wavelengths.

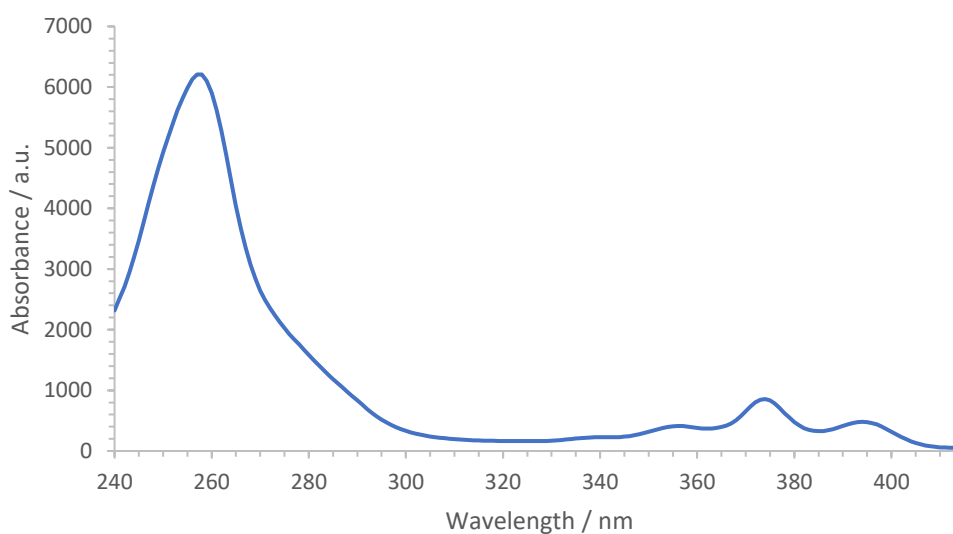


Figure 5.4: Absorbance spectrum of anthracene BRAF probe. 0.5 μM [DNA], 100 mM NaCl, 10 mM sodium phosphate buffer, pH 7.0, Milli-Q water.

Figure 5.5 shows the emission spectra of the anthracene probe. The detection wavelength for the sensing experiments discussed in this chapter was selected as 426 nm, where maximum fluorescence intensity is observed.

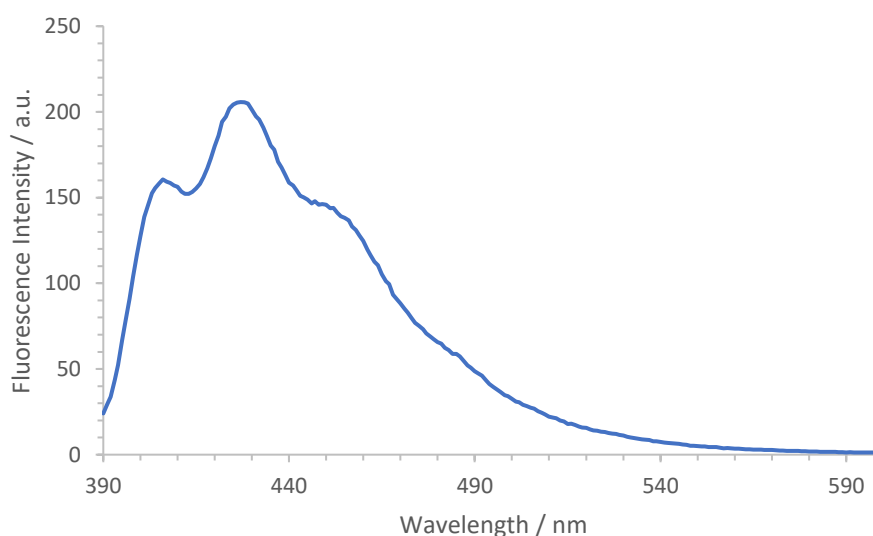


Figure 5.5: Fluorescence emission spectrum of anthracene BRAF probe. $\lambda_{ex} = 350$ nm, 298 K. 0.5 μ M [DNA], 100 mM NaCl, 10 mM sodium phosphate buffer, pH 7.0, Milli-Q water.

5.5.2. Fluorescence Sensing With Equimolar Amounts of Probe and Target

The melting temperatures of the ‘anthracene probe: target’ duplexes were sufficiently high, Table 5.2, $T_m = 46$ °C \pm 1 °C, 5 μ M [DNA], 100 mM NaCl, 10 mM sodium phosphate buffer, pH 7.0) for all probe strands to bind efficiently with the target strands at room temperature. In theory, this should enable the maximum fluorescence signal output to be achieved when sensing using equivalent concentrations of probe and target at room temperature. However in previous work, a slight excess of target had typically been used for the sensing experiments to generate the maximum output (i.e. to ensure all probe was bound to target). However, as discussed later in this chapter, when using PCR-amplified genomic DNA, the target was present in limited concentrations. Therefore, it was deemed important to determine the conditions at which the lowest concentration of probe and the lowest ratio of target to anthracene probe could be used in generating accurate sensing results. To begin with, the probe was tested using equimolar amounts of probe and target.

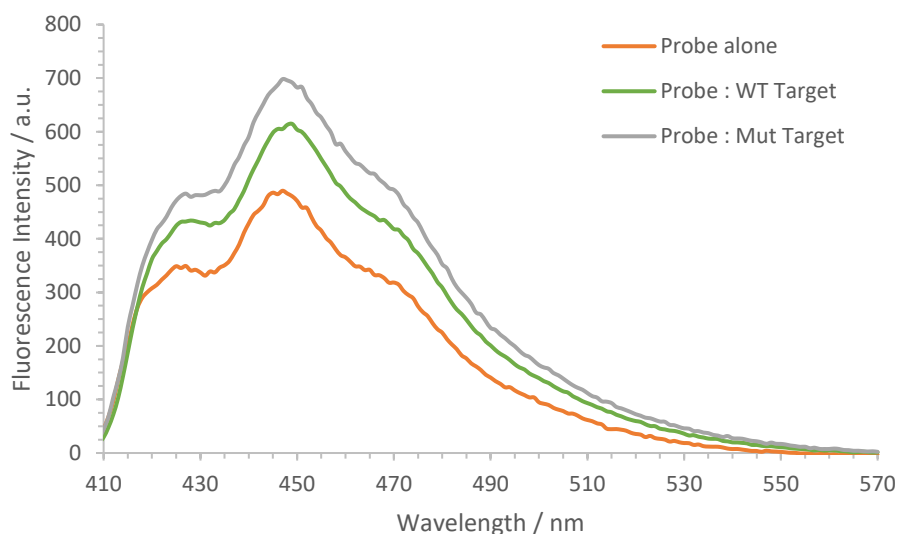


Figure 5.6: Emission spectra of anthracene probe when single-stranded (orange) and when duplexed with WT (green) and Mut (grey) 15-mer target. $\lambda_{ex} = 350 \text{ nm}$, 298 K, 0.5 μM probe: 0.5 μM target (100 mM NaCl, 10 mM sodium phosphate buffer pH 7.0, aqueous solution).

Figure 5.6 shows the emission spectra of the anthracene probe and the changes in the fluorescence signal upon binding the WT and Mut target variants. For detailed sensing conditions, see Experimental 7.7.2. The figure shows the fluorescence signals recorded from samples containing equimolar concentrations of probe and target strands (0.5 μM).

There are minimal changes in fluorescence intensity between duplexes containing 100% WT and 100% Mut targets, implying that when using equimolar concentrations of probe and target, duplex formation is not sufficient. The indistinctive intensity changes between samples containing either the WT or Mut target reduces the accuracy and effectiveness of the sensing system. Increasing the target concentration relative to the probe concentration should drive duplex formation and lead to more distinctive fluorescence intensity changes between WT and Mut samples.

5.5.3. Fluorescence Sensing With 1 Equivalent of Probe and 3 Equivalents of Target

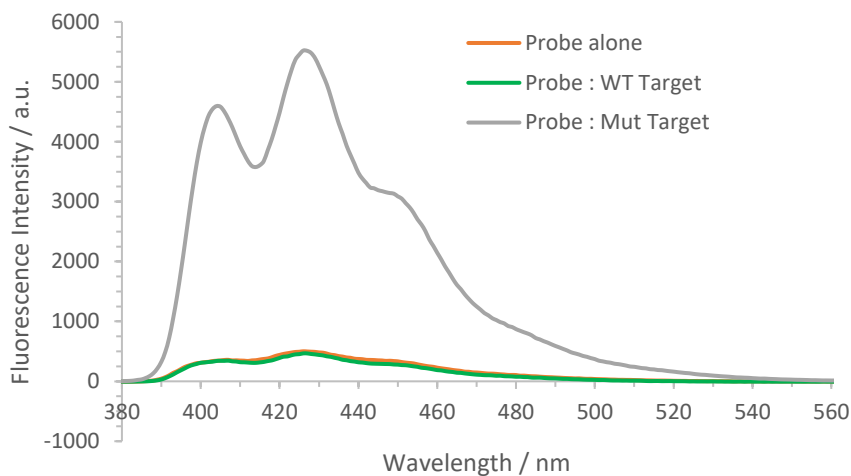


Figure 5.7: Emission spectra of anthracene probe when single-stranded (orange) and when duplexed with WT (green) and Mut (grey) 15-mer targets. $\lambda_{ex} = 350$ nm, 298 K, 0.5 μ M probe: 1.5 μ M target (100 mM NaCl, 10 mM sodium phosphate buffer pH 7.0, aqueous solution).

Next, studies with an excess of target (three equivalents) were performed. Although this required higher target concentrations, the results obtained allow for more accurate sensing due to the more significant enhancement in fluorescence signal between samples containing 100% WT (T) target and 100% Mut (A) target, as shown in Figure 5.7. Figure 5.8 shows a plot between the anthracene fluorescence intensity recorded at 426 nm and the percentage of Mut (A) target within samples of varying ratios of WT (T)/Mut (A) target. Although data points include samples containing up to 100% Mut target, in reality the testing range is 0-50% for a fully cancerous sample as it is heterozygous. The data shown in Figure 5.8 demonstrates a good linear correlation effect and confirms the ability of the system to detect allelic ratios within unknown samples with reasonable accuracy.

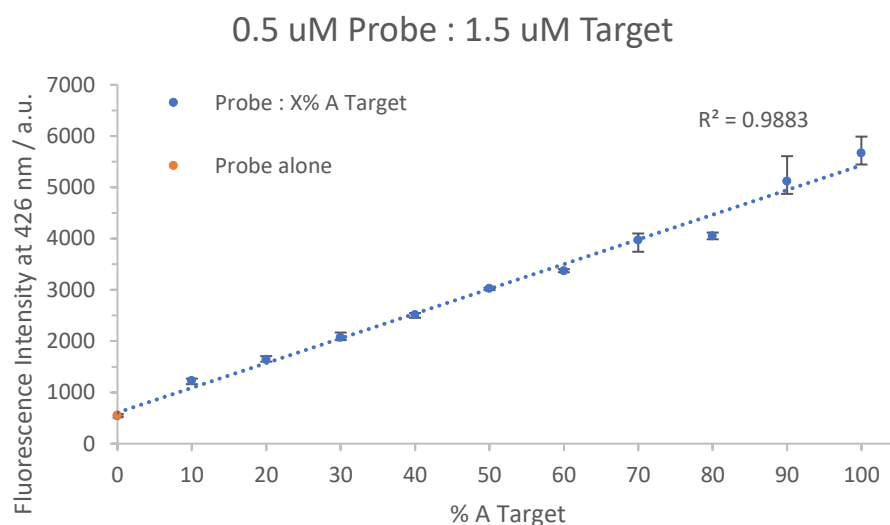


Figure 5.8: Linear correlation plot showing anthracene fluorescence intensity recorded at 426 nm. Fluorescence intensity of the probe alone is shown in orange and the fluorescence intensity once duplexes are formed with varying ratios of A/T target variants are shown in blue. Triplicates were recorded for each data point; error bars are shown, with the data points being the mean value. 0.5 μM probe: 1.5 μM target (100 mM NaCl, 10 mM sodium phosphate buffer pH 7.0, aqueous solution). λ_{ex} = 350 nm, 298 K.

As an excess of target was required to produce accurate sensing results, sensing using a lower concentration of probe was studied in order to help reduce the required target concentration. The correlation plot obtained from sensing at a lower probe concentration of 0.1 μM with a three-fold excess of target is depicted in Figure 5.9. However, clearly the correlation plot is less reliable/accurate, which indicates that lowering the probe concentration to 0.1 μM or less results in compromised sensing ability. The limits of detection of the anthracene sensing system are explored further in the following section.

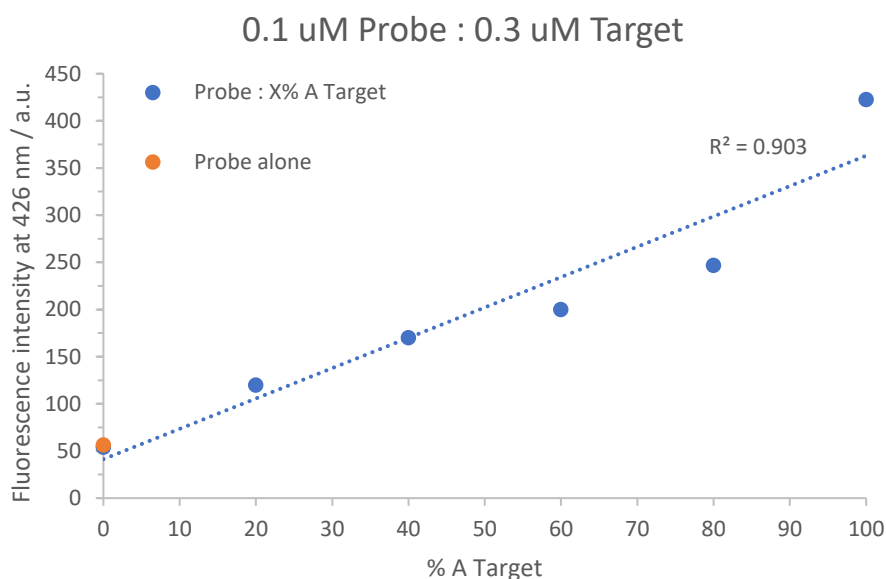


Figure 5.9: Linear correlation plot showing anthracene fluorescence intensity recorded at 426 nm. Fluorescence intensity of the probe alone is shown in orange and the fluorescence intensity once duplexes are formed with varying ratios of A/T target variants are shown in blue. 0.1 μ M probe: 0.3 μ M target (100 mM NaCl, 10 mM sodium phosphate buffer pH 7.0, aqueous solution). λ_{ex} = 350 nm, 298 K.

5.6. BRAF V600E Sensing Using Long (173-mer) Oligonucleotide Targets

Work in the above section confirms prior data reported by the group, demonstrating a good linear correlation between the anthracene fluorescence signal and the amount of Mut target within a sample. However, although using short oligonucleotide targets (15-mers) demonstrates the potential ability of the anthracene probe for use as a clinical detection assay, short oligomer targets are not truly representative of commercially available sensing assays. Most commercial mutation detection assays of this type involve PCR amplification of known sections of genomic DNA, resulting in target DNA strands far greater than 15 nucleotides in length. For this reason, the anthracene sensing system was tested using longer DNA fragments. With the ultimate aim of using PCR-amplified DNA targets resulting from genomic DNA, a known sequence of the BRAF gene was selected at the region of interest which contains the T > A mutation site within the core of this sequence and comprises of 173 nucleobases. Oligonucleotide target strands with this selected sequence were purchased from Sigma Aldrich and

sequences are shown in Table 5.3. A 173-mer target strand was deemed to be sufficiently long enough to allow for effective PCR amplification to take place in future experimental steps but not too long to compromise the sensing signal.

5.6.1. Fluorescence Sensing With 1 Equivalent of Probe and 1.2 Equivalents of Target

Initial sensing experiments involved using a slight excess of the long 173-mer target oligos, with probe concentrations of 0.5 μM and target concentrations of 0.6 μM .

Fluorescence sensing of the 173-mer WT and Mut targets was successful, as shown by the increase in fluorescence signal observed upon binding the Mut target in comparison to the probe alone and WT target, Figure 5.10. However, the fluorescence intensity difference between the WT and Mut targets, is not as significant as expected from experiments using the short oligo target strands. As demonstrated earlier, this is most likely a result of insufficient duplex formation caused by the use of smaller equivalents of target relative to the probe. As shown above, using a larger excess of target will aid duplex formation and produce optimal fluorescence signals, conditions which are explored below.

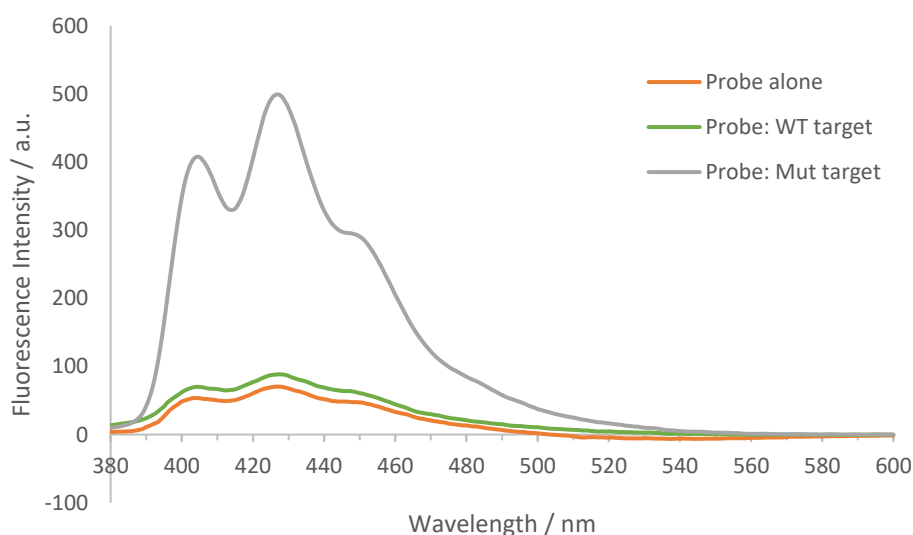


Figure 5.10: Emission spectra of the anthracene probe when single-stranded (orange) and when duplexed to WT (green) and Mut (grey) 173-mer targets. $\lambda_{\text{ex}} = 350 \text{ nm}$, 298 K, 0.5 μM probe: 0.6 μM target (100 mM NaCl, 10 mM sodium phosphate buffer pH 7.0, aqueous solution).

Figure 5.11 shows the correlation between the fluorescence intensity at 426 nm and the amount of Mut target within a sample. A fairly linear correlation is observed when sensing with only 1.2 equivalents of target, however this linear correlation effect is more significant in previous examples. This suggests that allelic ratio discrimination may be possible using a slight excess of target, but results may not be as sensitive as when using a larger excess of target.

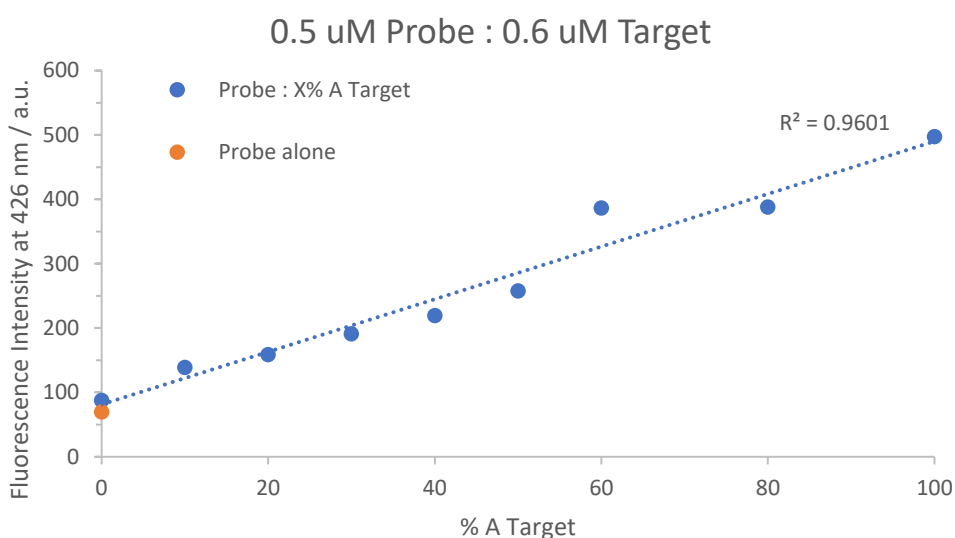


Figure 5.11: Linear correlation plot showing anthracene fluorescence intensity recorded at 426 nm. Fluorescence intensity of the probe alone is shown in orange and the fluorescence intensity once duplexes are formed with varying ratios of A/T target variants are shown in blue. 0.5 μ M probe: 0.6 μ M target (100 mM NaCl, 10 mM sodium phosphate buffer pH 7.0, aqueous solution). λ_{ex} = 350 nm, 298 K.

5.6.2. Fluorescence Sensing With 1 Equivalent of Probe and 3 Equivalents of Target

With a large excess of target strand relative to the probe established as the optimal sensing conditions, fluorescence sensing using the 173-mer synthetic target strands was performed as above. This involved a probe concentration of 0.5 μ M and target concentration of 1.5 μ M, Figure 5.12 and Figure 5.13.

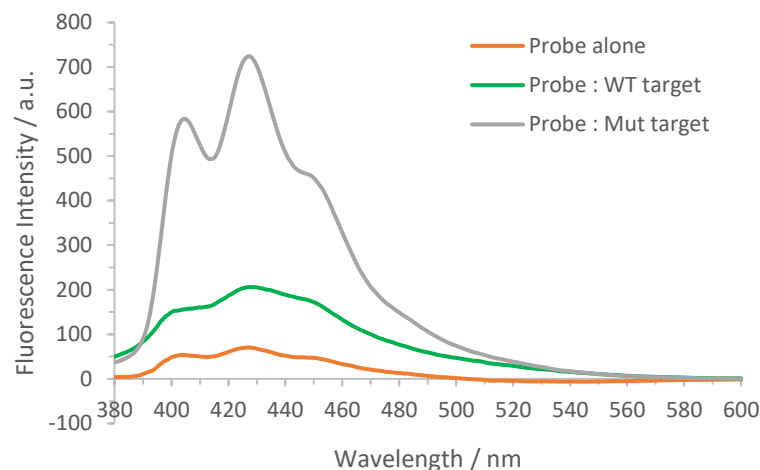


Figure 5.12: Emission spectra of the anthracene probe when single-stranded (orange) and when duplexed to WT (green) and Mut (grey) 173-mer targets. $\lambda_{ex} = 350 \text{ nm}$, 298 K, 0.5 μM probe: 1.5 μM target (100 mM NaCl, 10 mM sodium phosphate buffer pH 7.0, aqueous solution).

On first inspection, it was shown that the anthracene probe system was effective at sensing 100% WT (T) samples from 100% Mut (A) samples containing the 173-mer targets, as evidenced by the significantly enhanced fluorescence intensity upon binding the Mut (A) samples, Figure 5.12. Additionally, a fairly linear correlation was observed between the anthracene fluorescence signal and the percentage of Mut (A) target within a sample, Figure 5.13. While this complements results obtained in the previous section using the 15-mer targets, Figure 5.8, the correlation is less linear. In addition, a further difference concerned the fluorescence intensity of the probe alone compared with the ‘probe: 100% WT target’ duplex; data gathered from the 15-mer targets showed a very similar fluorescence intensity between the two, whereas the data displayed using the 173-mer targets shows a slight increase in fluorescence for the ‘probe: 100% WT target’ duplex when compared to the probe alone. This effect is observed for all samples containing the longer targets and is discussed in later sections (5.6.3).

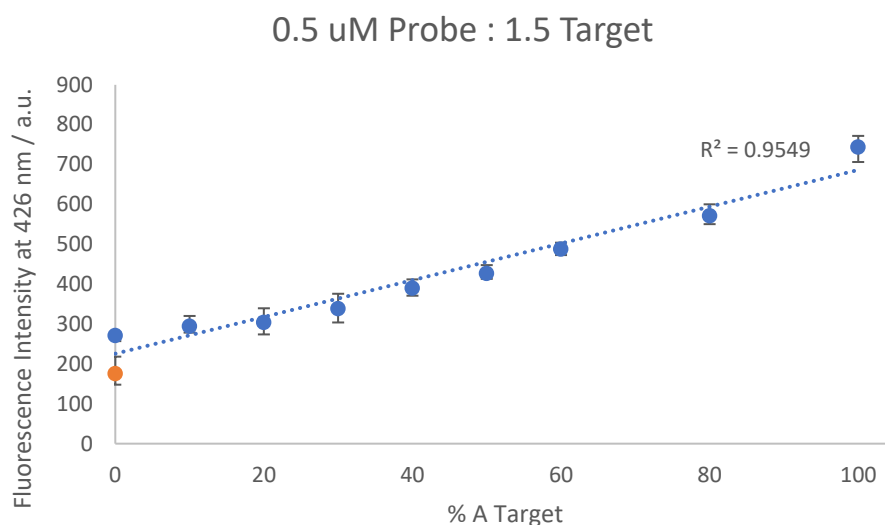


Figure 5.13: Linear correlation plot showing anthracene fluorescence intensity recorded at 426 nm. Fluorescence intensity of the probe alone is shown in orange and the fluorescence intensity once duplexes are formed with varying ratios of A/T target variants are shown in blue. Triplicates were recorded for each data point; error bars are shown, with the data points being the mean value. 0.5 μ M probe: 1.5 μ M target (100 mM NaCl, 10 mM sodium phosphate buffer pH 7.0, aqueous solution). λ_{ex} = 350 nm, 298 K.

Subsequently, the sensing system was analysed at various concentrations with the aim of trying to reduce the overall amount of target DNA required. Figure 5.14 to Figure 5.18 show the linear correlation plots of the anthracene signal at 426 nm for different samples with varying amounts of Mut (A) target.

Firstly, the results indicate that at all concentrations the anthracene probe can effectively discriminate between samples containing 100% WT (T) target and 100 % Mut (A) targets, with an enhanced anthracene fluorescence signal observed for the 100 % Mut (A) target. However, at a probe concentration of 0.1 μ M and 0.2 μ M (Figure 5.14 and Figure 5.15, respectively) a linear correlation between the anthracene fluorescence signal and the amount of Mut (A) target present in the sample could not be obtained. There was also a less significant change between the anthracene signal observed with the 'probe: 100% WT target' duplex and the 'probe: 100% Mut target' duplex. This reduced sensitivity of the sensing system at these lower concentrations is most likely due to the

weakness of the anthracene fluorescence signal and the difficulty in detecting the very small changes in fluorescence intensity between the various 'probe: X% A target' duplexes.

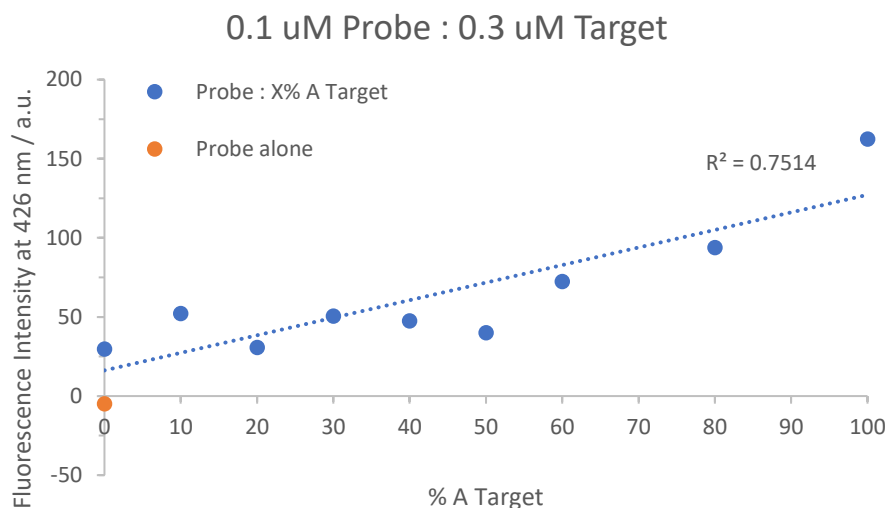


Figure 5.14: Linear correlation plot showing anthracene fluorescence intensity recorded at 426 nm. Fluorescence intensity of the probe alone is shown in orange and the fluorescence intensity once duplexes are formed with varying ratios of A/T target variants are shown in blue. 0.1 μ M probe: 0.3 μ M target (100 mM NaCl, 10 mM sodium phosphate buffer pH 7.0, aqueous solution). λ_{ex} = 350 nm, 298 K.

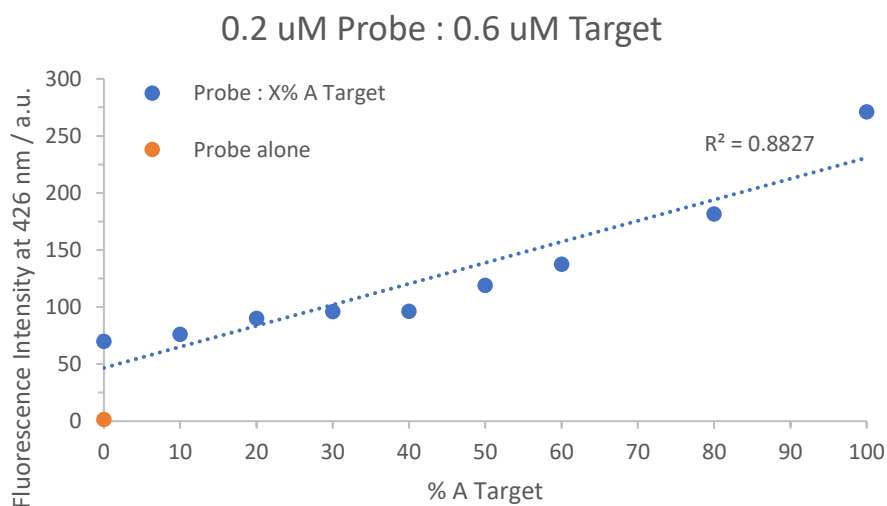


Figure 5.15: Linear correlation plot showing anthracene fluorescence intensity recorded at 426 nm. Fluorescence intensity of the probe alone is shown in orange and the fluorescence intensity once duplexes are formed with varying ratios of A/T target variants are shown in blue. 0.2 μ M probe: 0.6 μ M target (100 mM NaCl, 10 mM sodium phosphate buffer pH 7.0, aqueous solution). λ_{ex} = 350 nm, 298 K.

Moving to higher probe concentrations of 0.3 μM , and 0.4 μM (Figure 5.16 and Figure 5.17, respectively) improvements in the linear correlation effect and the sensitivity of detection were observed due to the anthracene fluorescence signal being now sufficiently strong enough.

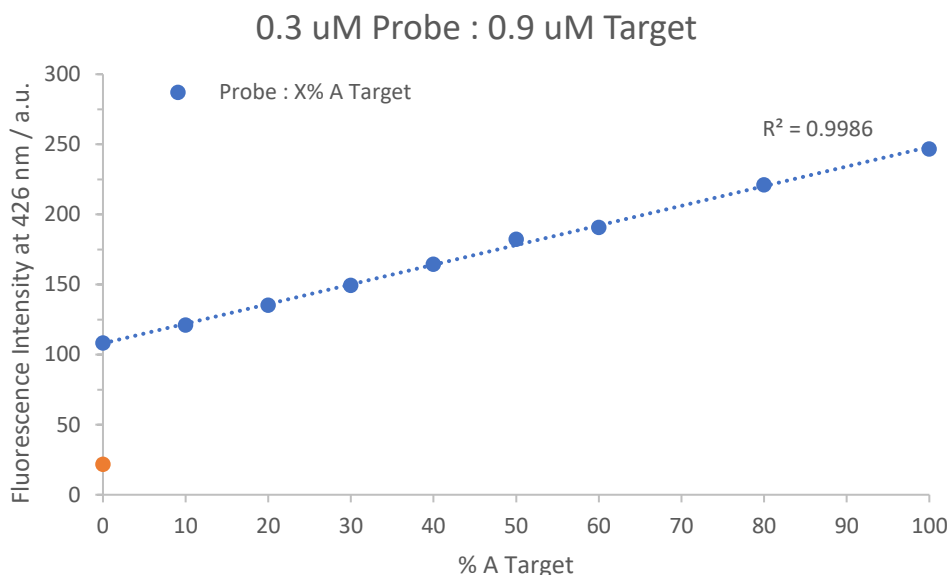


Figure 5.16: Linear correlation plot showing anthracene fluorescence intensity recorded at 426 nm. Fluorescence intensity of the probe alone is shown in orange and the fluorescence intensity once duplexes are formed with varying ratios of A/T target variants are shown in blue. 0.3 μM probe: 0.9 μM target (100 mM NaCl, 10 mM sodium phosphate buffer pH 7.0, aqueous solution). $\lambda_{\text{ex}} = 350 \text{ nm}$, 298 K.

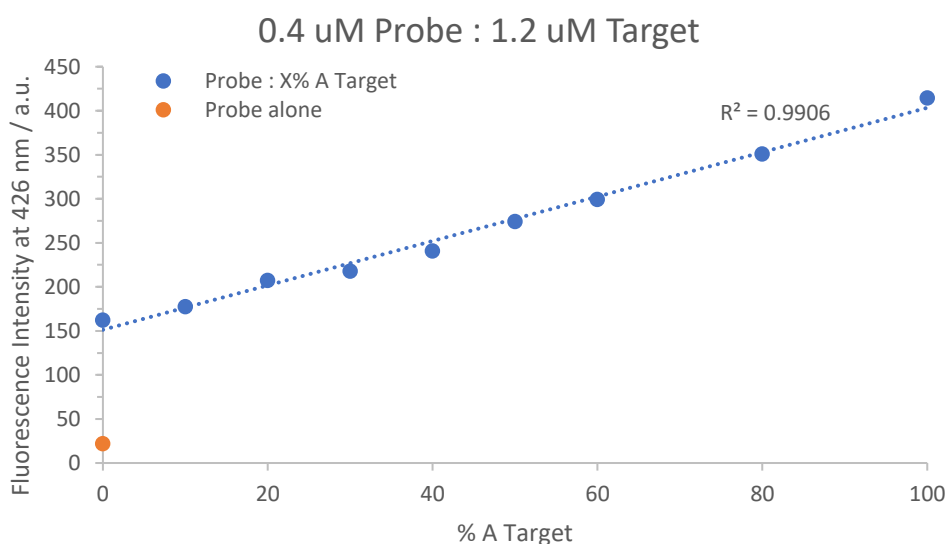


Figure 5.17: Linear correlation plot showing anthracene fluorescence intensity recorded at 426 nm. Fluorescence intensity of the probe alone is shown in orange and the fluorescence intensity once duplexes are formed with varying ratios of A/T target variants are shown in blue. 0.4 μM probe: 1.2 μM target (100 mM NaCl, 10 mM sodium phosphate buffer pH 7.0, aqueous solution). $\lambda_{\text{ex}} = 350 \text{ nm}$, 298 K.

Interestingly, at the highest probe concentration of 1 μM , Figure 5.18, there was again a noticeable deviation from linearity, which could be caused by non-specific interactions between probe and target strands which become enhanced at higher target concentrations.

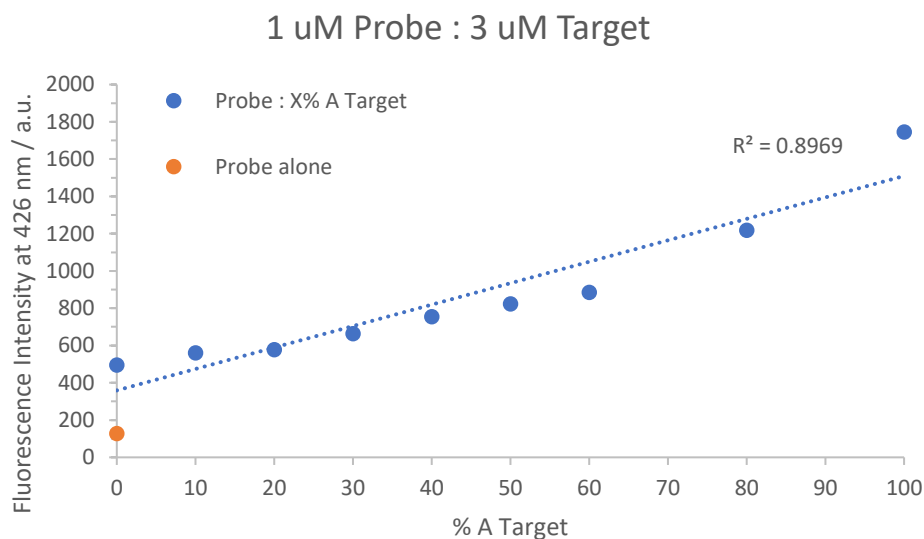


Figure 5.18: Linear correlation plot showing anthracene fluorescence intensity recorded at 426 nm. Fluorescence intensity of the probe alone is shown in orange and the fluorescence intensity once duplexes are formed with varying ratios of A/T target variants are shown in blue. 1 μM probe: 3 μM target (100 mM NaCl, 10 mM sodium phosphate buffer pH 7.0, aqueous solution). $\lambda_{\text{ex}} = 350 \text{ nm}$, 298 K.

Sensing results obtained at these various probe concentrations suggest that there is an optimal probe concentration range in which reliable and accurate data can be obtained to produce effective linear correlation plots. This range lies somewhere between a probe concentration of 0.3 μM and 0.5 μM for the 173-mer targets. A probe concentration of 0.5 μM was chosen for future experiments as at this concentration, a good linear correlation effect is observed and there is a steeper gradient between samples containing 100% WT and 100% Mut targets allowing for increased accuracy.

5.6.3. Investigating the Increase in Fluorescence Observed Upon Formation of Duplexes Containing Long Oligonucleotide Targets

As mentioned above, one of the main differences between the data gathered using the 15-mer and 173-mer target oligos was the slight differences in the magnitude of fluorescence intensity increases upon target binding relative to the unbound probe. Observations using the 15-mer targets showed very similar fluorescence signals between those for the probe alone and the 'probe: 100% WT target' duplex, with an increased fluorescence intensity for the 'probe: 100% Mut target' duplex. As for the 173-mer targets, a slight increase in fluorescence intensity was observed for the 'probe: 100% WT target' duplex in comparison to the unbound probe and an even larger increase upon binding the 100% Mut target.

To investigate this further, the fluorescence emission profiles of the two unbound 173-mer target strands at 1.5 μM were recorded, Figure 5.19. Although very minimal, some background fluorescence was observed at roughly 440 nm, which can explain the slight increase in emission for the WT duplexes compared to the probe alone. This may be a result of impurities in the purchased oligo stock samples, such as salts/buffers remaining from the DNA synthesis and purification processes. NAP desalting columns were used in an attempt to remove any impurities from these samples; however, this only led to a loss in sample, while the background fluorescence emission remained.

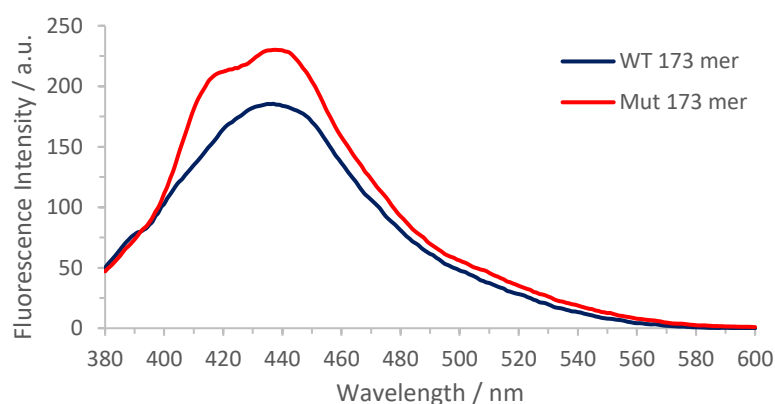


Figure 5.19: Fluorescence spectra of the 173-mer WT (blue) and Mut (orange) targets. $\lambda_{ex} = 350 \text{ nm}$, 298 K, 1.5 μM [DNA], 100 mM NaCl, 10 mM sodium phosphate buffer pH 7.0, aqueous solution.

Overall, since this background fluorescence was very minimal it was concluded that this issue should not greatly interfere with the sensing results.

5.7. BRAF V600E Sensing Using PCR-Amplified DNA From Genomic DNA

Following the promising results obtained when sensing the 15-mer and 173-mer synthetic targets, the sensing ability of the anthracene BRAF V600E probe was tested using extracted genomic DNA targets from healthy and BRAF V600E mutated cell line samples, with the aim of replicating patient samples more closely. PCR amplification of the extracted genomic DNA is required to increase the amount of target DNA so that a sufficient amount of anthracene probe can be used to generate a detectable fluorescence signal. After PCR amplification it was anticipated that there would be sufficient amounts of target for the anthracene probe to bind at a probe concentration that could provide a strong enough emission signal.

5.7.1.1. Producing Single-Stranded DNA Targets From the PCR Amplicon

The development of a sensing protocol using PCR-amplified DNA targets obtained from genomic DNA is not straightforward, due to the need of the anthracene probe to bind to single-stranded DNA targets only, while standard PCR amplification methods produce double-stranded amplicons. There are many known methods for producing single-stranded DNA *during* PCR amplification, such as asymmetric PCR,¹⁹⁻²² or *post* PCR amplification, such as magnetic bead separation²³⁻²⁵ or enzymatic digestion methods.^{26,27} Asymmetric PCR methods may seem the simplest way of producing single-stranded DNA in one step, but asymmetric PCR methods are often not as specific as other PCR methods. Such methods often favour the amplification of one variant over another (this is especially the case if one variant has a much lower copy number), which produces amplicon mixtures that do not truly represent the allelic ratio in the original sample.^{20,22} On the other hand, the use of 'one-step' methods for the amplification of genomic DNA to single-stranded DNA targets is of high importance for clinical assays to reduce the chances of contamination. However, the possibility of unequal amplification of WT and

Mut DNA was considered to be too great a risk and therefore *post* amplification separation methods were deemed more appropriate. It was decided that enzymatic digestion methods would be used due to the high cost of magnetic bead separation methods, as well as there being previous success within the group employing enzymatic digestion methods for this purpose.¹²

5.7.2. PCR Amplification of Genomic DNA

Prior to amplification, the genomic DNA was extracted from colorectal cancer (CRC) cell lines using Qiagen DNeasy® Blood and Tissue Kit. The method is outlined in the Experimental 7.7.5. The extracted genomic DNA was then amplified at the region of interest using PCR, as outlined below.

5.7.2.1. Primer Design

Primers were designed specific to the region of the BRAF gene where the T > A point mutation occurs, amplifying a region containing 173 base pairs. The primer sequences are shown in Table 5.4 and were purchased from Sigma Aldrich. The forward primer contains several phosphorothioate modifications at the 5' end. Post amplification, the presence of these phosphorothioate modifications enables the formation of single-stranded DNA targets *via* the use of a T7 exonuclease DNA polymerase. Several phosphorothioate modifications are required to ensure stability.²⁸ This T7 exonuclease DNA polymerase is not able to recognise and digest the strand containing the phosphorothioate modifications at the 5' end of the sequence, resulting in ssDNA formed from the forward primer being left intact.

The melting temperature (T_m) of the primers are important in determining the annealing temperature employed during the PCR cycles.²⁹ These are shown in Table 5.4.

Table 5.4: PCR primer sequences for the amplification of the region of interest in the BRAF gene containing the point mutation. The melting temperature (T_m) of each primer corresponds to the hybridisation of the primers with their complementary targets.

	Sequence	T_m (°C)
Forward Primer	5' – T*G*C* T*TG CTC TGA TAG GAA AAT G - 3' Where * denotes phosphorothioate modification	63.1
Reverse Primer	5' – CCA CAA AAT GGA TCC AGA CA – 3'	63.4

PCR amplification using the above primers has been already reported within the group.¹² Previously reported sequencing results confirm that the primers successfully amplify the selected region of the BRAF gene to give sequences identical to those in Table 5.3.¹²

5.7.2.2. PCR Reaction Conditions

Starting with 200 ng genomic DNA and 0.5 μ M of each primer (a 50 μ L scale reaction) and employing the optimal conditions shown in Table 5.5, PCR was performed using a Phusion® High-Fidelity PCR Kit on a BioRad C1000 Touch Thermal Cycler.

Table 5.5: PCR cycling conditions used for optimal DNA concentration output.

Step	Temperature (°C)	Time Length (s)	
Initial Denaturation	98	30	
Denaturation	98	10	35 Cycles
Annealing	61	30	
Extension	72	45	
Final Extension	72	600	
Hold	4	∞	

PCR cycling was also performed under a variety of other conditions, shown in the Experimental 7.7.4, in order to determine which conditions yielded the amplified DNA in concentrations sufficient for the fluorescence sensing experiments. A negative control sample was included with each PCR run, consisting of all the PCR reagents and primers whilst not containing any genomic DNA for amplification.

The ScreenTape (High Sensitivity D1000 ScreenTape® using Agilent Technologies TapeStation Analysis) shown in Figure 5.20 confirms the formation of the expected PCR amplicon, showing a band with the expected size of around 173 bp. A ScreenTape is a DNA electrophoresis technique, with higher precision and control than gel electrophoresis. Both WT (lanes B1 and C1) and Mut (lanes D1 and E1) samples display this band, whereas the PCR negative control (lane F1) does not. There are also bands present across all lanes equating to a size of around 20 bp which corresponds to the presence of primers remaining in the sample (ScreenTape performed prior to purification steps).

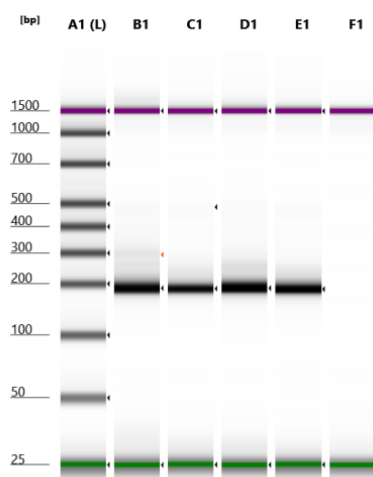


Figure 5.20: High sensitivity ScreenTape showing the successful PCR amplification of Mut and WT genomic DNA from cell lines. Lane A1: Ladder (bp); Lane B1: PCR product from WT sample; Lane C1: PCR product from WT sample; Lane D1: PCR product from Mut sample.

5.7.3. T7 Exonuclease Digestion of PCR Amplicon

Prior to probe hybridisation and fluorescence sensing, the double-stranded PCR amplicon is digested to single-stranded DNA using a T7 exonuclease DNA polymerase enzyme. As outlined earlier, the target strand formed from the extension of the phosphorothioate primers remains intact as the enzyme does not recognise and digest the phosphorothioate modifications at the 5' end of the amplified target; Figure 5.21 demonstrates this schematically. In contrast, the complementary strand formed from the unmodified primer is recognised and subsequently digested by the T7 exonuclease. After clean and

purification steps using Monarch PCR & DNA Cleanup Kit, only the single-stranded target (173-mer) remains, with sequences identical to those in Table 5.3.

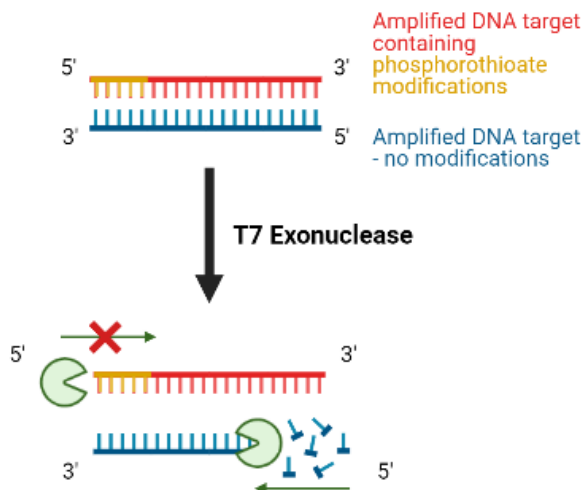


Figure 5.21: Schematic diagram showing the mechanism of action of the T7 exonuclease. The amplified target strands extended from the phosphorothioate primers are not digested by the exonuclease and remain intact. The unmodified target strands are digested and removed in subsequent wash steps.

The PAGE image, Figure 5.22, shows the effect of the exonuclease digestion of the PCR amplicon to produce single-stranded DNA containing the phosphorothioate modified primer. The PCR amplicon (prior to the exonuclease digestion step) (Lane 4) is of the expected size when compared to the Hyperladder 25 bp (Lane 3 and Lane 6) and contains only one band, indicating that PCR amplification has been successful. The product remaining from the exonuclease digestion step (Lane 5) appears further down the gel as expected, indicating the presence of the undigested single-stranded DNA formed from the phosphorothioate primers during PCR amplification. There are several bands that appear in this lane, most probably due to the different folding that can occur within the long target strand.

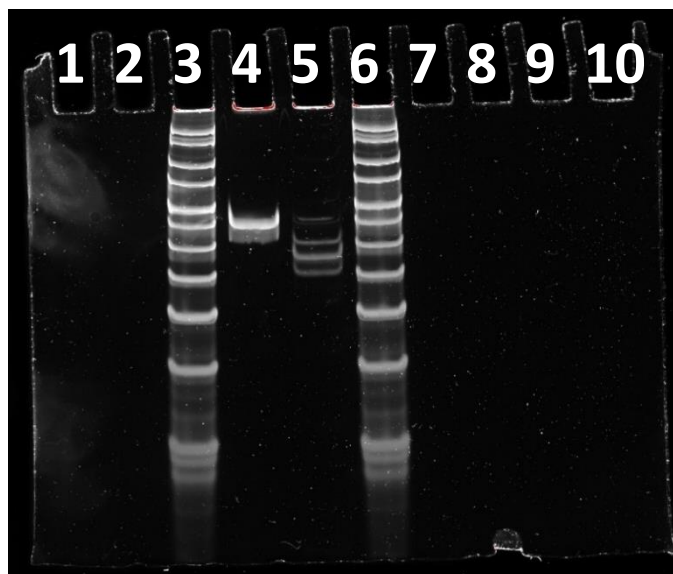


Figure 5.22: PAGE image of PCR amplicon and ssDNA product remaining from the exonuclease digestion step. 5% polyacrylamide, 100 V, run time = 1 h 15 min. Lane 1-2: empty. Lane 3: Hyperladder 25 bp. Lane 4: ds PCR amplicon (roughly 0.5 μ M). Lane 5: ssDNA product remaining from the exonuclease digestion step (roughly 0.5 μ M). Lane 6: Hyperladder 25 bp. Lane 7-10: empty. Stained using Diamond™ dye.

5.7.4. Fluorescence Sensing of the Single-Stranded PCR Product

Initial fluorescence sensing studies tested the probe in the simple detection of fully WT and fully Mut BRAF samples. It is important to note that the fully Mut BRAF samples are heterozygous, containing 50% WT (T) variant and 50% Mut (A) variant, rather than consisting of just one nucleobase target variant, and this must therefore be considered when comparing fluorescence intensity changes between the fully WT and fully Mut samples.

A single PCR amplification reaction did not produce a high enough concentration of target DNA to carry out fluorescence sensing experiments (target concentrations were calculated using a QuBit ssDNA Assay Kit), despite efforts to optimise the PCR protocol and cycling conditions. A single PCR reaction, involving 38 cycles, yielded roughly 500 ng DNA, or 0.8 μ M in 15 μ L (after purification steps). The relatively large number of PCR cycles increased the time taken for each PCR reaction, a potential barrier to the development of a more rapid detection assay. In addition, the amount of DNA produced was much lower than the concentration levels required for anthracene sensing. As outlined earlier,

anthracene sensing at probe concentrations of 0.3-0.5 μM are required for more accurate results and fluorescence sensing was carried out on a 50 μL scale because of limitations on cuvette size. Additionally, the purification steps following PCR amplification and exonuclease digestion resulted in sample loss, thus further reducing sample concentrations. For this reason, 8-12 individual PCR experiments were combined to generate target concentrations that were high enough for fluorescence sensing to be conducted.

Due to limited amounts of target sample being produced, it was initially decided to test the BRAF anthracene probe using a very low probe concentration of 0.05 μM . When sensing was performed at this lower concentration using the 15-mer targets, the WT and Mut variants could at least be discriminated, even if the correlation plot was not linear (Appendix 8.3.4).

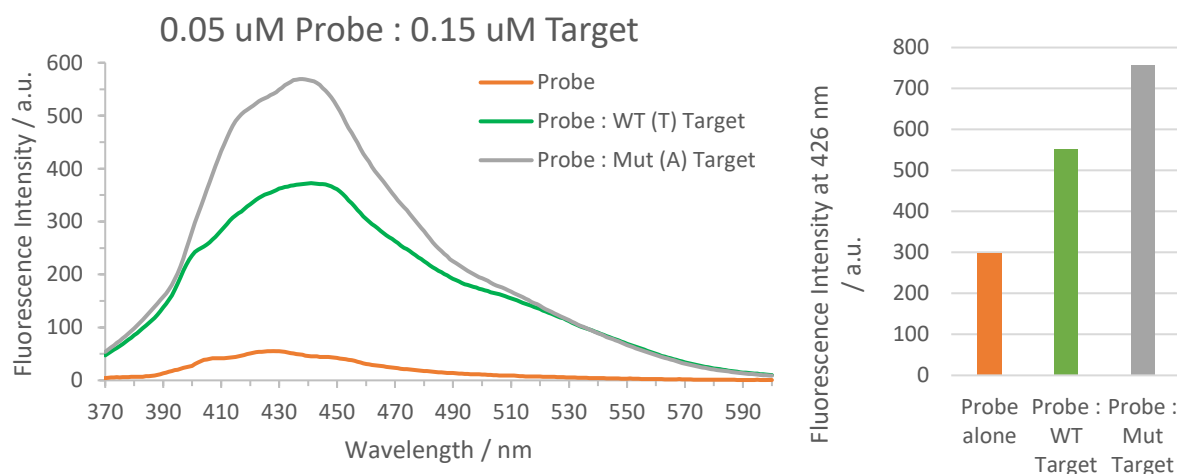


Figure 5.23: (Left) Fluorescence emission of anthracene BRAF probe when single-stranded (orange), duplexed with WT PCR derived target (green) and Mut PCR derived target (grey). (Right) Bar chart showing fluorescence intensity at 426 nm. $\lambda_{\text{ex}} = 350 \text{ nm}$, 298 K. 0.05 μM probe: 0.15 μM target, 100 mM NaCl, 10 mM sodium phosphate buffer pH 7.0, aqueous solution.

Figure 5.23 displays the fluorescence signal of the anthracene BRAF probe at this lower concentration, unbound and when binding a three-fold excess of WT and Mut BRAF target strands derived from PCR-amplified genomic DNA. A detectable fluorescence intensity change was observed between the WT and Mut samples, demonstrating the ability of the probe to detect the BRAF V600E biomarker. As observed with the 173-mer synthetic targets described earlier, increases in fluorescence intensity were

observed for both duplexed samples. Similarly, this increase results from the background fluorescence from the PCR samples as shown in Figure 5.24. Although minimal, this background fluorescence is most likely due to small amounts of impurities remaining in the sample from the PCR reaction or subsequent wash steps. The buffers used in the various purification kits contain reagents that may be contributing to this background fluorescence. It can be very difficult to completely remove all traces of buffers within the sample and any trace amounts of buffer may be detected due to the high sensitivity of the fluorescence sensing parameters that were employed (fluorescence sensing parameters can be found in the Experimental 7.7.2).

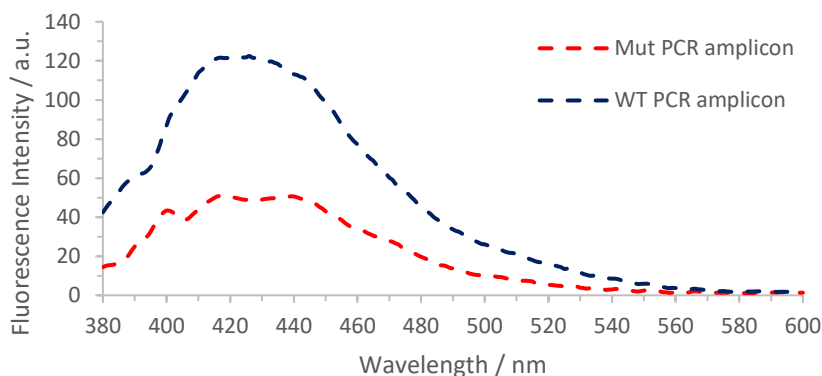


Figure 5.24: Background fluorescence emission resulting from the PCR-amplified targets. $\lambda_{ex} = 350 \text{ nm}$, 298 K, 0.6 μM [DNA], 100 mM NaCl, 10 mM sodium phosphate buffer pH 7.0, aqueous solution.

Probe concentrations of ca. 0.5 μM were shown earlier to produce optimal fluorescence sensing outputs and so this concentration was also tested using the 173-mer targets derived from PCR-amplified genomic DNA, Figure 5.25. An excess amount of target was added once again, however due to the limited amounts of target species produced, this amounted to just over a two-fold excess.

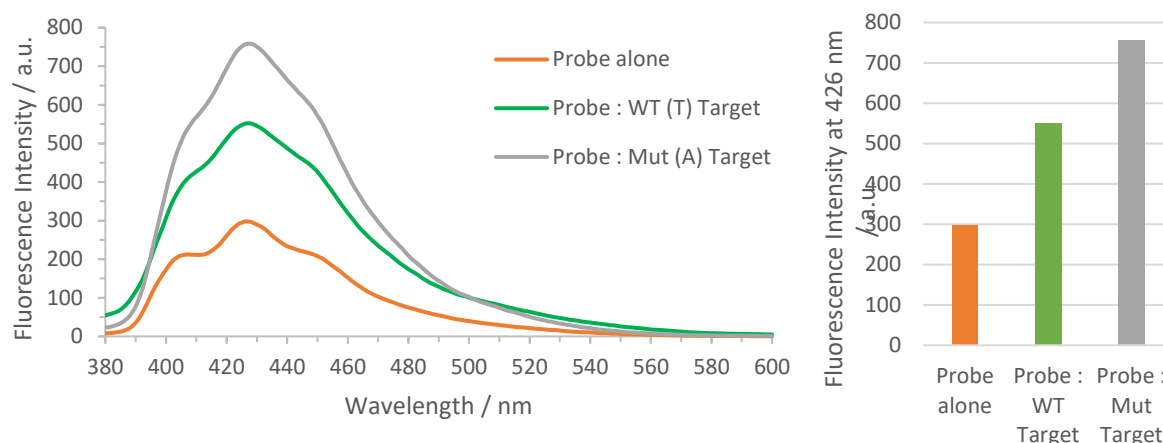


Figure 5.25: (Left) Fluorescence emission of anthracene BRAF probe when single-stranded (orange), duplexed with WT PCR derived target (green) and Mut PCR derived target (grey). (Right) Bar chart showing fluorescence intensity at 426 nm. $\lambda_{ex} = 350$ nm, 298 K. Probe concentration 0.5 μ M, target concentration 1.1 μ M, 100 mM NaCl, 10 mM sodium phosphate buffer pH 7.0, aqueous solution.

At this higher probe concentration, the anthracene signal was more pronounced and again WT samples could be distinguished from Mut samples through differences in fluorescence intensity. If limited target concentration were not an issue and 3 equivalents rather than 2.2 equivalents of target were used, an even greater change in fluorescence intensity between the WT and Mut samples would be expected. The use of even fewer molar equivalents of target (1.2 equivalents) was also investigated at this concentration of probe. As might be expected, this resulted in reduced changes in the fluorescence intensity of the anthracene probe when discriminating between the WT and Mut samples, with the results presented in the Appendix 8.3.4.

5.8. Conclusions

Progress has been made into the development of the anthracene BRAF probe as a point mutation detection assay for the BRAF V600E biomarker, with the probe successfully distinguishing between Mut and WT targets derived from genomic DNA. A workflow has been established in which the specific region of interest in genomic DNA is amplified, digested to form single-stranded DNA targets and then hybridised with the probe to allow for the fluorescence sensing experiments to proceed. Furthermore, it has been shown that the linear correlation effect between anthracene fluorescence signal and

amount of Mut target present within a heterozygous sample is still effective when using longer targets (173-mer). This provides good evidence that the allelic ratios of unknown patient tumour samples can be accurately determined using the anthracene probe and a linear calibration curve.

It has also been shown that lower concentrations of probe and target can be employed for the sensing experiments and still yield relatively accurate outputs for the allelic ratio quantification. However, the concentration of target required for effective fluorescence sensing remains problematic. In particular, it is currently not possible to produce a sufficient amount of target DNA in one run from genomic DNA as is currently the case for many commercial assays (Cobas, TaqMan™, etc). The work in this chapter describes PCR experiments involving many PCR cycles for each run, producing samples with insufficient amount of DNA for fluorescent sensing. This led to the assay having increased sensing times and reagent costs. These issues would need to be addressed in future work.

5.9. Future Work

Future work on this project will aim to assess the sensing ability of the anthracene probe when using patient samples of unknown allelic ratios and use a linear calibration curve to determine the amount of Mut target within the sample. In order to achieve this and perform more tests on patient samples/genomic DNA, alternative methods employed for DNA amplification need to be explored. As mentioned above, the PCR methods adopted for this work would not be feasible for use as an assay due to the limited amount of sample produced, as well as the current 'open' workflow of the sensing system which introduces potential sample contamination. Other PCR techniques should be tested, including LATE PCR with the aim of producing single-stranded target DNA at higher concentrations.³⁰

In addition, different methods of producing single-stranded DNA from the PCR amplicon could be explored. Although the exonuclease digestion worked well for this purpose, there may be more effective methods which may help reduce sample loss during this process. Despite their increased cost, magnetic beads may be a good alternative choice to be explored.

5.10. References

1. R. Kumar, S. Angelini, K. Czene, I. Sauroja, M. Hahka-Kemppinen, S. Pyrhonen and K. Hemminki, *Clin Cancer Res*, 2003, **9**, 3362.
2. R. Houben, J. C. Becker, A. Kappel, P. Terheyden, E. B. Brocker, P. Goetz and U. R. Rapp, *J. Carcinog*, 2004, **3**, 6.
3. M. Libra, G. Malaponte, P. M. Navolanic, P. Gangemi, V. Bevelacqua, L. Proietti, B. Bruni, F. Stivala, M. C. Mazzarino, S. Travali and J. A. McCubrey, *Cell Cycle*, 2005, **4**, 1382.
4. E. Tiacci, V. Trifonov, G. Schiavoni, A. Holmes, W. Kern, M. P. Martelli, A. Pucciarini, B. Bigerna, R. Pacini, V. A. Wells, P. Sportoletti, V. Pettirossi, R. Mannucci, O. Elliott, A. Liso, A. Ambrosetti, A. Pulsoni, F. Forconi, L. Trentin, G. Semenzato, G. Inghirami, M. Capponi, F. DeRaimondo, C. Patti, L. Arcaini, P. Musto, S. Pileri, C. Haferlach, S. Schnittger, G. Pizzolo, R. Foa, L. Farinelli, T. Haferlach, L. Pasqualussi, R. Rabadan and B. Falini, *N Engl J Med*, 2011, **364**, 2305.
5. E. R. Cantwell-Dorris, J. J. O'Leary and O. M. Sheils, *Mol Cancer Ther*, 2011, **10**, 385.
6. C. McCourt, O. Dolan and G. Gormley, *The Ulster Medical Journal*, 2014, **83**, 103.
7. C. Willmore-Payne, J. A. Holden, S. Hirschowitz and L. J. Layfield, *Human Pathology*, 2006, **37**, 520.
8. I. Hudecova, *Clin. Biochem*, 2015, **48**, 948.
9. E. Day, P. H. Dear and F. McCaughan, *Methods*, 2013, **59**.
10. B. Vogelstein and K. W. Kinzler, *Proc. Natl. Acad. Sci. U.S.A.*, 1999, **96**, 9236.
11. Z. Zhao, M. San, J. H. A. Duprey, J. R. Arrand, J. S. Vyle and J. H. R. Tucker, *Bioorg. & Med. Chem. Lett.*, 2012, **22**, 129.
12. A. Ali, University of Birmingham, 2018.
13. S. Benlloch, A. Paya, C. Alenda, X. Bessa, M. Andreu, R. Jover, A. Castells, X. Llor, F. I. Aranda and B. Massuti, *J Mol Diagn*, 2006, **6**, 540.
14. F. E. A. McGuigan and S. H. Ralston, *Psychiatric Genetics*, 2002, **12**, 133.

15. P.-J. Lamy, F. Castan, N. Lozano, C. Montelion, P. Audran, F. Bibeau, S. Roques, F. Montels and A.-C. Laberrenne, *J Mol Diagn*, 2015, **17**, 366.
16. B. Malicherova, T. Burjanivova, M. Grendar, E. Minarikova, M. Bobrovskaya, B. Vanova, K. Jasek, E. Jezkova, A. Kapinova, M. Antosova, I. Homola, T. Pecova, Z. Lasabova and L. Plank, *Am J Transl Res*, 2018, **10**, 3773.
17. J.-L. H. A. Duprey, PhD Thesis, University of Birmingham, 2010.
18. J.-L. H. A. Duprey, Z.-Y. Zhao, D. M. Bassani, J. Manchester, J. S. Vyle and J. H. R. Tucker, *Chem. Commun.*, 2011, **47**, 6629.
19. P. C. McCabe, *PCR Protocols, A Guide to Methods and Applications*, Academic Press, New York, 1990.
20. U. B. Gyllensten and H. A. Erlich, *Proc. Natl. Acad. Sci. U.S.A.*, 1988, **85**, 7652.
21. K. E. Pierce, J. E. Rice, J. A. Sanchez and L. J. Wangh, *Mol. Hum. Reprod*, 2003, **9**, 815.
22. J. A. Sanchez, K. E. Pierce, J. E. Rice and L. J. Wangh, *Proc. Natl. Acad. Sci. U.S.A.*, 2004, **101**, 1933.
23. R. Wilson, *Nucleic Acid Therapeutics*, 2011, **21**, 437.
24. J. B. H. Tok and N. O. Fischer, *Chem. Commun.*, 2008, **28**, 1883.
25. A. Wochner, B. Cech, M. Menger, V. A. Erdmann and J. Glokler, *BioTechniques*, 2007, **43**, 344.
26. L. A. McReynolds and N. M. Nichols, *Curr. Protoc. Mol. Biol.*, 2011, **96**, 3.11.
27. N. A. Straus and R. J. Zagursky, *Biotechniques*, 1991, **10**, 376.
28. J. H. Chan, S. Lim and W. S. Wong, *Clin Exp Pharmacol Physiol*, 2006, **33**, 533.
29. N. E. BioLabs, Tm Calculator, <https://tmcalculator.neb.com/#!/main>, (accessed 12/01/2021, 2021).
30. J. A. Sanchez, K. E. Pierce, J. E. Rice and L. J. Wangh, *PNAS*, 2004, **101**, 1933.

6. The Development of Naphthalimide Nucleic Acid Probes for Use in Fluorescence In Situ Hybridisation (FISH) and Super-Resolution Imaging Experiments

6.1. Introduction

Fluorescently-modified DNA is widely used for probing biological environments in situ using microscopy. Progressing from the Tucker group's initial developments into anthracene modified nucleic acid probes, naphthalimide modified probes improve on these first-generation probes owing to their longer wavelength absorption and emission profiles which make them more well-suited to microscopy imaging techniques. The increased absorption wavelengths allow for the use of a 405 or 488 nm laser as a source of excitation, which is common in most microscope set-ups. In addition, their absorption and emission profiles residing at longer wavelengths (in comparison anthracenes) are beneficial to sensing biological environments in situ as the longer wavelengths reduce any background fluorescence from cellular environments.

Work in this chapter focuses on the use of naphthalimide probes in two imaging techniques; "fluorescence in situ hybridisation" (FISH) and "DNA points accumulation for imaging in nanoscale topography" (DNA PAINT). These techniques will be discussed in more detail in the following sections, along with the suitability of the naphthalimide probes for these techniques.

6.1.1. Fluorescence In Situ Hybridisation (FISH)

Fluorescence in situ hybridisation (FISH) is a molecular cytogenetic technique that enables the specific binding of fluorescent probes to complementary nucleic acid sequences within chromosomes to allow researchers to locate those specific sequences.¹ Since the development of the first FISH techniques in 1977,² today there are a variety of FISH procedures that are available which are used to diagnose many types of chromosomal abnormalities in patients, including deletions, duplications and translocations.

FISH techniques were initially performed on metaphase chromosomes but can now also be performed on interphase chromosomes.³ This development provides many advantages, especially regarding sample preparation, as cells no longer need to be cultured for long periods of time before using for analysis and also allows chromosomes from solid tumour specimens to be analysed (samples which do not divide frequently). However, chromosomal DNA is more compact in metaphases, which allows for site localisation of hybridised probes within specific chromosomes of defined shape and size, making chromosome analysis easier to perform with samples containing metaphases in comparison to samples containing only interphase nuclei.

FISH methods involve a fluorescent probe targeting a specific DNA sequence in chromosomal preparations that have been fixed on slides, also known as target DNA, as shown in Figure 6.1. Firstly, samples are heated to a temperature that denatures all double-stranded DNA in a sample so that single-stranded DNA remains. The sample is then cooled slowly to allow for controlled and specific hybridisation of the probe with the complementary region of interest within the chromosome. Subsequent wash steps allow for the removal of any unbound probe. Fluorescence microscopy is then used to detect and/or visualise the location of the bound probes.

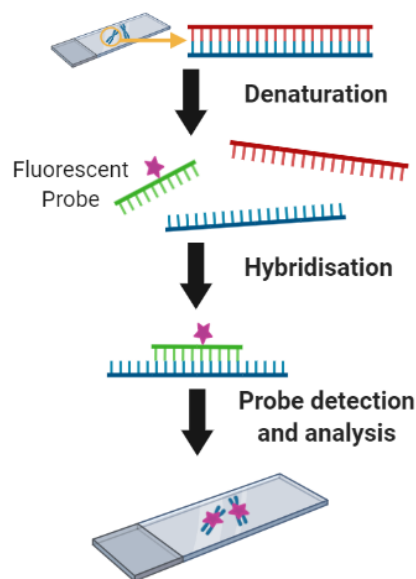


Figure 6.1: Schematic diagram demonstrating a typical FISH experiment.

Many commonly used FISH probes are commercially available and were developed from DNA fragments (collected during the Human Genome Project) cloned in bacterial artificial chromosomes (BACs). The BAC library contains hundreds of probes, usually with lengths in the region of kilobases, which are used for detecting specific genes/regions of interest. There are several types of probes commonly used in FISH techniques; locus-specific, centromeric, telomeric and whole chromosome paint.⁴ Work in this chapter focusses on the development of centromeric probes. Centromeric probes target highly repetitive α -satellite regions found within centromeres of chromosomes.⁵ Centromeric probes are generally used as enumeration probes, to detect chromosome abnormalities such as loss or gain of chromosomes (aneuploidy). Such abnormalities may be caused during cell division and are linked to many types of cancers.

Centromeres are specialised constricted regions of DNA that separate a chromosome into a short arm and a long arm, as demonstrated in Figure 6.2. During cell division, a chromosome replicates so that each daughter cell receives a complete set of chromosomes. Following DNA replication (in metaphases), the chromosome consists of two identical structures called sister chromatids joined at the centromere. The specialised DNA constituting the centromere is a highly repetitive region of non-coding DNA. These regions are made up of monomer units of 171 base pair (bp) sequences which are A-T rich and make up higher order repeats that are tandemly repeated potentially hundreds to thousands of times within the centromeres.⁶ The repeating monomer units found in centromeres are roughly 50-70% similar across all chromosomes, thus making probe design tricky as probes are required to be highly specific to the centromere of a single chromosome.⁶⁻⁸ Probes are designed to target chromosome specific repeating units, sequences which remain identical throughout the higher order repeats. Work by O'Keefe *et al.* demonstrated the use of oligo probes to detect these higher order repeats that are specific to chromosome 17. The probes were designed to target a region of interest at which there are two known variant sequences with humans. Each variant is highly homologous, only differing in base variants at four different positions within this sequence. Probes

developed by O'Keefe *et al.* were able to distinguish between these two variants and their work demonstrates how oligoprobes can be used to detect polymorphisms at a molecular level enabling the differentiation between chromosomes that are cytogenetically indistinguishable.⁹

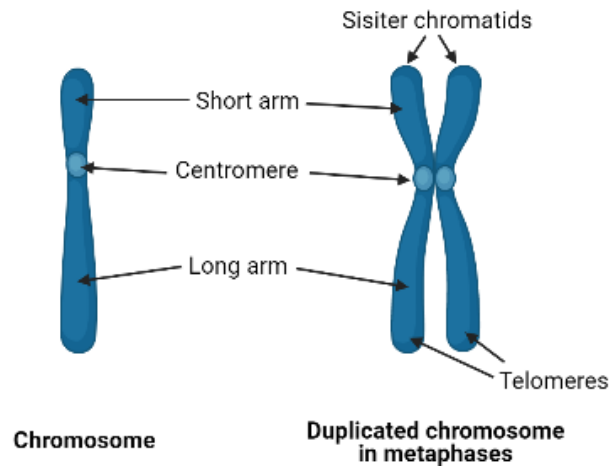


Figure 6.2: Diagram of a chromosome, showing the specific centromere and telomere regions. Following DNA replication, cells in metaphase contain two sister chromatids which are held together at the centromere.

6.1.1.1. OligoFISH

OligoFISH utilises relatively short oligo probes of around 50 nucleobases in length. These short probes are synthetically produced, unlike the most commonly used FISH probes mentioned above which are produced using BACs. The shorter length of these probes allows for more streamlined FISH protocols due to the shorter hybridisation times that can be adopted. OligoFISH probes also provide greater specificity for their target. Reducing hybridisation times, which can be up to 16 hours with traditional methods, results in reduced waiting times for diagnostic testing procedures. Additionally, as oligoFISH probes are synthetically made, this gives more freedom over the region of interest/abnormalities that can be targeted and are not restricted to those only present in the BAC library.

Due to their increased specificity, oligoFISH probes are able to detect differences in only a few bases in DNA sequences within the region of interest. These small structural changes would not be distinguishable under traditional cytogenetic methods.^{8,9}

6.1.2. DNA PAINT

After the Nobel Prize was given for 'the development of super-resolved fluorescence microscopy' in 2014, super-resolution microscopy methods have advanced biomedical research, allowing imaging to occur at molecular-level resolution inside cells. There are several methods to achieve super-resolution microscopy. Localisation microscopy methods, such as DNA PAINT, aim to control the fluorescence of molecules so that only a few fluorophores are detected at the same time. Each method has their advantages and disadvantages in terms of fluorophore selection, experimental set-up and experimental design. Localisation-based techniques, such as (fluorescence) photo-activated localisation microscopy ((f)PALM),^{10,11} stochastic optical reconstruction microscopy (STORM)^{12,13} and points accumulation for imaging in nanoscale topography (PAINT),¹⁴ utilise the reversible binding of fluorescent probes to surpass the diffraction limited resolution of standard optical systems, with each method using different types of probe to do so. The work in this chapter, concerns a PAINT technique to achieve super-resolution imaging and so this will be the focus of the discussion.

PAINT is a diffusion-based super-resolution microscopy technique in which a target molecule is exposed to a constant flux of probe molecules. The association between the probe and target molecules causes transient binding of the two and results in a burst of fluorescence from the probe molecule. These bursts of fluorescence can be localised (their positions determined with sub-diffraction limit resolution, typically of the order of 20 nm) by recording a video of the 'switch on' of fluorescent molecules per frame. The exact position of a localisation ('burst' of fluorescence) within every frame across the imaging experiment can then mapped onto a single plot.^{14,15} Upon dissociation of the probe from the target (or photobleaching of the probe), the fluorescence signal ceases as the

fluorescent molecules diffuse out of the imaging plane, known as the TIRF angle which is explained below. This hybridisation and dissociation process is repeated throughout the imaging experiment. In theory, the collisions should occur indefinitely which suits the long experiment times required for localisation microscopy. In addition, the PAINT method is less affected by photobleaching when compared to other localised super-resolution methods such as PALM or STORM due to the constant flux of 'fresh' fluorescent molecules in the imaging solution producing the fluorescence signal.

The major disadvantage of using PAINT based methods is the reduced signal-to-noise ratio that affects the quality of the image obtained. The freely diffusing probe in the imaging solution produces background fluorescence which makes it more difficult to differentiate between bound and unbound probe. The signal-to-noise ratio is optimised by using total internal reflection fluorescence (TIRF) microscopes which allows only the excitation and visualisation of fluorophores within an evanescent field of the incident laser; a region just above the sample/slide in the imaging solution.¹⁶ Fluorophores that lie outside this region are not directly excited. Figure 6.3 schematically demonstrates TIRF microscopy.

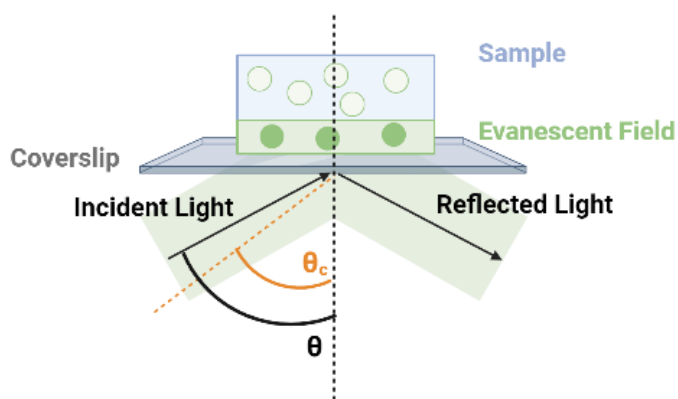


Figure 6.3: TIRF. The incident light enters the sample at the incidence angle, θ , which is greater than the critical angle, θ_c . The incident light is reflected off the coverslip: sample interface. An evanescent field is created on the other side of the coverslip: sample interface, within the sample. Only samples in the evanescent field are excited.

The most common variant of PAINT, DNA PAINT, draws upon the highly specific nature of DNA binding between two complementary oligo strands and is the method used to form the basis of the work in

this chapter. In this technique, short fluorescently-modified oligos, named ‘imager’ strands, transiently bind to their complementary targets, named ‘docking’ strands, as shown in Figure 6.4. For this to occur, the imager strands must have a thermal melting temperature (T_m) just below room temperature (imaging experiments performed at room temperature). This transient binding mode creates the blinking behaviour that is requisite for localisation microscopies. The blinking is created by the transient interaction of the imager strands and docking strands which produces a burst of fluorescence that can be localised. Similarly to other localised super-resolution microscopy methods, the fluorescence signal ceases upon dissociation of the imager strand from the docking strand and the process is continuously repeated.¹⁷

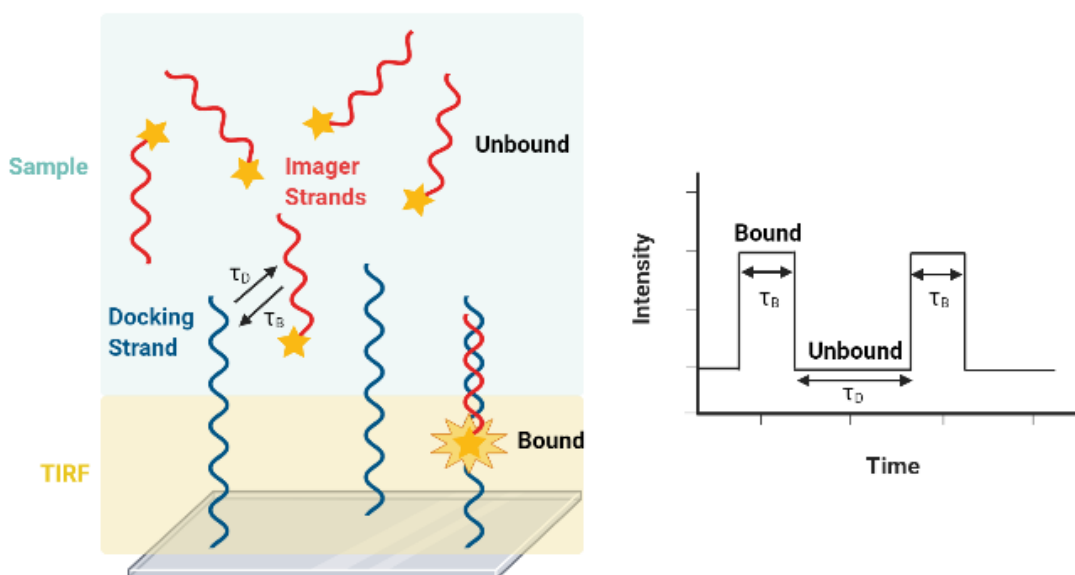


Figure 6.4: Schematic diagram demonstrating the DNA PAINT technique, showing the reversible binding of the imager strands to the docking strands on the surface. The fluorescent imager strand is only imaged when bound to the docking strand and in the TIRF field. In the naphthalimide system, the emission intensity increases upon binding of the imager strand to the docking strand.

DNA PAINT was first used as an assay to probe the single-molecule hybridisation kinetics of DNA origami.¹⁸ Since then, there have been many in vitro and cellular examples of the DNA PAINT technique where docking strands are linked to antibodies or other biological structures.¹⁹

The binding event that occurs in DNA PAINT controls the effectiveness of the imaging technique and the quality of the image produced; it is therefore important to be able to control the hybridisation kinetics. Although hybridisation between target and freely diffusing probe is stochastic, the binding kinetics can be engineered to produce high quality super-resolution images. For instance, altering the concentration of the imager strand will increase the frequency of collisions between imager strand and docking strand and thus increase the number of localisations per frame within the imaging experiment – this in turn reduces the experimental run time. However, there is an upper limit of concentration of imager strand that can be employed. An excessively high imager strand concentration will lead to an increase in background fluorescence from unbound imager probes diffusing close to the TIRF angle and therefore contribute to reduced signal-to-noise ratios. Salt/buffer concentration can also affect the binding strength between imager and docking strands. Higher salt concentrations can lead to longer binding durations, with the ‘switch on’ fluorescence signal spanning many frames and may improve the quality of the super-resolution image. Another factor affecting the hybridisation kinetics, is the length of the imager strand, an effect which has been explored in detail by Jungmann *et al.*¹⁸ It was shown that increasing the length of the complementary binding region between imager and docking strand also leads to an increase in the length of the binding event. Salt concentration and strand length are factors that affect the thermal melting temperature of the duplexes formed between imager and docking strands and need to be carefully considered when designing DNA PAINT experiments. It is important to achieve hybridisation kinetics where both bound and dissociated states are sufficiently long enough to allow for the bursts of fluorescence to be visualised and detected to produce high quality super-resolution images. Most DNA PAINT experiments use probes with lengths between 7-12 nucleobases long and salt concentrations of around 50-100 mM MgCl₂.¹⁸⁻²⁰

As mentioned above, the main disadvantage of this type of technique is reduced signal-to-noise ratios observed within samples. The (unbound) fluorescent imager strands, in the imaging solution at the edge of the evanescent TIRF field, contribute to the background fluorescence (‘noise’) and reduce the

quality of the super resolution images produced, especially when imager strand concentrations are increased to optimise the hybridisation kinetics of the imaging experiment. This chapter shows the development of fluorogenic imager strands, based on the naphthalimide nucleotide analogue. We use these probes to circumvent the limitation of current approaches for DNA PAINT by employing imager strands that have relatively low fluorescence intensity when single-stranded in the imaging solution and whose intensity increases upon hybridisation with docking strands. Employing imager strands that have low fluorescence emission when unbound and show increased fluorescence emission when bound reduces any background emission resulting from imager strands in the imaging solution close to the imaging surface.

6.2. [Project Aims](#)

The suitability of naphthalimide-modified oligonucleotides as probes for microscopy is demonstrated. Building on the simple nucleic acid sensing experiments performed using solutions of synthetic oligonucleotides in Chapter 4, the naphthalimide probes are applied to more complex sensing environments. The photophysical properties of naphthalimide compounds, with an absorption band in the region of 450 nm and a reasonable quantum yield might result in a probe that can be used for sensing in microscopy. Here, the suitability of naphthalimide probes for this purpose is investigated.

Firstly, the use of naphthalimide probes in oligoFISH techniques is explored. Relatively short probes of any sequence are easily synthesised using automated solid-phase DNA synthesis methods and can incorporate the naphthalimide modification as a nucleotide substitution at any position. Building on work by Dr A. Rushton in the Neely group,²¹ short oligoFISH probes were used as centromeric probes. Oligo probes were designed to target α -satellite regions at centromeres of chromosomes to investigate chromosome enumeration. It was expected that the highly repetitive nature of these regions would enable the naphthalimide probes to bind many times to produce a strong enough signal for detection without the need for DNA amplification of the region of interest. In particular, the α -satellite region at

the centromeres of chromosome 17 will be investigated. The decision for targeting this region of interest was due to the discovery of sequence polymorphisms within the highly repetitive chromosome-specific α -satellite region of DNA which was reported by O'Keefe *et al.*⁹ The sequence of this chromosome-specific region is known and so an oligo probe complementary to a section of this sequence was synthesised. Within this sequence, there are 4 positions at which the base may vary (polymorphisms) and one of these sites was selected to be incorporated into the targeted region of interest for the naphthalimide oligoFISH probe. The naphthalimide probes show shifts in their emission spectra that are sensitive to the base opposite the naphthalimide tag. Hence, the ability of these probes to detect and differentiate between the polymorphisms using standard oligoFISH methods, coupled with spectral imaging was to be investigated.

In Chapter 4, it was recognised that one variant of naphthalimide probes containing the Naph¹_{Dimethyl} modifications, produce very low fluorescence signals when single-stranded, but once annealed to its complement, the fluorescence intensity of these probes increases by a factor of up to 10 in some cases. This phenomenon is ideally suited to DNA PAINT methods as it increases the signal-to-noise ratio of imaging by reducing the background emission. Background emission is often problematic during the imaging experiment from fluorophores in close proximity to the imaging surface. When background fluorescence is heightened, the signal-to-noise ratio is reduced and localisation precision is lessened, producing images of reduced quality.²²

In addition, DNA PAINT probes containing fluorescent nucleotide analogues have not been reported in the literature and will be the first of their kind for use in DNA PAINT procedures. As with many DNA PAINT probes in the literature, the naphthalimide probes will firstly be tested on a DNA origami structure as a control for imaging nanoscale structures. DNA origami involves the sequence specific binding of many short synthetic staple strands to a long single-stranded DNA molecule, such as the 7249-nucleotide long genome of the M13mp18 bacteriophage used in this research. DNA origami

provides a defined structure to which docking strands can be added with precision making it an ideal starting point for many DNA PAINT techniques. We use a modified DNA origami triangle for this purpose which was made by Dr D. Smith from the Neely group, which uses the design principles of the Rothmund triangle.²³ The visualisation of this origami triangle structure will be attempted using super-resolution imaging of naphthalimide-modified imager strands.

6.3. The Development of OligoFISH Centromeric Probes for the Detection and Discrimination of Known Polymorphisms at α -Satellite DNA Regions Within Centromeres of Chromosome 17

6.3.1. Probe Design

OligoFISH probes were designed to target α -satellite repetitive DNA regions at the centromeres of chromosome 17. Loss of chromosome 17 (along with other factors) is associated with acute lymphocytic leukaemia (ALL) and is currently tested for using FISH methods.²⁴ However, standard FISH methods have very long hybridisation times (up to 16 hours) due to the nature of the long probes that are used (derived from BACs). The oligoFISH probe developed in this work was designed to be significantly shorter than the length of a standard FISH probe, with the aim of reducing testing times owing to the shortened hybridisation times made possible by these shorter DNA fragments. The probe sequences were adapted from work by O'Keefe *et al.* and were verified by a BLAT search which confirmed that the sequence is selective for chromosome 17.^{9, 25} Work by O'Keefe *et al.* showed that the target sequence of DNA has two highly homologous variants, which differ at four known base positions. Humans are thought to have either one of the variants or a mixture of both within the centromeres of chromosome 17. Previous chapters have demonstrated the naphthalimide probes successful at sensing a single base change. Therefore, the oligoFISH probe designed herein selectively targets a section of the α -satellite repeated sequence discovered by O'Keefe *et al.* which includes only one of the four base variants. The sequence of the naphthalimide oligoFISH probe (Naph17CEN) and the sequence variants of the targeted region of interest are shown in Table 6.1.

Table 6.1: Sequence of oligoFISH probes used for sensing centromeres of chromosome 17 and their corresponding target variant sequences.

Name	Sequence
Naph 17CEN	5' - AGT GCA AT \mathbf{X} ATC CCC TTG CA - 3' Where \mathbf{X} = Naphthalimide nucleotide analogue modification Naph ^A _{Short} , Naph ^A _{Long} , Naph ^L _{Dimethyl}
17CEN Target Variant 1	5' - TGC AAG GGG AT \mathbf{C} ATT GCA CT - 3'
17CEN Target Variant 2	5' - TGC AAG GGG AT \mathbf{A} ATT GCA CT - 3'

6.3.1.1. Naphthalimides as Fluorescence Reporter Groups

In Chapter 3, the synthesis of various naphthalimide nucleotide analogues were discussed. In Chapter 4, the different readout signals that these various naphthalimide modifications produce upon sensing DNA mutations and base discrimination were also explored. It was found that each variant of naphthalimide modification displayed differing changes in fluorescence intensity and spectral shifts depending on the base it was sensing. It is also known that altering the bases either side of the nucleotide modification may also affect the local sensing environment and the fluorescent signals observed. Therefore, because the 17CEN probe sequence is different from that previously studied, changes to the naphthalimide fluorescent signals are expected. Probes were synthesised with three of the naphthalimide modifications synthesised in Chapter 3; Naph^A_{Short}, Naph^A_{Long} and Naph^L_{Dimethyl}. Probes containing both L and D stereochemistry (resulting from either the L or D threoninol nucleotide analogue used in the synthesis) of each variant were synthesised. Unfortunately, due to limited sample, the Naph^L_{Amine} variant could not be made, but previous results proved this tag to be least effective at base discrimination, showing limited fluorescence intensity changes and spectral shifts between variants.

6.3.2. Naph 17CEN Probe Strand Synthesis

The naphthalimide-modified oligoFISH strands mentioned above (Naph 17CEN Probe, Table 6.1) were synthesised using automated solid-phase DNA synthesis using ultramild conditions in a similar method

to those outlined in Chapter 3 and further details can be found in the Experimental 7.3 and 7.4. The oligoFISH probe strands were then purified using semi-preparative reverse phase HPLC using a Clarity Oligo column. 0.1 M triethylammonium acetate buffer was used with an increasing acetonitrile gradient from 5-18% acetonitrile over 25 minutes (see Experimental 7.4 for full method). The strands were characterised using mass spectrometry, for full characterisation data see Appendix 8.4.1.

6.3.3. Preliminary Fluorescence Sensing Studies With Duplexes

Initial fluorescence sensing experiments were carried out using the naphthalimide oligoFISH probes and the short complementary synthetic target oligos shown in Table 6.1. These initial fluorescence sensing experiments were carried out to determine which of the naphthalimide probes gave best results for distinguishing between the two target variants (i.e. C/A base discrimination). As previously shown, base discrimination is achieved *via* changes in the fluorescence intensity and spectral shifts, owing to the solvatochromic nature of the naphthalimide tags. With the expected application of using our probes in FISH experiments coupled with spectral imaging, work in this section focuses on base discrimination *via* spectral shifts (for intensity change data see Appendix 8.4.3). Fluorescence intensity changes are difficult to measure and compare during imaging experiments for a number of reasons; the uncertainty in number of bound probes, and technical challenges such as homogeneous laser irradiation and comparable focal planes. However, any spectral shifts between the two target variants, if significant enough, may be detectable using spectral imaging. Spectral imaging refers to techniques that collect both spectroscopic data and imaging data, simultaneously.

Prior to sensing, the probe and target strands were annealed together by combining 0.5 μM probe with 1.5 μM target (excess of target) in an aqueous solution of 100 mM NaCl and 100 mM sodium phosphate buffer, pH 7.0. The aqueous mixture was then heated to 95 $^{\circ}\text{C}$ for 5 mins before allowing to cool to room temperature over roughly 30 minutes to 1 hour.

Duplex melting temperature studies were also performed to prove the viability and strength of probe binding at room temperature during the sensing and imaging experiments. The melting temperatures of all duplexes are shown in Table 6.2 and are sufficiently above room temperature, hence stable duplexes are formed at room temperature. The duplex melting temperatures are high enough, that any slight temperature increases that may arise during imaging experiments caused by the heating of the sample by the laser will not greatly affect the duplex stability or sensing.

The spectral shifts displayed by the various probes (Naph 17CEN) upon binding of the two targets (17CEN Target Variant 1 and 2) are shown in Table 6.2. It has been shown that most probes (apart from the probe containing the L Naph^I_{Dimethyl} modification) are successful in discriminating between the two target variants by showing changes in the maximum emission wavelength, λ_{max} . The nature and extent of the spectral shift depends on the interaction of the naphthalimide tag with the surrounding environment (solvent molecules) and target strand. As discussed in Chapter 4, the naphthalimide tag exhibits positive solvatochromism, meaning that the emission profile of the naphthalimide will display a bathochromic shift if the local environment is less polar, or a hypsochromic shift if more polar. The structure of the tag, along with its duplex intercalating ability will ultimately affect the positioning of the tag and how the tag interacts with the target strand. The nature of nucleobase variant present in the target strand will also provide differing interactions with the naphthalimide tags. All of these factors ultimately affect the overall local environment in which the naphthalimide tag resides and is the reason we observe shifts in the emission spectra.

Table 6.2: 17CEN duplex fluorescence sensing results and duplex melting temperatures (T_m). The maximum fluorescence emission intensity wavelength (λ_{max}) is shown for the probe alone (red) and upon duplex formation with each of the target variants. The shift in the wavelength upon duplex formation is also shown for comparison. T_m values reported as an average of triplicate repeats with error shown in brackets (\pm), to the nearest 0.5 °C.

	Probe modification	T_m / °C	λ_{max} / nm	Wavelength shift (compared to probe alone) /nm
Unmod probe: 17CEN Target Variant 1 (C)	None	73.0 (\pm 0.5)	-	-
Unmod probe: 17CEN Target Variant 2 (A)	None	70.2 (\pm 0.5)	-	-
Naph 17CEN	L Naph ^A _{Short}	-	524	-
Naph 17CEN : 17CEN Target Variant 1 (C)	L Naph ^A _{Short}	70.0 (\pm 1.5)	511	-13
Naph 17CEN : 17CEN Target Variant 2 (A)	L Naph ^A _{Short}	69.0 (\pm 0.5)	514	-10
Naph 17CEN	D Naph ^A _{Short}	-	524	-
Naph 17CEN : 17CEN Target Variant 1 (C)	D Naph ^A _{Short}	63.5 (\pm 2.5)	519	-5
Naph 17CEN : 17CEN Target Variant 2 (A)	D Naph ^A _{Short}	65.5 (\pm 0.5)	513	-11
Naph 17CEN	L Naph ^A _{Long}	-	531	-
Naph 17CEN : 17CEN Target Variant 1 (C)	L Naph ^A _{Long}	64.5 (\pm 0.5)	528	-3
Naph 17CEN : 17CEN Target Variant 2 (A)	L Naph ^A _{Long}	65.0 (\pm 0.5)	530	-1
Naph 17CEN	D Naph ^A _{Long}	-	532	-
Naph 17CEN : 17CEN Target Variant 1 (C)	D Naph ^A _{Long}	64.5 (\pm 0.5)	530	-2
Naph 17CEN : 17CEN Target Variant 2 (A)	D Naph ^A _{Long}	66.0 (\pm 0.5)	534	2
Naph 17CEN	L Naph ^I _{Dimethyl}	-	529	-
Naph 17CEN : 17CEN Target Variant 1 (C)	L Naph ^I _{Dimethyl}	67.0 (\pm 0.5)	528	-1
Naph 17CEN : 17CEN Target Variant 2 (A)	L Naph ^I _{Dimethyl}	69.5 (\pm 0.5)	528	-1
Naph 17CEN	D Naph ^I _{Dimethyl}	-	524	-
Naph 17CEN : 17CEN Target Variant 1 (C)	D Naph ^I _{Dimethyl}	68.5 (\pm 1.0)	531	7
Naph 17CEN : 17CEN Target Variant 2 (A)	D Naph ^I _{Dimethyl}	67.0 (\pm 0.5)	528	4

The most effective probe for base discrimination is the D Naph^A_{Short} 17CEN probe, demonstrating a large shift of 6 nm between the two target variants. It is plausible that this wavelength difference between the two will be detectable using spectral imaging;²⁶ therefore, this will be the probe employed in later work during FISH experiments. Upon duplex formation with the targets, the Naph^A_{Short} probes display shifts in their emission to lower wavelengths, thus implying that once duplexed, the naphthalimide tag experiences a more hydrophobic (less polar) environment. This correlates well with sensing results obtained from Chapter 4 and can be explained by the rigid positioning of the

naphthalimide tag within the probe. The naphthalimide tag in probes containing the Naph^A_{Short} modification are held closely to the DNA backbone and may intercalate slightly into the duplex upon hybridisation with the target strand and are therefore slightly removed from the polar aqueous environment. Any hypsochromic shifts suggest the opposite, implying that the naphthalimide is positioned overall in a more polar environment, which may be a result of the naphthalimide tag protruding out of the duplex into the more aqueous external environment. This effect was also observed in previous chapters, owing to the different structures/orientations of the naphthalimide tags and what position they reside within the probe strand.

6.3.4. FISH Sensing Using the Naph 17CEN Oligo Probe

The Naph 17CEN probe is used in this experiment as a proof-of-concept study to demonstrate the ability of solvatochromic probes to enable the detection of single nucleobase variants during cellular imaging experiments. As mentioned earlier, the region of interest in the α -satellite regions at the centromere of chromosome 17 has two known variants, comprising of single nucleobase changes and is therefore ideal for studying these probes.

Fixed patient sample slides (patient samples from anonymised 46 XX/XY white blood cell suspensions) were kindly provided by Birmingham Women's NHS Foundation Trust. Slide sample density was checked using an optical microscope prior to use. The fixed patient slides contain interphase and metaphase cells. The presence of metaphases helps to confirm the specific binding of the Naph 17CEN probe to centromeres of chromosome 17.

A full experimental procedure for the FISH sensing is detailed in the Experimental 7.8.1. Typically, FISH protocols include the following steps: (i) denaturation of the fixed cell DNA, (ii) hybridisation of the probe to the region of interest within the fixed cell DNA, (iii) wash steps to remove any unbound probe. As mentioned earlier, standard FISH procedures use long hybridisation times (up to 16 h) due to the longer length of the probes that are typically employed. Here, much shorter oligo probes are used,

meaning that hybridisation times are successfully reduced to 15 min, as previously demonstrated by Dr A. Rushton.²¹ Reducing the hybridisation times is very beneficial for diagnostic testing as it can significantly improve the diagnosis wait times for patients. In addition to the hybridisation times, the composition of the hybridisation buffer may also be altered to accommodate for the use of the shorter oligo probes; this will be discussed later in the section.

6.3.4.1. FISH Sensing Using the TAMRA 17CEN Probe

As the behaviour of the naphthalimide molecules under the microscope and in cellular environments are not well understood, it was first decided to test the FISH protocol with a probe containing a known fluorophore.

An oligo probe labelled with a TAMRA fluorescent dye (ex/em, 555/580 nm) and consisting of 26 nucleobases was initially tested. The probe sequence targets the 17CEN region of interest and the probe sequence can be found in the Appendix 8.4.2. The oligo probe used for this test experiment was one designed by Dr A. Rushton.²¹ This TAMRA 17CEN probe was hybridised to the region of interest for 15 minutes at 37 °C using the method described in the Experimental 7.8.1. DAPI was used as a nuclear stain, a commonly used nuclear counterstain for fluorescence microscopy, flow cytometry, and chromosome staining. The sample was visualised using an epifluorescence microscope (RAMM system, Applied Scientific Instrumentation) equipped with a 100x objective lens (Nikon, 1.49/oil TIRF) and cooled EMCCD camera (Photometrics, Evolve[®] 512 Delta). Excitation lasers (Coherent, OBIS) at 405 nm for DAPI and 561 nm for TAMRA 17CEN probe were used. Figure 6.5 shows the visualisation of the TAMRA 17CEN probe by FISH on human interphase cells. The presence of two localised binding events within each nucleus suggests the selective binding of the TAMRA 17CEN probes to the centromeres of chromosome 17. The visualisation of the 17CEN probes by FISH on human metaphases may have given a stronger indication of selective binding; however, within the samples tested metaphases could not

be found. Nevertheless, the images in Figure 6.5 still show promise and indicate that the sample preparation and FISH protocol methods are effective.

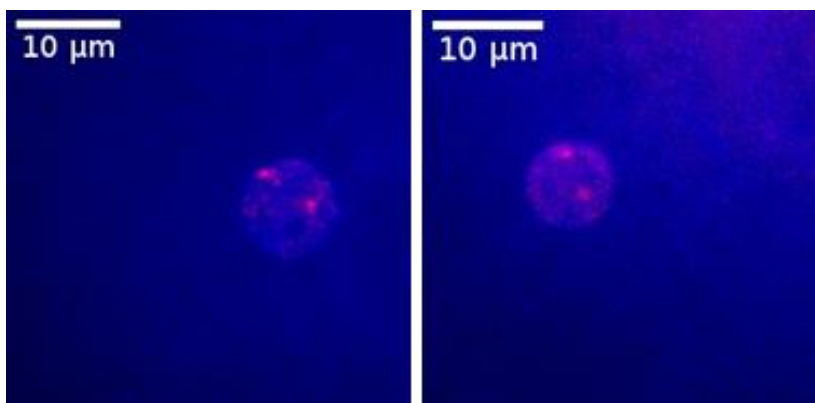


Figure 6.5: TAMRA 17CEN probe visualised by FISH on human interphases using DAPI nuclear stain. Two images showing nuclei from different surface areas within the same sample. ~75 ng of TAMRA 17CEN probe used.

With the correct sample preparation and FISH protocol in place, the Naph 17CEN probes were then investigated using FISH.

6.3.4.2. FISH Sensing Using the Naph 17CEN Probe

As above, the Naph 17CEN probes were hybridised to the region of interest for 15 minutes at 37 °C using the method described in the Experimental 7.8.1. Initially, DAPI was used as a nuclear counterstain, however, the excitation and emission wavelengths (ex/em, 358/461 nm) of this common nuclear stain lie too close to those of the naphthalimide fluorophore (ex/em, 449/524 nm), see Figure 6.6. The 405 nm excitation laser, used to excite DAPI, also excites the naphthalimide fluorophore and this crossover of excitation spectra results in images where the Naph 17CEN probes could not be visualised. As both DAPI and naphthalimide emit within a similar region, bandpass filters cannot be used to separate the emission of each dye. To resolve this, it was decided to use a nuclear stain with excitation and emission wavelengths shifted towards the red, GelRed® (Biotium). The excitation spectra of GelRed® is shown in Figure 6.6C and when using an excitation laser of 405 nm to excite the naphthalimide probes, the GelRed® dye should not be fully excited. Instead, the 561 nm laser was used

to excite GelRed[®]. Figure 6.7 shows images produced from FISH using the GelRed[®] nuclear stain. As observed before with the DAPI nuclear stain, the Naph 17CEN probe cannot be visualised. In this instance, the problem may arise from any minimal excitation of GelRed[®] that may occur at 405 nm. Owing to the higher density of the stain within the sample compared to the naphthalimide molecules, any minimal excitation of GelRed[®] may result in fluorescence emission that is stronger than that of the naphthalimide molecules and therefore swamp any localised signals resulting from the naphthalimide probes. Filters were used in an effort to separate the GelRed[®] emission from the naphthalimide emission; however, owing to the slight overlap in emission profiles of the two dyes, this was not successful. Finally, another long wavelength dye was tested, TOTO[™]-3. However, again, similar results were obtained where the Naph 17CEN probes were not visualised over the emission of the DNA intercalating dye. This is probably a result of the similar effect that occur when we stain using GelRed[®]. As the nuclear stains are present at higher density within the sample than the naphthalimide probes, the emission signals produced from these stains may be swamping the naphthalimide emission signal.

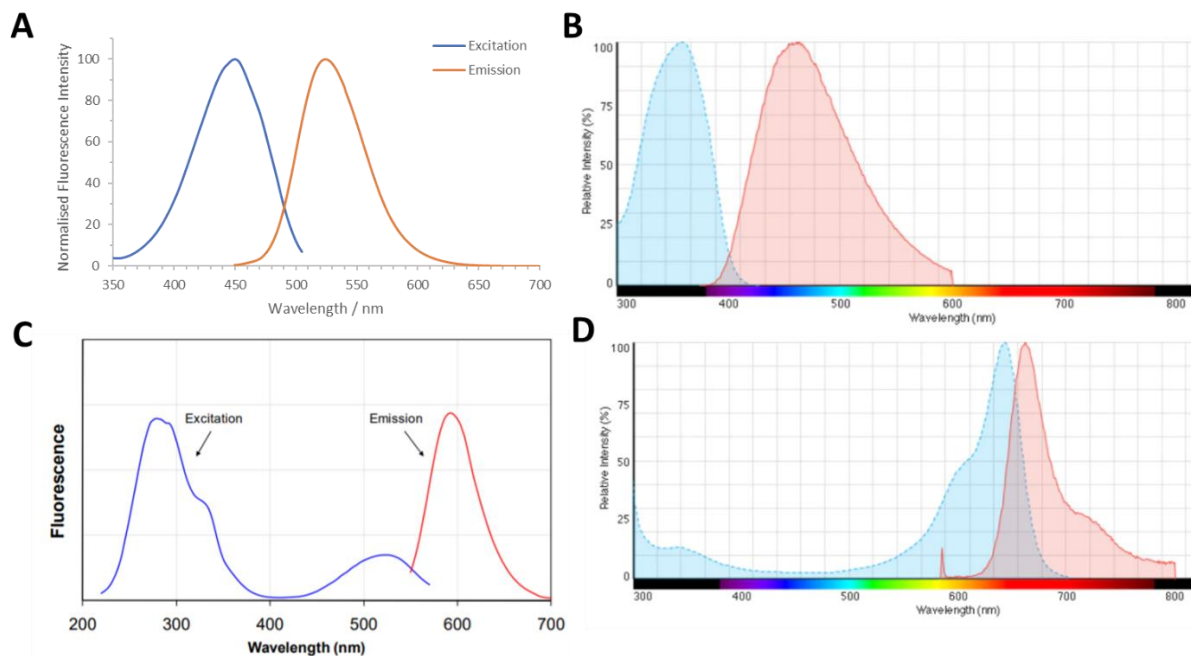


Figure 6.6: Excitation and emission spectra of (A) Naph 17CEN Probe, (B) Nuclear stain DAPI (image taken from ThermoFisher, <https://www.thermofisher.com/order/catalog/product/D1306#/D1306>), (C) Nuclear stain GelRed[®] (image taken from Biotium, <https://biotium.com/product/gelred-nucleic-acid-gel-stain/>), (D) Nuclear stain TOTO[™]-3 (image taken from ThermoFisher, <https://www.thermofisher.com/order/catalog/product/T3604#/T3604>).

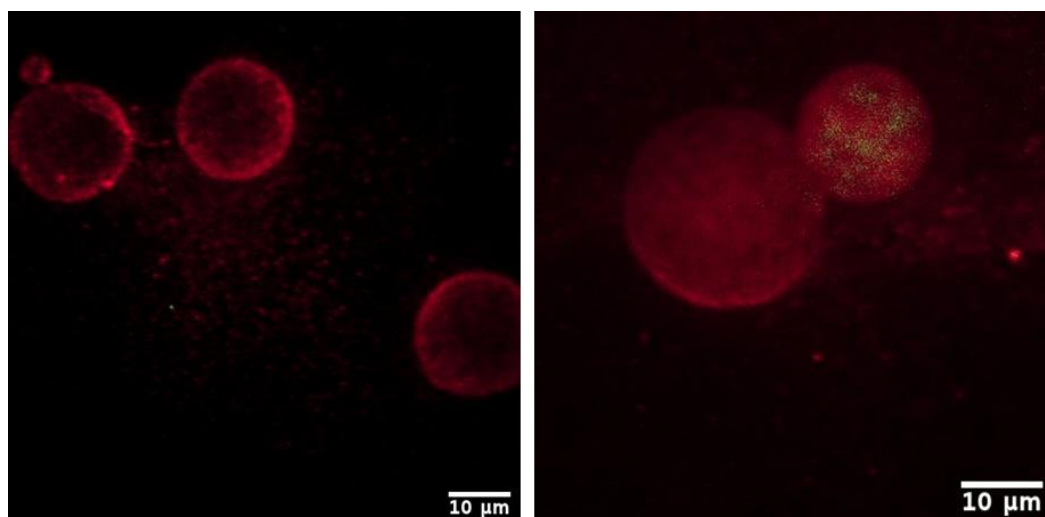


Figure 6.7: Images produced by FISH on human interphases using GelRed® nuclear stain. Two images showing different surface areas from different samples. ~75 ng Naph 17CEN probe.

Clearly, the use of a nuclear counterstain is problematic. The emission from the probe is too weak to overcome the emission of the nuclear stain, which is present at a much higher density across the sample. However, another possibility for the lack of Naph 17CEN probe visualisation by FISH may be attributed to an ineffective FISH protocol. The FISH protocol was altered to rule out that the problems with probe visualisation may have arisen from the FISH protocol.

It is possible that the wash steps are too long, resulting in the complete (or almost complete) removal of the hybridised Naph 17CEN probes within the sample. Owing to the shorter nature of the Naph 17CEN oligoFISH probes, longer wash times may be causing the denaturation of the bound probes. However, reducing the wash steps from 5 min to 2 min did not improve the visualisation of the probes by FISH. Alternatively, the amount of formamide in the hybridisation buffer may be altered to aid stronger binding. Different percentages of formamide were tested (30%, 40%, 50%, 60%, 70%, 80%); however, again, improvements in the images produced were not achieved and the Naph 17CEN probes were still not successfully visualised by FISH.

The above experiments along with the successful visualisation of the TAMRA oligoFISH probe using the same FISH protocol, confirm that the problems with naphthalimide probe visualisation are most likely

due to the weak emission of the naphthalimide probe. Additionally, the probe may not bind to the region of interest strongly enough/with enough specificity which may be a result of the naphthalimide modification disrupting the probe sequence and duplex stability. This is demonstrated by a reduction in thermal melting temperatures (T_m) of roughly 5 °C for the 17CEN D Naph^A_{Short} probe in comparison to the unmodified probe, Table 6.2. A longer probe sequence may improve the sensing capability of the naphthalimide probe, however, unfortunately work on this project had to conclude, owing to patient sample slide degradation, so further studies were not conducted.

6.4. The Development of Imaging Probes for DNA PAINT Super-Resolution Imaging Methods

6.4.1. Experimental Set-Up and Probe Design

The use of naphthalimide modified probes for super-resolution imaging is explored. In this section, research will not focus on base discrimination as in previous sections; instead the interesting fluorescent properties of one of the naphthalimide modifications discovered in Chapter 4 will be explored.

A major downside to DNA PAINT imaging methods is the difficulty in optimising the signal-to-noise ratio. Typically, small signal-to-noise ratios are observed because of the highly fluorescent nature of the unbound imaging probes in the imaging solution just outside of the TIRF imaging angle, Figure 6.3. The naphthalimide-modified imaging probes aim to increase this signal-to-noise ratio owing to their interesting fluorescent properties that were discovered in Chapter 4. The Naph^L_{Dimethyl} tag molecules display relatively low fluorescence when present in single-stranded probe form and upon binding of these probes to their complementary targets, the fluorescence intensity vastly increases. This effect is heightened when using the L Naph^L_{Dimethyl} isomer modification and hence is the chosen fluorescent tag for incorporation into the imager probe strands in this work. It is this phenomenon that is envisaged

to help reduce the background fluorescence ('noise') that is commonly observed with other common fluorescently labelled imager probes.

It is important to design imager probes of a specific length which enable transient binding between the imager probe strands and the docking strands. As mentioned earlier, the length of the imager strand can greatly influence the binding strength and the length of the binding interaction between the imager and docking strands. Typically, imager strand length is between 7-12 nucleobases long for DNA PAINT experiments. Predicted thermal melting temperatures obtained from the IDT oligo analyser tool gave a good indication as to the correct strand length for the particular sequences used in this research.²⁷ A duplex melting temperature of just under 25 °C should provide suitable conditions that promote this transient stochastic binding motion of imager and docking strands. As the disruption to duplex stability caused by the naphthalimide modification within the probe strand is unknown, it was decided to synthesise imager strands of varying lengths to test which of the strands will provide the best imaging conditions.

Initial experiments involved the design of a naphthalimide imager strand that was complementary to a biotinylated oligo sequence (IDT DNA, sequences shown in Table 6.3). Similarly to previous probe designs, the naphthalimide modification is present at the centre of the strand as a base substitution. The biotinylated docking strand will be bound to the coverslip surface using NeutrAvidin and biotinylated BSA as shown in Figure 6.8. Although this test experiment set-up does not produce super-resolution images of defined structures, this preliminary experiment allowed the study of the fluorescence properties of these short imager strands and the establishment of a flow chamber-like sample preparation set-up without wasting any of the limited DNA origami sample used in later experiments.

Table 6.3: Sequences of imager and docking strands used in preliminary DNA PAINT experiments. Complementary regions are highlighted in blue. The predicted melting temperatures were obtained from IDT oligo analyser, without the modification X taken into consideration; 0.1 μ M, 75 mM MgCl₂.²⁷

Strand name	Sequence 5'→3'	Predicted T _m (without modification, X) (°C)
Naph imager test	GATAXCTCG (where X = L Naph ¹ _{Dimethyl})	23.3
Biotinylated docking strand test	BiotinTEG-TTTTTGATCTCGCTTACGTCGAGCTATGG	-

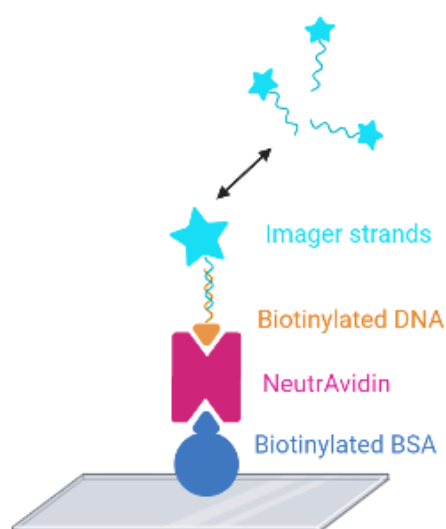


Figure 6.8: Schematic representation of the preliminary DNA PAINT imaging experiment attaching biotinylated docking strands to a coverslip surface via NeutrAvidin and biotinylated BSA. Transient binding of the imaging strands to docking strands produces bursts of fluorescence.

Following on, super-resolution imaging of a DNA origami triangle structure was attempted using DNA PAINT methods. The origami triangle design provides a structure with known nanoscale dimensions which can be easily designed/modified to incorporate docking strand sequences at specific and predictable sites within the triangle structure.

The DNA origami triangle was adapted from work by Rothemund *et al.* and prepared by another member of the Neely group.²⁸ The origami triangle was prepared by the folding of a long sequence of DNA using many short staple strands; the 7249 nucleotide long genome of the M13mp18

bacteriophage was used for this purpose. See Appendix 8.4.5 for staple strand sequences. The origami triangle was designed to incorporate 'loose end' or 'tail' DNA sequences which are not fully utilised in the origami folding design and therefore provide single-stranded DNA that is free for binding. In this work, two variants of 'loose end' DNA sequences were incorporated into the origami. One sequence is specific for the complementary binding of biotinylated DNA strands which were used to anchor the origami triangle to the surface. These anchoring strands contain poly-T sequences which bind to biotinylated complementary poly-A strands for the attachment to the surface using NeutrAvidin and biotinylated BSA. The other 'loose end' sequence is the docking strand sequence to which the imager probe strands transiently bind to produce the super-resolution image. Figure 6.9 demonstrates how the origami triangle is bound to the surface and how the imager strands bind to the docking strands on and off to produce 'bursts' of fluorescence. The origami triangle was programmed to incorporate docking strand sequences on each side of the triangle in the ratio 6:3:1, as shown in Figure 6.10. The naphthalimide-modified probe strands and docking strand sequences are shown in Table 6.4. As mentioned earlier, the imager strand length can alter the length of the binding interaction between the imager and docking strand and the thermal melting temperature gives an indication to a suitable length. Here two strand lengths are synthesised with a melting temperature of around 25 °C (however, the incorporation of the naphthalimide modification will affect this melting temperature slightly). The effect of the strand length on the quality of the super-resolution images produced will be discussed later.

Table 6.4: Sequences of the imager and docking strands used for DNA PAINT experiments using origami triangle structures. The predicted melting temperatures were obtained from IDT oligo analyser, without the modification X taken into consideration; 0.02 μ M, 75 mM MgCl₂.²⁷

Strand name	Sequence 5'→3'	Predicted T _m (without modification, X) (°C)
Naph imager -11	CTAGAXGTATA (where X = L Naph ¹ _{Dimethyl})	21.5
Naph imager -12	CTAGAXGTATAA (where X = L Naph ¹ _{Dimethyl})	26.6
Origami docking strand	(staple sequence)...TTTTTTTTTATACATCTA	-

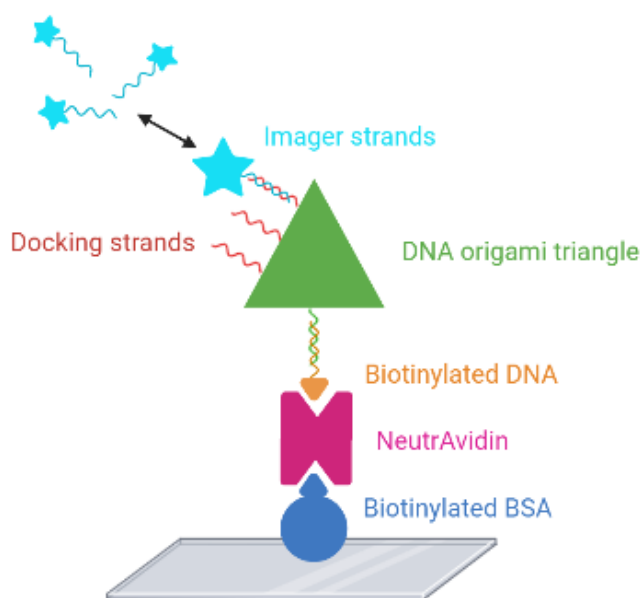


Figure 6.9: Schematic representation of DNA PAINT imaging experiment using an origami triangle attached to a coverslip surface via biotinylated DNA, NeutrAvidin and biotinylated BSA. Transient binding of the imaging strands to docking strands on the origami surface produces bursts of fluorescence.

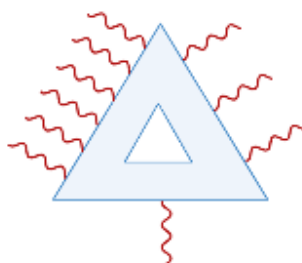


Figure 6.10: DNA origami triangle showing the docking strands (red) positioned on each side of the triangle structure in the ratio 6:3:1.

6.4.2. Imager Probe Strand Synthesis

The naphthalimide-modified imager strands mentioned above were synthesised using automated solid-phase DNA synthesis using ultramild conditions in a similar method to those mentioned in Chapter 3 (see Experimental 7.3). The imager strands were then purified using semi-preparative reverse phase HPLC using a Clarity Oligo column. 0.1 M triethylammonium acetate buffer was used with an increasing acetonitrile gradient from 5-18% acetonitrile over 25 minutes (see Experimental 7.4 for full method). The strands were characterised using mass spectrometry, for full characterisation data see Appendix 8.4.4.

6.4.3. Preliminary Duplex Studies to Test the Suitability of the Naphthalimide Imager Strands for DNA PAINT Imaging

To investigate the fluorescent properties of the naphthalimide imager strands and to determine the correct conditions for the DNA PAINT experiment, simple duplex fluorescence studies were conducted.

In aqueous solution, the Naph imager test strands (5' – GATAXCTCG – 3', Table 6.3) were annealed to their fully complementary targets (5' – CGAGCTATC – 3') and the fluorescence recorded. The addition of MgCl₂ to the aqueous solution drives the formation of duplex DNA. As previously stated, the binding of the imager probes to the complementary regions on the docking strands must occur transiently to produce super-resolution images and this binding event can be altered by varying the salt concentration. Increasing the Mg²⁺ concentration stabilises duplex formation by reducing the electrostatic repulsion between the negative phosphate backbones of the imager and docking DNA strands, resulting in more binding events/localisations per docking strand. Figure 6.11 shows the fluorescence emission spectra of the imager strand upon duplex formation with the fully complementary target and the effect of varying the concentration of MgCl₂ in solution. On first inspection, as hoped, the figure demonstrates a signal increase in naphthalimide-modified imager strand emission upon duplex formation. It also highlights the significance of altering the MgCl₂

concentration to aid duplex formation. The fluorescence intensity change observed between single-stranded and duplex forms is enhanced as MgCl_2 concentration is increased. For the Naph imager test strands, a salt concentration of 100 mM MgCl_2 was shown to produce optimal fluorescence signals. At this salt concentration, the duplex melting temperature was recorded at 24.0 °C which is in the expected range to promote transient stochastic binding between imager and docking strands at room temperature. However, the salt concentration used in later experiments is lowered slightly to account for the increase in imager strand length which results in higher thermal melting temperatures than the imager strands used in this example. IDT oligo analyser was used to adapt the salt concentrations for later experiments.²⁷

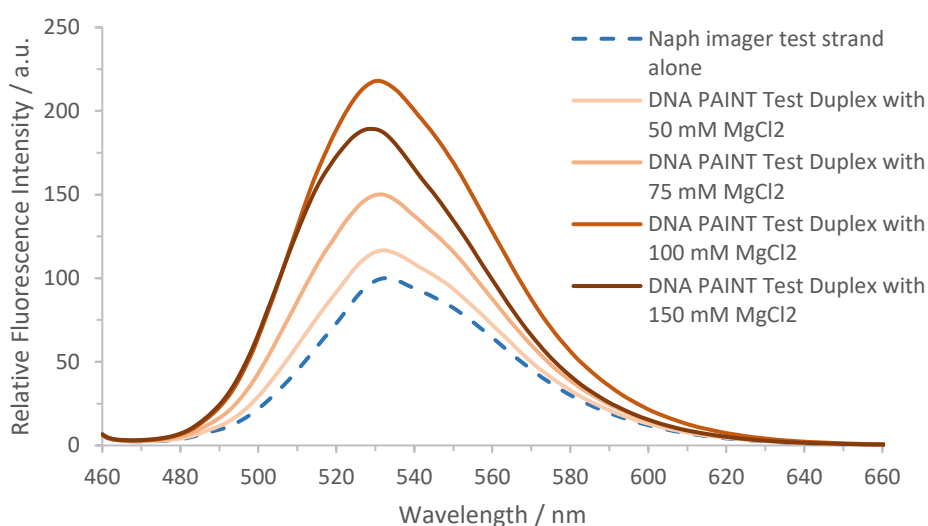


Figure 6.11: Relative fluorescence intensity of the Naph imager test strand upon duplex formation with its fully complementary target (5'-CGAGCTATC-3'). 0.5 μM imager strand: 0.5 μM target, aqueous solution of varying MgCl_2 concentration (50 mM, 75 mM, 100 mM, 150 mM). $\lambda_{\text{ex}} = 450 \text{ nm}$, 298 K.

Following on from the fluorescence studies on duplex oligo DNA, the test DNA PAINT set-up involving the attachment of biotinylated docking strands to the surface was employed. CoverWell™ perfusion chambers were attached to a borosilicate glass coverslip to allow for easy addition and removal of reagents. Traditionally, flow chambers are created for this purpose, however, from previous experience this method causes difficulties with wash steps and with the removal of reagents from the

flow chamber, especially when very low volumes are used such as in this instance. Biotinylated BSA was added to the CoverWell™ chamber and bound to the clean coverslip slide, followed by the binding of NeutrAvidin and the biotinylated docking test strand, sequence shown in Table 6.3. The Naph imager test strand in imaging solution was then finally added to the chamber. Incubation times and wash steps were included after addition of each reagent. See Experimental 7.8.2.2 for detailed protocol. The sample was then imaged using an epifluorescence microscope equipped with a 100x objective lens (Nikon, 1.49/oil TIRF) and cooled EMCCD camera (Photometrics, Evolve® 512 Delta). Excitation lasers (Coherent, OBIS) at 405 nm and 488 nm were used to find the sample imaging surface and to excite the Naph imager test strand in solution, respectively. At the imaging surface, the TIRF angle was adjusted to enhance the signal-to-noise ratio and the samples were imaged over a period of time to produce a video comprising of multiple frames.

A negative control sample was also imaged in which the imager solution contained a non-fluorescent imager strand (5' - CGA GCT ATC – 3'). The imager sequences were the same length and both samples were prepared in the same way and imaged under the same parameters so that they could be directly compared, making it easier to draw conclusions about the DNA PAINT images.

Typically, a large number of frames are recorded (≥ 8000) to produce high quality super-resolution images of defined structures. However, a relatively small number of frames (1000) were recorded during these initial experiments as no defined structures were present, only oligo DNA bound to a surface. Super-resolution images were processed using Igor Pro and the Localizer package. The Localizer software produces localisation plots in which fluorescent localisations from every frame throughout the course of the imaging experiment are mapped onto a single plot. This produces a scatter plot of all localisations and a bitmap image across all frames as demonstrated in Figure 6.12.

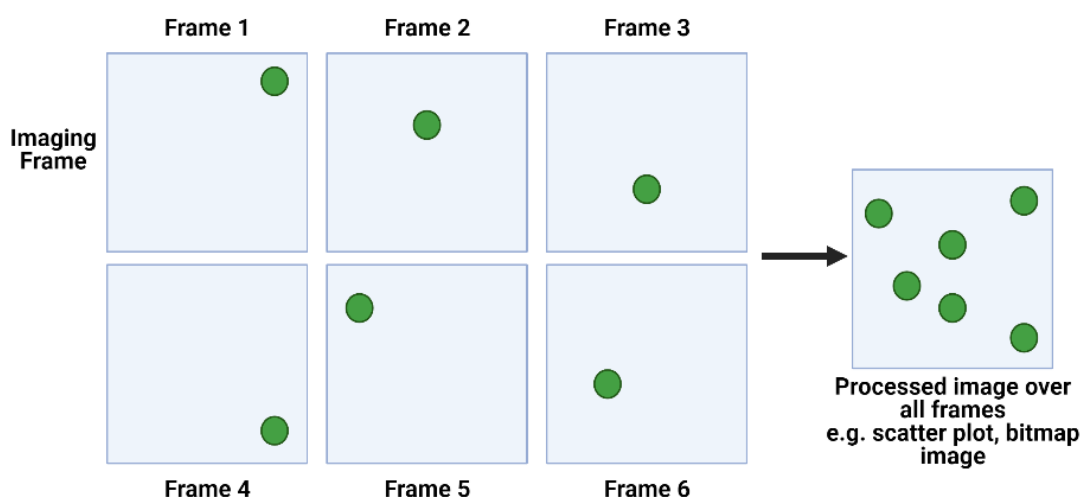


Figure 6.12: Schematic diagram showing the generation of scatter plots and bitmap images. Each imaging frame over different time points is superimposed to generate the overall image.

The experiment described above is simple in design and allows for a straightforward assessment of probe binding to DNA strands immobilised on a surface, relative to a control experiment. Using this approach, the probe specificity and binding kinetics are investigated. These initial experiments show promise. Upon comparing the images produced from the negative control sample to the sample containing the Naph imager test strand, an increased number of localisations are observed in the sample containing the fluorescent naphthalimide imager strand, Table 6.5. In addition, the scatter plots, Figure 6.13, showing the localisation density demonstrate that more localisation clusters are formed in samples containing the Naph imager test strands. The negative control samples show localisations at a more random distribution within the sample (i.e. lacking cluster formation). These are promising observations and although defined structures were not imaged, the increase in number of localisations implies that probe binding/dissociation is occurring within the sample. Introducing a defined structure to which the imager strands bind help confirm that the localisations observed are definitely caused by a binding event between imager and docking strands. Thus, DNA origami triangles were incorporated into the DNA PAINT design set-up.

Table 6.5: Total number of localisations calculated over 1000 frames for each sample used in DNA PAINT test experiments. 20 nM imager strand, 75 mM MgCl₂, imaging buffer.

Sample	Total Number of Localisations
Negative control	5401
Naph imager test strands	13572

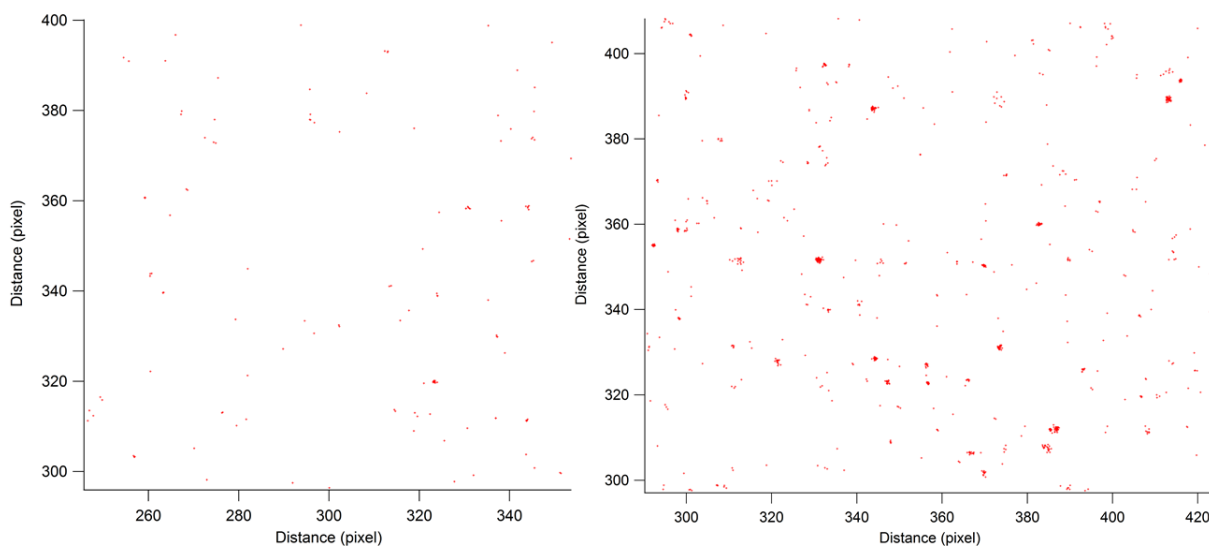


Figure 6.13: Scatter plots showing localisation density of DNA PAINT test experiments with negative control (left) and Naph imager test strands (right). Scatter plots generated from 1000 frames. 20 nM imager strand, 75 mM MgCl₂, imaging buffer.

6.4.4. DNA PAINT Imaging Using Naphthalimide Imager Strands to Produce Super-Resolution Images of DNA Origami Triangles

A DNA origami triangle, based on a published design was used for these experiments.²⁸ Staple strands were used to fold the M13mp18 bacteriophage genome (staple strand sequences are listed in Appendix 8.4.5) into the desired structure. The successful synthesis of the origami triangle was shown by the AFM images in Figure 6.14 (courtesy of W. Vanderlinden, J. Lipfert, LMU Munich) and shows each structure to have dimensions of roughly 100 nm.

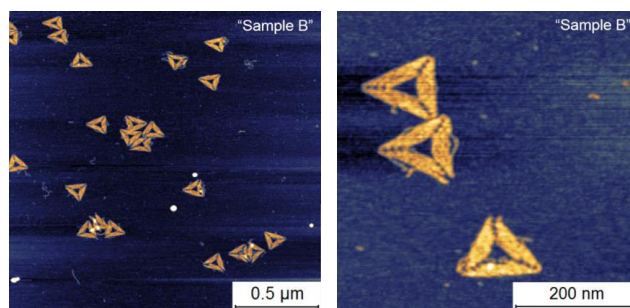


Figure 6.14: AFM images of DNA origami triangle. Images show the successful synthesis of the adapted Rothemund's origami triangle with diameter of roughly 100 nm. Images courtesy of W. Vanderlinden and J. Lipfert, LMU Munich.

Prior to assembly of the imaging chamber, the origami triangle was annealed to biotinylated poly-A strands. As mentioned earlier, the origami triangle structure was designed to contain poly-T loose ends which enable the anchoring of the triangle structure to a surface *via* binding to the biotinylated poly-A strands.

The sample was prepared as before on a borosilicate glass coverslip using CoverWell™ perfusion chambers to allow for the addition and removal of reagents. The following reagents were sequentially added to the chamber; biotinylated BSA, NeutrAvidin, followed by the origami triangle with the biotinylated DNA strands pre-annealed. The imaging solution, containing the imager probe is finally added to the chamber (see Experimental 7.8.2.3 for detailed protocol).

Control experiments were also prepared in a similar way. A negative control sample was prepared in which the imaging solution contained a non-fluorescent imager strand. This negative control should therefore not produce any specific fluorescent signals and any fluorescence observed will be background fluorescence ('noise') produced from fluorescent species within the sample. In contrast, the positive control sample contains an ATTO 488-labelled imager strand within the imaging solution. This positive control experiment helped to confirm that any localisations observed with the Naph imager strands are due to the specific binding of the imager strands to docking strands on the origami triangle. In addition, the positive control experiment was also used to directly compare and investigate the signal-to-noise ratio produced by the two samples. It was hypothesised that the Naph imager

strands will exhibit enhanced signal-to-noise ratios and higher quality super-resolution images, a result of their fluorogenic response to the transient DNA duplex formation. DNA imager strands labelled with an ATTO 488 dye were chosen for the positive control because of their similar excitation and emission profiles to that of the naphthalimide fluorophores used in this work.

The prepared samples were imaged using an epifluorescence microscope equipped with a 100x objective lens (Nikon, 1.49/oil TIRF) and cooled EMCCD camera (Photometrics, Evolve® 512 Delta). Excitation lasers (Coherent, OBIS) at 405 nm and 488 nm were used to find the sample imaging surface and to excite the Naph imager strand and ATTO 488 control imaging strand, respectively. The TIRF angle was modified to optimise the signal-to-noise ratio and reduce the background fluorescence from any unbound fluorescent imaging strands in the imaging solution close to the TIRF angle. Up to 8000 sequential imaging frames were recorded.

The two variants of the Naph imager strands differ in length by one nucleobase; with Naph imager -11 having 11 nucleobases and Naph imager -12 having 12 nucleobases (including the naphthalimide nucleoside analogue, Table 6.4). This difference of one nucleobase, an A-T base pair, will affect the stability of the duplex formed between the imager strands and docking strand and the more stable the duplex, the more localisations are observed per target. However, if the duplex formed is too stable then the imager strand will remain bound to the docking strand and the transient stochastic binding motion required for super-resolution imaging will not occur.

Samples containing Naph imager -12 strands have an increased number of localisations compared to samples containing Naph -11 strands, as shown in Table 6.6. Comparing the scatter plots generated from the two samples, Figure 6.15, the localisation density between samples can be compared. It is observed from the scatter plots in Figure 6.15 that more localisation clusters are formed in samples containing the longer imaging strand, Naph imager -12, compared to the sample containing Naph imager -11 strands. Thus, implying that the longer imager strands form more stable duplexes which

results in more localisations per target, however, they do not form such a stable duplex that the strands do not dissociate back into the imaging solution.

Table 6.6: Total number of localisations calculated over 3000 frames for each sample used in the DNA PAINT origami experiments. 20 mM imager strand concentration, 75 mM MgCl₂, imaging buffer.

Sample	Total Number of Localisations	Localisation Error; X,Y (nm)
Naph imager -11	4022	40, 40
Naph imager -12	18790	38, 38

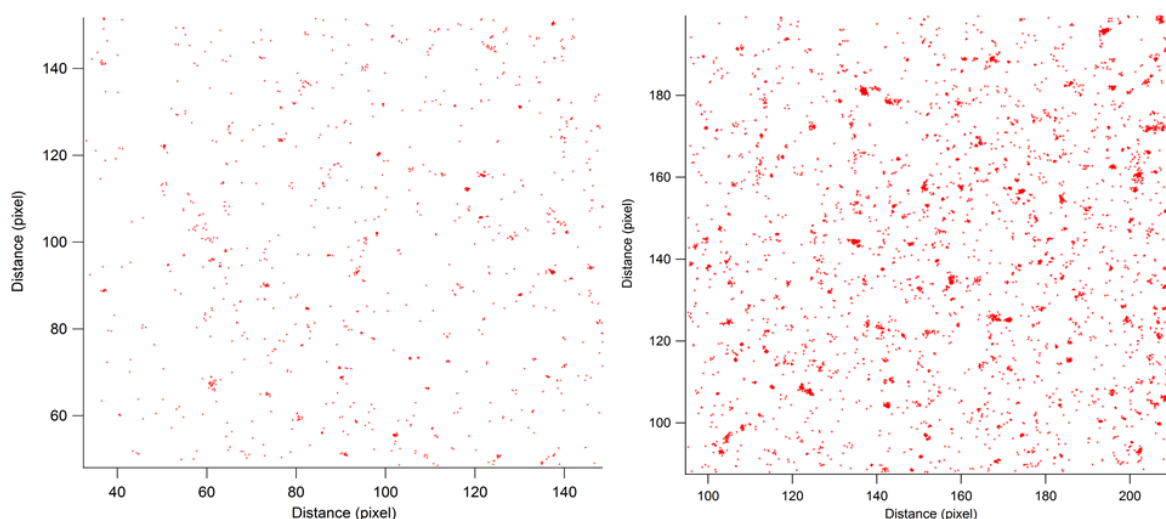


Figure 6.15: Scatter plots showing the localisation density within the sample containing Naph imager -11 strands (left) and Naph imager -12 strands (right). Scatter plots generated from 3000 frames, 20 mM imager strand concentration, 75 mM MgCl₂, imaging buffer.

Bitmap images were generated by displaying the localised emitters with a 2D Gaussian-shaped model of the emitter's point spread function (PSF) with a width of 0.05 CCD pixels (8 nm) and then combining all localisations within every frame over the imaging experiment. The bitmap images generated show that the localisation clusters have shape and size that resemble that of the DNA origami, Figure 6.16. The AFM images above, show the size of the origami triangle to have a size of approximately 100 nm across which correlates with the sizes of the structures shown in Figure 6.16 (considering any localisation error, 30-40 nm, Table 6.6). The object in Figure 6.17 shows particular promise, the bitmap

image shows localisations which correspond to the position of the docking strands incorporated into the DNA origami triangle. A high density of localisations is present along one side of the object which likely corresponds to the side of the triangle containing 6 docking strands (10 – 15 nm apart). The other sides of the object contain fewer localisations, corresponding to the remaining sides of the origami triangle containing 3 and 1 docking strands.

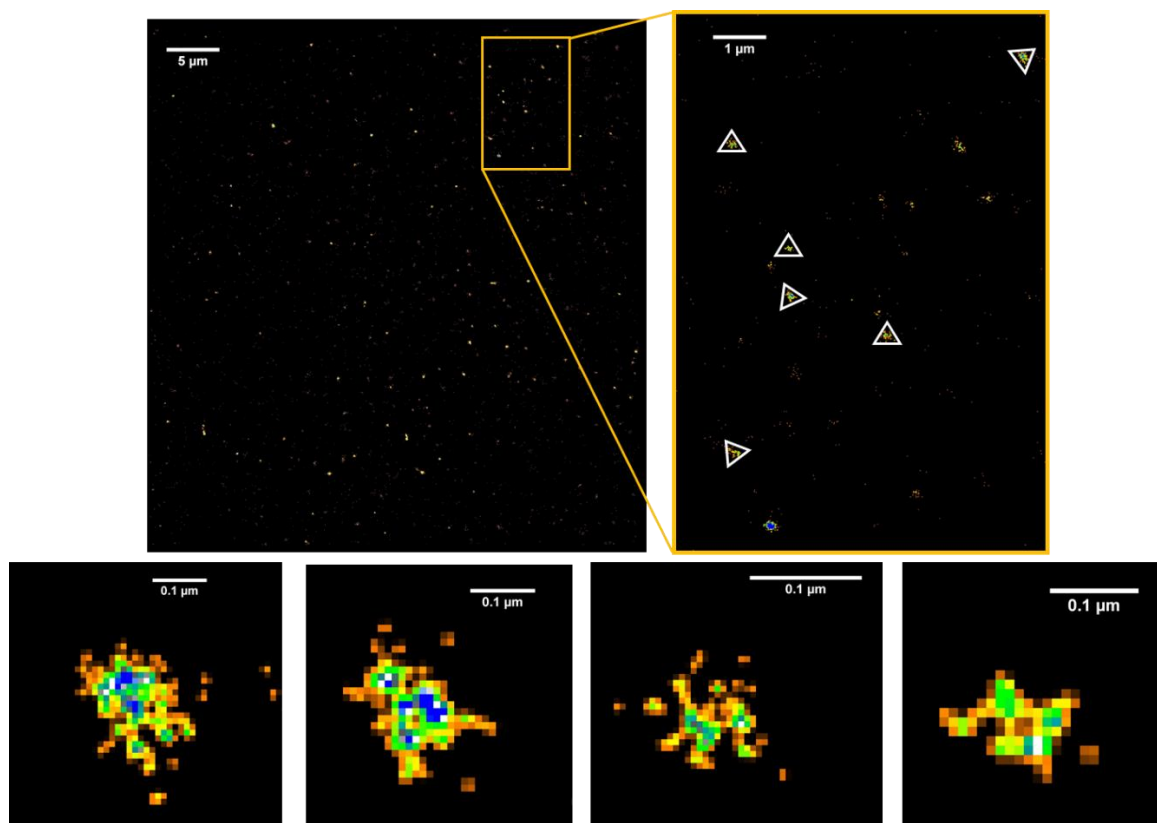


Figure 6.16: Bitmap image generated of samples containing the origami triangle and Naph imager -12 strands. A magnified section of the image in the insert shows highlighted clusters which are assumed to be the origami structures. Each of these structures is magnified further to highlight the shape and size, which corresponds to the origami structure. Image produced from 8000 frames, 60 ms exposure, excitation laser 488 nm. 20 mM imager strand concentration, 75 mM MgCl₂, imaging buffer.

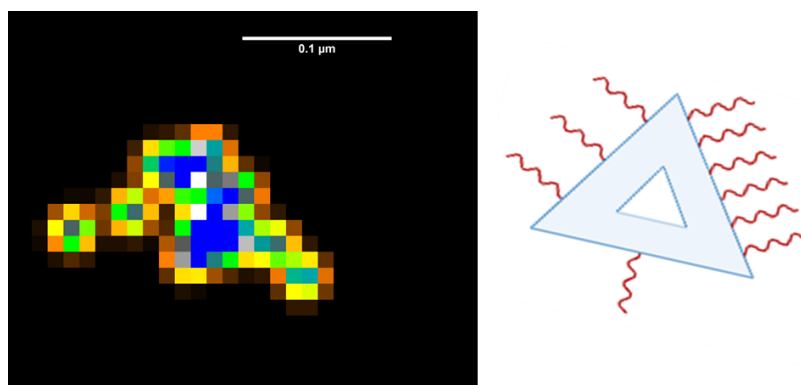


Figure 6.17: Magnified bitmap image of one cluster of localisations of a sample containing the Naph imager -12 strand (left) and the design of the DNA origami triangle (right) showing the probable orientation of the triangle in the image based on the density of the localisations observed in the bitmap image. Image produced from 8000 frames, 60 ms exposure, excitation laser 488 nm. 20 mM imager strand concentration, 75 mM MgCl₂, imaging buffer.

For confirmation of successful PAINt imaging, the data produced from samples containing the Naph imager -12 strands were compared with the data produced from the positive and negative control samples. Table 6.7 shows the total number of localisations present across the 8000 frames collected during the experiment for each sample.

Table 6.7: Total number of localisations calculated over 8000 frames for each sample used in the DNA PAINt origami experiments. 20 nM imager strand concentration, 75 mM MgCl₂, imaging buffer.

Sample	Total Number of Localisations	Localisation Error; X,Y (nm)
Negative control Unmodified imager strands	3522	59, 59
Naph imager -12 strands	11992	40, 40
Positive control ATTO 488 imager strands	105522	43, 43

The negative control sample contains the fewest localisations, Table 6.7. The scatter plot of localisation density, Figure 6.18 (top left), also implies the absence of probe binding/dissociation within this sample, with localisations randomly distributed and the reduced numbers of localisation cluster formed. Any localisation clusters observed are probably caused by artifacts/contaminants on the surface or in the imaging solution.

The positive control samples have a large total number of localisations across all frames as shown in Table 6.7, and a high density of localisations producing clusters as shown the scatter plots, Figure 6.18 (bottom left and bottom right). Figure 6.18 includes two scatter plots of the positive control sample containing ATTO 488 imager strands. The scatter plots are generated from the same sample but analysed using slightly different parameters. The scatter plot shown Figure 6.18 (bottom left) was generated using identical parameters to the negative control sample and the samples containing the Naph imager -12 strands for direct comparison (with GLRT insensitivity of 25). This plot shows that the parameters used for samples containing the naphthalimide imager strands are not well suited to those containing the ATTO 488 imaging strands as the parameters used are mostly fitting 'noise' in this example. The ATTO 488 dye is much brighter and as a result background fluorescence is increased, meaning that the GLRT threshold needs to be adjusted to account for this (GLRT insensitivity raised to 35). This adjusted scatter plot (bottom right, Figure 6.18) reveals localisation clusters across the sample, again implying probe binding and dissociation is occurring.

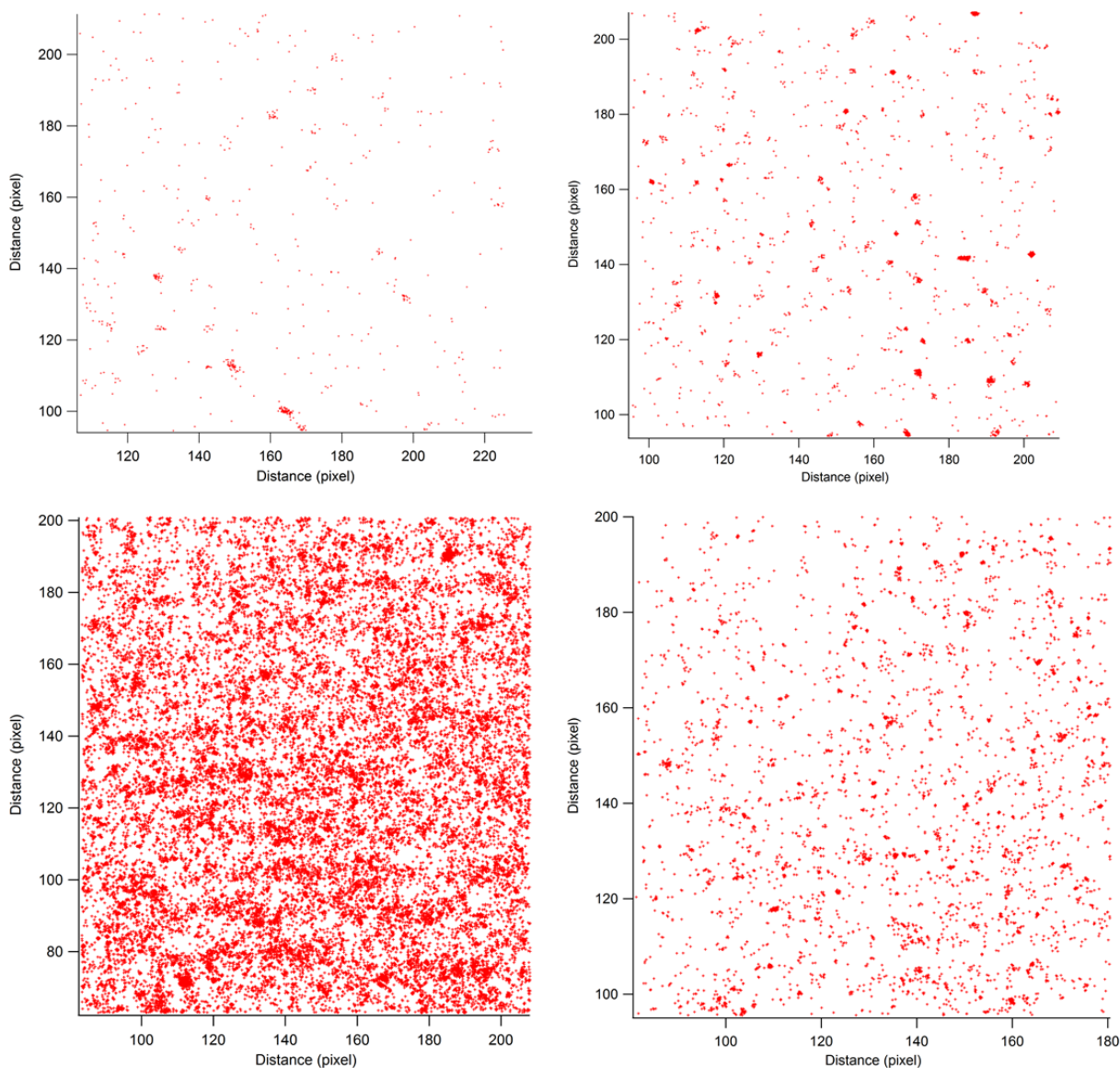


Figure 6.18: Scatter plots showing localisation density within samples containing; negative control unmodified imager strands (top left), Naph imager -12 strands (top right), positive control ATTO 488 imager strands (bottom left). This data was analysed using the same parameters (GLRT insensitivity of 25) to allow for direct comparison, however, the plot showing the ATTO 488 imager strands (bottom left) appears to be fitting noise and so the analysis parameters were adjusted (GLRT sensitivity of 35) as appropriate for this brighter dye to produce a more representative scatter plot for this sample (bottom right). All samples contain 20 nM imager strand, 75 mM MgCl₂, imaging buffer. Scatter plots produced from 8000 frames, 60 ms exposure, excitation laser 488 nm.

Furthermore, the positive control sample contains higher background fluorescence when compared to the sample containing Naph imager -12 strands, an observation that demonstrates the advantage of using the naphthalimide imager strands to increase the signal-to-noise ratio. To compare the background fluorescence of the two samples, the intensity of emission was taken across a set distance within an imaging frame. This set distance was a straight line drawn through a region of an imaging

frame, including background regions and a single emitter region. Several different areas, frames and emitters were selected to give a good representation of the whole sample. Figure 6.19 and Figure 6.20 show the emission plots which measure the intensity of the background vs the single emitters for the samples containing Naph imager -12 strands and ATTO 488 strands, respectively. Upon inspection of Figure 6.19 and Figure 6.20, samples containing ATTO 488 have a significantly higher background fluorescence to those containing Naph imager -12 strands, with background emission intensity of roughly 5000 compared to 2500, respectively. The ATTO 488 strands are highly fluorescent even when present as an unbound imager strand in the imaging solution. The highly fluorescent nature causes fluorescence of the imaging solution close to the surface and may be detected within the TIRF imaging angle which results in the increased background emission observed. However, the increase of background emission intensity for the ATTO 488 strands is offset by the increase in signal intensity for a single emitter, with ATTO 488 emitters showing intensities of around 7500 counts, compared to naphthalimide emitters which have emission intensities of 4000 counts. Despite this, the signal-to-noise ratios calculated for the Naph imager -12 sample is slightly increased (average S/N of 1.6) compared to the ATTO 488 sample (average S/N of 1.5).

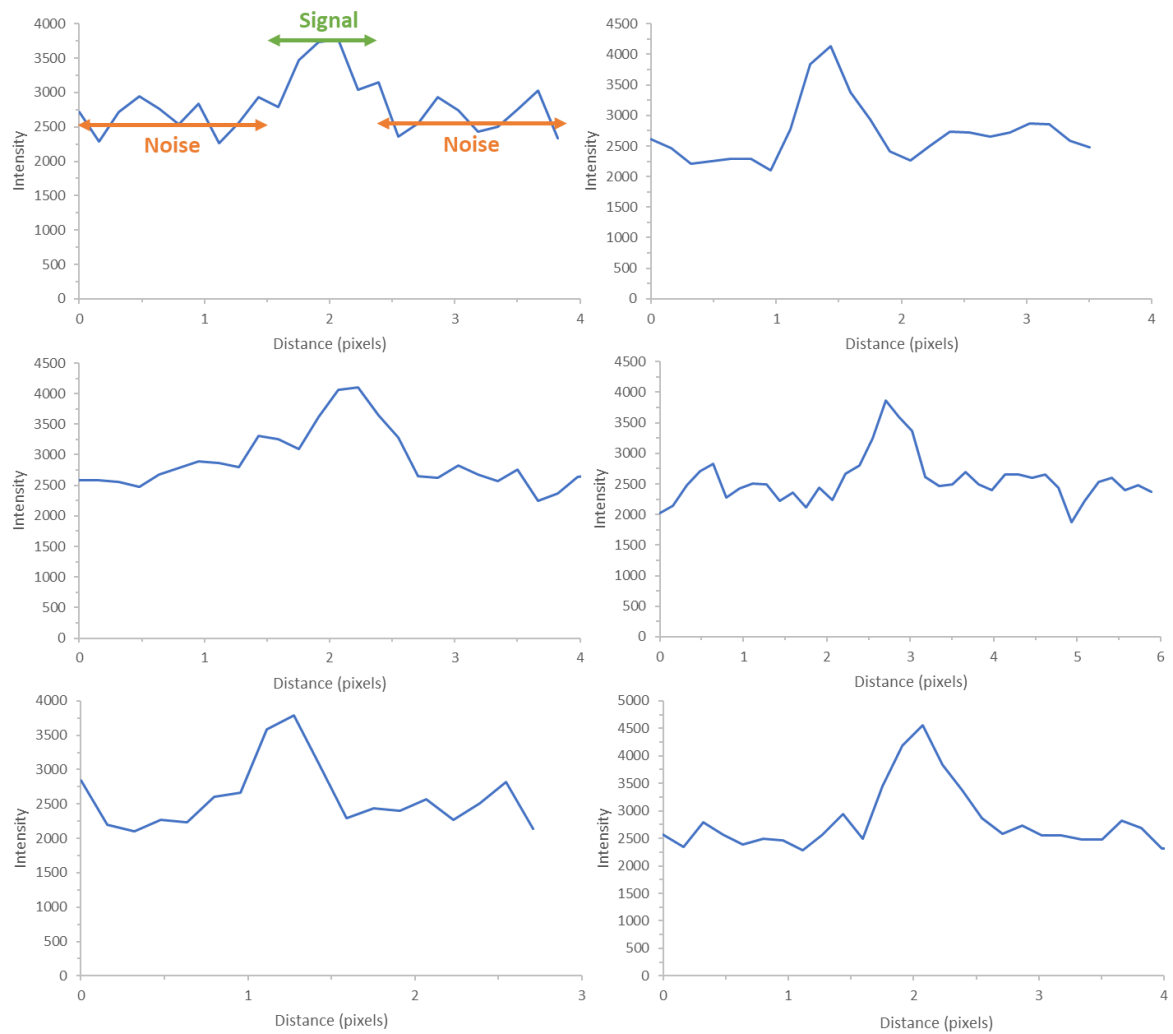


Figure 6.19: Intensity plots across set distances with a sample containing Naph imager -12 strands to measure the intensity of the background (noise) vs the signal of single emitters. Showing six different single emitters from six different imaging frames within the same sample. 20 nM Naph imager -12 strand concentration, 75 mM MgCl₂, imaging buffer.

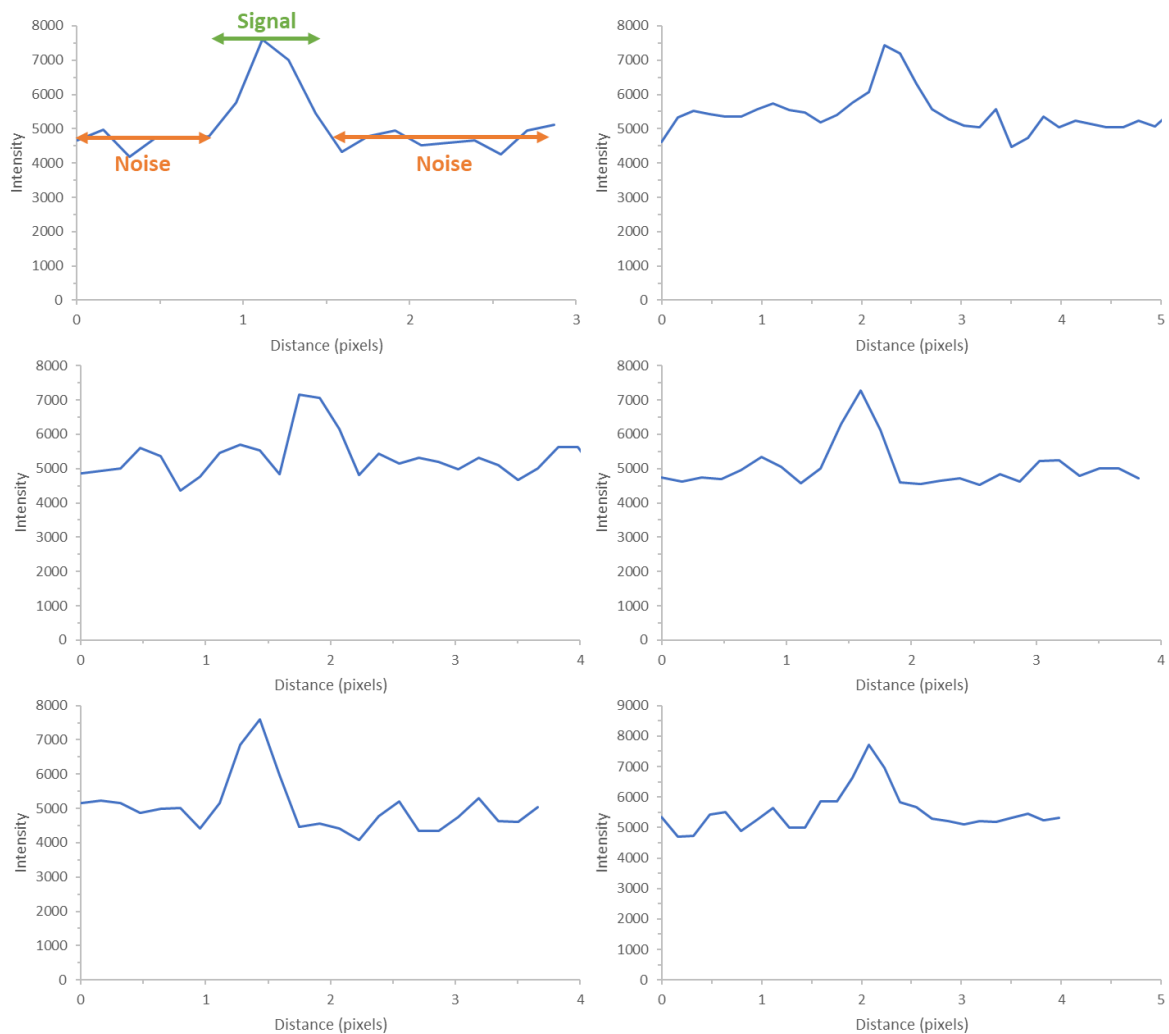


Figure 6.20: Intensity plots across set distances with samples containing ATTO 488 strands to measure the intensity of the background (noise) vs the signal of single emitters. Showing six different single emitters from six different imaging frames within the same sample. 20 nM ATTO 488 imager strand concentration, 75 mM MgCl₂, imaging buffer.

The scatter plots produced from samples containing the Naph imager -12 strands, Figure 6.18, show several clusters of localisations in the field of view. However, it would be expected to observe a comparable cluster density to the sample containing the ATTO 488 imager strands, see Figure 6.18, as both samples were prepared in the same way. The naphthalimide molecules are not as bright as the ATTO 488 dye (molar absorptivity values of roughly 90000 for the ATTO dye compared to 8000 for naphthalimides). In addition, the incorporation of the naphthalimide tags into the Naph imager strands may be resulting in lower binding affinity between the imager strand and docking strands. A

combination of these two factors may be resulting in the reduced localisations that are observed. In an attempt to overcome these factors, the concentration of the Naph imager -12 strands in the imaging solution was increased. Increasing the imager strand concentration was assumed to increase the number of collisions between imager strand and docking strands and hopefully increase the number of localisations observed in the super-resolution image. Various imager strand concentrations were employed (20 nM, 50 nM, 100 nM) to see if any trends emerged upon increasing the concentration. Increasing the concentration shows the opposite effect of what was expected, Table 6.8. This is a result of increased background fluorescence at these higher concentrations, as shown by the emission plots of samples at these higher concentrations. Figure 6.21 and Figure 6.22 show the emission intensity plots of samples containing 50 nM and 100 nM imager strand respectively, see Figure 6.19 for 20 nM. The emission plots demonstrate the lower signal-to-noise ratios for the samples containing higher concentrations of imager strand. The average signal-to-noise ratio is 1.6 for samples containing 20 nM imager strand (as stated earlier), 1.43 for samples containing 50 nM imager strand and 1.40 for samples containing 100 nM imager strand. The increase of background signals at these higher concentrations may overpower or mask any low emitting signals residing from samples containing the Naph imager strands. These low emitting signals are therefore not detected when the background fluorescence is increased above a certain threshold. It was concluded that 20 nM Naph imager -12 strand concentration produces best the super-resolution images.

Table 6.8: Total number of localisations calculated over 8000 frames for samples containing various concentrations of Naph imager -12 strands in DNA PAINT experiments. 20, 50 and 100 nM imager strand concentration, 75 mM MgCl₂, imaging buffer.

Sample	Total number of localisations
20 nM Naph imager -12	11992
50 nM Naph imager -12	10441
100 nM Naph imager -12	9242

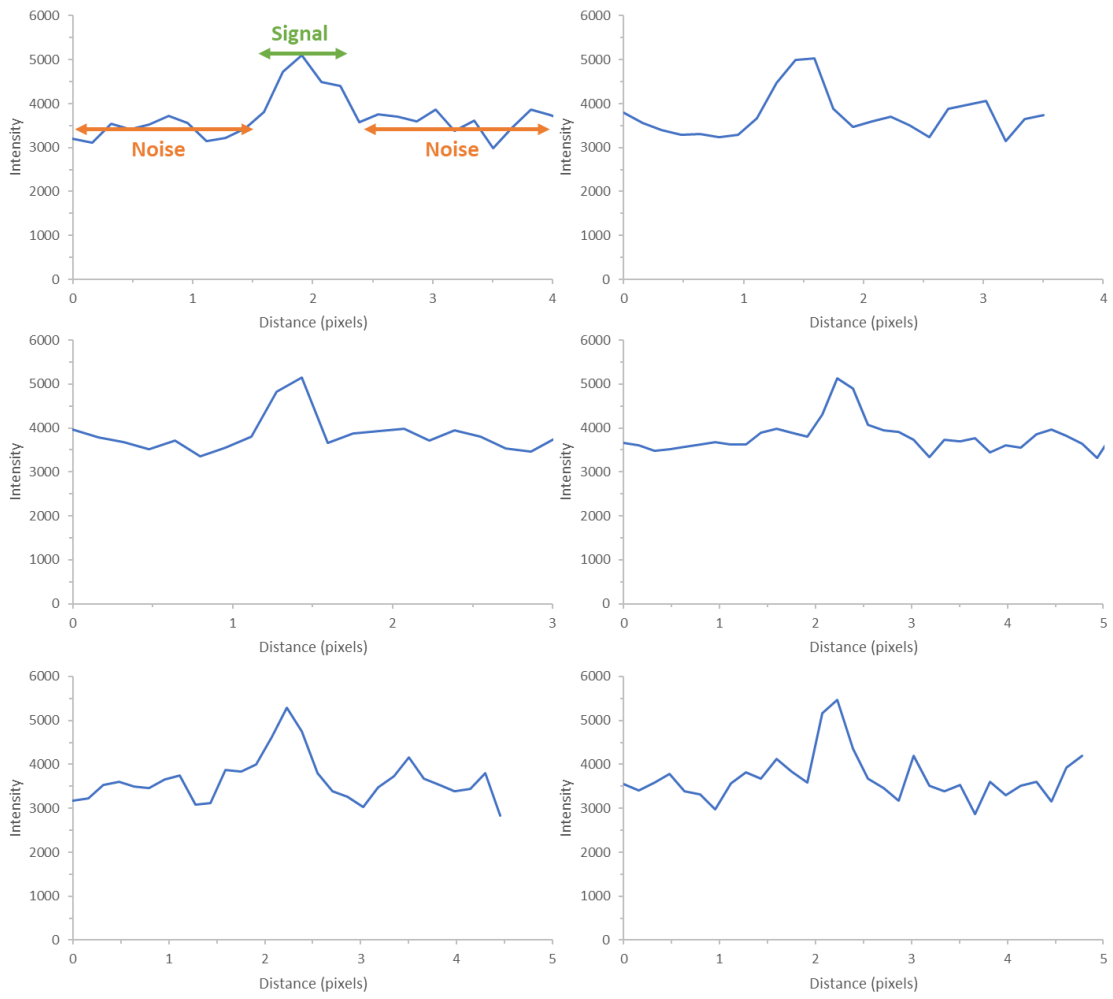


Figure 6.21: Intensity plots across set distances with samples containing 50 nM Naph -12 imaging strand to measure the intensity of the background (noise) vs the signal of single emitters. Showing six different single emitters from six different imaging frames within the same sample. 50 nM Naph imager -12 strand concentration, 75 mM MgCl₂, imaging buffer.

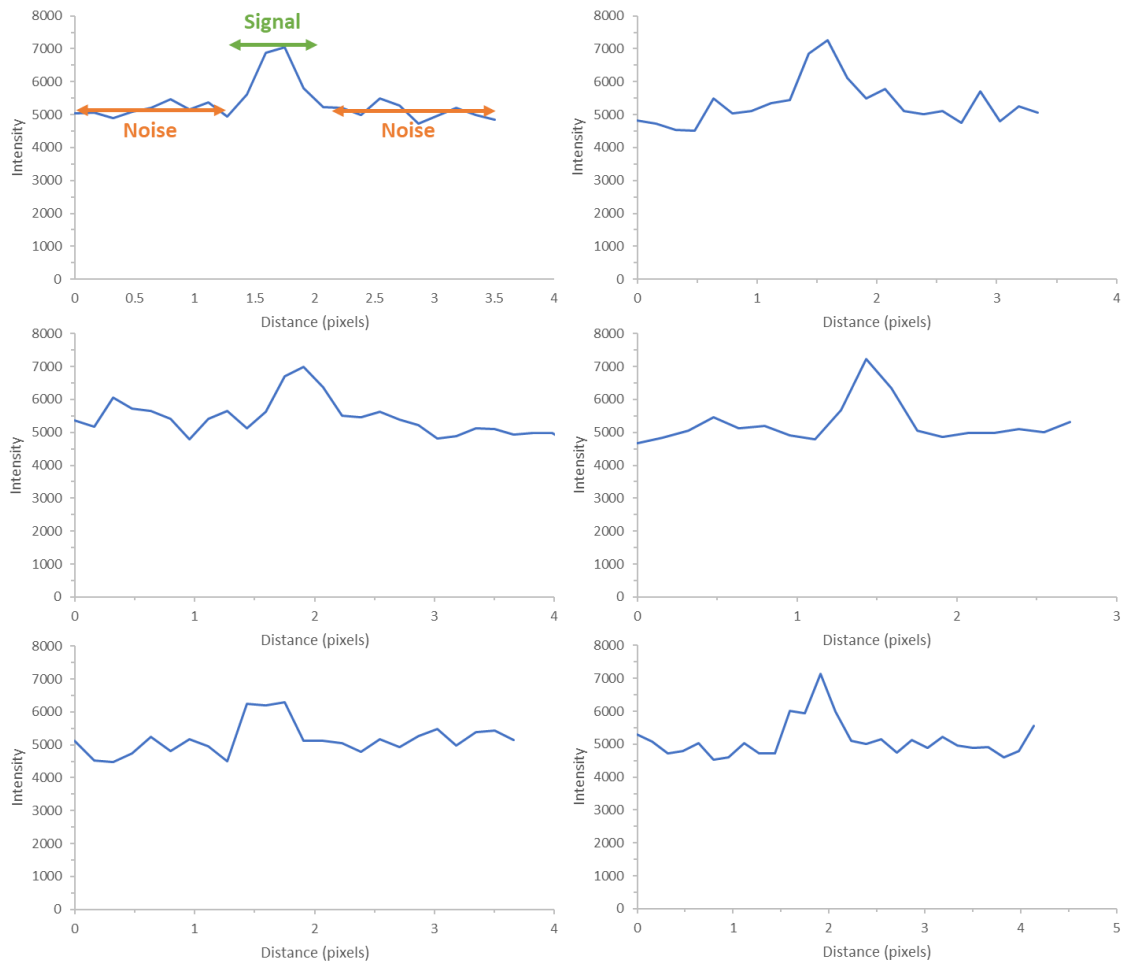


Figure 6.22: Intensity plots across set distances with samples containing 100 nM Naph -12 imaging strand to measure the intensity of the background (noise) vs the signal of single emitters. Showing six different single emitters from six different imaging frames within the same sample. 100 nM Naph imager -12 strand concentration, 75 mM MgCl₂, imaging buffer.

6.5. Conclusions and Future Work

It has been shown that naphthalimide-modified DNA probes can be adopted for more complex sensing environments such as the imaging experiments described in this chapter.

Firstly, the Naph 17CEN probes were successfully synthesised and duplex studies demonstrated the ability of these probes to discriminate between two target variants which differ in sequence by a single nucleobase. Upon binding of the probes to each target variant (17CEN target variant 1 and 2), a shift in the probe fluorescence emission profile is observed and provides a way of sensing between the two. One naphthalimide probe in particular provided a significant spectral shift between the two target variants of 6 nm. However, problems arose when using these probes in a cellular environment. Unfortunately, it was not possible to visualise the naphthalimide probes by FISH. This is most likely attributed to the use of nuclear counterstain and weakly emitting naphthalimide probe (compared to commercially available dyes such as TAMRA), and the weaker binding of the naphthalimide probe to the region of interest.

One way of overcoming these problems could be to omit a nuclear counterstain from the protocol and instead use brightfield imaging and a telomeric probe (using a dye of higher wavelength) to aid naphthalimide probe visualisation and confirm the selective binding of the naphthalimide probes to the region of interest. Omitting the highly fluorescent nuclear counterstain from the protocol, will hopefully remove the higher density of fluorescent signals observed in the nuclear region, which may have been masking the lower density fluorescent signals of the naphthalimide probes. The length of the probe sequence could also be increased to aid the formation of more stable duplexes. Future work would involve the continuing working on probe visualisation by FISH and if proven successful, coupling FISH methods with spectral imaging to discriminate between the target variants.

DNA PAINT imaging using naphthalimide-modified imager strands proved more successful, with the seemingly effective binding of imager probes to docking strands on DNA origami structures to produce super-resolution images containing structures that resemble the origami triangle shape and size.

Docking sites were incorporated into a DNA origami triangle to which complementary naphthalimide imager strands could bind. The data produced showed localisations which resembles the specific positioning of these docking strands within the origami triangle. The effect of changing the imager strand length and other experimental conditions such as imager strand and salt concentration were also explored. A longer imager strand length (12 nucleobases) produced images containing a higher number of localisations owing to the increased binding affinity between the imager and docking strands. The positive and negative control samples also aided the conclusion that the structures observed in the images are most probably due to the specific binding of the imager strands to docking strands on the origami triangle structures.

It was also shown, that the naphthalimide probes successfully reduce the background fluorescence within the samples, as hoped. This is a major advantage for super-resolution imaging techniques and increases localisation precision and the quality of images produced.

Future work would involve tweaking the design of the DNA PAINT imaging experiment to improve the binding kinetics (i.e. increasing the probe strand length). This would hopefully lead to the visualisation of increased number of localisations within samples containing Naph imager strands. Following on from this, the use of the naphthalimide probes in a well-defined biological target can be explored, such as the imaging of antibodies to investigate cellular activity.

6.6. References

1. R. Bishop, *Bioscience Horizons*, 2010, **2**, 85.
2. G. T. Rudkin and B. D. Stollar, *Nature*, 1977, **265**, 472.
3. B. J. Trask, *Nat Rev Genet*, 2002, **3**, 769.
4. T. Liehr, H. Starke, A. Weise, H. Lehrer and U. Claussen, *Histol. Histopathol.* , 2004, **19**, 229.
5. D. L. Grady, R. L. Ratliff, D. L. Robinson, E. C. McCanlies, J. Meyne and R. K. Moyzis, *Proc. Natl. Acad. Sci. U.S.A.*, 1992, **89**, 1695.
6. J. S. Waye and H. F. Willard, *Mol Cell Biol*, 1986, **6**, 3156.
7. A. Baumgartner, J. F. Weier and H. U. G. Weier, *J. Histochem. Cytochem.*, 2006, **54**, 1363.
8. C. L. O'Keefe and A. G. Matera, *Genome Res.*, 2000, **10**, 1342.
9. C. L. O'Keefe, P. E. Warburton and A. G. Matera, *Human Molecular Genetics*, 1996, **5**, 1793.
10. E. Betzig, G. H. Patterson, R. Sougrat, O. W. Lindwasser, S. Olenych, J. S. Bonifacino, M. W. Davidson, J. Lippincott-Schwartz and H. F. Hess, *Science*, 2006, **313**, 1642.
11. S. T. Hess, T. P. K. Girirajan and M. D. Mason, *Biophys. J.* , 2006, **91**, 4258.
12. M. J. Rust, M. Bates and X. Zhuang, *Nat. Methods*, 2006, **3**, 793.
13. M. Heilemann, S. v. d. Linde, M. Schuttpelz, R. Kasper, B. Seefeldt, A. Mukherjee, P. Tinnefeld and M. Sauer, *Angew. Chem. Int. Ed. Engl.*, 2008, **47**, 6172.
14. A. Sharonov and R. M. Hochstrasser, *Proc. Natl. Acad. Sci. U.S.A.*, 2006, **103**, 18911.
15. E. Mei, F. Gao and R. M. Hochstrasser, *Phys. Chem. Chem. Phys.*, 2006, **8**, 2077.
16. D. Axelrod, *Traffic*, 2001, **2**, 764.
17. D. J. Nieves, K. Gaus and M. A. B. Baker, *Genes*, 2018, **9**, 621.
18. R. Jungmann, C. Steinhauer, M. Scheible, A. Kuzyk, P. Tinnefeld and F. C. Simmel, *Nano Lett.*, 2010, **10**, 4756.
19. J. Schnitzbauer, M. T. Strauss, T. Schlichthaerle, F. Schueder and R. Jungmann, *Nature Protocols*, 2017, **12**, 1198.

20. F. Schueder, J. Stein, F. Stehr, A. Auer, B. Sperl, M. T. Strauss, P. Schwille and R. Jungmann, *Nature Methods*, 2019, **16**, 1101.
21. A. E. Rushton, Ph.D., University of Birmingham 2019.
22. H. Shroff, S. T. Hess, E. Betzig, H. F. Hess, G. H. Patterson, J. Lippincott-Schwartz and M. W. Davidson, <http://zeiss-campus.magnet.fsu.edu/print/superresolution/palm/practicalaspects-print.html>, 2020).
23. P. Rothemund, *Nature*, 2006, **440**, 297.
24. K. Mrozek, D. P. Harper and P. D. Aplan, *Hematol Oncol Clin North Am*, 2009, **23**, 991.
25. J. W. Kent, *Genome Res.*, 2002, **12**, 656.
26. T. Haraguchi, T. Shimi, T. Koujin, N. Hashiguchi and Y. Hiraoka, *Genes to Cells*, 2002, **7**, 881.
27. Oligo Analyzer, <https://eu.idtdna.com/calc/analyzer>, 2020).
28. A. Gopinath and P. W. K. Rothemund, *ACS Nano*, 2014, **8**, 12030.

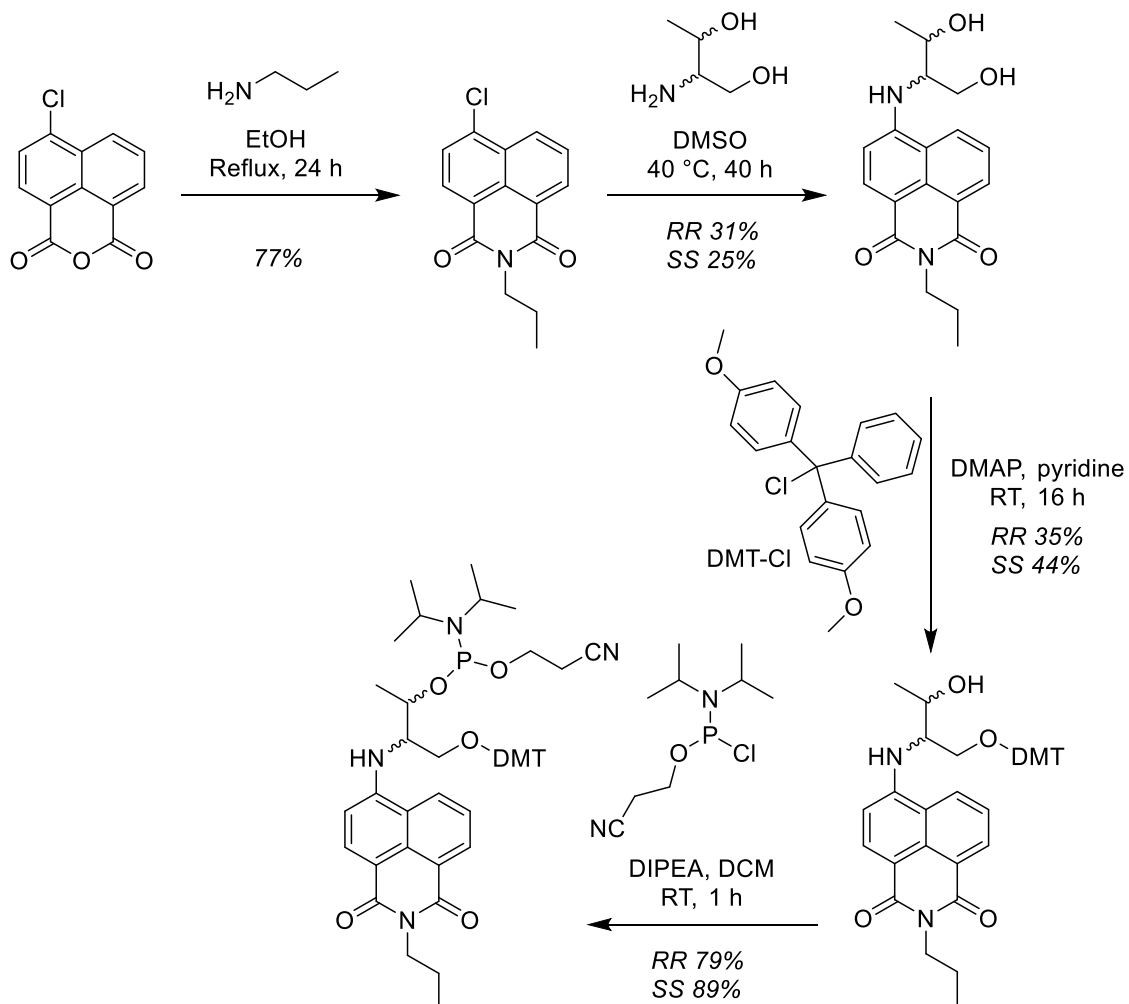
7. Experimental

7.1. Materials and Methods

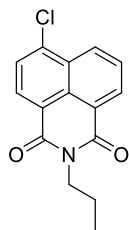
All chemicals and reagents were purchased from commercial suppliers and used without further purification. Purification by column chromatography was carried out using open columns packed with Merck grade 60 silica gel. ^1H , ^{13}C , and ^{31}P NMR spectra were obtained on Bruker AVIII300, AVIII400 or AVNEO500 spectrometers. NMR data was analysed with MestReNova v14.1.2. Electrospray mass (ESI-MS) spectra were measured by either Waters micromass LCT electrospray time-of-flight (ESTOF), Waters Xevo G2-XS, or Synapt G2S mass spectrometers. IR spectroscopy was performed on dry samples with a Varian 660-IR FT-IR spectrometer. Milli-Q water used for DNA sample preparation was purified with a Millipore Elix-Gradient A10 system (resistivity $> 18 \mu\Omega\cdot\text{cm}$, TOC ≤ 5 ppb, Millipore, France).

7.2. Monomer Synthesis

7.2.1. Naph^A_{Short} Synthesis



7.2.1.1. 6-chloro-2-propyl-1H-benzo[de]isoquinoline-1,3(2H)-dione¹



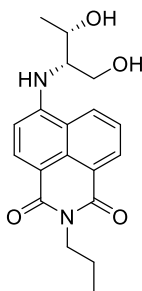
4-chloro-1,8-naphthalic anhydride (4.00 g, 17.2 mmol) was added to propylamine (2.83 mL, 34.4 mmol) and EtOH (70 mL). The solution was heated at reflux under argon overnight. The reaction mixture was left to cool and precipitate formed. The precipitate was filtered and washed with EtOH to give the stated product as a yellow solid (3.64 g, 77%). ¹H NMR (400 MHz, CDCl₃, δ ppm): 8.66 (dd, J = 7.3, 1.1 Hz, 1H, Naph Ar CH), 8.59 (dd, J = 8.5, 1.1 Hz, 1H, Naph Ar CH), 8.50 (d, J = 7.9 Hz, 1H, Naph Ar CH), 7.89 – 7.80 (m, 2H, Naph Ar CH), 4.17 – 4.11 (m, 2H, N-CH₂), 1.83 – 1.70 (m, 2H, CH₂), 1.02 (t, J = 7.5 Hz, 3H, CH₃). ¹³C NMR (101 MHz, CDCl₃, δ ppm): 163.92 (C=O), 139.11 (C-Cl), 132.13 (Ar CH), 131.25 (Ar CH), 130.71 (Ar CH), 129.48 (Ar C), 129.26 (Ar C), 127.98 (Ar CH), 127.51 (Ar CH), 123.33 (Ar C), 121.84 (Ar C), 42.20 (N-CH₂), 21.52 (CH₂), 11.64 (CH₃). HRMS (TOF-ESI +ve) (*m/z*): [M]⁺ calculated for C₁₅H₁₂NO₂Cl₃₅, 273.0557; found 273.0559. IR ν_{\max} /cm⁻¹: 1655.4 (C=O), 784.3 (C-Cl).

7.2.1.2. 6-(((2R,3R)-1,3-dihydroxybutan-2-yl)amino)-2-propyl-1H-benzo[de]isoquinoline-1,3(2H)-dione



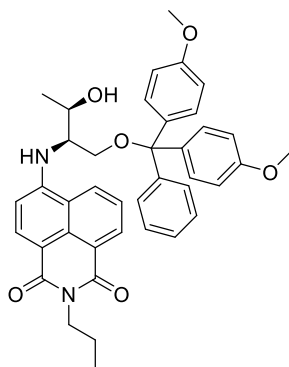
L-threoninol (0.384 g, 3.65 mmol) was dissolved in DMSO (4.00 mL) and 6-chloro-2-propyl-1H-benzo[de]isoquinoline-1,3(2H)-dione (0.500 g, 1.83 mmol) was added. The solution was heated at 40 °C under argon for 48 h. The solution was cooled and H₂O was added to produce a precipitate. 1 M HCl was used to neutralise the mixture and the product extracted into DCM (4 x 20 mL) and washed with H₂O (2 x 20 mL). The solution was dried over magnesium sulfate, filtered and the solvent removed *in vacuo* to give the crude product as an orange oil. Column chromatography on silica (DCM/MeOH, 90:10) gave the stated product as an orange solid (0.197 g, 31%). ¹H NMR (300 MHz, CDCl₃) δ 8.41 (dd, *J* = 7.3, 1.0 Hz, 1H, Naph Ar CH), 8.21 (d, *J* = 8.4 Hz, 1H, Naph Ar CH), 8.09 (dd, *J* = 8.6, 1.1 Hz, 1H, Naph Ar CH), 7.56 (dd, *J* = 8.4, 7.3 Hz, 1H, Naph Ar CH), 6.59 (d, *J* = 8.5 Hz, 1H, Naph Ar CH), 6.15 (d, *J* = 8.2 Hz, 1H, NH), 4.49 (q, *J* = 6.4 Hz, 1H, CH), 4.23 (d, *J* = 11.5 Hz, 1H, CH₂-O), 4.08 – 3.97 (m, 3H, CH₂-O, N-CH₂), 3.68 – 3.58 (m, 1H, CH), 1.72 (dt, *J* = 15.1, 7.5 Hz, 2H, CH₂), 1.32 (d, *J* = 6.4 Hz, 3H, CH₃-CH(OH)), 0.99 (t, *J* = 7.4 Hz, 3H, CH₃). ¹³C NMR (101 MHz, CDCl₃, δ ppm): 164.52 (C=O), 164.10 (C=O), 149.58 (Ar C-NH), 134.33 (Ar CH), 131.22 (Ar C), 129.86 (Ar C), 126.40 (Ar CH), 124.56 (Ar C), 122.84 (Ar CH), 120.38 (Ar C), 109.69 (Ar C), 104.40 (Ar CH), 67.83 (CH-OH), 62.62 (N-CH), 57.81 (CH), 41.66 (CH₂-OH), 21.44 (CH₂), 20.45 (CH(OH)-CH₃), 11.54 (CH₃). HRMS (TOF-ESI +ve) (*m/z*); [M]⁺ calculated for C₁₉H₂₁N₂O₄, 341.1501; found 341.1502. IR ν_{max}/cm⁻¹: 3353.8 (OH), 2961.9 (NH), 1631.3 (C=O).

7.2.1.3. 6-(((2S,3S)-1,3-dihydroxybutan-2-yl)amino)-2-propyl-1H-benzo[de]isoquinoline-1,3(2H)-dione



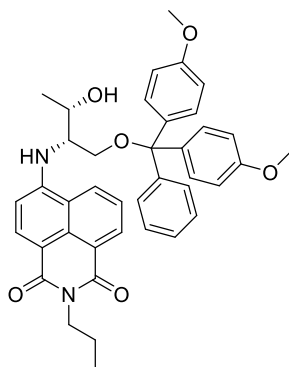
D-threoninol (0.390 g, 3.71 mmol) was dissolved in DMSO (4.00 mL) and 6-chloro-2-propyl-1H-benzo[de]isoquinoline-1,3(2H)-dione (0.507 g, 1.85 mmol) was added. The solution was heated at 40 °C under argon for 48 h. The solution was cooled and H₂O was added to produce a precipitate. 1 M HCl was used to neutralise the mixture and the product extracted into DCM (4 x 20 mL) and washed with H₂O (2 x 20 mL). The solution was dried over magnesium sulfate, filtered and the solvent removed *in vacuo* to give the crude product as an orange oil. Column chromatography on silica (DCM/MeOH, 90:10) gave the stated product as an orange solid (0.158 g, 25%). ¹H NMR (500 MHz, CDCl₃) δ 8.62 (d, *J* = 7.3 Hz, 1H, Naph Ar CH), 8.44 (d, *J* = 8.4 Hz, 1H, Naph Ar CH), 8.25 (d, *J* = 8.4 Hz, 1H, Naph Ar CH), 7.74 – 7.63 (m, 1H, Naph Ar CH), 6.66 (d, *J* = 8.4 Hz, 1H, Naph Ar CH), 6.02 (d, *J* = 9.7 Hz, 1H, NH), 4.88 (dd, *J* = 6.4, 1.3 Hz, 1H, CH), 4.21 (dd, *J* = 11.6, 1.8 Hz, 1H, CH₂-O), 4.15 – 4.13 (m, 2H, N-CH₂), 3.96 (dd, *J* = 11.5, 1.7 Hz, 1H, CH₂-O), 3.70 (d, *J* = 9.7 Hz, 1H, CH), 1.76 (qd, *J* = 7.5, 1.4 Hz, 2H, CH₂), 1.30 (dd, *J* = 6.5, 1.2 Hz, 3H, CH₃-CH(OH)), 1.00 (td, *J* = 7.4, 1.2 Hz, 3H, CH₃). ¹³C NMR (101 MHz, CDCl₃, δ ppm): 164.77 (C=O), 164.20 (C=O), 148.85 (Ar C-NH), 134.31 (Ar CH), 131.53 (Ar CH), 130.19 (Ar C), 126.21 (Ar CH), 125.17 (Ar CH), 123.45 (Ar C), 120.76 (Ar C), 111.03 (Ar C), 104.40 (Ar CH), 75.53 (CH-OH), 70.04 (N-CH), 50.88 (CH), 41.83 (CH₂-OH), 21.59 (CH₂), 18.22 (CH(OH)-CH₃), 11.70 (CH₃). HRMS (TOF-ESI +ve) (*m/z*); [M]⁺ calculated for C₁₉H₂₃N₂O₄, 343.1658; found 343.1657. IR ν_{max}/cm⁻¹: 3338.8 (OH), 2961.8 (NH), 1630.8 (C=O).

7.2.1.4. 6-(((2R,3R)-1-(bis(4-methoxyphenyl)(phenyl)methoxy)-3-hydroxybutan-2-yl)amino)-2-propyl-1H-benzo[de]isoquinoline-1,3(2H)-dione^{2,3}



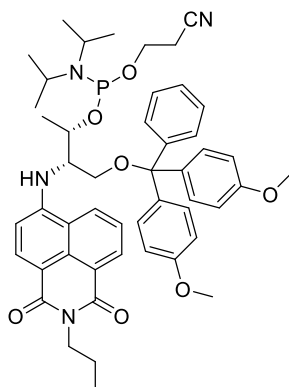
6-(((2R,3R)-1,3-dihydroxybutan-2-yl)amino)-2-propyl-1H-benzo[de]isoquinoline-1,3(2H)-dione (0.197 g, 0.575 mmol) was dissolved in pyridine (30 mL). DMT-Cl (0.195 g, 0.575 mmol) and DMAP (0.0105 g, 0.0862 mmol) was added and the solution left to stir under argon for 24 h. The reaction mixture was poured onto H₂O (50 mL) and the product extracted with DCM (2 x 50 mL). The remaining solution was dried over MgSO₄, filtered and the solvent removed in *vacuo*. Column chromatography on silica (EtOAc/hexane/TEA, 59:40:1) to leave the stated product as an orange solid oil (0.131 g, 35%).¹H NMR (300 MHz, CD₃CN) δ 8.38 (dd, *J* = 7.3, 0.9 Hz, 1H, Naph Ar CH), 8.32 – 8.23 (m, 1H, Naph Ar CH), 8.18 (d, *J* = 8.5 Hz, 1H, Naph Ar CH), 7.58 – 7.46 (m, 1H, Naph Ar CH), 7.46 – 7.37 (m, 2H, DMT CH), 7.33 – 7.10 (m, 7H, DMT CH), 6.81 – 6.67 (m, 4H, DMT CH), 6.58 (d, *J* = 8.7 Hz, 1H, Naph Ar CH), 6.10 (d, *J* = 8.8 Hz, 1H, NH), 4.38 (dd, *J* = 6.4, 3.8 Hz, 1H, CH), 4.04 – 3.95 (m, 2H, CH₂-O), 3.85 – 3.74 (m, 1H, CH), 3.69 (d, *J* = 5.6 Hz, 6H, DMT O-CH₃), 3.47 (dd, *J* = 9.8, 5.5 Hz, 1H, N-CH₂), 3.33 (dd, *J* = 9.8, 4.9 Hz, 1H, N-CH₂), 1.76 – 1.61 (m, 2H, CH₂), 1.28 – 1.25 (m, 3H, CH(OH)-CH₃), 1.00 – 0.93 (m, 3H, CH₃). ¹³C NMR (101 MHz, CD₃CN, δ ppm): 164.91 (C=O), 164.17 (C=O), 159.18 (Ar C-O), 150.55 (Ar C-NH), 145.79 (Ar C), 136.47 (Ar CH), 134.22 (Ar CH), 131.20 (Ar CH), 130.54 (Ar C), 128.47 (Ar CH), 128.36 (Ar CH), 127.56 (Ar CH), 127.35 (Ar CH), 125.17 (Ar CH), 123.61 (Ar C), 121.06 (Ar C), 113.52 (Ar CH), 110.16 (Ar C), 105.50 (Ar CH), 86.84 (DMT C), 66.90 (CH-OH), 63.34 (CH₂-O), 58.90 (CH), 55.43 (DMT O-CH₃), 41.73 (CH₂), 21.80 (CH₂), 20.33 (CH(OH)-CH₃), 11.43 (CH₃). HRMS (TOF-ESI +ve) (*m/z*): [M]⁺ calculated for C₄₀H₃₉N₂O₆, 643.2810; found 643.2808. IR ν_{\max} / cm⁻¹: 3400 (OH), 2965.70 (NH), 1580.83 (C=O).

7.2.1.5. 6-(((2S,3S)-1-(bis(4-methoxyphenyl)(phenyl)methoxy)-3-hydroxybutan-2-yl)amino)-2-propyl-1H-benzo[de]isoquinoline-1,3(2H)-dione^{2,3}



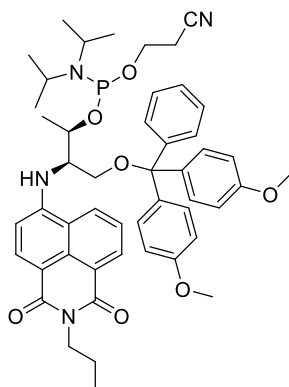
6-(((2R,3R)-1,3-dihydroxybutan-2-yl)amino)-2-propyl-1H-benzo[de]isoquinoline-1,3(2H)-dione (0.158 g, 0.462 mmol) was dissolved in pyridine (30 mL). DMT-Cl (0.157 g, 0.462 mmol) and DMAP (0.0085 g, 0.0693 mmol) was added and the solution left to stir under argon for 24 h. The reaction mixture was poured onto H₂O (50 mL) and the product extracted with DCM (2 x 50 mL). The remaining solution was dried over MgSO₄, filtered and the solvent was removed in *vacuo*. Column chromatography on silica (EtOAc/hexane/TEA, 59:40:1) yielded the stated product as an orange solid oil (0.179 g, 44 %). ¹H NMR (300 MHz, CDCl₃) δ 8.56 (dd, *J* = 7.3, 0.9 Hz, 1H, Naph Ar CH), 8.31 (d, *J* = 8.4 Hz, 1H, Naph Ar CH), 8.14 (dd, *J* = 8.6, 1.1 Hz, 1H, Naph Ar CH), 7.58 (dd, *J* = 8.4, 7.3 Hz, 1H, Naph Ar CH), 7.41 – 7.33 (m, 2H, DMT CH), 7.29 – 7.15 (m, 7H, DMT CH), 6.76 – 6.61 (m, 4H, DMT CH), 6.47 (d, *J* = 8.6 Hz, 1H, Naph Ar CH), 6.04 (d, *J* = 7.7 Hz, 1H, NH), 4.50 – 4.37 (m, 1H, CH), 4.14 – 4.08 (m, 3H, CH₂-O), 3.70 (d, *J* = 6.5 Hz, 6H, DMT O-CH₃), 3.65 (d, *J* = 7.8 Hz, 2H, CH), 3.47 (t, *J* = 6.0 Hz, 1H, N-CH₂), 3.35 – 3.25 (m, 1H, N-CH₂), 1.82 – 1.69 (m, 2H, CH₂), 1.32 (d, *J* = 6.4 Hz, 3H, CH(OH)-CH₃), 1.00 (t, *J* = 7.4 Hz, 3H, CH₃). ¹³C NMR (101 MHz, CDCl₃, δ ppm): 164.65 (C=O), 164.09 (C=O), 158.63 (Ar C-O), 149.14 (Ar C-NH), 144.49 (Ar C), 135.23 (Ar CH), 134.30 (Ar CH), 131.19 (Ar CH), 129.88 (Ar C), 127.98 (Ar CH), 127.00 (Ar CH), 126.03 (Ar CH), 124.72 (Ar CH), 123.09 (Ar C), 120.48 (Ar C), 113.24 (Ar CH), 110.08 (Ar C), 104.78 (Ar CH), 87.06 (DMT C), 67.77 (CH-O), 63.17 (CH₂-O), 57.29 (CH), 55.16 (DMT O-CH₃), 41.68 (CH₂), 21.49 (CH₂), 20.54 (CH(O)-CH₃), 11.58 (CH₃). HRMS (TOF-ESI +ve) (*m/z*): [M]⁺ calculated for C₄₀H₃₉N₂O₆, 643.2807; found 643.2808. IR *v*_{max}/cm⁻¹: 3421.38 (OH), 2963.27 (NH), 1578.50 (C=O).

7.2.1.6. (2R,3R)-4-(bis(4-methoxyphenyl)(phenyl)methoxy)-3-((1,3-dioxo-2-propyl-2,3-dihydro-1H-benzo[de]isoquinolin-6-yl)amino)butan-2-yl (2-cyanoethyl) diisopropylphosphoramidite³



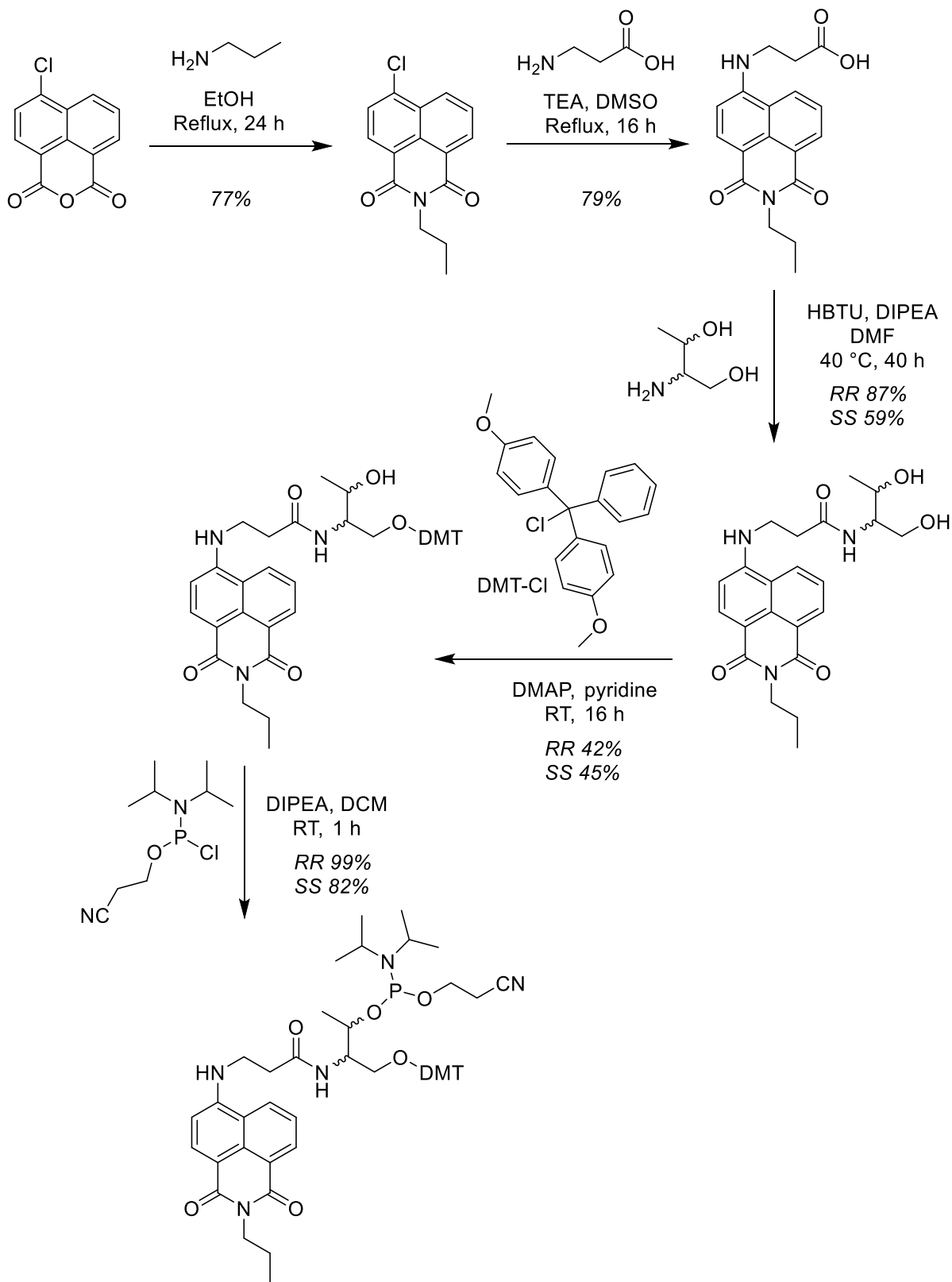
Under argon, 6-(((2R,3R)-1-(bis(4-methoxyphenyl)(phenyl)methoxy)-3-hydroxybutan-2-yl)amino)-2-propyl-1H-benzo[de]isoquinoline-1,3(2H)-dione (0.197 g, 0.304 mmol) was dissolved in anhydrous DCM (50 mL). DIPEA (0.16 mL, 0.911 mmol) and 2-cyanethyl-diisopropylchlorophosphoramidite (0.08 mL, 0.364 mmol) were added and the solution left to stir under argon for 1 h. Methanol (1 mL) was added to quench the reaction and left to stir for a further 30 min. The solid was filtered off and rinsed with EtOAc (50 mL). The remaining solution was washed with sodium hydrogen carbonate (2 x 50 mL), water (50 mL) and brine (50 mL). The organic layer was dried over MgSO₄, filtered and solvent removed in *vacuo*. Column chromatography on alumina (EtOAc/hexane/TEA, 59:40:1) afforded the stated product as a yellow oil (0.203 g, 79%). ¹H NMR (300 MHz, CD₃CN) δ 8.45 (ddd, *J* = 7.2, 5.1, 0.8 Hz, 1H, Naph Ar CH), 8.29 – 8.24 (m, 1H, Naph Ar CH), 8.24 – 8.18 (m, 1H, Naph Ar CH), 7.64 (dd, *J* = 8.4, 7.4 Hz, 1H, Naph Ar CH), 7.47 – 7.42 (m, 2H, DMT CH), 7.28 (td, *J* = 8.2, 7.8, 3.9 Hz, 7H, DMT CH), 6.82 – 6.77 (m, 5H, DMT CH), 6.71 (d, *J* = 8.7 Hz, 1H, Naph Ar CH), 5.97 (d, *J* = 8.6 Hz, 1H, NH), 4.57 – 4.48 (m, 1H, CH), 4.03 – 3.97 (m, 3H, CH₂-O), 3.82 – 3.77 (m, 1H, CH), 3.72 (d, *J* = 2.6 Hz, 6H, DMT O-CH₃), 3.69 – 3.52 (m, 6H, N-CH, N-CH₂), 2.66 (t, *J* = 6.0 Hz, 2H, CH₂), 2.54 (t, *J* = 6.0 Hz, 2H, CH₂), 1.67 (s, 2H, CH₂), 1.32 (d, *J* = 6.3 Hz, 3H, CH(O)-CH₃), 1.21 – 1.15 (m, 16H, ¹Pr₂-N), 0.95 (td, *J* = 7.4, 1.3 Hz, 4H, CH₃). ³¹P NMR (121 MHz, CD₃CN, δ ppm): 148.84, 148.42 (P(III)), 147.21 (P(III)).

7.2.1.7. (2S,3S)-4-(bis(4-methoxyphenyl)(phenyl)methoxy)-3-((1,3-dioxo-2-propyl-2,3-dihydro-1H-benzo[de]isoquinolin-6-yl)amino)butan-2-yl (2-cyanoethyl) diisopropylphosphoramidite³

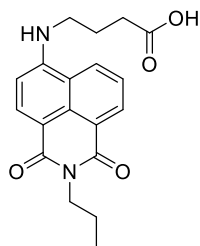


Under argon, 6-(((2R,3R)-1-(bis(4-methoxyphenyl)(phenyl)methoxy)-3-hydroxybutan-2-yl)amino)-2-propyl-1H-benzo[de]isoquinoline-1,3(2H)-dione (0.167 g, 0.259 mmol) was dissolved in anhydrous DCM (50 mL). DIPEA (0.14 mL, 0.776 mmol) and 2-cyanoethyl-diisopropylchlorophosphoramidite (0.07 mL, 0.310 mmol) were added and the solution left to stir under argon for 1 h. Methanol (1 mL) was added to quench the reaction and left to stir for a further 30 min. The solid was filtered off and rinsed with EtOAc (50 mL). The remaining solution was washed with sodium hydrogen carbonate (2 x 50 mL), water (50 mL) and brine (50 mL). The organic layer was dried over MgSO₄, filtered and solvent removed in *vacuo*. Column chromatography on alumina (EtOAc/hexane/TEA, 59:40:1) afforded the stated product as a yellow oil (0.194 g, 89%). ¹H NMR (300 MHz, CD₃CN) δ 8.38 (ddd, *J* = 7.3, 3.8, 1.0 Hz, 1H, Naph Ar CH), 8.17 (dd, *J* = 8.5, 2.8 Hz, 1H, Naph Ar CH), 8.10 (ddd, *J* = 18.0, 8.6, 1.1 Hz, 1H, Naph Ar CH), 7.56 (ddd, *J* = 8.5, 7.3, 4.5 Hz, 1H, Naph Ar CH), 7.33 (ddd, *J* = 7.2, 4.0, 1.5 Hz, 2H, DMT CH), 7.25 – 7.03 (m, 7H, DMT CH), 6.75 – 6.65 (m, 4H, DMT CH), 6.61 (t, *J* = 8.9 Hz, 1H, Naph Ar CH), 5.82 (dd, *J* = 27.7, 8.8 Hz, 1H, NH), 4.42 (ddt, *J* = 8.7, 6.2, 3.1 Hz, 1H, CH), 3.93 (ddd, *J* = 9.8, 6.5, 2.4 Hz, 2H, CH₂-O), 3.81 – 3.66 (m, 2H, CH), 3.63 (dd, *J* = 4.0, 1.9 Hz, 6H, DMT O-CH₃), 3.61 – 3.35 (m, 5H, N-CH, N-CH₂), 2.63 – 2.52 (m, 2H, CH₂), 2.48 – 2.40 (m, 1H, CH₂), 1.59 (qd, *J* = 7.5, 1.8 Hz, 2H, CH₂), 1.23 (dd, *J* = 9.4, 6.3 Hz, 3H, CH(O)-CH₃), 1.11 – 1.03 (m, 13H, ⁱPr₂-N), 0.89 – 0.84 (m, 3H, CH₃). ³¹P NMR (121 MHz, CDCl₃, δ ppm): 149.32 (P(III)), 148.14 (P(III)).

7.2.2. Naph^ALong Synthesis

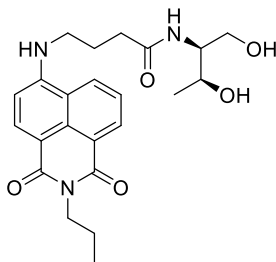


7.2.2.1. 4-((1,3-dioxo-2-propyl-2,3-dihydro-1H-benzo[de]isoquinolin-6-yl)amino)butanoic acid



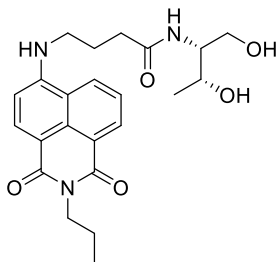
γ -aminobutyric acid was dispersed in dimethyl sulfoxide (15 mL). Trimethylamine (3.05 mL, 21.9 mmol) and 6-chloro-2-propyl-1H-benzo[de]isoquinoline-1,3(2H)-dione (0.999 g, 3.65 mmol) was added. The solution was heated to reflux under argon overnight. The reaction mixture was left to cool to room temperature. Water was added to the reaction mixture (50 mL) and 4 M hydrochloric acid was added to produce a precipitate. The precipitate was filtered and washed with water to leave the stated product as a yellow solid (0.332 g, 27%). ^1H NMR (300 MHz, CD_3OD) δ 8.56 – 8.46 (m, 2H, Naph Ar CH), 8.37 (d, J = 8.6 Hz, 1H, Naph Ar CH), 7.65 (dd, J = 8.4, 7.4 Hz, 1H, Naph Ar CH), 6.85 (d, J = 8.7 Hz, 1H, Naph Ar CH), 4.14 – 4.04 (m, 2H, N-CH₂), 3.51 (t, J = 7.1 Hz, 2H, NH-CH₂), 2.50 (t, J = 7.0 Hz, 2H, CH₂-COOH), 2.08 (p, J = 7.0 Hz, 2H, CH₂), 1.74 (dt, J = 14.9, 7.4 Hz, 2H, CH₂-CH₃), 0.99 (t, J = 7.5 Hz, 3H, CH₃). ^{13}C NMR (101 MHz, MeOD) δ 177.32 (C=OOH), 166.18 (C=O), 165.67 (C=O), 152.45 (Naph Ar C-NH), 135.88 (Naph Ar CH), 132.07 (Naph Ar CH), 131.08 (Naph Ar C), 129.20 (Naph Ar CH), 125.37 (Naph Ar CH), 123.26 (Naph Ar C), 121.72 (Naph Ar C), 109.31 (Naph Ar C), 105.01 (Naph Ar CH), 43.88 (N-CH₂), 42.59 (N-CH₂), 32.44 (CH₂-COOH), 24.68 (CH₂), 22.44 (CH₂), 11.78 (CH₃). HRMS (TOF-ESI +ve) (m/z): $[\text{M}]^+$ calculated for $\text{C}_{19}\text{H}_{21}\text{N}_2\text{O}_4$, 341.1501; found 341.1502.

7.2.2.2. N-((2S,3S)-1,3-dihydroxybutan-2-yl)-4-((1,3-dioxo-2-propyl-2,3-dihydro-1H-benzo[de]isoquinolin-6-yl)amino)butanamide



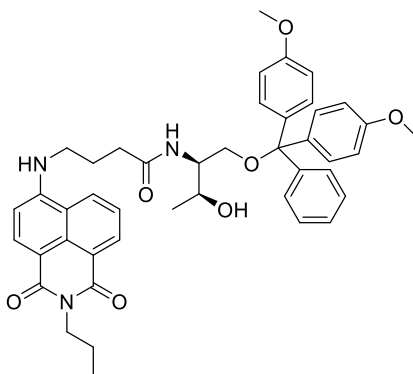
4-((1,3-dioxo-2-propyl-2,3-dihydro-1H-benzo[de]isoquinolin-6-yl)amino)butanoic acid (0.295 g, 0.865 mmol) was dissolved in anhydrous DMF (20 mL). HBTU (0.332 g, 0.876 mmol) was added and left to stir under argon at room temperature for 15 min. D-threoinol (0.0972 g, 0.924 mmol) and DIPEA (0.15 mL, 0.882 mmol) were added and reaction left to stir under argon at 40°C for 51 h. The reaction mixture was cooled to room temp and diluted with MeOH/DCM (1:2, 100 mL) and washed with H₂O (3 x 50 mL), then dried over MgSO₄. The solvent was removed in *vacuo* and the crude solid purified by silica column chromatography using a gradient eluent system (99:1 DCM/ammonia solution increasing to 90:9:1 DCM/MeOH/ammonia solution) to give the stated product as a yellow solid (0.223 g, 59%). ¹H NMR (300 MHz, CD₃OD) δ 8.53 (t, *J* = 8.6 Hz, 2H, Naph Ar CH), 8.37 (d, *J* = 8.6 Hz, 1H, Naph Ar CH), 7.70 – 7.61 (m, 1H, Naph Ar CH), 6.82 (d, *J* = 8.6 Hz, 1H, Naph Ar CH), 4.13 – 4.04 (m, 2H, N-CH₂), 3.98 (dd, *J* = 6.4, 3.3 Hz, 1H, CH-OH), 3.91 – 3.83 (m, 1H, CH), 3.70 – 3.53 (m, 2H, CH₂-OH), 3.50 (t, *J* = 7.0 Hz, 2H, NH-CH₂), 2.48 (t, *J* = 7.1 Hz, 2H, CH₂-CO), 2.15 – 2.06 (m, 2H, CH₂), 1.72 (q, *J* = 7.5 Hz, 2H, CH₂-CH₃), 1.13 (d, *J* = 6.4 Hz, 3H, CH₃-CH(OH)), 0.98 (t, *J* = 7.5 Hz, 3H, CH₃). ¹³C NMR (126 MHz, MeOD) δ 176.25 (C=ONH), 166.51 (C=O), 166.02 (C=O), 152.85 (Naph Ar C-NH), 136.26 (Naph Ar CH), 132.41 (Naph Ar CH), 131.50 (Naph Ar C), 129.62 (Naph Ar CH), 125.69 (Naph Ar CH), 123.63 (Naph Ar C), 122.12 (Naph Ar C), 109.56 (Naph Ar C), 105.28 (Naph Ar CH), 67.29 (CH-NH), 63.03 (CH-OH), 57.67 (CH₂-OH), 44.21 (N-CH₂), 42.74 (CH₂), 34.72 (CH₂-CO), 25.65 (CH₂), 22.63 (CH₂-CH₃), 20.61 (CH₃-C(H)OH), 11.92 (CH₃). HRMS (TOF-ESI +ve) (*m/z*): [M]⁺ calculated for C₂₃H₂₉N₃O₅Na, 450.2005; found 450.2002. IR *v*_{max}/cm⁻¹ 3338 (N-H), 3288 (N-H), 3052 (OH), 2966 (N-H), 2933 (N-H), 1679 (C=O, s), 1633 (C=O, s).

7.2.2.3. N-((2R,3R)-1,3-dihydroxybutan-2-yl)-4-((1,3-dioxo-2-propyl-2,3-dihydro-1H-benzo[de]isoquinolin-6-yl)amino)butanamide



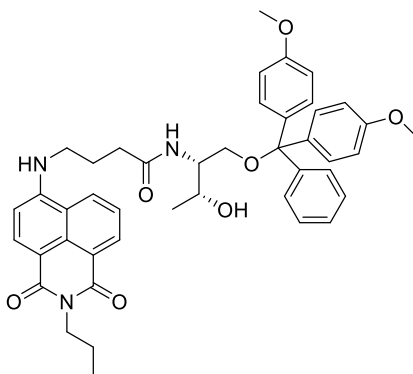
4-((1,3-dioxo-2-propyl-2,3-dihydro-1H-benzo[de]isoquinolin-6-yl)amino)butanoic acid (0.194 g, 0.572 mmol) was dissolved in anhydrous DMF (20 mL). HBTU (0.223 g, 0.588 mmol) was added and left to stir under argon at room temperature for 15 min. L-threoninol (0.0618 g, 0.588 mmol) and DIPEA (0.10 mL, 0.5.88 mmol) were added and reaction left to stir under argon at 40°C for 43 h. The reaction mixture was cooled to room temp and diluted with MeOH/DCM (1:2 100 mL) and washed with H₂O (3 x 50 mL), then dried over MgSO₄. The solvent was removed in *vacuo* and the crude solid was purified by silica column chromatography using a gradient eluent system (99:1 DCM/ammonia solution increasing to 90:9:1 DCM/MeOH/ammonia solution) to give the stated product as a yellow solid (0.220 g, 87%). ¹H NMR (300 MHz, CD₃OD) δ 8.54 (ddd, *J* = 8.6, 7.9, 1.1 Hz, 2H, Naph Ar CH), 8.38 (d, *J* = 8.6 Hz, 1H, Naph Ar CH), 7.66 (dd, *J* = 8.4, 7.4 Hz, 1H, Naph Ar CH), 6.83 (d, *J* = 8.7 Hz, 1H, Naph Ar CH), 4.14 – 4.05 (m, 2H, N-CH₂), 4.04 – 3.94 (m, 1H, CH-OH), 3.88 (td, *J* = 6.1, 3.3 Hz, 1H, CH), 3.71 – 3.56 (m, 2H, CH₂-OH), 3.50 (t, *J* = 7.0 Hz, 2H, NH-CH₂), 2.49 (t, *J* = 7.1 Hz, 2H, CH₂-CO), 2.12 (p, *J* = 7.1 Hz, 2H, CH₂), 1.73 (h, *J* = 7.5 Hz, 2H, CH₂-CH₃), 1.14 (d, *J* = 6.4 Hz, 3H, CH₃-CH(OH)), 0.99 (t, *J* = 7.5 Hz, 3H, CH₃). ¹³C NMR (126 MHz, MeOD) δ 176.09 (C=ONH), 166.35 (C=O), 165.86 (C=O), 152.69 (Naph Ar C-NH), 136.11 (Naph Ar CH), 132.26 (Naph Ar CH), 131.34 (Naph Ar C), 129.47 (Naph Ar CH), 125.53 (Naph Ar CH), 123.46 (Naph Ar C), 121.96 (Naph Ar C), 109.37 (Naph Ar C), 105.12 (Naph Ar CH), 67.10 (CH-NH), 62.84 (CH-OH), 57.49 (CH₂-OH), 44.03 (CH₂), 42.57 (CH₂), 34.54 (CH₂-CO), 25.47 (CH₂), 22.46 (CH₂-CH₃), 20.44 (CH₃-C(H)OH), 11.75 (CH₃). HRMS (TOF-ESI +ve) (*m/z*): [M]⁺ calculated for C₂₃H₂₉N₃O₅Na, 450.2005; found 450.2007. IR *v*_{max}/cm⁻¹ 3340 (N-H), 3289 (N-H), 3057 (OH), 2966 (N-H), 2934 (N-H), 1680 (C=O), 1632 (C=O).

7.2.2.4. N-((2S,3S)-1-(bis(4-methoxyphenyl)(phenyl)methoxy)-3-hydroxybutan-2-yl)-4-((1,3-dioxo-2-propyl-2,3-dihydro-1H-benzo[de]isoquinolin-6-yl)amino)butanamide^{2,3}



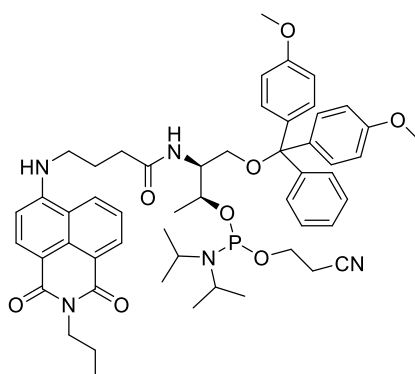
N-((2S,3S)-1,3-dihydroxybutan-2-yl)-4-((1,3-dioxo-2-propyl-2,3-dihydro-1H-benzo[de]isoquinolin-6-yl)amino)butanamide (0.172 g, 0.402 mmol) was dissolved in anhydrous pyridine (30 mL). Dimethoxytritylchloride (0.139 g, 0.410 mmol) and DMAP (0.0094 g, 0.0769 mmol) were added and the reaction mixture left to stir under argon at room temperature for 20 h. The reaction mixture was poured onto H₂O (50 mL) and the product extracted with DCM (3 x 50 mL), then dried over MgSO₄. The solvent was removed in *vacuo* and the product purified by column chromatography on silica (EtOAc/Hex/TEA, 89:10:1) to give the desired product as an orange solid (0.132 g, 45%). ¹H NMR (300 MHz, CD₃CN) δ 8.29 (dd, *J* = 7.3, 1.0 Hz, 1H, Naph Ar CH), 8.25 – 8.18 (m, 1H, Naph Ar CH), 8.12 (d, *J* = 8.4 Hz, 1H, Naph Ar CH), 7.41 (dd, *J* = 8.4, 7.3 Hz, 1H, Naph Ar CH), 7.23 – 7.17 (m, 2H, DMT CH), 7.08 – 7.01 (m, 7H, DMT CH), 7.00 – 6.96 (m, 1H, Naph Ar CH), 6.63 – 6.56 (m, 4H, DMT CH), 6.48 (dd, *J* = 14.6, 8.9 Hz, 2H, NH), 3.87 – 3.84 (m, 3H, N-CH₂, CH-OH), 3.52 (d, *J* = 2.4 Hz, 6H, DMT O-CH₃), 3.24 (d, *J* = 5.7 Hz, 2H, CH₂-O), 2.95 (dd, *J* = 9.3, 4.8 Hz, 1H, CH), 2.88 – 2.77 (m, 2H, NH-CH₂), 2.34 (dd, *J* = 12.6, 9.5 Hz, 2H, CH₂-CO), 1.92 (s, 2H, CH₂), 1.57 – 1.47 (m, 2H, CH₂), 1.19 (d, *J* = 13.7 Hz, 4H, CH₃-CH(OH)), 1.04 (t, *J* = 7.1 Hz, 3H, CH₃). HRMS (TOF-ESI +ve) (*m/z*): [M]⁺ calculated for C₄₄H₄₇N₃O₇Na, 752.3312; found 752.3315.

7.2.2.5. N-((2R,3R)-1-(bis(4-methoxyphenyl)(phenyl)methoxy)-3-hydroxybutan-2-yl)-4-((1,3-dioxo-2-propyl-2,3-dihydro-1H-benzo[de]isoquinolin-6-yl)amino)butanamide^{2,3}



N-((2R,3R)-1,3-dihydroxybutan-2-yl)-4-((1,3-dioxo-2-propyl-2,3-dihydro-1H-benzo[de]isoquinolin-6-yl)amino)butanamide (0.169 g, 0.397 mmol) was dissolved in anhydrous pyridine (30 mL). Dimethoxytritylchloride (0.138 g, 0.407 mmol) and DMAP (0.0088 g, 0.0720 mmol) were added and the reaction mixture left to stir under argon at room temperature for 20 h. The reaction mixture was poured onto H₂O (50 mL) and the product extracted with DCM (3 x 50 mL), then dried over MgSO₄. The solvent was removed in *vacuo* and the product purified by column chromatography on silica (EtOAc/Hex/TEA, 89:10:1) to give the desired product as an orange solid (0.122 g, 42%). ¹H NMR (300 MHz, CD₃CN) δ 8.30 (dd, *J* = 7.3, 0.8 Hz, 1H, Naph Ar CH), 8.24 – 8.18 (m, 1H, Naph Ar CH), 8.14 (d, *J* = 8.4 Hz, 1H, Naph Ar CH), 7.45 – 7.39 (m, 1H, Naph Ar CH), 7.38 – 7.33 (m, 2H, DMT CH), 7.29 – 7.05 (m, 8H, DMT CH, Naph Ar CH), 6.77 – 6.69 (m, 4H, DMT CH), 6.50 (d, *J* = 8.6 Hz, 1H, NH), 4.02 – 3.96 (m, 3H, N-CH₂, CH-OH), 3.65 (d, *J* = 1.6 Hz, 6H, DMT O-CH₃), 3.31 (q, *J* = 7.1, 6.6 Hz, 2H, CH₂-O), 3.21 – 3.09 (m, 1H, NH-CH₂), 3.01 (dd, *J* = 9.2, 5.8 Hz, 1H, NH-CH₂), 2.79 (t, *J* = 7.6 Hz, 1H, CH), 2.69 (s, 2H, OH), 2.51 (p, *J* = 7.1 Hz, 2H, CH₂-CO), 2.09 (td, *J* = 15.7, 13.8, 8.8 Hz, 2H, CH₂), 1.74 – 1.59 (m, 2H, CH₂), 1.02 (d, *J* = 6.1 Hz, 3H, CH₃-CH(OH)), 0.94 (d, *J* = 7.4 Hz, 3H, CH₃). HRMS (TOF-ESI +ve) (*m/z*): [M]⁺ calculated for C₄₄H₄₇N₃O₇Na, 752.3312; found 752.3301.

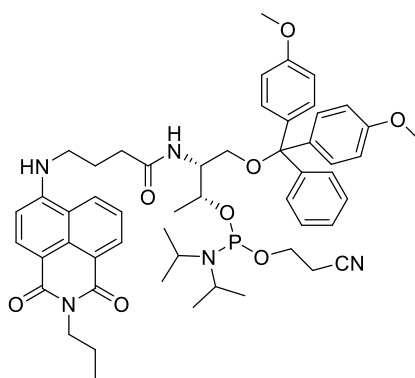
7.2.2.6. (2S,3S)-4-(bis(4-methoxyphenyl)(phenyl)methoxy)-3-(4-((1,3-dioxo-2-propyl-2,3-dihydro-1H-benzo[de]isoquinolin-6-yl)amino)butanamido)butan-2-yl (2-cyanoethyl) diisopropylphosphoramidite³



Under argon N-((2S,3S)-1-(bis(4-methoxyphenyl)(phenyl)methoxy)-3-hydroxybutan-2-yl)-4-((1,3-dioxo-2-propyl-2,3-dihydro-1H-benzo[de]isoquinolin-6-yl)amino)butanamide, (0.131 g, 0.180 mmol) was dissolved in anhydrous DCM (15 mL). DIPEA (0.10 mL, 0.53 mmol) and 2-cyanoethyl-diisopropylchlorophosphoramidite (0.04 mL, 0.216 mmol) were added and the solution left to stir under argon for 1 h. Methanol (1 mL) was added to quench the reaction and left to stir as before for a further 30 min. EtOAc (10 mL) was added to the remaining solution was washed with sodium hydrogen carbonate (2 x 50 mL), water (50 mL) and brine (50 mL). The organic layer was dried over MgSO₄, filtered and solvent removed in *vacuo*. Column chromatography on alumina (EtOAc/hexane/TEA, 59:40:1) afforded the stated product as a yellow oil (0.108 g, 82%). ¹H NMR (400 MHz, CD₃CN) δ 8.40 – 8.34 (m, 2H, Naph Ar CH), 8.20 (d, *J* = 8.5 Hz, 1H, Naph Ar CH), 7.54 – 7.47 (m, 1H, Naph Ar CH), 7.37 (dtd, *J* = 7.0, 3.5, 1.9 Hz, 2H, DMT CH), 7.22 (tdd, *J* = 7.7, 4.0, 2.5 Hz, 7H, DMT CH), 7.13 (tdd, *J* = 7.2, 3.3, 2.1 Hz, 1H, Naph Ar CH), 6.75 (ddd, *J* = 8.7, 7.2, 1.3 Hz, 4H, DMT CH), 6.58 (dd, *J* = 8.4, 2.6 Hz, 1H, NH), 4.24 (dq, *J* = 8.3, 5.2, 4.2 Hz, 1H, CH-O), 4.03 – 3.97 (m, 2H, N-CH₂), 3.69 (d, *J* = 1.7 Hz, 1H, CH), 3.69 – 3.65 (m, 6H, DMT O-CH₃), 3.53 – 3.41 (m, 2H, CH₂-O), 3.41 – 3.33 (m, 2H, HN-CH₂), 3.15 – 3.08 (m, 2H, CH₂-CO), 2.47 (t, *J* = 6.0 Hz, 2H, CH₂-CN), 2.25 (tt, *J* = 8.8, 5.4 Hz, 1H, CH-N), 2.09 (tdd, *J* = 12.9, 7.2, 4.6 Hz, 2H, CH-N), 1.71 – 1.63 (m, 2H, CH₂), 1.58 – 1.46 (m, 3H, CH₂), 1.13 – 1.01 (m, 13H, ⁱPr₂-N), 0.96 – 0.93 (m, 4H, CH₃-CH(OH)), 0.87 (d, *J* = 3.7 Hz, 3H, CH₃). ³¹P NMR (162 MHz, CD₃CN) δ 147.56 (P(III)),

147.15 (P(III)), 8.25 (P(V)), 7.58 (P(V)), 7.49 (P(V)), 7.19 (P(V)). HRMS (TOF-ESI +ve) (m/z): $[M]^+$ calculated, 930.4571; found 930.4572.

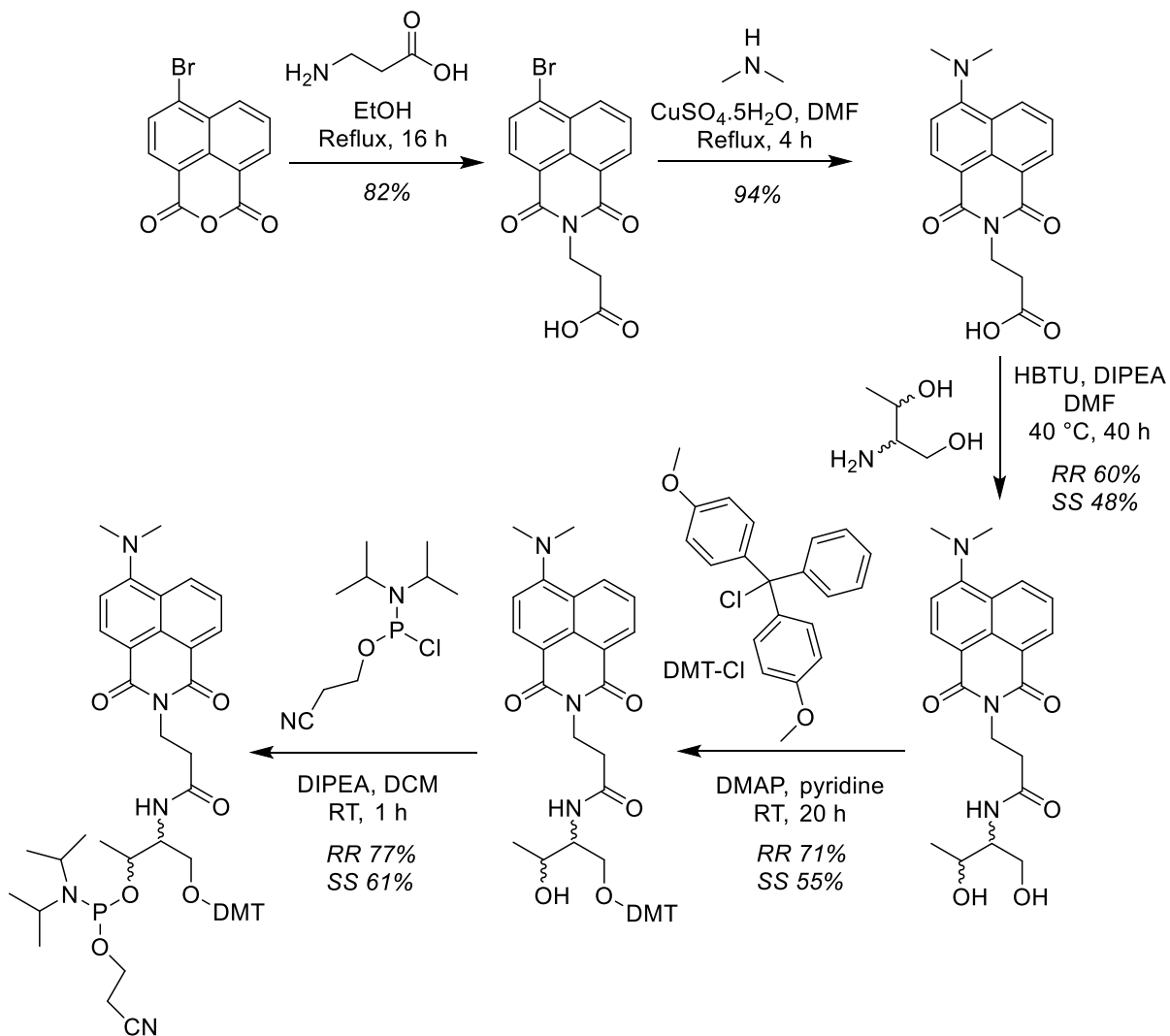
7.2.2.7. (2R,3R)-4-(bis(4-methoxyphenyl)(phenyl)methoxy)-3-(4-((1,3-dioxo-2-propyl-2,3-dihydro-1H-benzo[de]isoquinolin-6-yl)amino)butanamido) butan-2-yl (2-cyanoethyl) diisopropylphosphoramidite³



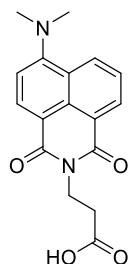
Under argon N -((2R,3R)-1-(bis(4-methoxyphenyl)(phenyl)methoxy)-3-hydroxybutan-2-yl)-4-((1,3-dioxo-2-propyl-2,3-dihydro-1H-benzo[de]isoquinolin-6-yl)amino)butanamide, (0.121 g, 0.166 mmol) was dissolved in anhydrous DCM (15 mL). DIPEA (0.09 mL, 0.499 mmol) and 2-cyanoethyl-diisopropylchlorophosphoramidite (0.04 mL, 0.199 mmol) were added and the solution left to under argon for 1 h. Methanol (1 mL) was added to quench the reaction and left to stir as before for a further 30 min. EtOAc (10 mL) was added to the remaining solution and washed with sodium hydrogen carbonate (2 x 50 mL), water (50 mL) and brine (50 mL). The organic layer was dried over $MgSO_4$, filtered and solvent removed in *vacuo*. Column chromatography on alumina (EtOAc/hexane/TEA, 69:30:1) afforded the stated product as a yellow oil (0.1526 g, 99%). 1H NMR (300 MHz, CD_3CN) δ 8.42 – 8.35 (m, 2H, Naph Ar CH), 8.24 – 8.19 (m, 1H, Naph Ar CH), 7.52 (dd, J = 8.4, 7.3 Hz, 1H, Naph Ar CH), 7.40 – 7.34 (m, 2H, DMT CH), 7.23 (ddd, J = 6.7, 4.6, 2.3 Hz, 7H, DMT CH), 7.16 – 7.10 (m, 1H, Naph Ar CH), 6.76 (tdt, J = 6.7, 5.4, 1.2 Hz, 4H, DMT CH), 6.59 (dd, J = 8.5, 2.3 Hz, 1H, NH), 4.28 – 4.21 (m, 1H, CH-O), 4.05 – 3.97 (m, 2H, N-CH₂), 3.69 (d, J = 1.3 Hz, 1H, CH), 3.55 (s, 6H, DMT O-CH₃), 3.47 (ddt, J = 13.4, 6.8, 3.2 Hz, 2H, CH₂-O), 3.41 – 3.35 (m, 2H, HN-CH₂), 3.16 – 3.07 (m, 2H, CH₂-CO), 2.50 – 2.44 (m, 2H, CH₂-CN), 2.25 (tt, J = 8.6, 5.5 Hz, 3H, CH-N, CH-N), 1.72 – 1.58 (m, 4H, CH₂, CH₂), 1.15 – 1.02 (m,

15H, $^1\text{Pr}_2\text{-N}$, 0.89 – 0.85 (m, 12H, $\text{CH}_3\text{-CH(OH)}$, CH_3). ^{31}P NMR (121 MHz, CD_3CN) δ 147.53 (P(III)), 147.15 (P(III)), 13.79 (P(V)), 7.51 (P(V)), 7.20 (P(V)).

7.2.3. Naph¹Dimethyl Synthesis

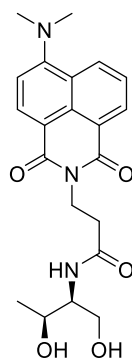


7.2.3.1. 3-(6-(dimethylamino)-1,3-dioxo-1H-benzo[de]isoquinolin-2(3H)-yl)propanoic acid⁴



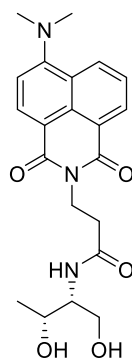
3-(6-bromo-1,3-dioxo-1H-benzo[de]isoquinolin-2(3H)-yl)propanoic acid was dissolved in DMF (6 mL). Dimethylamine (2 mL, 40% aqueous solution) and $\text{CuSO}_4 \cdot 5\text{H}_2\text{O}$ (0.04 g, 0.144 mmol) was added and the reaction mixture heated to reflux under argon and left to stir. After 3.5 h the reaction mixture was left to cool and the solvent removed in *vacuo*. Column chromatography on silica (gradient eluent system, DCM/methanol/ammonia solution, 96:3:1 to 90:9:1) afforded the stated product as an orange solid (0.84 g, 94%). ^1H NMR (300 MHz, MeOD) δ 8.59 – 8.50 (m, 2H, Naph Ar CH), 8.43 (d, J = 8.3 Hz, 1H, Naph Ar CH), 7.73 (dd, J = 8.5, 7.3 Hz, 1H, Naph Ar CH), 7.23 (d, J = 8.3 Hz, 1H, Naph Ar CH), 4.47 – 4.35 (m, 2H, N-CH₂), 3.14 (s, 6H, N(CH₃)₂), 2.69 – 2.62 (m, 2H, CH₂-COOH). MS (TOF-ESI +ve) (m/z): [M]⁺ calculated for C₁₇H₁₆N₂O₄Na, 335.10; found 335.10.

7.2.3.2. N-((2S,3S)-1,3-dihydroxybutan-2-yl)-3-(6-(dimethylamino)-1,3-dioxo-1H-benzo[de]isoquinolin-2(3H)-yl)propanamide



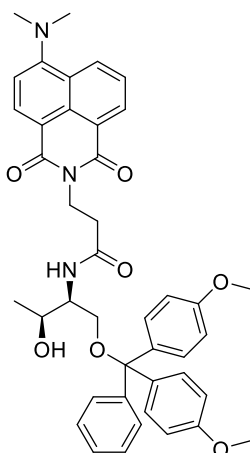
3-(6-(dimethylamino)-1,3-dioxo-1H-benzo[de]isoquinolin-2(3H)-yl)propanoic acid (0.80 g, 2.56 mmol) was dissolved in DMF (20 mL). HBTU (0.98 g, 2.58 mmol) was added and left to stir at room temperature, under argon for 15 min. D-threoninol (0.28 g, 2.62 mmol) and DIPEA (0.45 mL, 2.56 mmol) was added and reaction mixture heated to 40 °C. The solution was left to stir under argon for 71 h. The reaction mixture was allowed to cool slightly and then diluted with methanol/DCM 1:2 solution and washed with water (2 x 50 mL). Organic layer dried over MgSO₄, filtered and solvent removed in *vacuo*. Column chromatography on silica (gradient eluent system, DCM/methanol, 96:4 to 94:6) afforded the stated product as a yellow solid (0.49 g, 48%). ¹H NMR (500 MHz, MeOD) δ 8.60 – 8.48 (m, 2H, Naph Ar CH), 8.43 (d, *J* = 8.3 Hz, 1H, Naph Ar CH), 7.72 (dd, *J* = 8.5, 7.3 Hz, 1H, Naph Ar CH), 7.22 (d, *J* = 8.4 Hz, 1H, Naph Ar CH), 4.50 – 4.39 (m, 2H, N-CH₂), 3.96 (dd, *J* = 6.5, 3.5 Hz, 1H, CH), 3.79 (td, *J* = 6.1, 3.5 Hz, 1H, CH), 3.65 – 3.53 (m, 2H, CH₂-OH), 3.14 (s, 6H, N-(CH₃)₂), 2.67 (t, *J* = 7.2 Hz, 2H, CH₂-CO), 1.10 (d, *J* = 6.5 Hz, 3H, CH(OH)-CH₃). ¹³C NMR (126 MHz, MeOD) δ 173.96 (C=O), 165.85 (Naph C=O), 165.36 (Naph C=O), 158.78 (Naph Ar C), 133.83 (Naph Ar C), 132.94 (Naph Ar C), 131.99 (Naph Ar C), 131.45 (Naph Ar C), 126.24 (Naph Ar C), 125.78 (Naph Ar C), 123.76 (Naph Ar C), 115.01 (Naph Ar C), 114.13 (Naph Ar C), 66.94 (CH), 62.51 (CH₂), 57.4 (CH), 44.87 (N(CH₃)₂), 37.81 (N-CH₂), 35.60 (CH₂), 20.02 (CH(OH)-CH₃). HRMS (TOF-ESI +ve) (*m/z*): [M]⁺ calculated for C₂₁H₂₅N₃O₅Na, 422.1692; found 422.1693. IR ν_{max}/cm⁻¹ 3324.94 (NH), 2919.60 (OH), 1677.31 (C=O), 1644.35 (C=O).

7.2.3.3. N-((2R,3R)-1,3-dihydroxybutan-2-yl)-3-(6-(dimethylamino)-1,3-dioxo-1H-benzo[de]isoquinolin-2(3H)-yl)propanamide



3-(6-(dimethylamino)-1,3-dioxo-1H-benzo[de]isoquinolin-2(3H)-yl)propanoic acid (0.80 g, 0.00256 mol) was dissolved in DMF (20 mL). HBTU (0.97 g, 2.56 mmol) was added and left to stir at room temperature, under argon for 15 min. L-threoninol (0.27 g, 2.57 mmol) and DIPEA (0.45 mL, 2.56 mmol) was added and reaction mixture heated to 40 °C. The solution was left to stir under argon for 71 h. The reaction mixture was allowed to cool slightly and then diluted with methanol/DCM 1:2 solution and washed with water (2 x 50 mL). Organic layer dried over MgSO₄, filtered and solvent removed in *vacuo*. Column chromatography on silica (gradient eluent system, DCM/methanol, 96:4 to 94:6) afforded the stated product as a yellow solid (0.61 g, 60%). ¹H NMR (500 MHz, MeOD) δ 8.58 – 8.50 (m, 2H, Naph Ar CH), 8.42 (d, *J* = 8.3 Hz, 1H, Naph Ar CH), 7.72 (dd, *J* = 8.5, 7.3 Hz, 1H, Naph Ar CH), 7.22 (d, *J* = 8.3 Hz, 1H, Naph Ar CH), 4.44 (qt, *J* = 13.0, 7.2 Hz, 2H, N-CH₂), 3.97 (qd, *J* = 6.4, 3.5 Hz, 1H, CH), 3.79 (td, *J* = 6.1, 3.5 Hz, 1H, CH), 3.66 – 3.55 (m, 2H, CH₂-OH), 3.14 (s, 6H, N-(CH₃)₂), 2.67 (t, *J* = 7.2 Hz, 2H, CH₂-CO), 1.10 (d, *J* = 6.4 Hz, 3H, CH(OH)-CH₃). ¹³C NMR (126 MHz, MeOD) δ 174.13 (C=O), 166.00 (Naph C=O), 165.50 (Naph C=O), 158.93 (Naph Ar C), 133.99 (Naph Ar C), 133.10 (Naph Ar C), 132.14 (Naph Ar C), 131.60 (Naph Ar C), 126.39 (Naph Ar C), 125.94 (Naph Ar C), 123.91 (Naph Ar C), 115.16 (Naph Ar C), 114.29 (Naph Ar C), 67.11 (CH), 62.68 (CH₂), 57.58 (CH), 45.04 (N(CH₃)₂), 37.98 (N-CH₂), 35.77 (CH₂), 20.19 (CH(OH)-CH₃). HRMS (TOF-ESI +ve) (*m/z*): [M]⁺ calculated for C₂₁H₂₅N₃O₅Na, 422.1692; found 422.1691. IR ν_{\max} /cm⁻¹ 3323.81 (NH), 2919.26 (OH), 1676.97 (C=O), 1643.98 (C=O).

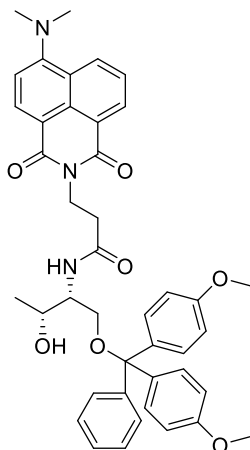
7.2.3.4. N-((2S,3S)-1-(bis(4-methoxyphenyl)(phenyl)methoxy)-3-hydroxybutan-2-yl)-3-(6-(dimethylamino)-1,3-dioxo-1H-benzo[de]isoquinolin-2(3H)-yl)propanamide^{2, 3}



N-((2S,3S)-1,3-dihydroxybutan-2-yl)-3-(6-(dimethylamino)-1,3-dioxo-1H-benzo[de]isoquinolin-2(3H)-yl)propanamide (0.20 g, 0.506 mmol) was dissolved in pyridine (15 mL). DMT-Cl (0.17 g, 0.505 mmol) and DMAP (0.01 g, 0.0859 mmol) were added and left to stir under argon at room temperature. After 19 h, the reaction mixture was poured onto water (50 mL) and product extracted with DCM (4 x 50 mL). The organic layer was dried over MgSO₄, filtered and solvent removed in *vacuo*. Column chromatography on silica (hexane/EtOAc/TEA, 10:89:1) afforded the stated product as a yellow oil (0.19 g, 55%). ¹H NMR (400 MHz, CD₃CN) δ 8.21 – 8.14 (m, 2H, Naph Ar CH), 8.03 (d, *J* = 8.2 Hz, 1H, Naph Ar CH), 7.45 – 7.35 (m, 3H, DMT CH), 7.33 – 7.20 (m, 6H, DMT CH), 7.18 – 7.10 (m, 1H, Naph Ar CH), 6.89 (d, *J* = 9.0 Hz, 1H, Naph Ar CH), 6.83 – 6.78 (m, 4H, DMT CH), 4.30 – 4.20 (m, 2H, N-CH₂), 4.00 (dt, *J* = 6.3, 4.3 Hz, 1H, CH), 3.93 (dq, *J* = 9.5, 5.2 Hz, 1H, CH), 3.68 (d, *J* = 1.1 Hz, 6H, DMT O-CH₃), 3.09 (ddd, *J* = 46.0, 9.2, 5.4 Hz, 2H, CH₂-O), 2.92 (s, 6H, N-(CH₃)₂), 2.62 (t, *J* = 7.7 Hz, 2H, CH₂-CO), 1.01 (d, *J* = 6.3 Hz, 3H, CH(OH)-CH₃). ¹³C NMR (101 MHz, CD₃CN) δ 171.92 (C=O), 164.87 (Naph C=O), 164.22 (Naph C=O), 159.48 (DMT C-O), 157.58 (Ar C), 146.19 (Ar C), 137.00 (Ar C), 136.96 (Ar CH), 132.97 (Ar CH), 132.12 (Ar CH), 131.23 (Ar CH), 130.91 (Ar CH), 130.64 (Ar C), 128.95 (Ar CH), 128.74 (Ar CH), 127.67 (Ar CH), 125.48 (Ar CH), 125.39 (Ar C), 123.37 (Ar C), 114.64 (Ar C), 113.95 (Ar CH), 113.68 (Ar CH), 86.71 (DMT C), 67.23 (CH), 64.34 (CH₂), 55.83 (O-CH₃), 55.55 (CH), 44.97 (N-(CH₃)₂), 37.56 (N-CH₂), 35.38

(CH₂), 20.55(CH(OH)-CH₃). MS (TOF-ESI +ve) (*m/z*): [M]⁺ calculated for C₄₂H₄₃N₃O₇Na, 724.30; found 724.30.

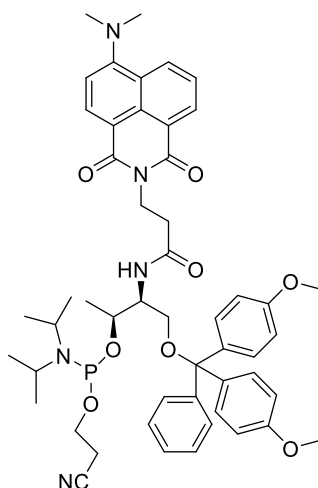
7.2.3.5. N-((2R,3R)-1-(bis(4-methoxyphenyl)(phenyl)methoxy)-3-hydroxybutan-2-yl)-3-(6-(dimethylamino)-1,3-dioxo-1H-benzo[de]isoquinolin-2(3H)-yl)propanamide^{2, 3}



N-((2R,3R)-1,3-dihydroxybutan-2-yl)-3-(6-(dimethylamino)-1,3-dioxo-1H-benzo[de]isoquinolin-2(3H)-yl)propanamide (0.20 g, 0.505 mmol) was dissolved in pyridine (15 mL). DMT-Cl (0.17 g, 0.502 mmol) and DMAP (0.01 g, 0.0917 mmol) were added and left to stir under argon at room temperature. After 20 h, the reaction mixture was poured onto water (50 mL) and product extracted with DCM (4 x 50 mL). The organic layer was dried over MgSO₄, filtered and solvent removed in *vacuo*. Column chromatography on silica (hexane/EtOAc/TEA, 10:89:1) afforded the stated product as a yellow oil (0.25 g, 71%). ¹H NMR (300 MHz, CD₃CN) δ 8.18 (ddd, *J* = 7.3, 4.8, 1.2 Hz, 2H, Naph Ar CH), 8.04 (d, *J* = 8.3 Hz, 1H, Naph Ar CH), 7.47 – 7.35 (m, 3H, DMT CH), 7.33 – 7.20 (m, 6H, DMT CH), 7.18 – 7.11 (m, 1H, Naph Ar CH), 6.87 (d, *J* = 8.9 Hz, 1H, Naph Ar CH), 6.84 – 6.78 (m, 4H, DMT CH), 4.25 (t, *J* = 7.6 Hz, 2H, N-CH₂), 4.06 – 3.89 (m, 2H, CH, CH), 3.69 (s, 6H, DMT O-CH₃), 3.10 (ddd, *J* = 34.4, 9.2, 5.4 Hz, 2H, CH₂-O), 2.93 (s, 6H, N-(CH₃)₂), 2.62 (t, *J* = 7.6 Hz, 2H, CH₂-CO), 1.01 (d, *J* = 6.2 Hz, 3H, CH(OH)-CH₃). ¹³C NMR (101 MHz, CD₃CN) δ 171.92 (C=O), 164.85 (Naph C=O), 164.20 (Naph C=O), 159.47 (DMT C-O), 157.56 (Ar C), 146.18 (Ar C), 136.99 (Ar C), 136.95 (Ar CH), 132.96 (Ar CH), 132.11 (Ar CH), 131.23 (Ar CH), 130.90 (Ar CH), 130.61 (Ar C), 128.95 (Ar CH), 128.73 (Ar CH), 127.66 (Ar CH), 125.46 (Ar CH), 125.35 (Ar C), 123.34 (Ar C), 114.61 (Ar C), 113.94 (Ar CH), 113.64 (Ar CH), 86.71 (DMT C), 67.23 (CH),

64.34 (CH₂), 55.82 (O-CH₃), 55.54 (CH), 44.96 (N-(CH₃)₂), 37.55 (N-CH₂), 35.37 (CH₂), 20.55 (CH(OH)-CH₃). MS (TOF-ESI +ve) (*m/z*): [M]⁺ calculated for C₄₂H₄₃N₃O₇Na, 724.30; found 724.30.

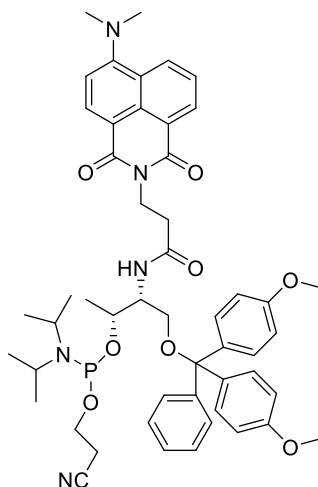
7.2.3.6. (2*S*,3*S*)-4-(bis(4-methoxyphenyl)(phenyl)methoxy)-3-(3-(6-(dimethylamino)-1,3-dioxo-1*H*-benzo[de]isoquinolin-2(3*H*)-yl)propanamido)butan-2-yl (2-cyanoethyl) diisopropylphosphoramidite³



Under argon, N-((2*S*,3*S*)-1-(bis(4-methoxyphenyl)(phenyl)methoxy)-3-hydroxybutan-2-yl)-3-(6-(dimethylamino)-1,3-dioxo-1*H*-benzo[de]isoquinolin-2(3*H*)-yl)propanamide (0.19 g, 0.268 mmol) was dissolved in anhydrous DCM (15 mL). DIPEA (0.14 mL, 0.803 mmol) and 2-cyanoethyl-diisopropylchlorophosphoramidite (0.07 mL, 0.321 mmol) were added and the solution left to under argon for 1 h. Methanol (1 mL) was added to quench the reaction and left to stir as before for a further 30 min. EtOAc (10 mL) was added to the remaining solution and washed with sodium hydrogen carbonate (2 x 50 mL), water (50 mL) and brine (50 mL). The organic layer was dried over MgSO₄, filtered and solvent removed in *vacuo*. Column chromatography on alumina (EtOAc/hexane/TEA, 69:30:1) afforded the stated product as a yellow oil (0.15 g, 61%). ¹H NMR (400 MHz, CD₃CN) δ 8.39 (dt, *J* = 8.5, 1.0 Hz, 1H), 8.34 (ddd, *J* = 7.3, 2.1, 1.1 Hz, 1H, Naph Ar CH), 8.22 (dd, *J* = 8.3, 2.9 Hz, 1H, Naph Ar CH), 7.58 (ddd, *J* = 8.3, 7.3, 0.9 Hz, 1H, Naph Ar CH), 7.42 (ddd, *J* = 8.2, 2.8, 1.8 Hz, 2H, DMT CH), 7.33 – 7.24 (m, 6H, DMT CH), 7.24 – 7.16 (m, 1H, Naph Ar CH), 7.04 (dd, *J* = 8.4, 1.2 Hz, 1H, Naph Ar CH), 6.87 – 6.80 (m, 4H, DMT CH), 6.44 (dd, *J* = 18.0, 9.1 Hz, 1H, NH), 4.31 (dddd, *J* = 13.2, 11.7, 5.7, 1.6 Hz, 2H, N-CH₂), 4.26 – 4.19 (m, 1H, CH), 4.12 (td, *J* = 6.1, 3.4 Hz, 1H, CH), 3.76 – 3.72 (m, 6H, DMT

O-CH₃), 3.53 – 3.43 (m, 2H, CH₂), 3.15 – 3.07 (m, 2H, CH₂-O), 3.04 (s, 6H, N-(CH₃)₂), 2.66 – 2.52 (m, 3H, CH₂, N-CH), 2.46 (t, *J* = 6.0 Hz, 1H, CH₂-CO), 1.13 – 1.02 (m, 12H, ¹Pr₂N), 0.94 (d, *J* = 6.8 Hz, 3H, CH(O)-CH₃). ³¹P NMR (162 MHz, CD₃CN) δ 147.49 (P(III)), 147.10 (P(III)), 7.51 (P(IV)), 6.92 (P(IV)). HRMS (TOF-ESI +ve) (*m/z*): [M]⁺ calculated for C₅₁H₆₀N₅O₈NaP, 924.4077; found 924.4075.

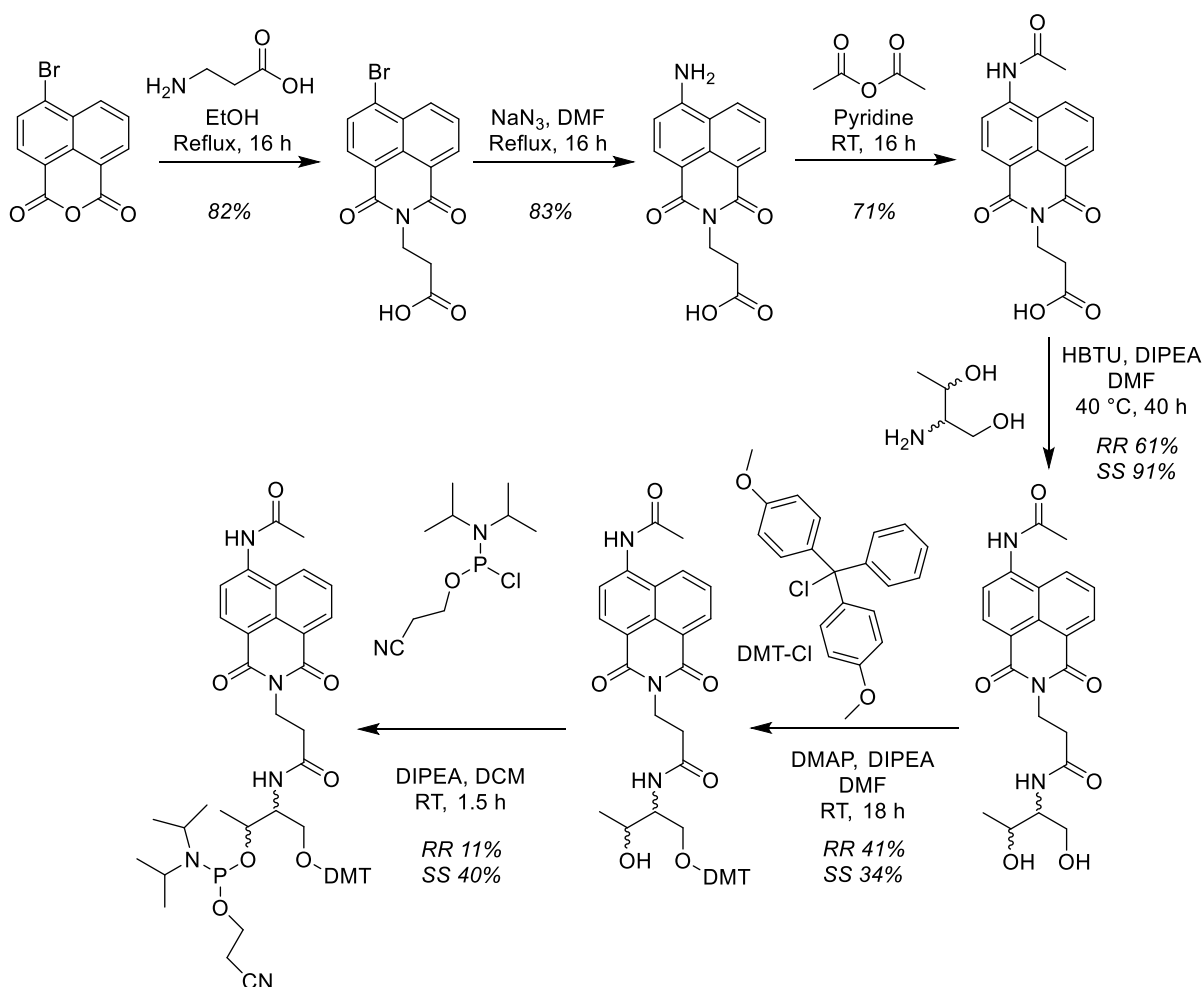
7.2.3.7. (2R,3R)-4-(bis(4-methoxyphenyl)(phenyl)methoxy)-3-(3-(6-(dimethylamino)-1,3-dioxo-1H-benzo[de]isoquinolin-2(3H)-yl)propanamido)butan-2-yl (2-cyanoethyl) diisopropylphosphoramidite³



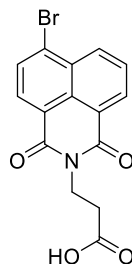
Under argon, N-((2R,3R)-1-(bis(4-methoxyphenyl)(phenyl)methoxy)-3-hydroxybutan-2-yl)-3-(6-(dimethylamino)-1,3-dioxo-1H-benzo[de]isoquinolin-2(3H)-yl)propanamide (0.16 g, 0.227 mmol) was dissolved in anhydrous DCM (15 mL). DIPEA (0.12 mL, 0.680 mmol) and 2-cyanoethyl-diisopropylchlorophosphoramidite (0.06 mL, 0.272 mmol) were added and the solution left to under argon for 1 h. Methanol (1 mL) was added to quench the reaction and left to stir as before for a further 30 min. EtOAc (10 mL) was added to the remaining solution and washed with sodium hydrogen carbonate (2 x 50 mL), water (50 mL) and brine (50 mL). The organic layer was dried over MgSO₄, filtered and solvent removed in *vacuo*. Column chromatography on alumina (EtOAc/hexane/TEA, 69:30:1) afforded the stated product as a yellow oil (0.16 g, 77%). ¹H NMR (300 MHz, CD₃CN) δ 8.46 – 8.33 (m, 2H, Naph Ar CH), 8.24 (dd, *J* = 8.2, 2.2 Hz, 1H, Naph Ar CH), 7.60 (dd, *J* = 8.5, 7.3 Hz, 1H, Naph Ar CH), 7.47 – 7.35 (m, 3H, DMT CH), 7.29 (dtd, *J* = 9.0, 3.3, 1.9 Hz, 6H, DMT CH), 7.06 (d, *J* = 8.3 Hz, 1H, Naph Ar CH), 6.84 (dq, *J* = 8.8, 3.2 Hz, 4H, DMT CH), 6.43 (dd, *J* = 13.3, 9.1 Hz, 1H, NH), 4.33 (ddt, *J* =

10.8, 7.2, 2.1 Hz, 2H, N-CH₂), 4.26 – 4.18 (m, 1H, CH), 4.14 – 4.08 (m, 1H, CH), 3.74 (d, *J* = 1.7 Hz, 6H, DMT O-CH₃), 3.54 – 3.45 (m, 2H, CH₂), 3.10 (dd, *J* = 6.4, 2.1 Hz, 2H, CH₂-O), 3.05 (s, 6H, N-(CH₃)₂), 2.59 (ddd, *J* = 15.1, 7.6, 4.6 Hz, 3H, CH₂, N-CH), 2.46 (t, *J* = 6.0 Hz, 1H, CH₂-CO), 1.12 – 1.03 (m, 12H, ⁱPr₂-N), 0.94 (d, *J* = 6.8 Hz, 3H, CH(O)-CH₃). ³¹P NMR (121 MHz, CD₃CN) δ 147.48 (P(III)), 147.09 (P(III)). HRMS (TOF-ESI +ve) (*m/z*): [M]⁺ calculated for C₅₁H₆₁N₅O₈P, 902.4258; found 902.4256.

7.2.4. Naph¹Amine Synthesis

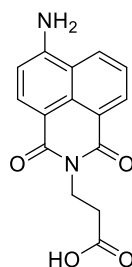


7.2.4.1. 3-(6-bromo-1,3-dioxo-1H-benzo[de]isoquinolin-2(3H)-yl)propanoic acid⁵



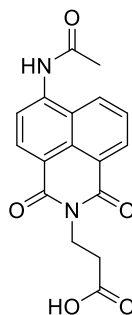
4-bromonaphthalic anhydride (2.50 g, 9.02 mmol) was dispersed in ethanol (30 mL) and 3-aminopropanoic acid (0.96 g, 10.8 mmol) was added. The solution was heated at reflux under argon overnight. The reaction mixture was left to cool and the solid filtered and washed with EtOH to give the stated product as a grey solid (2.58 g, 82%). ¹H NMR (300 MHz, DMSO-*d*₆) δ 8.50 (t, *J* = 6.8 Hz, 2H, Naph Ar CH), 8.28 (d, *J* = 7.8 Hz, 1H, Naph Ar CH), 8.17 (d, *J* = 7.8 Hz, 1H, Naph Ar CH), 7.94 (t, *J* = 7.9 Hz, 1H, Naph Ar CH), 4.18 (t, *J* = 7.7 Hz, 2H, N-CH₂), 2.52 (t, *J* = 7.7 Hz, 2H, CH₂-COOH). ¹³C NMR (101 MHz, DMSO) δ 172.54 (C=OOH), 162.88 (Naph C=O), 162.84 (Naph C=O), 132.75 (Naph Ar C), 131.66 (Naph Ar C), 131.45 (Naph Ar C), 131.05 (Naph Ar C), 129.89 (Naph Ar C), 129.21 (Naph Ar C), 128.91 (Naph Ar C), 128.42 (Naph Ar C), 122.88 (Naph Ar C), 122.10 (Naph Ar C), 35.95 (N-CH₂), 32.22 (CH₂-COOH). HRMS (TOF-ESI +ve) (*m/z*): [M]⁺ calculated for C₁₅H₁₀NO₄Na⁷⁹Br, 369.9691; found 369.9691. IR $\nu_{\max}/\text{cm}^{-1}$ 2901.42 (OH), 1697.42 (C=O), 1648.34 (C=O).

7.2.4.2. 3-(6-amino-1,3-dioxo-1H-benzo[de]isoquinolin-2(3H)-yl)propanoic acid



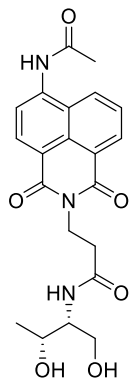
3-(6-bromo-1,3-dioxo-1H-benzo[de]isoquinolin-2(3H)-yl)propanoic acid (2.21 g, 6.36 mmol) was dissolved in DMF (20 mL). NaN_3 (0.62 g, 9.55 mmol) was added and the solution heated to reflux for 18 h under argon. The reaction mixture was left to cool and solvent removed in *vacuo*. Column chromatography on silica (DCM/methanol, 90:10) afforded the stated product as an orange solid (1.50 g, 83%). ^1H NMR (400 MHz, DMSO) δ 8.62 (d, $J = 8.4$ Hz, 1H, Naph Ar CH), 8.42 (d, $J = 7.2$ Hz, 1H, Naph Ar CH), 8.19 (d, $J = 8.4$ Hz, 1H, Naph Ar CH), 7.69 – 7.61 (m, 1H, Naph Ar CH), 7.46 (s, 2H, NH_2), 6.84 (d, $J = 8.4$ Hz, 1H, Naph Ar CH), 4.22 (dd, $J = 9.3, 6.2$ Hz, 2H, N- CH_2), 2.54 (d, $J = 8.0$ Hz, 2H, $\text{CH}_2\text{-COOH}$). HRMS (TOF-ESI +ve) (m/z): $[\text{M}]^+$ calculated for $\text{C}_{15}\text{H}_{13}\text{N}_2\text{O}_4$, 285.0875; found 285.0875. IR $\nu_{\text{max}}/\text{cm}^{-1}$ 3354.11 (NH), 3257.41 (NH), 2923.12 (OH), 1715.35 (C=O), 1650.48 (C=O).

7.2.4.3. 3-(6-acetamido-1,3-dioxo-1H-benzo[de]isoquinolin-2(3H)-yl)propanoic acid⁶



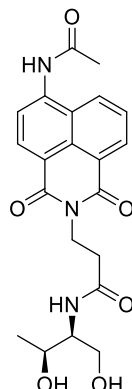
3-(6-amino-1,3-dioxo-1H-benzo[de]isoquinolin-2(3H)-yl)propanoic acid (0.64 g, 2.26 mmol) was dissolved in pyridine (30 mL) and acetic anhydride (0.43 mL, 4.50 mmol) was added. Reaction left to stir at room temperature for 16 h under argon. The solvent was removed in *vacuo*. Column chromatography on silica (DCM/methanol, 90:10) afforded the stated product as a yellow solid (0.52 g, 71%). ¹H NMR (300 MHz, DMSO) δ 10.28 (s, 1H, NH), 8.53 (d, J = 7.7 Hz, 1H, Naph Ar CH), 8.34 (dd, J = 15.5, 7.3 Hz, 2H, Naph Ar CH), 8.12 (d, J = 8.2 Hz, 1H, Naph Ar CH), 7.73 (dd, J = 8.5, 7.3 Hz, 1H, Naph Ar CH), 4.13 – 4.04 (t, J = 6, 2H, N-CH₂), 2.45 – 2.38 (t, J = 6, 2H, CH₂-COOH), 2.11 (s, 3H, CH₃). ¹³C NMR (101 MHz, DMSO) δ 173.27 (C=OOH), 170.31 (C=O), 163.86 (Naph C=O), 163.28 (Naph C=O), 140.82 (Naph Ar C), 132.03 (Naph Ar C), 131.35 (Naph Ar C), 129.96 (Naph Ar C), 128.69 (Naph Ar C), 126.85 (Naph Ar C), 124.50 (Naph Ar C), 122.52 (Naph Ar C), 119.98 (Naph Ar C), 117.82 (Naph Ar C), 36.21 (N-CH₂), 32.88 (CH₂-COOH), 24.49 (CH₃). HRMS (TOF-ESI +ve) (m/z): [M]⁺ calculated for C₁₇H₁₃N₂O₅, 369.9691; found 325.0827. IR ν_{\max} /cm⁻¹ 3406.70 (NH), 2925.87 (OH), 1697.42 (C=O), 1698.61 (C=O), 1637.00 (C=O).

7.2.4.4. (2R,3R)-1,3-dihydroxybutan-2-yl 3-(6-acetamido-1,3-dioxo-1H-benzo[de]isoquinolin-2(3H)-yl)propanoate



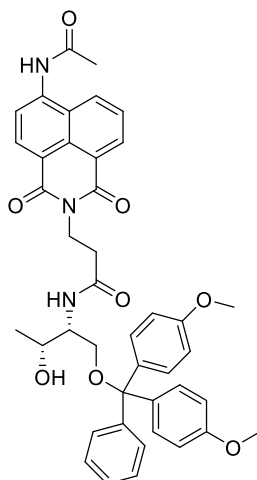
3-(6-acetamido-1,3-dioxo-1H-benzo[de]isoquinolin-2(3H)-yl)propanoic acid (0.52 g, 1.61 mmol) was dissolved in DMF (20 mL) and HBTU (0.62 g, 1.63 mmol) was added and stirred at room temperature for 15 minutes. L-threoninol (0.17 g, 1.64 mmol) and DIPEA (0.28 mL, 1.61 mmol) were added and reaction mixture heated to 40 °C and stirred under argon for 41 h. Solvent removed in *vacuo*. Column chromatography on silica (gradient eluent system, DCM/methanol, 98:2 to 90:10) afforded the stated product as a yellow solid (0.41 g, 61%). ¹H NMR (300 MHz, MeOD) δ 8.65 – 8.51 (m, 3H, Naph Ar CH), 8.22 (d, *J* = 8.1 Hz, 1H, Naph Ar CH), 7.85 (dd, *J* = 8.6, 7.3 Hz, 1H, Naph Ar CH), 4.52 – 4.42 (m, 2H, N-CH₂), 3.97 (dd, *J* = 6.5, 3.4 Hz, 1H, CH), 3.78 (dd, *J* = 6.0, 3.4 Hz, 1H, CH), 3.64 – 3.52 (m, 2H, CH₂-OH), 2.69 (t, *J* = 7.1 Hz, 2H, CH₂-CO), 2.34 (s, 3H, CH₃C=O), 1.10 (d, *J* = 6.5 Hz, 3H, CH(OH)-CH₃). ¹³C NMR (126 MHz, MeOD) δ 174.57 (C=O), 173.13 (C=O), 166.14 (Naph C=O), 165.64 (Naph C=O), 141.90 (Naph Ar C), 133.36 (Naph Ar C), 132.90 (Naph Ar C), 130.78 (Naph Ar C), 130.58 (Naph Ar C), 128.32 (Naph Ar C), 127.14 (Naph Ar C), 124.58 (Naph Ar C), 122.64 (Naph Ar C), 120.65 (Naph Ar C), 67.60 (CH), 63.17(CH₂-OH), 58.05 (CH), 38.64 (N-CH₂), 36.18 (CH₂), 24.32 (CH₃), 20.71 (CH(OH)-CH₃). HRMS (TOF-ESI +ve) (*m/z*): [M]⁺ calculated for C₂₁H₂₃N₃O₆Na, 436.1485; found 436.1492.

7.2.4.5. 3-(6-acetamido-1,3-dioxo-1H-benzo[de]isoquinolin-2(3H)-yl)-N-((2S,3S)-1,3-dihydroxybutan-2-yl)propanamide



3-(6-acetamido-1,3-dioxo-1H-benzo[de]isoquinolin-2(3H)-yl)propanoic acid (0.12 g, 0.374 mmol) was dissolved in DMF (20 mL) and HBTU (0.15 g, 0.384 mmol) was added and stirred at room temperature for 15 minutes. D-threoninol (0.06 g, 0.570 mmol) and DIPEA (0.07 mL, 0.374 mmol) were added and reaction mixture heated to 40 °C and stirred under argon for 66 h. Solvent removed in *vacuo*. Column chromatography on silica (gradient eluent system, DCM/methanol, 98:2 to 90:10) afforded the stated product as a yellow solid (0.14 g, 91%). ¹H NMR (300 MHz, MeOD) δ 8.64 – 8.51 (m, 3H, Naph Ar CH), 8.21 (d, *J* = 8.2 Hz, 1H, Naph Ar CH), 7.85 (dd, *J* = 8.6, 7.3 Hz, 1H, Naph Ar CH), 4.47 (td, *J* = 7.0, 4.2 Hz, 2H, N-CH₂), 4.01 – 3.93 (m, 1H, CH), 3.79 (tt, *J* = 6.1, 3.3 Hz, 1H, CH), 3.65 – 3.53 (m, 2H, CH₂-OH), 2.69 (t, *J* = 7.1 Hz, 2H, CH₂-CO), 2.34 (s, 3H, CH₃), 1.10 (d, *J* = 6.5 Hz, 3H, CH(OH)-CH₃). ¹³C NMR (126 MHz, MeOD) δ 174.23 (C=O), 172.78 (C=O), 165.79 (Naph C=O), 165.29 (Naph C=O), 141.56 (Naph Ar C), 133.02 (Naph Ar C), 132.56 (Naph Ar C), 130.43 (Naph Ar C), 130.23 (Naph Ar C), 127.97 (Naph Ar C), 126.77 (Naph Ar C), 124.23 (Naph Ar C), 122.28 (Naph Ar C), 120.29 (Naph Ar C), 67.26 (CH), 62.83 (CH₂-OH), 57.71 (CH), 38.29 (N-CH₂), 35.84 (CH₂), 23.99 (CH₃), 20.37 (CH(OH)-CH₃). HRMS (TOF-ESI +ve) (*m/z*): [M]⁺ calculated for C₂₁H₂₃N₃O₆Na, 436.1485; found 436.1497.

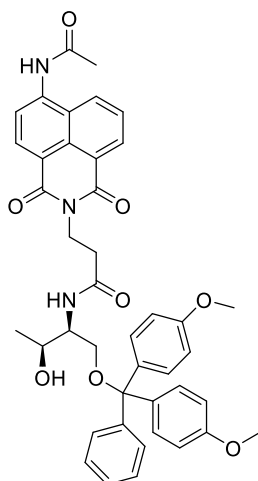
7.2.4.6. 3-(6-acetamido-1,3-dioxo-1H-benzo[de]isoquinolin-2(3H)-yl)-N-((2R,3R)-1-(bis(4-methoxyphenyl)(phenyl)methoxy)-3-hydroxybutan-2-yl)propanamide^{2,3}



3-(6-acetamido-1,3-dioxo-1H-benzo[de]isoquinolin-2(3H)-yl)-N-((2R,3R)-1,3-dihydroxybutan-2-yl)propanamide (0.15 g, 0.368 mmol) and DMAP (0.02 g, 0.124 mmol) was dissolved in DMF (10 mL). DMT-Cl (0.15 g, 0.452 mmol) and DIPEA (0.06 mL, 0.368 mmol) were added. Solution was left to stir under argon at room temperature for 18 h. Solvent was removed in *vacuo*. Column chromatography purification on silica (DCM/methanol/TEA, 97:2:1) afforded the stated product as a yellow oil (0.11 g, 41%). ¹H NMR (300 MHz, CD₃CN) δ 8.32 – 8.22 (m, 2H, Naph Ar CH), 8.18 (d, *J* = 8.2 Hz, 1H, Naph Ar CH), 8.10 – 8.02 (m, 2H, Naph Ar CH), 7.55 (dd, *J* = 8.5, 7.3 Hz, 1H, DMT Ar CH), 7.44 – 7.37 (m, 2H, DMT Ar CH), 7.30 – 7.16 (m, 6H, DMT Ar CH), 6.86 – 6.80 (m, 4H, DMT Ar CH), 6.55 – 6.50 (m, 1H, NH), 4.35 – 4.26 (m, 2H, N-CH₂), 4.02 – 3.95 (m, 1H, CH), 3.91 (m, 1H, CH), 3.73 (s, 6H, DMT O-CH₃), 3.15 – 2.97 (m, 2H, CH₂-O), 2.63 (t, *J* = 7.5 Hz, 2H, CH₂-CO), 2.27 (s, 3H, CH₃), 1.00 (d, *J* = 6.3 Hz, 4H, CH(OH)-CH₃). ¹³C NMR (101 MHz, CD₃CN) δ 171.96 (C=O), 170.87 (C=O), 164.73 (Naph C=O), 164.17 (Naph C=O), 159.55 (DMT C-O), 150.20 (Ar CH), 146.21 (Ar C), 140.81 (Ar C), 137.02 (Ar C), 132.28 (Ar CH), 131.59 (Ar CH), 130.95 (Ar CH), 130.93 (Ar CH), 129.32 (Ar CH), 129.19 (Ar CH), 128.98 (Ar CH), 128.77 (Ar CH), 127.72 (Ar CH), 127.17 (Ar CH), 124.94 (Ar C), 123.43 (Ar C), 120.24 (Ar CH), 118.89 (Ar C), 113.98 (Ar CH), 86.74 (DMT C), 67.13(CH), 64.25(CH₂), 55.87 (CH), 55.55 (CH), 39.24 (CH₃), 37.75(N-CH₂), 35.26 (CH₂), 24.65 (CH₃), 20.46 (CH(OH)-CH₃). HRMS (TOF-ESI +ve) (*m/z*): [M]⁺ calculated for C₄₂H₄₁N₃O₈Na,

738.2791; found 738.2783. IR $\nu_{\max}/\text{cm}^{-1}$ 3286.80 (NH), 2932.29 (OH), 1697.42 (C=O), 1695.13 (C=O), 1650.00 (C=O).

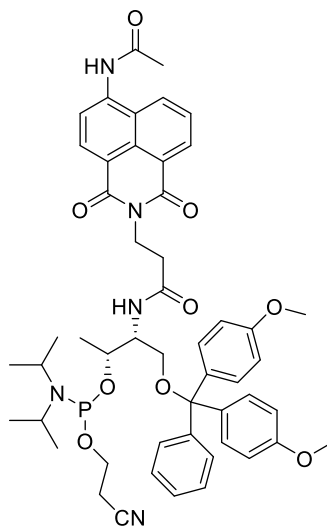
7.2.4.7. 3-(6-acetamido-1,3-dioxo-1H-benzo[de]isoquinolin-2(3H)-yl)-N-((2S,3S)-1-(bis(4-methoxyphenyl)(phenyl)methoxy)-3-hydroxybutan-2-yl)propanamide^{2,3}



3-(6-acetamido-1,3-dioxo-1H-benzo[de]isoquinolin-2(3H)-yl)-N-((2S,3S)-1,3-dihydroxybutan-2-yl)propanamide (0.13 g, 0.321 mmol) and DMAP (0.02 g, 0.129 mmol) was dissolved in DMF (10 mL). DMT-Cl (0.17 g, 0.501 mmol) and DIPEA (0.06 mL, 0.321 mmol) were added. Solution was left to stir under argon at room temperature for 18 h. Solvent was removed in *vacuo*. Column chromatography purification on silica (DCM/methanol/TEA, 97:2:1) afforded the stated product as a yellow oil (0.08 g, 34%). ¹H NMR (400 MHz, CD₃CN) δ 9.07 (s, 1H, OH), 8.21 (dd, $J = 7.6, 3.0$ Hz, 2H, Naph Ar CH), 8.11 (d, $J = 8.2$ Hz, 1H, Naph Ar CH), 8.01 (d, $J = 8.2$ Hz, 1H, Naph Ar CH), 7.53 – 7.45 (m, 1H, DMT Ar CH), 7.45 – 7.38 (m, 2H, DMT Ar CH), 7.29 – 7.17 (m, 6H, DMT Ar CH), 6.82 (dd, $J = 8.9, 1.4$ Hz, 4H, DMT Ar CH), 6.52 (d, $J = 5.3$ Hz, 1H, NH), 4.28 (dd, $J = 8.4, 6.7$ Hz, 2H, N-CH₂), 3.98 (qd, $J = 6.3, 3.9$ Hz, 1H, CH), 3.94 – 3.86 (m, 1H, CH), 3.72 (s, 6H, DMT O-CH₃), 3.06 (ddd, $J = 39.9, 9.2, 5.5$ Hz, 2H, CH₂-O), 2.63 (t, $J = 7.5$ Hz, 2H, CH₂-CO), 2.27 (s, 3H, CH₃), 1.00 (d, $J = 6.3$ Hz, 3H, CH(OH)-CH₃). ¹³C NMR (101 MHz, CD₃CN) δ 172.00 (C=O), 170.89 (C=O), 164.67 (Naph C=O), 164.11 (Naph C=O), 159.54 (DMT C-O), 149.95 (Ar CH), 146.20 (Ar C), 140.75 (Ar C), 137.01 (Ar C), 132.23 (Ar CH), 131.55 (Ar CH), 130.95 (Ar CH), 130.92 (Ar CH), 129.23 (Ar CH), 129.14 (Ar CH), 128.97 (Ar CH), 128.77 (Ar CH), 127.72 (Ar CH), 127.12 (Ar CH),

124.86 (Ar C), 123.33 (Ar C), 120.19 (Ar CH), 118.80 (Ar C), 113.97 (Ar CH), 86.74 (DMT C), 67.14 (CH), 64.26 (CH₂), 55.86 (CH), 55.57 (CH), 39.26 (CH₃), 37.74 (N-CH₂), 35.25 (CH₂), 24.66 (CH₃), 20.47 (CH(OH)-CH₃). HRMS (TOF-ESI +ve) (*m/z*): [M]⁺ calculated for C₄₂H₄₁N₃O₈Na, 738.2791; found 738.2782.

7.2.4.8. (2R,3R)-3-(3-(6-acetamido-1,3-dioxo-1H-benzo[de]isoquinolin-2(3H)-yl)propanamido)-4-(bis(4-methoxyphenyl)(phenyl)methoxy)butan-2-yl (2-cyanoethyl) diisopropylphosphoramidite³

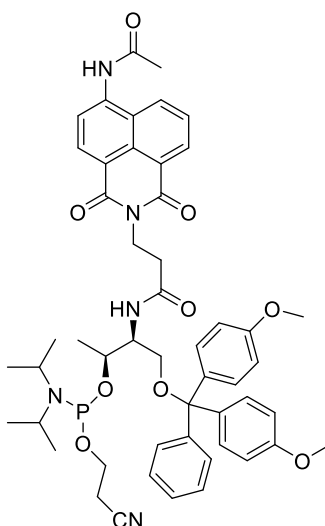


3-(6-acetamido-1,3-dioxo-1H-benzo[de]isoquinolin-2(3H)-yl)-N-((2R,3R)-1-(bis(4-methoxyphenyl)(phenyl)methoxy)-3-hydroxybutan-2-yl)propanamide (0.11 g, 0.152 mmol) was dissolved in anhydrous DCM (10 mL). DIPEA (0.08 mL, 0.456 mmol) and 2-cyanethyl-diisopropylchlorophosphoramidite (0.04 mL, 0.183 mmol) were added and the solution left to stir under argon. After 1.5 h, methanol (1 mL) was added to quench the reaction and left to stir for a further 30 min under argon. EtOAc (10 mL) was added to the reaction mixture and washed with sodium hydrogen carbonate (2 x 50 mL), water (50 mL) and brine (50 mL). The organic layer was dried over MgSO₄, filtered and solvent removed in *vacuo*. Column chromatography on alumina (hexane/EtOAc/TEA, 15:84:1) afforded the stated product as a yellow oil (0.02 g, 11%). ¹H NMR (300 MHz, CD₃CN) δ 8.92 (s, 1H, OH), 8.44 – 8.14 (m, 5H Naph Ar CH), 7.75 – 7.64 (m, 1H, DMT Ar CH), 7.45 – 7.37 (m, 3H, DMT Ar CH), 7.30 – 7.23 (m, 7H, DMT Ar CH), 6.86 – 6.82 (m, 4H, DMT Ar CH), 4.37 – 4.29 (m, 2H, N-CH₂), 4.11 – 3.99 (m, 2H, CH, CH), 3.74 (d, *J* = 1.2 Hz, 6H, DMT O-CH₃), 3.50 (d, *J* = 5.3 Hz, 2H, CH₂), 3.13 – 2.99 (m, 2H, CH₂-O), 2.69 – 2.53 (m, 4H, CH₂-CN,

N-CH, N-CH), 2.46 (t, $J = 5.9$ Hz, 1H, CH₂-CO), 2.29 (s, 3H, CH₃), 1.27 – 1.01 (m, 15H, ¹Pr₂N, CH(O)-CH₃).

³¹P NMR (121 MHz, CD₃CN) δ 147.49 (P(III)), 147.09 (P(III)), 7.55 (P(IV)), 7.50 (P(IV)), 6.98 (P(IV)).

7.2.4.9. (2S,3S)-3-(3-(6-acetamido-1,3-dioxo-1H-benzo[de]isoquinolin-2(3H)-yl)propanamido)-4-(bis(4-methoxyphenyl)(phenyl)methoxy)butan-2-yl (2-cyanoethyl) diisopropylphosphoramidite³



3-(6-acetamido-1,3-dioxo-1H-benzo[de]isoquinolin-2(3H)-yl)-N-((2S,3S)-1-(bis(4-methoxyphenyl)(phenyl)methoxy)-3-hydroxybutan-2-yl)propanamide (0.11 g, 0.152 mmol) was dissolved in anhydrous DCM (10 mL). DIPEA (0.08 mL, 0.456 mmol) and 2-cyanethyl-diisopropylchlorophosphoramidite (0.04 mL, 0.183 mmol) were added and the solution left to stir under argon. After 1.5 h, methanol (1 mL) was added to quench the reaction and left to stir for a further 30 min under argon. EtOAc (10 mL) was added to the reaction mixture and washed with sodium hydrogen carbonate (2 x 50 mL), water (50 mL) and brine (50 mL). The organic layer was dried over MgSO₄, filtered and solvent removed in *vacuo*. Column chromatography on silica (DCM/methanol/ammonia solution, 97:2:1) afforded the stated product as a yellow oil (0.05 g, 40%). ¹H NMR (300 MHz, CD₃CN) δ 8.96 (s, 1H, OH), 8.34 (dd, $J = 7.6$, 2.3 Hz, 2H, Naph Ar CH), 8.27 (dd, $J = 8.2$, 3.5 Hz, 1H, Naph Ar CH), 8.16 (dd, $J = 8.2$, 1.3 Hz, 1H, Naph Ar CH), 7.64 (td, $J = 7.8$, 1.4 Hz, 1H, DMT Ar CH), 7.41 (dq, $J = 6.4$, 1.7 Hz, 2H, DMT Ar CH), 7.27 (ddd, $J = 8.8$, 3.6, 2.2 Hz, 6H, DMT Ar CH), 6.89 – 6.81 (m, 4H, DMT Ar CH), 6.56 – 6.46 (m, 1H, NH), 4.39 – 4.28 (m, 2H, N-CH₂), 4.23 – 4.10 (m, 2H, CH, CH), 3.74 (s, 6H, DMT O-CH₃), 3.54 – 3.45 (m, 2H, CH₂), 3.07 (q,

$J = 5.4, 4.7$ Hz, 2H, $\text{CH}_2\text{-O}$), 2.69 – 2.51 (m, 4H, $\text{CH}_2\text{-CN}$, N-**CH**, N-**CH**), 2.46 (t, $J = 6.0$ Hz, 1H, $\text{CH}_2\text{-CO}$), 2.29 (s, 3H, CH_3), 1.24 – 1.03 (m, 16H, $^1\text{Pr}_2\text{N}$, CH(O)-CH_3). ^{31}P NMR (121 MHz, CD_3CN) δ 147.49 (P(III)), 147.10 (P(III)), 13.86 (P(IV)), 9.56 (P(IV)), 7.50 (P(IV)).

7.3. [DNA Synthesis](#)

Oligos were synthesised using solid-phase DNA synthesis performed on an Applied Biosystems ABI 394 DNA/RNA synthesiser. All modified probe strands were synthesised using Ultramild DNA synthesis methods, whilst all unmodified target strands were synthesised using standard DNA synthesis methods.

7.3.1. Standard Synthesis – Unmodified DNA

Phosphoramidites (Bz-dA, iBu-dG, Ac-dC, and dT) were purchased from Link Technologies and dissolved in anhydrous acetonitrile to 0.1 M prior to synthesis. Synbase CPG 1000/110 solid supports were purchased from Link Technologies. Oligos were synthesised on the solid supports at a 1 μmol scale. Activation of phosphoramidites was achieved with 5-ethylthio-1H-tetrazole (0.5 M) in acetonitrile. Subsequent coupling occurred with a coupling time of 25 seconds for nucleosides. Capping of unreacted material was achieved using acetic anhydride and methylimidazole followed by oxidation of the phosphotriester using iodine (0.1 M) in THF/pyridine/water (78:20:2). Following completion of sequence synthesis, strands were cleaved from the resin by treating with aqueous ammonia (30% solution) for 1 hour. To fully deprotect, oligos were heated in aqueous ammonia (30% solution) at 60 $^\circ\text{C}$ for 6 hours followed by removal of solvent on a Thermo Scientific speed vac.

7.3.2. Ultramild Synthesis - Modified Probe DNA

Phosphoramidites (Pac-dA, iPr-Pac-dG, Ac-dC, dT) were purchased from Link Technologies and 1,8-naphthalimide phosphoramidites were also used for ultramild synthesis. All phosphoramidites were dissolved in anhydrous acetonitrile to 0.1 M prior to synthesis. Synbase CPG 1000/110 solid supports

were purchased from Link Technologies. Oligos were synthesised on the solid supports at a 1 μ mol scale. Activation of phosphoramidites was achieved with 5-ethylthio-1H-tetrazole (0.25 M) in acetonitrile. Subsequent coupling occurred with a coupling time of 25 seconds for nucleoside phosphoramidites and 10 seconds for 1,8-naphthalimide phosphoramidites. For low yielding 1,8-naphthalimide coupling steps, the coupling time was increased to 15 min. Capping of unreacted material was achieved using phenoxyacetic anhydride and methylimidazole followed by oxidation of the phosphotriester using iodine (0.02 M) in THF/pyridine/water (7:2:1). Following completion of sequence synthesis, strands were cleaved from the resin and deprotected by placing resin in 1 mL potassium carbonate (0.05 M) in methanol and left overnight. Resulting solutions were neutralised with acetic acid (6 μ L) and solvent removed on a Thermo Scientific speed vac. The remaining dry solid was dissolved in 1 mL ultra-pure (Milli-Q) water and desalted using a NAP-10 column (GE Healthcare) prior to purification.

7.4. [DNA Purification](#)

Semi-preparative reversed-phase HPLC purification of all oligos was performed on an Agilent Technologies 1260 Infinity system using a Phenomenex Clarity 5 μ M Oligo-RP LC 250x10 mm column. 0.1 M triethylammonium acetate buffer was used with an increasing acetonitrile gradient depending on the method used. All unmodified oligonucleotides and 1,8-naphthalimide modified oligonucleotides were purified using HPLC method 1, shown in Table 7.1, and all anthracene modified probes were purified using HPLC method 2, shown in Table 7.2. Each sample run had a flow rate of 3 mL/min and 1 μ L of sample was injected for each run. The UV-Vis absorbance was monitored at 260 nm for all oligos and additionally at 430 nm for probes containing naphthalimide. Fractions collected were evaporated to dryness and dissolved in 1 mL ultra-pure (Milli-Q) water. Collected sample was then desalted using a NAP-10 column (GE Healthcare). The purity of the collected oligo sample was determined by analytical HPLC on an Agilent Technologies 1260 Infinity system using a Phenomenex Clarity 5 μ M Oligo RP LC 250x4.6 mm column. The solvent gradients used were identical to that used

via semi-preparative methods but with each run at a flow rate of 1 mL/min with a 20 μ L sample injection. The UV-Vis absorbance was monitored at 260 nm for all oligos and additionally at 430 nm for naphthalimide-modified probes or 320 nm for any anthracene-modified probes. Samples with purity over 95% were acceptable for use.

Table7.1: HPLC method 1.

Time /min	% 0.1M triethylammoniumn buffer	% acetonitrile
0	95	5
25	82	18
30.0	0	100
40	0	100
40.1	95	5
45	95	5

Table7.2: HPLC method 2.

Time /min	% 0.1M triethylammoniumn buffer	% acetonitrile
0	85	15
30	75	25
30.1	0	100
40	0	100
40.1	85	5
45	85	5

7.5. [DNA Characterisation](#)

Oligonucleotide samples were characterised using negative mode electrospray mass spectrometry on a Waters Xevo G2-XS. Sample concentrations were determined by optical density at 260 nm using a BioSpecnano micro-volume UV-Vis spectrophotometer (nanodrop) from Shimadzu. Predicted molar extinction coefficients of oligonucleotides were calculated using the IDT OligoAnalyser tool.⁷ Calculated masses of modified oligonucleotides were obtained using ChemDraw (using the exact mass

value). Calculated masses of unmodified oligonucleotides were calculated using the IDT OligoAnalyser tool.⁷

7.6. Naphthalimide Duplex Sensing

7.6.1. Duplex Annealing Conditions

Probe and target strands in aqueous solution of 100 mM NaCl, 10 mM sodium phosphate buffer, pH 7.0 in Milli-Q water were combined. Strands heated to 95 °C and left to cool slowly to room temperature over 30 min to 1 h.

7.6.2. Fluorescence Sensing Parameters

Fluorescence sensing for naphthalimide systems were carried out on Jasco FP-8500 spectrofluorometer using a 50 µL quartz fluorescence cuvette. Parameters listed below.

Excitation wavelength: 450 nm

Data Interval: 1 nm

Scan speed: 200 nm/min

Bandwidth: 5 nm

Sensitivity: Medium

Temperature control: 25 °C

7.6.3. Duplex Melting Temperatures

Duplex melting temperatures determined using SYBR Green. Aqueous probe (10 µM) and target DNA (10 µM) in NaCl (100 mM) and sodium phosphate buffer (10 mM, pH 7.0) (Milli-Q) samples were prepared. 19 µL of sample was added to 1 µL of 20 x SYBR Green dye from Bio-Rad. The thermal melting experiment was carried out on a M550 double beam scanning UV-visible spectrophotometer with a temperature controlled 96-well plate. Samples were heated from 15 °C to 90 °C and cooled from 90 °C

to 20 °C at a rate of 1 °C/min. Melt curves were produced, and T_m values taken from the maxima of the negative first derivative of the melting curve.

7.7. Fluorescent Nucleic Acid Assay for the Detection and Quantification of the BRAF V600E Mutation

7.7.1. Duplex Annealing Conditions

Probe and target strands in aqueous solution of 100 mM NaCl, 10 mM sodium phosphate buffer, pH 7.0 in Milli-Q water were combined. Strands left in the dark at room temperature for 5 min to anneal.

7.7.2. Fluorescence Sensing Parameters

Fluorescence sensing for anthracene systems were carried out on Jasco FP-8500 spectrofluorometer using a 50 µL quartz fluorescence cuvette. Samples kept in the dark. Parameters detailed below.

Excitation wavelength: 350 nm

Data Interval: 1 nm

Scan speed: 200 nm/min

Bandwidth: 5 nm

Sensitivity: High

Temperature control: 25 °C

7.7.3. DNA Extraction

Colorectal cell lines (HT-29 (ATCC® HTB-38™) and HCT 116 (ATCC® CCL-247™)) were donated by Dr Andrew Beggs, University of Birmingham.

DNA was extracted from the cultured cells using QIAGEN DNeasy® Blood and Tissue Kit. Procedure followed as per kit instructions without modification. DNA eluted in 200 µL AE buffer.

7.7.4. PCR Amplification

PCR amplification was performed using QIAGEN Multiplex PCR Kit or New England BioLabs Phusion® High-Fidelity PCR Kit on a BioRad C1000 Touch Thermal Cycler. All PCR reagents were thawed and prepared on ice.

7.7.4.1. QIAGEN Multiplex PCR Kit

The PCR reaction mixture included WT or Mut genomic DNA (between 2-200 ng), forward and reverse primers (at a final concentration of 0.2 μ M), 2 x QIAGEN Master Mix (25 μ L), 5 x Q-solution (10 μ L) made up to a final volume of 50 μ L with RNase free water.

The PCR cycling conditions were as follows (several conditions were attempted, as shown by conditions in brackets[]):

1. Heat activation: 15 min at 95 °C
 2. Denaturation: 20 [30] sec at 94 °C
 3. Annealing: 30 [90] sec at 50 °C [57 °C]
 4. Extension: 30 [90] sec at 72 °C
- Steps 2-4 repeated 38 times, cycling.

5. Final Extension: 5 [10] min 72 °C
6. Hold: ∞ at 4 °C

7.7.4.2. New England BioLabs Phusion® High-Fidelity PCR Kit

The PCR mixture included WT or Mut genomic DNA (between 2-200 ng), forward and reverse primers (at a final concentration of 0.5 μ M), 5 x Phusion® HF Buffer (10 μ L), 10 mM dNTPs (1 μ L), Phusion® DNA polymerase (0.5 μ L) made up to a final volume of 50 μ L with RNase free water. Phusion DNA polymerase was the last component to be added.

The PCR cycling conditions were as follows:

1. Heat activation: 30 sec at 98 °C
2. Denaturation: 10 sec at 98 °C
3. Annealing: 30 sec at 61 °C
4. Extension: 43 sec at 72 °C

Steps 2-4 repeated 35 times, cycling.

5. Final extension: 10 min at 72 °C
6. Hold: ∞ at 4 °C

7.7.5. DNA Clean and Purification

DNA clean and purification steps were performed after PCR amplification and after T7 exonuclease digestion steps.

Post PCR amplification, the ZYMO Research DNA Clean and Concentrator™ Kit was used. The method was followed as per kit protocol without modification. DNA was eluted in 15 µL elution buffer.

Post T7 exonuclease digestion, the Monarch® PCR and DNA Cleanup Kit was used. The method was followed as per oligonucleotide clean-up protocol without modification. DNA was eluted in 15 µL nuclease free water.

7.7.6. T7 Exonuclease Digestion

The double-stranded PCR product was digested to single-stranded DNA so that fluorescence sensing experiments can be carried out. This was achieved by the use of phosphorothioate primers used during PCR amplification steps. Strands formed from these phosphorothioate primers are not recognised by the exonuclease and therefore remain intact during the digestion step, forming the target strands for sensing. The complementary strand formed from the unmodified primers is digested by the exonuclease. The T7 exonuclease was purchased from New England BioLabs. The reaction included 10 x NEBuffer 4 (5 µL), T7 exonuclease (1 µL), DNA (PCR product at varied concentrations not exceeding

1 µg) made up to 50 µL with nuclease free water. The reaction mixture was incubated at 25 °C for 30 min. the reaction was then stopped *via* the addition of EDTA (to 11 mM).

7.7.7. TapeStation DNA Electrophoresis

TapeStation (Agilent Technologies) analysis was performed by the Genomics Centre at The University of Birmingham. The DNA High Sensitivity D1000 ScreenTape was used to determine if the PCR amplification had been successful. 2 µL sample or ladder and 2 µL of Buffer loaded into each lane.

7.7.8. QuBit DNA Quantification

All DNA concentrations were performed using QuBit Fluorometric Quantification (ThermoFisher).

For double-stranded DNA, the High Sensitivity DNA assay was used. For single-stranded DNA, the ssDNA assay was used. Samples were prepared as stated in the protocol. Standards (S1 and S2) were used prior to each use for calibration and a stranded was tested to ensure the dye mix had been correctly made.

7.7.9. Polyacrylamide Gel Electrophoresis (PAGE)

8% polyacrylamide gel was prepared by combing 8 mL polyacrylamide (40%), 8 mL 5 x TBE buffer, 300 µL APS and 30 µL TEMED. The gel was left to set for around 30 min. the gel was then pre-run in 1 x TBE buffer at 100 V in the fridge for around 20 min. The gel was then loaded: Lanes 3 and 6 contained 6 µL Hyperladder (BioLine) 25 bp; lane 4 contained 1 uL Gel Loading dye, 6X (New England BioLabs), 4 µL PCR product, 2 µL Milli-Q water; lane 5 contained 1 uL Gel Loading dye, 6X (New England BioLabs), 1 µL ssDNA from exonuclease digestion, 2 µL Milli-Q water. The loaded gel was run in 1 x TBE buffer at 100 V in the fridge for 1 h 15 min. The gel was stopped and stained using Diamond nucleic acid stain for 10 min, shaking.

7.8. Naphthalimide Modified Nucleic Acid Probes for Use in Imaging Techniques

7.8.1. Fluorescence In Situ Hybridisation

7.8.1.1. Sample Preparation

Slides were kindly donated and prepared by the Birmingham Women's NHS Foundation Trust. Slides contain fixed patient samples from anonymised 46 XX/XY white blood cell suspensions. Slides contain a mixture of metaphases and interphases.

7.8.1.2. Probe Hybridisation

Prior to hybridisation, 50 mL denaturation solution (0.07 M NaOH, 70% formamide) was heated to 72 °C. The fixed patient sample slides were placed in denaturation solution for 2 min at 72 °C. The fixed patient sample slides were then placed in a dehydration series of 70% methanol, 85% methanol, 100 % methanol for 2 min each (room temp). the samples were removed from the dehydration series and briefly left to air dry. 5 µL of probe (roughly 75 ng DNA) was combined with 5 µL hybridisation buffer (6 mM NaOH, 30-70% formamide, 20 % dextran sulfate) and 1 µL COT-1. The entire mixture was applied to the slide. A coverslip was placed over the slide and any air bubbles removed. The slide was then left to hybridise at 37 °C for 15 min.

7.8.1.3. Wash Steps

Following hybridisation, the coverslip was removed. Slides were washed at high stringency (0.4X SSC, 0.3% IGEPAL, room temp) for 2-5 min, followed by low stringency (2X SSC, 0.1% IGEPAL, room temp). samples were left to briefly air dry.

7.8.1.4. Staining

7.5-10 μL nuclear stain in mountant was applied to each slide as a counterstain (DAPI, ex 358 nm/em 461 nm; GelRed[®], ex 510 nm/em 600 nm; TOTO[™]-3, ex 642 nm/em 660 nm, were used). A coverslip was placed on top and any air bubbles removed.

7.8.1.5. Imaging Slides

Samples were imaged using an inverted epifluorescence microscope equipped with a 100X objective lens (Nikon, 1.49/oil TIRF) and cooled EMCCD camera (Photometrics, Evolve[®] 512 Delta). Excitation lasers (Coherent, OBIS) were used at wavelengths corresponding to the dye being visualised.

Images were analysed using FUJI Image J.

7.8.2. DNA PAINT

7.8.2.1. Buffer Components

- Imaging Buffer; X mM MgCl_2 , 5 mM Tris HCl (pH 8.0), 1 mM EDTA, 0.05% Tween 20.
- Buffer B; 10 mM MgCl_2 , 5 mM Tris HCl (pH 8.0), 1 mM EDTA, 0.05% Tween 20.

All stock solutions were made up in buffer B solution.

7.8.2.2. Sample Preparation for Preliminary DNA PAINT Experiment

CoverWell[™] perfusion chambers were fixed to borosilicate glass coverslips which had been placed in a furnace (~ 400 °C) prior to use to reduce any surface contamination. CoverWell[™] perfusion chambers allow for the easy addition and removal of reagents up to 40 μL in volume.

The following reagents (40 μL) were sequentially added to the chamber; BSA: BSA-biotin (20:1, Sigma Aldrich), NeutrAvidin (Thermo Scientific, 0.2 mg mL^{-1}), biotinylated DNA (500 pM). Incubation times proceeded each step; 15 minutes after addition of BSA: BSA-biotin and then 10 minutes after every

other step. Wash steps also proceeded every step to remove any unbound solution; 2 x 40 μL buffer B. The imager strand (5 nM in imaging buffer, 100 mM MgCl_2) was then added to the chamber. The prepared coverslip slide was then placed on the objective lens with the CoverWell™ chamber in place above with the coverslip side down.

7.8.2.3. Sample Preparation for DNA PAINT Experiments Using Origami Triangle

CoverWell™ perfusion chambers were fixed to borosilicate glass coverslips which had been placed in a furnace (~ 400 °C) prior to use to reduce any surface contamination. CoverWell™ perfusion chambers allow for the easy addition and removal of reagents up to 40 μL in volume.

Prior to sample preparation, biotinylated poly A strands were annealed to poly T anchor sites on the origami triangle. This biotinylated annealed origami structure was added to the sample as one.

The following reagents (40 μL) were sequentially added to the chamber; BSA: BSA-biotin (20:1, Sigma Aldrich), NeutrAvidin (Thermo Scientific, 0.2 mg mL^{-1}), origami triangle with biotinylated DNA pre-annealed (2 ng/ μL). Incubation times proceeded each step; 15 minutes after addition of BSA: BSA-biotin and then 10 minutes after every other step. Wash steps also proceeded every step to remove any unbound solution; 2 x 40 μL buffer B. The imager strand (5-100 nM in imaging buffer, 75 mM MgCl_2) was then added to the chamber. The prepared coverslip slide was then placed on the objective lens with the CoverWell™ chamber in place above with the coverslip side down.

7.8.2.4. Optical Set-Up for DNA PAINT Imaging and Imaging Parameters

Samples were imaged using an epifluorescence microscope equipped with a 100x objective lens (Nikon, 1.49/oil TIRF) and cooled EMCCD camera (Photometrics, Evolve® 512 Delta). Sample excitation was achieved using a 488 nm laser (Coherent, OBIS) for the naphthalimide imager strands and ATTO 488 labelled imager strands. The samples were imaged under the following conditions: 1000-8000

frames (depending on sample type), 60 ms exposure, 50 mW laser power, EM gain set to 100, TIRF angle $\sim 3^\circ$.

7.8.2.5. Data Analysis

Data analysis was performed using Igor Pro and localisation images were achieved using the Localizer software. The super-resolution image was displayed as both a density scatter plot and a bitmap image. The super-resolution images map the positions of each localisation across all frames (of equal position and dimensions) onto a single plot. The generalised likelihood ratio test (GLRT) algorithm was used to separate the pixels into signal and background. The GLRT insensitivity was adjusted depending on the emission intensity within each sample so that both low and bright emitters are detected. Gaussian fitting was used as the localisation algorithm so that each signal position is localised in the frame according to the coordinates of the maxima obtained from the gaussian plot.

7.9. References

1. K. N. Oliveira, P. Costa, J. R. Santin, L. Mazzambani, C. Burger, C. Mora, R. J. Nunes and M. N. Souza, *Bioorg. Med. Chem*, 2011, **19**, 4295-4306.
2. A. Pike, L. C. Ryder, B. R. Horrocks, W. Clegg, M. R. J. Elsegood, B. A. Connolly and A. Houlton, *Chem. Eur. J.* , 2002, **8**, 2891-2899.
3. N. Moran, PhD Thesis, University of Exeter, 2006.
4. K. J. Kilpin, C. M. Clavel, F. Edafe and P. J. Dyson, *Organometallics*, 2012, **31**, 7031-7039.
5. Q. Zeng, Q. Guo, Y. Yuan, Y. Yang, B. Zhang, L. Ren, X. Zhang, Q. Luo, M. Liu, L.-S. Bouchard and X. Zhou, *Anal. Chem.*, 2017, **89**, 2288-2295.
6. J. C. Kim, M. Kim, J. Jung, J. Lee, B. J. Ree, H. Kim, I. J. Kim, J. R. Kim and M. Ree, *J. Polym. Sci., Part A: Polym. Chem.*, 2015, **53**, 1151.
7. Oligo Analyzer, <https://eu.idtdna.com/calc/analyzer>, 2020.

8. Appendix

8.1. DNA Synthesis, Purification, Characterisation and Quantification

8.1.1. Oligonucleotide Mass Spectrometry Results

Table 8.1: Summary of the oligonucleotide sequences synthesised, their masses and molar extinction coefficients, ϵ .

Name	Modification (X)	Sequence 5' → 3'	Calculated Mass (g mol ⁻¹)	Mass Found (m/z)	ϵ /L mol ⁻¹ cm ⁻¹
P1AL	L Naph ^A _{Short}	TGG ACT CXC TCA ATG	4642.84	4642.8	137361
P1AD	D Naph ^A _{Short}	TGG ACT CXC TCA ATG	4642.84	4642.5	137727
P1BL	L Naph ^A _{Long}	TGG ACT CXC TCA ATG	4725.91	4726.02	136174
P1BD	D Naph ^A _{Long}	TGG ACT CXC TCA ATG	4725.91	4726.03	135815
P1CL	L Naph ^I _{Dimethyl}	TGG ACT CXC TCA ATG	4697.88	4698.0	138678
P1CD	D Naph ^I _{Dimethyl}	TGG ACT CXC TCA ATG	4697.88	4697.98	136733
P1DL	L Naph ^I _{Amine}	TGG ACT CXC TCA ATG	4669.85	4669.96	140536
P1DD	D Naph ^I _{Amine}	TGG ACT CXC TCA ATG	4669.85	4670.00	141083
P1	-	TGG ACT CGC TCA ATG	4568	4567.75	139400
P2AL	L Naph ^A _{Short}	AGA TTT CXC TGT AGC	4655.86	4655.74	141461
P2AD	D Naph ^A _{Short}	AGA TTT CXC TGT AGC	4655.86	4656.80	141827
P2Anth	Anthracene 5L	AGA TTT CXC TGT AGC	4708.91	4708.95	185444
P2	-	AGA TTT CAC TGT AGC	4567	4564.84	146400
T1G	-	CAT TGA GGG AGT CCA	4617.1	4617.0	150800
T1A	-	CAT TGA GAG AGT CCA	4601.1	4600.9	153900
T1C	-	CAT TGA GCG AGT CCA	4577	4576.6	147300

T1T	-	CAT TGA GTG AGT CCA	4592	4591.8	149400
T1MM	-	CAT TGA GAA AGT CCA	4585.1	4587.5	154600
T1mC	-	CAT TGA GmCG AGT CCA	4591.06	4591.0	147300
T2WT	-	GCT ACA GTG AAA TCT	4576	4573.93	148500
T2Mut	-	GCT ACA GAG AAA TCT	4585.1	4582.95	153000

8.1.2. Purified Oligonucleotide HPLC Traces

8.1.2.1. Unmodified Oligonucleotides

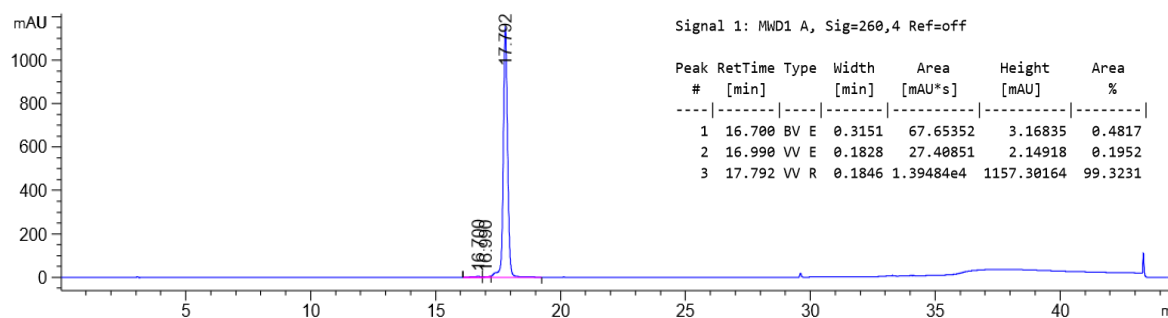


Figure 8.1: HPLC trace of purified T1C oligonucleotide. Detection wavelength is 260 nm for DNA.

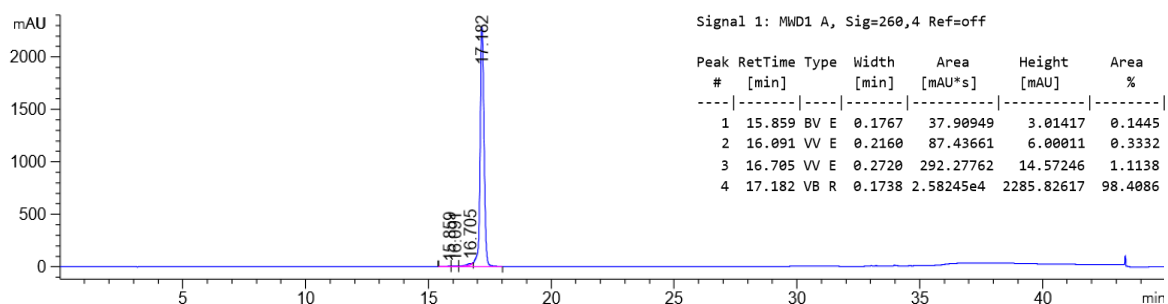


Figure 8.2: HPLC trace of purified T1G oligonucleotide. Detection wavelength is 260 nm for DNA.

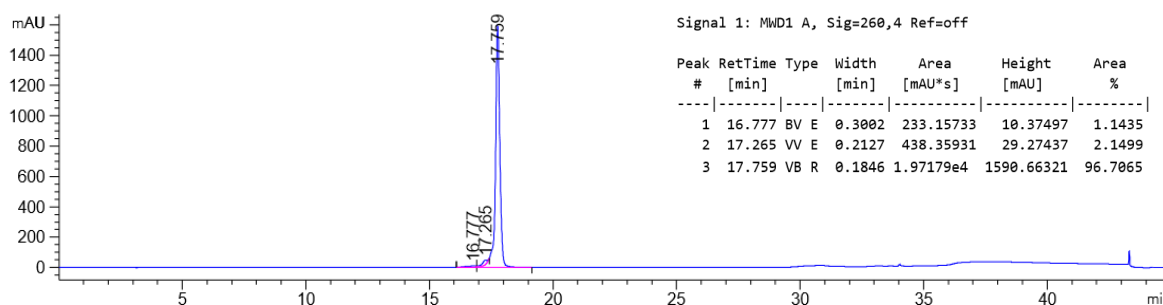


Figure 8.3: HPLC trace of purified T1T oligonucleotide. Detection wavelength 260 nm for DNA.

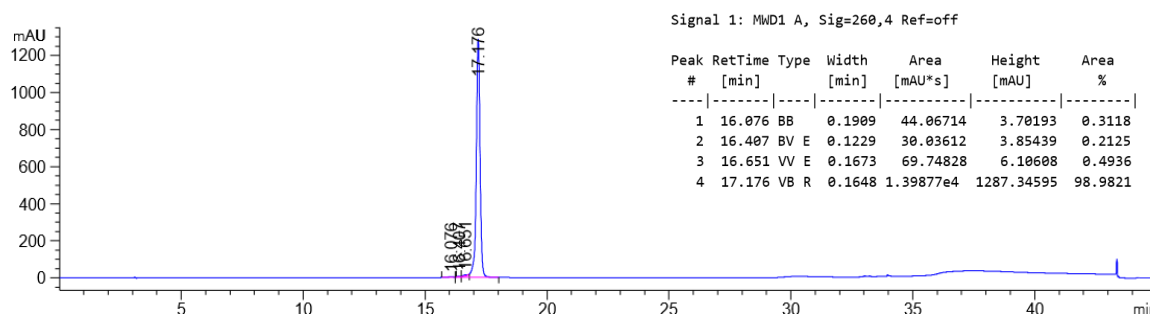


Figure 8.4: HPLC trace of purified T1A oligonucleotide. Detection wavelength is 260 nm for DNA.

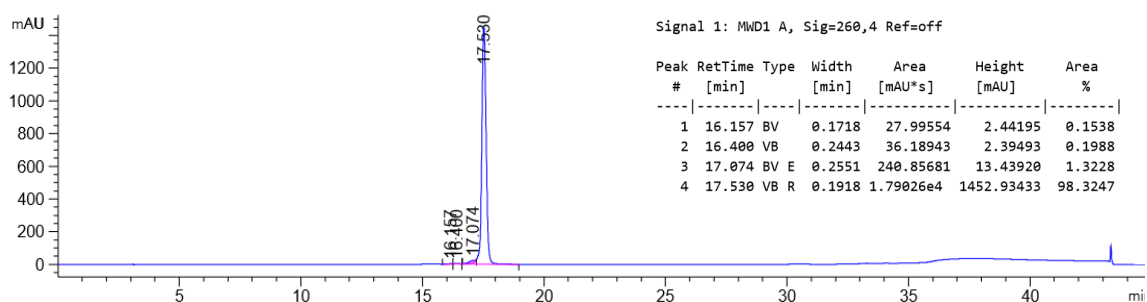


Figure 8.5: HPLC trace of purified T1MM oligonucleotide. Detection wavelength is 260 nm for DNA.

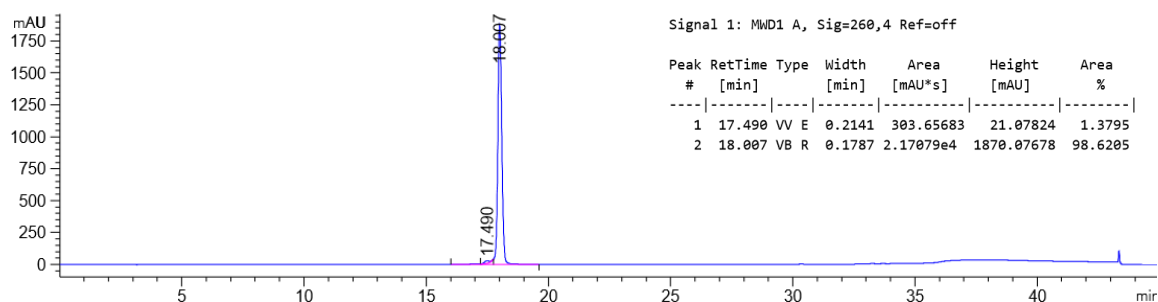


Figure 8.6: HPLC trace of purified T1mC oligonucleotide. Detection wavelength is 260 nm for DNA.

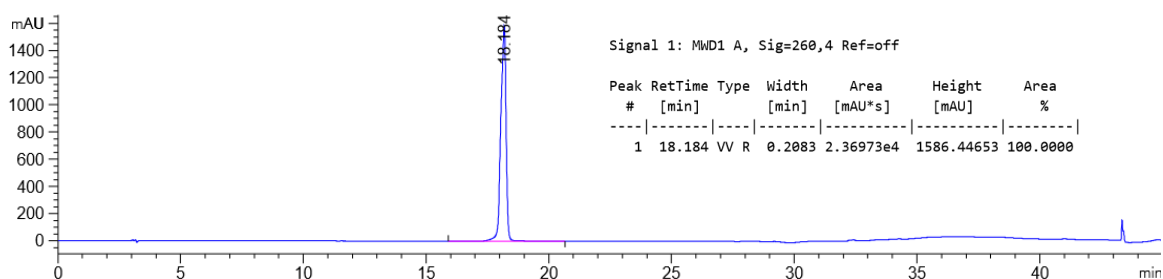


Figure 8.7: HPLC trace of purified P2 oligonucleotide. Detection wavelength is 260 nm for DNA.

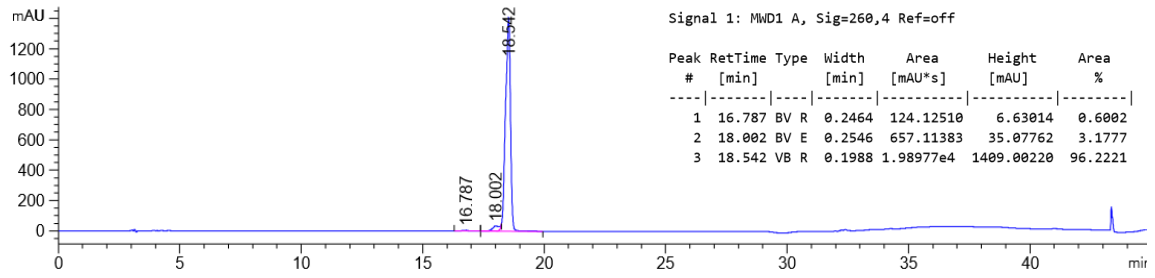


Figure 8.8: HPLC trace of purified T2WT oligonucleotide. Detection wavelength is 260 nm for DNA.

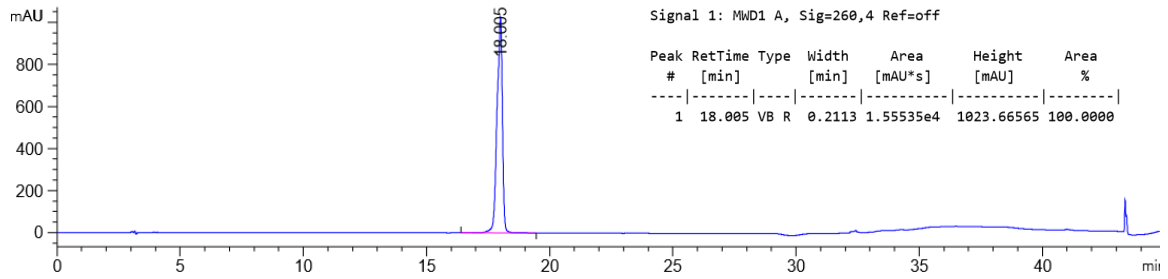


Figure 8.9: HPLC trace of purified T2Mut oligonucleotide. Detection wavelength is 260 nm for DNA.

8.1.2.3. Modified Oligonucleotides

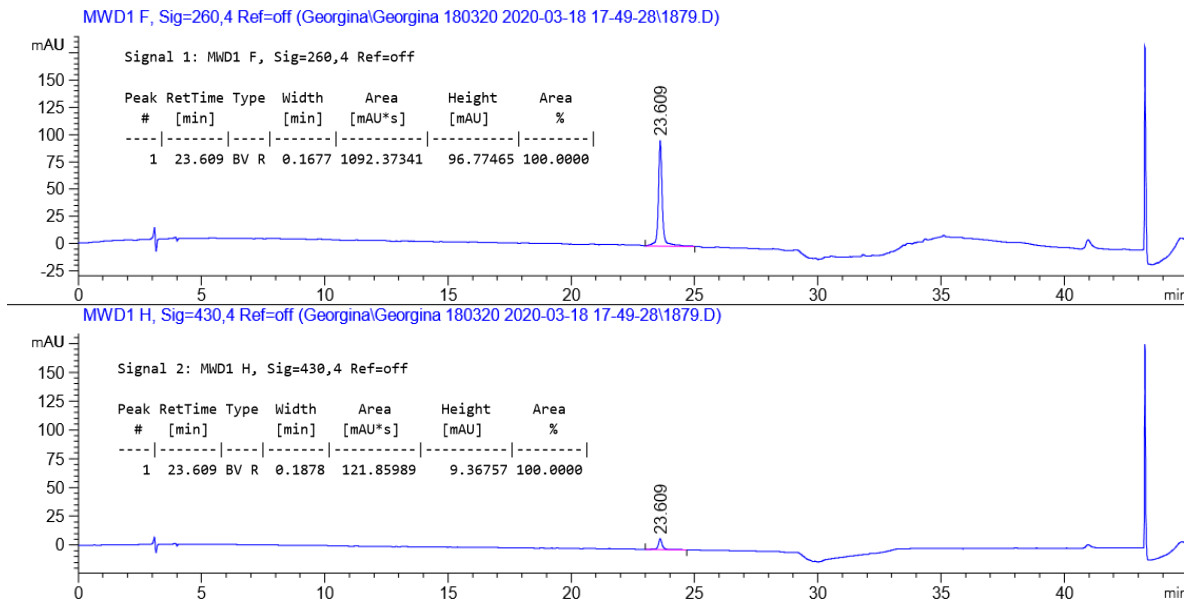


Figure 8.10: HPLC trace of purified P1AL modified oligonucleotide. Detection wavelength is 260 nm for DNA (top) and 430 nm for naphthalimide modification (bottom).

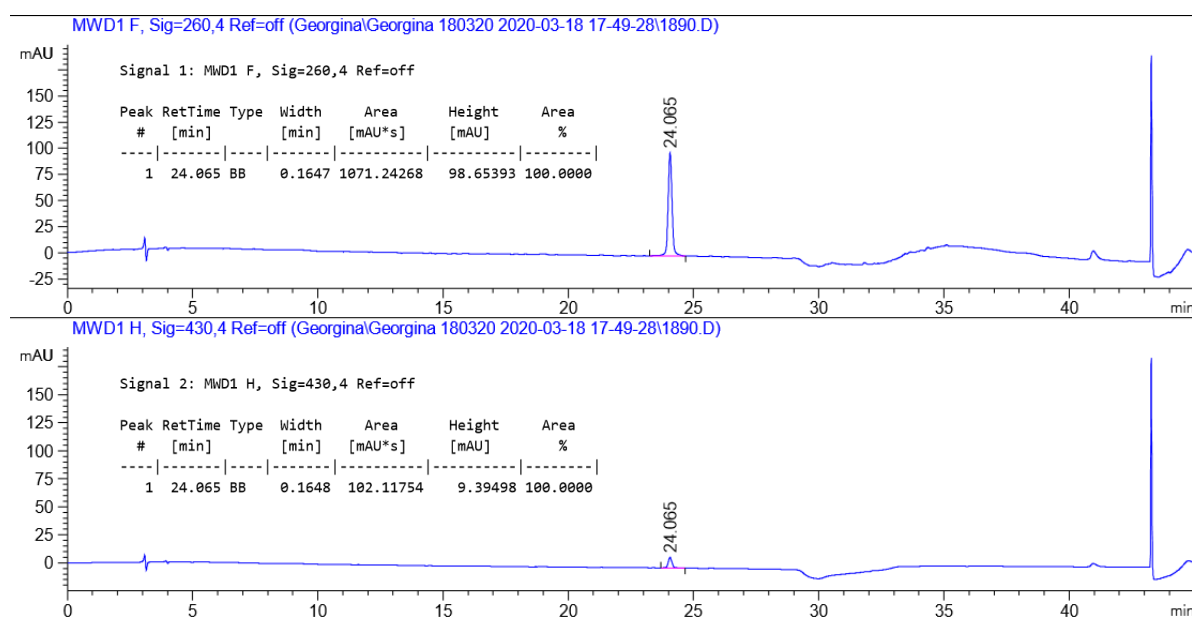


Figure 8.11: HPLC trace of purified P1AD modified oligonucleotide. Detection wavelength is 260 nm for DNA (top) and 430 nm for naphthalimide modification (bottom).

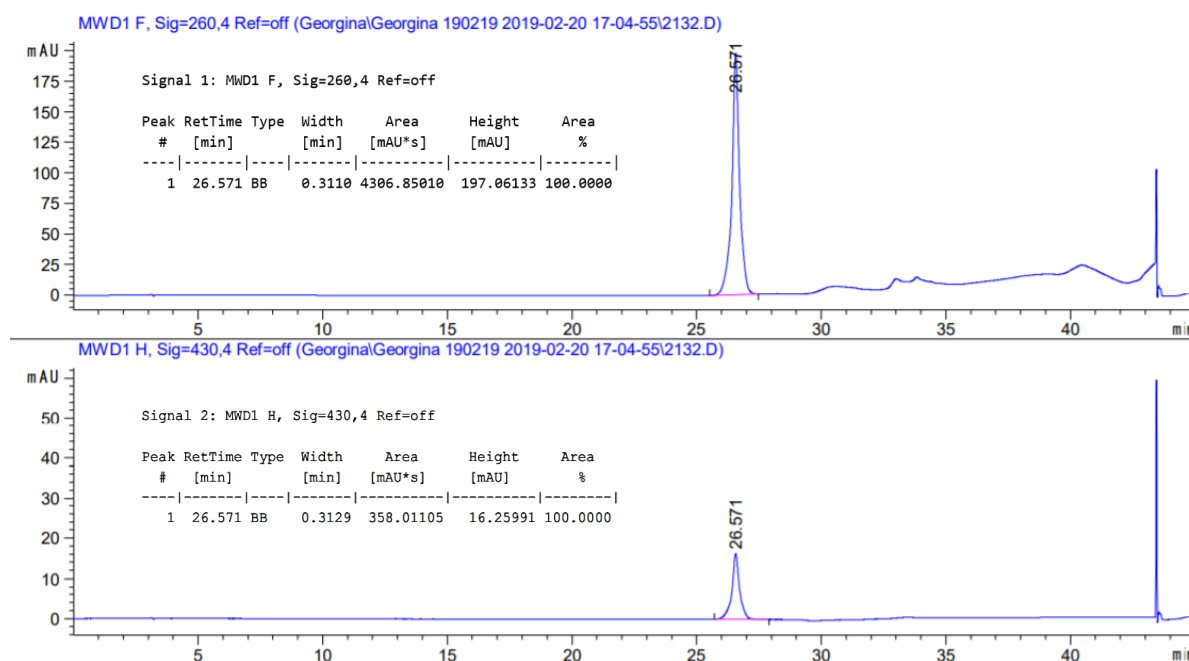


Figure 8.12: HPLC trace of purified P1BL modified oligonucleotide. Detection wavelength is 260 nm for DNA (top) and 430 nm for naphthalimide modification (bottom).

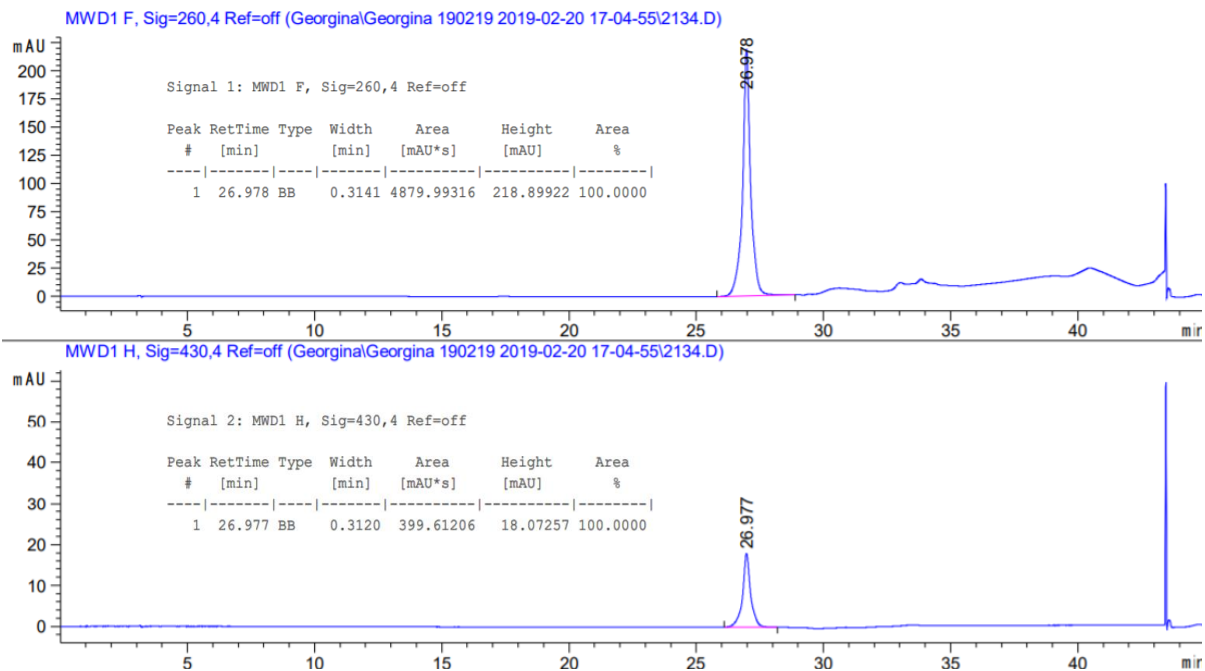


Figure 8.13: HPLC trace of purified P1BD modified oligonucleotide. Detection wavelength is 260 nm for DNA (top) and 430 nm for naphthalimide modification (bottom).

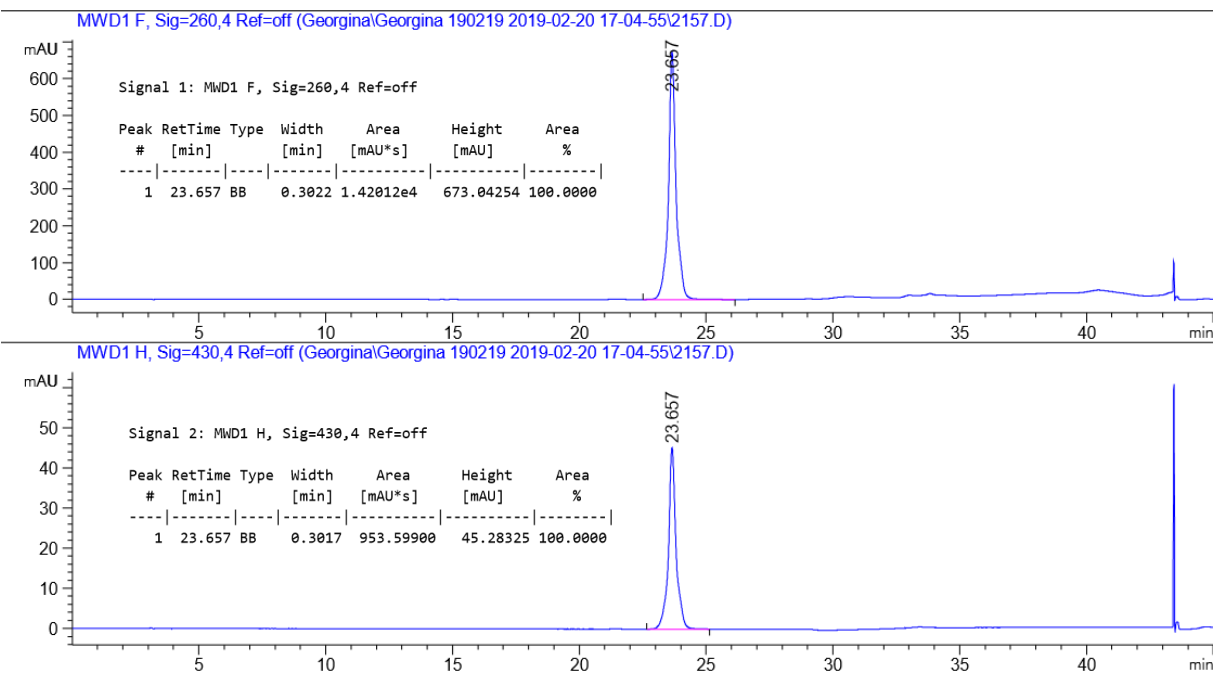


Figure 8.14: HPLC trace of purified P1CL modified oligonucleotide. Detection wavelength is 260 nm for DNA (top) and 430 nm for naphthalimide modification (bottom).

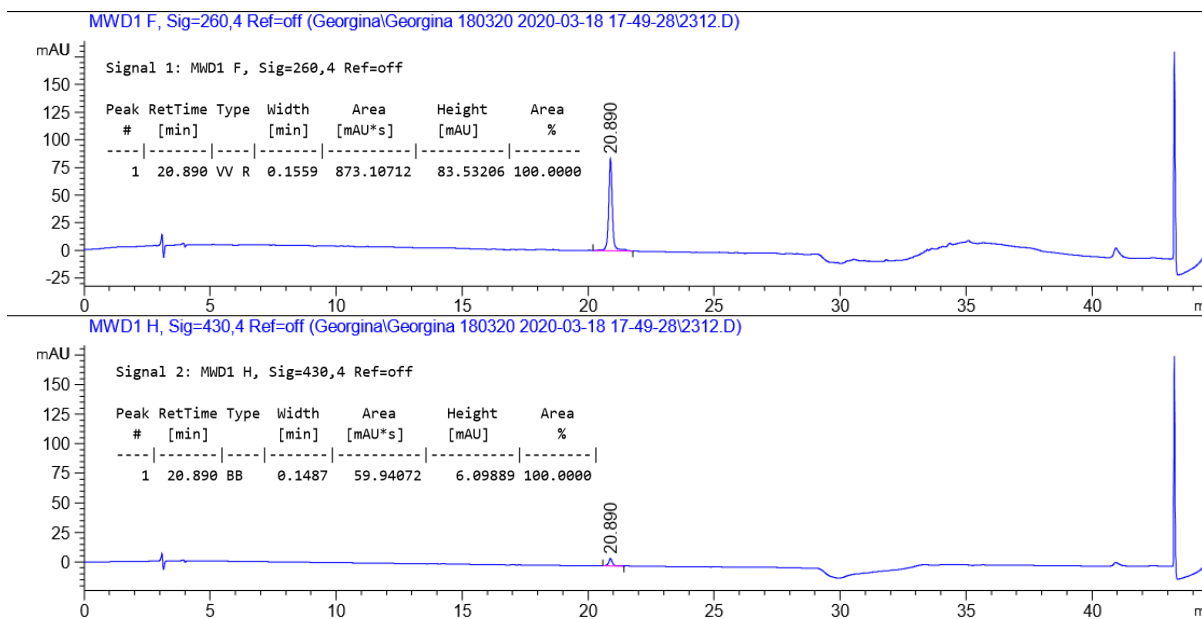


Figure 8.16: HPLC trace of purified P1DL modified oligonucleotide. Detection wavelength is 260 nm for DNA (top) and 430 nm for naphthalimide modification (bottom).

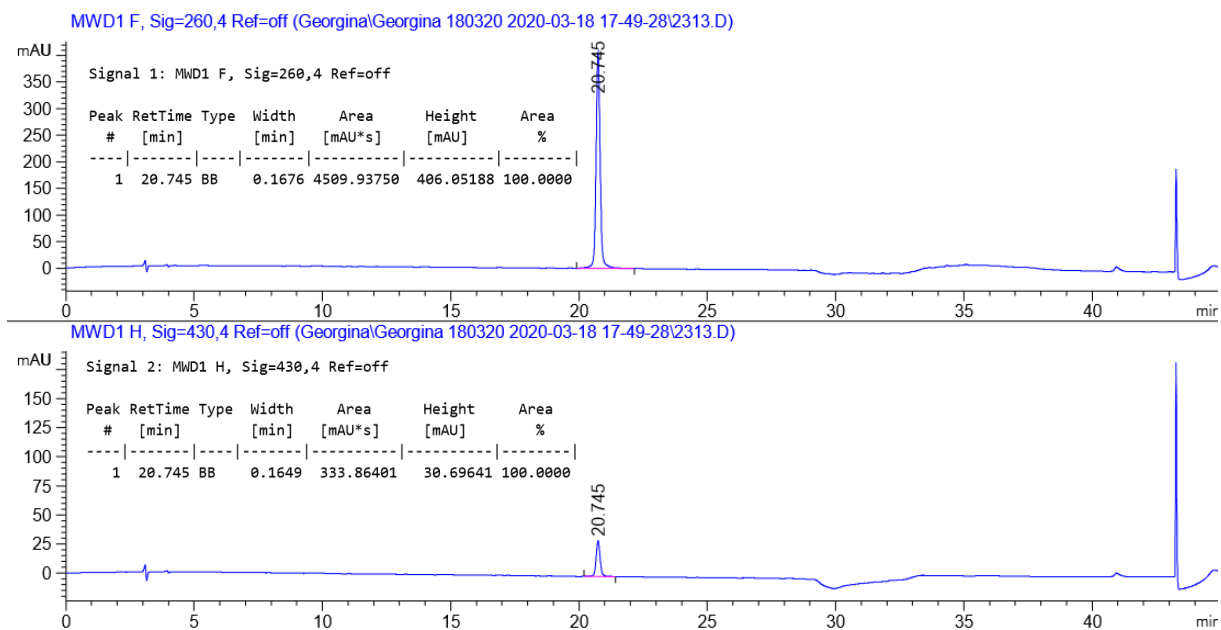


Figure 8.17: HPLC trace of purified P1DD modified oligonucleotide. Detection wavelength is 260 nm for DNA (top) and 430 nm for naphthalimide modification (bottom).

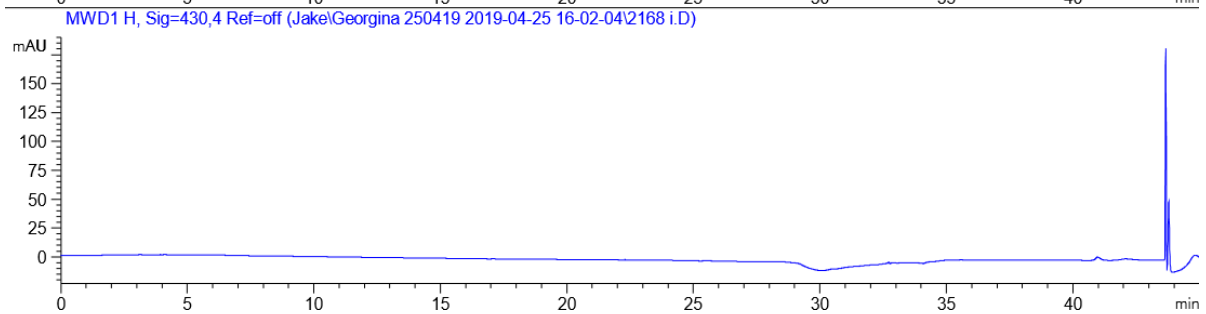
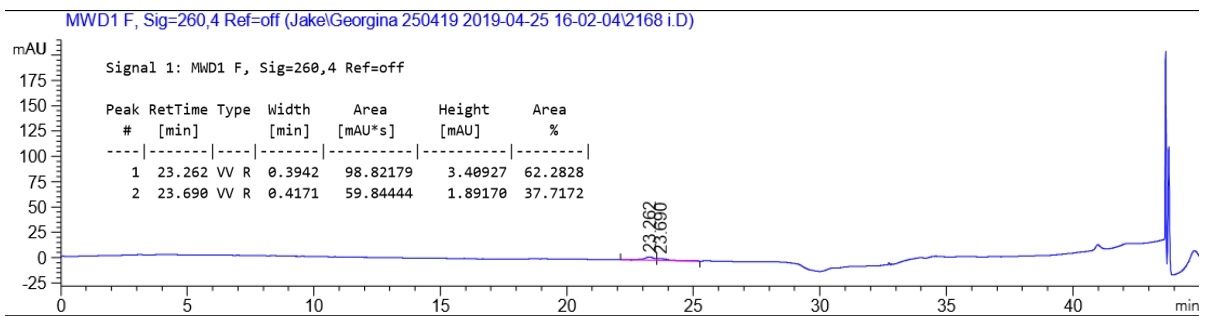


Figure 8.18: HPLC trace of purified P2AL modified oligonucleotide. Detection wavelength is 260 nm for DNA (top) and 430 nm for naphthalimide modification (bottom).

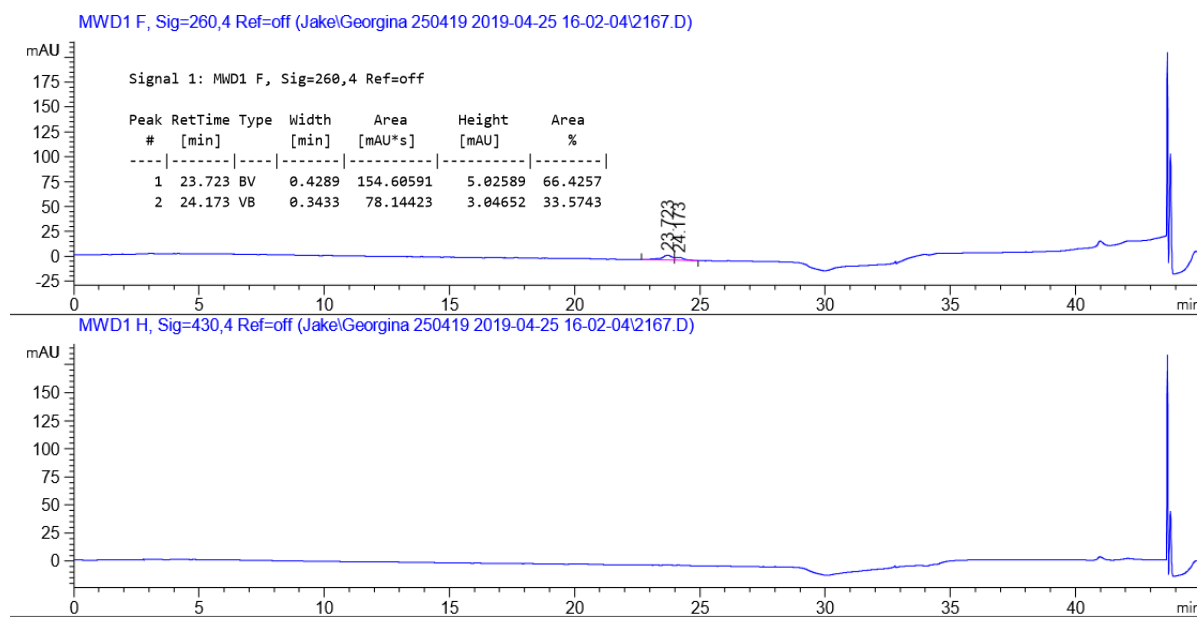


Figure 8.19: HPLC trace of purified P2AD modified oligonucleotide. Detection wavelength is 260 nm for DNA (top) and 430 nm for naphthalimide modification (bottom).

8.1.3. Determining Molar Extinction Coefficients

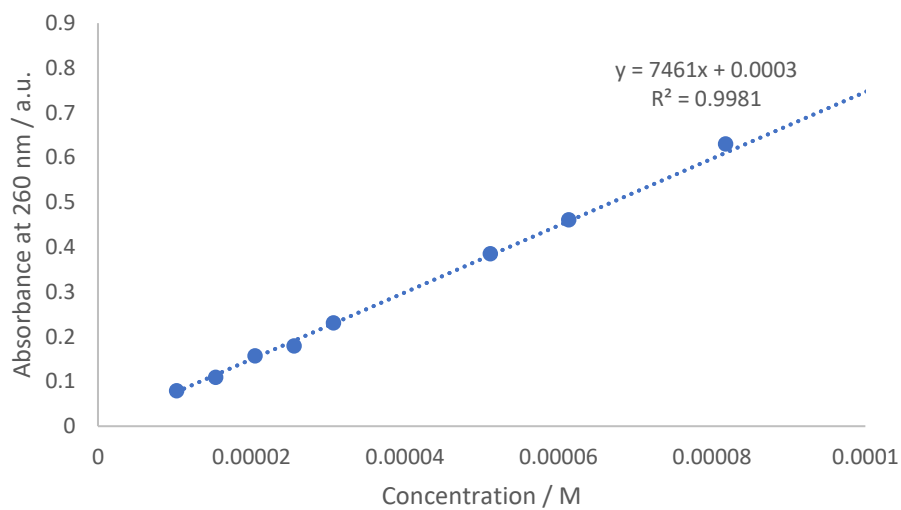


Figure 8.20: Determining the molar extinction coefficient of $L\text{ Naph}^A_{\text{Short}}$.

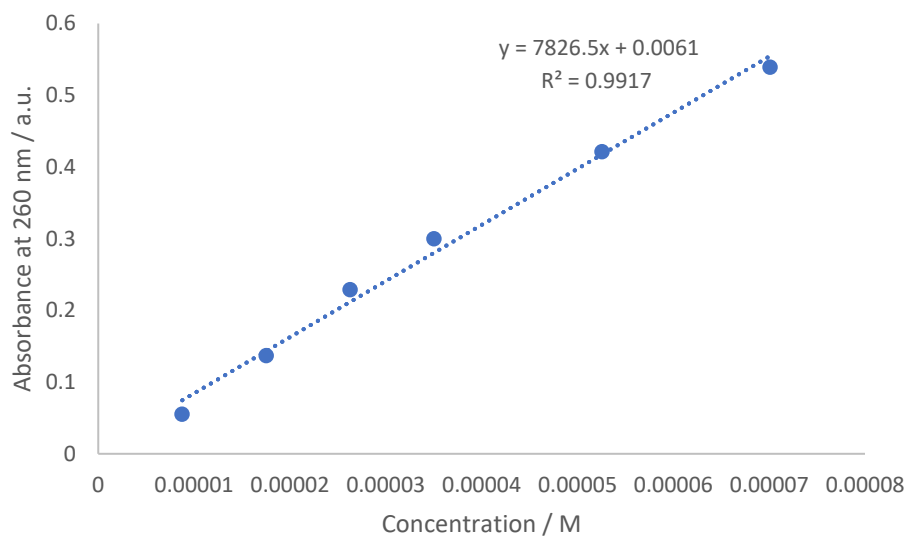


Figure 8.21: Determining the molar extinction coefficient of $D\text{ Naph}^A_{\text{Short}}$.

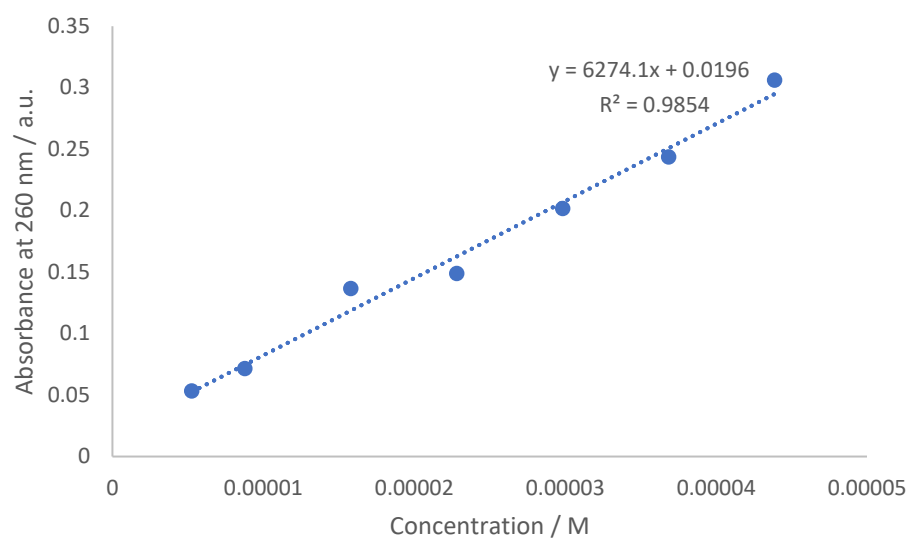


Figure 8.22: Determining the molar extinction coefficient of L Naph^A_{Long}.

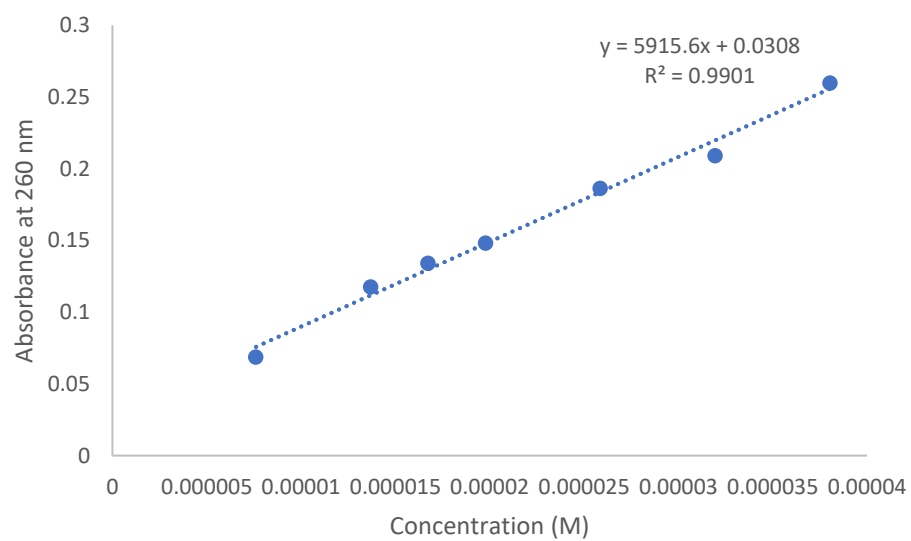


Figure 8.23: Determining the molar extinction coefficient of D Naph^A_{Long}.

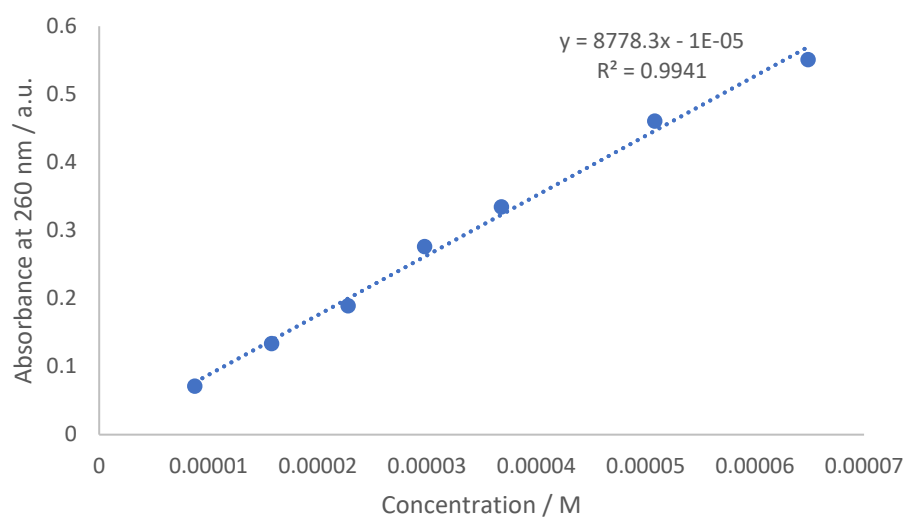


Figure 8.24: Determining the molar extinction coefficient of L Naph^{Dimethyl}.

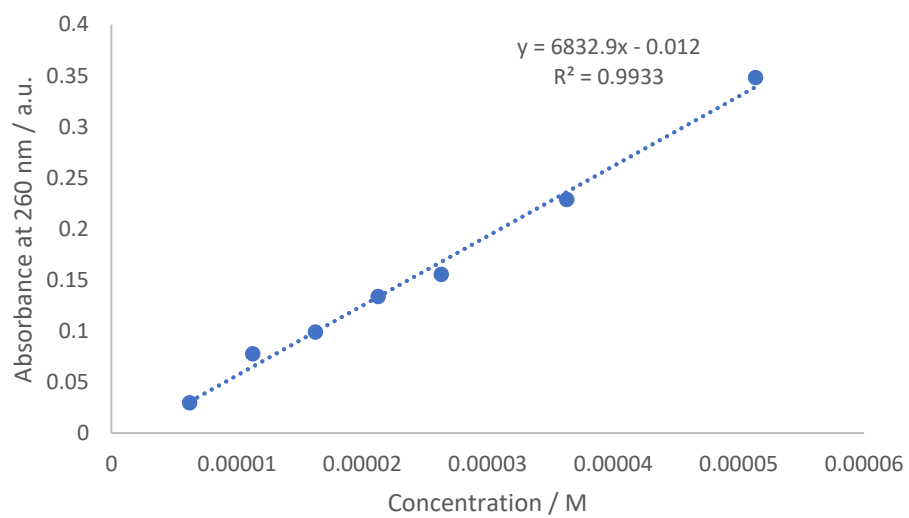


Figure 8.25: Determining the molar extinction coefficient of D Naph^{Dimethyl}.

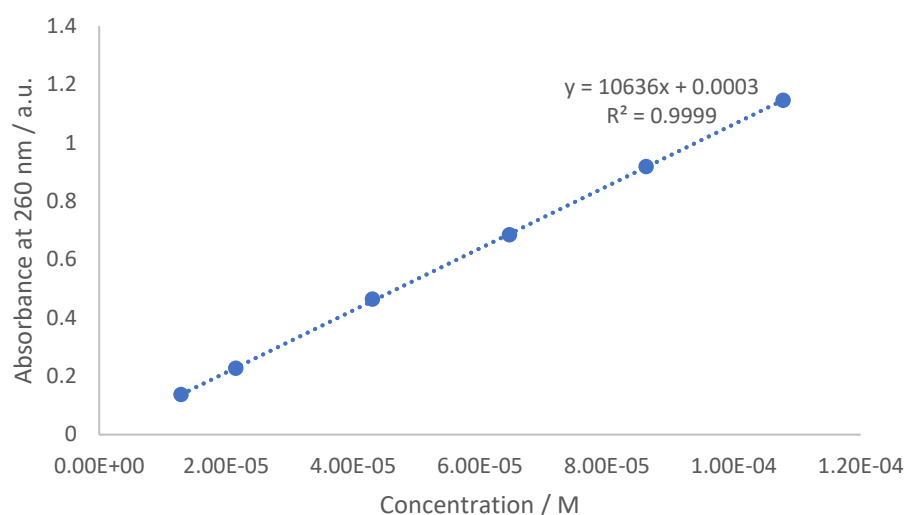


Figure 8.26: Determining the molar extinction coefficient of L Naph^I_{Amine}.

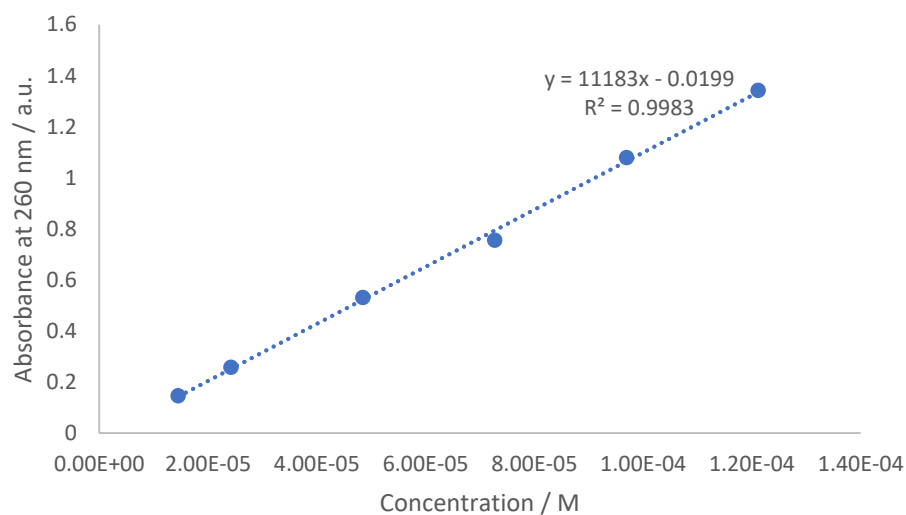


Figure 8.27: Determining the molar extinction coefficient of D Naph^I_{Amine}.

Table 8.2: Summary of the molar extinction coefficients of the 1,8-naphthalimide modifications.

Modification	Molar extinction coefficient, ϵ / L mol ⁻¹ cm ⁻¹
L Naph ^A _{Short}	7461
D Naph ^A _{Short}	7827
L Naph ^A _{Long}	6274
D Naph ^A _{Long}	5915
L Naph ^I _{Dimethyl}	8778
D Naph ^I _{Dimethyl}	6833
L Naph ^I _{Amine}	10636
D Naph ^I _{Amine}	11183

8.2. Exploring the Photophysical Properties of 1,8-Naphthalimide Reporter Groups and Their Ability as Base Discriminating Probes

8.2.1. Absorption Spectra of 1,8-Naphthalimide Tag Monomers

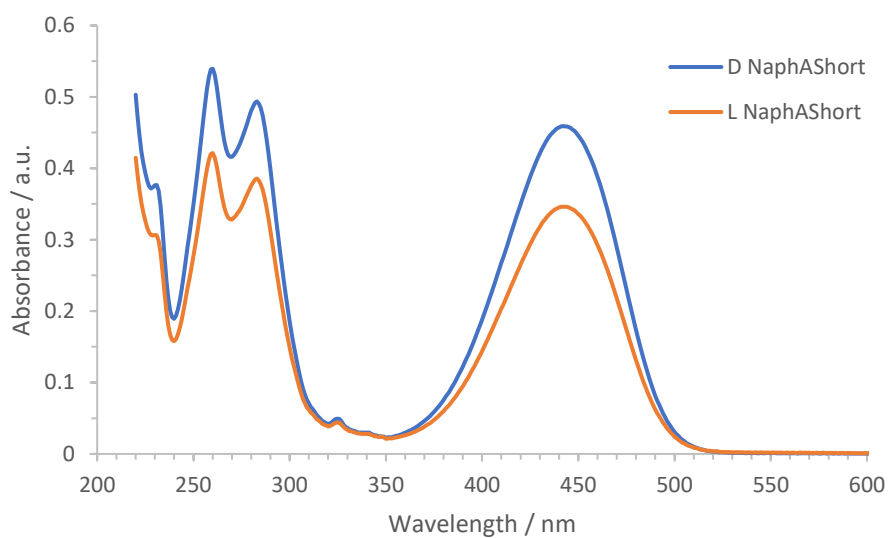


Figure 8.28: Absorption spectra of D Naph^A_{Short} tag monomer, 0.70×10^{-4} M (blue) and L Naph^A_{Short} tag monomer, 0.53×10^{-4} M (orange) in water/acetonitrile 85:15.

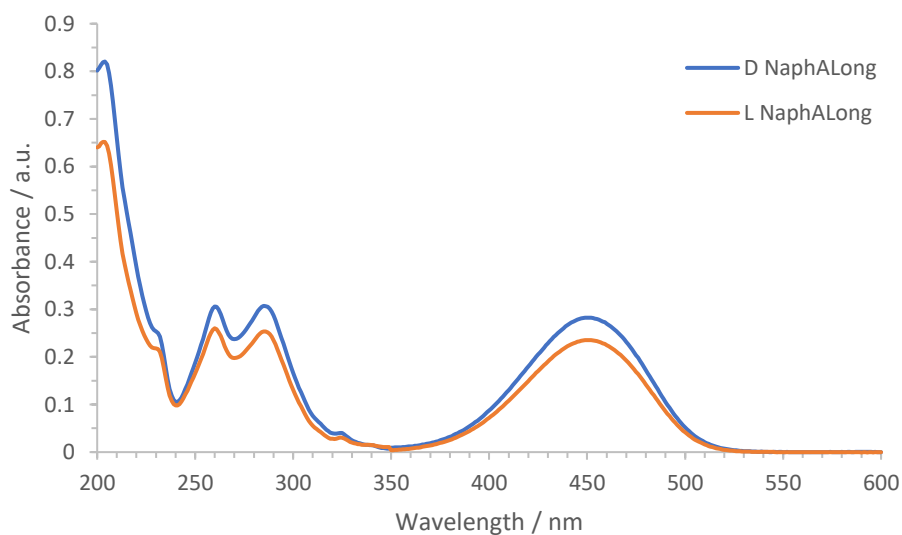


Figure 8.29 Absorption spectra of D Naph^A_{Long} tag monomer, 0.44×10^{-4} M (blue) and L Naph^A_{Long} tag monomer, 0.38×10^{-4} M (orange) in water/acetonitrile 85:15.

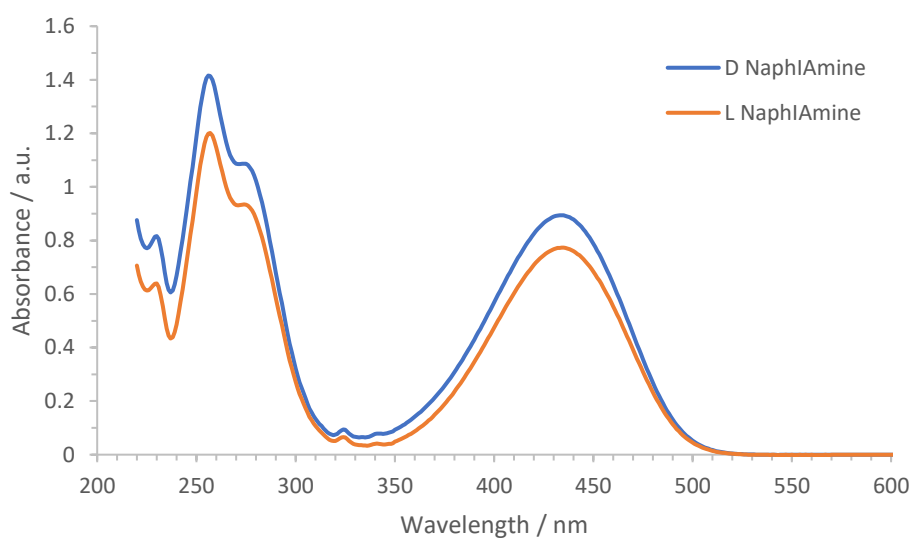


Figure 8.30: Absorption spectra of *D Naph^IAmine* tag monomer, 1.21×10^{-4} M (blue) and *L Naph^IAmine* tag monomer, 1.08×10^{-4} M (orange) in water/acetonitrile 85:15.

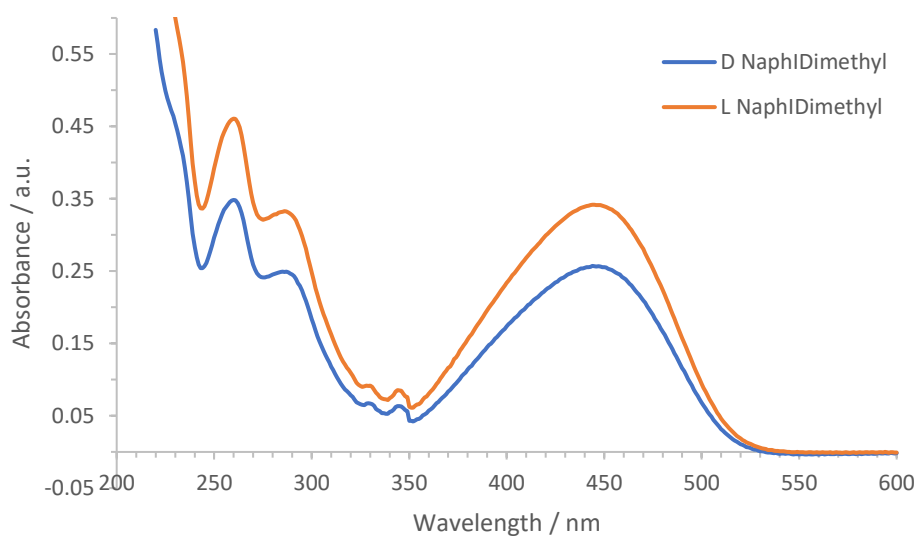


Figure 8.31: Absorption spectra of *D Naph^IDimethyl* tag monomer, 0.51×10^{-4} M (blue) and *L Naph^IDimethyl* tag monomer, 0.51×10^{-4} M (orange) in water/acetonitrile 85:15.

8.2.2. Effect of Solvent on the Absorption Profiles of the Naphthalimide Tag Monomers

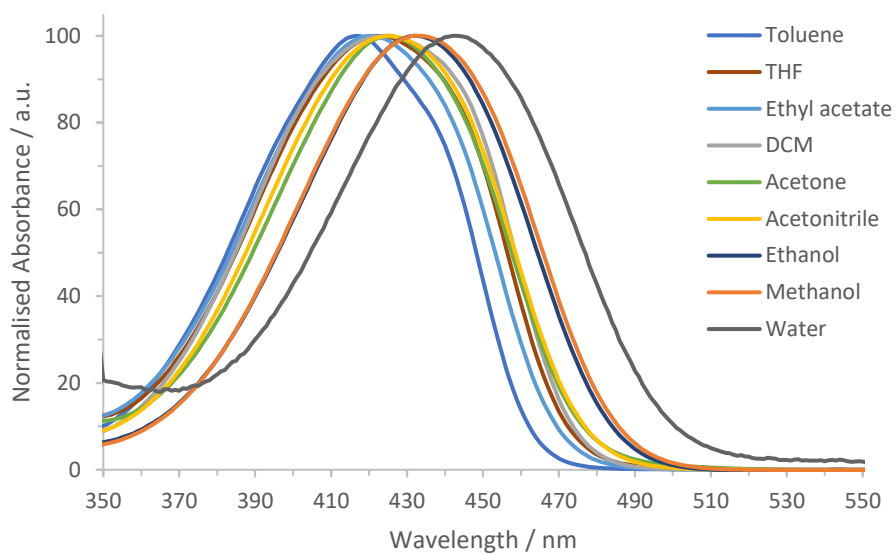


Figure 8.32: Normalised absorption profiles of L Naph^{A_Short} tag in different solvents.

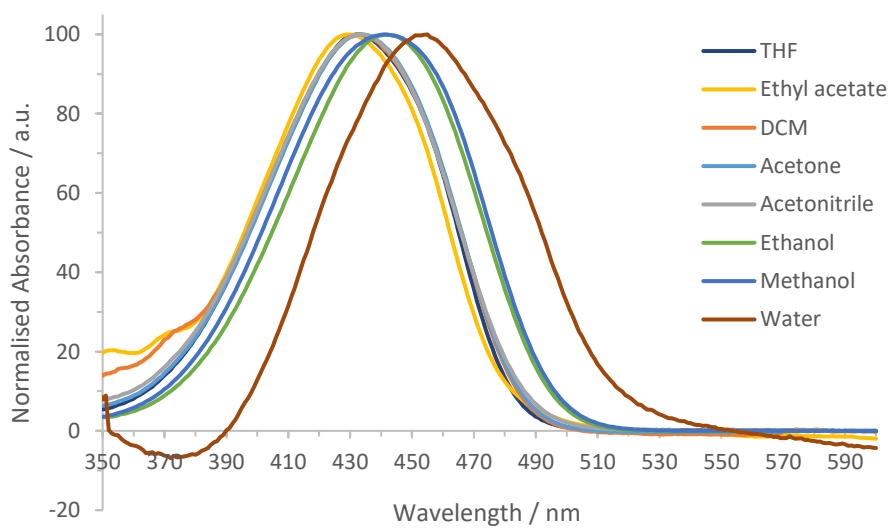


Figure 8.33: Normalised absorption profiles of D Naph^{A_Long} tag in different solvents.

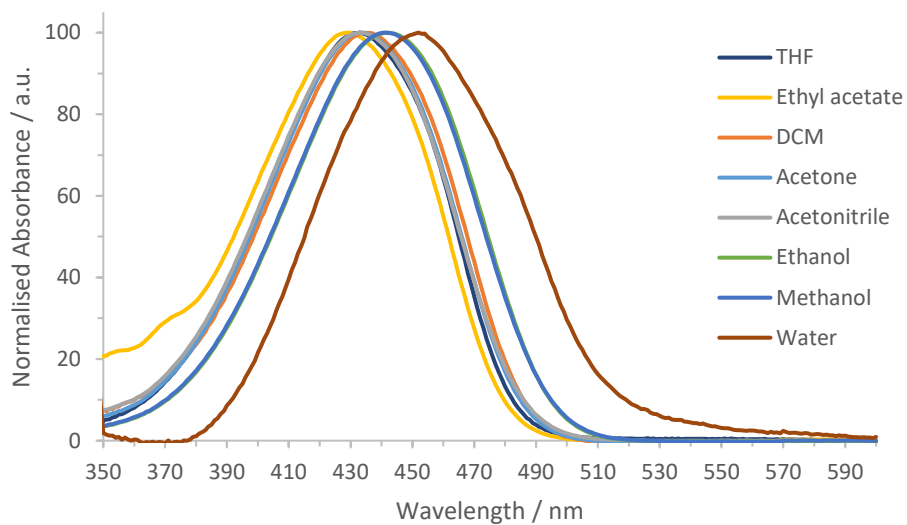


Figure 8.34: Normalised absorption profiles of L Naph^A_{Long} tag in different solvents.

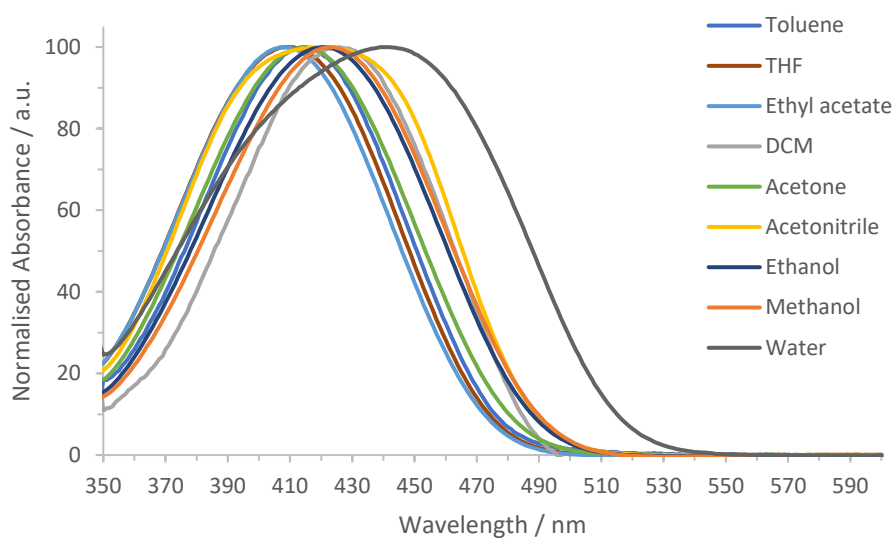


Figure 8.35: Normalised absorption profiles of D Naph^I_{Dimethyl} tag in different solvents.

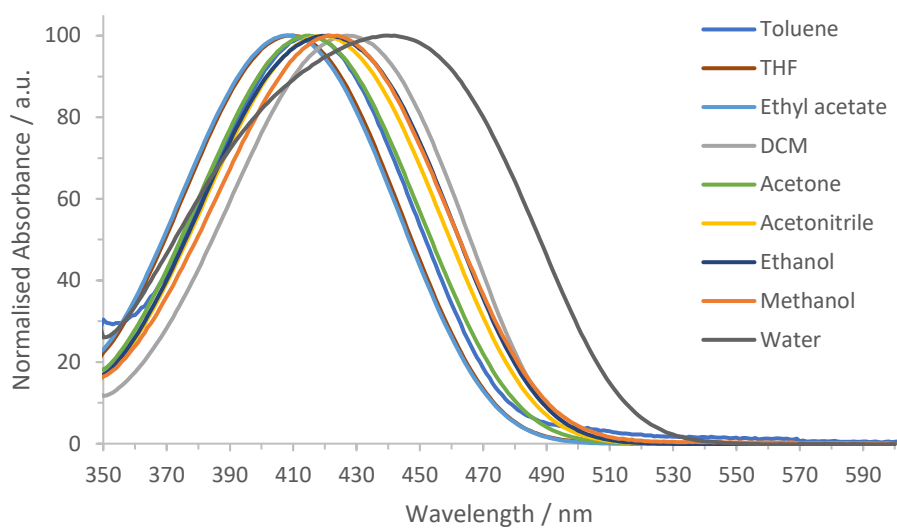


Figure 8.36: Normalised absorption profiles of *L Naph¹Dimethyl tag* in different solvents.

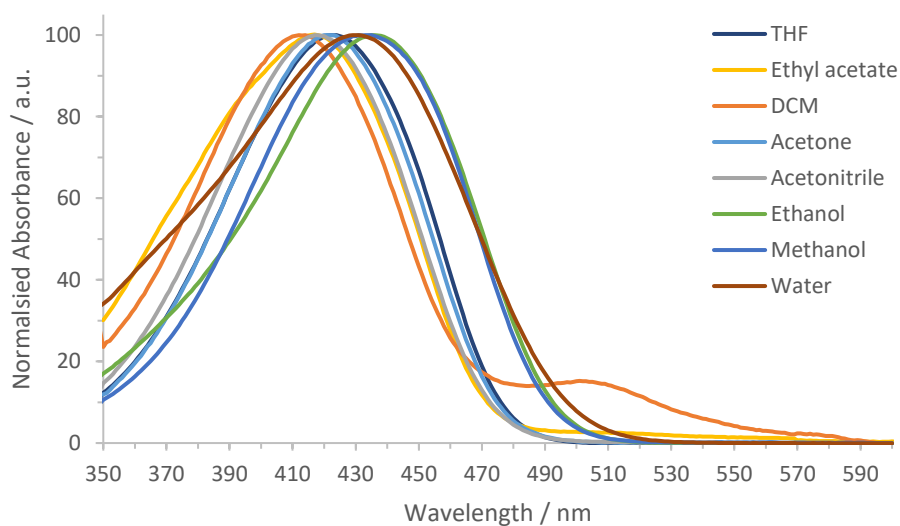


Figure 8.37: Normalised absorption profiles of *D Naph¹Amine tag* in different solvents.

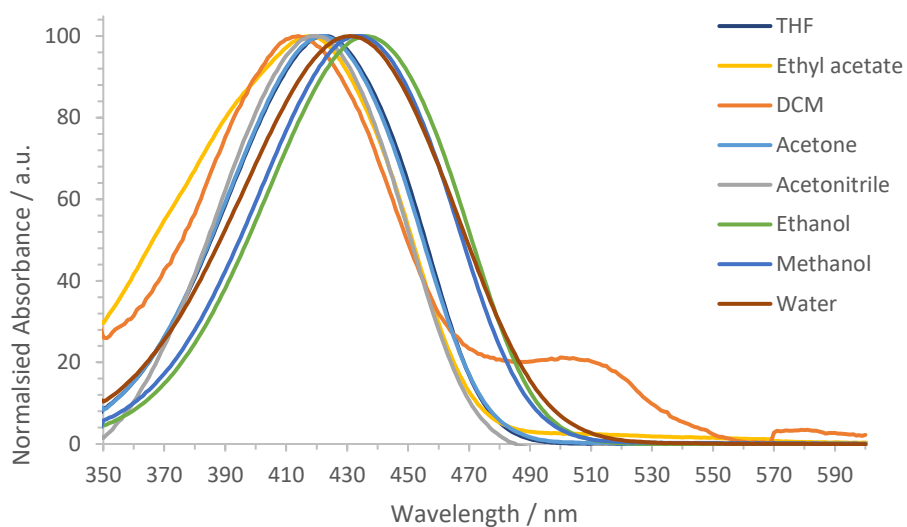


Figure 8.38: Normalised absorption profiles of $L\text{ Naph}^{\text{Amine}}$ tag in different solvents.

Table 8.3: Maximum absorption wavelength, λ_{max} of naphthalimide tag monomer units in different solvents of varying polarity, described using the Dimroth-Reichardt parameter, $E_{\text{T}}(30)$. Dash (-) indicates that an accurate reading could not be made due to solubility.

Solvent	$\lambda_{\text{max}} / \text{nm}$								$E_{\text{T}}(30)$ / kcal mol^{-1}
	D $\text{Naph}^{\text{A}_{\text{Short}}}$	L $\text{Naph}^{\text{A}_{\text{Short}}}$	D $\text{Naph}^{\text{A}_{\text{Long}}}$	L $\text{Naph}^{\text{A}_{\text{Long}}}$	D $\text{Naph}^{\text{Dimethyl}}$	L $\text{Naph}^{\text{Dimethyl}}$	D $\text{Naph}^{\text{Amine}}$	L $\text{Naph}^{\text{Amine}}$	
Water	443	442	453	452	440	440	431	431	63.1
Methanol	433	432	441	441	424	424	433	433	55.4
Ethanol	432	432	442	442	421	421	436	436	51.9
Acetonitrile	425	425	433	433	421	420	418	419	45.6
Acetone	425	425	433	433	414	414	421	422	42.2
DCM	424	424	433	433	426	427	412	414	40.7
Ethyl acetate	421	421	429	429	408	408	417	418	38.1
THF	422	422	433	433	409	410	424	422	37.4
Toluene	417	417	-	-	415	415	-	-	33.9

8.2.3. Absorption Studies of 1,8-Naphthalimide Tag Monomers and the Affect Upon Incorporation Into DNA

Table 8.4: Maximum absorption wavelength, λ_{max} , of the naphthalimide tag monomers and probes.

	λ_{max} 1,8-naphthalimide tag monomer / nm	λ_{max} 1,8-naphthalimide probe / nm
L Naph ^A _{Short}	442	447
D Naph ^A _{Short}	443	450
L Naph ^A _{Long}	452	459
D Naph ^A _{Long}	453	459
L Naph ^I _{Dimethyl}	440	455
D Naph ^I _{Dimethyl}	440	455
L Naph ^I _{Amine}	431	444
D Naph ^I _{Amine}	431	444

8.2.4. Fluorescence Spectra of Naphthalimide Tag Monomers in Water

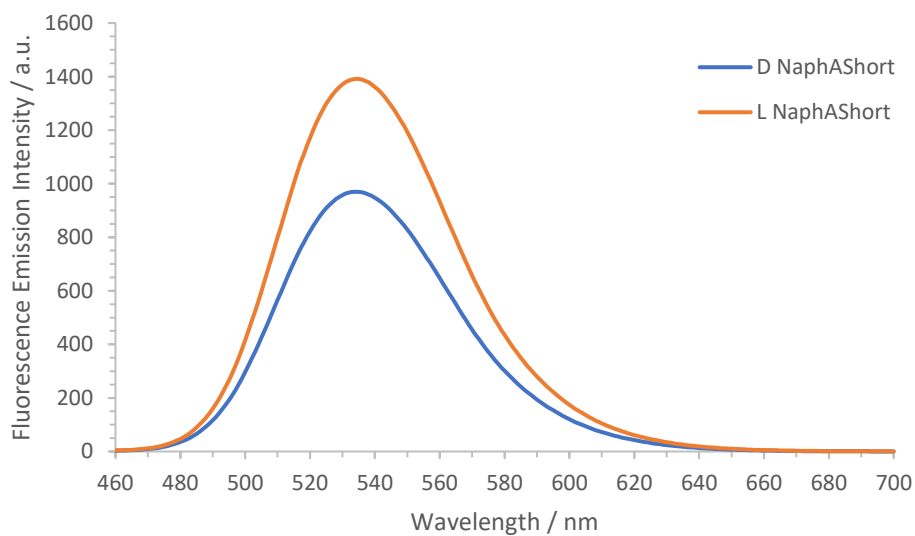


Figure 8.39: Fluorescence spectra of D Naph^A_{Short} (blue) and L Naph^A_{Short} (orange) in Milli-Q water. $\lambda_{ex} = 450$ nm, 298 K.

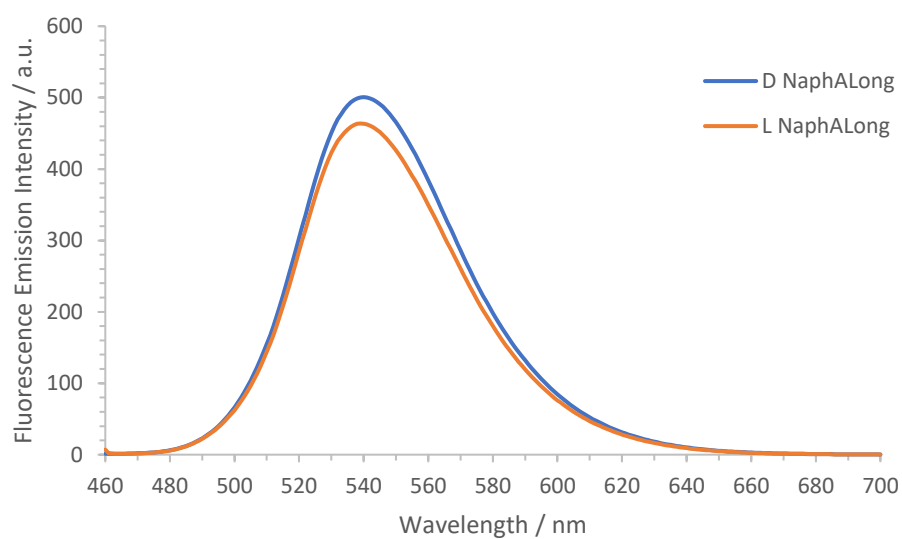


Figure 8.40: Fluorescence spectra of D Naph^A_{Long} (blue) and L Naph^A_{Long} (orange) in Milli-Q water. $\lambda_{ex} = 450$ nm, 298 K.

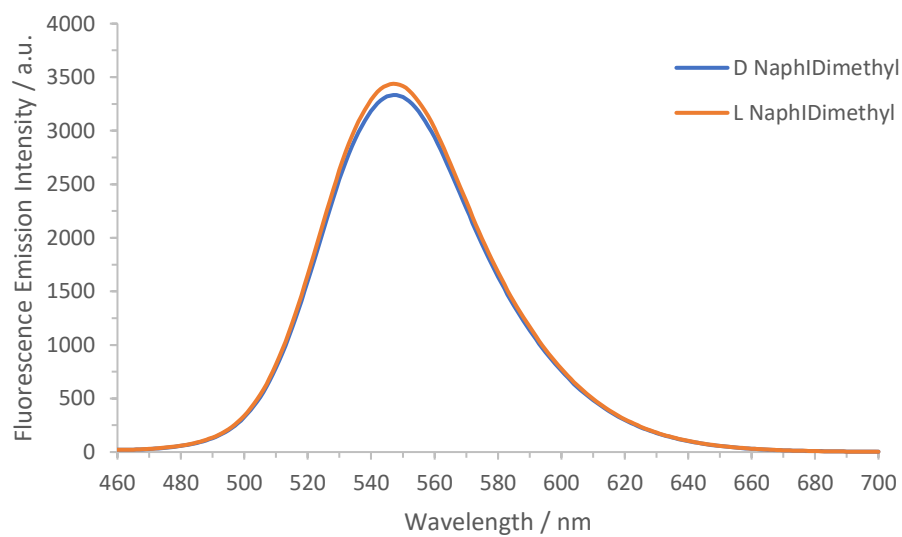


Figure 8.41: Fluorescence spectra of D Naph^I_{Dimethyl} (blue) and L Naph^I_{Dimethyl} (orange) in Milli-Q water. $\lambda_{ex} = 450$ nm, 298 K.

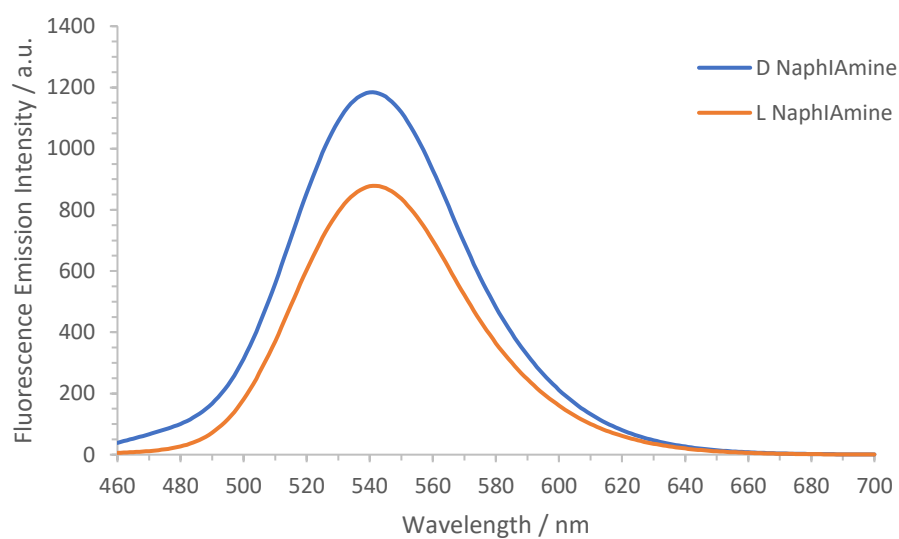


Figure 8.42: Fluorescence spectra of D Naph^IAmine (blue) and L Naph^IAmine (orange) in Milli-Q water. $\lambda_{ex} = 450$ nm, 298 K.

8.2.5. Solvatochromic Properties of Naphthalimide Tag Monomers

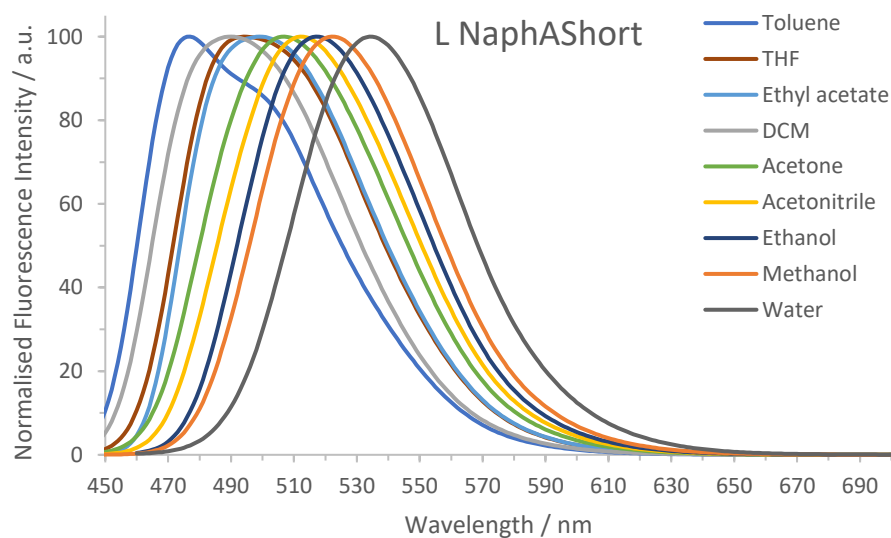


Figure 8.43: Normalised fluorescence profiles of L Naph^A_{Short} tag in different solvents.

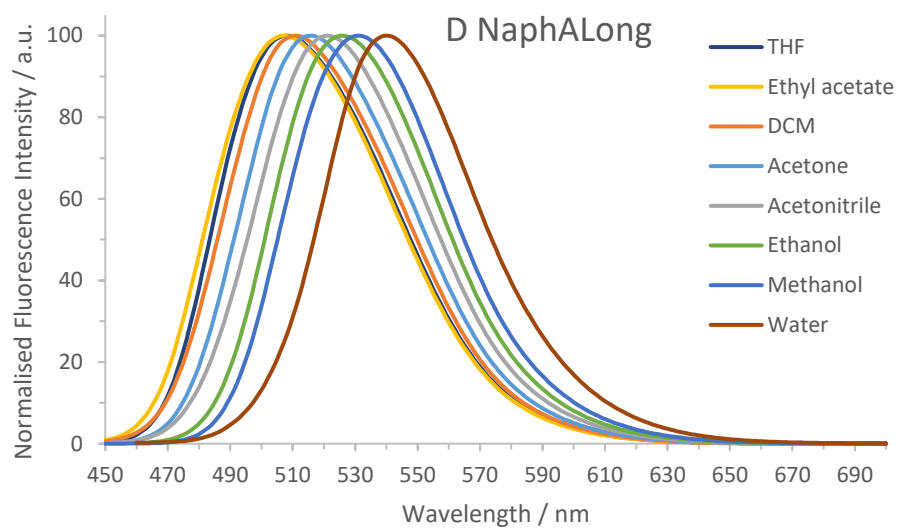


Figure 8.44: Normalised fluorescence profiles of D Naph^A_{Long} tag in different solvents.

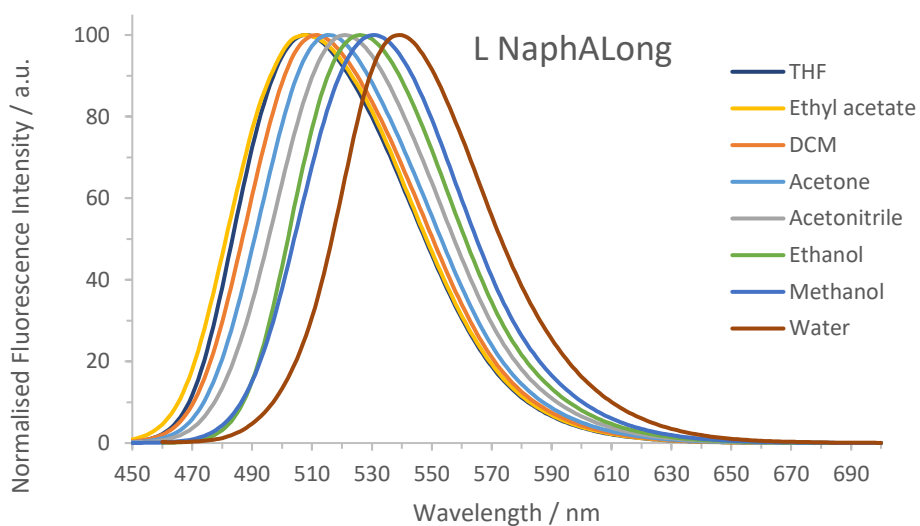


Figure 8.45: Normalised fluorescence profiles of L Naph^A_{Long} tag in different solvents.

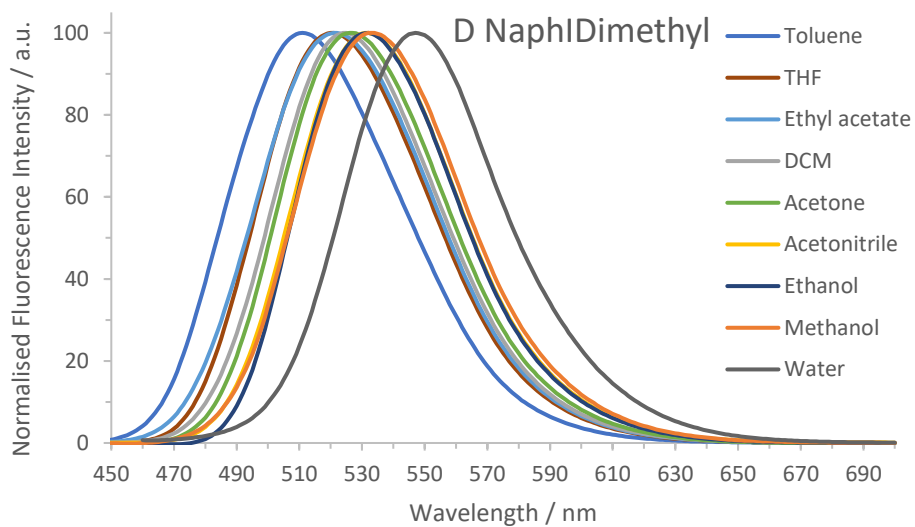


Figure 8.46: Normalised fluorescence profiles of D Naph^l_{Dimethyl} tag in different solvents.

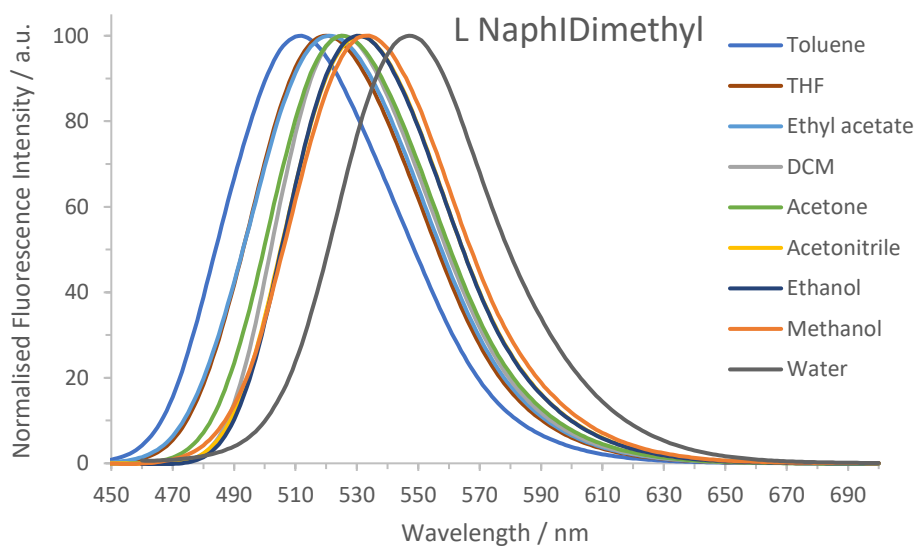


Figure 8.47: Normalised fluorescence profiles of L Naph^l_{Dimethyl} tag in different solvents.

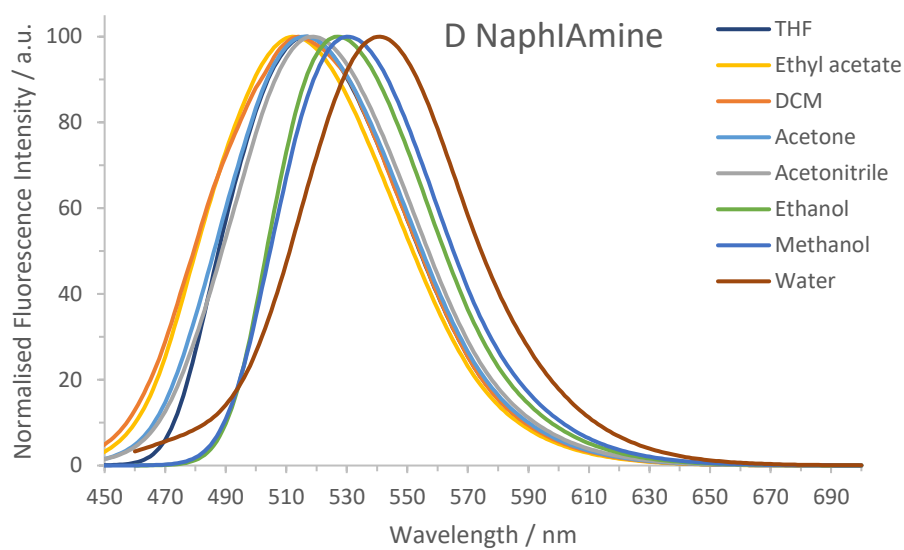


Figure 8.48: Normalised fluorescence profiles of D Naph^IAmine tag in different solvents.

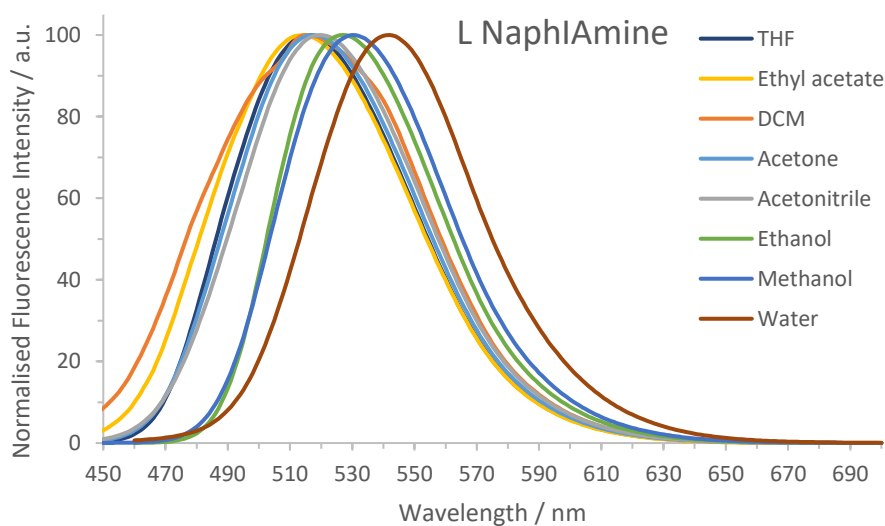


Figure 8.49: Normalised fluorescence profiles of L Naph^IAmine tag in different solvents.

Table 8.5 Maximum fluorescence emission wavelength, λ_{max} , of naphthalimide tag monomer units in different solvents of varying polarity, described using the Dimroth-Reichardt parameter, $E_T(30)$. Dash (-) indicates that an accurate reading could not be made due to solubility.

Solvent	$\lambda_{max} / \text{nm}$								$E_T(30)$ / kcal mol^{-1}
	D Naph ^A _{Short}	L Naph ^A _{Short}	D Naph ^A _{Long}	L Naph ^A _{Long}	D Naph ^I _{Dimethyl}	L Naph ^I _{Dimethyl}	D Naph ^I _{Amine}	L Naph ^I _{Amine}	
Water	534	534	540	539	547	547	542	541	63.1
Methanol	522	522	531	531	533	532	530	530	55.4
Ethanol	517	517	526	526	530	530	527	527	51.9
Acetonitrile	512	512	521	521	532	531	519	520	45.6
Acetone	507	507	516	515	526	525	516	517	42.2
DCM	501	500	511	511	524	525	514	515	40.7
Ethyl acetate	498	499	507	508	521	521	512	514	38.1
THF	496	494	508	508	520	520	517	516	37.4
Toluene	478	477	-	-	511	512	-	-	33.9

8.2.6. Sensing Results With 1:1 Probe: Target Equivalents

8.2.6.1. Naph^A_{Short}

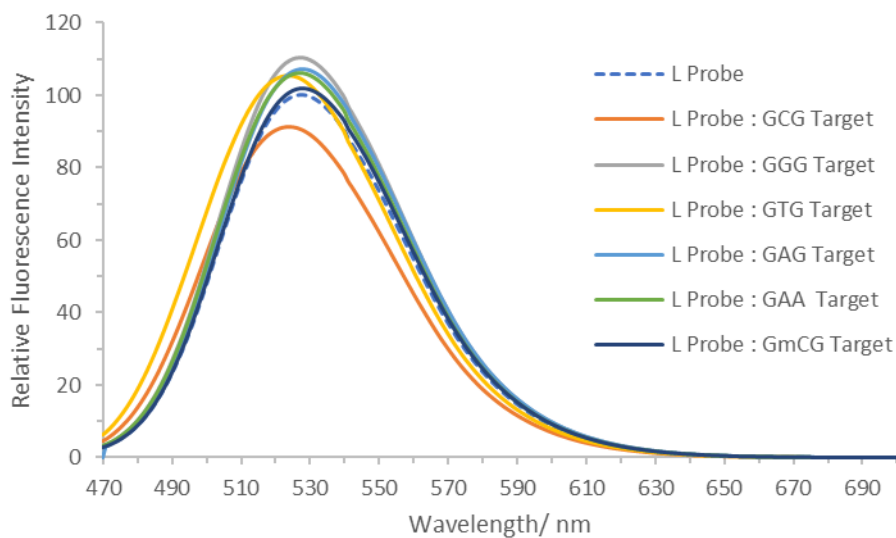


Figure 8.50: Sensing results of L Naph^A_{Short} probes upon duplex formation with target strand. 0.5 μM [Probe], 0.5 μM [Target], 100 mM NaCl, 10 mM sodium phosphate buffer pH 7.0, Milli-Q water. $\lambda_{ex} = 450 \text{ nm}$, 298 K.

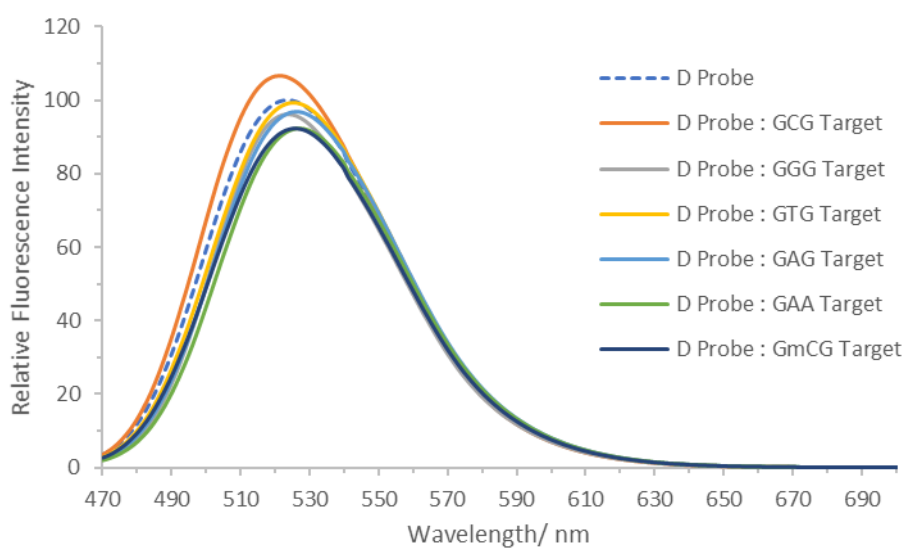


Figure 8.51: Sensing results of D Naph^{A_Short} probes upon duplex formation with target strand. 0.5 μ M [Probe], 0.5 μ M [Target], 100 mM NaCl, 10 mM sodium phosphate buffer pH 7.0, Milli-Q water. λ_{ex} = 450 nm, 298 K.

8.2.6.2. Naph^{A_Long}

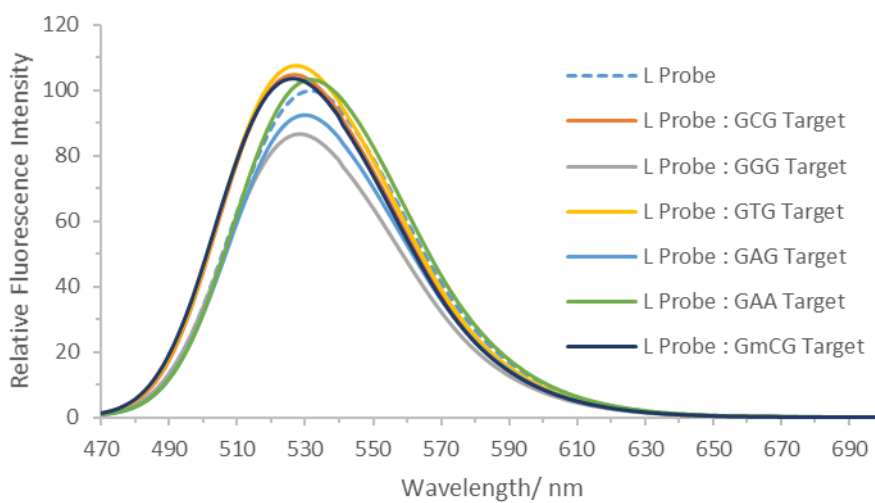


Figure 8.52: Sensing results of L Naph^{A_Long} probes upon duplex formation with target. 0.5 μ M [Probe], 0.5 μ M [Target], 100 mM NaCl, 10 mM sodium phosphate buffer pH 7.0, Milli-Q water. λ_{ex} = 450 nm, 298 K.

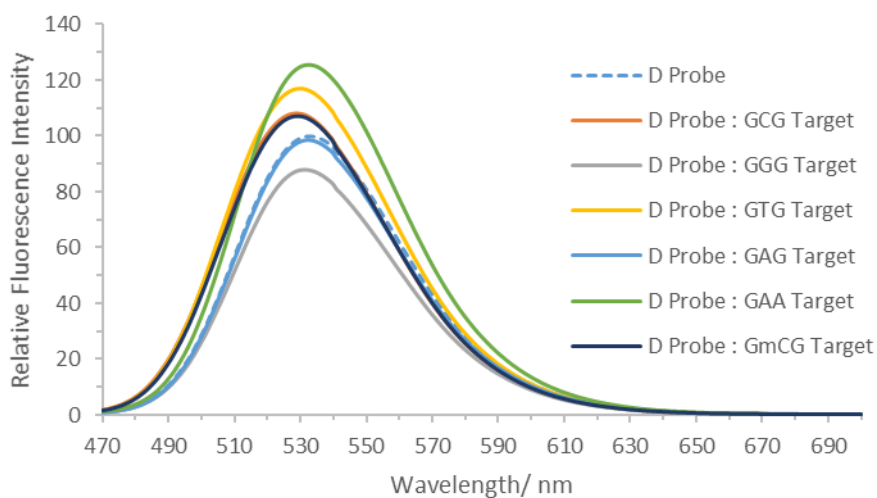


Figure 8.53: Sensing results of D $Naph^A_{Long}$ probes upon duplex formation with target. $0.5 \mu M$ [Probe], $0.5 \mu M$ [Target], 100 mM NaCl , $10 \text{ mM sodium phosphate buffer pH 7.0}$, Milli-Q water. $\lambda_{ex} = 450 \text{ nm}$, 298 K .

8.2.6.3. $Naph^{Dimethyl}$

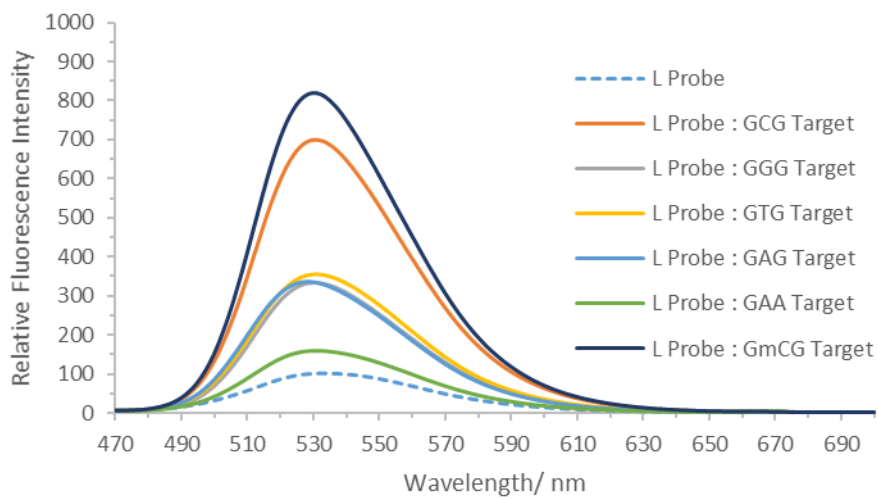


Figure 8.54: Sensing results of L $Naph^{Dimethyl}$ probes upon duplex formation with target. $0.5 \mu M$ [Probe], $0.5 \mu M$ [Target], 100 mM NaCl , $10 \text{ mM sodium phosphate buffer pH 7.0}$, Milli-Q water. $\lambda_{ex} = 450 \text{ nm}$, 298 K .

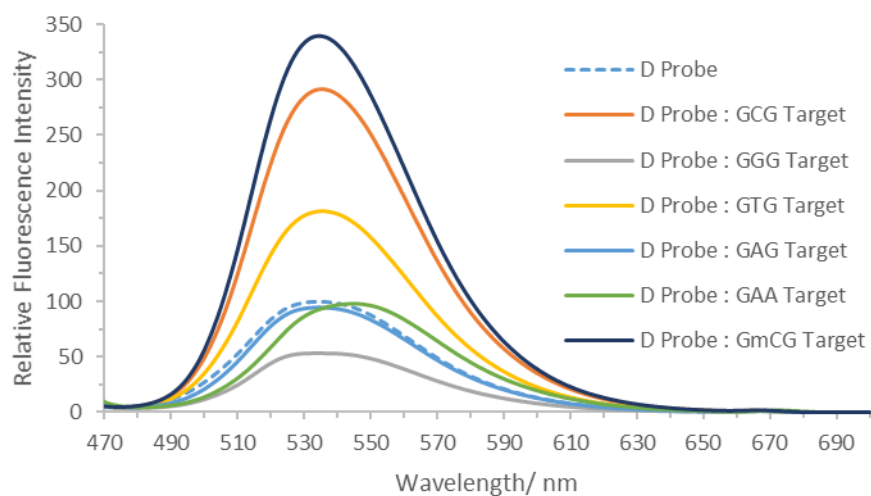


Figure 8.55: Sensing results of D Naph¹_{dimethyl} probes upon duplex formation with target. 0.5 μM [Probe], 0.5 μM [Target], 100 mM NaCl, 10 mM sodium phosphate buffer pH 7.0, Milli-Q water. $\lambda_{\text{ex}} = 450 \text{ nm}$, 298 K.

8.2.6.4. Naph¹_{Amine}

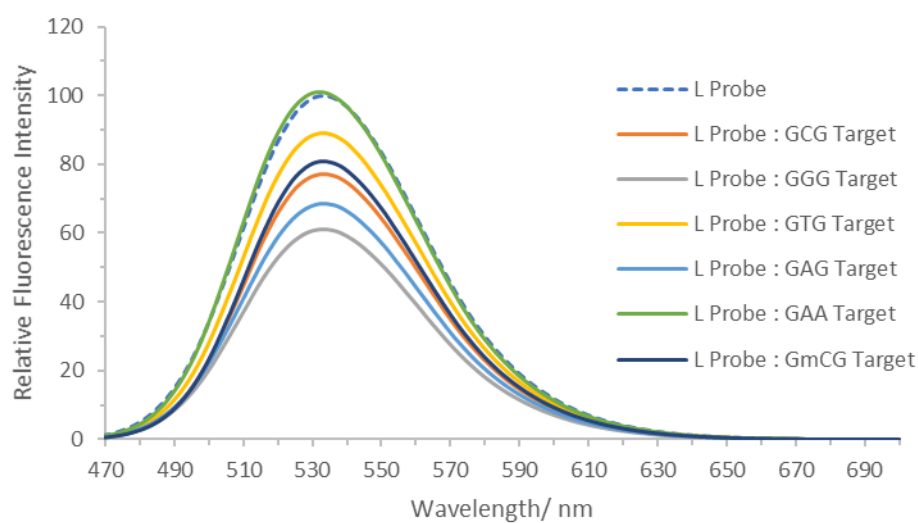


Figure 8.56: Sensing results of L Naph¹_{amine} probes upon duplex formation with target. 0.5 μM [Probe], 0.5 μM [Target], 100 mM NaCl, 10 mM sodium phosphate buffer pH 7.0, Milli-Q water. $\lambda_{\text{ex}} = 450 \text{ nm}$, 298 K.

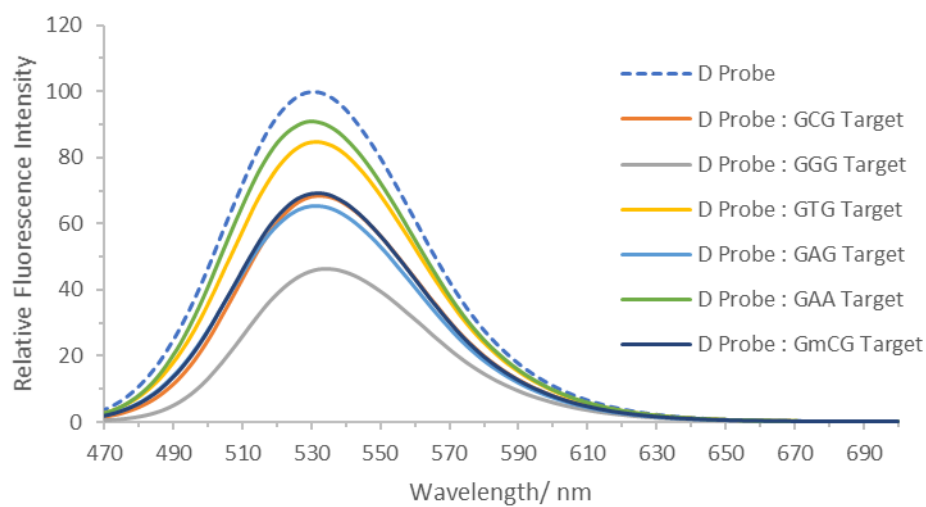


Figure 8.57: Sensing results of D Naph^{Amine} probes upon duplex formation with target. 0.5 μM [Probe], 0.5 μM [Target], 100 mM NaCl, 10 mM sodium phosphate buffer pH 7.0, Milli-Q water. $\lambda_{\text{ex}} = 450 \text{ nm}$, 298 K.

8.3. The Development of a Fluorescent Nucleic Acid Sensing Assay to Detect and Quantify the BRAF V600E Mutation

8.3.1. Previous Work

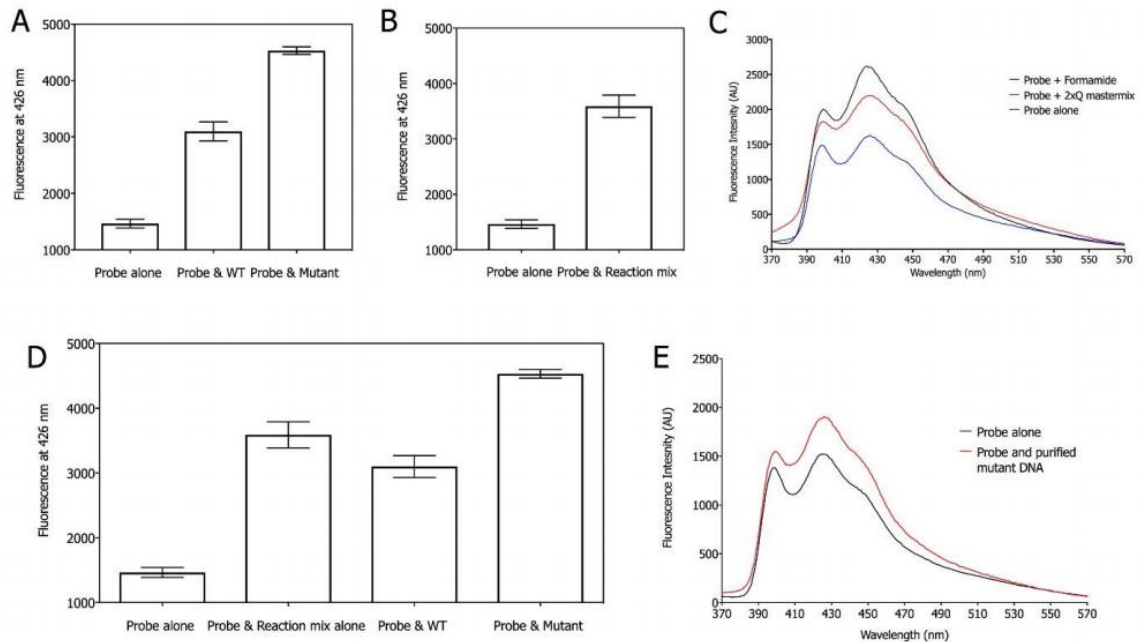


Figure 8.58: Prior BRAF sensing work using PCR-amplified target DNA, taken from A. Ali Thesis. A) The emission data from the study of the un-purified PCR samples compared to the emission of the probe alone, B) the emission data from the study of the probe alone compared to the emission of the probe in the reaction mix, C) the emission data from the study of the probe with formamide or 2xQ mastermix, demonstrating the components that caused a fluorescence increase in the probe, D) the emission data from the study of; the probe alone, the probe and the reaction mix and the PCR samples. All samples except the probe alone were still present in the reaction mix in A-D and finally E) shows the emission data from the study of the purified mutant genomic PCR sample at (0.03 μM) and the probe at 1 μM (0.03 equivalence). The purified products were in 10 mM sodium phosphate buffer, 100 mM NaCl at pH 7. The λ_{ex} = 350 nm, RT, λ_{em} = 426 nm, room temperature. The error bars show one standard deviation from three experimental repeats.

8.3.2. Probe Synthesis and Characterisation

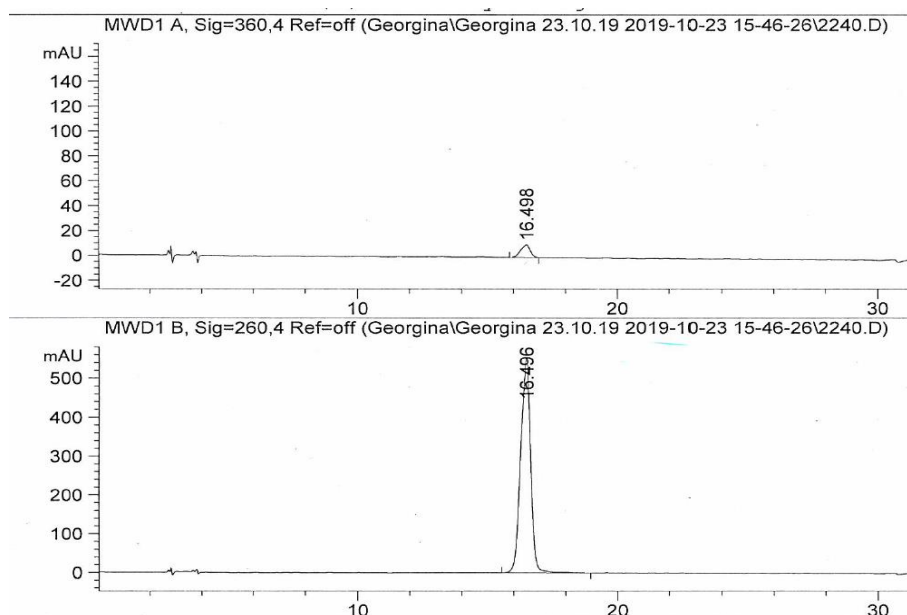


Figure 8.59: Anthracene BRAF probe analytical HPLC trace. Detection wavelengths for DNA at 260 nm and anthracene tag modification at 360 nm. Purity shown as 100%.

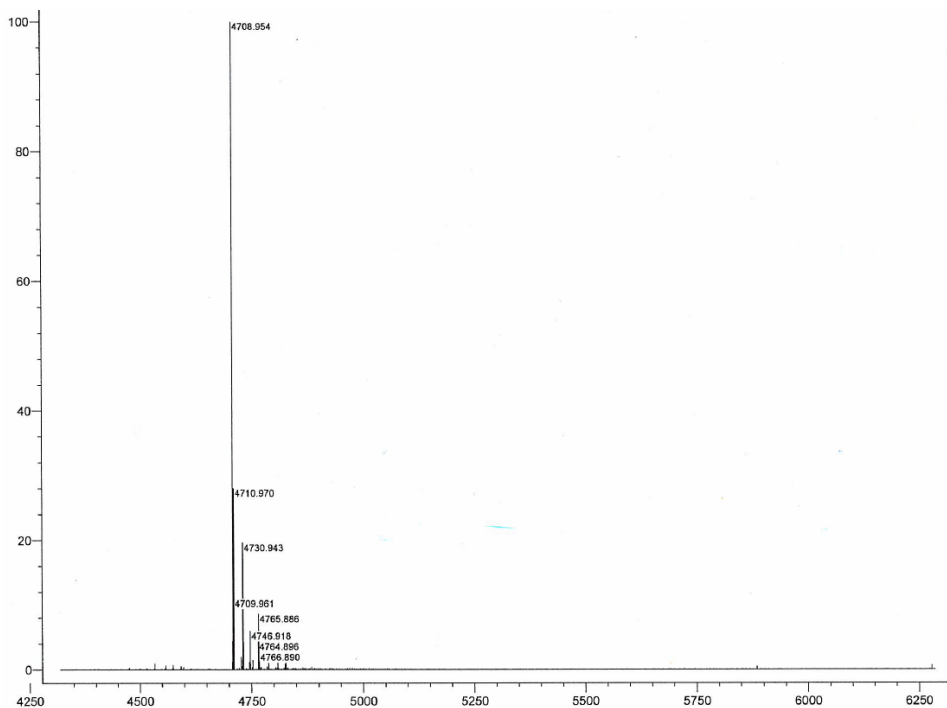


Figure 8.60: Mass spectrum of purified anthracene BRAF V600E probe.

Table 8.6: Mass Spectrometry oligonucleotide characterisation results.

	Calculated Mass	Mass Found
Anthracene BRAF V600E Probe	4708.91 g mol ⁻¹	4708.954 m/z

8.3.3. Raman Scattering From Water

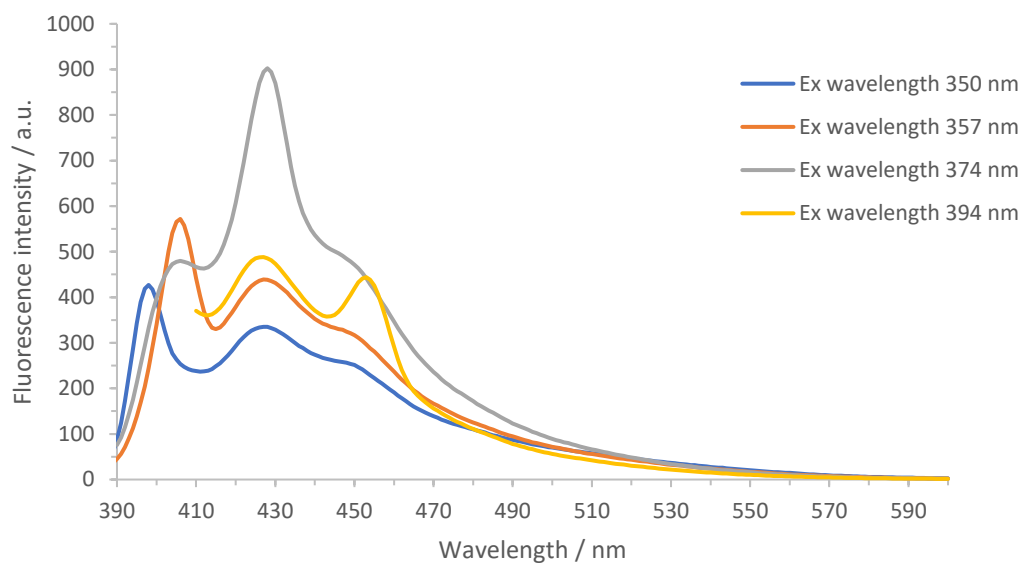


Figure 8.61: Fluorescence emission spectra of anthracene probe at varied excitation wavelengths to show the effect of the Raman scatter peak on the emission profile. [DNA] = 0.5 μ M, aqueous solution

8.3.4. Fluorescence Sensing of PCR Product

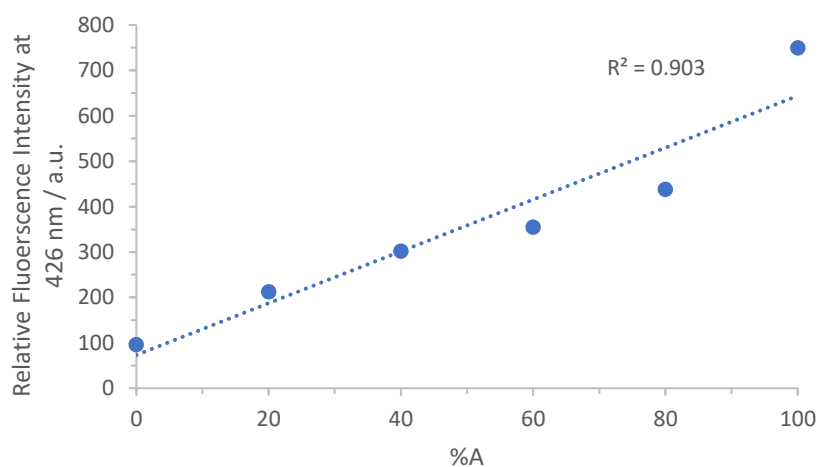


Figure 8.62: Linear correlation plot showing anthracene fluorescence intensity recorded at 426 nm. Fluorescence intensity of the probe alone is 100. The fluorescence intensity once duplexes are formed with varying ratios of A/T target variants are shown relative to the probe strand. 0.1 μ M probe: 0.3 μ M target (100 mM NaCl, 10 mM sodium phosphate, aqueous solution). λ_{ex} = 350 nm, 298 K.

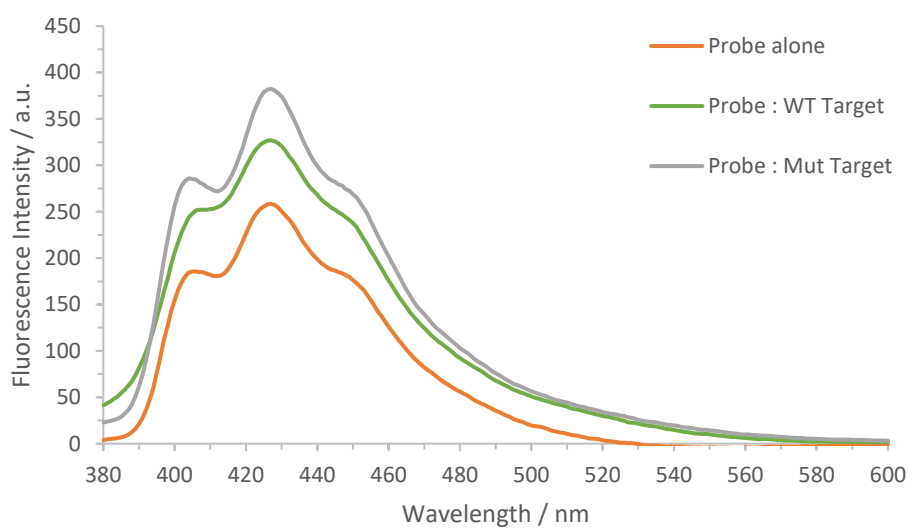


Figure 8.63: Fluorescence emission of anthracene BRAF probe when single-stranded (orange), duplexed with WT PCR derived target (green) and Mut PCR derived target (grey). $\lambda_{ex} = 350 \text{ nm}$, 298 K. Probe concentration, 0.5 μM , target concentration 0.6 μM , 100 mM NaCl, 10 mM sodium phosphate buffer pH 7.0, aqueous solution.

8.4. The Development of Naphthalimide Nucleic Acid Probes for Use in Fluorescence In Situ Hybridisation (FISH) and Super-Resolution Imaging Experiments

8.4.1. Naph 17CEN Probe and Target Characterisation

All modified and unmodified probe and target oligos were purified using HPLC method 1 from Experimental 7.4.

8.4.1.1. HPLC Traces

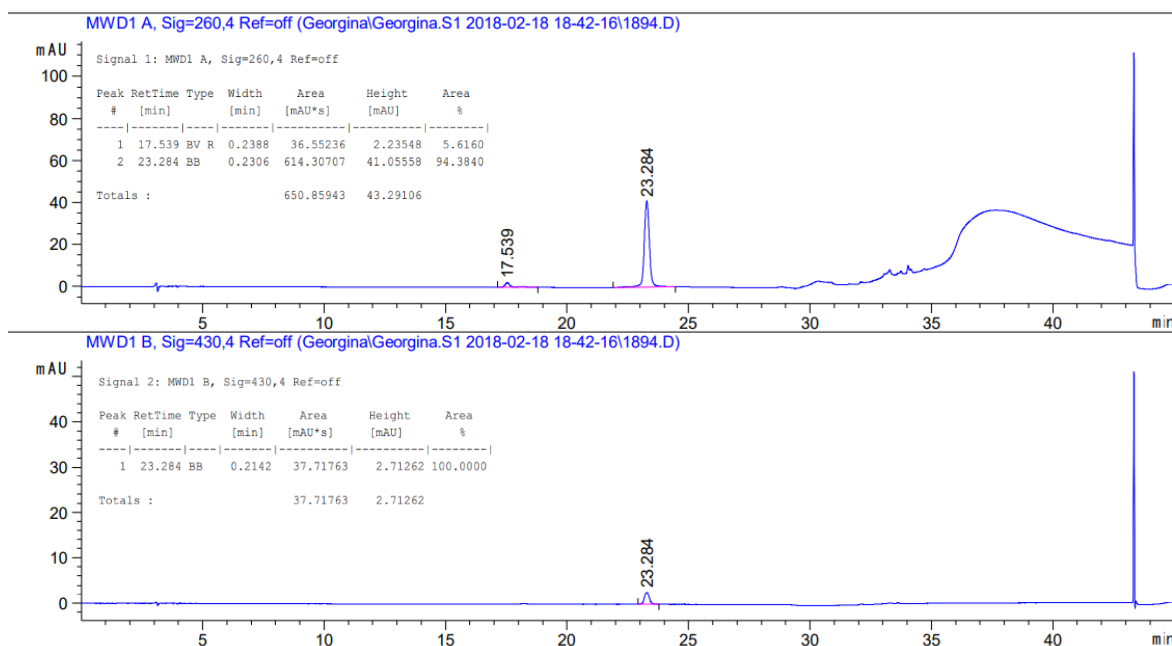


Figure 8.64: Analytical HPLC trace of purified Naph 17CEN probe with L Naph^A_{Short} modification. Detection wavelength is 260 nm for DNA (top) and 430 nm for naphthalimide modification (bottom).

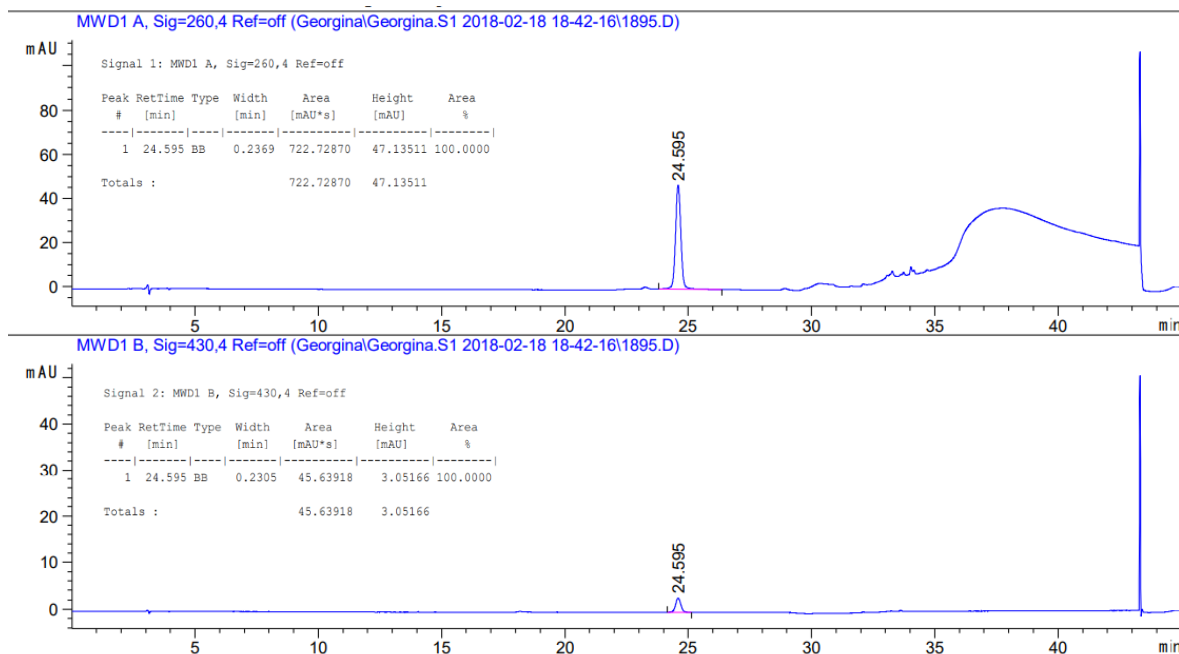


Figure 8.65: Analytical HPLC trace of purified Naph 17CEN probe with D Naph^A_{Short} modification. Detection wavelength is 260 nm for DNA (top) and 430 nm for naphthalimide modification (bottom).

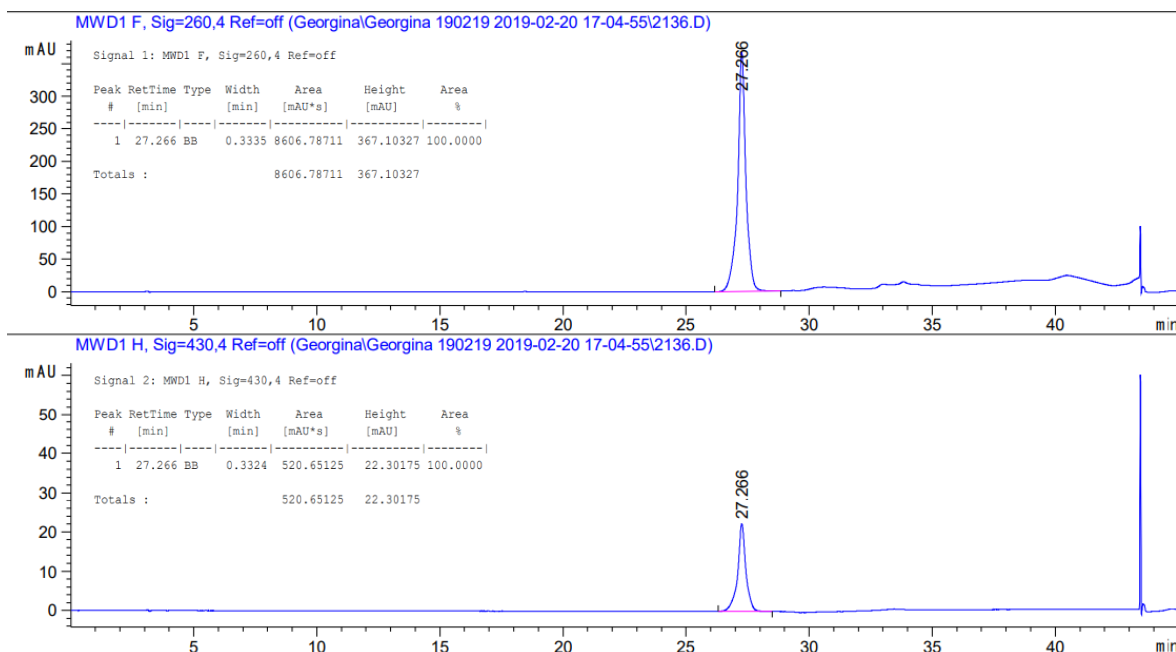


Figure 8.66: Analytical HPLC trace of purified Naph 17CEN probe with L Naph^A_{Long} modification. Detection wavelength is 260 nm for DNA (top) and 430 nm for naphthalimide modification (bottom).

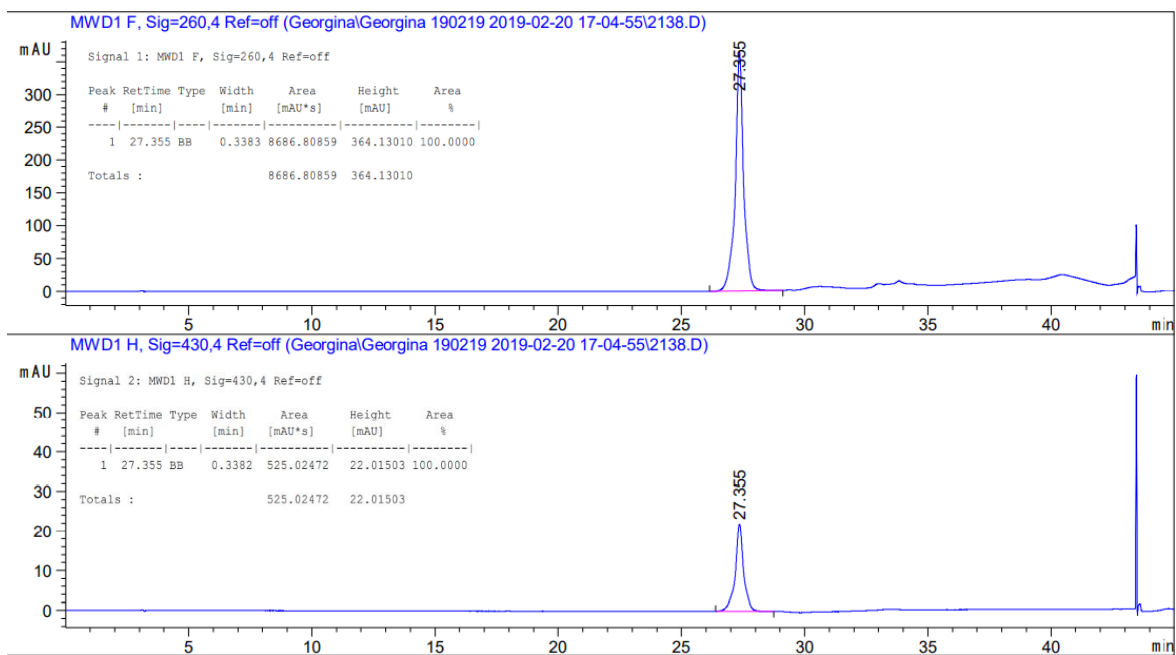


Figure 8.67: Analytical HPLC trace of purified Naph 17CEN probe with D Naph^A_{Long} modification. Detection wavelength is 260 nm for DNA (top) and 430 nm for naphthalimide modification (bottom).

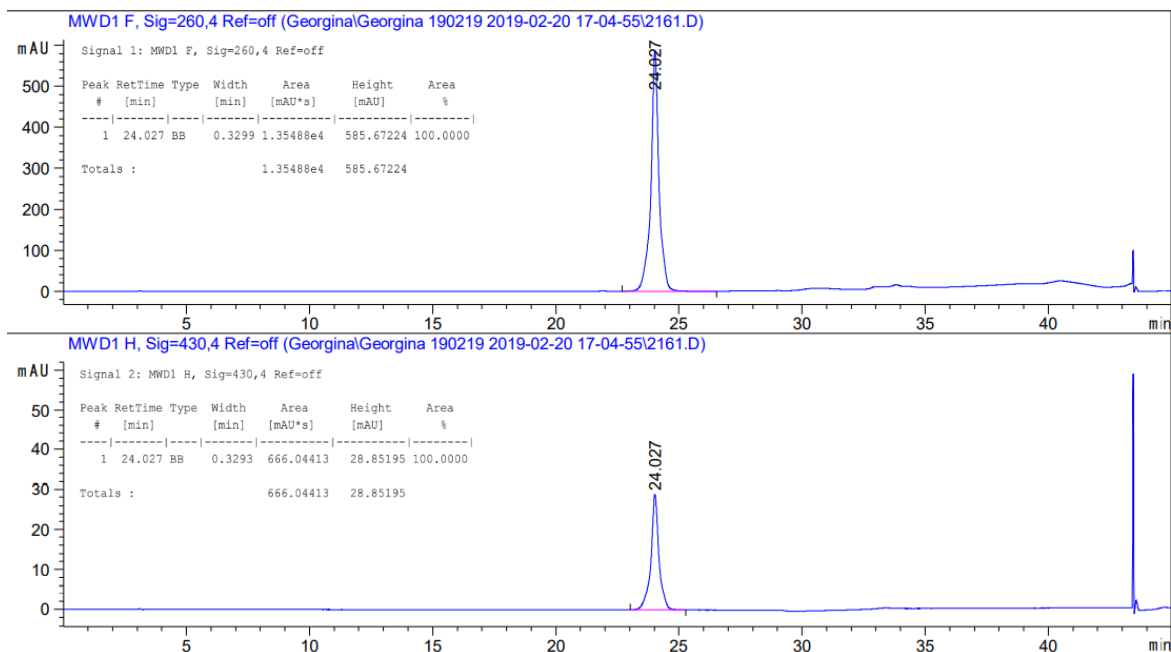


Figure 8.68: Analytical HPLC trace of purified Naph 17CEN probe with L Naph^{Dimethyl} modification. Detection wavelength is 260 nm for DNA (top) and 430 nm for naphthalimide modification (bottom).

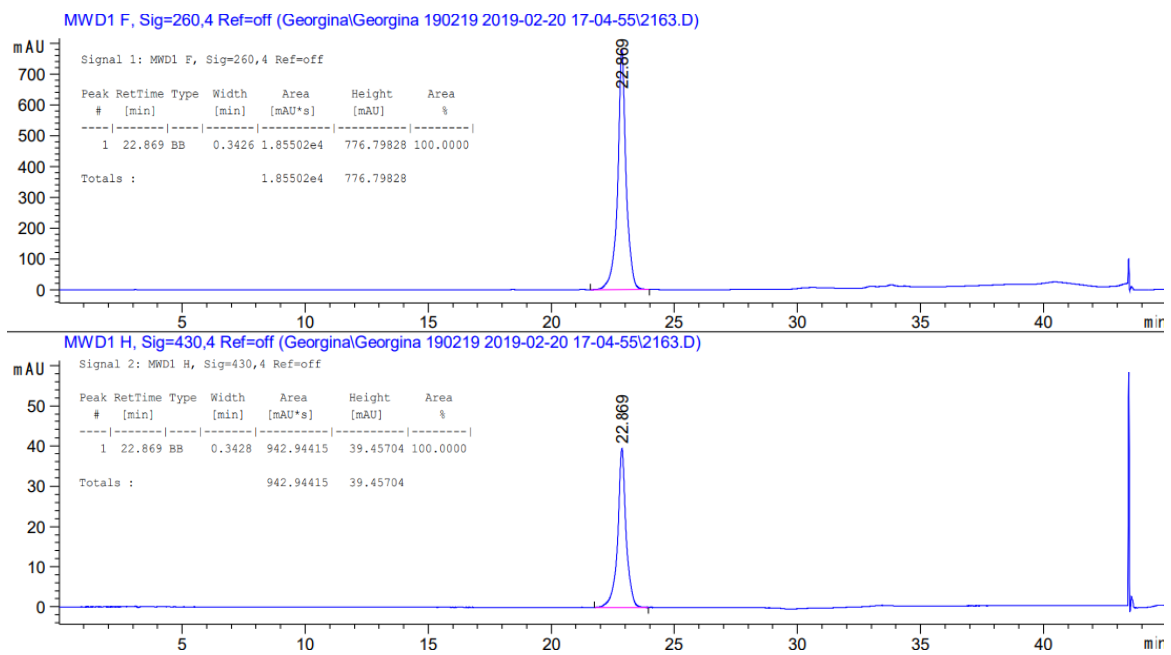


Figure 8.69: Analytical HPLC trace of Naph 17CEN probe with D Naph^{Dimethyl} modification. Detection wavelength is 260 nm for DNA (top) and 430 nm for naphthalimide modification (bottom).

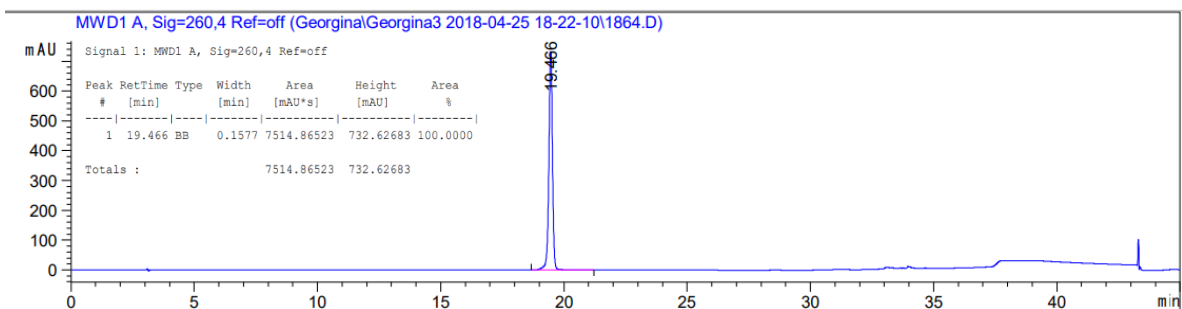


Figure 8.70: Analytical HPLC trace of purified unmodified probe (T). Detection wavelength is 260 nm for DNA.

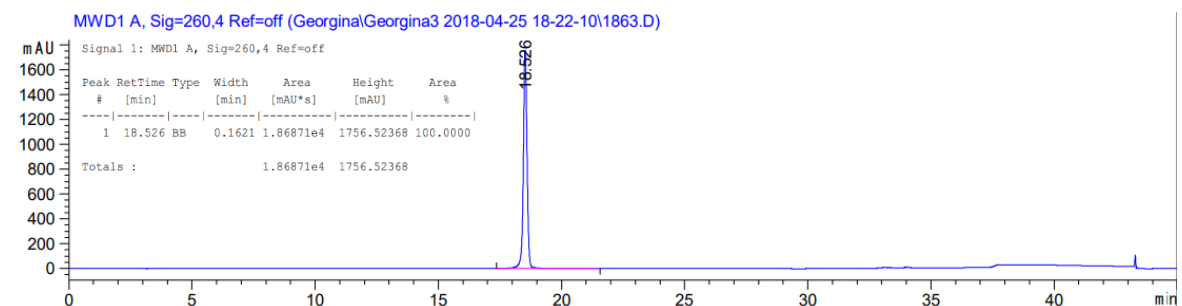


Figure 8.71: Analytical HPLC trace of purified unmodified probe (G). Detection wavelength is 260 nm for DNA.

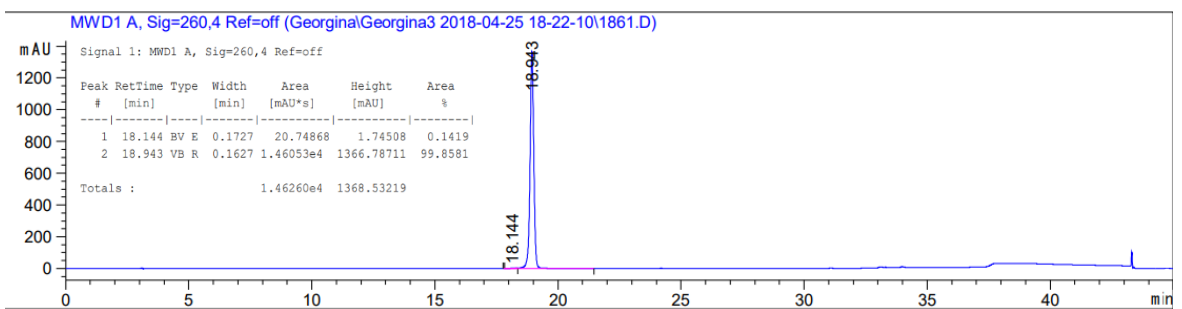


Figure 8.72: Analytical HPLC trace of purified 17CEN Target Variant 1 (C). Detection wavelength is 260 nm for DNA.

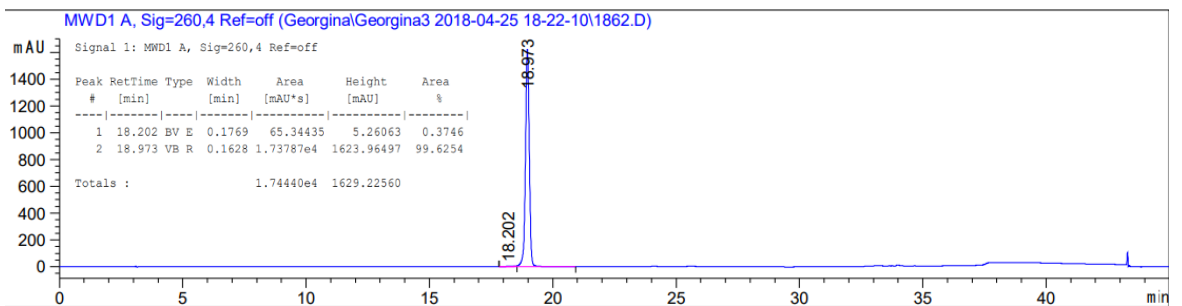


Figure 8.73: Analytical HPLC trace of purified 17CEN Target Variant 2 (A). Detection wavelength is 260 nm for DNA.

8.4.1.2. Mass Spectrometry

Table 8.7: Mass spectrometry oligonucleotide characterisation results.

	Modification (X)	Sequence (5' →3')	Calculated Mass (g mol⁻¹)	Mass Found (m/z)
Unmodified Probe (G)	-	AGT GCA ATG ATC CCC TTG CA	6077	6080.8
Unmodified Probe (T)	-	AGT GCA ATT ATC CCC TTG CA	6052	6156.6
Naph 17CEN Probe	L Naph ^A _{Short}	AGT GCA ATX ATC CCC TTG CA	6152.15	6151.7
Naph 17CEN Probe	D Naph ^A _{Short}	AGT GCA ATX ATC CCC TTG CA	6152.15	6151.8
Naph 17CEN Probe	L Naph ^A _{Long}	AGT GCA ATX ATC CCC TTG CA	6234.16	6234.33
Naph 17CEN Probe	D Naph ^A _{Long}	AGT GCA ATX ATC CCC TTG CA	6234.16	6234.81
Naph 17CEN Probe	L Naph ^I _{Dimethyl}	AGT GCA ATX ATC CCC TTG CA	6206.13	6206.81
Naph 17CEN Probe	D Naph ^I _{Dimethyl}	AGT GCA ATX ATC CCC TTG CA	6206.13	6206.85
17CEN Target Variant 1 (C)	-	TGC AAG GGG ATC ATT GCA CT	6157	6162.3
17CEN Target Variant 2 (A)	-	TGC AAG GGG ATA ATT GCA CT	6178.07	6181.1

8.4.2. TAMRA 17CEN1 Probe

The 17CEN1 Probe was designed and bought by a previous group member, A. Rushton. The probe was labelled with the TAMRA dye.

Table 8.8: TAMRA labelled 17CEN1 probe sequence.

	Sequence
TAMRA 17CEN1 Probe	5' – ATCATTGCACTCTTTGAGGAGTACCG – 3'

8.4.3. FISH Sensing

Table 8.9: Fluorescence sensing results using the Naph 17CEN probes and the short complementary targets. Showing changes in the probe fluorescence intensity. 0.5 μ M Probe: 1.5 μ M Target. Aqueous solution 100 mM NaCl, 10 mM sodium phosphate buffer, pH 7.0. λ_{ex} = 450 nm, 298 K.

	Probe modification	Normalised Intensity at λ_{max} of probe alone	Shift in intensity (in comparison to probe alone)
L probe	Naph ^A _{Short}	100	-
L probe : C Target	Naph ^A _{Short}	171	71
L Probe : A Target	Naph ^A _{Short}	168	68
D Probe	Naph ^A _{Short}	100	-
D Probe : C Target	Naph ^A _{Short}	183	83
D Probe : A Target	Naph ^A _{Short}	186	86
L probe	Naph ^A _{Long}	100	-
L probe : C Target	Naph ^A _{Long}	96	-4
L Probe : A Target	Naph ^A _{Long}	93	-7
D Probe	Naph ^A _{Long}	100	-
D Probe : C Target	Naph ^A _{Long}	94	-6
D Probe : A Target	Naph ^A _{Long}	88	-12
L probe	Naph ^I _{Dimethyl}	100	-
L probe : C Target	Naph ^I _{Dimethyl}	258	158
L Probe : A Target	Naph ^I _{Dimethyl}	174	74
D Probe	Naph ^I _{Dimethyl}	100	-
D Probe : C Target	Naph ^I _{Dimethyl}	80	-20
D Probe : A Target	Naph ^I _{Dimethyl}	46	-54

8.4.4. DNA PAINT Imager Strand Characterisation

All modified and unmodified probe and target oligos were purified using HPLC method 1 from Experimental 7.4.

8.4.4.1. HPLC Traces

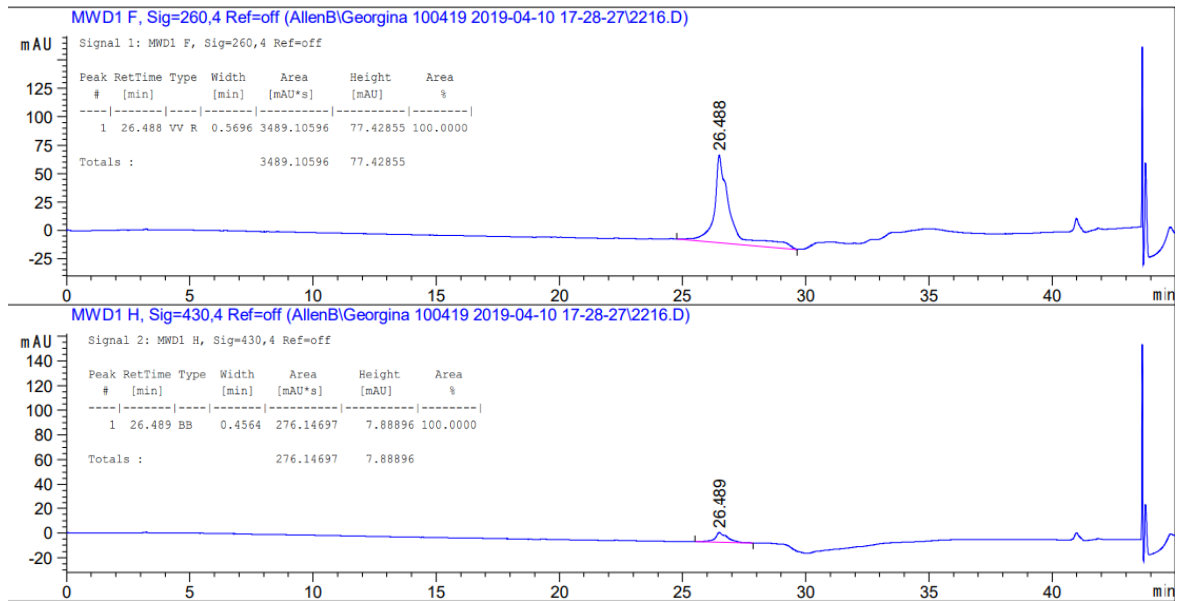


Figure 8.74: Analytical HPLC trace of purified Naph Imager test strand. Detection wavelength is 260 nm for DNA (top) and 430 nm for naphthalimide modification (bottom).

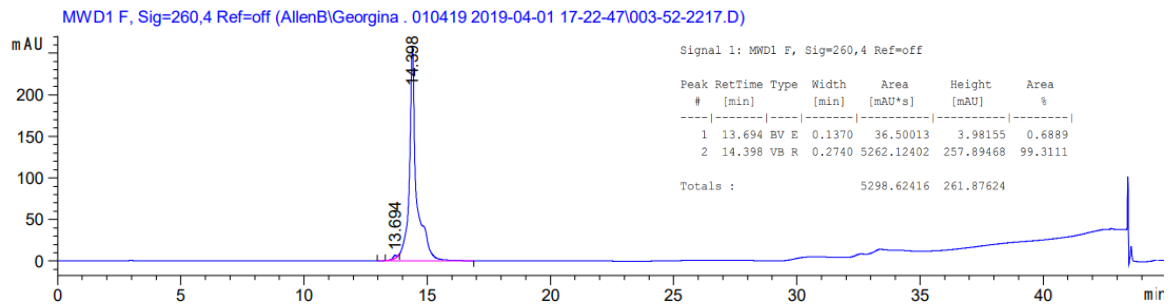


Figure 8.75: Analytical HPLC trace of purified complementary target for the Naph Imager test strand. Detection wavelength is 260 nm for DNA.

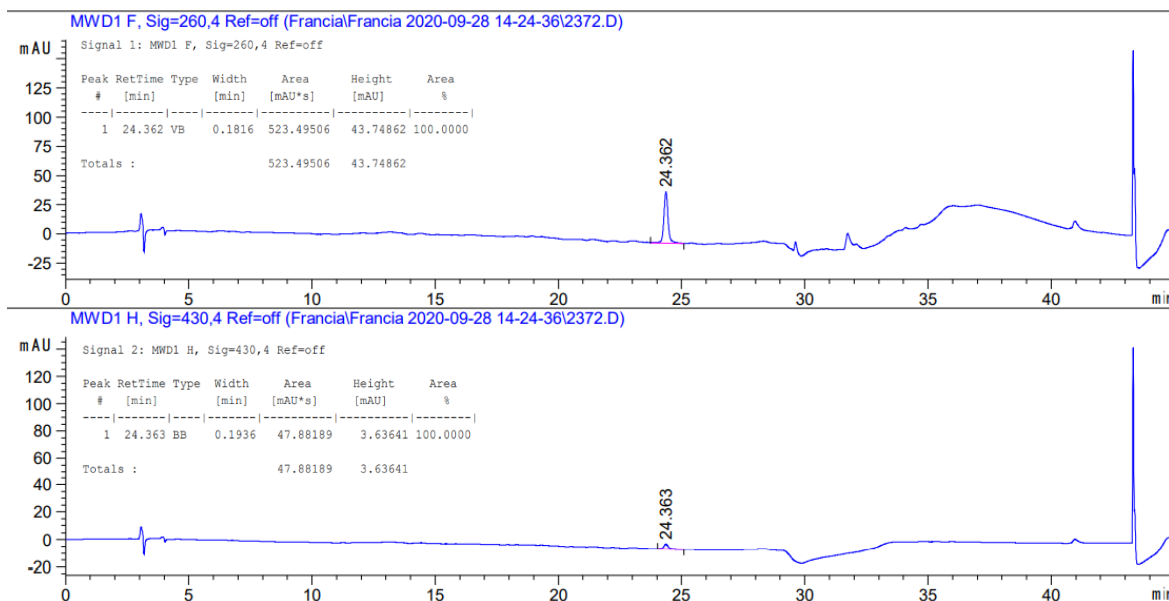


Figure 8.76: Analytical HPLC trace of purified Naph Imer -11 strand. Detection wavelength is 260 nm for DNA (top) and 430 nm for naphthalimide modification (bottom).

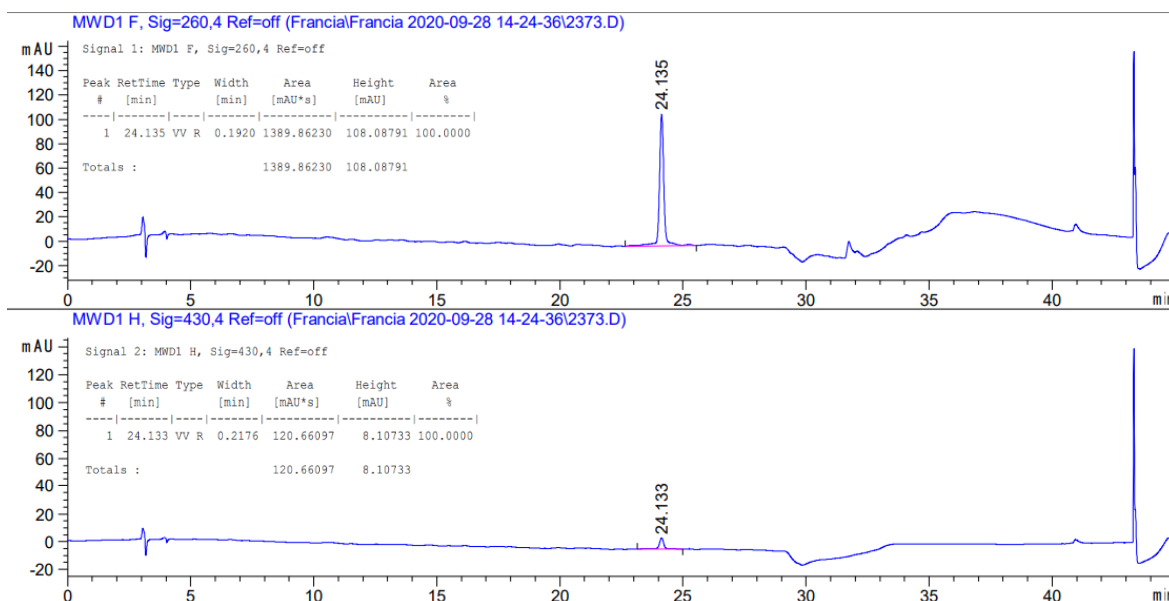


Figure 8.77: Analytical HPLC trace of purified Naph Imer -12 strand. Detection wavelength is 260 nm for DNA (top) and 430 nm for naphthalimide modification (bottom).

8.4.4.2. Mass Spectrometry

Table 8.10: Mass spectrometry oligonucleotide characterisation results.

	Modification (X)	Sequence (5' →3')	Calculated Mass (g mol⁻¹)	Mass Found (m/z)
Naph DNA PAINT Im Test	L Naph ⁱ _{Dimethyl}	GATAXCTCG	2869.58	2869.51
Unmodified Test target	-	CGAGCTATC	2697.5	2697.42
Naph DNA PAINT Imager -11	L Naph ⁱ _{Dimethyl}	CTAGAXGTATA	3510.70	3510.76
Naph DNA PAINT Imager -12	L Naph ⁱ _{Dimethyl}	CTAGAXGTATAA	3823.76	3823.83

8.4.5. DNA Origami Triangle Staple Strand Sequences

Table 8.11: DNA origami triangle. Plate: Triangle core 1.

Well Position	Sequence Name	Sequence
A1	s0t127	TTAAATTGAGATCTACAAAGGCTACTGATAAA
B1	s0t191	TCATATGTGTAATCGTAAAACCTAGTCATTTTC
C1	s0t223	CCGCCACCCAAGCCCAATAGGAACGTAAATGA
D1	s0t255	TACCGCCATGAGTTTCGTCACCAGGATCTAAA
E1	s1t176	GATGAACGACCCCGTTGATAATCAGAAAAGC
F1	s1t208	AGGGATAGCTCAGAGCCACCACCCATGTCAA
G1	s1t240	CGTAACACCCCTCAGAACCGCCACCCTCAGAA
H1	s1t272	ACAACGCCTATCACCGTACTCAGGAGGTTTAG
A2	s2t127	TTAATGCCTATTTCAACGCAAGGGCAAAGAA
B2	s2t191	GTGAGAAAATGTGTAGGTAAAGATACAACCTT
C2	s2t223	ATTTTCTGTCAGCGGAGTGAGAATACCGATAT
D2	s2t255	GTTTTGTCAGGAATTGCGAATAATCCGACAAT
E2	s3t91	ACCCTGTAATACTTCAGAGCA
F2	s3t112	AGAAGCCTGGAGAGGGTAG
G2	s3t176	CCTGAGTAGCCGGAGACAGTCAAAGAGAATC
H2	s3t208	CAACAGTTTATGGGATTTTGCTAATCAAAGG
A3	s3t240	ACAACCTAAGTCTTTCCAGACGTTACCATGTAC
B3	s3t272	CACGTTGATCATAGTTAGCGTAACTACAACT
C3	s4t95	TAAAGCTATATAACAGTTGATTCCCATTTTTG

D3	s4t127	TTAGCAAATAGATTTAGTTTGACCAGTACCTT
E3	s4t191	GGCATCAAATTTGGGGCGCGAGCTAGTTAAAG
F3	s4t223	ATTCGGTCTGCGGGATCGTCACCCGAAATCCG
G3	s4t255	GACAACAAGCATCGGAACGAGGGTGAGATTTG
H3	s4t287	AACAGCTTGCTTTGAGGACTAAAGCGATTATA
A4	s5t59	AAAGTACGGTGTCTGAATATAA
B4	s5t80	TCATTCCAAATCGGTTGTA
C4	s5t112	CGAACGAGATTAAGCAATAAAGCCTTTGCGGG
D4	s5t176	ATATTTTCTTCTACTAATAGTAGTATGCAATG
E4	s5t208	GCCGCTTTGCTGAGGCTTGCAAGGGGAAAAGGT
F4	s5t240	GAAAGACACCATCGCCACGCATAAGAAAGGA
G4	s5t272	CTACAGAGGATACCGATAGTTGCGAATTTTTT
H4	s5t304	ATGAGGAACTTGCTTTGAGGTGAGGCTCCAA
A5	s6t63	TGCTGTAGATCCCCCTCAAATGCTGCGAGAGG
B5	s6t95	CGGATGGCACGAGAATGACCATAATCGTTTAC
C5	s6t127	TAATTGCTTTACCCTGACTATTATGAGGCATA
D5	s6t191	TTCGAGCTAAGACTTCAAATATCGGGAACGAG
E5	s6t223	CGACCTGCGGTCAATCATAAGGGAACGGAACA
F5	s6t255	TATCATCGTTGAAAGAGGACAGATGGAAGAAA
G5	s6t287	CCAAGCGCAGGCGCATAGGCTGGCAGAACTGG
H5	s6t319	AAAACACTTAATCTTGACAAGAACTTAATCAT
A6	s7t27	ACTGCGGAATCGTAGGGGGTAATAGTAAAATGTTTAGACT
B6	s7t48	TTCATTGACTCAACATGTT
C6	s7t80	TTCAGAAATTAGAGCTTAATTGCTTGGAAGTT
D6	s7t112	TCAGGTCTCCTTTTGATAAGAGGTCAATTCTG
E6	s7t176	AAGCCCGATCAAAGCGAACCAGACGTTTAGCT
F6	s7t208	GCGCAGACTCCATGTTACTTAGCCCGTTTTAA
G6	s7t240	GACCAACTCCTGATAAATTGTGTCTCAGCAGC
H6	s7t272	TACAGACCGAAACAAAGTACAACGAGCAACGG
A7	s7t304	ATCAAGAGCATCTTTGACCCCCAGACTTTTTTC
B7	s7t336	CATTACCCACGAAAGAGGCAAAAGTAAAATAC
C7	s8t63	CTTTTGCAAAGAAGTTTTGCCAGCATAAATATTTTTTTTATAACATCTA
D7	s8t95	CAGACGACGATAAAAACCAAATATTAACAG
E7	s8t127	GTAAGAGCAACACTATCATAACCCATCAAAAATTTTTTTTATAACATCTA
F7	s8t191	AGATTTAGGAATACCACATTCAACTTAAGAGGTTTTTTTATAACATCTA
G7	s8t223	ACATTATTACAGGTAGAAAGATTCATCAGTTG
H7	s8t255	AATCTACGTTAATAAAACGAACTAACCGAACTTTTTTTTATAACATCTA
A8	s8t287	CTCATTATACCAGTCAGGACGTTGGAACGGTG
B8	s8t319	TGTGAATTACCTTATGCGATTTTATGACCTTCTTTTTTTATAACATCTA
C8	s8t351	GCTTGAGATGGTTTAATTTCAACTCGGATATT
A9	s2t290-notail	ACAGACAGCCCAAATCTCCAAAAAAAATTTCTTA

B9	s4t322-notail	CGGTTTATCAGGTTTCCATTAACGGGAATACACT
C9	s6t354-notail	ACCAACCTAAAAAATCAACGTAACAAATAAATTGG
D9	s8t386-notail	CCTGACGAGAAACACCAGAACGAGTAGGCTGCTCATT TTTTTTTATAACATCT A
A10	s1t280-brdg- notail-3T	TGTAGCATTCCTTTTATAAACAGTT
B10	s3t304-brdg- 2T	AAGGAGCCTTTAATTGTATTTCCACCAGAGCCGCC
C10	s5t336-brdg- 1T	GTAATGCCACTACGAAGGCTTAGCACCATTACCA
D10	s7t368-brdg- 0T	TTCAGTGAATAAGGCTTGCAACAAAGTTACCAG
A11	s1t144	TTGCCTGACAGGAAGATTGTATAAGCAAATAT
B11	s3t144	TTTTAGAATATTCAACCGTTCTAGTCAGGTCA
C11	s5t144	CATTCGCAAATCATAACAGGCAAGATAAAAAAT
D11	s7t144	GCAAAGCGCAGGTCAGGATTAGAGATTAGATA
A12	s0t159	CCCAAAAAGAGTCTGGAGCAAACAATCACCAT
B12	s2t159	CAATATGACCCTCATATATTTTAAAGCATTAA
C12	s4t159	CATCCAATAAATGGTCAATAACCTCGGAAGCA
D12	s6t159	AACTCCAAGATTGCATCAAAAAGATAATGCAG
E12	s8t159	ATACATAACGCCAAAAGGAATTACAGTCAGAA

Table 8.12: DNA origami triangle. Plate: Triangle core 2.

Well Position	Sequence Name	Sequence
A1	s10t127	AATAGGTGAATGCCCCCTGCCTATGGTCAGTG
B1	s10t191	CGGGGTTTCCTCAAGAGAAGGATTTTGAATTA
C1	s10t223	ATTAATTAATGGAAACAGTACATTAGTGAAT
D1	s10t255	GAAGATGAGTGAATAACCTTGCTTATAGCTTA
E1	s9t176	CTGAGACTTGCTCAGTACCAGGCGGATAAGTG
F1	s9t208	CCTTTTTTCATTTAACAATTTTCATAGGATTAG
G1	s9t240	ATATGTGATGAAACAAACATCAAGAAAACAAA
H1	s9t272	CGTCGCTATTCATTTCAATTACCTGAGCAAAA
A2	s12t127	CCTTGAGTCAGACGATTGGCCTTGCGCCACCC
B2	s12t191	AGCGTCATGTCTCTGAATTTACCGACTACCTT
C2	s12t223	TTATCAAACCGGCTTAGGTTGGGTAAGCCTGT
D2	s12t255	GATTAAGAAATGCTGATGCAAATCAGAATAAA
E2	s11t91	GCCAGCATTGACACCACCCTC
F2	s11t112	AGGCAGGTAACAGTGCCCG
G2	s11t176	AAAGCGCAACATGGCTTTTGATGATTAAGAGG
H2	s11t208	TTAACCTATCATAGGTCTGAGAGTTCCAGTA

A3	s11t240	TATATGTACGCTGAGAAGAGTCAAAAATCAAT
B3	s11t272	AGACAAAGCCTTGAAAACATAGCGCTGTAAT
C3	s14t95	AGAGCCGCACCATCGATAGCAGCATGAATTAT
D3	s14t127	TCAGAACCCAGAATCAAGTTTGCCGGTAAATA
E3	s14t191	TTCATAATCCCCTTATTAGCGTTTTTCTTACC
F3	s14t223	TTAGTATCGCCAACGCTCAACAGTCGGCTGTC
G3	s14t255	CACCGGAATCGCCATATTTAACAAAATTTACG
H3	s14t287	GTGTGATAAGGCAGAGGCATTTTCAGTCCTGA
A4	s13t59	TTAGCAAGGCCGGGGGAATTA
B4	s13t80	CCAATGAACACCAGAACCA
C4	s13t112	AGTAGCGAGCCACCCTCAGAGCCAGGAGGTTG
D4	s13t176	GTCATAGCCAAAATCACCGGAACCCAGAATGG
E4	s13t208	AGTATAAAATATGCGTTATACAAAGCCATCTT
F4	s13t240	ATTGAGAATCATAATTACTAGAAATATATAAC
G4	s13t272	TGTAATTTAATAAGGCGTTAAATACAATCGCA
H4	s13t304	AATAAGAGATTTAATGGTTTGAAATTCAAATA
A5	s16t63	GAGCCAGCGAATACCCAAAAGAACATGAAATA
B5	s16t95	CACCGTCACCTTATTACGCAGTATTGAGTTAA
C5	s16t127	TTGACGGAAATACATACATAAAGGGCGCTAAT
D5	s16t191	ATGGTTTATGTCACAATCAATAGATATTAAC
E5	s16t223	TTTCCTTAGCACTCATCGAGAACAATAGCAGC
F5	s16t255	AGCATGTATTTTCATCGTAGGAATCAAACGATT
G5	s16t287	ACAAGAAAGCAAGCAAATCAGATAACAGCCAT
H5	s16t319	GCGCCTGTTATTCTAAGAACGCGATTCCAGAG
A6	s15t27	AAGGAAACCGAGGTTTTTAAGAAAAGTAAGCAGATAGCCG
B6	s15t48	TAATAACGAAAATCACCAG
C6	s15t80	TTAAGACTCCGACTTGAGCCATTTAAACGTCA
D6	s15t112	ACGTAGAAAATTATTCATTAAGGCCGTAATC
E6	s15t176	GTTTATTTCCAGCGCCAAAGACAACATTTTCG
F6	s15t208	CAAGTACCTCATTCCAAGAACGGGAAATTCAT
G6	s15t240	GTTTTTATGAAACCAATCAATAATAGGGCTTA
H6	s15t272	GCCCAATAAATAATATCCCATCCTCGCCAACA
A7	s15t304	TTATCCGGTTATCAACAATAGATAGAGCCAGT
B7	s15t336	AGCGAACCCAACATGTTTCAGCTAAAAAAGGTA
C7	s18t63	GCAATAGCTATCTTACCGAAGCCCAAACGCAA
D7	s18t95	GCCCAATAATAAGAGCAAGAAACATGGCATGA
E7	s18t127	ATCAGAGAGATAACCCACAAGAATGTTAGCAATTTTTTTTATACATCTA
F7	s18t191	GCGCATTAGACGGGAGAATTAACCTCGGAATAA
G7	s18t223	CTTTACAGAGAGAATAACATAAAAAACAGGGAATTTTTTTTATACATCTA
H7	s18t255	TTTTGTTTAAACGTCAAAAATGAAAAGCAAGCC
A8	s18t287	ATTATTTATCCCAATCCAATAAGATTACCGC

B8	s18t319	CCTAATTTGCCAGTTACAAAATAATAGAAGGCTTTTTTTTATACATCTA
C8	s18t351	TCTTACCAACGCTAACGAGCGTCTGGCGTTTT
A9	s12t290-notail	TCCCTTAGAATAACGCGAGAAAACTTTTACCGACC
B9	s14t322-notail	TTCTGACCTAAAATATAAAGTACCGACTGCAGAAC
C9	s16t354-notail	ACGACAATAAATCCCGACTTGCGGGAGATCCTGAA
D9	s18t386-notail	TGCTATTTTGACCCAGCTACAATTTTGTTTTGAA
A10	s9t280-brdg-notail-3T	TTAATTAATTTTTTACCATATCAAA
B10	s11t304-brdg-2T	TATTTTAGTTAATTTTCATCTTAGACTTTACAAACA
C10	s13t336-brdg-1T	AAGTAATTCTGTCCAGACGTATACCGAACGAACC
D10	s15t368-brdg-0T	GCCTTAAATCAAGATTAGTGTAGCAATACTTCT
A11	s9t144	CTATTATTAGGGTTGATATAAGTATAGCCCGG
B11	s11t144	AAACAAATTAATAAGTTTTAACGGTTCGGAAC
C11	s13t144	CAGACTGTCCGCCTCCCTCAGAGCATATTCAC
D11	s15t144	TATAAAAGCGATTGAGGGAGGGAATTTAGCGT
A12	s10t159	CCGTCGAGCTGAAACATGAAAGTATACAGGAG
B12	s12t159	TGTA CTGGAAATCCTCATTAAAGCAGAGCCAC
C12	s14t159	CACCGAAAGCGCGTTTTTCATCGGAAGGGCGA
D12	s16t159	CATTCAACAAACGCAAAGACACCAGAACACCC
E12	s18t159	TGAACAAAGTCAGAGGGTAATTGATGGCAACA

Table 8.13: DNA origami triangle. Plate: Triangle core 3.

Well Position	Sequence Name	Sequence
A1	s20t127	GCGAATTAATTATTTGCACGTAAATTCTGAAT
B1	s20t191	TCGGGAGATATACAGTAACAGTACAAATAATT
C1	s20t223	TTTAACCAGCCTTCCTGTAGCCAGGCATCTGC
D1	s20t255	TCGCATTAATGTGAGCGAGTAACACACGTTGG
E1	s17t176	CAGATGAAAACAATAACGGATTTCGCCTGATTG
F1	s17t208	CGCGTCTGATAGGAACGCCATCAACTTTTACA
G1	s17t240	AACATTAATAATTTTTGTTAAATCAGCTCATT
H1	s17t272	GATTCTCCTAAACGTTAATATTTTGTAAAAT
A2	s22t127	AATGGAAGCGAACGTTATTAATTTCTAACAAC
B2	s22t191	CCTGATTAAGGAGCGGAATTATCTCGGCCTC
C2	s22t223	CAGTTTGACGCACTCCAGCCAGCTAAACGACG
D2	s22t255	TGTAGATGGGTGCCGAAACCAGGAACGCCAG
E2	s19t91	ATTCGACAACCTCGTAATACAT
F2	s19t112	CCTTTGCCGGTTAGAACCT
G2	s19t176	ACCACCAGTCAGATGATGGCAATTTTAAACGT
H2	s19t208	AGGAAGATGGGGACGACGACAGTAATCATATT

A3	s19t240	CCGCTTCTGGCGCATCGTAACCGTCTTTCATC
B3	s19t272	CATTCGCCCCGTAATGGGATAGGTACCCGTCG
C3	s24t95	TTGAGGATGGTCAGTATTAACACCTTGAATGG
D3	s24t127	TAATAGATCGCTGAGAGCCAGCAGAAGCGTAA
E3	s24t191	GCAAATCACCTCAATCAATATCTGCAGGTCGA
F3	s24t223	GCCAGTGCATCCCCGGTACCGAGTTTTTCT
G3	s24t255	GGTTTTCCATGGTCATAGCTGTTTGAGAGGCG
H3	s24t287	TGCTGCAAATCCGCTCACAATCCCAGCTGCA
A4	s21t59	ACCAGCAGAAGATGATAGCCC
B4	s21t80	GGTGAGGCTTAGAAGTATT
C4	s21t112	CAGTGCCATAGAGCCGTC AATAGATATTAAT
D4	s21t176	TATCAAACACAGTTGAAAGGAATTACAAAGAA
E4	s21t208	CTCTAGAGCAAGCTTGCATGCCTGGTCAGTTG
F4	s21t240	TCGTAATCCAGTCACGACGTTGTATTCCGGCA
G4	s21t272	AAATTGTTGGCGATTAAGTTGGGTCAAAGCGC
H4	s21t304	TACGAGCCACGCCAGCTGGCGAAATGTTGGGA
A5	s26t63	TAAAACATTAGAAGAACTCAAACCTTTTTATAA
B5	s26t95	CTATTAGTATATCCAGAACAATATCAGGAACG
C5	s26t127	GAATACGTAACAGGAAAAACGCTCCTAAACAG
D5	s26t191	CGACCAGTACATTGGCAGATTCACCTGATTGC
E5	s26t223	TTTCACCAGCCTGGCCCTGAGAGAAAGCCGGC
F5	s26t255	GTTTGCCTCACGCTGGTTTGCCCAAGGGAGC
G5	s26t287	TTAATGAAGTTTGATGGTGGTTCCGAGGTGCC
H5	s26t319	TTCCAGTCCTTATAAATCAAAGAGAACCATC
A6	s23t27	TTGATTAGTAATAGTCTGTCCATCACGCAAATTAACCGTT
B6	s23t48	TGCCTGAGCGCCATTA AAA
C6	s23t80	TGCTGGTACTTTAATGCGCGAACTAAAACAGA
D6	s23t112	GCCATTGCGGCACAGACAATATTTGCCTGCAA
E6	s23t176	GATTATTTAATAAAAAGGGACATTCACCTCAA
F6	s23t208	CCTTACCCTGAGACGGCAACAGCAGTCACA
G6	s23t240	AAGCGGTCATTGGGCGCCAGGGTGGCTCGAAT
H6	s23t272	AAAATCCTTCGGCCAACGCGCGGGCCTGTGTG
A7	s23t304	CAAATCCGGGAAACCTGTCTGTGCACACAACA
B7	s23t336	AGATAGGGATTGCGTTGCGCTCACAAGCCTGG
C7	s28t63	TCAGTGAGGCCACCGAGTAAAAGAACATCACT
D7	s28t95	GTACGCCAGAATCCTGAGAAGTGTATCGGCCT
E7	s28t127	GAGGCCGATTAAAGGGATTTTAGATACCGCCA
F7	s28t191	TGGTTGCTTTGACGAGCACGTATACTGAAATG
G7	s28t223	GAACGTGGCGAGAAAGGAAGGGAAGCGTACTATTTTTTTTATACATCT A
H7	s28t255	CCCCGATTTAGAGCTTGACGGGGAGTTGCAGC
A8	s28t287	GTAAAGCACTAAATCGGAACCCTAAGCAGGCG

B8	s28t319	ACCCAAATCAAGTTTTTTGGGGTCGAAATCGG
C8	s28t351	TATCAGGGCGATGGCCCACTACGTATAGCCCCG
A9	s22t290-notail	CGGCGGATTGAATTCAGGCTGCGCAACGGGGGATG
B9	s24t322-notail	TCTTCGCTATTGGAAGCATAAAGTGTATGCCCGCT
C9	s26t354-notail	AACTCACATTATTGAGTGTTGTTCCAGAAACCGTC
D9	s28t386-notail	ACGTGGACTCCAACGTCAAAGGGCGAATTTGGAAC
A10	s17t280-brdg-notail-3T	GTGGGAACAAATTTCTATTTTTGAG
B10	s19t304-brdg-2T	AGGGCGATCGGTGCGGGCCTTCCAAAAACATTATG
C10	s21t336-brdg-1T	GGTGCCTAATGAGTGAGCTTTTAAATATGCAACT
D10	s23t368-brdg-0T	AAGAGTCCACTATTAAGAGGATAGCGTCCAAT
A11	s17t144	AAAGAAATACCAAGTTACAAAATCGCGCAGAG
B11	s19t144	TGAGTAACATTGTTTGGATTATACACAGAAAT
C11	s21t144	AAATCTAAAATATCTTTAGGAGCATAAAAAGTT
D11	s23t144	ACCTACATAACCCTTCTGACCTGACAAATGAA
A12	s20t159	CTTTGAATTGCGTAGATTTTCAGGCATCAATA
B12	s22t159	TAATCCTGATTATCATTTTGC GGAGAGGAAGG
C12	s24t159	TTATCTAAAGCATCACCTTGCTGATGGCCAAC
D12	s26t159	AGAGATAGTTTGACGCTCAATCGTACGTGCTT
E12	s28t159	TCCTCGTTAGAATCAGAGCGGGAGATGGAAAT

Table 8.14: DNA origami triangle. Plate: Triangle 18T inner core.

Well Position	Sequence Name	Sequence
A1	s0t127-18T	TTTTTTTTTTTTTTTTTTTTAAATTGAGATCTACAAAGGCTACTGATAAA
B1	s0t159-18T	TTTTTTTTTTTTTTTTTTTTCCCAAAAAGAGTCTGGAGCAAACAATCACCAT
C1	s0t191-18T	TTTTTTTTTTTTTTTTTTTTCATATGTGTAATCGTAAAAC TAGTCATTTTC
D1	s0t223-18T	TTTTTTTTTTTTTTTTTTTTCCGCCACCCAAGCCCAATAGGAACGTAAATGA
E1	s0t255-18T	TTTTTTTTTTTTTTTTTTTTACCGCCATGAGTTTCGTCACCAGGATCTAAA
A2	s10t127-18T	TTTTTTTTTTTTTTTTTTTTAATAGGTGAATGCCCCCTGCCTATGGTCAGTG
B2	s10t159-18T	TTTTTTTTTTTTTTTTTTTTCCGTGCGAGCTGAAACATGAAAGTATACAGGAG
C2	s10t191-18T	TTTTTTTTTTTTTTTTTTTTCGGGGTTTCCTCAAGAGAAGGATTTTGAATTA
D2	s10t223-18T	TTTTTTTTTTTTTTTTTTTTATTAATTAATGAAACAGTACATTAGTGAAT
E2	s10t255-18T	TTTTTTTTTTTTTTTTTTTTGAAGATGAGTGAATAACCTTGCTTATAGCTTA
A3	s20t127-18T	TTTTTTTTTTTTTTTTTTTTGCGAATTAATTATTTGCACGTAAATTCTGAAT
B3	s20t159-18T	TTTTTTTTTTTTTTTTTTTTCTTTGAATTGCGTAGATTTTCAGGCATCAATA
C3	s20t191-18T	TTTTTTTTTTTTTTTTTTTTCGGGAGATATACAGTAACAGTACAAATAATT
D3	s20t223-18T	TTTTTTTTTTTTTTTTTTTTAACCAGCCTTCTGTAGCCAGGCATCTGC
E3	s20t255-18T	TTTTTTTTTTTTTTTTTTTTCGCATTAAATGTGAGCGAGTAACACACGTTGG
A4	21A - Amine	AAA AAA AAA AAA AAA AAA AAA /3AmMO/

8.4.6. DNA PAINT Background Intensity Plots

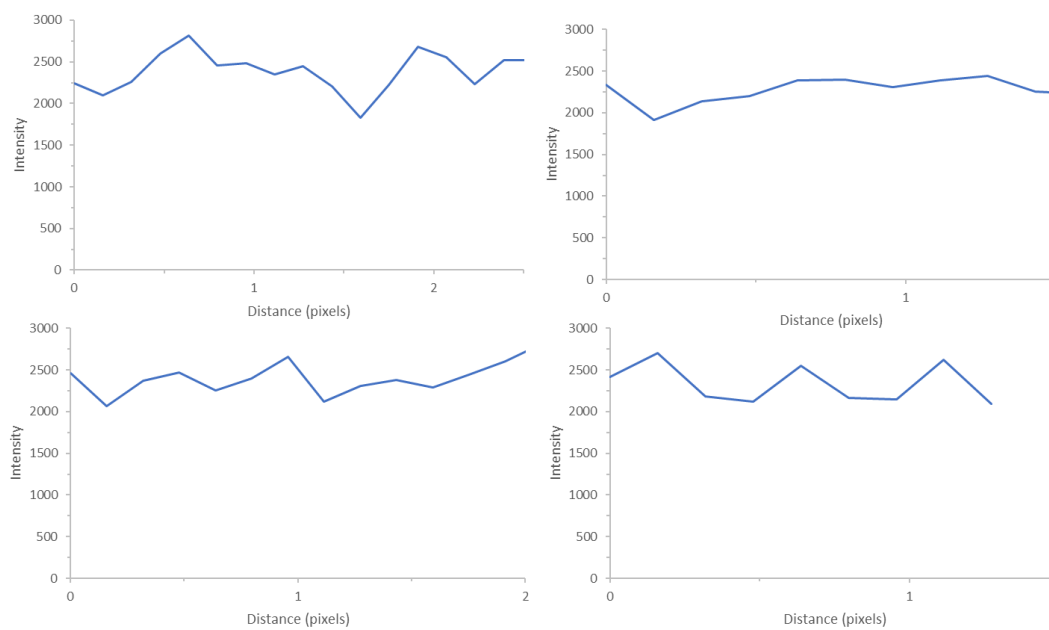


Figure 8.78: Intensity plots across set distances within negative control samples (20 nM, 75 mM MgCl₂, imaging buffer) to measure the intensity of the background (noise). Various sections across 8000 frames were analysed.

8.5. Naphthalimide Oligo Probe Mass Spectra

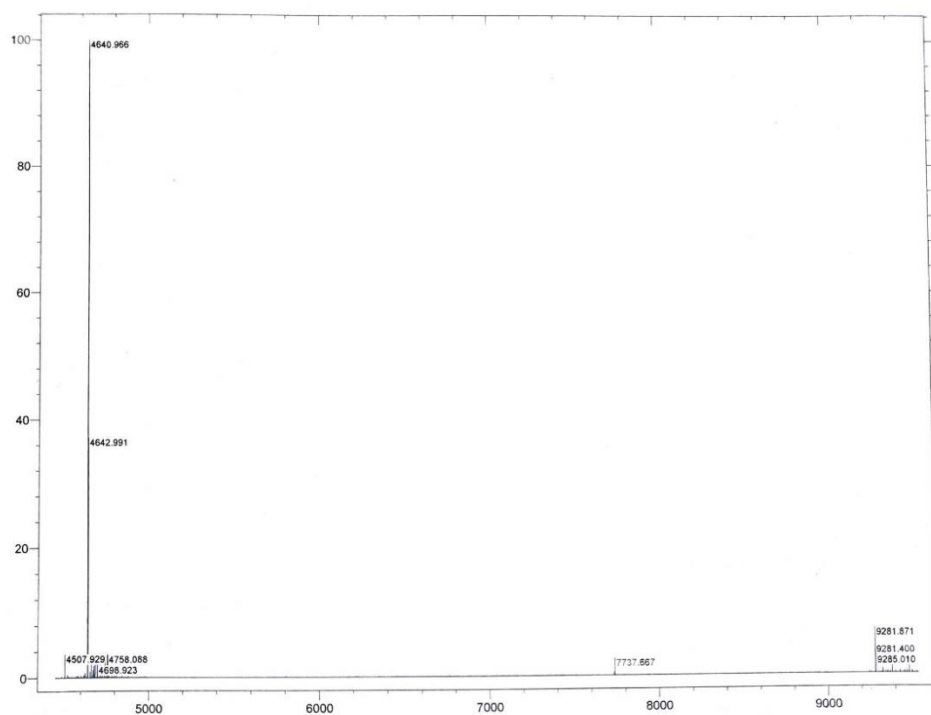


Figure 8.79: Mass spectrum of P1AL.

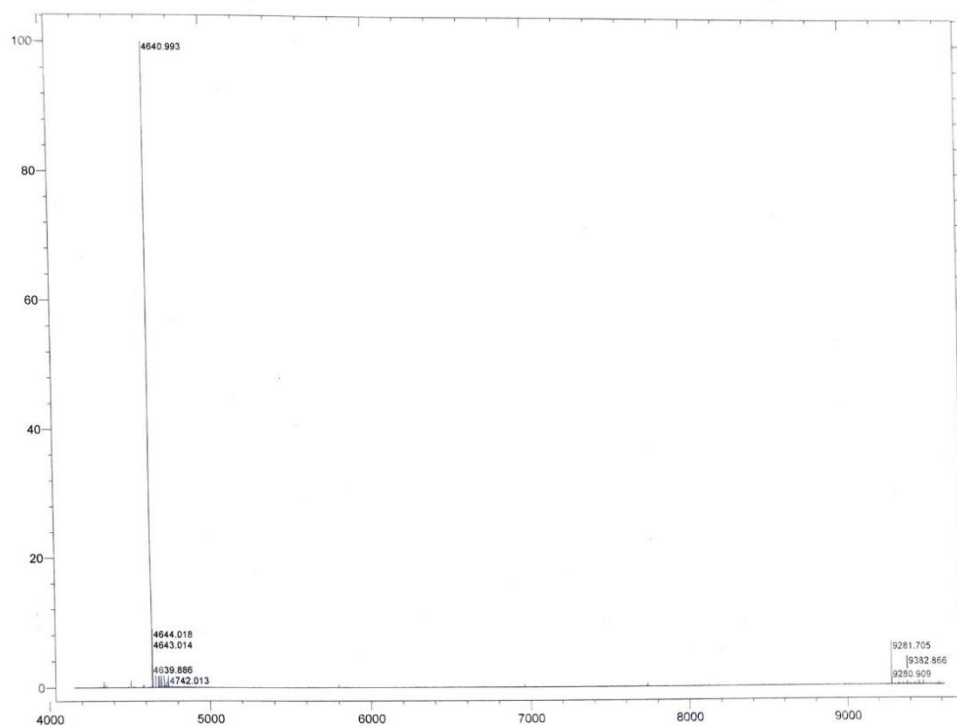


Figure 8.80: Mass spectrum of P1AD.

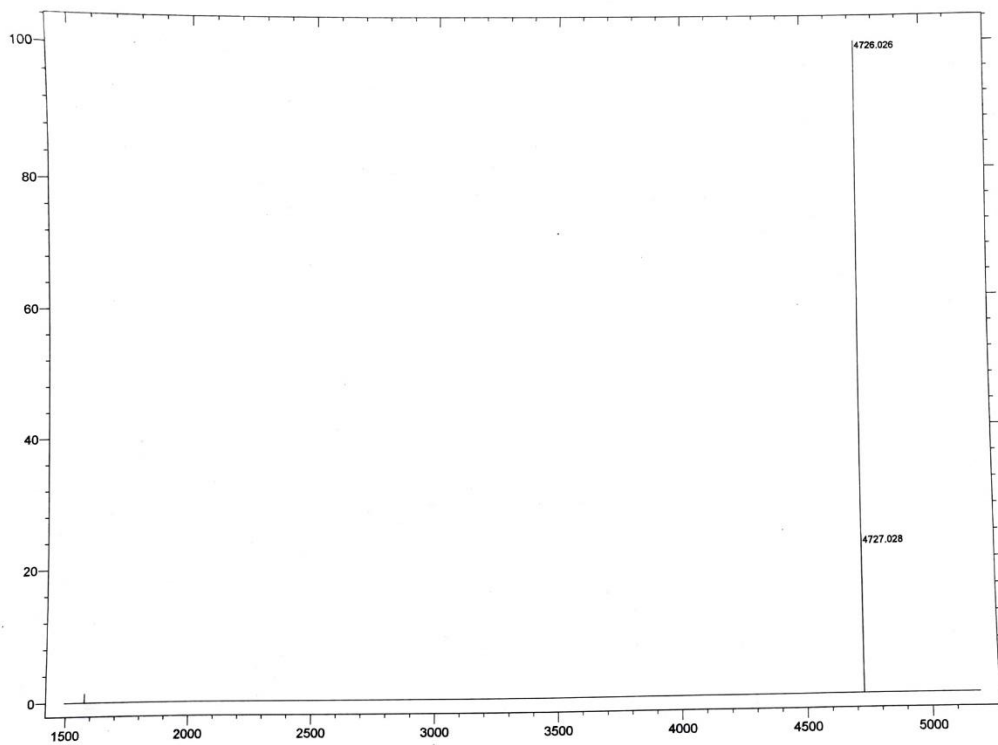


Figure 8.81: Mass spectrum of P1BD.

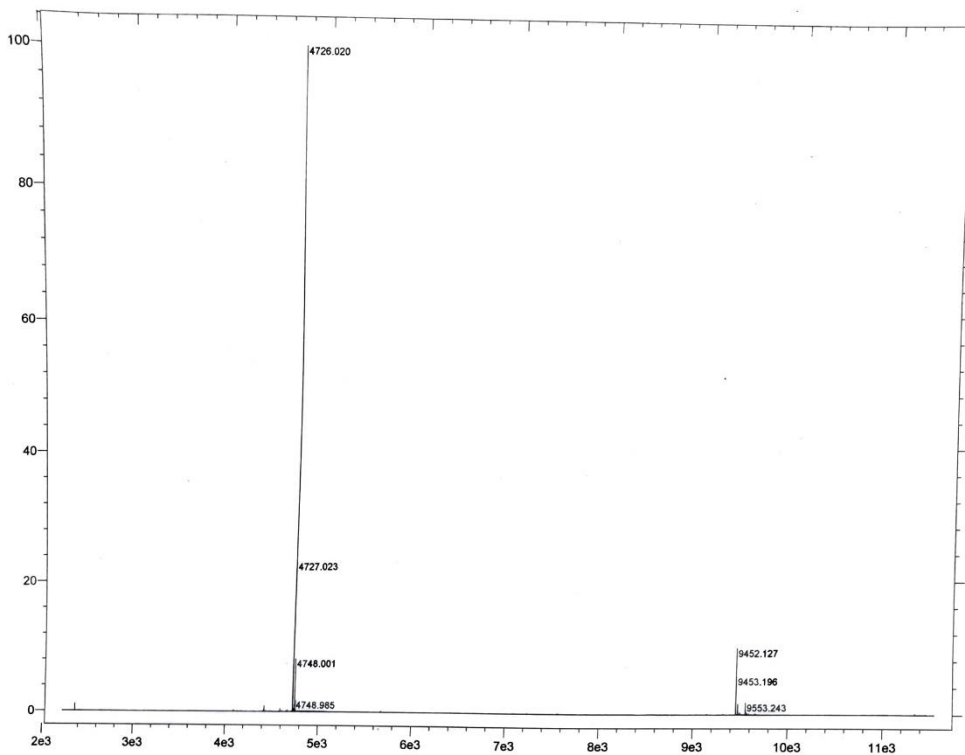


Figure 8.82: Mass spectrum of P1BL.

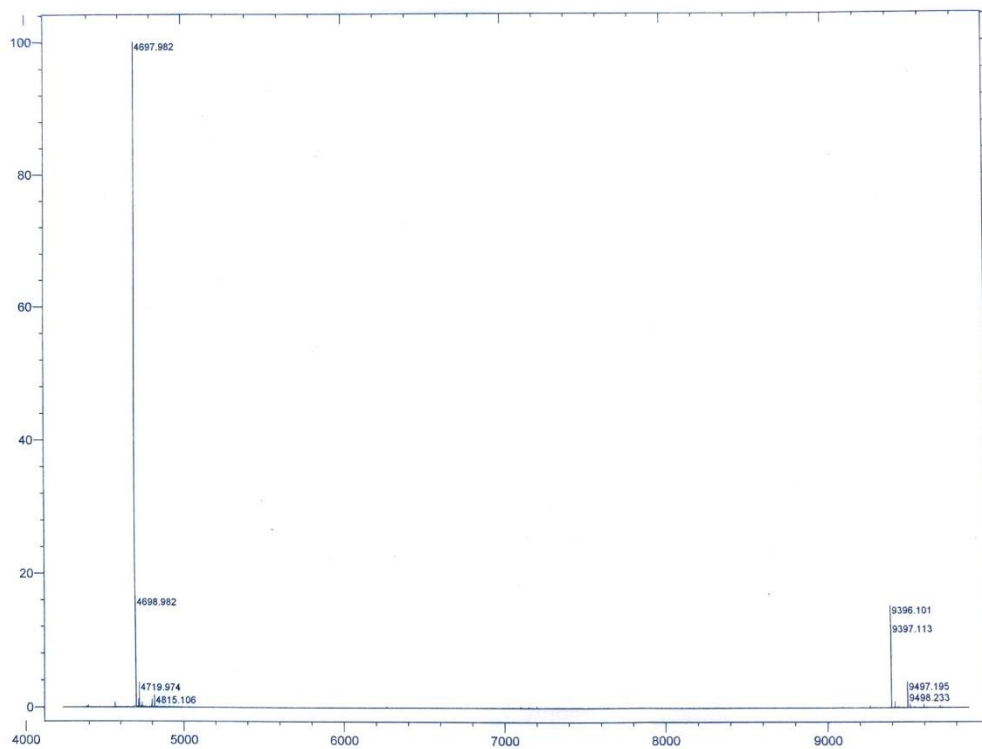


Figure 8.83: Mass spectrum of P1CD.

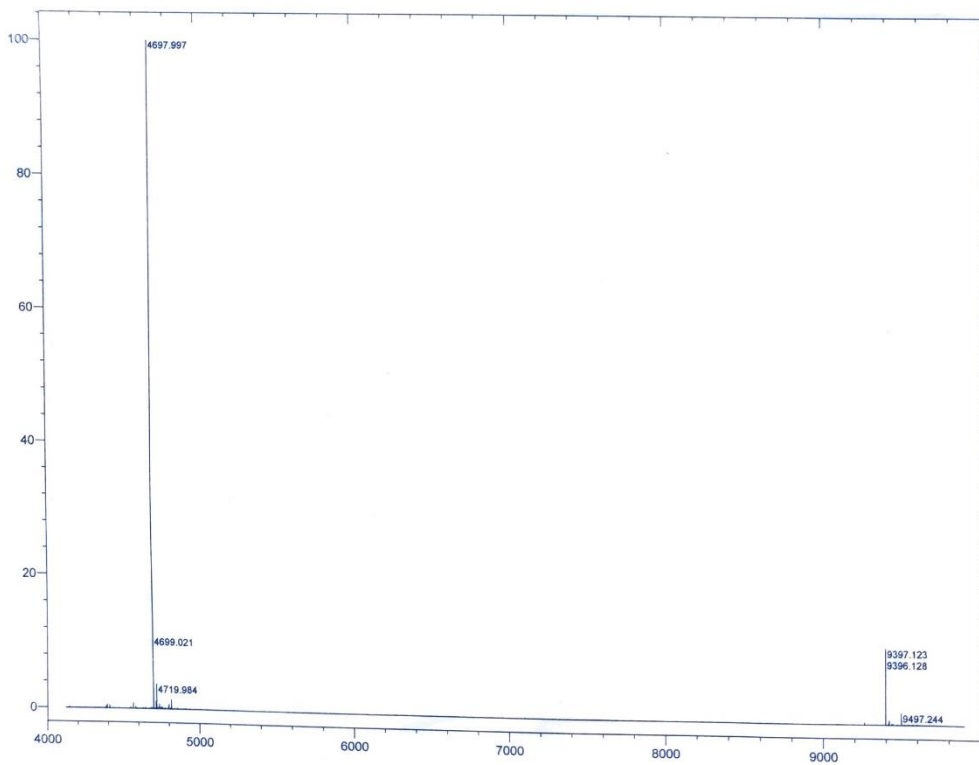


Figure 8.84: Mass spectrum of P1CL.

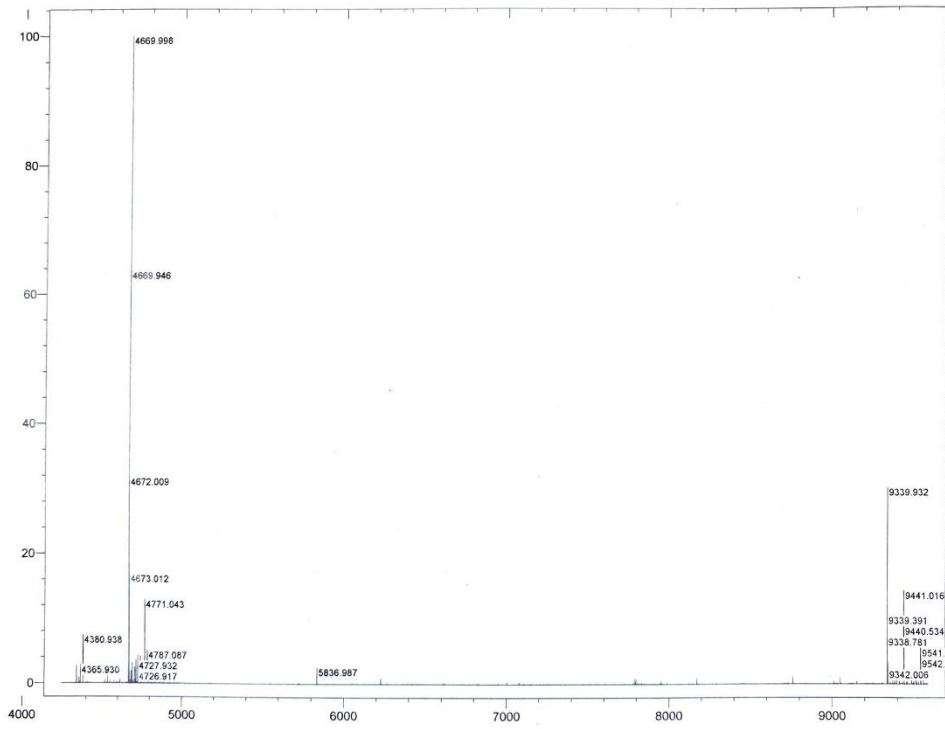


Figure 8.85: Mass spectrum of P1DD.

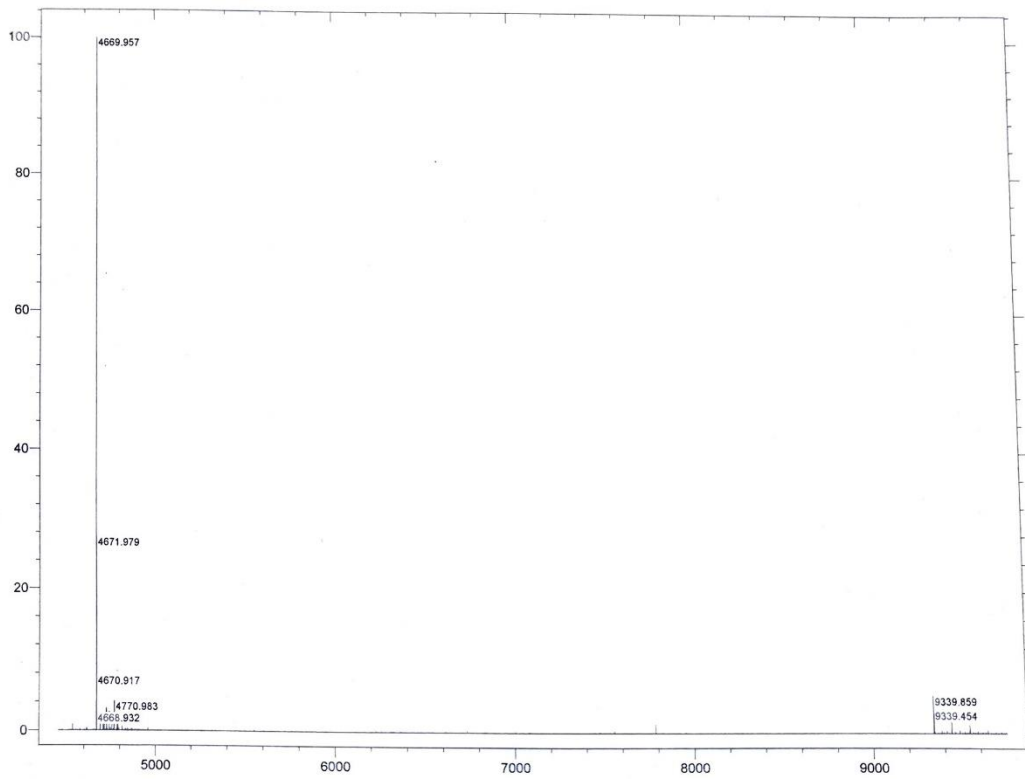


Figure 8.86: Mass spectrum of P1DL.

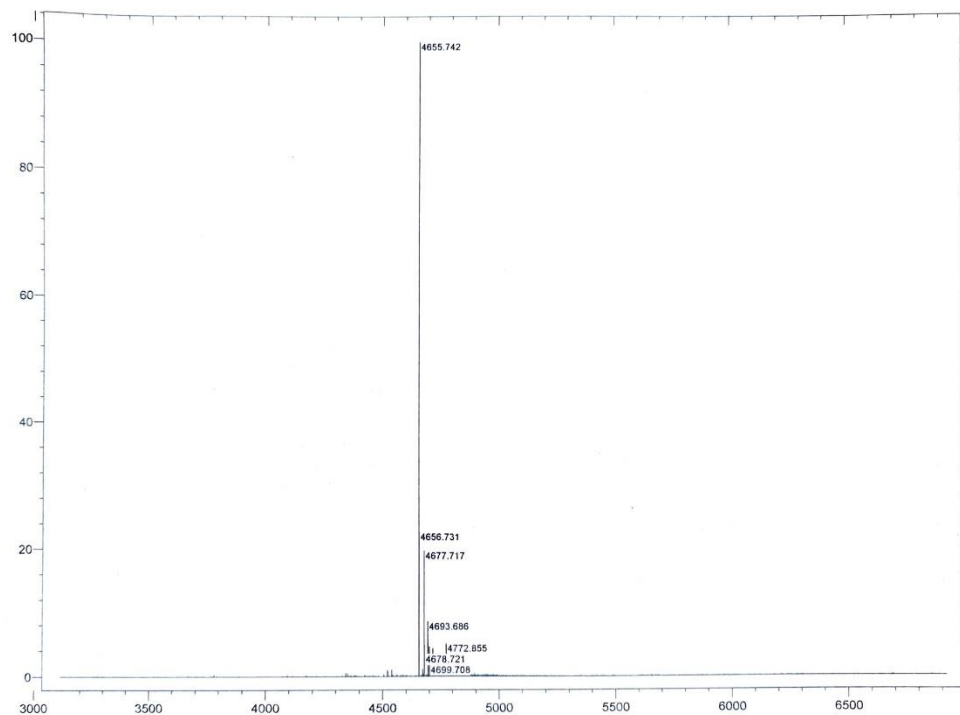


Figure 8.87: Mass spectrum of P2AD.

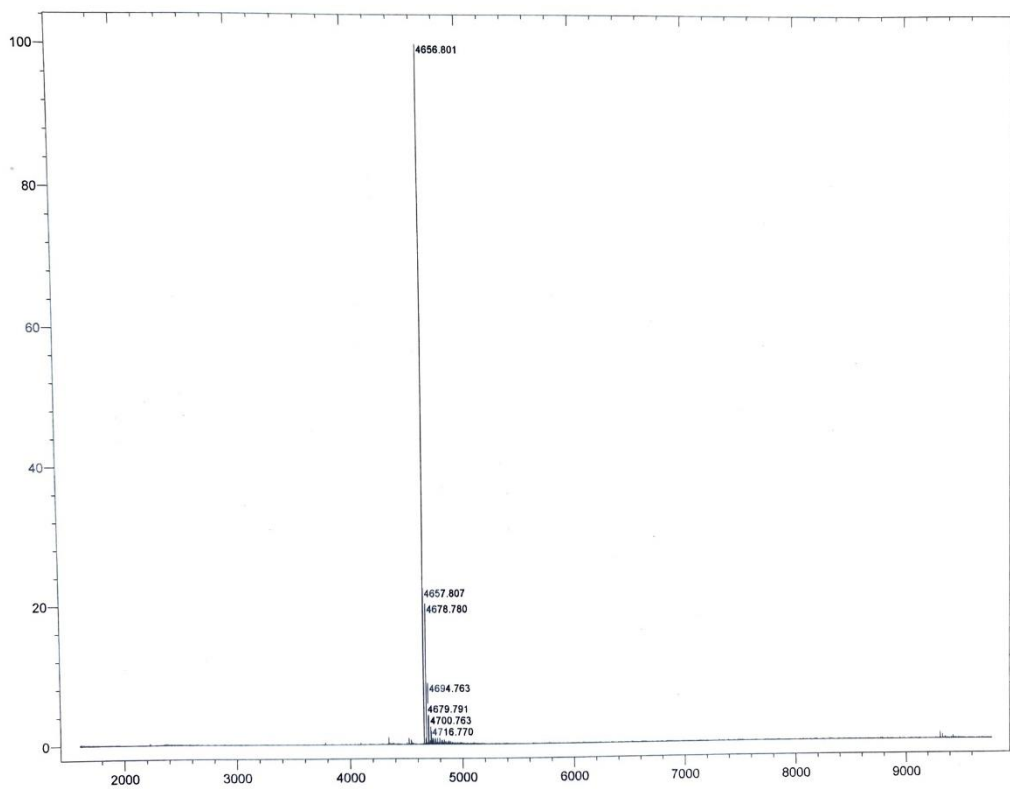


Figure 8.88: Mass spectrum of P2AL.

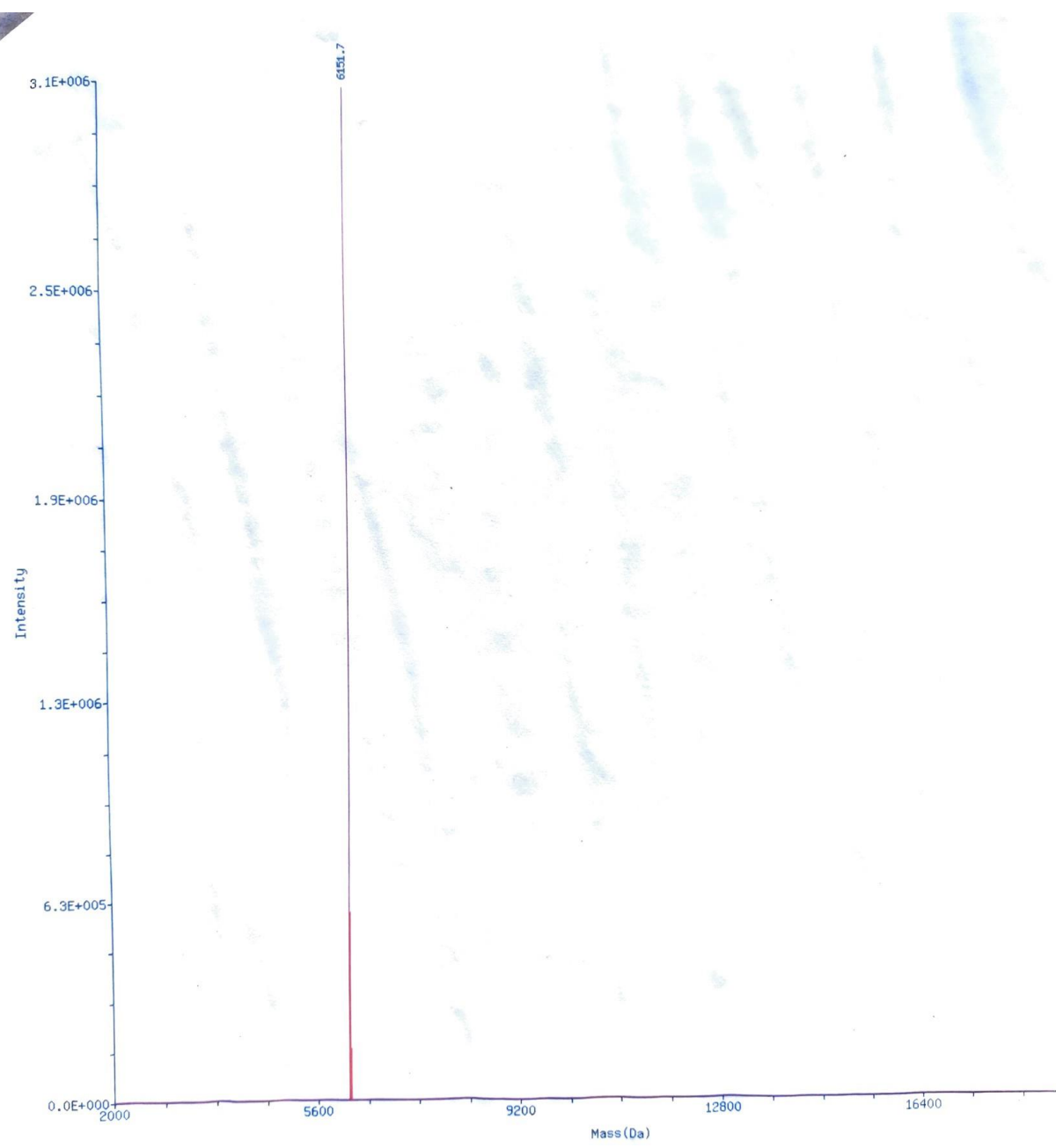


Figure 8.89: Mass spectrum of 17CEN Naph^A_{Short} probe.

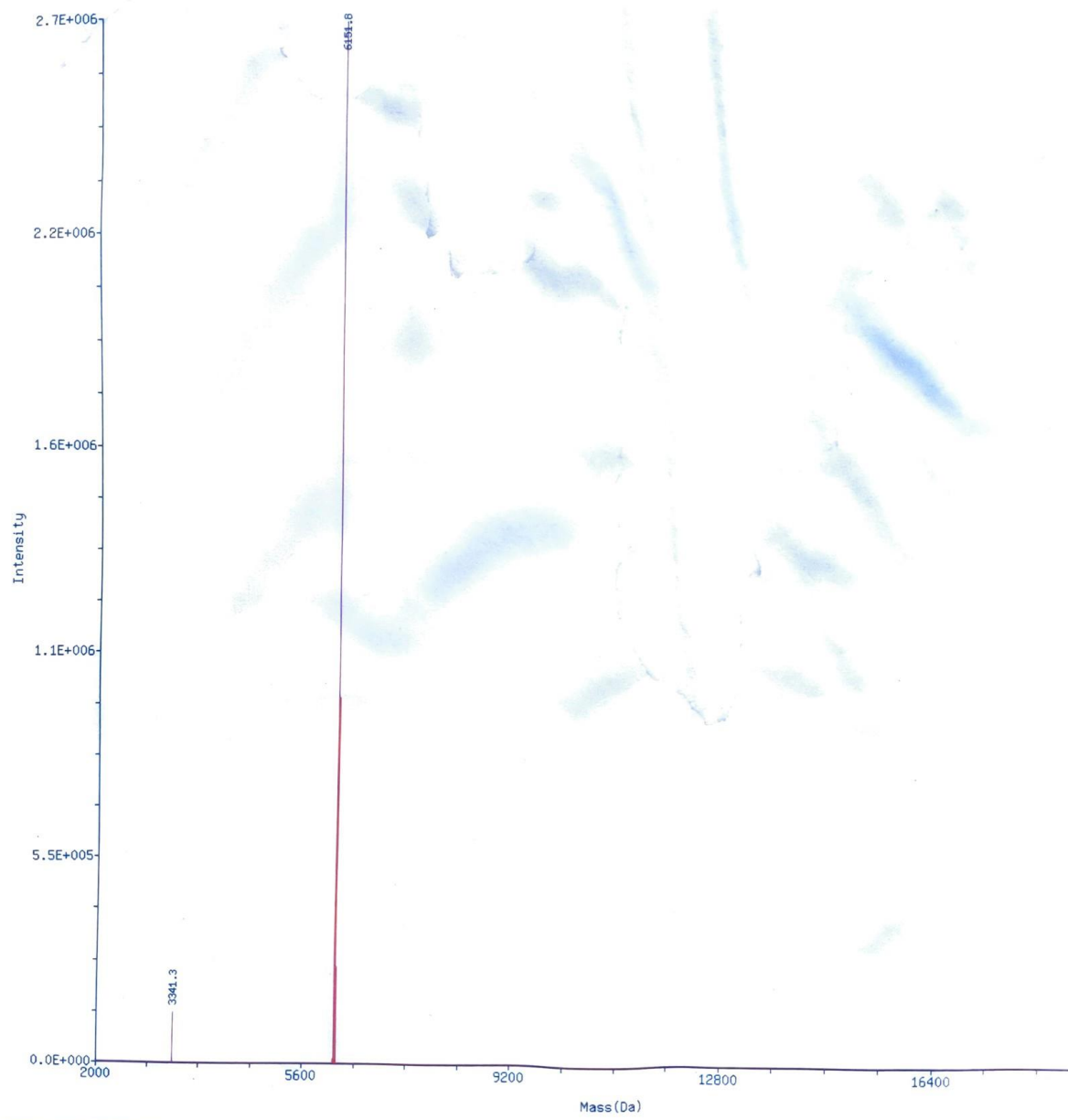


Figure 8.90: Mass spectrum of 17CEN D Naph^A_{Short} probe.

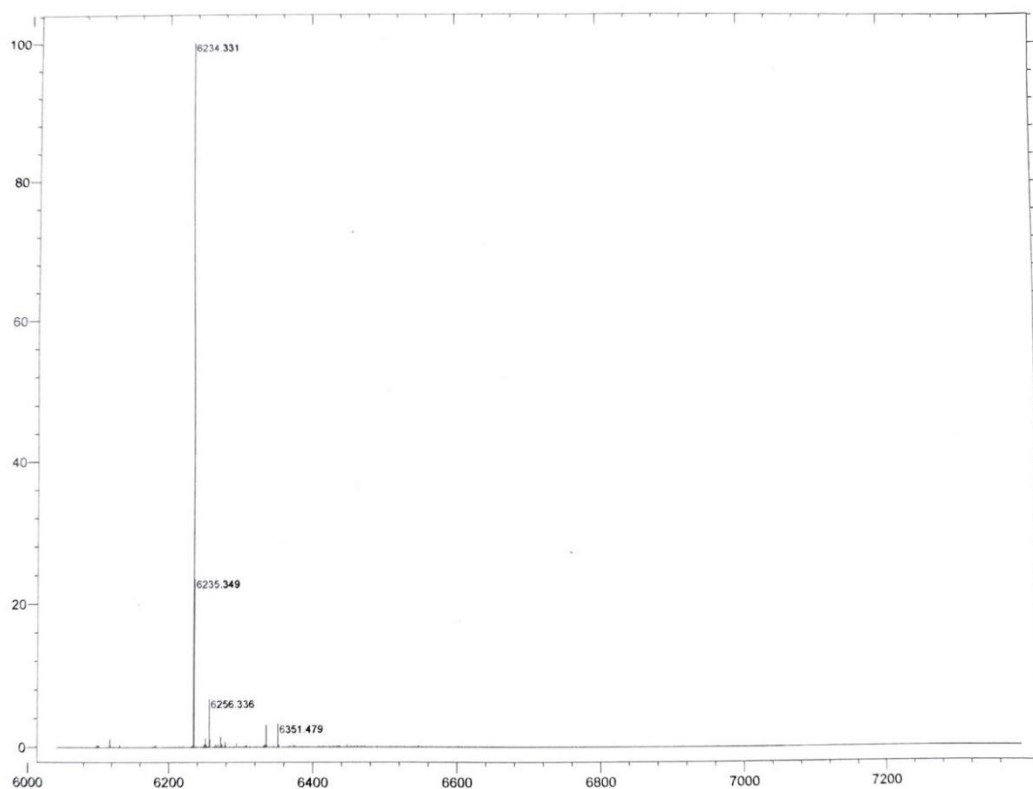


Figure 8.91: Mass spectrum of 17CEN L Naph^A_{LoNg} probe.

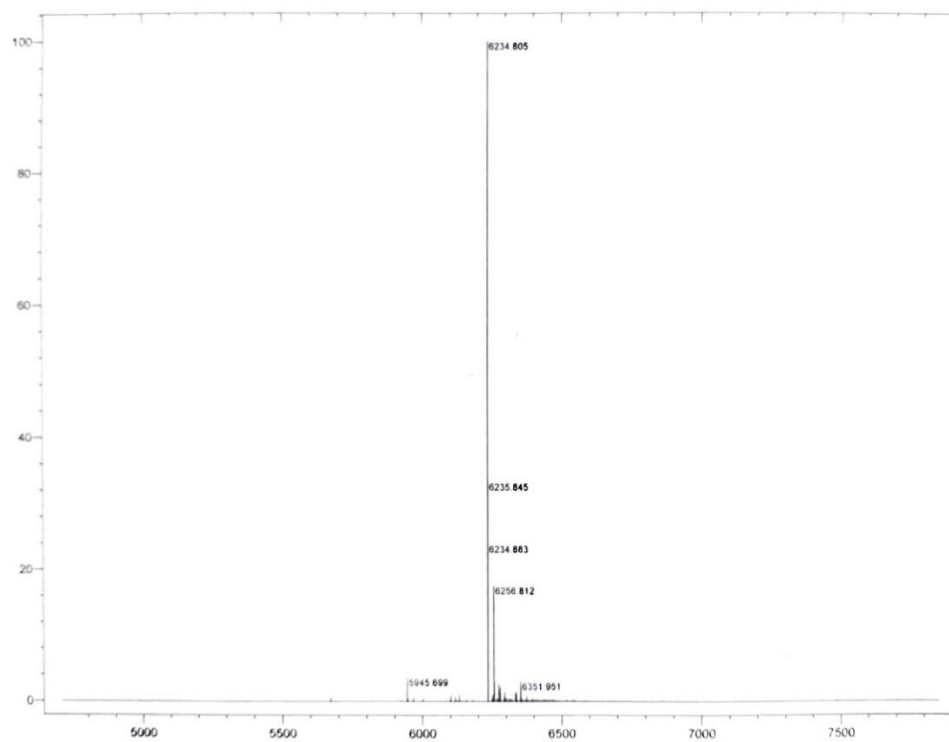


Figure 8.92: Mass spectrum of 17CEN D Naph^A_{LoNg} probe.

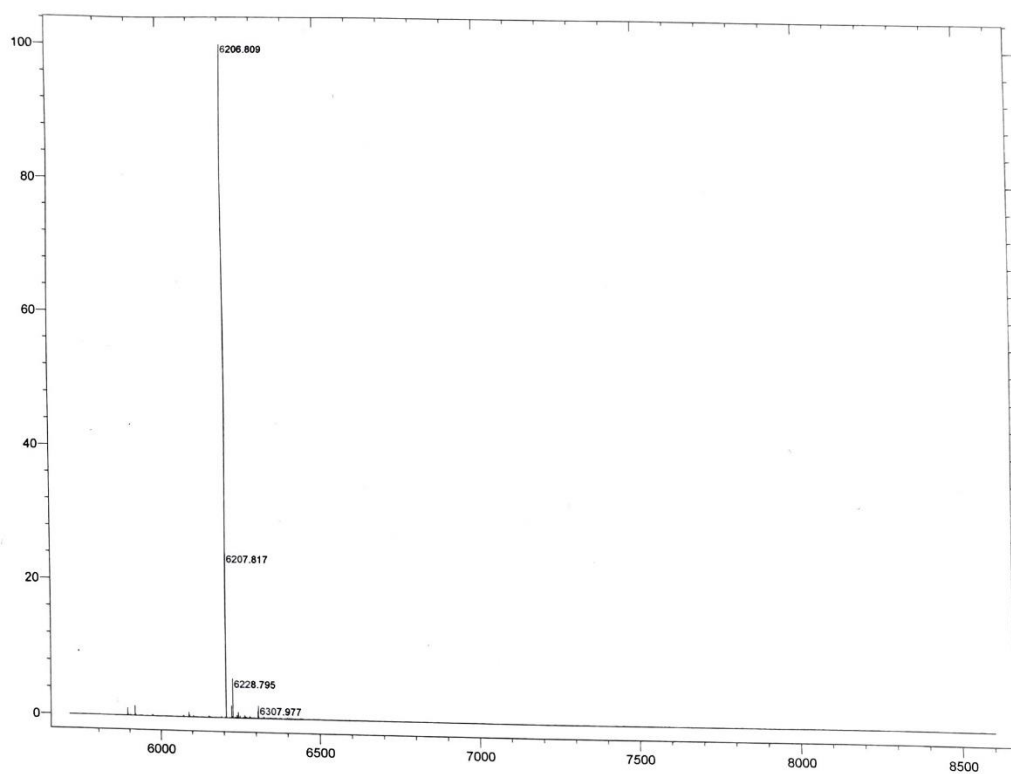


Figure 8.93: Mass spectrum of 17CEN L Naph¹Dimethyl probe.

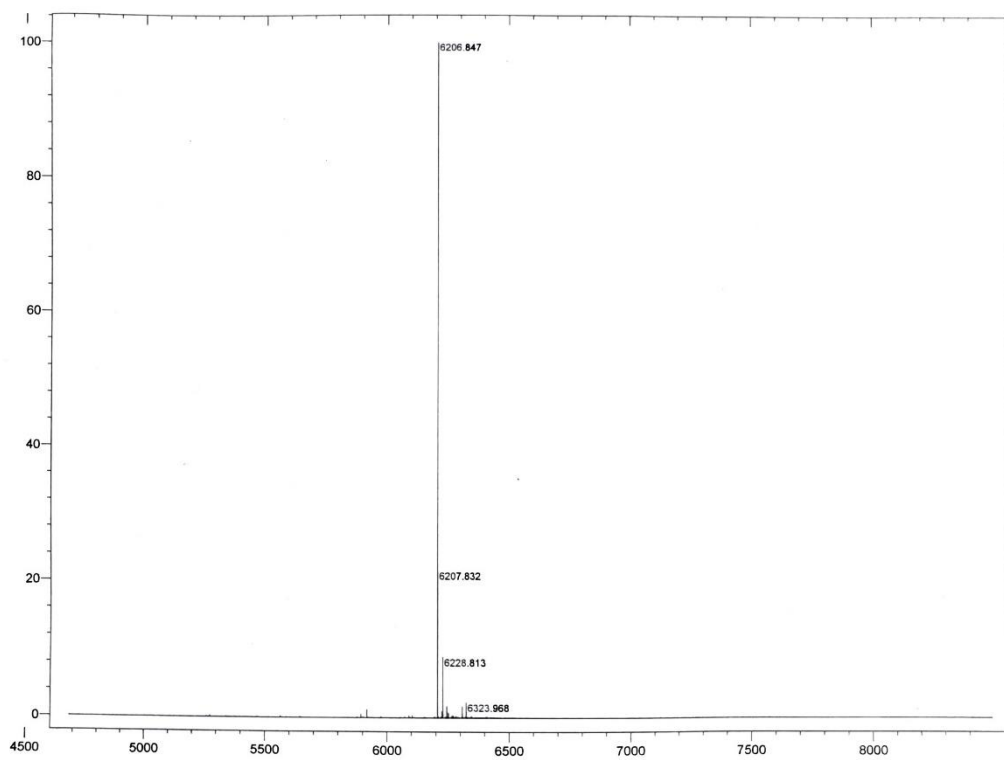


Figure 8.94: Mass spectrum of 17CEN D Naph¹Dimethyl probe.

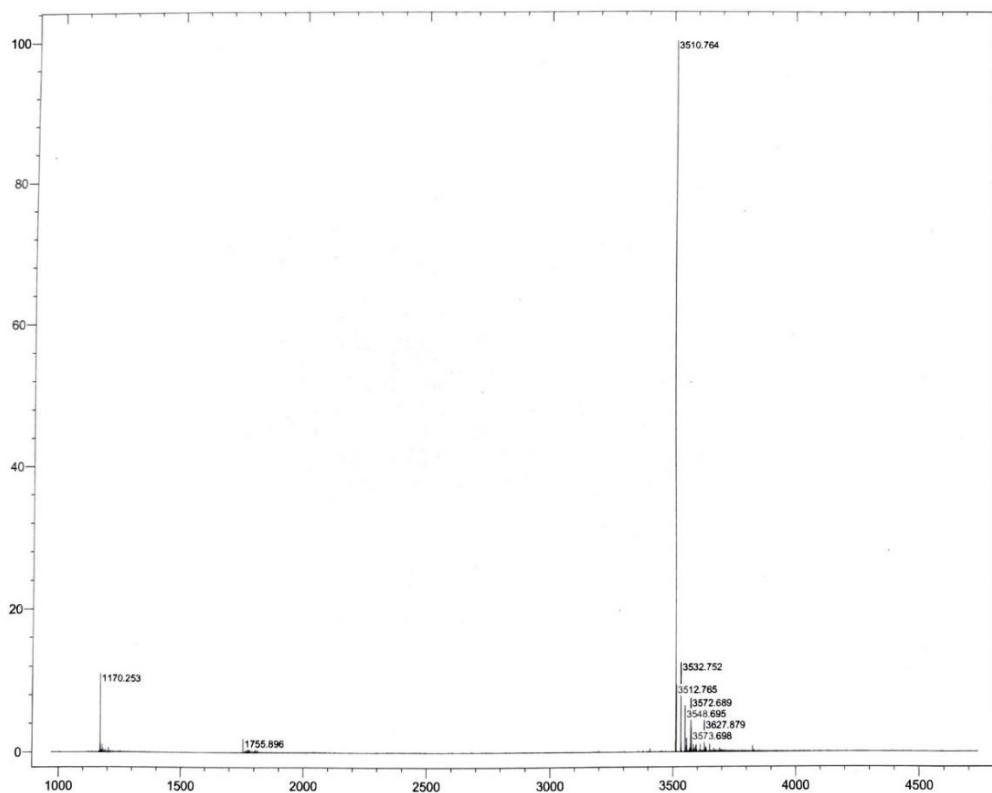


Figure 8.95: Mass spectrum of Naph -11 imager strand.

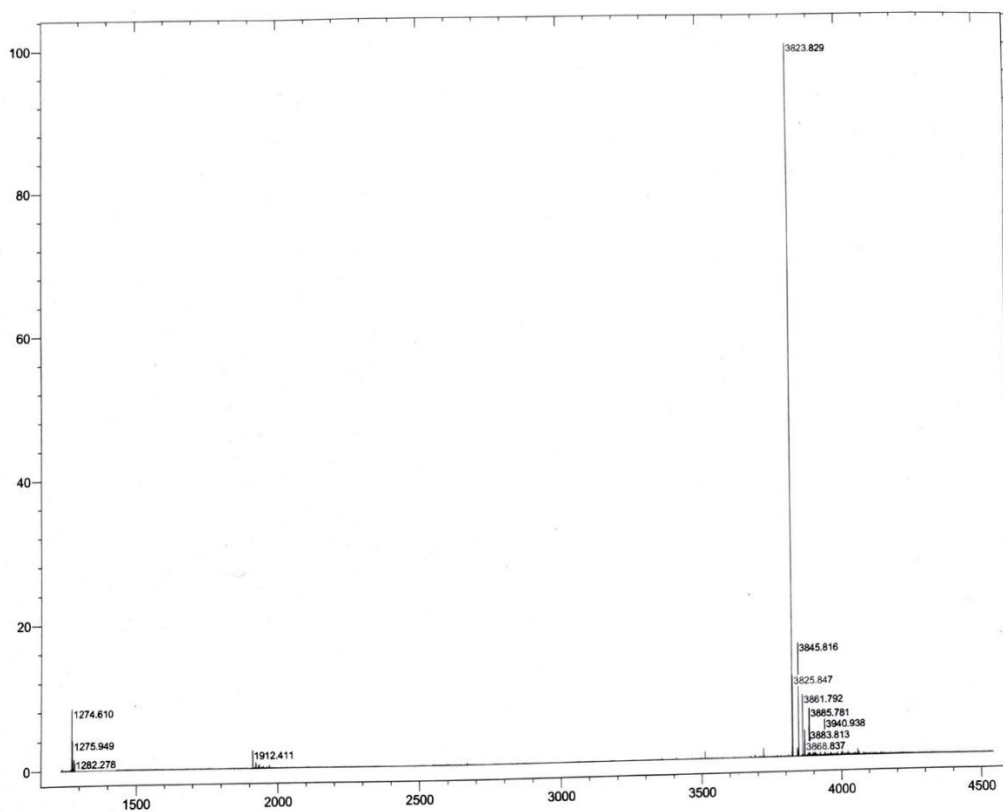


Figure 8.96: Mass spectrum of Naph -12 imager strand.

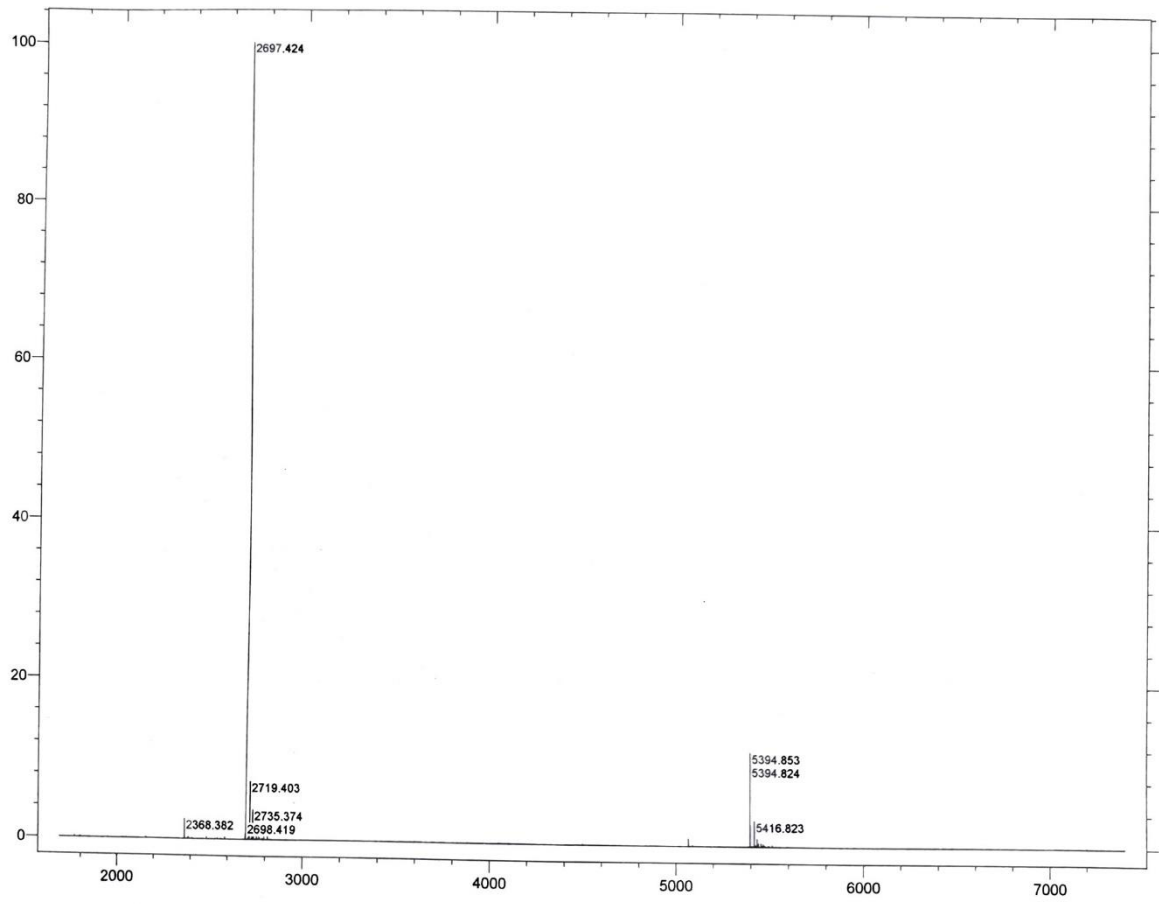


Figure 8.97: Mass spectrum of Naph DNA PAINT Im test strand.